Progress in Theoretical Chemistry and Physics A 25
Series Editors: J. Maruani · S. Wilson

Anders Lund
Masaru Shiotani *Editors*

EPR of Free Radicals in Solids II

Trends in Methods and Applications

2nd Edition

Springer

EPR of Free Radicals in Solids II

Progress in Theoretical Chemistry and Physics

VOLUME 25

For further volumes:
http://www.springer.com/series/6464

EPR of Free Radicals in Solids II

Trends in Methods and Applications

Second Edition

Edited by

ANDERS LUND
University of Linköping, Sweden

MASARU SHIOTANI
University of Hiroshima, Japan

Springer

Editors
Anders Lund
Department of Physics, Chemistry and Biology
Linköping University
Linköping
Sweden

Masaru Shiotani
Graduate School of Engineering
Hiroshima University
Higashi-Hiroshima
Japan

ISSN 1567-7354
ISBN 978-94-007-4886-6 ISBN 978-94-007-4887-3 (eBook)
DOI 10.1007/978-94-007-4887-3
Springer Dordrecht Heidelberg New York London

Library of Congress Control Number: 2012951322

Printed on acid-free paper

Springer is part of Springer Science+Business Media (www.springer.com)

PTCP Aim and Scope

Progress in Theoretical Chemistry and Physics

A series reporting advances in theoretical molecular and material sciences, including theoretical, mathematical and computational chemistry, physical chemistry and chemical physics and biophysics.

Aim and Scope

Science progresses by a symbiotic interaction between theory and experiment: theory is used to interpret experimental results and may suggest new experiments; experiment helps to test theoretical predictions and may lead to improved theories. Theoretical Chemistry (including Physical Chemistry and Chemical Physics) provides the conceptual and technical background and apparatus for the rationalisation of phenomena in the chemical sciences. It is, therefore, a wide ranging subject, reflecting the diversity of molecular and related species and processes arising in chemical systems. The book series *Progress in Theoretical Chemistry and Physics* aims to report advances in methods and applications in this extended domain. It will comprise monographs as well as collections of papers on particular themes, which may arise from proceedings of symposia or invited papers on specific topics as well as from initiatives from authors or translations.

The basic theories of physics – classical mechanics and electromagnetism, relativity theory, quantum mechanics, statistical mechanics, quantum electrodynamics – support the theoretical apparatus which is used in molecular sciences. Quantum mechanics plays a particular role in theoretical chemistry, providing the basis for the valence theories, which allow to interpret the structure of molecules, and for the spectroscopic models employed in the determination of structural information from spectral patterns. Indeed, Quantum Chemistry often appears synonymous with Theoretical Chemistry: it will, therefore, constitute a major part of this book series. However, the scope of the series will also include other areas of theoretical

chemistry, such as mathematical chemistry (which involves the use of algebra and topology in the analysis of molecular structures and reactions); molecular mechanics, molecular dynamics and chemical thermodynamics, which play an important role in rationalizing the geometric and electronic structures of molecular assemblies and polymers, clusters and crystals; surface, interface, solvent and solidstale effects; excited-state dynamics, reactive collisions, and chemical reactions.

Recent decades have seen the emergence of a novel approach to scientific research, based on the exploitation of fast electronic digital computers. Computation provides amethod of investigationwhich transcends the traditional division between theory and experiment. Computer-assisted simulation and design may afford a solution to complex problems which would otherwise be intractable to theoretical analysis, and may also provide a viable alternative to difficult or costly laboratory experiments. Though stemming from Theoretical Chemistry, Computational Chemistry is a field of research in its own right, which can help to test theoretical predictions and may also suggest improved theories.

The field of theoretical molecular sciences ranges from fundamental physical questions relevant to the molecular concept, through the statics and dynamics of isolated molecules, aggregates and materials, molecular properties and interactions, and to the role of molecules in the biological sciences. Therefore, it involves the physical basis for geometric and electronic structure, states of aggregation, physical and chemical transformations, thermodynamic and kinetic properties, as well as unusual properties such as extreme flexibility or strong relativistic or quantum-field effects, extreme conditions such as intense radiation fields or interaction with the continuum, and the specificity of biochemical reactions.

Theoretical Chemistry has an applied branch – a part of molecular engineering, which involves the investigation of structure-property relationships aiming at the design, synthesis and application of molecules and materials endowed with specific functions, now in demand in such areas as molecular electronics, drug design and genetic engineering. Relevant properties include conductivity (normal, semi- and supra-), magnetism (ferro- and ferri-), optoelectronic effects (involving nonlinear response), photochromism and photoreactivity, radiation and thermal resistance, molecular recognition and information processing, biological and pharmaceutical activities, as well as properties favouring self-assembling mechanisms and combination properties needed in multifunctional systems.

Progress in Theoretical Chemistry and Physics is made at different rates in these various research fields. The aim of this book series is to provide timely and in-depth coverage of selected topics and broad-ranging yet detailed analysis of contemporary theories and their applications. The series will be of primary interest to those whose research is directly concerned with the development and application of theoretical approaches in the chemical sciences. It will provide up-to-date reports on theoretical methods for the chemist, thermodynamician or spectroscopist, the atomic, molecular or cluster physicist, and the biochemist or molecular biologist who wish to employ techniques developed in theoretical, mathematical and computational chemistry in their research programmes. It is also intended to provide the graduate student with a readily accessible documentation on various branches of theoretical chemistry, physical chemistry and chemical physics.

Preface

During the last ten years, significant progress has been made in the study of free radical processes in solids by applying modern EPR (ESR) methods. The progress has been possible by instrumental advancements in continuous wave (CW) and pulse EPR, by development of sensitive detection methods, by the application of sophisticated matrix isolation techniques and by the advancement in quantitative EPR, to mention a few recent experimental trends. On the theoretical side, methods based on first principles have been developed and applied for the calculation of hyperfine couplings, zero-field splittings and g-factors as well as in spectral simulations. Software for these purposes, developed during the last decade, is also available. Not all of those developments can be treated in detail in a single volume. We have therefore asked several main contributors to the development of the field to present chapters in selected areas, where recent reviews seem to be missing. In this respect, the book is an update of a previous edition of this work, with a similar organization of the content.

The first volume is concerned with trends in experimental and theoretical methods. In the first chapter, CW EPR and ENDOR methods for studies of radical structure in single crystals and powders are reviewed. Most of the following seven chapters give accounts of novel developments that so far are only available in the journal literature. The chapter by Brustolon and Barbon describes the different pulsed techniques as applied to radicals and spin probes in solid matrices. Methods to extract dynamical parameters from CW and pulsed EPR are summarised in the chapter by Benetis and Dmitriev, which also contains an account of relaxation phenomena. New simulation schemes, including the influence of dynamics, are also presented. Single crystal measurement is the most straightforward but not always applicable method for complex systems, where often only powder spectra can be obtained. For these systems, analyses by simulation techniques based on exact diagonalisation are beginning to replace the previously used perturbation methods, as described in the chapter by Hanson and coworkers. An extended version of the software presented in the previous edition is outlined, including now also procedures for the analysis of pulse EPR and several other new features. The software is marketed by Bruker. Studies of quantum effects in isotopically labelled methyl

radicals trapped in inert matrices at low temperature is a major part of the chapter by Shiotani and Komaguchi. A detailed theoretical analysis was possible due to the extremely high resolution of the EPR spectra at low temperature. The chapter by Boyd and coworkers illustrates the usefulness of advanced quantum chemistry methods for the theoretical interpretation of hyperfine coupling tensors. Ab initio and density functional methods are applicable even for the biological systems. The calculated parameters have been frequently employed for the assignment of experimental spectra in recent work. The methods for the calculation of *g*-tensors have been developed even more during the last ten years as described in the chapter by Kaupp. The accurate *g*-tensor data obtained by high-field EPR measurements can for instance now be analyzed taking into account environmental interactions with the radical. A new chapter on the calculation of the zero-field splitting tensors was introduced in this edition. The subject is of relevance for high-spin clusters and molecules treated in two chapters in the second volume. The theory is also applicable in EPR studies of systems containing pairs of radicals.

The second volume presents applications involving studies of radiation and photo-induced inorganic and organic radicals in inert matrices. High-spin molecules and complexes are also considered as well as radical processes in photosynthesis. Recent advancements in environmental applications including EPR dosimetry are summarised. There are trends both towards simplification by using matrix isolation in frozen noble gas matrices with accompanying increase of resolution as illustrated in the chapter by Kunttu and Eloranta and in the work by Shiotani and Komaguchi in the first volume, and towards studies of complex systems treated in the chapters by Takui et al., by Baumgarten, Kawamori and by Feldman. In the former case, an overview of the matrix isolation technique for the studies of atoms and small radicals embedded in solid rare gases is presented, while Feldman presents recent development in the EPR studies of reactive intermediates from irradiation of moderately large organic molecules using matrix isolation. Two chapters address the issue of high-spin systems, the one by Baumgarten in organic systems, the other by Takui et al. also in metal-based molecular clusters. Both subjects have relevance for the development of molecular magnets. The potential application of EPR for quantum computing is also considered in a newly written chapter, with emphasis on pulse ENDOR methods. The chapter by Kawamori describes studies of plant photosystem II by pulsed EPR, dual mode CW EPR and pulsed electron-electron double resonance, the latter to obtain distances between radical pairs trapped after illumination. Accurate measurement of the concentration of radicals is an important issue in EPR dosimetry and other kinds of quantitative EPR, which is addressed in the chapter by Yordanov et al. This subject relates to other applications of EPR in the environmental sciences, discussed in a chapter by Rhodes. In this context, myon spin resonance provides new means to considerably lower the detection limit in heterogeneous systems. In the final chapter, recent developments of optical detection to lower the detection limit and to obtain time-resolution in the characterisation of defect centres in semiconductor materials are presented by Chen.

The titles of the chapters have been retained from the old edition, with one exception. The content of each chapter in the new edition differs in general from that

in the old by the addition of new results and deletion of older material, however. The size has nevertheless increased, in part also due to the inclusion of two new chapters. Some technical problems with the printing of figures, figure legends and the index of the previous work have been corrected. The chapters of the first edition were frequently referred to as additional reading in a work we recently prepared for a broader audience [Anders Lund, Masaru Shiotani, Shigetaka Shimada: 'Principles and Applications of ESR Spectroscopy', Springer (2011)]. We hope that the new edition will be of value for this purpose as well as for future research involving free radicals.

May 2012

Anders Lund
Masaru Shiotani

Contents

Contributors

Martin Baumgarten Max Planck Institute for Polymer Research, Mainz, Germany

Weimin M. Chen Department of Physics, Chemistry and Biology, Linköping University, Linköping, Sweden

Jussi Eloranta Department of Chemistry and Biochemistry, California State University at Northridge, Northridge, CA, USA

Vladimir I. Feldman Department of Chemistry, M.V. Lomonosov Moscow State University, Moscow, Russia

Kou Furukawa Department of Chemistry and Molecular Materials Science, Graduate School of Science, Osaka City University, Osaka, Japan

Veselka Gancheva National Center of EPR Spectroscopy, Institute of Catalysis, Bulgarian Academy of Sciences, Sofia, Bulgaria

Yordanka Karakirova National Center of EPR Spectroscopy, Institute of Catalysis, Bulgarian Academy of Sciences, Sofia, Bulgaria

Asako Kawamori AGAPE Kabutoyama Institute of Medicine, Nishinomiya, Japan

Masahiro Kitagawa Department of System Innovation, Graduate School of Engineering Science, Osaka University, Toyonaka, Japan

Henrik Kunttu Department of Chemistry, University of Jyväskylä, Jyväskylä, Finland

Hideto Matsuoka Department of Chemistry and Molecular Materials Science, Graduate School of Science, Osaka City University, Osaka, Japan

Yasushi Morita Department of Chemistry, Graduate School of Science, Osaka University, Toyonaka, Japan

Shigeaki Nakazawa Department of Chemistry and Molecular Materials Science, Graduate School of Science, Osaka City University, Osaka, Japan

Shinsuke Nishida Department of Chemistry and Molecular Materials Science, Graduate School of Science, Osaka City University, Osaka, Japan

Robabeh D. Rahimi Department of Chemistry and Molecular Materials Science, Graduate School of Science, Osaka City University, Osaka, Japan

Christopher J. Rhodes Fresh-lands Environmental Actions, Caversham, Berkshire, UK

Kazunobu Sato Department of Chemistry and Molecular Materials Science, Graduate School of Science, Osaka City University, Osaka, Japan

Daisuke Shiomi Department of Chemistry and Molecular Materials Science, Graduate School of Science, Osaka City University, Osaka, Japan

Takeji Takui Department of Chemistry and Molecular Materials Science, Graduate School of Science, Osaka City University, Osaka, Japan

Kazuo Toyota Department of Chemistry and Molecular Materials Science, Graduate School of Science, Osaka City University, Osaka, Japan

Nicola D. Yordanov National Center of EPR Spectroscopy, Institute of Catalysis, Bulgarian Academy of Sciences, Sofia, Bulgaria

Tomohiro Yoshino Department of Chemistry and Molecular Materials Science, Graduate School of Science, Osaka City University, Osaka, Japan

Chapter 1
EPR Studies of Atomic Impurities in Rare Gas Matrices

Henrik Kunttu and Jussi Eloranta

Abstract In this article we give an overview of the matrix isolation technique combined with electron paramagnetic resonance (EPR) detection for embedded atomic impurities in solid rare gases. A special emphasis is put on impurity – matrix coupling effects combining both experimental and theoretical approaches.

1.1 Introduction

Chemical dynamics in condensed phases forms a rapidly evolving field of research dealing with a wide range of phenomena from simple point defect diffusion to the broad field of chemical reaction dynamics. In the strict sense such dynamics in dense media is always dictated by interactions with strong many-body nature, thus detailed understanding of even the most elementary events at a molecular level remains a challenge. A convergence of quantitative modelling and interpretation of various processes is attained only by synergy between experiment and theory. Experimental methods at one's disposal range from optical absorption and emission based techniques to magnetic spectroscopies among which electron paramagnetic resonance (EPR) has a long tradition as a versatile tool for interrogation of open shell species [1]. Due to the rapidly increasing computational resources and development of new efficient algorithms, microscopic description of the observed spectroscopy, optical and magnetic, can now be pursued at the first-principles level in highly multi-dimensional models approaching the size and complexity of a realistic chemical system.

H. Kunttu (✉)
Department of Chemistry, University of Jyväskylä, P.O. Box 35, FIN-40351 Jyväskylä, Finland
e-mail: Henrik.M.Kunttu@jyu.fi

J. Eloranta
Department of Chemistry and Biochemistry, California State University, 18111 Nordhoff St., Northridge, CA 91330, USA
e-mail: Jussi.Eloranta@csun.edu

A. Lund and M. Shiotani (eds.), *EPR of Free Radicals in Solids II*, Progress in Theoretical Chemistry and Physics 25, DOI 10.1007/978-94-007-4887-3_1,

Rare gases (Rg) solidify in cryogenic conditions and form more or less ordered structures, namely, glassy crystalline or strongly light scattering powder like substances which are commonly called matrices. The inertness of the Group VIII elements against chemical reactivity is reflected in their other name, the noble gases. As such, they provide a versatile medium for studies of elementary physico-chemical processes. In particular, doping these solids with atomic or small molecular impurities, i.e. matrix isolation, is ideally suited for spectroscopic observations of highly reactive transient species in inert frozen environment. This was, in fact, the original goal of the matrix isolation technique [2]. Besides providing spectral reference data for investigations in related fields [3], such as atmospheric and combustion chemistry, understanding of trapping, transport, and reactivity in these conceptually simple solids has also more practical applications. Chemical energy storage in cryogenic solids by trapping reactive atoms, radicals or chemical intermediates, and controlling their subsequent recombination by annealing is an example of such developments [4]. Moreover, matrix isolation in solid hydrogen is actively used is research aiming at development of advanced propellants called "high energy density materials" [5, 6]. Besides their role in isolation, Rg matrices can be used as excellent media to investigate chemical species containing rare gas atoms [7, 8]. A new development in the field comes from the application of superfluid helium in condensing nanometer scale inert gas clusters to form a porous solid -like structure within the liquid ("impurity helium solid") [9–15]. Extremely high concentrations of hydrogen and nitrogen atoms (densities in the range of 10^{19}–10^{20} cm^{-3}) have been isolated in such structures, which are much higher than achieved earlier in traditional matrix isolation experiments [12, 13].

The information gathered from experiments in solids is subject to perpetual averaging processes of dynamical and structural origin. Therefore, as the spectroscopic methods become blunted in this respect, the need for theoretical aid in interpretation becomes evident. On the other hand, cryogenic solids provide an ideal testing ground for theoretical treatments. Either way around, the theoretical approaches encounter challenging obstacles due to the immense number of interacting species and degrees of freedom that need to be considered. This is why purely quantum mechanical approaches, that is, solving the time-dependent Schrödinger equation by some affordable way are rarely used in large-scale simulations and, instead, various approximations of semi-classical nature are usually employed [16].

EPR spectroscopy has proven to be a powerful experimental technique for elucidating details of the electronic structure of open shell molecules and ions in crystals and solutions. Because EPR transitions (1) are dominated by the properties of the electronic ground state, (2) exhibit very narrow line widths in dilute samples, and (3) are very sensitive to small changes in the environment of the paramagnetic species under investigation, this method seems conceptually ideally suited for studies of atomic trapping and dynamics in low temperature matrices. However, detection of atoms with orbitally degenerate ground states has turned out to be difficult, and most of the available EPR data on atoms or ions in Rg matrices have concerned cases with isotropic g values and hyperfine interaction [1]. Even for these spherical atoms theoretical treatment of the isotropic hyperfine coupling

(IHC) is a relatively problematic task for modern ab initio electronic structure methods. The challenge here is the local nature of the spin density, and the isotropic component of the hyperfine interaction, which may also be composed of indirect effects such as spin polarization and electron correlation [17–19]. A proper theoretical approach would therefore necessitate a high quality basis set combined with a substantial effort in treatment of electron correlation. Since a typical matrix shift for the IHC of an atom is some tens of MHz, the accuracy needed for such computation is exceedingly high. Consequently, a combined quantum-classical approach with an assumption of pair additive hyperfine coupling is by far the only choice for computation of magnetic properties of atoms trapped in matrix environments [20–22].

In this review we briefly summarize some of the previous EPR spectroscopic observations of atomic impurities isolated in rare gas matrices and impurity helium solids as well as introduce the theoretical tools applicable for analysis of the obtained spectra.

1.2 Experimental Techniques

In this section we consider some of the special experimental aspects related to matrix EPR measurements. A detailed overview of the experimental techniques can be found from the existing literature [1, 23, 24]. For impurity helium solids, the early work of Gordon et al. and the recent work of Lee et al. and Kunttu et al. describes the relevant experimental techniques [9, 13, 15].

Most of the matrix EPR experiments that have been carried out below 10 K have employed a liquid He bath cryostat. For example, the first study of Bowers et al. on atomic impurities in rare gas matrices employed this type of arrangement [25]. For studies above 10 K, a standard closed-cycle He cryostat is a convenient choice. An example of such setup is shown in Fig. 1.1, where both EPR and optical measurements can be performed from the same sample. In both approaches the cryostat is used to cool down a copper or sapphire substrate (cold target) on which the thin matrix film is grown at low temperature. During the measurement the substrate resides in the microwave cavity of a EPR spectrometer, and thus care must be taken in designing the substrate geometry and in its proper positioning inside the cavity. For example, a copper substrate interacts strongly with the electrical component of the microwave radiation field, and even small mechanical vibrations will greatly increase noise in the EPR signal. In the case of a standard TE102 microwave resonator the signal-to-noise ratio can be improved by making the copper substrate flat (for example, 4 mm $\times$ 30 mm $\times$ 0.4 mm) and placing it carefully in the nodal plane of the electric field. Mechanical vibrations do not exist when He bath cryostats are used but most of the closed cycle cryostat based systems suffer from this problem.

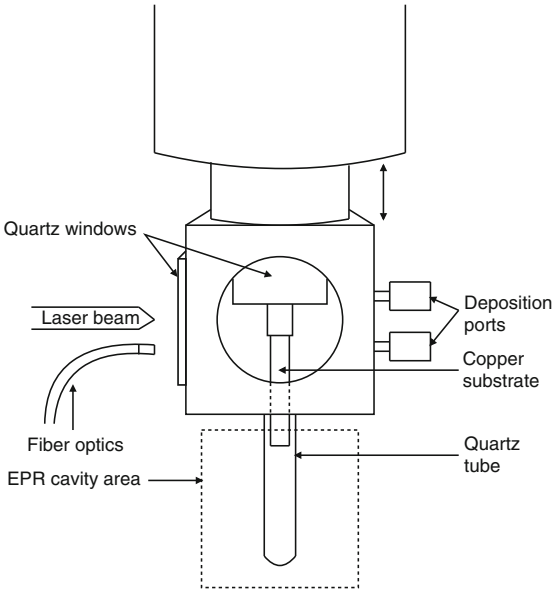

Fig. 1.1 Sketch of a matrix EPR/luminescence apparatus is shown [26]. The flat copper substrate can be moved from the area with optical access to the quartz tube fitting the microwave cavity of the EPR spectrometer

Once the cold substrate is at a suitable temperature, a gaseous mixture can be slowly sprayed on it. In magnetic measurements the optical quality of the matrix is not important, and thus low temperature (4–10 K) deposition, which usually results in very "snowy" looking and strongly scattering solids, can be applied. In some cases low temperature deposition has a great advantage over high temperature deposition (20–50 K) as it prevents diffusion of the impurity atoms or molecules during the freezing stage of the matrix. The impurities can be premixed with the rare gas before deposition, or they can be deposited from separate inlets as shown in Fig. 1.1.

Reactive species, like most atoms, can not be premixed in the rare gas due to practical limitations. Hence, various alternative methods have been developed for producing such species in the rare gas matrices. The most common techniques include in situ photolysis of a suitable parent molecule in the matrix, laser ablation, various thermal vaporization sources, chemical reactions in the matrix, and discharge based methods. For example, photodissociation of hydrogen halides will yield hydrogen atoms and halogen atoms in the matrix [27]. A comparison of the laser ablation and Knudsen oven based techniques for generating trapped atomic species rare gas matrices has been studied in detail [28]. A sketch of a laser ablation apparatus is shown in Fig. 1.2.

Atomic species in impurity helium solids are typically produced by directing a gaseous jet on the surface of superfluid helium forming a porous solid, which eventually falls to the bottom of the liquid helium bath cryostat by gravity and can then be studied directly by EPR. The gas jet consists of a dilute mixture of the atomic precursor, the matrix inert gas and the main component is helium gas. To produce the atomic species in the jet prior to injection into the superfluid, a radio frequency discharge is typically used to dissociate the molecular precursor into the

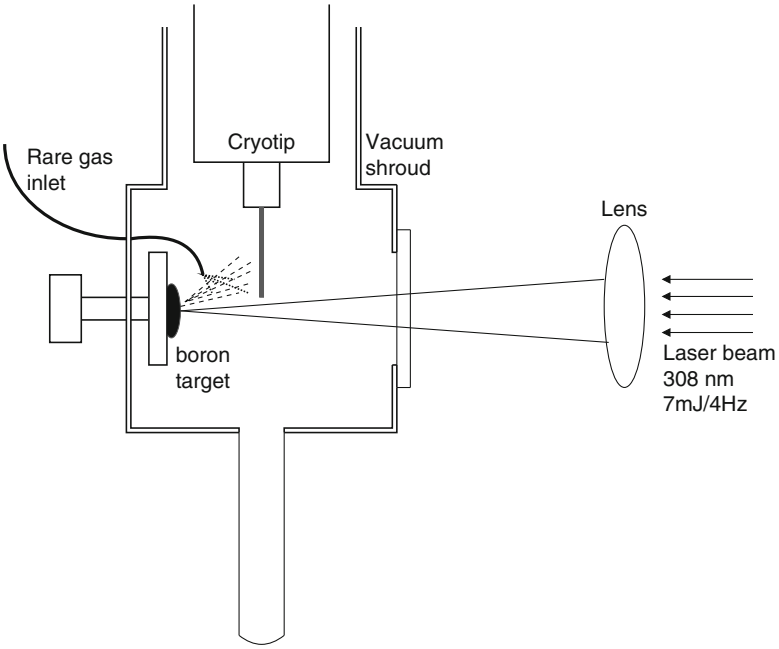

Fig. 1.2 Laser ablation/EPR apparatus [22, 28]. To preserve laser ablation efficiency the copper target was rotated periodically

corresponding atomic species. For example, a dilute N_2 in helium gas leads to the formation of impurity helium solid consisting of N_2 matrix with N atoms embedded inside N_2 clusters or on their surface [9, 11, 15]. This technique has been applied to prepare atomic hydrogen and nitrogen trapped in solid H_2, Ne, Kr and N_2 at $T < 2.1$ K (i.e., below the superfluid lambda temperature) [9–15].

1.3 Atomic Impurities in Rare Gas Matrices

1.3.1 ^2S State Atoms

For ^{2}S state atoms trapped in rare gas matrices the EPR spectrum is highly isotropic. Depending on the impurity, the spectrum may contain resonances due to multiple trapping sites of different size and symmetry with slightly different g and/or A values. For example, in the case of hydrogen atom doped argon matrix, two distinct trapping sites occur as shown in Fig. 1.3 [25, 29]. These sites have been identified as singly substitutional (12 nearest neighbors) and interstitial octahedral sites (6 nearest neighbors) in the face-centered-cubic (FCC) lattice [21, 30]. This assignment is based on a theoretical treatment which will be discussed in Sect. 1.4.

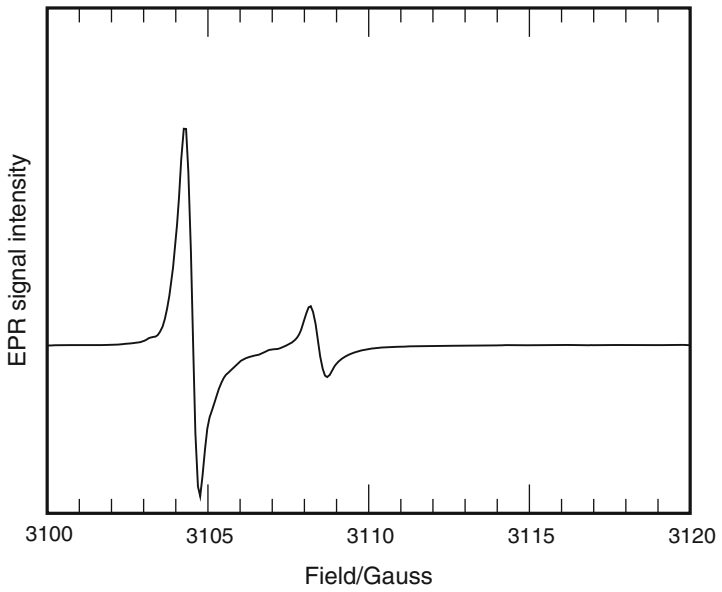

Fig. 1.3 Low field resonance lines of H atom trapped in Ar matrix as produced by UV photodissociation of HCl precursor. Two distinct trapping site resonances (interstitial octahedral and substitutional) are separated by approximately 4 G. In this sample the interstitial octahedral site is more populated than the substitutional site. Center of the spectrum is located at *ca.* 3,350 Gauss

An empirical and relatively well justified rule of thumb is that when the interaction pair potential between the impurity atom and the rare gas atom is much more repulsive than the rare gas – rare gas potential, then a distribution of trapping sites with varying number of lattice vacancies is usually observed. An example of such situation in rare gas matrices is provided by the alkali metal atoms, where the atoms may reside in sites involving multiple lattice vacancies [20, 28]. In this case, thermally activated dynamics, characterized by activation barrier of few meV, within the trapping cavity has been reported [31]. Due to their distinct structures, different trapping sites have usually characteristic thermal stabilities, which allows one to use sample annealing at suitably high temperatures to simplify the observed spectrum significantly. In most favorable cases EPR resonances due to a single trapping configuration is observed after annealing. Annealing of impurity helium samples above the superfluid lambda temperature leads to the recombination of the trapped atomic species, which releases large amounts of excess energy leading to the destruction of the sample.

The resulting EPR spectra can be simulated by standard methods using isotropic g and hyperfine coupling matrix A. It should, however, be carried out with caution since atomic species may have large A and therefore higher than first order corrections become very important. An interesting example of such case is provided by Cu atoms trapped in rare gas matrices as this species shows rather peculiar EPR spectrum in which only two lines are seen for a particular Cu isotope [32, 33].

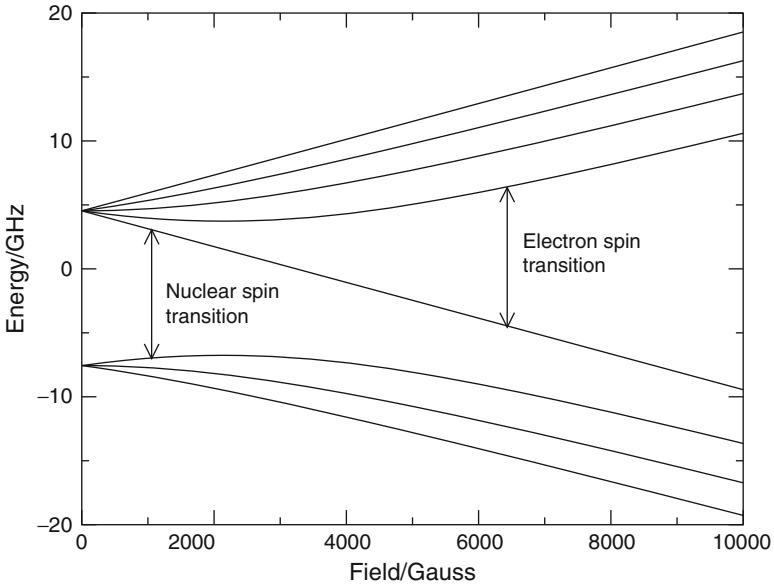

Fig. 1.4 Energy level diagram as a function of magnetic field strength for a single Cu atom. At X-band only two transitions are seen below 10,000 G which can be approximately classified as being electron spin and nuclear spin types by numerically evaluating the transition moments

The origin of this spectrum can be understood by inspecting the energy level diagram of Fig. 1.4. In order to carry out a rigorous theoretical analysis for these systems, one must obtain both g and A matrices with proper accuracy. For this reason, it is suggested that spectrum simulation with iterative parameter fitting with highly accurate evaluation of the exact spin Hamiltonian is used (see Sect. 1.4.4). Furthermore, the transition moments should be evaluated based on the proper eigenvectors in order to get the intensities reliably. In the previous Cu atom example both dominantly electron spin and dominantly nuclear spin transitions are observed. Summary of experimental magnetic parameters for ^{2}S state atoms trapped in solid rare gases is shown in Table 1.1.

Trapped atoms may be thermally activated provided that the barrier for diffusion can be overcome with thermal energies. By measuring the time decay profiles of the EPR signals at specified temperatures one can obtain kinetic information of the impurity atom diffusion. Thermal behaviour usually depends on the site structure around the impurity as was already noted in the context of sample annealing. For example, this method has been used to determine the diffusion rates of atomic hydrogen in rare gas matrices [29]. In this case the substitutional sites are thermally stable up to the matrix evaporation temperatures, whereas the octahedrally trapped atoms are mobilized at low temperatures (in Ar at 16 K and in Kr at 24 K). No new resonances are observed as the final products are not paramagnetic (H_2 and thermally formed rare gas compounds) [7, 8]. In the case of metal atoms (Li [36],

Table 1.1 Summary of relevant magnetic parameters of ^{2}S state atoms in solid rare gases is shown

Atom	I	Matrix	g_{iso}	A_{iso}	Site	Source
H		Ar(1)	2.0012	+17	Int.	Refs. [21, 25, 29, 30]
H		Ar(1)	2.0017	−6	Subst.	Refs. [21, 25, 29, 30]
H		Kr(1)	1.9992	+8	Int.	Refs. [21, 25, 29, 30]
H		Kr(1)	2.0013	−11	Subst.	Refs. [21, 25, 29, 30]
H		Kr(4)	–	−12	Subst.?	Ref. [13]
H		H_2(4)	–	−4.4	Subst.?	Ref. [13]
H		Xe(5)	–	−15	Int.	Ref. [34]
^{1}H	1/2	Free	2.00226	1420.4		Ref. [1]
Li		Ar(2)	2.0018	−7	12 vac.	Refs. [20, 35]
Li		Ar(2)	2.0010	+12	8 vac.	Refs. [20, 35]
Li		Ar(3)	1.9984	+56	Subst.	Refs. [20, 28]
Li		Ar(3)	1.9998	+14	8 vac.	Refs. [20, 28]
Li		Kr(2)	1.9987	−7	12 vac.	Refs. [20, 35]
Li		Kr(2)	1.9966	+9	6 vac.	Refs. [20, 35]
Li		Kr(3)	1.9860	+44	Subst.	Refs. [20, 28]
Li		Xe(2)	1.9914	−5	12 vac.	Refs. [20, 35]
^{7}Li	3/2	Free	2.00231	401.7		Ref. [1]
Na		Ar(2)	*Broad distribution of sites*			Refs. [28, 35]
Na		Ar(3)	*Broad distribution of sites*			Refs. [28, 35]
Na		Kr(2)	1.9917	−14	12 vac.	Refs. [20, 28, 35]
Na		Kr(2)	1.9872	+11	6 vac.	Refs. [20, 28, 35]
Na		Kr(3)	1.9832	+115	Subst.	Refs. [20, 28]
Na		Xe(2)	1.9925	−12	12 vac.	Refs. [20, 28, 35]
Na		Xe(3)	1.9925	+97	Subst.	Refs. [20, 28]
^{23}Na	3/2	Free	2.00231	885.81		Ref. [1]
K		Ar(2)	*Broad distribution of sites*			Ref. [35]
K		Kr(2)	1.9964	−3	–	Ref. [35]
K		Kr(2)	1.9849	+15	–	Ref. [35]
K		Xe(2)	1.9857	+4	–	Ref. [35]
^{39}K	3/2	Free	2.00231	230.86		Ref. [1]
Rb		Ar(2)	*Broad distribution of sites*			Ref. [35]
Rb		Kr(2)	*Broad distribution of sites*			Ref. [35]
Rb		Xe(2)	1.9821	−16	–	Ref. [35]
^{85}Rb	5/2	Free	2.00241	1,012		Ref. [1]
Cs		Ar(2)	2.0051	+11	–	Ref. [35]
Cs		Kr(2)	2.0015	−21	–	Ref. [35]
^{133}Cs	7/2	Free	2.00258	2,298		Ref. [1]
Cu		Ar(2)	1.9994	+282	–	Ref. [33]
Cu		Kr(2)	1.9955	+176	–	Ref. [33]
Cu		Kr(3)	1.996	+181	–	Ref. [32]
Cu		Xe(2)	1.9942	+29	–	Ref. [33]
^{63}Cu	3/2	Free	2.0023	5,867		Ref. [1]

(continued)

Table 1.1 (continued)

Atom	I	Matrix	g_{iso}	A_{iso}	Site	Source
Ag		Ar(2)	1.9998	+98	–	Ref. [33]
Ag		Kr(2)	1.9942	+65	–	Ref. [33]
Ag		Xe(2)	1.9922	+17	–	Ref. [33]
^{107}Ag	1/2	Free	2.0023	−1,713		Ref. [1]
Au		Ar(2)	2.0012	+85	–	Ref. [33]
Au		Kr(2)	1.9962	+43	–	Ref. [33]
Au		Xe(2)	1.9970	−27	–	Ref. [33]
Au	3/2	Free	2.0023	3053		Ref. [1]

Atom preparation method is denoted as: (1) photodissociation, (2) thermal source (Knudsen oven), (3) laser ablation, (4) impurity helium solid or (5) electron bombardment. Hyperfine coupling shifts with respect to the gas phase values (labelled as free) are expressed in MHz. Data for most abundant isotopes are shown

Na [37], K [37, 38], Cu [39, 40] and Ag [39]) formation of paramagnetic clusters has been observed. However, the alkali metal clusters were formed during sample deposition within the semiliquid interface between the solid and vacuum, and Cu and Ag were mobilized thermally in solid neon only. Therefore, these atoms do not exhibit real diffusion behavior in solid Ar, Kr, or Xe. It appears that only hydrogen exhibits diffusion mediated propagation in these solids, which suggests the importance of tunneling in the mechanism. This is consistent with the observed different thermal behaviour for H and D atoms [29]. When the initial concentration of the H/D atoms is high, interesting spin-paired species can be observed without thermal activation [41]. Based on the magnetic parameters it was estimated that the distances between the impurity centres was greater than 7 Å in the matrix.

1.3.2 High Spin S State Atoms

Atoms having half-filled *np* shells (e.g., N (^{4}S), P (^{4}S), As (^{4}S)) all have isotropic electron distribution and hence the rare gas – atom interaction potentials are isotropic. The matrix – impurity interaction ground state potentials dictate the trapping site symmetry and for purely substitutional trapping the site symmetry will be spherical. Thus, the EPR spectra are expected to be isotropic. If multiple substitutional trapping occurs then deviation from the spherical symmetry results and electron spin–spin interaction may be observed. For rare gas matrices this can not be seen but, for example, N atoms in N_2 matrix shows signs of this interaction [42]. Both g and hyperfine coupling A experience deviation from their gas phase values and similar analysis as presented for the ^{2}S atoms may be applied. In general, it has been observed that the relative matrix induced shifts for these atoms are larger than for the ^{2}S atoms indicating stronger impurity – matrix coupling. Data for some ^{4}S state atoms is listed in Table 1.2. A simple theory employing isotropic hyperfine coupling shifts predicts that these atoms occupy sites that resemble closely substitutional sites in the FCC lattice.

Table 1.2 Summary of relevant magnetic parameters for ^{4}S state atoms in solid rare gases is shown

Atom	I	Matrix	g_{iso}	A_{iso}	Site	Source
N		Ar(1,2)	2.0020	+1.6	Subst.	Refs. [26,43]
N		Kr(1,2)	2.0019	+1.9	Subst.	Refs. [26,43]
N		Xe(1,2)	2.0019	+1.9	Subst.	Refs. [26,43]
N		N_2(3)	2.0019	+1.2	–	Refs. [44,45]
^{14}N	1	Free	2.0022	10.45		Ref. [1]
P		Ar(2)	2.0012	+26	Subst.	Ref. [43]
P		Kr(2)	2.0001	+28	Subst.	Ref. [43]
P		Xe(2)	–	+30	Subst.	Ref. [43]
^{31}P	1/2	Free	2.0019	55.06		Ref. [1]
As		Ar(2)	1.9960	−31	Subst.	Ref. [43]
As		Kr(2)	1.9951	−35	Subst.	Ref. [43]
As		Xe(2)	1.9943	–	–	Ref. [43]
^{75}As	3/2	Free	1.9965	−66.20		Ref. [1]

Atom preparation method is denoted as: (1) photodissociation, (2) γ-irradiation of suitable molecular species or (3) impurity helium solid. Hyperfine coupling constant shifts with respect to gas phase values (labelled as free) are expressed in MHz. Data for most abundant isotopes are shown

Thermal mobility of ^{4}S state atoms has not been reported in the literature. The experimental data show that at least nitrogen atoms [26], produced by photolysis, were stable up to the evaporation temperatures of the matrix. The N–Ar pair potential (minimum located approximately at 3.6 Å with a depth of 8 meV; CCSD(T)/aug-cc-pvqz level calculation) is comparable to the H–Ar (minimum at 3.6 Å with 4 meV well depth) pair potential and yet no thermal mobility is observed [21]. However, only one trapping site was observed for nitrogen atoms and therefore it is quite probable that N atoms occupy pure substitutional sites in the lattice. Hydrogen atoms trapped in substitutional cavities are also stable and this thermal stability can also be related to the site structure. No reports for diffusive cluster formation in this group of atoms has been reported. In highly concentrated matrices N atoms show spin-pairing spectra similar to the H atoms [46]. Other observed high spin atoms in rare gas matrices include Cr (^{7}S) and Mn (^{6}S), which yield nearly isotropic EPR spectra [47].

1.3.3 Superhyperfine Interaction

Both ^{83}Kr (11.6% of I = 9/2) and ^{129,131}Xe (26.4% of I = 1/2; 21.2% of 3/2) atoms have magnetic isotopes, which may affect the observed EPR spectra. If the interaction between impurity and the matrix atom is sufficiently strong (i.e., there is sufficient mixing of matrix atom and impurity orbitals) then the EPR spectrum may exhibit additional structure due to electron spin (impurity) – nuclear spin (matrix) coupling. This effect is usually called as superhyperfine coupling. An interesting demonstration of this effect was given by Morton et al. who isolated hydrogen

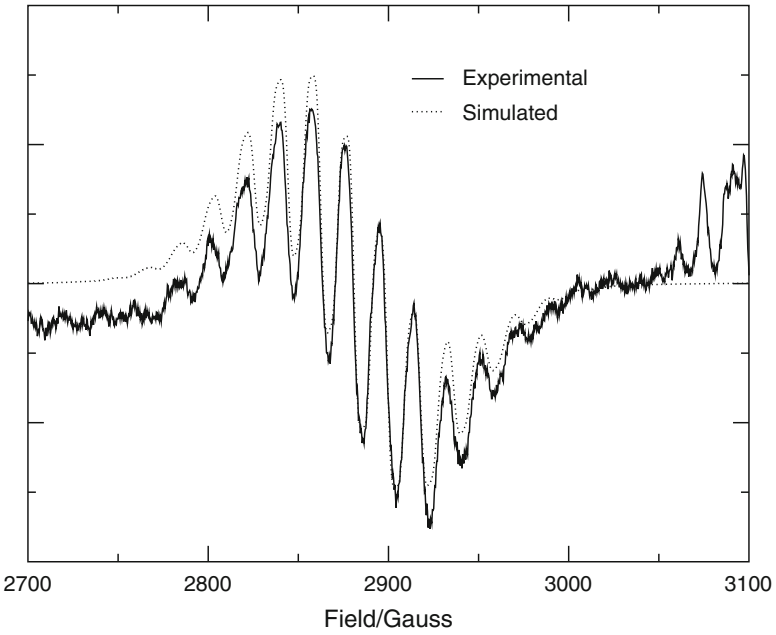

Fig. 1.5 Superhyperfine structure of Na atoms trapped in solid Xe (only single Na resonance line is shown). Simulation assumes statistical distribution of 12 Xe atoms with their natural isotope distribution around the alkali metal center. Only isotropic hyperfine interaction ($A_{iso} \approx 115$ MHz) has been included in calculation [28]

atoms in solid isotopically enriched ^{129}Xe (37%) [34, 48]. The authors were able to simulate the resulting anisotropic EPR spectrum by assuming octahedral trapping site and proper statistical distribution of magnetic matrix atoms. A similar approach was used in explaining the observed superhyperfine structure for sodium atoms trapped in solid Xe [28]. Experimental and simulated spectra for one of the sodium EPR lines are shown in Fig. 1.5. Accurate EPR spectrum simulations can be effectively used to predict the number of magnetic matrix atoms around the impurity and therefore conclusions on the trapping site structure can be made.

1.3.4 ^{2}P State Atoms

Detection of ^{2}P atoms in rare gas matrices has turned out to be a difficult task [1]. Atoms with a single electron in their outer p-shell (B, Al, and Ga) show powder spectra with axial symmetry and, consequently, EPR detection sensitivity is greatly reduced [22, 49–51]. As will be justified in Sect. 1.4, the axial symmetry is caused by locking of the unpaired electron orbital to a preferential direction with respect to an origin placed on the impurity. On the other hand, the sample will contain atoms with random distribution of p-orbital orientations with respect to the direction

of the external magnetic field. The other extreme, a hole in the p-orbital frame (e.g., halogens), is even more difficult to detect by EPR [1]. The only clean observation of this group of atoms concerns F atom in a Kr matrix, which appear to form a relatively tightly bound tri-atomic Kr_2F molecule, again in axial symmetry [52]. Other halogen atoms have only been observed in strongly quenched states [53, 54]. However, in these few observed cases, the EPR spectrum revealed detailed information about the lattice structure around the impurity. Simulation of the EPR spectra of ^{2}P state atoms involves powder integration along axial symmetry, and depending on the atom, higher order corrections may be necessary to include. For loosely bound atoms (i.e., B, Al, and Ga), by explicitly including spin-orbit coupling, orbital Zeeman, and crystal field interactions, one can obtain the associated parameters from the spectrum. This has been carried out in detail for B atom in Ar, Kr, and Xe matrices by Kiljunen et al. [22]. In this case the Hamiltonian was written as:

$$H = \beta_e H \cdot (L + g_e S - g_N I) + \xi L \cdot S + S \cdot A \cdot I + H_{tetr}(L)$$
$$\text{where } H_{tetr}(L) = \alpha_t \left[3L_d^2 - L(L+1)\mathbf{1}\right], d = x, y, z \qquad (1.1)$$

and was solved numerically in the uncoupled representation. Note that $\alpha_t = -\Delta/2$ where Δ is the crystal field splitting parameter. By performing parameter fitting between simulated and experimental powder EPR spectra, values for spin-orbit and crystal field parameter α_t can be obtained. As explained in more detail in the theoretical part of the text, the external heavy atom effect can be included in this model by artificially reducing the value of the spin-orbit coupling constant. By way of an example experimental and simulated EPR spectra of boron atoms trapped in solid Ar and Kr are shown in Fig. 1.6. The external heavy atom effect is seen clearly as exchange in the magnitude of $g_{xx,yy}$ and g_{zz} as the EPR spectrum changes its overall phase completely. A summary of magnetic parameters for selected atoms in solid rare gases is shown in Table 1.3.

The theoretical analysis of boron atom has accounted for the external heavy atom effect, whereas Al and Ga were treated essentially by assuming the gas-phase values for the spin-orbit coupling constants. As already demonstrated for boron, this assumption fails for heavier rare gases. It is thus expected that the crystal field splitting in Table 1.3 for Al and Ga is too large for Kr and Xe matrices. This was noted in the work by Schlosnagle et al. [49], where the calculations indicated that the crystal field splitting is infinite in Xe matrix. Since the experimental EPR spectrum can only yield information on the ratio between the crystal field splitting and the spin-orbit coupling constant, additional theoretical calculations are required to determine either of the free parameters separately.

As was noted by Kunttu et al. [22] and Weltner et al. [50], diffusion of B atoms can be thermally activated, and in some cases formation of B_2 as well as impurity related products H_2BO (presumably originating from the H_2O + B reaction) and BO (from O_2 + B) are observed. The existence of these species clearly demonstrate that the matrix environment is well suited for studying reactions between molecular species and B atoms. No information of thermal stability of Al and Ga atoms is available in the literature.

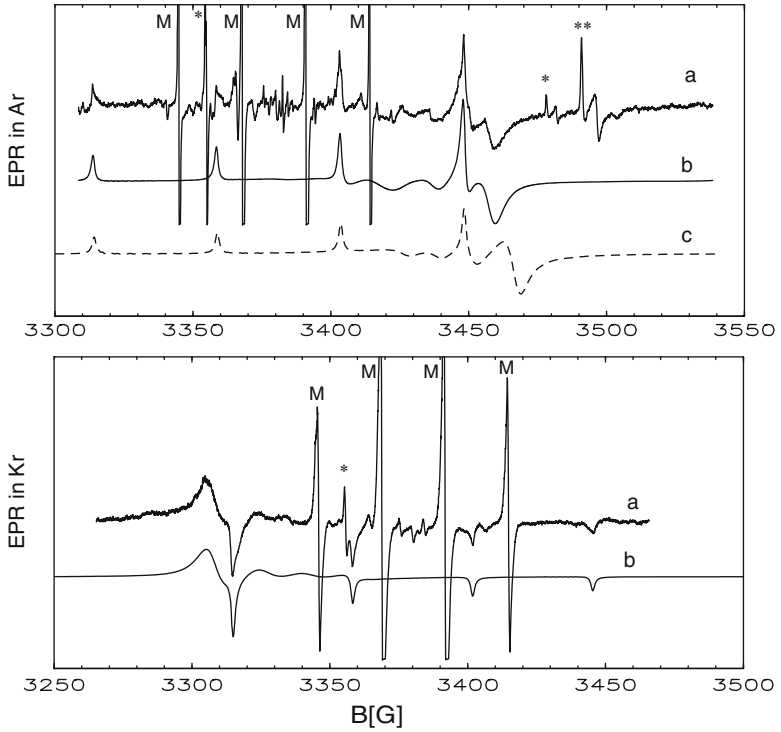

Fig. 1.6 Experimental and simulated EPR spectra of boron atoms in solid Ar and Kr: (**a**) experimental, (**b**) axially symmetric simulation [22], (*c*) axially symmetric simulation [50]. The methyl radical impurities are marked by M, ^{10}BO by *, and ^{11}BO by **

1.4 Theoretical Treatment of Atomic Impurities

The first theoretical analysis of matrix induced shifts of the isotropic g and A values was presented by Adrian [30]. For isotropic hyperfine coupling shifts, the impurity atom – matrix interaction was assumed to be pair-wise additive and to consist of two types of interactions: van der Waals attraction and Pauli repulsion. The van der Waals attraction causes expansion of the impurity atom electron cloud and, in simple cases like H atom, yields reduced spin density at the nucleus. This is the origin of the negative shift in the isotropic hyperfine coupling constant. The Pauli repulsion has an opposite effect for the shift since it causes compression of the unpaired electron orbital. The experiments on atoms in rare gas matrices measure the delicate balance between these two effects. For this reason different trapping sites exhibit distinct isotropic hyperfine coupling constants. The origin for g-value shift is more difficult to visualize but essentially it is caused by mixing of the outer atomic orbitals of the rare gas into the wavefunction of the impurity by exchange interaction. This increases the effective spin-orbit coupling of the atom, and hence

Table 1.3 Summary of relevant magnetic parameters for ^{2}P state atoms in solid rare gases is shown

Atom	I	Matrix	g_{zz}	$g_{xx,yy}$	A_{zz}	$A_{xx,yy}$	ξ	Δ	Source
^{11}B		Ar(1)	2.0012	1.9645	126	−33	10.7	380	Ref. [50]
^{11}B		Ar(2)	2.0014	1.970	126.1	−46.9	7.8	361	Ref. [22]
^{11}B		Kr(2)	2.0018	2.032	122.3	−44.9	−4.7	224	Ref. [22]
^{11}B		Xe(2)	2.002	2.10	100	−36	−11.4	168	Ref. [22]
^{11}B	3/2	free	–	–	11.6	11.6	10.7	–	Ref. [1]
^{27}Al		Ar(1)	2.000	1.954	143.0	−101.5	74.9	2,100	Ref. [49]
^{27}Al		Kr(1)	2.001	1.989	135.8	−89.9	74.9	7,540	Ref. [49]
^{27}Al		Xe(1)	1.997	1.962	173.9	−75.8	74.9	–	Ref. [49]
^{27}Al	5/2	free	–	–	−4.6	−4.6	74.9	–	Ref. [1]
^{69}Ga		Ar(1)	1.943	1.591	433	−598	550.8	2,068	Ref. [49]
^{69}Ga		Kr(1)	1.956	1.688	394	−536	550.8	2,643	Ref. [49]
^{69}Ga		Xe(1)	1.968	–	342	–	550.8	3,460	Ref. [49]
^{69}Ga	3/2	free	–	–	−146	−146	550.8	–	Ref. [1]

Atom preparation method is denoted as: (1) thermal source or (2) laser ablation of the solid. Hyperfine coupling constant shifts with respect to gas phase values (labelled as free) are expressed in MHz. Data for most abundant isotopes are shown. A_{ii} ($ii = xx, yy, zz$) refers to the anisotropic components of the hyperfine coupling, ξ is the effective spin-orbit coupling constant (cm^{-1}), and Δ is the crystal field splitting parameter as defined by Eq. 1.1 (cm^{-1}). When clearly distinguishable sites for Al and Ga exist then the data shown is the average over these sites

we expect a negative shift in isotropic g-value. This is, indeed, observed for ^{2}S impurities as shown in Table 1.1. In the following paragraphs, we will consider theoretical calculation of g and A shifts using the pair-wise additive model.

1.4.1 Calculation of Isotropic Hyperfine Coupling Constants

A number of theoretical studies have demonstrated that ab initio calculation of isotropic hyperfine coupling constants is very sensitive to the proper treatment of electron correlation and the quality of the applied basis set. The same conclusion applies for calculation of pair potentials, which similarly consist of the van der Waals attraction and the Pauli repulsion contributions. To a good approximation the Pauli repulsion can be described by single determinant calculations (Hartree-Fock), whereas the van der Waals part requires the inclusion of electron correlation. For atomic hydrogen the maximum negative IHC shifts have been calculated to occur at slightly larger internuclear distances than the van der Waals potential energy minimum. The simple interpretation of van der Waals expansion / Pauli compression fits these results very well.

As a representative case, we will consider the pair interaction between atomic hydrogen and Ne, Ar, Kr, and Xe atoms. For Ne and Ar Dunning's augmented basis set aug-cc-pvqz [55] was applied, whereas for the heavier rare gases the effective core potential basis set of the Stuttgart group [56] with additional augmentation was used.

In the latter case the effective core potential basis set reduces the number of explicit electrons and makes the calculation computationally more affordable. In both cases the diffuse basis functions are important for obtaining accurate results. The isotropic hyperfine coupling constant a can be obtained from the Fermi contact analysis [57]:

$$a = \frac{2}{3h}\mu_0 g_e g_N \mu_B \mu_N \, |\psi(0)|^2 \tag{1.2}$$

where μ_0 is the vacuum permeability, g_e and g_N are the electron and nuclear g values, and μ_B and μ_N are the Bohr and nuclear magnetons, respectively. The spin density $|\psi(0)|^2$ can be obtained from the single particle density matrices by standard methods [57]. Efficient methods for including electron correlation are provided by the coupled cluster (CC) and Møller-Plesset (MP) theories [58]. For evaluation of the pair potentials, methods such as CCSD(T) (single, double, and perturbative triple excitations) and MP4 have proven to be very accurate. For hydrogen atom – rare gas systems the calculated van der Waals minima account for about 80% of the binding energy when compared with experimental results. Unfortunately, most of the available quantum chemistry programs allow evaluation of the required single particle density matrices only at the less accurate CCD and MP4(SDQ) levels.

Since finite basis expansion calculations are prone to artificial basis set superposition errors, one must use the counterpoise procedure of Boys and Bernardi for both pair potentials and isotropic hyperfine coupling shifts [59]. In both cases it is not necessary to obtain fully converged results for the asymptotic region (e.g., infinite nuclear separation) since we are only interested in relative energies and shifts (Δa). In the latter case the following equation is applied [21]:

$$\Delta a(R) = a_{\mathrm{RGH}}(R) - a_{\mathrm{RG"H}}(R) \tag{1.3}$$

where $a_{\mathrm{RGH}}(R)$ is the calculated isotropic hyperfine coupling constant shift for H–RG system and $a_{\mathrm{RG"H}}(R)$ is the same quantity when the rare gas atom is included as a "ghost atom". For ghost atoms the calculation involves all basis functions for the center but no electrons. By way of an example, the calculated isotropic hyperfine coupling shifts for {Kr, Xe}–H as function of internuclear distance are shown in Fig. 1.7. All the obtained curves show sudden collapse at short distances. The onset for Xe–H can be seen in Fig. 1.7, whereas for Kr–H the turn over occurs at shorter bond lengths. At short distances it is expected that the contribution of diatomic Rydberg states increases dramatically and this, consequently, causes shielding of the unpaired electron from the impurity nucleus. Most of the available ground state optimized basis sets are not sufficient in describing these Rydberg states properly, and the collapse in Δa may in fact occur even at longer distances than the calculations have indicated so far. This may have, for example, considerable effect for line broadening in the Xe–H system. In fact, experiments show that sensitivity for detecting hydrogen atoms in Xe matrix via EPR is strongly reduced [34]. However, the lack of sensitivity is mostly caused by broadening caused by the

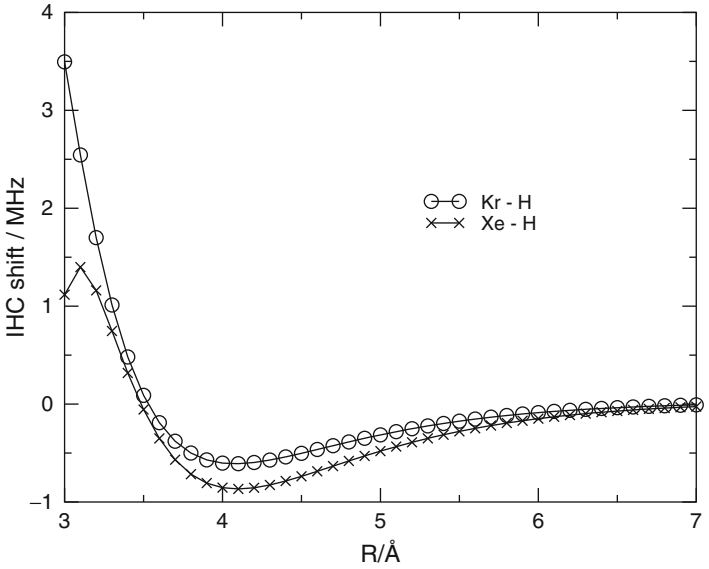

Fig. 1.7 The distance dependence of IHC shifts for {Kr, Xe}–H systems from MP4(SDQ) calculations is shown [21]

superhyperfine interaction. Finally, we note that the anisotropic hyperfine coupling will exhibit small shifts as well, but comparison with the experimental observations is not easy because of the poor resolution in the powder spectra.

1.4.2 Calculation of g Shift and Anisotropy

The g value shift may be estimated by calculating the induced spin-orbit coupling change by the approaching rare gas atom. In the case of free hydrogen atom, no spin-orbit interaction exists, and thus the rare gas atom is solely responsible for spin-orbit interaction in this case. The spin-orbit matrix elements in a diatomic system can be conveniently evaluated by a method presented by Knowles et al. by using multi-reference configuration interaction wave functions [60]. Both regular and effective core potential basis sets can be applied in these calculations. This type of calculation has been carried out in detail for boron atom trapped in rare gas matrices where anisotropic interactions also occur [22]. The g-shift can be approximated by the sum over states bilinear formula [57, 61]:

$$g_{ab} = g_e \delta_{ab} + g_e \sum_{n \neq 0} \frac{\langle 0 | L_a S_a | n \rangle \langle n | L_b | 0 \rangle}{E_n - E_0} \tag{1.4}$$

where $a, b = x, y, z$, $L_a S_a$ is the spin-orbit operator, L_b is the orbital Zeeman operator (gauge dependent) and summation is taken over the excited states. Provided that the matrix element of L_b would not change much for different impurity – rare gas combinations, then it can be seen that it is the spin-orbit operator that is responsible for mixing in the electronically excited states. These excited states have considerable contributions from the rare gas atoms and, in the case of Xe, the ionic charge transfer state (B^- Xe^+) plays a significant role. In this case it was possible to account for the isotropic g shift by reducing the effective value of the spin-orbit coupling constant as shown in Table 1.3.

In addition to the isotropic g value shifts, the ^{2}P state atoms experience strong splitting of the p-orbital frame by the surrounding crystal field. For example, boron atom trapped in rare gas matrices produce axially symmetric powder spectra. This can be understood in terms of the Σ and Π pair potentials for B–Rg, which are sufficiently different to produce an axially symmetric trapping site (see Fig. 1.8). In terms of the crystal field theory, this means that the surrounding matrix removes the orbital degeneracy and therefore quenches the orbital angular momentum. It can be shown that a simple relation between the crystal field splitting energy (ΔE) and $\Delta g_{xx,yy}$ holds:

$$\Delta g_{xx,yy} = g_e - 2\frac{\xi}{\Delta E} \tag{1.5}$$

In most previous theoretical analysis the spin-orbit (ξ) coupling has been taken as a constant corresponding to the free atom limit. However, as discussed earlier, the external heavy atom effect of the matrix atoms alters the effective value of spin-orbit coupling, and therefore the above expression will yield increasingly incorrect results when heavier rare gas matrices are treated. This behaviour was in fact observed by Ammeter et al. in their study of crystal field splitting in Al and Ga atoms embedded in rare gas matrices (see Table 1.3), where too large crystal field splitting were observed [49]. Furthermore, this expression does not allow for a change of sign in Δg, which was observed experimentally for B atoms in Kr matrix. Thus a careful analysis of the effective spin-orbit coupling constant must always be carried out when using this equation.

1.4.3 Molecular Dynamics Simulations

Once the pair-wise additive potentials and isotropic hyperfine coupling shifts have been calculated, trapping of the impurity in the rare gas lattice can be simulated. Although light atoms such as H and B have considerable quantum mechanical zero-point spread associated with them, to a first approximation we can treat them classically. Classical molecular dynamics simulations for these systems have been carried [21, 22]. Electronic and nuclear degrees of freedom were separated in these calculations by assuming that the electronic part adiabatically follows the nuclear motion. For hydrogen atoms these simulations are able to yield correct trapping sites (i.e., they produce the experimentally observed isotropic hyperfine coupling

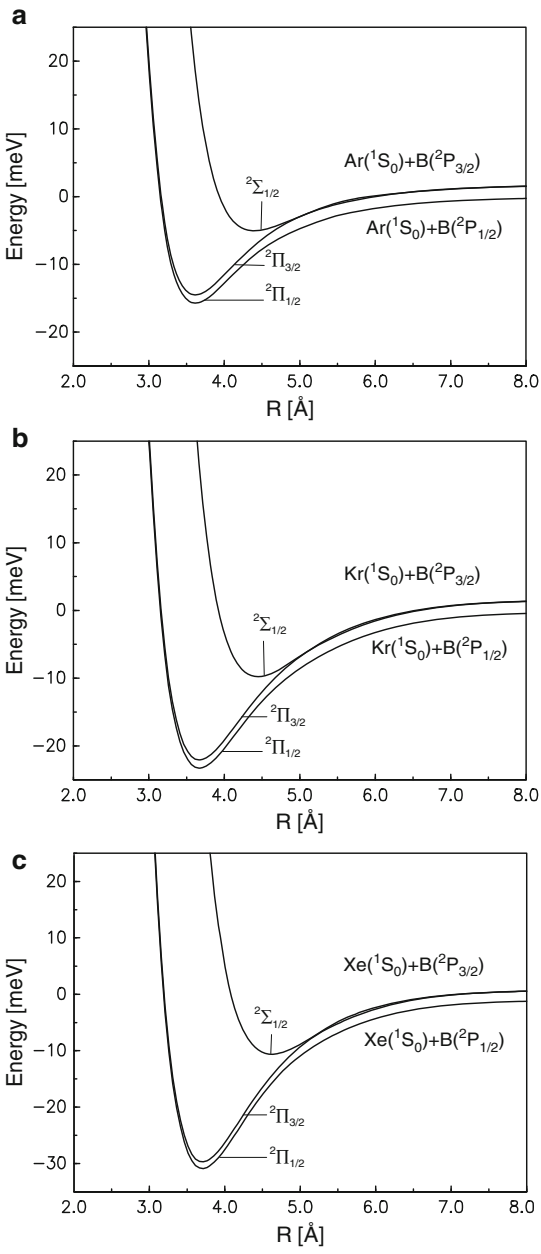

Fig. 1.8 The potential energy curves for B–Rg pairs including spin-orbit coupling are shown [22]

shifts as shown in Table 1.1). This method was the basis in identifying the trapping sites for atomic hydrogen. Simulation of ^{2}P state atoms requires a more complex way of evaluating the potential energy surface used in the molecular dynamics simulations because the B–Rg Σ and Π potentials are different from each other.

For this purpose a minimal diatomics-in-molecules (DIM) description is well suited. The DIM Hamiltonian is given as [22]:

$$H^{DIM} = \sum_{i<j} E(i,j) \otimes \mathbf{1} + \sum_{i} \begin{pmatrix} E_i\left(^2\Pi\right) + x_i^2 \Delta_i & x_i y_i \Delta_i & x_i z_i \Delta_i \\ x_i y_i \Delta_i & E_i\left(^2\Pi\right) + y_i^2 \Delta_i & y_i z_i \Delta_i \\ x_i z_i \Delta_i & y_i z_i \Delta_i & E_i\left(^2\Pi\right) + z_i^2 \Delta_i \end{pmatrix} \tag{1.6}$$

where $\Delta_i = E_i\left(^2\Sigma\right) - E_i\left(^2\Pi\right)$, x_i, y_i, z_i denote the direction cosines between the ^{2}P atom and matrix atom i, $E(i,j)$ is the Rg–Rg pair potential and $\mathbf{1}$ is the 3×3 unit matrix. The first summation is over the ^{1}S matrix atom pairs and the second over the surrounding matrix atoms. Numerical diagonalization of this real symmetric matrix can be efficiently performed, for example, by the DSYEV routine in LAPACK [62]. This diagonalization yields three eigenstates and the effective orientation of the unpaired electron orbital is given by the eigenvectors. It should be noted that atoms that have a hole in their p-orbital frame must be treated differently as the ionic states have major contributions to the ground state. By including vacancies around the boron atom, it was observed that in the lowest state the p-orbital direction became locked in space. Based on the experimental EPR spectrum this is the correct behavior. The calculated crystal field splitting (i.e., the difference between the eigenvalues) correspond very nicely with the experimental observations. Spatial locking of the p-orbital can be conveniently represented by the orbital autocorrelation function of the ith state:

$$C(t) = \langle c_i(t) \cdot c_i(0) \rangle \tag{1.7}$$

where $c_i(t)$ is the eigenvector of the ith state at time t. By way of an example, the autocorrelation function of the unpaired electron orbital of boron in various Rg hosts is shown in Fig. 1.9.

The calculated crystal field splittings obtained by this method are listed in Table 1.3. From the simple g value shift expression in Eq. 1.5 it can be seen that experiments can only yield the ratio between the effective spin-orbit and the crystal field splitting. In practice this means that the theoretical calculations are mandatory in order to obtain proper results. The DIM model can be easily extended to include interactions that are important for EPR spectroscopy (DIM-SH). When spin-orbit interaction is included the Hamiltonian becomes a complex 6×6 matrix since electron spin has to be added to the basis set. It then depends on the problem weather Cartesian, uncoupled, or coupled basis representation is the most efficient one to use. One should observe that a consistent phase convention is used in transformations between different schemes [63].

The DIM-SH method combined with molecular dynamics calculations is expected to be very useful, for example, in modelling of spin dynamics in solids. Ensemble averages for spins can be performed by averaging over multiple trajectories with different initial conditions. Even inhomogeneities can be included

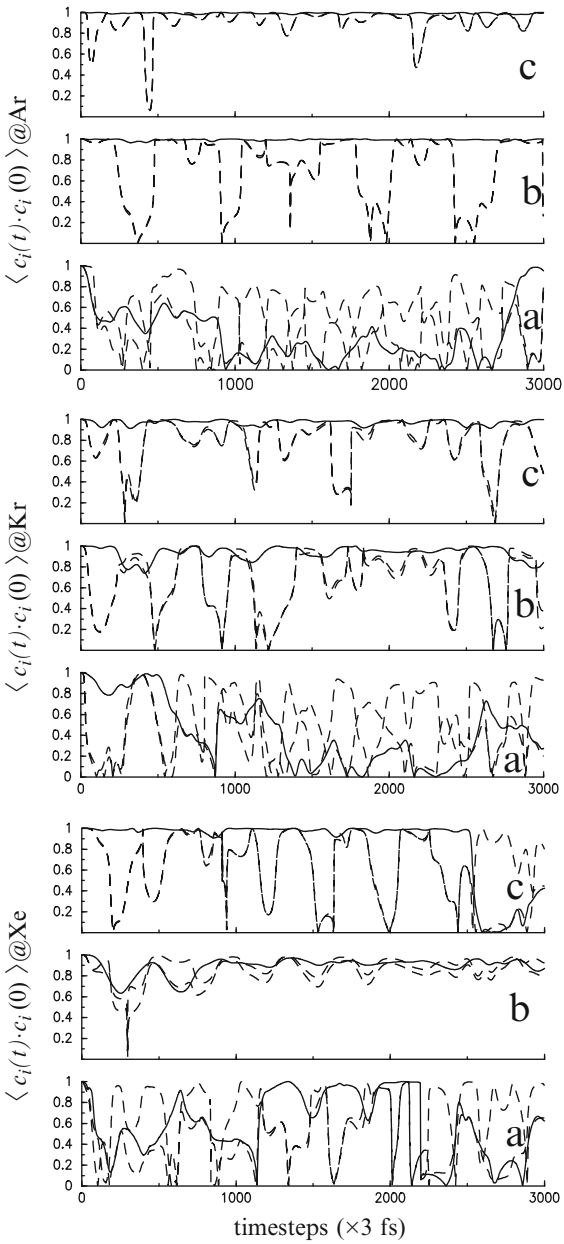

Fig. 1.9 The p-orbital autocorrelation function for B atom in Ar, Kr, and Xe matrices are shown [22]. Case (**a**) no vacancies, (**b**) one vacancy, and (**c**) two vacancies. The *solid lines* correspond to the lowest eigenstate (z) and the *dashes lines* to nearly degenerate excited eigenstates (xy)

by introducing different trapping sites in the averaging process. However, long simulation times and extensive ensemble averaging may lead to excessive computation times.

1.4.4 Simulation of EPR Spectra

Simulation of EPR spectra for ^{2}S atoms in rare gas matrices can be carried out very efficiently by using *effective* isotropic g and a values. However, the ^{2}P state case requires a more complex approach as the spin Hamiltonian of Sect. 1.3.4 must be solved numerically. Furthermore, as the orientation of the p-orbital is most often locked in solids, a powder spectrum with an axial symmetry must be generated. For this purpose, we have implemented a generic spin engine, which can deal with an arbitrary number of spins and their operations in the uncoupled representation. Given the spin Hamiltonian of (1.2), this routine builds the required spin Hamiltonian matrix efficiently, diagonalizes it, and calculates the transition moments between the requested states. In most EPR experiments the magnetic field is varied instead of the microwave field frequency and therefore the simulation algorithm obtains transition energies and moments at several different magnetic field values within the spectral range and uses a linear interpolation to obtain the intermediate values. Since the obtained energy levels may cross within the interpolation interval, it is important to correlate correct states with each other. To find the state that correlates with state i, state k is chosen such that it maximizes the overlap between i and k:

$$\max_k \left| \left\langle c_i \left(B_j \right) | c_k \left(B_{j+1} \right) \right\rangle \right|^2 \tag{1.8}$$

where B's indicate the magnetic field values and c's are the eigenvectors of the spin Hamiltonian obtained at the given magnetic field values.

For powder spectrum integration, a cubic spline interpolation of the transition energies and transition moments was applied. This greatly reduces the number of orientations at which the spin Hamiltonian must be diagonalized. After the powder integration procedure, the EPR lineshape is convoluted into spectrum by using the Fast Fourier Transform (FFT) approach where the convolution is carried out in the Fourier space as a direct multiplication [64]. For boron atom trapped in rare gas matrices, we have used different linewidths for parallel and perpendicular transitions, which makes the lineshape calculation computationally more demanding by requiring the FFT convolution to be carried out for each single crystal orientation separately. In this particular case, it was observed that the perpendicular lines were 7–9 times broader than the parallel lines. Coupling of the p_z orbital with $p_{x,y}$ by the external magnetic field is the most likely source for this effect. The x-y frame is more strongly coupled to the lattice and hence its presence causes severe line broadening. This type of effect is in fact quite general and it has been observed in more complex systems as well [65].

The simulated EPR spectrum can be fitted to the experimental spectrum by using the least squares minimization process where any of the parameters of Hamiltonian in Eq. 1.2 can be simultaneously optimized. Since the analytic gradients are very difficult to obtain, a minimization method that does not require gradients is preferred. Three such methods were used in the simulations: Monte Carlo, Simplex, and

Marquardt [66]. Restrictions on the optimized parameters were included by penalty terms, which essentially increase the object function value if some parameters are out of their allowed range. In a typical application, the optimization starts with several thousand Monte Carlo cycles to avoid local minima, the solution is improved by the simplex method and then finally the Marquardt method is used to obtain a fully converged result. All the described spectral simulation methods have been implemented in Xemr program, which is available for free download through Internet [32].

References

1. Weltner W Jr (1983) Magnetic atoms and molecules. Dover Publications, New York
2. Whittle E, Dows D, Pimentel G (1954) Matrix isolation method for the experimental study of unstable species. J Chem Phys 22:1943–1944
3. Jacox M (2011) Vibrational and electronic energy levels of polyatomic transient molecules. http://webbook.nist.gov/chemistry/polyatom/. Accessed 7 Jul 2011
4. Bass A, Broida H (eds) (1960) Frormation and trapping of free radicals. Academic, New York
5. Palaszewski P, Ianovski L, Garrick P (1998) Propellant technologies: far-reaching benefits for aeronautical and space-vehicle propulsion. J Propul Power 14:641–648
6. Tam S, Macler M, DeRose M, Fajardo M (2000) Electronic spectroscopy of B atoms and B_2 molecules isolated in para-H_2, normal-D_2, Ne, Ar, Kr, and Xe matrices. J Chem Phys 113:9067–9078
7. Khriachtchev L, Pettersson M, Runeberg N, Lundell J, Räsänen M (2000) A stable argon compound. Nature 406:874–876
8. Pettersson M, Lundell J, Räsänen M (1999) New rare-gas-containing neutral molecules. Eur J Inorg Chem 1999:729–737
9. Boltnev R, Gordon E, Khmelenko V, Krushinskaya I, Martynenko M, Pelmenev A, Popov E, Shestakov A (1994) Luminescence of nitrogen and neon atoms isolated in solid helium. Chem Phys 189:367–382
10. Boltnev R, Bernard E, Järvinen J, Khmelenko V, Lee D (2009) Stabilization of hydrogen atoms in aggregates of krypton nanoclusters immersed in superfluid helium. Phys Rev B 79:180506
11. Gordon E, Mezhov-Deglin L, Pugachev O (1974) Stabilization of nitrogen atoms in superfluid helium. JETP Lett 19:63–65
12. Gordon E, Khmelenko V, Popov E, Pelmenev A, Pugachev O (1989) Impurity-helium van der Waals crystals. Chem Phys Lett 155:301–304
13. Khmelenko V, Lee D, Vasiliev S (2011) Matrix isolation of h atoms at low temperatures. J Low Temp Phys 162:105–120
14. Kiryukhin V, Keimer B, Boltnev R, Khmelenko V, Gordon E (1997) Inert-gas solids with nanoscale porosity. Phys Rev Lett 79:1774–1777
15. Popov E, Eloranta J, Ahokas J, Kunttu H (2003) On the formation mechanism of impurity-helium solids: evidence for extensive clustering. Low Temp Phys 29:510–514
16. Apkarian V, Schwentner N (1999) Molecular photodynamics in rare gas solids. Chem Rev 99:1481–1514
17. Chipman D (1992) The spin polarization model for hyperfine coupling constants. Theor Chim Acta 82:93–115
18. Feller D (1990) An ab initio study of the magnetic hyperfine properties of F_2^- ($^2\Sigma_u^+$). J Chem Phys 93:579–589

19. Feller D, Glendening E, Cullough EM Jr, Miller R (1993) A comparison of unrestricted Hartree-Fock and restricted openshell Hartree-Fockbased methods for determining the magnetic hyperfine parameters of NO ($X^2\Pi$). J Chem Phys 99:2829–2840
20. Ahokas J, Kiljunen T, Eloranta J, Kunttu H, Khriachtchev L, Pettersson M, Räsänen M (2000) Electronic structure and short-range recombination dynamics of S_2 in solid argon. J Chem Phys 112:7475–7482
21. Kiljunen T, Eloranta J, Kunttu H (1999) Ab initio and molecular-dynamics studies on rare gas hydrides: potential-energy curves, isotropic hyperfine properties, and matrix cage trapping of atomic hydrogen. J Chem Phys 110:11814–11822
22. Kiljunen T, Eloranta J, Ahokas J, Kunttu H (2001) Magnetic properties of atomic boron in rare gas matrices: an electron paramagnetic resonance study with ab initio and diatomics-in-molecules molecular dynamics analysis. J Chem Phys 114:7144–7156
23. Dunkin I (1998) Matrix-isolation techniques: a practical approach. Oxford University Press, New York
24. Weil J, Bolton J, Wertz J (1994) Electron paramagnetic resonance: elementary theory and practical applications. Wiley, New York
25. Foner S, Cochran E, Bowers V, Jen C (1960) Multiple trapping sites for hydrogen atoms in rare gas matrices. J Chem Phys 32:963–971
26. Eloranta J, Vaskonen K, Häkkänen H, Kiljunen T, Kunttu H (1998) 193 nm photodynamics of NO in rare gas matrices: fluorescence, thermoluminescence, and photodissociation. J Chem Phys 109:7784–7792
27. Eloranta J, Vaskonen K, Kunttu H (1999) Photogeneration of atomic hydrogen in rare gas matrices. J Chem Phys 110:7917–7925
28. Vaskonen K, Eloranta J, Kunttu H (1999) Trapping of laser-vaporized alkali metal atoms in rare-gas matrices. Chem Phys Lett 310:245–251
29. Vaskonen K, Eloranta J, Kiljunen T, Kunttu H (1999) Thermal mobility of atomic hydrogen in solid argon and krypton matrices. J Chem Phys 110:2122–2128
30. Adrian F (1960) Matrix effects on the electron spin resonance spectra of trapped hydrogen atoms. J Chem Phys 32:972–981
31. Schrimpf A, Rosendahl R, Bornemann T, Stöckmann HJ, Faller F, Manceron L (1992) Thermally activated processes in Li doped Ar matrices studied by electronic spin-lattice relaxation. J Chem Phys 96:7992–7999
32. Eloranta J (2011) Xemr – a general purpose electron magnetic resonance software. Available at: http://sourceforge.net/projects/xemr/files/. Accessed 7 Jul 2011
33. Kasai P, McLeod D Jr (1971) ESR studies of Cu, Ag, and Au atoms isolated in raregas matrices. J Chem Phys 55:1566–1575
34. Feldman V, Sukhov F, Orlov A (2008) Hydrogen atoms in solid xenon: trapping site structure, distribution, and stability as revealed by EPR studies in monoisotopic and isotopically enriched xenon matrices. J Chem Phys 128:214511
35. Jen C, Bowers V, Cochran E, Foner S (1962) Electron spin resonance of alkali atoms in inert-gas matrices. Phys Rev 126:1749–1757
36. Garland D, Lindsay D (1984) ESR spectra of matrix isolated Li_7 clusters. J Chem Phys 80:4761–4766
37. Thompson G, Tischler F, Lindsay D (1983) Matrix ESR spectra of polyatomic alkali metal clusters. J Chem Phys 78:5946–5953
38. Thompson G, Lindsay D (1981) ESR spectra of matrix isolated potassium atom clusters. J Chem Phys 74:959–968
39. Bach S, Garland D, Zee RV, Weltner W Jr (1987) Ag_7 cluster: pentagonal bipyramid. J Chem Phys 87:869–872
40. Zee RV, Weltner W Jr (1990) Cu_7 cluster: pentagonal bipyramid. J Chem Phys 92:6976–6977
41. Knight L Jr, Rice W, Moore L, Davidson E, Dailey R (1998) Theoretical and electron spin resonance studies of the H...H, H...D, and D...D spin-pair radicals in rare gas matrices: a case of extreme singlettriplet mixing. J Chem Phys 109:1409–1424

42. Cole T, McConnell H (1958) Zero field splittings in atomic nitrogen at 4.2 K. J Chem Phys 29:451–452
43. Jackel G, Nelson W, Gordy W (1968) Matrix perturbations of the ESR of trapped H, N, P, and As atoms at 4.2 K. Phys Rev 176:453–460
44. Boltnev R, Krushinskaya I, Pelmenev A, Popov E, Stolyarov D (2005) Study of the stabilization and recombination of nitrogen atoms in impurityhelium condensates. Low Temp Phys 31:547–555
45. Popov E, Gordon R, Khmelenko V, Martynenko M, Pelmenev A, Shidov E (1996) Cooperative effects in the low temperature optical and esr spectroscopy of atoms isolated in helium matrix. In: 2nd International conference on temperature chemistry, Kansas City, p 145
46. Knight L Jr, Bell B, Cobranchi D, Davidson E (1999) Electron spin resonance and theoretical studies of the $^{14}N\ldots{}^{14}N$ and $^{15}N\ldots{}^{15}N$ spin-pair radicals in neon matrices: the effects of mixing among the $^1\Sigma_g^+$, $^3\Sigma_u^+$, $^5\Sigma_g^+$, and $^7\Sigma_u^+$ electronic states. J Chem Phys 111:3145–3154
47. Kasai P (1968) Generation and trapping of charged species in rare-gas matrix at 4 K: ESR spectra of Cd^+, Cr^+, and Mn^+. Phys Rev Lett 21:67–69
48. Morton J, Preston K, Strach S, Adrian F, Jette A (1979) Anisotropic hyperfine interactions of raregas nuclei near trapped hydrogen atoms. J Chem Phys 70:2889–2893
49. Ammeter J, Schlosnagle D (1973) Electronic quenching of Al and Ga atoms isolated in rare gas matrices. J Chem Phys 59:4784–4820
50. Graham W, Weltner W Jr (1976) B atoms, B_2 and H_2BO molecules: ESR and optical spectra at 4 K. J Chem Phys 65:1516–1521
51. LB Knight J, Weltner W Jr (1971) ESR and optical spectroscopy of the AlO molecule at 4 K; Observation of an Al complex and its interaction with krypton. J Chem Phys 55:5066–5077
52. Boate A, Morton J, Preston K (1978) EPR spectrum of Kr_2F. Chem Phys Lett 54:579–581
53. Bhat S, Weltner W Jr (1980) ESR of matrix isolated bromine atoms produced in the $H+Br_2$ reaction. J Chem Phys 73:1498–1502
54. Iwasaki M, Toriyama K, Muto H (1979) Electron spin resonance of ^{127}I atoms trapped in Xe matrices. J Chem Phys 71:2853–2859
55. Woon D, Dunning T Jr (1994) Gaussian basis sets for use in correlated molecular calculations. IV. calculation of static electrical response properties. J Chem Phys 100:2975–2988
56. Nicklass A, Dolg M, Stoll H, Preuss H (1995) Ab initio energyadjusted pseudopotentials for the noble gases Ne through Xe: calculation of atomic dipole and quadrupole polarizabilities. J Chem Phys 102:8942–8952
57. Mcweeny R (1992) Methods of molecular quantum mechanics, 2nd edn. Academic, London
58. Jensen F (1999) Introduction to computational chemistry. Wiley, New York
59. Boys S, Bernardi F (1970) Calculation of small molecular interactions by differences of separate total energies – some procedures with reduced errors. Mol Phys 19:553–566
60. Berning A, Schweizer M, Werner HJ, Knowles P (2000) Spin-orbit matrix elements for internally contracted multireference conguration interaction wave functions. Mol Phys 98:1823–1833
61. Harriman J (1978) Theoretical foundations of electron spin resonance. Academic, New York
62. Anderson E, Bai Z, Bischof C (1999) LAPACK users' guide, 3rd edn. Society for industrial and applied mathematics, Philadelphia
63. Condon E, Shortley G (1970) The theory of atomic spectra. Cambridge University Press, Cambridge
64. Frigo M, Johnson S (2005) The design and implementation of FFTW3. Proc IEEE 93(2):216–231, special issue on "Program generation, optimization, and platform adaptation"
65. Du JL, Eaton G, Eaton S (1995) Temperature and orientation dependence of electron-spin relaxation rates for bis(diethyldithiocarbamato)copper(II). J Magn Reson A 117:67–72
66. Kirste B (1992) Methods for automated analysis and simulation of electron paramagnetic resonance spectra. Anal Chim Acta 265:191–200

Chapter 2
Organic Radical Cations and Neutral Radicals Produced by Radiation in Low-Temperature Matrices

Vladimir I. Feldman

Abstract Paramagnetic species produced by ionizing radiation in organic materials were studied extensively by EPR for 60 years. Using low temperature matrices made it possible to characterize a wide class of highly reactive radicals. More recently, the focus was shifted to the investigations of ionized molecules (radical cations). Several approaches based on frozen solution technique, trapping in porous media and rigorous matrix isolation method has been developed up to 1990s. The knowledge on structure and properties of radical ions is crucial for understanding fundamental processes in radiation chemistry and important for a number of various areas, including, radiobiology, physical organic chemistry and molecular electronics. This chapter presents a review of progress in the field during the past two decades with particular attention to the EPR studies of radical cations and radicals generated by high-energy irradiation of moderate-size organic molecules in solid noble gas matrices. The mechanisms and selectivity of the primary radiation-induced processes in organic solids are discussed with special impact on the role of "fine tuning" and matrix effects.

2.1 Introduction

Organic radicals and radical ions are the key reactive intermediates in a wide variety of chemical and biological processes induced by oxidising agents, heat, light, ionizing radiation, etc. Unstable radicals produced in thermal chemical reactions normally occur in very small concentrations, and their lifetimes are quite short (especially, in liquid phase), which limits direct detection of these species. Meanwhile, in the case of irradiation of organic solids and polymers, various-type

V.I. Feldman (✉)
Department of Chemistry, M.V. Lomonosov Moscow State University, Moscow, 11991, Russia
e-mail: vladimir.feldman@rad.chem.msu.ru

A. Lund and M. Shiotani (eds.), *EPR of Free Radicals in Solids II*, Progress in Theoretical Chemistry and Physics 25, DOI 10.1007/978-94-007-4887-3_2,

radicals and radical ions are easily produced and trapped in high concentrations, which makes it possible to investigate their structure and properties in detail. Probably, the first EPR study of organic radicals generated by high-energy radiation (X-rays) was reported in 1951 [1], so now we can celebrate 60 years of using EPR for characterization of the radiation-induced damage in organic materials. It is worthwhile noting that both EPR spectroscopy and radiation chemistry benefited greatly from these studies. Indeed, ionizing radiation has proved to be the most common tool to obtain various organic radicals, including highly reactive "high-energy" species, which can be hardly produced by other techniques. Many basic results concerning the structure and dynamics of free radicals were derived from the studies of irradiated systems. As an illustrative example, one can mention classical works on determination of proton hyperfine coupling tensors for aliphatic radicals trapped in irradiated single crystals [2]. On the other hand, high sensitivity and unique structural informativity of EPR spectroscopy gave invaluable help in elucidating the radiation-chemical mechanisms, and since the 1960s EPR was accepted as one of the basic experimental tools of radiation chemistry [3]. Extensive studies carried out during the first 30 years (1951–1980) resulted in dramatic progress in the field. In particular, the radicals trapped in different organic systems and polymers irradiated at 77 K were identified unambiguously, and the radiation-chemical yields were determined for a number of systems. A comprehensive review of the early work can be found in the book by Pshezhetskii et al. [4]. An important problem addressed (but not solved) in these studies is concerned with the possibility to differentiate primary radiation-induced chemical events from secondary reactions. At first, it was supposed that the secondary processes should be completely stopped in rigid media at 77 K. However, further experiments revealed that some reactions activated by local molecular motion in organic solids and polymers could occur well below this point [5–10]. Furthermore, although the EPR data on the radiolysis of organic systems at cryogenic temperatures (below 77 K) are still rather limited, it is clear that some primary radical species cannot be trapped even at lowest attainable temperatures. In general, it is suggested that the radical reactions occurring at very low temperatures are due to tunnelling phenomena. Meanwhile, in the case of radiation-induced radicals, one should also bear in mind possible involvement of "hot" or "unrelaxed" species.

At this point, it should be stressed out that even detection of "primary" neutral radicals resulting from dissociation of organic molecules is not sufficient to establish the basic mechanisms of radiation-induced damage. Actually, the *primary* event induced by radiation is ionization or electronic excitation rather than chemical bond rupture. The ionization process specific for high-energy radiation is generally favoured in condensed phases. An important role of ionic processes is clearly demonstrated by the observations of trapped electrons and radical anions in a number of irradiated organic systems [4]. Thus, from fundamental viewpoint, it is crucial to characterise the structure and reactivity of the primary ionized molecules, or radical cations. The radical cations are paramagnetic species, so they should be detectable by EPR. Nevertheless, most aliphatic radical cations were not observed in early studies. An obvious reason is extremely high reactivity of ionized aliphatic

molecules, which may undergo recombination with electrons, fast reactions with neighbouring neutral molecules, and "hot" fragmentation. In fact, none of these processes requires molecular diffusion, so the reactions of the primary radical cations cannot be stopped at low temperatures. To avoid the ion—molecule reactions, it is practicable to use matrix isolation, whereas the ion—electron recombination may be ceased in the presence of electron scavengers. A simple and efficient solution for the EPR studies of reactive radical cations, the so-called Freon matrix technique, was suggested by Shida and Kato in 1979 [11]. The method is based on irradiation of frozen solutions of organic substances in fluorinated halocarbons (mainly freons) at reasonably low temperatures (typically, 77 K). Detailed scheme, advantages and problems of the method will be discussed below. Extensive studies of a wide class of organic cations were carried out using this approach [12–14], and the up-to-date knowledge on electronic structure, geometry, and chemical properties of these species relies essentially on the data obtained in halocarbon matrices.

As a whole, up to early 1990s, the basic information on the structure of the radiation-induced paramagnetic species (radicals and radical ions) was available for many organic compounds and a number of important polymers (including macromolecules of biological interest). Nevertheless, general understanding the primary radiation-induced events in organic materials was still lacking. In particular, the following issues could be defined as major unresolved problems:

1. *The problem of localization*. Typically, molecular solids and polymers consist of molecules or units, which are chemically similar, but physically not exactly equivalent, because of conformation difference, variations in molecular interaction, packing, etc. The role of this dispersion in localisation of primary radiation-induced events is not clear.
2. *The problem of matrix effects*. Even in the case of chemically inert environment, the primary radiation-induced effects in solid media can be sensitive to the matrix nature, especially if we consider the relaxation and reactions of strongly interacting primary ionized molecules. However, the data on matrix effects on the early processes are rather ambiguous.
3. *The problem of excess energy* (involvement of "vibrationally hot" species). In general, it is assumed that the high-energy reaction paths involving "hot" species (vibrationally excited radical cations or radicals) are less significant in solids than in the gas phase. However, the formation of fragment radicals at low temperatures may imply effect of excess energy. The conclusions on this problem are speculative and not based on any direct experiment.
4. *The problem of selectivity*. Despite the intuitive reasoning on statistical primary bond rupture in "high-energy processes", the EPR data suggest non-random mode of radical formation. The interpretation is not straightforward since it is not easy to discriminate between primary and secondary events. The "selection rules" in the radiation chemistry of molecules in solids are still unclear.

It is worth noting that EPR spectroscopy is the most suitable experimental tool to shed a bit of light on these issues. Indeed, EPR spectra are quite sensitive to chemical structure and conformation of radicals and radical ions; matrix effects

can be often seen in magnetic parameters of the radical species. Although the EPR studies of the radiation-induced species during the past two decades were not as extensive as in early period, the results provide some important clues for basic problems outlined above. In addition, they have demonstrated new opportunities of using the radiation-chemical methods for detailed studies of structure, dynamics and reactivity of organic radicals and radical ions.

This chapter will present a review of results obtained mainly in the past 15 years with specific impact on experimental studies carried out in our laboratories. It will focus primarily on matrix isolation studies, but also include other kinds of relevant low-temperature works. The main goal is to show experimental basis of the matrix EPR experiments using high-energy radiation and to illustrate their potential for elucidation of the most spurious issues of solid-state radiation chemistry and related fields, with a large number of various implications (ranging from molecular electronics to biophysics and radiobiology).

2.2 Experimental Approaches and Overview of Results

2.2.1 Low-Temperature Radiation-Chemical Techniques for EPR Studies

Most commonly, the low-temperature EPR studies of radiation-induced radicals in organic solids are carried out at 77 K using standard equipment for irradiation and measurements, which is commercially available for tens of years. Meanwhile, as mentioned above, some chemical reactions of active species and local physical processes in matrices cannot be stopped at this temperature. Using "helium-range" temperatures (below 77 K) may be significant both for trapping of highly reactive intermediates and for visualisation of spatial distribution of the primary chemical events. Early EPR studies of the radiation damage in organic materials at very low temperatures (down to 1.5 K) were focused mainly on spatial distribution of the primary radicals, in particular, on the structure and dynamics of radical pairs produced by irradiation. Linear alkane crystals and polyethylene were the most popular objects in these works [5–10, 15–17]. In a few cases, it was possible to identify the radicals, which are unstable at 77 K (e.g., methoxy radicals in methanol [18]). An extensive work was made on DNA crystals irradiated at 4 K.[1]

Considering early studies from experimental viewpoint, one should note that the irradiation of organic crystals in ampules with X- or γ-rays was typically carried out in a liquid-helium bath (Dewar) at 4.2 K (or at even lower temperature, if the pump-out procedure was used [5]). The EPR measurements were made in the same Dewar at 4.2 K, or at higher temperatures (using liquid nitrogen Dewar or nitrogen-flow

[1]The results of the DNA-related studies are discussed in a separate chapter of this book.

Table 2.1 Mass absorption coefficients (in cm^2/g) for photons with E = 30 keV for some typical matrix media

H_2O	C_6H_{14}	C_2H_5OH	MTHF	$CFCl_3$	SF_6	Ar	Kr	Xe
0.156	0.0583	0.0971	0.0804	1.68	0.588	2.31	13.65	7.97

Calculated from the data presented in Ref. [25]

cryostat for the measurements at 77 K and above). Such an approach is somewhat limited, especially for detailed studies at intermediate temperatures (between 4 and 77 K); furthermore, it is not suitable for matrix isolation studies. A more versatile approach is based on using continuous-flow or closed-cycle helium cryostats operating in a wide temperature range. At present, the general-purpose helium-flow cryostats for the EPR measurements are commercially available and widely used in many laboratories. However, the cryostats for high-energy irradiation and EPR measurements under the conditions strictly avoiding intermediate heating of the sample are still custom-made devices used by a few groups. Most of these devices make use of X-ray radiation [19–21]. A different approach using fast electron irradiation produced by a Van-de-Graaf accelerator (typically, 1–1.2 MeV) has been developed at Karpov Institute [22–24]. One advantage of using fast electrons results from easy tunability of the beam parameters, i.e., electron energy and beam current. Thus, it is possible to tune the penetration depth and to vary the dose rate over a wide range. On the other hand, irradiation with X-rays is often more practicable because of easier experimental setup and opportunity of using local protection.

Beyond these technical features, one should bear in mind a basic *physical* difference in the energy absorption mechanisms between fast electrons and X-rays. In the case of fast electron irradiation, the absorption is mainly determined by inelastic collisions with the electrons of medium (ionization losses) and typically there is a rather weak effect of the chemical nature of absorber (at least, for materials used in matrix isolation studies). In other words, the absorbed dose is roughly similar for different substances irradiated under the same conditions. The same is also true for irradiation with γ-rays (high-energy photons with the energy of about 1 MeV), because the basic mechanism of photon interaction with matter in this energy range is Compton effect and the mass absorption coefficients for different substances are rather similar. However, in the case of X-rays with typical energy of 20–50 keV, the most important mechanism is photoelectric absorption and the absorber nature has dramatic effect on its cross-section. For most elements (except for H) the atomic absorption cross-section for photoelectric effect in this energy region is roughly proportional to Z^4 [3] (Z is atomic number of the absorber), provided that the photon energy is above K-edge. This means that the mass absorption coefficient increases approximately as Z^3 for heavier elements. The effect of heavy atom for irradiation of selected matrices 30-keV photons is illustrated by Table 2.1 (the data for different elements and photon energies may be found elsewhere [25]).

In practice, it means that, for instance, the dose in Freon-11 ($CFCl_3$) and in a hydrocarbon matrix may differ by more than an order of magnitude, when these matrices are irradiated with X-rays in the same geometry. This effect (often ignored

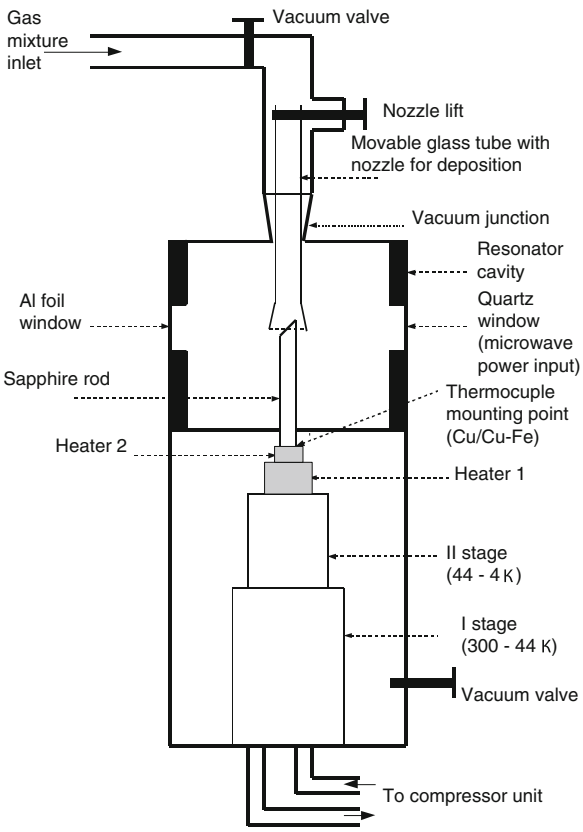

Fig. 2.1 Scheme of a custom-made closed-cycle cryostat for EPR matrix isolation studies of the radiation-induced species (Laboratory of Radiation Chemistry, Moscow State University, 2010)

in qualitative structural studies) should be definitely taken into account for proper planning of the experiment in terms of irradiation time and uniformity of dose distribution. The latter factor is especially important for heavy noble gases (the mass absorption coefficient of xenon is lower than that of krypton, because the K-edge for xenon lies above 30 keV). Indeed, due to huge mass absorption coefficient, the photons with energy of ca. 30 keV are mainly absorbed within the thin layer of krypton or xenon (200–400 μm) and the dose in this layer is quite high. As follows from experiments in our laboratory, a short-time exposure to X-rays often yields large amounts of trapped guest radicals in krypton and xenon matrices, whereas more prolonged irradiation is required for molecular media.

The EPR cryostat for matrix isolation studies used in our studies (Fig. 2.1) contains a cylindrical (H_{011} mode) vacuum resonator cavity. An early version designed at Karpov Institute was based on a continuous-flow scheme with the lowest attainable temperature of 8 K. The latest version of a portable cryostat used at present in our laboratory is based on a closed-cycle cryocooler (the sample temperature down to ca. 6 K) and can be applied for both X-ray and fast electron irradiation. A sample is obtained by slow controlled deposition of gaseous mixture onto the tip of a 4-mm cylindrical sapphire rod inserted into the cavity. There are

two options of rod tips: (a) a truncated conical tip, which corresponds naturally to the symmetry of the resonator cavity and (b) a cut-off at 45° (more suitable for photobleaching experiments). If the deposition is slow enough and the nozzle comes close to the tip, the shape of the growing sample follows the tip shape. In this case, the paramagnetic species produced in the sample show essentially random orientation in macroscopic scale. For this reason, the effect of preferential orientation often observed in the spot-like samples obtained on a flat rod [26] is of minor importance, especially for the samples prepared on the truncated conical tip. After the deposition is complete, the sample is irradiated with X-rays or fast electrons through an aluminium foil window, and then the cavity is connected to the microwave bridge of spectrometer.

2.2.2 Matrix Isolation for Radiation Chemistry

Matrix isolation is a widely used experimental approach for the studies of highly reactive intermediates. In general, it implies trapping of a reactive species in a rigid, chemically inert environment at low temperature. Classic procedure makes use of deposited matrices obtained mainly from noble gases; however, "compromise" techniques using dilute frozen solutions are also often referred to as matrix isolation methods. Meanwhile, the matrices used for the EPR studies of radiation-induced radicals and radical cations should meet a number of specific requirements. First, the matrix substance should have relatively high ionization and/or excitation potential. Indeed, the high-energy radiation is absorbed primarily by matrix, and the species from guest molecules are produced only by positive hole or excitation transfer. Second, as mentioned above, trapping of the primary radical cations is possible only in the presence of electron scavengers, which blocks ion—electron recombination. Third, the EPR spectra of paramagnetic species produced by matrix radiolysis should not overlap with the spectra of radicals under study (ideally, the matrix should yield no paramagnetic species under irradiation). Finally, the magnetic interactions of trapped radical with matrix nuclei should be negligible (the best choice is matrix without magnetic nuclei). These requirements result in significant restriction in the choice of suitable matrices for the radiation-chemical studies. Nevertheless, a number of approaches have been developed to overcome the above-mentioned limitations.

2.2.2.1 Low-Temperature Organic Glasses

Molecular glasses stable at 77 K (e.g., branched alkanes, MTHF, methylcyclohexane, alcohols and alkyl halides) have been used as matrices for optical spectroscopic studies of structure and photochemistry of organic radicals produced by different methods [27]. Using glassy matrices was found to be especially valuably for investigations of trapped electrons and radical anions [14]. In general, these media

are less suitable for the EPR studies of radical cations and neutral radicals produced by radiolysis, because the matrix radicals yield quite intense and complicated EPR signals. Among a few examples, it is possible to mention identification of the EPR signals of radical cations of tetramethylethylene and some long-chain alkanes with relatively low ionization potentials in 3-methylpentane and 3-methylhexane glasses [28, 29]. The problem of background signal can be partially solved by using perdeuterated matrices. Indeed, the hyperfine coupling constants for deuterons are 6.51 times smaller than the corresponding values for protons, so the EPR spectra of perdeuterated radicals show much smaller total spread. For this reason, the outer lines of the species produced from protiated solute molecules can be easily detected in perdeuterated glassy solvents. Such an approach was used for the studies of hydrogen atom abstraction from guest alkane molecules in glassy perdeuterated alcohols [30].

2.2.2.2 Freon Matrices

Freons are chemically inert fluorinated halocarbons widely used in general-purpose technologies. Actually, the "Freon matrix technique" is a modification of the halocarbon method for optical spectroscopic studies of radical cations suggested by Shida and Hamill [32]. As mentioned in Introduction, application of freons to the EPR studies of radiation-induced radical cations has been uniquely successful. General scheme of production of organic radical cations in the most popular matrix, Freon-11 (fluorotrichloromethane), may be represented as follows:

$$CFCl_3 - \bigwedge\!\!\bigwedge \rightarrow CFCl_3{}^{+\cdot} + e^- \tag{2.1}$$

$$CFCl_3^{+\cdot} + RH \rightarrow CFCl_3 + RH^{+\cdot} \tag{2.2}$$

$$CFCl_3 + e^- \rightarrow (CFCl_3{}^{-\cdot}) \rightarrow CFCl_2^{\cdot} + Cl^- \tag{2.3}$$

Here symbol "-⋀⋀->" denotes the action of ionizing radiation, and RH is a solute organic molecule. The problem of background EPR signal from matrix radicals is not crucial, because fluorinated radicals yield very broad and weak signals in macroscopically disordered media due to large anisotropy of ^{19}F hyperfine coupling. Other popular matrix substances are the isomers of trifluorotrichloroethane (Freon-113), mainly $CFCl_2CF_2Cl$ and CF_3CCl_3. The former matrix is especially useful for the studies of ion–molecule reactions, whereas the latter one may be helpful for investigation of unimolecular transformations of the radical cations. The mixture of CF_2BrCF_2Br (Freon-114B2) and Freon-11 suggested for optical studies [33] was also used in combination with EPR. In addition to freons, some other fluorinated compounds (in particular, perfluoroalkanes and SF_6) were applied for the EPR studies of radical cations.

The "golden age" in Freon matrix studies is associated with the 1980ths, and comprehensive reviews in the field are available [12–14]. Here I have to mention in short some later results (not covered in early reviews).

Identification of a large number of hydrocarbon radical cations was made in early works; meanwhile, new data became available during the past two decades. Despite the extensive studies of linear alkane radical cations in halocarbon matrices in the previous period, the discussion on the structure of these species is not closed, and some additional experimental and theoretical arguments have been presented [34, 35]. The peculiarities of ion–molecule reactions of the linear alkane radical cations occurring in alkane aggregates in frozen halocarbon solutions were studied by Ceulemans et al. [36–38]. EPR spectra of radical cations of some branched alkanes have been characterised in various Freons [39].

Several studies were concerned with the structure and reactions of the radical cations of unsaturated hydrocarbons, namely, long-chain linear alkenes (pentenes, hexenes and octenes) [39–43] and terminal alkynes [44]. Recently, the EPR spectrum of a branched terminal alkyne (3,3-dimethylbutyne-1) was first reported in freonic matrices [45]. An interesting feature of these species is remarkable weakening of a specific C—H bond in one of the methyl groups, which results in a very large hyperfine coupling constant for a corresponding γ-proton (3.0 mT) and may lead to specific reactivity. The radical cation of vinyl cyclopropane (VCP) and other C_5H_8-related species has been studied extensively in various Freon matrices [46, 47]. The reactions of primary and distonic radical cations produced from VCP are quite sensitive to environment, which leads to a very diverse chemistry, depending on the experimental conditions.

A number of papers reported EPR and ENDOR studies of structure and rearrangements of bicyclic and polycyclic hydrocarbon radical cations in halocarbon matrices [48–54]. The application of the Freon matrix technique for general organic chemistry may be illustrated by a study of trimethylene methane radical cation produced from methylene cyclopropane [55] and comparative investigation of benzene and Dewar benzene derivatives [55a].

In the case of aromatic hydrocarbons, the main problem is precise determination and assignment of small hyperfine couplings. Recent progress is associated with the application of ENDOR. The latter technique made it possible to characterise in detail the structure of both monomeric and dimeric cations [56–58]. Also to be mentioned, the EPR studies revealed dramatic effects of halocarbon matrix nature on the conformation of some alkyl benzene radical cations [59, 60]. In addition, the Freon matrix technique was applied to characterize the structure of diphenylamine radical cation [61] and dimeric radical cations of partially fluorinated benzenes [62].

A number of recent investigations using halocarbon matrices were related to heteroatomic aliphatic radical cations. An interesting example is given by characterisation of structure and reactions of methyl *tert*-buty ether (MTBE) radical cation [63]. This cation shows a major hyperfine coupling of $a(3\ \mathrm{H}) = 3.3$ mT due to methoxy group protons, which is substantially smaller than the corresponding value for dimethyl ether ($a(6\ \mathrm{H}) = 4.2$–4.3 mT [64, 65]). Unlike the radical cations of linear ethers, the MTBE radical cation easily undergoes methane loss at the temperatures above 100 K. Another example is represented by the studies of structure and reactions of various-type amine radical cations (including alkylamines,

allylamines and propargylamine) [66, 67]. One feature of these works is real-time kinetic monitoring of reactions in the Freon matrices by low-temperature EPR spectroscopy (the data of this kind are still rather limited). It has revealed intramolecular rearrangements via a hydrogen shift in the primary radical cations to yield the corresponding distonic-type species, which may occur by both classical and tunnelling mechanisms (the latter is probably the case for 1,2-shift). Kinetic aspects of the intramolecular H-shift were also analyzed for lactone radical cations [68].

Several papers reported the studies of the radical cations of vinyl monomers and related compounds, including vinyl ethers [69–71], dihydrofuranes [70–74], dihydropyranes [75, 76], and acrylates [77]. The latter species appear to be of special interest in view of practical significance of acrylates and confusing data of early studies. It was shown that ionization of acrylates occurred from the nonbonding orbital of carbonyl oxygen, which implies small hyperfine couplings in the primary cation yielding a broad unresolved singlet in the EPR spectra. The primary species easily undergo intramolecular H transfer (in the case of ethyl acrylate, the transformation starts at 40 K). Further reactions depend crucially on the matrix. In general, these studies provide a new insight into early stages of the radiation-induced polymerisation of vinyl monomers initiated by radical cations.

During the past decade, Freon matrices were applied to investigate the structure of heterocyclic radical cation with two heteroatoms, which present a challenge from the viewpoint of structural chemistry and considerable interest for model purposes. These works included re-examination of the radical cations of 1,4-dioxane [76] and *s*-trioxane [78] and characterization of previously unknown species (the radical cations of piperazine, morpholine, thiomorpholine and thioxane [79]). The EPR and ENDOR studies supported by extensive DFT calculations have clearly shown that all the studied radical cations of 1,4-diheterocycles adopt chair (or distorted chair) conformations, so there are no reasons to consider boat structures with intramolecular σ*-bonding. In the cases of 1,4-dioxane, piperazine and thiomorpholine, the spin population is almost equally distributed between the two heteroatoms, whereas for morpholine and thioxane the unpaired electron is mainly located at nitrogen and sulphur atoms, respectively.

For the most recent example of application of the Freon matrix technique for detailed characterization of complex heteroatomic species, one can refer to a study on aromatic thioether radical cations [80]. Interestingly, in this case, spin and charge were found to be almost equally distributed between the sulfur atom and the adjacent phenyl ring (unlike that for other aromatic cations).

Also to be mentioned, some new studies were made on the radical cations of organometallic compounds [81].

The results of our studies on “bridged” bifunctional radical cations will be discussed in detail in Sect. 2.3.2 and an extensive work of Shiotani group on specific deuterium labelling to analyse the low-temperature dynamics of the radical cations in halocarbon matrices is presented a separate chapter of this book (Chap. 4 of Volume 1).

Recent development in the field of “Freon matrix technique” also included extensive application of this method to the photochemistry of the radical cations.

Early investigations of the phototransformations of organic radical cations in solid halocarbons used mainly optical absorption spectroscopy [82, 83], whereas the application of EPR was restricted to the qualitative "photobleaching" experiments and photochemical studies of some hydrocarbon cations [12–14]. Systematic quantitative determination of the kinetic parameters of the photochemical reactions of a series of aliphatic functional radical cations based on combination of EPR and electronic absorption spectroscopy was made mainly in the past 15 years. The optical characteristics, quantum yields of decay and reaction products were determined for a number of various radical cations (including ethers and acetals, amides, alkanes, acetone and acetaldehyde). The results obtained before 2000 are summarized in a mini-review [84]. An important step for further studies was quantitative determination of optical and photochemical characteristics of the radiation-induced intermediates resulting from Freons [85]. More recently, this approach was applied to the radical cations of organotin compounds [86], and cyclic oxides and sulfides [87–89]. In general, these studies reveal three kinds of photoreactions of the radical cations: (i) "trivial pathway", i. e., photostimulated charge transfer to matrix followed by charge recombination, (ii) deprotonation, and (iii) specific reactions. The first channel is typically characterised by high quantum yields. It occurs in different freons, but shows maximum efficiency in a polycrystalline Freon-11 matrix. The proton loss occurring with much lower quantum efficiency (except for tetrahydrofuran and dimeric radical cations) can be revealed clearly in a sulphur hexafluoride matrix with high ionization potential, because the photoinduced charge transfer in this matrix is energetically unfavourable due to large "IP gap" (>5.5 eV). Such a process also may occur in some other media (e.g., in Freon-113); the nature of proton acceptor is not fully clear. Specific reactions (determined by chemical nature of the system under study) include fragmentation, intramolecular H transfer, ring cleavage, and other types of rearrangements. An unusual photochemical reaction, methyl group migration, was found for the radical cations of methyl *tert*-butyl ether [63] and 3,3-dimethylbutyne-1 [45].

In summary, the "Freon matrix technique" has played a very important role in the studies of radiation-induced radical cations, and it is still of certain potential value due to its simplicity and versatility (some examples will be shown below). Meanwhile, this approach suffers from several significant limitations:

- in fact, this method is *not a true matrix isolation technique.* Indeed, the typical procedure makes use of frozen solutions. The microstructure of these samples is unknown, and the aggregation of solute molecules cannot be excluded. Furthermore, the concentrations of guest molecules are often quite high (typically, 1 mol%, or even higher), so, in general, the assumption of isolation is invalid;
- the assumptions of "matrix inertness" and "low disturbance" for freons are questionable. Although irreversible chemical reactions of radical cations with these matrices were not observed, the formation of strong matrix—cation complexes was detected for in a number of cases [12];
- frozen halocarbon solutions, which seem to be excellent media for the EPR studies, are not so attractive for UV/VIS absorption studies because of strong

scattering (except for glassy Freon mixture matrix); they are even less suitable for IR spectroscopy due to intense absorption in the low-frequency region.

In order to overcome some of these limitations, we suggested to use matrix deposition technique for EPR and optical spectroscopic studies in halocarbon matrices [23]. However, in any case, one should look for some alternative (or complementary) approach to answer a number of basic issues.

2.2.2.3 Zeolites and Other Porous Media

The idea of using inorganic sorbents as matrices for the EPR studies of paramagnetic species produced from organic molecules by ionizing radiation was first tested for benzene adsorbed on silica gel more than 40 years ago [90], which led to identification of monomeric and dimeric benzene radical cations. However, the application of silica gel was probably limited to the studies of simple aromatic radical cations [91, 92]. A crucial step was turning to specific cavity-type hosts, namely, synthetic zeolites [93, 94]. In principle, the scheme of formation of radical cations in zeolites is similar to that given above for the halocarbon matrices; the nature of electron traps in this case is not fully clear. The basic difference between the radical cations trapped in halocarbon matrices and zeolites results from the fact that the cages (trapping sites) in zeolites have regular, well-defined geometry. Both trapping and reactions of radical cations in zeolites occur in a completely rigid environment. Extensive EPR studies of structure and reactions of hydrocarbon radical cations produced by γ-irradiation in zeolites[2] were made by the Argonne group (one may refer to reviews [95, 96]). The most popular matrices used for these studies were zeolites of ZSM family (mainly, ZSM-5). Other hosts tested were X, Y and Beta zeolites, mordenite, silicalite, and MCM-41 molecular sieve. Also to be mentioned, the studies of dynamics of amine radical cations produced by radiolysis in zeolites have been reported [97].

In general, zeolites are less suitable for specific studies of the structure of organic radical cations than halocarbons. For example, the radical cations of n-hexane and n-octane were stabilized in a ZSM-5 zeolite only at 4 K [96], whereas smaller alkane cations were not detected at all. The same problem occurs with the radical cations of small alkenes [96]. Furthermore, an attempt to observe the EPR spectra of radical cations produced by irradiation of many organic molecules (e. g., ethers or esters) in zeolites failed, probably, due to secondary reactions [96]. The stability of radical cations and neutral radicals produced in zeolites depends strongly of the size of guest species. Small paramagnetic species often decay rapidly even at 77 K, whereas larger radicals and radical cations may be observed at 200 K or above. On the other hand, large cations cannot be accommodated in the pores of ZSM-5, and

[2]It should be noted that radical cations and radicals in zeolites can be also produced from some organic molecules due to chemical or photochemical one-electron oxidation; these processes are not considered in the present chapter.

their trapping requires using the zeolite hosts with larger cage size (e.g., mordenite) [95, 96]. These "size effects" resulting from size-dependent molecular diffusion and geometrical constraints reveal both limitations and advantages of zeolites. As to the latter, one should note that the EPR spectra of radicals in zeolites typically show better resolution than in halocarbon hosts. This result is understandable in view of larger pore size in zeolites, which allows more rotational freedom for small guest species. Geometrical constraints also play an important role in selection of reaction channels in zeolites. Thus, zeolites can be described as "microreactors" with tunable pore size, polar interactions and acidity [95, 96].

Formation of radical cations is not the only process occurring upon radiolysis of hydrocarbon molecules adsorbed in zeolites, because of the importance of formation of H adducts for olefins, dienes and aromatic molecules [98].

Generally speaking, zeolites are fascinating matrices for the EPR studies of structure and dynamics of some radical cations and neutral radicals. Furthermore, radiolysis of adsorbed molecules in zeolites provides a powerful tool for designing "spin probes" of adsorption and valuable models for heterogeneous catalysis [96]. However, a wide-scale application of zeolites for basic studies of the radiation-induced processes in solids is questionable because of a lot of complications resulting from inhomogeneous adsorbate distribution, strong chemical interactions, etc.

2.2.2.4 Solid Noble Gas Matrices

Solid noble gases are classical media for matrix isolation studies, which have been used extensively for spectroscopic characterization of highly reactive intermediates for several decades. In particular, organic radical cations (mainly, of aromatic and conjugated systems) were widely studied in noble gas matrices by optical absorption spectroscopy [82, 83, 99]. A number of neutral organic radicals produced by different techniques (i.e., photolysis, pyrolysis, glow discharge, or chemical reactions) were characterized in solid argon and neon by EPR since the 1960s [100]. Meanwhile, up to recently, the application of solid noble gas matrices to the EPR investigations of paramagnetic species produced by the solid-state radiolysis was limited. First EPR studies of methane radiolysis in solid argon, krypton and xenon at 4.2 K reported by Bouldin and Gordy [101] used frozen solution technique ("ampule method") rather than the classical matrix isolation procedure. Several other groups applied the same technique to radiolysis of larger hydrocarbons in solid noble gases [102–104]. Obvious limitations of this method are concerned with aggregation of solute molecules, which is especially important for noble gas matrices since the solute—solute interactions are much stronger than the solute—matrix interactions. More recently, Qin and Trifunac reported the EPR spectrum of 1,1,2,2-tetramethylcyclopropane radical cation in a frozen xenon solution containing Freon-113 as an electron scavenger at 77 K [105]. To my knowledge, it was the only EPR observation of a large organic radical cation in solid noble gas matrices before 1996.

Rigorous matrix isolation technique was applied by Knight and co-workers for the studies of inorganic and small organic radical cations in neon matrices (see Refs. [106, 107] for review; recent results concerning organic cations may be found in Refs. [20, 26, 108–110]). Early studies of this group used a number of different techniques for generation of radical ions *during* the matrix deposition (in-situ photoionization, electron bombardment, pulsed laser and discharge treatment) [106, 107]. Meanwhile, it was found later that the X-ray radiolysis of solid deposited matrices was quite effective for producing of organic radical cations in high concentrations [20, 26]. Using neon as a matrix material made it possible to characterise the radical cations generated from small molecules with high IP (e.g., methane and methanol), which cannot be produced in halocarbon matrices. In some other cases (e.g., for acetaldehyde), the neon matrix provides a benefit of superior resolution of the EPR spectra (in comparison with freons). However the matrix isolation studies of organic radical cations in neon were restricted to a few small species (maximum, two carbon atoms). Other applications of this matrix for EPR studies of the species produced by solid-state radiolysis included investigations of small organometallic compounds [110].

Somewhat surprisingly, up to recently, the radiation-induced radical cations were not characterized by EPR in solid argon, which is the most common medium for matrix isolation studies. Attempts to produce very small cations in argon were reported to be unsuccessful [20, 26], whereas this matrix was not applied for the studies of larger species. Investigations of the X-ray radiolysis of several small molecules (in particular, methane) in argon [21] were concerned mainly with the studies of the low-temperature dynamics as considered in Chap. 4 of Volume 1 of this book.

Some 15 years ago we started an experimental program aimed at characterization of intermediates resulting from irradiation of various organic molecules in solid noble gas matrices. In contrast with the work of other groups, our main interest was focused on chemical aspects rather than spectroscopic or molecular dynamics problems. The experimental technique and apparatus used for these studies are described above.

The first experiments with heptane in a xenon matrix [23, 24, 111] revealed that irradiation of solid deposited mixtures (mole ratio of 1: 400 to 1: 1,000) yields nearly balanced amounts of trapped hydrogen atoms and alkyl radicals. Addition of an electron scavenger results in dramatic drop in the yield of hydrogen atoms, whereas the spectrum of neutral alkyl radicals is replaced by the spectrum of radical cation (known from previous studies in halocarbon matrices [12–14]). These observations may be rationalized in the frame of simple scheme [24, 112]:

$$\mathrm{Ng}\text{–}\!\bigwedge\!\!\bigwedge \rightarrow \mathrm{Ng}^{+\cdot} + \mathrm{e}^{-} \tag{2.4}$$

$$\mathrm{Ng}^{+} + \mathrm{RH} \rightarrow \mathrm{Ng} + \mathrm{RH}^{+\cdot} \tag{2.5}$$

$$\mathrm{RH}^{+} + \mathrm{e}^{-} \rightarrow \mathrm{RH}^{*} \rightarrow \mathrm{R}^{\cdot} + \mathrm{H}^{\cdot} \tag{2.6}$$

Here Ng denotes a noble gas atom, and RH^* is an excited organic molecule. In the presence of an electron scavenger S, the ion—electron recombination (2.6) is ceased, and the radical cation is trapped in the matrix:

$$S + e^- \rightarrow S^{-\cdot} \tag{2.7}$$

$$RH^{+\cdot} \rightarrow RH^{+\cdot}(tr) \tag{2.8}$$

Formal meaning of reaction (2.8) is *trapping (stabilization)* of the radical cation in matrix. It implies that the primary radical cation resulting from the positive hole transfer is in "unrelaxed" state (the sense of this difference will become clear from the later discussion). A strong effect of electron scavenger clearly suggests that the main primary process is positive hole transfer rather than excitation transfer. Further studies [113–119] have shown that the scheme given above should be basically valid for different organic molecules in solid noble gases. Indeed, in the absence of an electron scavenger, the yields of trapped radicals and hydrogen atoms were nearly balanced (in the case of xenon) or, at least, comparable (for argon and krypton matrices).[3] In all the cases, addition of electron scavengers resulted in drastic decrease in the yield of trapped H atoms (by one or two orders of magnitude). This effect may be used as criterion of electron scavenging (with Freons, high efficiency was achieved at low scavenger concentration, typically 0.1–0.2 mol%). Using Freons as electron scavengers is beneficial for spectroscopic reasons mentioned above. It should be noted that addition of scavenger was found to be vitally important for observation of the radical cations. Meanwhile, even in the presence of scavengers, the relative yields of trapped radical cations for some systems were low (or even zero). As the "hydrogen atom criterion" was met, the lack of radical cations should not be attributed to low efficiency of electron scavenging. Moreover, the composition of radicals resulting from organic molecules is often changed in the presence of electron scavengers. Thus, the most reasonable explanation implies reactions of "unrelaxed" radical cations before trapping, or in competition with trapping:

$$RH^{+\cdot} \rightarrow \text{products} \tag{2.9}$$

Essential characteristics of the noble-gas matrices are given in Table 2.2. From the spectroscopic point of view, argon appears to be the most suitable matrix for the EPR studies of moderate-size radicals and radical ions, because natural argon contains no isotopes with magnetic nuclei ($I \neq 0$). As a result, the EPR spectra

[3] In principle, dissociation of excited molecules may also yield the products of skeleton bond rupture. However, the probability of escape from the matrix cage is much lower for heavier fragments.

Table 2.2 Physical characteristics of solid noble gas matrices significant for EPR studies of the radiation-induced radicals

Matrix	Melting point, K	Operating temperature range, K	IP, eV	Polarizability, nm^3	Magnetic nuclei
Ne	24.6	Up to 11	21.56	$4 \cdot 10^{-4}$	^{21}Ne ($I = 3/2$, 0.27%)
Ar	84	Up to 39 – 42	15.75	$1.64 \cdot 10^{-3}$	No
Kr	116	Up to 60	14	$2.48 \cdot 10^{-3}$	^{83}Kr ($I = 9/2$)
Xe	164	Up to 90 – 100	12.13	$4.16 \cdot 10^{-3}$	^{129}Xe ($I = 1/2$, 26.44%); ^{131}Xe ($I = 3/2$, 21.18%)

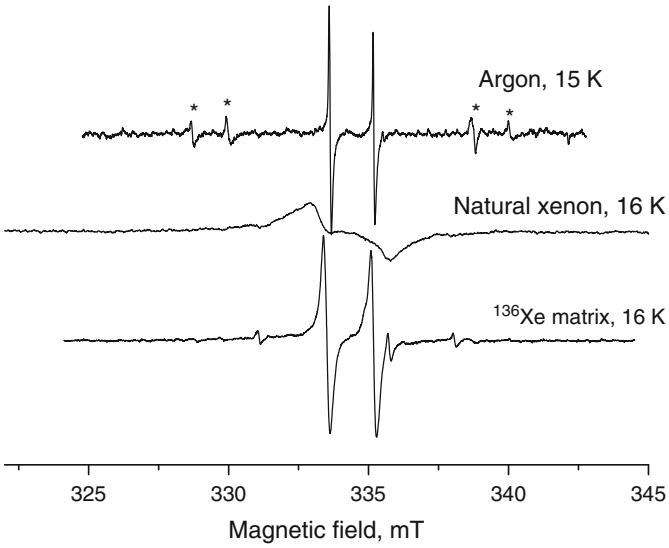

Fig. 2.2 Effect of matrix magnetic nuclei on the EPR spectra of ethynyl ($^{\cdot}C_2H$) radical obtained by irradiation of acetylene in solid argon and xenon (asterisks show the signals from vinyl radical)

in solid argon are often well resolved and exhibit sharp lines (see however, Sect. 2.4.1). A common shortcoming of argon matrix results from limited range of thermal stability (see Table 2.2).

On the other hand, a xenon matrix offers much wider temperature range, which makes it possible to study dynamics and reactions of the trapped radical species. The problem is that natural xenon contains large amounts of magnetic isotopes: ^{129}Xe (I=1/2) and ^{131}Xe ($I = 3/2$). This often leads to severe broadening of the EPR signals from trapped radicals, which means significant loss in resolution and sensitivity. In order to overcome this limitation, recently we suggested to use a specific isotopically pure non-magnetic xenon matrix of ^{136}Xe ($I = 0$) [120, 121]. In fact, this matrix can be described as an "argon-like xenon" from the viewpoint of EPR. Indeed, its magnetic properties are similar to those of argon, as illustrated by Fig. 2.2, but it is still xenon in terms of other properties.

It should be noted that using the ^{136}Xe matrix (instead of natural xenon) provides not only superior spectral resolution, but also a largely enhanced sensitivity (in certain cases, almost by two orders of magnitude, taking into account that the amplitude of the first-derivative EPR signal is inversely proportional to the square linewidth). The ^{136}Xe matrix has been used to get high-resolution EPR spectra of ethynyl and vinyl radicals over a wide temperature range [120]. This approach (in combination with controlled matrix doping with small amounts of magnetic xenon isotopes) was also applied for detailed assignment of the trapping site structure for radiolytically produced H atoms in xenon and elucidation of their spatial distribution and stability [121].

In summary, matrix isolation in solid noble gases in combination with EPR detection offers wide opportunities for basic studies of the primary radiation-induced processes in solids. Using these matrices makes it possible to study the reactions of both ionized molecules (radical cations) and neutral excited molecules. It is worthwhile noting that physical characteristics or the noble gas matrices (ionization potential, polarizability, rigidity) vary over a wide range when turning from neon to argon, krypton and xenon, which allows one to follow the most general matrix effects. The main disadvantage of this method is concerned with complex experimental procedure and relatively high cost of the equipment for matrix isolation studies.

2.2.3 Combination with Other Spectroscopic Methods

Obviously, as we are concerned about paramagnetic species, EPR is a very powerful structural method and a valuable kinetic tool. However, important information on the whole radiation-induced process is missing, if EPR is used as the only spectroscopic probe. Indeed, EPR is "silent" about the diamagnetic species (both neutral and charged). In particular, it gives no information on the state of parent molecule in the matrix prior to irradiation, which may be quite important for solid-state processes. Furthermore, one cannot estimate overall efficiency of a radiation-induced process from EPR data, so there is a chance that the observed formation of paramagnetic species represents only a minor channel.

The most widely used complementary method for the low-temperature studies of the radiation-induced species is electronic absorption (UV/VIS) spectroscopy. In the case of good absorbers, the sensitivity of this method is comparable to EPR. A combination of EPR and UV/VIS spectroscopy has been applied extensively to identification of radical cations and investigation of the photochemical reactions of the radiation-induced radicals (both neutral and charged) [27, 83, 84]. In certain cases, using electronic absorption spectroscopy also allows to follow the formation of diamagnetic ions and some molecular products. However, it should be noted that the electronic absorption spectra of radical ions in solid matrices typically exhibit broad featureless bands, which give no detailed structural information. Moreover,

the absorptions of neutral aliphatic radicals are often not characteristic, and the parent aliphatic molecules typically absorb only in the far UV region. Thus, being a valuable kinetic method (especially, for photochemical studies of the radiation-induced intermediates), UV/VIS spectroscopy is not very helpful for the problems outlined above.

The IR (vibrational) absorption spectroscopy offers an opportunity of getting rich structural information on different-type species, regardless of their magnetic properties. Using this method may allow one to characterise the state of parent molecule in the solid matrix in great detail, including conformation, molecule—matrix interactions and association. Often it is supposed that the main drawback of IR spectroscopy as applied to the studies of intermediate species is relatively low sensitivity of this method. However, this problem is not so crucial when using modern FTIR spectrometers, which provide high signal-to-noise ratio and fast scan speed. In particular, we have shown that it is possible to obtain the EPR and IR spectroscopic characteristics of radiolytic intermediates using the same dose range, which makes valid direct comparison of the results.

In general, a combination of EPR and FTIR spectroscopy is an important part of our experimental strategy in the studies of the radiation-induced processes in low-temperature matrices [23]. First, it was applied to the studies in halocarbon matrices [23, 42, 122]. This made it possible to obtain direct evidence for strong interaction between freon and solute molecules and gave indications of the IR features of the radiation-induced cations. The main problem is concerned with the meaning of "combination". In early studies [122] we just used a comparison between IR spectra obtained for deposited matrices and EPR data obtained by a conventional "ampule" (frozen solution) technique. Certainly, the validity of this approach is not evident, so later we turned to rigorous matrix isolation procedure (deposition technique) for both EPR and IR studies. In particular, this method was applied for the studies in noble gas matrices [23]. At present, the "combination" used in our laboratory implies obtaining the matrix samples in two cryostats from the same gaseous mixture with the same deposition system followed by irradiation with fast electrons or X-rays from the same source. Our cryostat for FTIR studies of electron irradiated matrix samples is described in detail elsewhere [22, 23]. Using FTIR spectroscopy allowed us to obtain the first direct estimate of overall efficiency of the radiation-induced transformation of guest molecules in noble gas matrices by measuring the intensity of IR absorptions of the parent molecules before and after irradiation. It was found [113, 123] that the total radiation-chemical yields of consumption of organic molecules in solid argon and xenon were quite high. Thus, the overall "energy transfer" (i.e., positive hole and excitation transfer) from noble gas matrices to the guest molecules is very effective, even at high dilution. Also, the FTIR studies revealed significance of non-radical paths in the radiation-induced degradation of organic molecules in solid noble gases (e.g., formation of olefins and methane from n-alkanes [123]).

Probably, the most challenging issue for the above-mentioned combination is assignment of the vibrational features of radicals and radical ions from comparison between the EPR and FTIR data. Direct experimental information on vibrational

spectra of organic radicals and radical ions in condensed phase is still rather limited in comparison with the EPR data (particularly, for polyatomic species) and EPR can be used as a reference tool. Such an approach was applied for investigation of thermally and photochemically produced radicals [124]. Recently, our version of EPR/FTIR combination was applied to characterisation of vibrational features of vinyl (C_2H_3·) and cyclohexadienyl (C_6H_7·) radicals in solid noble gas matrices [125, 126]. In the latter case, comparison with EPR, allowed us to assign tentatively six bands in the IR spectrum of cyclohexadienyl radical, which was previously unknown. Generally speaking, vibrational characteristics of radicals and radical ions are directly related to the bond properties, so they may give essential information for prediction of their chemical reactivity. There is still a large room for future work in this field, particularly for aliphatic radical ions.

2.3 Positive Hole Migration and Localization

Ionization of complex molecules in condensed phases is followed by a series of physical phenomena, including intermolecular and intramolecular migration of positive hole, conformational relaxation, etc. These fast processes typically occur before the first chemical step and they are of great significance for such fields as radiation chemistry, radiobiology, and molecular electronics. The time-resolved methods based on detection of optical absorption, luminescence or microwave conductivity are used for characterization of positive hole dynamics, but, in most cases, they do not provide any structural details. The low-temperature EPR spectroscopy is particularly helpful in this aspect since it shows detailed image of a trapped hole in molecular system. This sub-section presents the results of application of EPR spectroscopy for characterization of positive holes in two kinds of model systems, which reveal intermolecular and intramolecular effects.

2.3.1 Trap-to-Trap Positive Hole Transfer in Solid Matrices

The significance of distant positive hole transfer in low-temperature matrices (e.g., frozen halocarbons and solid noble gases) is well illustrated by high yields of guest organic radical cations under matrix isolation conditions. Specific interest is concerned with the case, when different traps with relatively close ionization energies are distributed in a rigid matrix. This seems to be a typical model of organic solid or polymer taking into account occurrence of different-type structural defects, chemical impurities, etc.; it can be also applied to heterogeneous systems (e.g., zeolites with adsorbed organic molecules). The questions are as follows: (i) what is the minimum "driving force" (ΔIP) for a distant trap-to-trap hole transfer? and (ii) what is the role of specific solid-state effects (i.e., the difference in conformation, molecular interactions, etc.) ?

2.3.1.1 Two-Trap Model

An indication of the occurrence of trap-to-trap hole transfer between organic solute molecules upon radiolysis in solid halocarbons was reported by Toriyama and Okazaki [127]. A simple quantitative model for analysis of this phenomenon was suggested recently by Werst et al. [128]. It implies irradiation of the frozen halocarbon solutions containing simultaneously two kinds of dissolved organic molecules at 77 K. If the EPR spectra of the radical cations resulting from the two solutes are substantially different, it is possible to determine the relative contributions of these species from computer simulation or additive least-square analysis. The bias in final population of the two "hole traps" can be expressed as $R_{mn} = (S_m/S_n)\cdot(N_n/N_m)$ [128]. Here indices *m* and *n* are related to the two solutes, $S_{m,n}$ denote the corresponding integrated intensities of the EPR signals (proportional to concentrations of the radical cations), and $N_{m,n}$ are the concentrations of parent neutral molecules. In principle, the bias in favor of the low-energy trap ($R_{mn} > 1$) may result either from different efficiency of the primary hole trapping or from trap-to-trap hole transfer. The former factor can be estimated by comparison of the radiation-chemical yields of the radical cations obtained in a usual ("single-trap") experiment. In general, the yields of radical cations in halocarbons may vary by a factor of up to 3, however, these values are rather close for solutes of similar chemical nature. The latter is most probably true for olefins and dienes used for the two-trap studies [128]. Anyway, the bias found for some pairs in a $CFCl_3$ matrix was so high (up to 10^3), that the dominating role of the trap-to-trap transfer was quite evident. The study of the concentration dependence made it possible to estimate the characteristic distance of hole transfer as 2–4 nm, which is supposed to be due to a single-step tunnelling.

A similar-type trap-to-trap positive hole transfer was observed in our studies of saturated functional molecules [129]. In particular, a rather effective transfer ($R_{mn} \sim 6$) was found for the system dimethyl ether–acetone ($\Delta IP = 0.33$ eV).

In addition to halocarbon matrices, the trap-to-trap hole transfer was also revealed in double loaded zeolites [128]. Meanwhile, in this case, the interpretation is complicated because of the effects of inhomogeneous adsorbate distribution and possible difference in the site energy.

2.3.1.2 Fine Tuning Effects in Positive Hole Transfer

Following the approach outlined above, recently we have applied the two-trap model to the analysis of the trap-to-trap hole transfer between benzene derivatives in different Freon matrices [60, 130]. Small difference in the gas-phase IP values (<0.5 eV) and similarity of the chemical structure of the traps warranted similar efficiency of the primary hole transfer from Freon to solutes. The total concentration of solute molecules was kept constant (1 mol%), whereas relative concentrations of the two traps varied by a factor of 5 to 10. The results are summarized in Table 2.3.

Table 2.3 Positive hole transfer between alkyl benzene molecules in Freon matrices [60, 131]

Solute molecule pair	Matrix	Direction of transfer	ΔIP_{gas}, eV	Controlling factor
Benzene/toluene (B/T)	$CFCl_2CF_2Cl$	B → T	0.43	ΔIP_{gas}
Toluene/ethyl benzene (T/EB)	$CFCl_3$	T → EB	0.06	Conformation
-"-	CF_3CCl_3	EB → T	−0.06	Conformation
Toluene/para-xylene (T/p-X)	$CFCl_2CF_2Cl$	T → p-X	0.38	ΔIP_{gas}
Para-xylene/metha-xylene (p-X/m-X)	$CFCl_2CF_2Cl$	No	0.12	–

In the case of pairs benzene/toluene and toluene/*para*-xylene, the results show distant hole transfer to a low-energy trap. Meanwhile, for pair *metha*-xylene/*para*-xylene ($\Delta IP \sim 0.12$ eV), bias in the trap population was not found ($R_{mn} \sim 1$).

The most interesting result was obtained for the pair toluene/ethyl benzene [131]. In this case, the gas-phase IP difference is quite small (ca. 0.06 eV), so it cannot provide sufficient "driving force" for the hole transfer. On the other hand, our studies revealed that ethyl benzene radical cation could be trapped in different conformations, depending on the Freon matrix used [5]. Conformer I with the hyperfine coupling constants of $a(2H) = 2.85$ mT and $a(1H) = 1.28$ mT is observed in a $CFCl_3$ matrix. In view of well-known "$\cos^2\theta$ rule", in this case, methyl group lies in the plane of phenyl ring ($\theta_1 = \theta_2 = 30°$; θ_i is the dihedral angle between the C_β–H_i bond and unpaired electron orbital axis). Conformer II is observed mainly in a CF_3CCl_3 matrix (with small contribution from I). This species exhibits the hyperfine coupling constants of $a(2H) = 0.95$ mT and $a(1H) = 1.25$ mT, which implies $\theta_1 = \theta_2 = 60°$. Both conformers were found in a $CFCl_2CF_2Cl$ matrix [60]. Note that conformer II ("vertical") corresponds to the most stable configuration of the parent neutral molecule (minimum steric repulsion between methyl and phenyl groups). It can be trapped, if the matrix hinders relaxation. On the other hand, conformer I can be described as "relaxed" conformer. Apparently, the ionization energy for the two conformers in matrix should be different. In fact, we observed inversion in the direction of positive hole transfer for the pair toluene/ethyl benzene in different matrices. This result may imply that the ionization energy of toluene just falls in the "gap" between the ionization energies of the two conformers of ethyl benzene in matrix. Different solvation of the two conformers of radical cations probably plays crucial role since the difference in the gas-phase IP is very small. The observation of the conformation-controlled hole transfer seems to be the first evidence of the "fine tuning" effects in distant charge migration in a solid matrix.

The conformation effects may also account for low efficiency of the positive hole transfer between alkane and alkene molecules found in our later work [129].

In conclusion, our findings suggest that at relatively large IP differences (>0.2 eV for molecules of comparable size and shape) a distant positive hole transfer should lead to charge trapping and localization of the primary radiation-induced chemical event at the low-energy trap. Meanwhile, in the region of small IP gaps (typical for systems with "natural" trap dispersion, e.g., polymers), specific effects (conformation, formation dimers, matrix interactions) may be significant.

2.3.2 "Bridged" Bifunctional Radical Cations

The "bridged" bifunctional molecules of general structure X-$(CH_2)_n$-Y (X and Y are functional groups separated by *n* methylene groups) represent an interesting class of models for studying the intramolecular aspects of positive hole trapping and transfer. Recently, we made a systematic EPR investigation of a series of "bridged" radical cations [132–135]. Basic findings are summarized in Table 2.4.

In the case of symmetrical species (X = Y), one might expect either localized or delocalized state of the positive hole, depending on the "bridge" length and conformation. Our experimental and computational results [132] clearly show that short "bridged" diketone radical cations (X = Y = MeCO, $n = 0$–2) are characterized by symmetrical delocalization of the spin density between two carbonyl groups, which yield poorly resolved EPR spectra with small hyperfine coupling constants (Table 2.4). This delocalization probably explains low reactivity of the ground-state diketone radical cations towards deprotonation.

Another interesting example is given by the radical cations of 1,n-diphenylalkanes ("bridged diphenyls", X = Y = Ph) [136]. In this case, symmetrical delocalization of spin between the two phenyl ring, again giving small proton coupling constants, was found for $n = 2$ and 3. However, for 1,2-*para*-ditolylethane

Table 2.4 Magnetic resonance parameters and structure of "bridged" bifunctional radical cations obtained in a Freon-113 matrix

X	Y	*n*	ΔIP_{XY}, eV[a]	Type	Isotropic hfc, mT	References
CH_3CO	CH_3CO	0	0	Delocalized	<0.3 (unresolved)	[132]
CH_3CO	CH_3CO	1[b]	0	Delocalized	<0.3 (unresolved)	[132]
CH_3CO	CH_3CO	2	0	Delocalized	0.67 (2H)	[132]
C_6H_5	C_6H_5	2	0	Delocalized	<0.4 (unresolved)	[136]
C_6H_5	C_6H_5	3	0	Delocalized	~0.5 (poorly resolved)	[136]
p-CH_3-C_6H_4	*p*-CH_3-C_6H_4	2	0	Localized	3.1 (1H); 1.8 (3H); 1.5 (1H)	[136]
				delocalized	1.62 (2H); 0.68 (2H); 0.9 (6H)	
CH_3O	CH_3CO	1	0.33	Delocalized	2.3 (1H); 1.2 (3H)[c]	[133]
$CH_3OC(O)$	$(CH_3)_2$ NC(O)	0 – 4	1.0	Localized	3.1 (6H)[d]	[134]
$(CH_3)_2$ NC(O)	$(CH_3)_2$N	3	1.4	Localized	2.45 (6H); 3.64 (1H)[d]	[135]
CH_3O	$(CH_3)_2$ N	3	2.2	Localized	2.61 (6H); 3.73 (1H); 0.45 (1H)[d]	[135]

[a]See explanation in text
[b]Ketonic form (enolic form is a C-centered *p*-electron species [132])
[c]Another conformer (also with delocalized spin density) was found in a Freon-11 matrix
[d]The coupling with nitrogen nuclei is strongly anisotropic with $a\perp(N) \sim 0$

with methyl substituents introduced to a *para*-position of both phenyl rings[4] we have found primary stabilization of the state with spin density localized at one phenyl ring at 77 K, as evidenced by relatively large coupling constants with the protons of one methyl and one methylene protons (similar to those for alkyl benzene radical cations). Upon slight warming (up to ca. 105 K), this metastable state relaxes irreversibly to yield a stable delocalized state with reduced proton hyperfine coupling constants, which clearly demonstrates involvement of two methyl groups (Table 2.4). This effect of "switching" between localized and delocalized states of a "bridged" radical cation in a solid matrix seems to be of particular interest and may have a number of implications.

In the case of non-symmetrical molecules ($X \neq Y$), the positive hole localization should be determined by the electronic properties of functional groups. In a rough approximation, one can use provisional values of ΔIP_{XY} (given in Table 2.4) defined as the IP difference for the corresponding monofunctional prototype molecules (e.g., dimethyl ether and acetone for etherketones). If the ΔIP_{XY} value is small enough (as for methoxyacetone [133]), the radical cation exhibits substantial (although non-symmetrical) delocalization of the spin density between functional groups.

Meanwhile, for a rather large ΔIP_{XY} (at least, 1 eV and above), major spin population is associated with the functional group with lower IP, independent of the bridge length (a "localized hole"). This situation was studied in detail for the substituted "bridged" amidoester radical cations with $n = 0$–4 [134]. The EPR spectra of all the studied species are similar to those of amide radical cations, i. e, ionization occurs from the amide moiety. Also, their thermal reactions are rather similar. However, it was found that the amidoester radical cation with $n = 3$ revealed selective and specific intramolecular phototransformation via H atom transfer from the "bridge' through a six-member cyclic transition state.

The reactions of this kind were not found for amide radical cations as well as for amidoesters with a shorter methylene "bridge". We have described this as a "magic bridge" A suggested explanation (confirmed by quantum-chemical calculations [134]) is concerned with specific conformation of the radical cation with $n = 3$, which provides a "conformational lock" due to interaction between the functional groups. Thus, a remote ester functional group (not directly involved in the primary ionization) may control the properties of the excited radical cation at a specific "bridge" length. This is a manifestation of a new kind of the "fine tuning" effect, which may be of significance for radiation chemistry and radiobiology. With further increasing the "bridge" length ($n = 4$) rearrangement also occurs, but it becomes non-selective (yielding a mixture of radicals), which may be attributed to conformational dispersion.

The effect of "magic bridge" (selective intramolecular photoreactions of the radical cations at $n = 3$) was also found for aminoamides and aminoethers [135], for instance:

[4]The idea of using methyl substituted molecules for such studies belongs to Prof. C.J. Rhodes, who kindly donated us 1,2-para-ditolylethane.

$$CH_3O(CH_2)_3N(CH_3)_2^{+\cdot} + h\nu \rightarrow CH_3O^{\cdot}\ CH(CH_2)_2N^{+}(H)(CH_3)_2 \qquad (2.10)$$

It is worth noting that, in both cases, the smaller radical cations ($n = 2$) show no photochemical transformations. Although the detailed mechanism of photochemical reactions is not clear, the results obtained for aminoethers make us suggest that the first step is intramolecular electron transfer between the functional groups in the excited state, followed by rapid proton transfer.

2.4 Matrix Effects on Trapping and Reactions of Radical Cations

Generally speaking, matrix environment has strong and rather complex influence on different stages of the radiation-induced chemical transformations of molecules in solids. Some of these effects are common for different-type species (e.g., effects of matrix rigidity or cage geometry). Meanwhile, the primary radical cations resulting from ionization of molecules are uniquely sensitive to the medium effects, because of strong electrostatic interactions of these species with surrounding molecules. "Matrix effects" for radical cations may imply a wide range of observations—from spectroscopic effects to matrix-controlled and matrix-assisted chemistry. In the case of molecular matrices, the nature of the effects may be very complicated, so, in most cases, it is difficult to rationalize them in clear physical terms. This section will focus on the basic effects of chemically inert noble gas matrices on trapping and properties of the radiation-induced radical cations as revealed by EPR studies in our laboratory.

2.4.1 Spectroscopic Effects: Noble Gas Matrices vs. Freons

In the past 15 years, we have succeeded in obtaining the EPR spectra of a number of larger cations in argon and xenon matrices, so a wider comparison is possible. The available data on isotropic hyperfine couplings in the radical cations obtained in solid noble gas and halocarbon matrices are given in Table 2.5.

In most cases, the coupling constants in rare gas and halocarbon matrices are rather close. An interesting exception is benzene radical cation. This cation is a typical Jahn—Teller species. The two distorted states denoted as $^2B_{1g}$ (acute minimum) and $^2B_{2g}$ (obtuse minimum) show essentially different spin density distribution, so they can be easily distinguished by EPR (Fig. 2.3).

Basic energy separation between these states is quite small (the $^2B_{1g}$ state lies 8 cm^{-1} lower as revealed by recent ZEKE studies [146]). Therefore, stabilization of a specific structure in the solid state should be determined mainly by the matrix effects. Previous studies gave clear evidence for preferential stabilization of the $^2B_{2g}$ state in a $CFCl_3$ matrix [57, 141]. Meanwhile, the results of our matrix isolation studies suggest trapping of the $^2B_{1g}$ state in an argon matrix [114].

Table 2.5 Comparison of the hyperfine coupling constants for organic radical cations trapped in solid rare gas and halocarbon matrices pair

Radical cation	Matrix	Isotropic hfc, mT	References	Isotropic hfc in halocarbon matrices, mT
$CH_2O^{+\cdot}$	Neon	13.29 (2H)	[137]	13.97 (2H) ($CFCl_3$, Ref. [138])
$CH_3CHO^{+\cdot}$	Neon	12.88 (1H)	[108]	13.7 (1H) ($CFCl_3$, Ref. [108])
$CH_3OCH_3{}^{+\cdot}$	Argon	4.5 (6H)	[113]	4.3 (6H) ($CFCl_3$, Ref. [64])
$CH_3OCH_2OCH_3{}^{+\cdot}$	Argon	14.0 (2H); 3.43 (2H)	[113, 116]	13.6 (2H); 3.13 (2H) ($CFCl_3$, Ref. [139])
$THF^{+\cdot}$	Argon	8.9 (2H); 4.0 (2H)	[117]	8.9 (2H); 4.0 (2H) ($CFCl_3$, Ref. [65])
$CH_3COCH_3{}^{+\cdot}$	Argon	<0.25 (unresolved)	[117]	$\leq$0.15 (CCl_4, Ref. [140])[a]
$C_6H_6{}^{+\cdot}$	Argon	0.64 (4H)[b]	[114]	0.82 (2H); 0.24 (4H)[c] ($CFCl_3$, Ref. [141])
$C_6H_5CH_3{}^{+\cdot}$	Argon	1.9 (3H); 1.3 (1H)	[115]	2.0 (3H); 1.25 (1H) (CF_3CCl_3, Ref. [142])
n-$C_7H_{16}{}^{+\cdot}$	Xenon	3.1 (2H)	[23, 24]	3.0 (2H) ($CFCl_2CF_2Cl$, Ref. [143])
cis-$CH_3CH=CHCH_3{}^{+\cdot}$	Argon	2.36 (6H); 1.05 (2H)	[118]	2.36 (6H); 0.95 (2H) (CF_3CCl_3, Ref. [144])
trans-$CH_3CH=CHCH_3{}^{+\cdot}$	Argon	2.6 (6H); 1.05 (2H)	[118]	2.74 (6H); 0.99 (2H) (CF_3CCl_3, Ref. [144])
$CH_3CH_2OCH=CH_2{}^{+\cdot}$	Argon	1.87 (2H); 0.48 (2H); 0.32 (1H)	[118]	1.9 (2H); 0.32 (2H) ($CFCl_3$, Ref. [145])

[a]ENDOR data
[b]$^2B_{1g}$ state
[c]$^2B_{2g}$ state

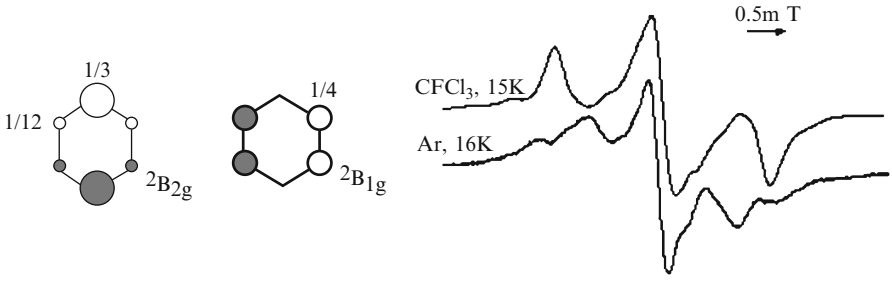

Fig. 2.3 Spin density distribution in the Jahn–Teller states of benzene radical cation and EPR spectra observed in Freon and argon matrices (See Refs. [114, 117] for details)

This difference can be explained by various-type matrix interactions [115]: a localised asymmetrical interaction with a Freon molecule leads to stabilization of the $^2B_{2g}$ state, whereas more symmetrical delocalised interaction in an argon matrix may favour stabilization of the $^2B_{1g}$ state.

It should be noted that superior resolution of the EPR spectra observed for small cations in neon matrices was not found in our argon matrix studies of larger organic species. Main reason of relatively poor resolution may be anisotropic line broadening for randomly oriented species. In conclusion, from spectroscopic point of view, using solid rare gas matrices may be justified in two cases: (i) for small radical cations, which cannot be trapped in halocarbon media or (ii) for the radical cations with nearly degenerate states, which can be extremely sensitive to the matrix effects.

2.4.2 Matrix-Assisted Deprotonation of Primary Radical Cations in Xenon

As stated in Sect. 2.2.2.3, in certain cases, the yields of the primary organic radical cations produced by irradiation in a xenon matrix in the presence of freons were found to be quite low (or even zero) [113, 116, 117]. Instead of this, we observed large yields of the radicals resulting from specific C—H bond rupture, which corresponds formally to proton loss in the primary radical cations (Fig. 2.4).

Similar results were obtained for a number of other compounds (Table 2.6). It is worth noting that, in all the cases studied, we observed formation of only

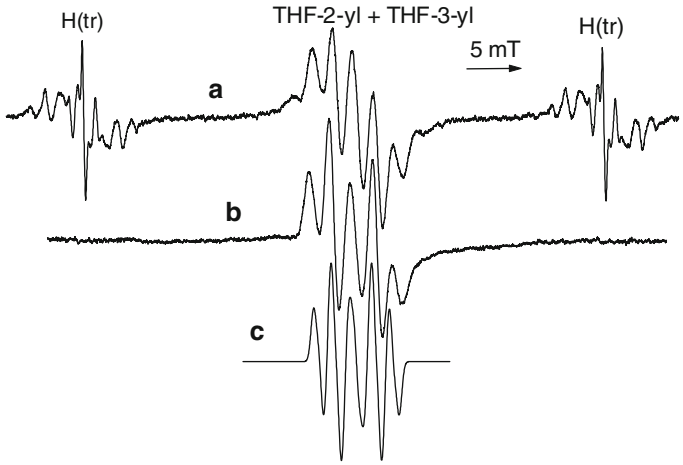

Fig. 2.4 EPR spectra of the radicals resulting from irradiation of THF in a xenon matrix at 16 K (*a*) in absence of electron scavenger and (*b*) in presence of Freon-11; (*c*) simulated EPR spectrum of THF-2-yl radical

Table 2.6 Radicals observed upon irradiation of organic molecules in a xenon matrix in the presence of Freon-11 at 16 K [113, 116, 117]

Parent radical cation	Observed radical
$CH_3OCH_3^{+\cdot}$	$CH_3OCH_2^{\cdot}$
$CH_3OCH_2OCH_3^{+\cdot}$	$CH_3O^{\cdot}CHOCH_3$
$CH_3CHO^{+\cdot}$	$CH_3^{\cdot}CO$
$THF^{+\cdot}$	THF-2-yl
1,3-Dioxolane$^{+\cdot}$	1,3-Dioxolane-2-yl

one specific radical for each parent cation. This means that deprotonation of the primary radical cations is a *regioselective* process (in contrast with the C—H bond cleavage in excited molecules observed in the absence of electron scavengers). The selectivity of this process correlates with spin density distribution in the radical cation (proton loss occurs at the maximum spin density position). The implication of this correlation will be discussed in more detail below.

Concerning the mechanism of proton transfer, the main problem is assignment of the proton acceptor site in a xenon matrix. At first glance, deprotonation might occur in dimers or larger molecular aggregates. However, such a possibility can be ruled out in view of the following arguments: (i) only deprotonation products were found even at high dilutions (above 1: 1000), when major part of guest molecules should be in monomeric form; (ii) under similar conditions, isolated monomeric radical cations were observed in an argon matrix, and there is no reason to suggest that aggregation of organic molecules in xenon is much stronger than in argon (in fact, the opposite is probably true for some systems). Thus, the observed reaction involves essentially isolated molecules, and the matrix plays an active role. Actually, the proton affinity of a xenon atom is relatively high (5.2 eV), that is, comparable to proton affinities of simple organic molecules and neutral radicals [147]. This means that, even in a gas-phase approximation, direct proton transfer from some highly acidic radical cations to xenon should be only slightly endothermic process. Meanwhile, in the case of solid xenon matrix, additional stabilization of proton results from specific collective solvation (formation of protonated xenon clusters of the Xe_nH^+ type) and long-range medium polarization. In particular, the formation of linear centrosymmetrical cation $XeHXe^+$ in solid xenon is well documented [148, 149]. Thus, direct deprotonation of radical cations to matrix may be justified reasonably (at least, from qualitative viewpoint). The reaction scheme for ether-type radical cations can be written as follows:

$$R_1CH_2OR_2^{+\cdot}(Xe) \rightarrow R_1^{\cdot}CHOR_2 + XeHXe^+ \qquad (2.11)$$

Verification of this scheme could be made by direct observation of the protonated species due to its characteristic vibrational spectrum (progression in a low-frequency region with the strongest band at 731 cm^{-1} [149]). In fact, we observed such an absorption by FTIR spectroscopy in some experiments; however, up to now, we were unable to establish the correlation between formation of $XeHXe^+$ and radical products of deprotonation. For this reason, it is of value to consider other possible mechanisms [84, 116, 117].

An alternative explanation can be based on recent theoretical finding [150], which shows that relatively polarizable rare gas atoms (in particular, xenon) may facilitate intramolecular rearrangement (H transfer to oxygen atom) in methanol radical cation due to formation of transition-state complex. In this case, the role of xenon is lowering potential barrier for the reaction, so the effect may be described as *matrix catalysis*. If such a model is applicable to the ether-type radical cations (and other oxygen-containing species), the observed transformation may be represented by the scheme:

$$R_1CH_2OR_2^{+\cdot}(Xe) \rightarrow R_1^{\cdot}CH(OH^{+})R_2 \qquad (2.12)$$

Note that the EPR spectra of the distonic radical cations resulting from reaction (2.11) may be indistinguishable from the spectra of the corresponding neutral radicals (deprotonation products) since the OH proton coupling should be small. Formally, reaction (2.11) is a hydrogen atom shift rather than proton transfer; however, in fact, the process is accompanied by substantial redistribution of positive charge. Theoretical analysis [150] shows that the catalytic effect directly correlates with the proton affinity of matrix atom, so the analogy with deprotonation is reasonable. Verification of this mechanism implies observation of the OH group in the radical product, which could come from IR spectroscopic studies or ENDOR measurements.

Finally, one may consider a combination of the two possibilities discussed above, namely matrix-assisted intermolecular proton transfer to oxygen atom of a distant molecule ("matrix pseudocatalysis"). In this case, the role of xenon matrix is providing a system of shallow traps ("conducting chain") for proton transport to a deeper trap (organic molecule).

2.4.3 *"Hot" Fragmentation and Rearrangements: Effect of Excess Energy*

Deprotonation of some primary radical cations was also observed in a krypton matrix [113, 116], however, this was not the case for argon. On the other hand, many aliphatic radical cations were not trapped in an argon matrix, and methylal radical cations were found only in trace amounts. In this case, the observed radicals result mainly from the skeleton bond fragmentation (i. e., cleavage of C—C or C—O bond). Formation of these products was attributed to the effect of excess energy resulting from high exothermicity of the positive hole transfer in the case of argon matrix [23, 84, 113, 116, 117]. In first approximation, one can estimate this excess energy from the difference in the IP values between matrix atom and guest organic molecule (IP gap). Typical IP values for simple organic molecules are ca. 9–10 eV, so, in the case of argon, the IP gap is around 6 eV. This value definitely exceeds the energy of chemical bonds in the resulting radical cations. Taking into account inefficient dissipation of excess energy to the argon lattice, one can conclude that the "hot" fragmentation should be highly probable. In fact, an indication of such process

Table 2.7 Radicals resulting from "hot" reactions of the primary radical cations upon irradiation of organic molecules in an argon matrix in the presence of Freon-11 at 16 K

Parent radical cation	Radical products	Relative yield of fragmentation/ rearrangement	References
$CH_3OCH_3^{+\cdot}$	$CH_3^{\cdot}$	Low	[84, 113]
$CH_3OCH_2OCH_3^{+\cdot}$	$CH_3^{\cdot}$, $CH_3O^{\cdot}$	High	[116]
n-$C_7H_{16}^{+\cdot}$, n-$C_5H_{12}^{+\cdot}$	$CH_3^{\cdot}$	Moderate high	[23]
$CH_3CHO^{+\cdot}$	$CH_3^{\cdot}$	Moderate high	[117]
$CH_3COCH_3^{+\cdot}$	$CH_3^{\cdot}$	Very low	[117]
$(CH_3)_3COCH_3^{+\cdot}$	$CH_3^{\cdot}$	Very high	[117]
$CH_3CH_2OCH=CH_2^{+\cdot}$	$CH_3^{\cdot}$	Low	[118]
$CH_3CH_2CH=CH_2^{+\cdot}$	*cis*-$CH_3CH=CHCH_3^{+\cdot}$	Very high	[118]
$CH_3COCOCH_3^{+\cdot}$	$CH_3^{\cdot}$	Very high	[151]
$CH_3COCH_2CH_2COCH_3^{+\cdot}$	$CH_3^{\cdot}$	Moderate high	[119]
$CH_3OCH_2COCH_3^{+\cdot}$	$CH_3^{\cdot}$	Moderate high	[119]

was obtained in early studies of the radiolysis of alkanes in argon and krypton [104]. In addition to fragmentation, excess energy may also result in rearrangement of the primary radical cations in a solid argon matrix [77, 82, 117]). The results of our studies on "hot" reactions of aliphatic radical cations in argon are summarized in Table 2.7.

It is worth noting that, in all the studied cases, the estimated excess energy (>5.5 eV) is high enough for bond cleavage or rearrangement of the primary radical cations (the corresponding processes always have lower threshold under the conditions of mass-spectrometry). However, as seen from Table 2.7, the efficiency of "hot" fragmentation of the radical cations in solid argon varies strongly, depending on the molecular structure of the guest species, even for rather similar electronic structure of radical cations (e. g., to compare dimethyl ether and methylal, or acetone and diacetonyl). Furthermore, it was shown that radical cations of 2-butene isomers retained not only molecular structure, but also spatial configuration (*cis*/*trans*) without any fragmentation or rearrangement, even though excess energy was ca 6.5 eV (to be compared with the fragmentation threshold of 2–2.2 eV found in the gas-phase studies [152]). These findings clearly suggest crucial significance of intramolecular relaxation of excess energy followed by its dissipation to a matrix lattice. In general, the relaxation processes are determined by vibronic interactions, coupling between different vibrational modes, and cation—matrix interactions. This may imply an important role of molecular symmetry and cage structure, which can be considered as another illustrative example for fine tuning in the high-energy chemistry in solids. In any case, it should be noted that the reactivity of "hot" radical cations generated in argon is quite different from the behaviour of electronically excited cations resulting from photoexcitation in halocarbon matrices [84]. It seems to be likely that indirect ionization in argon leads to population of high vibrational levels, which cannot be reached in photoprocesses. If it is the case, using argon matrices may provide unique information on the properties of vibrationally excited radical cations; however, further work is necessary to verify this assumption.

2.4.4 *"Matrix Switching" Between Reaction Channels*

One of the most interesting findings is concerned with observation of both reaction channels for the same species, when the yields of the primary radical cations are low for both xenon and argon matrices, but the observed products are quite different. An illustrative example of such effect of nearly complete *"matrix switching" between reaction channels* (deprotonation to fragmentation) is given by methylal radical cation [116]. In the case of xenon, the EPR spectra show dominating contribution from the $CH_3O{\cdot}CHOCH_3$ radicals (anisotropic doublet), which corresponds to selective deprotonation of the primary cation. Mainly fragmentation products ($CH_3{\cdot}$ and $CH_3O{\cdot}$, probably in the form of complex with $CH_2OCH_3{}^+$ ion) were found in argon [116]. Both processes occur in krypton (Fig. 2.5).

General consideration of the nature of matrix effects in chemically simplest and apparently inert environment should be addressed to the basic physical characteristics of the matrices used. As shown in Table 2.1, IP and polarizability of rare gas atoms vary over a rather wide range. While going from neon to xenon, the IP value decreases by more than 9 eV, whereas the polarizability increases roughly by an order of magnitude. In fact, the electronic characteristics of xenon are rather close to those of molecular matrices. High polarizability implies relatively strong interaction with the radical cations and appreciable proton affinity (basicity) of the xenon matrix.

As discussed above, the fragmentation of the primary radical cations in argon results from high IP value of the matrix used. From this point of view, one could be rather pessimistic about obtaining high yields of radiolytically produced complex organic radical cations in neon, because the excess energy (ΔIP) in this case is too large. The fragmentation of some radical cations was also found in a krypton

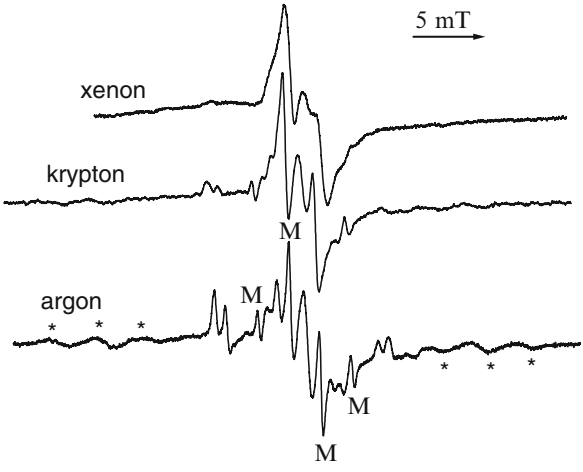

Fig. 2.5 Matrix switching between reaction channels for methylal radical cation: radical products resulting from irradiation of methylal in rare gas matrices in the presence of $CFCl_3$ at 16 K. Symbol M shows the *lines* from methyl radicals; *asterisks* indicate the components of the outer triplets from methylal radical cations (See Ref. [116] for details)

matrix [113–116], and (in a few cases) in xenon [151]. Thus, formally it is possible to estimate the threshold excess energy for "hot" fragmentation as 2.5–4 eV. Note, however, that matrix polarizability may also affect the probability of fragmentation, because energy dissipation to the matrix lattice becomes more efficient in krypton and especially in xenon.

Deprotonation of the studied radical cations becomes less important in krypton and does not occur in an "electronically rigid" (low-polarizable) argon matrix. Meanwhile, for the most "acidic" small radical cations (e.g., methane or methanol), even argon probably may act as a proton acceptor. In this case, neon should be the best choice because of its extremely low polarizability and proton affinity. In summary, trapping of organic radical cations in solid rare gas matrices is probably a matter of compromise between different electronic characteristics of the matrix used.

2.5 Selectivity of the Primary Radiation-Induced Chemical Events

The problem of selectivity of the primary chemical effects induced by ionizing radiation in molecular materials is of primary significance from both basic and practical points of view. In general, it implies determination of the factors, which control the reaction pathways of primary ionized and excited molecules in solid media. EPR studies in low-temperature matrices are especially valuable for model purposes, because they may reveal the mode of initial chemical bond rupture in various molecular systems.

2.5.1 Site-Selective Reactivity of Organic Radical Cations

The phenomenon of site-selective reactivity has been first clearly demonstrated by Toriyama and co-workers for deprotonation of linear alkane radical cations in halocarbon matrices, SF_6 and zeolites [93, 153, 154]. It was shown that ion—molecule reactions of linear alkane cations in the extended (planar zigzag) conformation resulted in selective proton loss from the chain-end position to yield terminal alkyl radicals:

$$CH_3(CH_2)_nCH_3^{+\cdot} + RH \rightarrow CH_3(CH_2)_nCH_2^{\cdot} + RH_2^{+} \qquad (2.13)$$

Here RH denotes neutral alkane molecule. The reactions of this type occur either in pre-existing dimers [93] and larger aggregates [36] or in the complexes formed due to molecular diffusion at intermediate temperatures [153, 154]. This process was also invoked to explain preferential formation of terminal alkyl radicals in the irradiated C_{10}—C_{25} linear alkane crystals [17]. Meanwhile, in the case of *gauche*-C_2

conformers of linear alkane cations, deprotonation occurs at the C_2 position to yield penultimate radicals [38, 153, 154]. Thus, in both cases, the most "acidic" proton is an in-plane proton, which bears maximum spin density in σ-delocalized alkane radical cations. In other words, it implies a correlation between the isotropic proton hyperfine coupling constant and probability of deprotonation.

The correlation of this kind was also found for linear alkene radical cations [39]. Meanwhile, extensive studies of alkyl radical formation in halocarbon matrices containing the parent radical cation has been for various alkyl-substituted cyclohexanes did not reveal direct relationship between the location of high spin density at protons in the cation and the site of the resulting π–type alkyl radicals [155]. The results obtained for ether and acetal radical cations in halocarbon matrices were also not so definitive [156, 157]. However, the studies in xenon matrices considered in Sect. 2.4.2, clearly reveal the same trend for all the radical cations examined. Certain difference between the data obtained in halocarbon and xenon matrices can be easily understood, if one takes into account that the ion-molecule reactions observed in halocarbons may imply not only proton transfer from the radical cation to neutral molecule, but also hydrogen atom transfer in the reverse direction. In the latter case, the radical cation acts similar to any neutral radical abstracting an H atom from neutral molecule. The selectivity of such process should be determined by the dissociation energies of specific C—H bonds in a neutral molecule; in the case of small difference, the relative yields of radicals may be essentially controlled by statistical and steric factors. In particular, this may be the reason for formation of relatively large amounts of the $\cdot CH_2OCH_2OCH_3$ radicals upon ion-molecule reactions of the methylal radical cation occurring at high methylal concentrations or at elevated temperatures in halocarbons [158]. As shown in the previous section, deprotonation in a xenon matrix yields only $CH_3O\cdot CHOCH_3$ radicals. Thus, one may conclude that deprotonation of the radical cations controlled by *electronic factors* is, in general, much more selective than thermal hydrogen atom abstraction. It is worth noting, however, that the theoretical interpretation of the correlation between spin density distribution and selectivity of deprotonation is still not straightforward, because it requires demanding calculations of the reaction barriers in the condensed phase taking into account environment effects.

One could note that "bond weakening" may also imply another possibility, namely hydrogen atom loss (dissociation of $RH^{+\cdot}$ to R^+ and $H\cdot$). This process may be favourable in gas phase; however, in the case of condensed phase, deprotonation should be favoured because of large gain in polarisation energy. In fact, H atoms were never found as significant products of reactions of organic cations in halocarbons or solid rare gases.

Deprotonation is probably the most important and the most widely studied site-selective process among the reactions of organic radical cations. Nevertheless, the concept of selective bond weakening is also applicable to the skeleton bonds in the radical cations. In particular, large elongation and weakening of specific C—C bonds upon ionization has been proved for branched alkanes [35]. Experimental evidences for the C—O bond weakening were reported for the radical cations of linear and cyclic acetals (1,1-diethers) [158]. In conclusion, the effect of strong

differentiation in the chemical bond energy upon ionization of organic molecules should be of key significance for understanding of specific selectivity of the primary events in the radiation chemistry of molecular systems and macromolecules.

2.5.2 Selectivity of Other Primary Processes

Formation of primary ionized molecules (radical cations) is a specific feature of the processes induced by high-energy radiation, so the selective reactivity of these species is of particular interest for radiation chemistry. Meanwhile, the radicals observed in molecular solids also result from dissociation of neutral excited molecules. Controversial results concerning the selectivity of the primary C—H bond rupture were reported for linear alkane crystals [16, 17, 159]. In general, amixture of different-type radicals (i.e., terminal, penultimate and interior alkyl radicals) is observed after irradiation of crystalline alkanes at 4.2 K [16, 17]. As deprotonation of the primary cations yields selectively terminal radicals (see above), other processes of radical formation are probably not so selective. In recent studies, we tried to estimate the mode of C—H bond rupture in isolated excited heptane molecules produced in a xenon matrix [24]. The experiment revealed formation of a mixture of penultimate and interior radicals, the former being predominated (detailed quantitative analysis was not made). Terminal alkyl radicals are not formed, as demonstrated in the studies of selectively deuterated heptane $CD_3(CH_2)_5CD_3$. Thus, the formation of radicals from neutral excited alkane molecules also seems to be non-random; however, the mode of C—H bond rupture is not so specific as in the case of deprotonation of the primary cations.

Little is known about the reactions of neutral excited molecules produced in the radiolysis of other simple aliphatic molecules in solid phase. As shown in Sect. 2.4.2 (Fig. 2.5 and related discussion), dissociation of excited THF molecules in solid xenon yields a mixture of THF-2-yl and THF-3-yl radicals in roughly comparable concentrations, which is characteristic of a non-selective process.

In addition to reactions of the primary radical cations and neutral excited molecules, the composition of radicals resulting from the low-temperature solid-state radiolysis is also determined by the reactions of hydrogen atoms. Strictly speaking, it is not a primary process; however, H atoms produced upon radiolysis are not trapped in solid alkanes (except for methane) and other organic systems even at 4 K, because they abstract hydrogen atoms from molecules via tunnelling mechanism [7]. Thus, the radicals produced by the reactions of hydrogen atoms are often treated as the "primary" radiolysis products. According to [30, 31], the selectivity of reactions of H atoms with alkanes in the solid phase depends strongly on the matrix physical state. In the case of crystalline linear alkanes, the abstraction yields both penultimate and interior radicals, whereas only penultimate radicals are formed selectively in glassy matrices of perdeuterated alcohols [30]. This effect was attributed to impeded C—C—C bending motion in low-temperature glasses; similar data were reported for glassy branched alkanes [31].

2.5.3 Application to Macromolecules

From practical point of view, studying the mode of radiation-induced damage in macromolecules and complex polymeric systems is one of the most important tasks of the solid-state radiation chemistry. It is also a challenging basic problem since it addresses to a number of issues, i.e., validity of local molecular models for description of the long-range effects, role of conformational defects, significance of molecular packing, etc. Numerous data on the radicals trapped in various irradiated polymers are available, however, the primary distribution of the radiation-induced events is not known, even for most widely studied macromolecules. A specific problem is associated with structural and chemical inhomogeneity of real polymers, which complicates the interpretation.

Here main focus will be made on recent results concerning the role of structural defects in the radiolysis of polyethylene (PE), chemically the simplest and practically the most important polymer. For linear polyethylene (if one disregards branching and chemical impurities), the most important type of defects is conformational defects, i.e. *gauche-trans* (GT) conformers. Although theoretical predictions for ideal macromolecules indicated possible role of the conformational defects in localization of primary events, experimental evidences for the effects of this type were unavailable for a long time. It is well known that irradiation of PE at low temperatures leads to formation of interior-type alkyl radicals $\sim CH_2{\cdot}CHCH_2 \sim$ [4], and only the radicals resulting from *trans-trans* (TT) conformers were detected in early EPR studies at 77 K [160]. However, the observed distribution of radicals may be affected by secondary processes, namely, local radical site migration, which was found to occur below 77 K [5–10]. Also, to make definite conclusions, it is important to deal with a chemically pure, well-organized and well-characterized polymer. Taking into account these points, we have reinvestigated the initial mode of radical formation in high-density linear PE irradiated at 15 K [161, 162]. In order to get an unequivocal test of the role of structural defects occurring in small concentrations, we used PE with extended chain crystals (ECC PE) obtained by high-temperature annealing of linear high-density PE under high pressure. These samples are characterized by extremely high crystallinity (95–98%) and very low concentration of conformational defects. In addition, using oriented samples allowed us to obtain high-quality EPR spectra and to get more information from the angular dependence.

The EPR spectrum shown in Fig. 2.6 clearly reveals the presence of substantial amounts of radicals resulting from GT conformers (the lines marked with arrows). Indeed, when external magnetic field is applied parallel to the draw axis, the TT conformer (dihedral angles $\theta = 30°$ for all the four β-protons) yields a nearly perfect sextet spectrum: $a(H_\alpha) \approx a(4H_\beta) \approx 3.3$ mT. An admixture of the GT conformer ($\theta_1 = 90°$, $\theta_2 = \theta_3 = \theta_4 = 30°$) is easily detected since in the latter case one β-proton takes a position in the nodal plane in respect to unpaired electron orbital axes, and the corresponding hyperfine coupling is lost. Detailed analysis [162] shows that the fraction of the radicals resulting from GT conformers is ca.

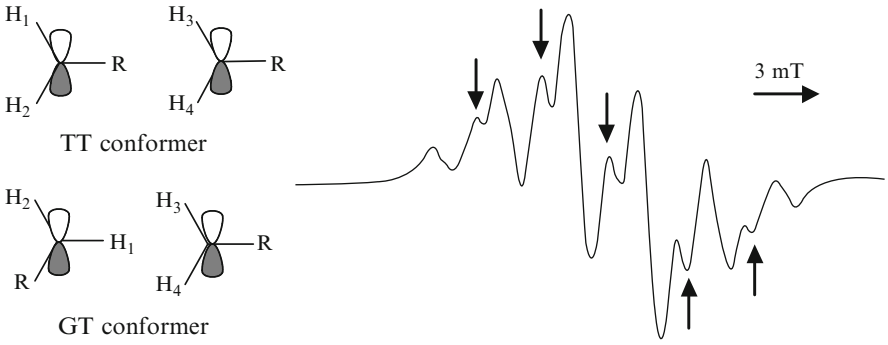

Fig. 2.6 EPR spectrum of oriented ECC PE irradiated at 15 K. Magnetic field is applied parallel to the direction of draw axis (See Refs. [161, 162] for details)

30%, despite the concentration of such conformers is very small. Thus, it was the first direct experimental evidence for highly preferential localization of the primary radiation-induced events at conformational defects in macromolecules. It is worthwhile noting that annealing of the irradiated samples at 80–90 K results in irreversible conversion of the defect-localized radicals to "normal" TT conformers, probably due to local "radical hopping" [162]. This result accounts for failure to observe the GT conformers in earlier studies carried out at 77 K.

To explain the nature of conformational selectivity in PE, it is logical to turn back to selective effects observed for the prototype molecules (linear alkanes). As stated above, deprotonation of the primary alkane radical cations occurs selectively, either at terminal methyl group (for extended all-*trans* conformers) or at *gauche* position (for *gauche*-C_2 conformers). This rule remains valid for rather long molecules (at least, up to C_{25} [17]). A similar consideration may be applied to the PE macromolecules: deprotonation of the primary positive hole may occur selectively at the defect position (again, the in-plane proton is lost preferentially).

In other words, this model implies that the *conformational defects act as "effective chain-ends"* for hole delocalization. Interestingly, the fraction of radicals localised at conformational defects in PE is very close to the fraction of terminal alkyl radicals resulting from selective deprotonation of the long-chain linear alkane cations.

Detailed information on the selectivity of early events in other polymer systems is lacking. It seems probable that the processes of long-range positive hole migration are basically important for the radiation chemistry of a wide class of polymeric systems [161]. In particular, in the case of polystyrene, the trap-to-trap hole migration may result in favourable localization of the radiation-induced events at specific conformers or dimeric associates of aromatic rings. In the case of microheterogeneous systems, the interphase migration of positive hole and electron may cause specific non-additive effects in the formation of radicals, especially, if the electronic properties of the components are different [163].

2.6 Conclusions and Outlook

In summary, EPR studies of the radiation-induced organic species in low-temperature matrices in the past two decades has led to significant progress in understanding basic mechanisms of the radiation effects in molecular solids and polymers and revealed some new trends.

The structure and reactivity of the primary ionized molecules (radical cations) remains in a focus of basic radiation chemistry and some other areas of physical chemistry. Using halocarbon matrices for the EPR characterization of organic radical cations has made a sort of "revolution" in the field some 30 years ago. Recent studies on "bridged" bifunctional radical cations have revealed new trends in this area, which may be useful not only for radiation chemistry, but also for radiobiology and molecular electronics. On the other hand, application of matrix isolation in solid rare gases to the EPR studies of relatively large organic radical cations was developed mainly during the past 15 years. Somewhat unexpectedly, this method has proved to be especially valuable for elucidation of chemical aspects rather than spectroscopic issues. I believe that the matrix isolation studies will eventually give the key to understanding of the matrix-assisted and matrix-controlled chemistry of ionized organic molecules in solids.

A new challenge is concerned with the studies of radiation-induced bifunctional radical anions. Recently, it was realized that the reactions of excess electrons producing unstable radical anions might play much more important role in radiation damage to biomolecules than it was suggested before. On the other hand, comparison of radical anions and radical cations in view of possible switching between localized and delocalized states may be of specific interest of molecular electronics and related fields. In particular, it would be of basic interest to establish the criteria of medium-controlled stabilization of the radical anions with weakly bound electron produced from molecules with negative electron affinity [164].

Regarding the radicals produced in complex organic systems and polymers, the most important finding is specific selectivity of the radiation-induced processes. In fact, it was clearly demonstrated that the primary chemical events induced by high-energy radiation were far more selective than it might be expected from formal energetic reasons; furthermore, the radiation damage was found to be sensitive to very "subtle" effects (e.g., molecule conformation or weak association). To a large extent, this selectivity is probably determined by long-range hole migration and specific bond weakening in the ionized molecules. There are still a few studies for complex systems, and more work should be done.

Important new information on the structure and reactivity of the radiation-induced paramagnetic species can be obtained using a combination of EPR with other spectroscopic techniques. In particular, IR spectroscopy is useful since it yields detailed structural data concerning parent molecules, primary paramagnetic species and diamagnetic products of their reactions. The most challenging issue is probably concerned with obtaining vibrational spectra of simple aliphatic radical cations. These characteristics may provide essential information on chemical

bonding in the radical cations, which should be crucial for testing the concept of selective bond weakening.

Recent development in theoretical methods made it possible to describe the geometry and magnetic resonance parameters of relatively large organic radicals with reasonably high accuracy. Meanwhile, the theoretical treatment of reactivity of radicals and, especially, radical cations is not so extensive. Probably, the most difficult problem is concerned with correct theoretical description of the effect of matrix environment on the reaction profile. Different ideas, including a concept of "matrix catalysis", should be considered.

Generally speaking, the results presented in this chapter have to illustrate the potential of using EPR spectroscopy for elucidation of the most challenging basic problems of radical chemistry (in particular, radiation chemistry) in solids. Some other aspects of the EPR studies of radiation-induced species related to radical dynamics, radiation damage in biomolecules and dosimetry are considered in other chapters of this book.

Acknowledgments I am indebted to all my collaborators and students, who took part in our research of the radiation-induced radicals in low-temperature matrices and polymers during the past two decades. The work in our laboratories was continuously supported by the Russian Foundation for Basic Research, INTAS and The Russian Academy of Sciences (projects no. 96-03-32949, 00-03-32041, 03-03-32717, 06-03-33104, 09-03-00848, IR-95-0008, IR-97-1262, and INTAS 2000-0093, programs no. 1 and 8 of the Division of Chemistry and Material Sciences of RAS). I appreciate a valuable comment of Prof. Shiotani regarding the selectivity of deprotonation during preparation of the first edition.

References

1. Schneider EE, Day MJ, Stein G (1951) Effects of X-rays upon plastics: paramagnetic resonance. Nature 168:645–664
2. Morton JR (1964) Electron spin resonance spectra of oriented radicals. Chem Rev 64: 453–471
3. Henly E, Johnson E (1969) The chemistry and physics of high energy reactions. University Press, Cambridge
4. Pshezhetskii SYa, Kotov AG, Milinchuk VK, Roginskii VA, Tupikov VI (1974) EPR of free radicals in radiation chemistry. Wiley, New York
5. Nunome K, Muto H, Toriyama K, Iwasaki M (1976) ESR studies of local concentrations of radicals in polyethylene irradiated at 1.5, 4.2 and 77 K. Chem Phys Lett 39:542–546
6. Iwasaki M, Toriyama K, Muto H, Nunome K (1976) Pairwise trapping of radicals in single-crystals of normal-decane irradiated at 1.5 and 4.2 degrees K. J Chem Phys 65:596–606
7. Toriyama K, Muto H, Nunome K, Fukaya M, Iwasaki M (1981) Radiation damages of organic materials at 4 —an electron spin resonance study of polyethylene and related hydrocarbons. Radiat Phys Chem 18:1041–1052
8. Feldman VI, Borzov SM, Sukhov FF, Slovokhotova NA (1987) Radical processes in polyethylene, irradiated at 10 – 100 K. Khimicheskaya fizika 6:477–483
9. Feldman VI, Borzov SM Sukhov FF, Slovokhotova NA (1988) Kinetics and mechanism of low-temperature radical reactions in high-crystalline polyethylene. Khimicheskaya fizika 7:781–787

10. Feldman VI, Borzov SM, Sukhov FF, Slovokhotova NA (1989) Effect of polymer structure and isotopic substitution on low-temperature radical reactions in irradiated polyethylene. Khimicheskaya fizika 8:949–955
11. Shida T, Kato T (1979) ESR and optical studies on the cation-radical of pyridine in a gamma-irradiated rigid matrix at low-temperatures. Chem Phys Lett 68:106–111
12. Symons MCR (1984) Radical cations in condensed phases. Chem Soc Rev 13:393–439
13. Shiotani M (1987) ESR studies of radical cations in solid matrices. Magn Reson Rev 12: 333–381
14. Radical ionic systems properties in condensed phases (1991) (Lund A, Shiotani M (eds)). Kluwer, Dordrecht
15. Gillbro T, Lund A (1975) High-yield of radical pairs in deuterated normal-alkane single-crystals gamma-irradiated at 4.2 K. Chem Phys Lett 34:375–377
16. Gillbro T, Lund A (1976) Deposition of radiation energy in solids as visualized by distribution, structure and properties of alkyl radicals in gamma-irradiated normal-alkane single-crystals. Int J Radiat Phys Chem 8:625–641
17. Iwasaki M, Toriyama K, Fukaya M, Muto H, Nunome K (1985) 4 K radiolysis of linear alkanes as studied by electron-spin resonance spectroscopy—selective formation of terminal alkyl radicals in the primary process. J Phys Chem 89:5278–5284
18. Toriyama K, Iwasaki M (1979) Electron spin resonance studies on radiolysis of crystalline methanol at 4.2 K. J Am Chem Soc 101:2516–2523
19. McKinley AJ, Michl J (1991) EPR-ENDOR spectroscopy of matrix-isolated NH_3+ and CH_3 radicals. J Phys Chem 95:2674–2679
20. Knight LB, Kerr K, Villanueva M, McKinley AJ, Feller D (1992) Theoretical and neon matrix electron-spin-resonance studies of the methanol cation—CH_3OH^+, CH_3OD^+, CH_2DOH^+, and $(CH_3OH^+)C^{13}$). J Chem Phys 97:5363–5376
21. Yamada S, Komaguchi K, Shiotani M, Benetis NP, Sornes AR (1999) High-resolution EPR and quantum effects on CH_3, CH_2D, CHD_2, and CD_3 radicals under argon matrix isolation conditions. J Phys Chem A 103:4823–4829
22. Sukhov FF (1988) Low-temperature radiation-chemical processes in polymers and their low-molecular-weight analogues. Dissertation, Karpov Institute of Physical Chemistry
23. Feldman VI (1997) Structure and properties of hydrocarbon radical cations in low-temperature matrices as studied by a combination of EPR and IR spectroscopy. Acta Chem Scand 51:181–192
24. Feldman VI, Sukhov FF, Nekhoroshev NS, Ivanchenko VK, Shmakova NA (1998) Radiation chemistry of organic molecules in solid rare gas matrices: 1. Formation of heptane radical cations in xenon at 15 K. High Energy Chem 32:15–19
25. Hubbell JH, Settler SM (1996) Tables of X-ray mass attenuation coefficients and mass energy-absorption coefficients from 1 keV to 20 MeV for elements $Z = 1$ to 92 and 48 additional substances of dosimetric interest. http://www.nist.gov/pml/data/xraycoef. Accessed 5 Sept 2011
26. Knight LB, King GM, Petty JT, Matsushita M, Momose T, Shida T (1995) Electron-spin-resonance studies of the methane radical cations ($(CH_4^+)C^{12,13}$, $(CDH_3+)C^{12,13}$, $(CD_2H_2+)C^{12}$, $(CD_3H^+)C^{12}$, $(CD_4^+)C^{12}$) in solid neon matrices between 2.5 and 11 K—analysis of tunnelling. J Chem Phys 103:3377–3386
27. Mel'nikov MYa, Smirnov VA (1996) Handbook of photochemistry of organic radicals. Begell House Inc Publishers, New York
28. Ichikawa T, Ludwig PK (1969) Electron spin resonance evidence on nature of trapped positive holes in gamma-irradiated 3-methylpentane systems at 77 degrees K. J Am Chem Soc 91:1023–1024
29. Ichikawa T, Ohta N (1987) Electron-spin-resonance and electronic-spectra of alkane radical cations formed in gamma-irradiated 3-methylpentane and 3-methylhexane glasses containing alkane solutes. J Phys Chem 91:3244–3248
30. Ichikawa T, Yoshida H (1992) Ichikawa T, Yoshida H (1992) Effect of solid-phase on the selectivity of hydrogen abstraction from branched alkanes—an electron spin resonance and electron spin echo study. J Phys Chem 96:7656–7661

31. Ichikawa T, Yoshida H (1992) Effect of solid-phase on the selectivity of hydrogen abstraction from n-alkanes—an electron-spin-resonance and electron-spin echo study. J Phys Chem 96:7661–7664
32. Shida T, Hamill WH (1966) Molecular ions in radiation chemistry I. Formation of aromatic-amine cations in CCl_4 by resonance charge transfer at 77°K. J Chem Phys 44:2369–2374
33. Grimpson A, Simpson GA (1968) Spectrophotometric identification of gamma-radiolytic intermediates in a new halogenic glassy matrix. J Phys Chem 72:1776–1779
34. Liu Y-J, Huang MB (2000) The asymmetric structure of the n-pentane radical cation: a theoretical study. Chem Phys Lett 321:89–94
35. Toriyama K, Okazaki M (1997) Asymmetric distortion of alkane radical cations as studied by EPR spectroscopy: The role of pseudo-Jahn-Teller effects and matrix interactions. Acta Chem Scand 51:167–173
36. Luyckx G, Ceulemans J (1991) Electron paramagnetic resonance evidence for the occurrence of hydrogen and/or proton-transfer between C-7, C-8 and C-11 normal-alkanes and their cations in irradiated CCl_3F matrices at 77 K. J Chem Soc Faraday Trans 87:3499–3504
37. Stienlet D, Ceulemans J (1992) Dependence on conformation of the site of proton-transfer from alkane radical cations—nature of the octyl radicals formed by proton-transfer from octane radical cations to octane molecules in CCl_3F matrices at 77-K. J Chem Soc Perkin Trans 2:1449–1453
38. Stienlet D, Ceulemans J (1993) Site selectivity in the proton transfer reaction from alkane radical cations to alkane molecules—selective formation of 1-octyl radicals by proton-transfer from octane radical cations to pentane molecules in gamma-irradiated n-C_5D_{12}/n-C_8H_{18} crystals at 77-K. J Phys Chem 97:8595–8601
39. Ohta N, Shiotani M, Ichikawa T (1991) Electron-paramagnetic resonance and indo-mo studies of 2-methylbutane, 3-methylpentane and 3-methylhexane cations produced in several halocarbon matrices gamma-irradiated at 77 K. J Chem Soc Faraday Trans 87: 3869–3874
40. Sjökvist L, Shiotani M, Lund A (1990) The structure of trans-3-hexene and cis-3-hexene radical cations stabilized in halocarbon matrices at low-temperature—an ESR and MNDO AM1 study. Chem Phys 141:417–430
41. Erikson LA, Sjökvist L, Lunell S, Shiotani M, Usui M, Lund A (1993) Effects of ionization in linear alkenes—a study of the radical cations of 1-pentene and 2-pentene. J Am Chem Soc 115:3244–3249
42. Ulyukina EA, Feldman VI, Borzov SM, Sukhov FF, Slovokhotova NA (1990) Spectroscopic study of formation, structure and properties of cation radicals of linear trans-alkenes in Freon matrix. Khimicheskaya fizika 8:1053–1059
43. Feldman VI, Ulyukina E A, Sukhov FF, Slovokhotova NA (1993) Selectivity of ion-molecular reactions of cation-radicals of linear alkenes in freon-113 matrix. Khimicheskaya fizika 12:1613–1621
44. Tachikawa H, Shiotani M, Ohta K (1992) Structure and formation mechanisms of methyl- and dimethylacetylene dimer cations: ESR and ab initio MO studies. J Phys Chem 96:164–171
45. Tyurin DA, Shiryaeva ES, Feldman VI (2010) Structure and photochemical rearrangement of the 3,3-dimethylbut-1-yne radical cation. Mendeleev Commun 20:205–206
46. Shchcapin IYu, Feldman VI, Belevskii VN (1994) Rearrangements of vinylcyclopropane radical cations studied by ESR in freonic matrices. Dokl Akad Nauk 334:338–342
47. Belevskii VN, Shchapin IYu (1997) Rearrangement and ion-molecular reactions of C_5H_8 + center dot-related radical cations as studied by EPR spectroscopy in the solid and liquid phase. Acta Chem Scand 51:1085–1091
48. Chen G-F, Williams F (1992) Cope rearrangement of the endo-5-vinylbicyclo[2 2 1]hept-2-ene (endo-5-vinylnorborn-2-ene) radical cation to the cis-bicyclo[4 3 0]nona-3,7-diene (cis-3a,4,7,7a-tetrahydroindene) radical cation at 100–150-K—a matrix-isolation ESR study. J Chem Soc Chem Commun 670–672
49. Faucitano A, Butttafava A, Martinotti F, Sustman R, Korth (1992) Matrix-isolation EPR study of novel radical cations from bicyclic[3 2 0] and monocyclic C_7H_8 and C_7H_{10} compounds. J Chem Soc Perkin Trans 2: 865–869

50. Gerson F (1994) Applications of ENDOR spectroscopy to radical cations in freon matrices. Acc Chem Res 27:63 -69
51. Bally T, Truttman L, Wang JT, Williams F (1995) Electronic structure and photochemical interconversions of dihydropentalene radical cations. J Am Chem Soc 11:7923–7934
52. Bally T, Truttman L, Wang JT, Williams F (1993) The radical-cation of 1,4-dihydropentalene and its photochemical formation from bicyclo[3 3 0]octa-2,6-diene-4,8-diyl cation. Chem Phys Lett 212:141–149
53. Bally T, Truttman L, Dai S, Williams F (1995) The C_8H_8 radical cations of cyclooctatetraene, semibullvalene, and their common bisallylic rearrangement product electronic structure and potential energy surfaces. J Am Chem Soc 117:7916–7922
54. Shchapin IYu, Feldman VI, Belevskii VN, Khoroshutin AV, Bobylyova AA (1999) Ion-molecule reactions and thermal isomerization of tricyclo[4 3 0 0(3 7)]nona-4,8-diene radical cations to tricyclo[4 2 1 0(4,9)]nona-2,7-diene radical cations in a gamma-irradiated frozen Freon matrix. Radiat Phys Chem 55:559–563
55. Komaguchi K, Shiotani M, Lund A (1997) An ESR study of trimethylenemethane radical cation. Chem Phys Lett 265:217–223
55a. Rhodes CJ (2003) An electron spin resonance investigation of the radiolysis of hexamethylbenzene and hexamethyl(Dewar)benzene. Prog React Kinet Mechanism 28:57–74
56. Erickson R, Benetis NP, Lund A, Lindgren M (1997) Radical cation of naphthalene on H-ZSM-5 zeolite and in $CFCl_3$ matrix A theoretical and experimental EPR, ENDOR, and ESEEM study. J Phys Chem A 101:2390–2396
57. Kadam RM, Erickson R, Komaguchi K, Shiotani M, Lund A (1998) ENDOR and EPR studies of benzene radical cations in halocarbon matrices: the static Jahn-Teller distortion of the monomer and geometry of the dimer cation. Chem Phys Lett 290:371–378
58. Itagaki Y, Benetis NP, Kadam RM, Lund A (2000) Structure of dimeric radical cations of benzene and toluene in halocarbon matrices: an EPR, ENDOR and MO study. Phys Chem Chem Phys 2:2683–2689
59. Kubozono Y, Okada, Miyamoto T, Ata M, Gomodo Y, Shiotani M, Yasutake S (1992) Matrix dependence of the conformations of the 1,4-diethylbenzene radical cation at low-temperatures. Spectrochim Acta Part A 48:213–218
60. Zezin AA, Feldman VI (2000) Formation of radical cations and hole migration upon irradiation of frozen solutions of aromatic hydrocarbons. Dokl Akad Nauk 370:481–485
61. Liu W, Lund A (2005) Geometric and electronic structure of the diphenylamine radical cation: an EPR, ENDOR and MO study. J Mol Struct 733:13–17
62. Itagaki Y, Yanagida N, Shiotani, M (2002) Formation and structure of dimer radical cations of fluorinated benzenes in solid matrices. Phys Chem Chem Phys 4:5982–5987
63. Tyurin DA, Belevskii VN (2001) Structure and reactivity of the radical cations of methyl tert-butyl ether in condensed phase: An ESR and quantum chemical study. High Energy Chem 35:404–416
64. Wang JT, Williams F (1981) Electron spin resonance detection of the dimethyl ether radical cation. J Am Chem Soc 103:6994–6996
65. Kubodera H, Shida T, Shimokoshi K (1981) Electron spin resonance evidence for the cation radicals of tetrahydrofurans and dimethyl ether produced in a gamma-irradiated frozen matrix of trichlorofluoromethane. J Phys Chem 85:2583–2586
66. Janovsky I, Knolle W, Naumov S, Williams F (2004) EPR studies of amine radical cations, part 1: Thermal and photoinduced rearrangements of n-alkylamine radical cations to their distonic forms in low-temperature freon matrices. Chem A Eur J 10:5524–5534
67. Knolle W, Janovsky I, Naumov S, Williams F (2004) EPR studies of amine radical cations. Part 2. Thermal and photo-induced rearrangements of propargylamine and allylamine radical cations in low-temperature freon matrices. J Phys Chem A 110:13816–13826
68. Naumov S, Janovsky I, Knolle W, Mehnert R, Turin, DA (2005) Low-temperature EPR and quantum chemical study of lactone radical cations and their transformations Radiat Phys Chem 73:206–212

69. Knolle W, Yanovsky I, Naumov S, Mehnert R (1999) Low-temperature EPR study of radical cations of vinyl ethers in a freon matrix. Radiat Phys Chem 55:625–631
70. Naumov S, Janovsky I, Knolle W, Mehnert R (2005) Role of distonic dimer radical cations in the radiation-induced polymerisation of vinyl ethers. Nucl Instrum Methods Phys Res B 236:461–467
71. Janovsky I, Naumov S, Knolle W, Mehnert R (2005) Radiation-induced polymerisation of 2,3-dihydrofuran: free-radical or cationic mechanism? Radiat Phys Chem 72:125–133
72. Knolle W, Yanovsky I, Naumov S, Mehnert R (1999) Low-temperature EPR study of radical cations of 2,5-and 2,3-dihydrofuran and their transformations in freon matrices. J Chem Soc Perkin Trans 2:2447–2453
73. Naumov S, Janovsky I, Knolle W, Mehnert R (2003) Distonic dimer radical cation of 2,3-dihydrofuran: Quantum chemical calculations and low-temperature EPR results. Nucl Instrum Methods Phys Res B 208:385–389
74. Naumov S, Janovsky I, Knolle W, Mehnert R (2003) Formation of 3,4-dihydrofuran radical cation through intramolecular H-shift: quantum chemical calculations and low-temperature EPR study. Radiat Phys Chem 67:243–246
75. Naumov S, Janovsky I, Knolle W, Mehnert R (2003) Radical cation, dimer radical cation and neutral radical of 2,3-dihydropyran—possible initiators of its polymerisation? Macromol Chem Phys 204:2099–2104
76. Naumov S, Janovsky I, Knolle W, Mehnert R (2003) Radical cations of tetrahydropyran and 1,4-dioxane revisited: quantum chemical calculations and low-temperature EPR results. Phys Chem Chem Phys 5:3133–3139
77. Knolle W, Feldman VI, Yanovsky I, Naumov S, Mehnert R, Langguth H, Sukhov FF, Orlov AYu (2002) EPR study of methyl and ethyl acrylate radical cations and their transformations in low-temperature matrices. J Chem Soc Perkin Trans 2:687–699
78. Janovsky I, Naumov S, Knolle W, Mehnert R (2003) Radical cations of tetrahydropyran and 1,4-dioxane revisited: quantum chemical calculations and low-temperature EPR results. Radiat Phys Chem 67:237–241
79. Nuzhdin KB, Nesterov SV, Tyurin DA, Feldman VI, Wei L, Lund A (2005) Structure of radical cations of saturated heterocyclic compounds with two heteroatoms as studied by electron paramagnetic resonance, electron ─ nuclear double resonance, and density functional theory. J Phys Chem A 109:6166–6173
80. Dondi D, Cimino P, Barone V, Buttafava A, Lanzalunga O, Faucitano A (2011) Matrix EPR and QM study of a model aromatic thioether radical-cation. Tetrahedron Lett 52:4097–4102
81. Belevskii VN, Belopushkin SI, Mel'nikov MYa, Feldman VI (1998) Fragmentation and ion-molecule reactions of radical cations of diethylmercury as studied by EPR and UV spectroscopy. Acta Chem Scand 52:903–910
82. Bally T (1991) Electronic structure, spectroscopy, and photochemistry of organic radical cations. In: Lund A, Shiotani M (eds) Radical ionic. Kluwer, Dordrecht
83. Shida T (1988) Electronic absorption spectra of radical ions. Elsevier, Amsterdam
84. Feldman VI, Mel'nikov MYa (2000) Matrix effects in the reactions of organic radical cations in ground and excited states in solid phase. High Energy Chem 34:236–245
85. Mel'nikov MY, Baskakov DV, Feldman VI (2003). Spectral characteristics and transformations of intermediates in irradiated Freon 11, Freon 113, and Freon 113a. High Energy Chem 36:309–315
86. Belokon EA, Pergushov VI, Tyurin DA, Egorov M, Mel'nikov MY (2005) Photoinduced transformations in low-temperature matrices containing radical cations of organotin compounds. High Energy Chem 39:224–231
87. Mel'nikov MY, Kalugina AD, Mel'nikova OL, Pergushov VI, Tyurin DA (2009). Photochemistry of trimethylene oxide and trimethylene sulfide radical cations in freonic matrices at 77 K. High Energy Chem 43:303–311
88. Sorokin ID, Feldman VI, Mel'nikova OL, Pergushov VI, Tyurin DA, Mel'nikov MY (2011) Reversible photochemical transformations of cis- and trans-2,3-dimethyloxirane radical cations in freonic matrices at 77 K. Mendeleev Commun 21:153–154

89. Sorokin ID, Feldman VI, Mel'nikova OL, Pergushov VI, Tyurin DA, Mel'nikov MY (2011) The nature and photochemistry of 2,2-dimethyloxirane radical cations in freonic matrices at 77 K. Mendeleev Commun 21:155–156
90. Edlund O, Kinell P-O, Lund A, Shimizu A (1967) Electron spin resonance spectra of monomeric and dimeric cations of benzene. J Chem Phys 46:3679–3680
91. Komatsu T, Lund A (1972) Electron spin resonance studies on irradiated heterogeneous systems. IX. Anisotropy of g-factor and hyperfine coupling-constant of benzene cation in adsorbed state. J Phys Chem 76:1727–1728
92. Erickson R, Lindgren M, Lund A, Sjökvist L (1993) Ionic radicals on silica surfaces—an EPR, ENDOR AND ESE study of benzene radical cations adsorbed on HY and silica-gel. Colloids Surf A 72:207–216
93. Toriyama K, Nunome K, Iwasaki M (1987) Linear alkane radical cations prepared in synthetic zeolites by irradiation at 4 K—electron spin resonance evidence for ion molecule reaction to form 1-alkyl radicals. J Am Chem Soc 109:4496–4500
94. Qin X-Z, Trifunac AD (1990) Radiolytic generation of organic radical cations in zeolite NA-Y. J Phys Chem 94:4751–4754
95. Werst DW, Trifunac AD (1998) Observation of radical cations by swiftness or by stealth. Acc Chem Res 31:651–657
96. Werst DW, Trifunac AD (1998) Spin probes of adsorption and chemistry in solids: zeolites as model systems. Magn Res Rev 17:163
97. Liu W, Wang P, Komaguchi K, Shiotani M, Michalik J, Lund A (2000) Structure and dynamics of $[(CH_3)(_3)N\text{-}CH_2]$(+center dot) radical generated in gamma-irradiated Al-offretite. Phys Chem Chem Phys 2:2515–2519
98. Werst DW, Han P, Choure SC, Vinokur EI, Xu L, Trifunac AD, Eriksson LA (1999) Hydrogen atom addition to hydrocarbon guests in radiolyzed zeolites. J Phys Chem B 103:9219–9230
99. Andrews L (1991) Infrared and optical absorption spectroscopy of molecular ions in solid argon. In: Lund A, Shiotani M (eds) Radical ionic. Kluwer, Dordrecht
100. Andrews L, Moskovits M (eds) (1989) Chemistry and physics of matrix isolated species. Elsevier, Amsterdam
101. Bouldin WV, Gordy W (1964) Energy migration + isotopic effects in irradiated solids at low temperature. Phys Rev 135:A806-A814
102. Bhattachrya D, Willard JE (1981) Radiolytic production of trapped hydrogen atoms from organic compounds in Xe, Kr, and Ar at 10 K. J Phys Chem 85:154–159
103. Muto H, Toriyama K, Nunome K, Iwasaki M (1982) Radiolysis of alkanes and olefins in xenon matrices at 4.2 K as studied by electron spin resonance—formation and trapping of hydrogen atoms and their subsequent reactions at cryogenic temperatures. Radiat Phys Chem 19:201–208
104. Gotoh K, Miyazaki T, Fueki K, Lee K-P (1987) Electron spin resonance study of radiolysis of solid rare-gas alkane mixtures at 4.2 K—ionic fragmentation and initial energy of hot H-atoms. Radiat Phys Chem 30:89–89
105. Qin X-Z, Trifunac AD (1990) Radiolytic generation of radical cations in xenon matrices—tetramethylcyclopropane radical cation and its transformations. J Phys Chem 94:3188–3192
106. Knight LB (1986) ESR investigations of molecular cation radicals in neon matrices at 4 K: generation, trapping, and ion—neutral reactions. Acc Chem Res 19:313–321
107. Knight LB (1991) Generation and study of inorganic cations on rare gas matrices. In: Lund A, Shiotani M (eds) Radical ionic. Kluwer, Dordrecht
108. Knight LB, Gregory BW, Cobranchi ST, Williams F, Qin X-Z (1988) High-resolution electron-spin-resonance spectroscopy and structure of the acetaldehyde radical cation (CH_3CHO^+) in neon matrices at 4 K—comparison with results in freon matrices. J Am Chem Soc 110:327–342
109. Knight LB, Gregory BW, Hill DW, Arrington CA, Momose T, Shida T (1991) Electron-spin-resonance studies of $(CH_3F^+)C^{12}$, $(CH_3F^+)C_,^{13}$ and $(CH_2DF^+)C^{12}$ in neon matrices at 4 K—comparison with theoretical calculations. J Chem Phys 94:67–79

110. Karakyriakos E, Davis JR, Wilson CJ, Yates SA, McKinley AJ, Knight LB, Babb R, Tyler DJ (1999) Neon and argon matrix ESR and theoretical studies of the (CH_3Cd)-C^{12}, (CD_3Cd)-C^{12}, (CH_3Cd)-C^{13}, (CH_3)-C^{12} Cd^{111}, and (CH_3)-C^{12} Cd^{113} radicals. J Chem Phys 110:3398–3410
111. Feldman VI, Sukhov FF, Orlov AYu (1997) Further evidence for formation of xenon dihydride from neutral hydrogen atoms: a comparison of ESR and IR spectroscopic results. Chem Phys Lett 280:507–512
112. Feldman VI (1999) Radiation-induced transformations of isolated organic molecules in solid rare gas matrices. Radiat Phys Chem 55:565–571
113. Feldman VI, Sukhov FF, Orlov AYu (1999) An ESR study of benzene radical cation in an argon matrix: evidence for favourable stabilization of $^2B_{1g}$ rather than $^2B_{2g}$ state. Chem Phys Lett 300:713–718
114. Feldman VI, Sukhov FF, Orlov AYu, Kadam R, Itagaki Y, Lund A (2000) Effect of matrix and substituent on the electronic structure of trapped benzene radical cations. Phys Chem Chem Phys 2:29–35
115. Feldman VI, Sukhov FF, Orlov AYu, Shmakova NA (2000) Effect of matrix electronic characteristics on trapping and degradation of organic radical cations in solid ware gases: A case study of methylal radical cation. J Phys Chem A 104:3792–3799
116. Feldman VI, Sukhov FF, Orlov AYu, Shmakova NA (2001) Radiation chemistry of organic molecules in solid rare gas matrices: 2 Selective deprotonation of the primary radical cations upon irradiation of oxygen-containing molecules in xenon matrices. High Energy Chem 35:319–327
117. Feldman V, Sukhov F, Orlov A, Tyulpina I (2003) Stabilization and reactions of aliphatic radical cations produced by fast electron irradiation in solid argon matrices. Phys Chem Chem Phys 5:1769–1774.
118. Feldman VI, Sukhov FF, Orlov AYu, Tyulpina IV, Ivanchenko VK (2006) Stabilization and isomerization of radical cations generated by fast electron irradiation of unsaturated organic molecules in a solid argon matrix. Radiat Phys Chem 75:106–114
119. Feldman VI, Baranova IA, Kobzarenko AV, Tyulpina IV (2011) Fragmentation of the primary radical cations of methoxyacetone and diacetonyl in a solid argon matrix. High Energy Chem 45:351–352
120. Feldman VI, Sukhov FF, Orlov AYu, Tyulpina IV (2008) High-resolution EPR spectroscopy of small radicals in a solid ^{136}Xe matrix. Mendeleev Commun 18:121–122
121. Feldman VI, Orlov AYu, Sukhov FF (2008) Hydrogen atoms in solid xenon: Trapping site structure, distribution, and stability as revealed by EPR studies in monoisotopic and isotopically enriched xenon matrices. J Chem Phys 128:214511
122. Feldman VI, Borzov SM, Sukhov FF, Slovokhtova NA (1986) Spectroscopic investigation of trans-butene-2 cation-radical formation and transformations in freon matrices Khimictskaya fizika 5:510–516
123. Feldman VI, Sukhov FF, Slovokhotova NA, Bazov VP (1996) Radiation-induced degradation of alkane molecules in solid rare gas matrices. Radiat Phys Chem 48: 261–269
124. Baskir EG, Misochko EY, Nefedov OM (2009) Spectroscopy and structure of free radicals stabilized in cryogenic matrices. Russ Chem Rev 78:638–715
125. Tanskanen H, Khriachtchev L, Räsänen M, Feldman VI, Sukhov FF, Orlov AY, Tyurin DA (2005) Infrared absorption and electron paramagnetic resonance studies of vinyl radical in noble-gas matrices. J Chem Phys 123:064318
126. Feldman VI, Sukhov FF, Logacheva EA, Orlov AYu, Tyulpina IV, Tyurin DA (2007) Reactions of H atoms produced by electron irradiation of benzene in solid xenon: IR spectrum of cylohexadienyl radical and possible involvement of $HXeC_6H_5$. Chem Phys Lett 2007: 207–211
127. Toriyama K, Okazaki M (1992) Selectively weakened carbon-carbon sigma-bond in cation radicals of linear and branched pentanes as studied by electron spin resonance. J Phys Chem 96:6986–6991
128. Werst DW, Han P, Trifunac AD (1997) Trap-to-trap hole transfer studied by radiolysis/EPR Radical cations in freon and zeolite matrices. Chem Phys Lett 269:333–340

129. Egorov AV, Baranova IA, Zezin AA, Andriyanova AA, Feldman VI (2007) Positive hole transfer between organic molecules of different classes in Freon matrices. High Energy Chem 41:409–414
130. Belevskii VN (1990) Reactions of radical cations in condensed phase. Dissertation, Moscow State University
131. Egorov AV, Zezin AA, Feldman VI (2003) An EPR study of positive hole transfer and trapping in irradiated frozen solutions containing aromatic traps. Radiat Phys Chem 67: 231–235
132. Nuzhdin KB, Feldman VI, Kobzarenko AV (2007) Diketone radical cations: Ketonic and enolic forms as revealed by matrix EPR studies and DFT Calculations. J Phys Chem A 111:3294–3301
133. Nuzhdin KB, Feldman VI, Kobzarenko AV (2008) Delocalized methoxyacetone radical cation: structure and reactivity. Mendeleev Commun. 18:69–70
134. Nuzhdin KB, Feldman VI Structure and photochemistry of "bridged" bifunctional radical cations: amidoesters vs. amides. Radiat Phys Chem 77:416–427
135. Nuzhdin KB, Kobzarenko AV, Barabanov II, Feldman VI (2009) A "magic bridge": effect of methylene chain length on the photochemistry of radical cations produced from bifunctional X-$(CH_2)_n$-Y molecules. Mendeleev Commun 19:268–269
136. Egorov AV (2004) Experimental modeling of early stages of the radiation-chemical processes in aromatic hydrocarbons and polystyrene. Dissertation, Moscow State University
137. Knight LB, Steadman J (1984) An electron-spin-resonance investigation of the formaldehyde cation radicals ($H_2(CO^+)C^{12}$ and $H_2(CO_+)C^{13}$) in neon matrices at 4-K. J Chem Phys 80:1018–1025
138. Rhodes CJ, Symons MCR (1988) The radical cation of formaldehyde in a freon matrix—an electron-spin resonance study. J Chem Soc Faraday Trans 1 84:4501–4507
139. Snow LD, Wang JT, Williams F (1982) Delocalized pi-radical cations of acetals. J Am Chem Soc 104:2062–2064
140. Boon PJ, Harris L, Olm MT, Wyatt L, Symons MCR (1984) The acetone cation—a C^{13} electron spin resonance and ENDOR study. Chem Phys Lett 106:408–412
141. Iwasaki M, Toriyama K, Nunome H (1983) Electron-spin-resonance evidence for the static distortion of $^2E_{1g}$ benzene cations giving $^2B_{2g}$ with D_{2h} symmetry in low-temperature matrices. J Chem Soc Chem Commun:320–322
142. Tabata M, Lund A (1983) Electron spin resonance of cation radicals of methyl-substituted benzenes in a CF_3CCl_3 matrix. Z Naturforsch A 38:428–433
143. Toriyama K, Nunome K, Iwasaki M (1981) Sigma-delocalized radical cations $[H(CH_2)NH]^+$ of primary alkanes—electron spin resonance evidence. J Phys Chem 85:2149–2152
144. Fujisawa J, Sato S, Shimokoshi K, Shida T (1985) Stereospecific conversion of butene cations into methylallyl radicals: an ESR study. J Phys Chem 89:5481–5486
145. Symons MCR, Wren B (1984) Electron spin resonance spectra of ether radical cations generated by radiolysis. J Chem Soc Perkin 2:687–689
146. Lindner R, Muller-Dethlefs K, Wedum E, Haber K, Grant ER (1996) On the shape of $C_6H_6^{+\cdot}$. Science 271:1698–1702
147. NIST Chemistry Webbook. NIST Standard Reference Database Number 69 (2011). http://webbook.nist.gov/chemistry/. Accessed 5 Sept 2011
148. Karatun AA, Sukhov FF, Slovokhotova NA (1981) Stabilization of HAr_n^+, HKr_n^+, and HXe_n^+ in solid inert-gases on irradiation of 2-chloropropane in them by fast electrons. Khim Vys Energ 156:371–372
149. Kunttu H, Seetula J, Rasanen M, Apkarian A (1992) Photogeneration of ions via delocalized charge-transfer states 1 Xe_2H^+ and Xe_2D^+ in solid Xe. J Chem Phys 96:5630–5635
150. Fridgen TD, Parnis JM (1999) A density functional theory study of the catalytic role of Ar, Kr, Xe, and N_2 in the CH_3OH center dot + to CH_2OH_2 center dot + isomerization reaction. Int J Mass Spectrom Ion Processes 190–191:181–194
151. Kobzarenko AV, Sukhov FF, Orlov AY, Kovalev GV, Baranova IA, Feldman VI (2012) Effect of molecular structure on fragmentation of organic molecules in solid rare gas matrices. Radiat Phys Chem 81:1434–1439

152. Hiseh T, Gilman JP, Weiss MJ, Meisels GG (1981) Competition between isomerization and fragmentation of gaseous ions. I. Kinetic and thermodynamic control for $C_4H_8^+$ ions. J Phys Chem 85:2722–2725
153. Toriyama K, Nunome, Iwasaki M (1982) Structures and reactions of radical cations of some prototype alkanes in low-temperature solids as studied by electron spin resonance spectroscopy. J Chem Phys 77:5891–5912
154. Toriyama K, Nunome K and Iwasaki M (1986) Structures and reactions of radical cations of linear alkanes—electron spin resonance evidence for selective deprotonation. J Phys Chem 90:6836–6842
155. Shiotani M, Lindgren M, Takahashi F, Ichikawa T (1990) On the alkyl radical formation from alkane cations in halocarbons—results for various alkyl-substituted cyclohexanes. Chem Phys Lett 170:201–205
156. Williams F, Qin X-Z (1988) Electron spin resonance studies of ion molecule reactions of ether, thioether, and olefin radical cations in the $CF_2ClCFCl_2$ matrix. Radiat Phys Chem 32:299–308
157. Baranova IA, Belevskii VN, Belopushkin SI, Feldman VI (1991) EPR study of reactions of methylal and dimethoxyethane cation radicals in condensed phase. High Energy Chem 25:450–457
158. Baranova IA, Feldman VI, Belevskii VN (1988) Reactions of radical cations of acetals—evidence for unimolecular decomposition. J Radioanal Nucl Chem Lett 126:39–51
159. Chappas WJ, Silverman J (1980) The radiation chemistry of crystalline alkanes. Radiat Phys Chem 16:437–443
160. Shimada S, Kashiwabara H, Sohma J, Nara S (1969) Anisotropic hyperfine constant in ESR spectrum of irradiated solution grown polyethylene. Jap J Appl Phys 8:145–150
161. Feldman VI, Sukhov FF, Slovokhotova NA (1994) Selectivity of radiation-induced chemical processes in low-molecular-mass and high-molecular-mass hydrocarbons. Vysokomolek soedin B 36:519–543
162. Feldman VI (1996) Selective localization of primary radiation-chemical events in solid aliphatic hydrocarbons and related polymers as evidenced by ESR. Appl Radiat Isot 47: 1497–1501
163. Zezin AA, Feldman VI (2002) Formation and reactions of paramagnetic species in irradiated microheterogeneous copolymer systems with different electronic characteristics of components. Radiat Phys Chem 63:75–80
164. Saenko EV, Laikov DN, Baranova IA, Feldman VI (2011) Stabilization of radical anions with weakly bound electron in condensed media: a case study of diacetonyl radical anion. J Chem Phys 135:10103

Chapter 3
Molecule-Based Exchange-Coupled High-Spin Clusters: Conventional, High-Field/High-Frequency and Pulse-Based Electron Spin Resonance of Molecule-Based Magnetically Coupled Systems

Takeji Takui, Shigeaki Nakazawa, Hideto Matsuoka, Kou Furukawa, Kazunobu Sato, and Daisuke Shiomi

Abstract Syntheses and magnetic functionalities of exchange-coupled magnetic systems in a controlled fashion of molecular basis have been the focus of the current topics in chemistry and materials science; particularly extremely large spins in molecular frames and molecular high-spin clusters have attracted much attention among the diverse topics of molecule-based magnetics and high spin chemistry. Magnetic characterizations of molecule-based exchange-coupled high-spin clusters are described in terms of conventional as well as high-field/high-frequency ESR spectroscopy. Off-principal-axis extra lines as a salient feature of fine-structure ESR spectroscopy in non-oriented media are emphasized in the spectral analyses. Pulse-ESR-based two-dimensional electron spin transient nutation spectroscopy applied to molecular high-spin clusters is also dealt with, briefly. Solution-phase fine-structure ESR spectroscopy is reviewed in terms of molecular magnetics. In addition to finite molecular high-spin clusters, salient features of molecule-based low-dimensional magnetic materials are dealt with. Throughout the chapter, electron spin resonance for high-spin systems is treated in a general manner in terms of theory. Hybrid eigenfield method is formulated in terms of direct products, and is described as a powerful and facile approach to the exact numerical calculation of resonance fields and transition probabilities for molecular high spin systems. Exact analytical expressions for resonance fields of high spin systems in their principal orientations are for the first time given.

T. Takui (✉) • S. Nakazawa • H. Matsuoka • K. Furukawa • K. Sato • D. Shiomi
Department of Chemistry and Molecular Materials Science, Graduate School of Science, Osaka City University, Osaka 558-8585, Japan
e-mail: takui@sci-osaka-cu.ac.jp

A. Lund and M. Shiotani (eds.), *EPR of Free Radicals in Solids II*, Progress in Theoretical Chemistry and Physics 25, DOI 10.1007/978-94-007-4887-3_3,

3.1 Introduction

Magnetic-ion-based exchange-coupled systems and their fine-structure ESR spectral analyses have been long-standing issues in electron magnetic resonance spectroscopy. Many standard or advanced ESR textbooks have been published, which have dealt with the issues, more or less [1]. Among these, the most comprehensive one devoted to the issues appeared in 1987 [1f]. Recently, syntheses of exchange-coupled magnetic systems in a controlled fashion of molecular basis have been the focus of the current topics in chemistry and materials sciences; particularly extremely high spins in molecular frames and high-spin molecular clusters, or large nonvanishing angular momentum systems have attracted much attention among the diverse topics of molecule-based magnetics and high spin chemistry [2]. This is partly due to the potential applications of the quantum nature of spins and orbital angular momenta controlled in well-designed molecular frames, emphasizing molecular designs such as for spin-mediated memory devices, spin magnetization oscillations, single-spin (extremely large S) detection and its dynamics, and the utilizations of dynamic (transverse) phase transitions of spin magnetizations; these issues can be termed molecular spinics in future science and technology. Organic molecular systems give exceptional diversity as subjects of novel quantum magnetic phenomena or functionalities. Organic super high-spin magnetics utilizing through-bond approaches is closely related to conceptual advances in magnetics which underlie novel molecular functionality devices such as genuine liquid-phase magnets and magnetic spin quantum well effects. In this context, spin dynamics for superparamagnets or extremely large molecular spins is expected to develop.

Also, from the theoretical side, molecule-based magnetics underlain by high spin chemistry is an important testing ground for a variety of theoretical models, whether they are established or not. In favorable conditions, electron magnetic resonance of molecular magnetic materials plays a crucial role to understand novel aspects of their magnetic property. For example, organic ferrimagnetics demonstrate a breakdown of classical and conventional pictures for ferrimagnetics [1, 3]. Experimentally direct detection of molecular systems with large fine-structure constants due to spin-orbit couplings has been challenged in the recent progress with high-field/high-frequency ESR spectroscopy. Findings of the quantum tunneling of spin magnetization from exchange-coupled transition metal ion clusters have affected research trends in interdisciplinary fields between chemistry and physics, emphasizing general interests in single-molecule magnets (SMM's) exhibiting stepwise magnetic hysteresis of the magnetization at low temperatures. Also, magnetic-ion clustering systems of biological importance have been elucidated, attracting general attention.

In a magnetically ordered molecular substance, the macroscopic magnetization as cooperative property is described in terms of dynamics of microscopic details (molecular spins). There are a variety of magnetic excitations, where the excitation does not remain localized at a given spin site but propagates in the form of coherent waves. The collectivized coherency (collective excitation) typically

originates in quantum-mechanical exchange interactions, forming the simplest type of magnetic excitation as spin waves or magnons. The exchange interaction is of short range. There is another type of spin waves, which is driven by an electron-spin dipolar interaction, i.e., a Walker mode. In terms of spin carriers, all documented spin waves are not molecule-based, but atom-based. These conventional spin waves are standing waves along the direction perpendicular to the thin film. Recently, novel types of quantum modes for standing spin waves have appeared which arise from artificial superlattices of ferromagnetic thin films on a micron size. One of the novel quantum modes is a lateral Walker's mode, and another is a dipolar spin wave from gigantic magnetic moments of one- or two-dimensionally arrayed ferromagnetic islands. Experimental identifications of the quantum modes have been carried out by electron spin (ferromagnetic) resonance spectroscopy [4]. Those artificial superlattices of ferromagnetic microstructures are an intermediate substance between bulk magnetic materials and molecular magnetic clusters with extremely high spins. In this context, magnetic resonance phenomena on a semi-microscopic scale are new applications of electron spin resonance spectroscopy. The spin dynamics of both magnetic substances on a semi-microscopic scale and molecular superparamagnets with internal spin (polar) structures is one of the current issues in molecule-based magnetics and spin science.

This chapter surveys the recent progress in fine-structure ESR spectroscopy of exchange-coupled molecular systems with finite spin multiplicities, both experimentally and theoretically, focusing on the documentation that has appeared recently after the book by Bencini and Gatteschi was published [1f]. The molecular systems included in the book are mainly inorganic ones, and genuinely organic high-spin clusters of chemical and spectroscopic importance are dealt with as well. Throughout the present chapter, molecular high-spin clusters mean intermolecularly exchange-coupled spin systems in chemistry terms. Thus, high-spin oligopolynitrenes or high-spin hydrocarbons such as oligopolycarbenes [4] or cyclopentanediyl-based hydrocarbons [5] with large high-spin multiplicities, whose high spins arise from the topological symmetry of their π-conjugation network of chemical bonding, are not dealt with in the present chapter except in theoretical terms. They are grouped into intramolecularly exchange-coupled systems and are dealt with in Chap. 5 by Baumgarten. In terms of the effective spin-Hamiltonian approach, both inter- and intramolecularly exchange-coupled systems can be treated on the same theoretical background, but in microscopic terms both systems show remarkably different magnetic properties and they require intrinsic molecular designs. In harmony with the book title, the issues treated in this chapter are associated with solid states. Nevertheless, in terms of spin dynamics in high-spin ESR spectroscopy and future technology, solution ESR spectroscopy for stable high-spin molecular systems with hyperfine interactions of comparable order to fine-structure ones is of particular importance. The chapter spares pages for this issue.

Referred to electron magnetic resonance in ordered regimes such as low dimensional magnetic systems, superparamagnetic ones and spin frustration ones, readers are recommended to consult recent reviews and monographs [1f, 2, 6]. The magnetic properties of magnetic materials such as low dimensional magnetic systems appearing on a macro- or semi-macroscopic scale are characterized by

invoking both magnetic resonance and magnetic susceptibility measurements. Approaches in terms of both micro- and macroscopic magnetic measurements are complementary for molecular exchange-coupled systems. Methodological establishments for molecular systems with nonvanishing and sizable orbital angular momenta and their assemblages are one of the current topics in the field of molecule-based magnetics and related fields [2a, 2f, 7–8]. Electron spin resonance spectroscopy applied to such molecular magnetic systems and their exchange-coupled assemblages in the crystal is immature, where analyses include magnetic interactions between orbital angular momenta. Treatments are beyond conventional Heisenberg-Dirac types of exchange couplings.

Electron-nuclear multiple resonance spectroscopy devoted to molecule-based high-spin systems is not included here, although it gives crucially important microscopic details such as spin density distributions, direct determination of spin sublevels involved in the ESR transitions, and thus the signs of the fine-structure constants in the high-spin systems [9]. Electron-nuclear multiple resonance spectroscopy in solid-state oriented media can afford direct evidence of inverted large negative molecular spins anticipated for antiferromagnetically exchange-coupled hetero-spin systems [9]. Applications of the multiple resonance technique to molecular high-spin systems in solid states are still premature [10].

3.2 Theoretical Background

The most striking feature of electron magnetic resonance phenomena due to molecule-based magnetically coupled clusters is that a variety of high spin states arising from the strength of exchange couplings give rise to a diversity of anisotropic ESR spectra. In this context, single-crystal fine-structure ESR spectroscopy is apparently the most powerful method for giving us anisotropic information on various magnetic tensors, which can be related to crystallographic structural data and electronic spin structures of molecular high-spin clusters. Nevertheless, single-crystal work is not always feasible simply because well-defined and magnetically diluted molecular systems are not available for most cases. In order to characterize magnetic properties of molecules or molecular clusters themselves, magnetically diluted molecular systems are required to suppress intermolecular exchange interactions, yielding anisotropic information on microscopic details with high accuracy. Thus, fine-structure ESR spectroscopy in non-oriented media is particularly important from the experimental side. Magnetically concentrated high-spin molecular clusters (molecule-based multinuclear high-spin clusters) are intriguing targets for fine-structure ESR spectroscopy in view of the molecularly controlled exchange couplings, intramolecular or intermolecular. In most magnetically concentrated high-spin nuclear clusters, hyperfine structures are smeared out in the ESR spectra. ESR spectroscopy gives unique microscopic information on their electronic and molecular structures with the help of their bulk magnetic properties based on magnetic susceptibility.

Generally, the fine-structure spectroscopy in non-oriented media requires spectral simulations to acquire spin Hamiltonian parameters with high accuracy from the observed fine-structure spectra for most cases except special cases with $S = 1$. Then, facile and easy-to-access interpretive approaches for high-spin identification in the ESR spectroscopy are useful. This chapter aims to present those approaches to readers who do not specialize in high-spin ESR spectroscopy and which allow them to extract spin Hamiltonian parameters from the observed fine-structure spectra. Under favorable conditions, the analytical exact expressions for the resonance fields described in this chapter help to extract the parameters without spectral simulations. Indeed, the exact analytical expressions for any resonance fields in triplet spin states are available [1f, 2e, g, 10b], but the counterparts in spin states higher than triplet have never been documented. This has been conceived of as mainly due to putative mathematical difficulties. This issue is solved as described in Sect. 3.3.3.

It should be noted that spectral simulations with the help of theoretical considerations for the electronic molecular structures of systems under study can afford us much information on magnetic properties of both high-spin molecules and molecular high-spin clusters. The theory-based or theoretically oriented spectral simulations are applicable to intramolecularly exchange-coupled high-spin systems under some restrictions, e.g., high-spin oligonitrenes whose high spin alignments are governed by the topological symmetry of π-spin polarizations [5]. In high-spin nitrene chemistry, there have been serious controversial issues between the documented fine-structure constants and quantum-chemistry-based spin structures. Those apparently puzzling issues have been disclosed by theory-based simulations [5]. Such a theoretical approach has been underlain by tensor-based analyses for the fine-structure spin-spin interaction, exemplifying a novel organic-radical-based molecule in Sect. 3.2.3. The approach is applicable to metal-based dinuclear high-spin clusters when spin sites are apart in the range of 0.3–0.8 nm and a classical magnetic dipole-dipole interaction is operative.

In terms of anisotropic ESR spectroscopy, another striking feature is the appearance of off-principal-axis lines, which correspond to the stationary points with the static magnetic field $\mathbf{B}_0$ along an off-principal-axis of the fine-structure tensor. Off-principal-axis absorption peaks in ESR spectroscopy are called extra lines (or off-axis extra lines). The occurrence of extra lines is inherent in fine-structure ESR spectra due to high spin molecular systems with $S > 1$. Referred to triplet states, an extra line appears only in the region for forbidden transitions [10b, 11]; the extra resonance line in fine-structure ESR spectra from randomly oriented samples has been called $B_{min.}$ The occurrence of extra lines complicates the fine-structure spectra from molecular high-spin systems, but correct identifications give a rationale for experimentally determined sets of spin Hamiltonian parameters with high accuracy [10b, 11].

Molecule-based infinite systems of exchange couplings feature low dimensionality of the systems. A long-time transverse relaxation occurring in the magnetic assemblages with extremely high purity depends on the dimensionality of the systems under study. This issue will be treated in a later section of this chapter.

3.2.1 *Effective Spin Hamiltonian Approach to Exchange-Coupled Systems: Tensor Analyses Underlying Theoretical Spectral Simulations*

Spectral and theoretical analyses in fine-structure ESR spectroscopy formolecular exchange-coupled high-spin clusters require the following two-site spin Hamiltonian to start,

$$\widehat{\mathrm{H}}^{\mathrm{spin}} = \widehat{\mathrm{H}}_{\mathrm{A}}{}^{\mathrm{spin}} + \widehat{\mathrm{H}}_{\mathrm{B}}{}^{\mathrm{spin}} + (-2J_{\mathrm{AB}})\,\mathbf{S}_{\mathrm{A}}\cdot\mathbf{S}_{\mathrm{B}} + \mathbf{S}_{\mathrm{A}}\cdot D_{\mathrm{AB}}\cdot\mathbf{S}_{\mathrm{B}} + d_{\mathrm{AB}}\cdot\mathbf{S}_{\mathrm{A}}\times\mathbf{S}_{\mathrm{B}} \quad (3.1)$$

$$\widehat{\mathrm{H}}_{\alpha}{}^{\mathrm{spin}} = \beta\mathbf{B}_0\cdot\boldsymbol{g}_{\alpha}\cdot\mathbf{S}_{\alpha} + \mathbf{S}_{\alpha}\cdot\boldsymbol{D}_{\alpha}\cdot\mathbf{S}_{\alpha} + \sum\nolimits_{\mathrm{k}}\mathbf{I}^{\mathrm{k}}\cdot A_{\alpha}{}^{\mathrm{k}}\cdot\mathbf{S}_{\alpha} \quad (\alpha = \mathrm{A},\mathrm{B}) \quad (3.2)$$

where we simply assume an isotropic exchange interaction between spins, $\boldsymbol{S}_{\mathrm{A}}$ and $\boldsymbol{S}_{\mathrm{B}}$, and also we neglect nuclear Zeeman terms, nuclear quadrupolar interactions and group-theoretically allowed quartic or higher-order fine-structure terms of even numbers such as $B_0{S_{\mathrm{m}}}^3$, ${S_{\mathrm{m}}}^2{S_n}^2$, and ${S_{\mathrm{m}}}^3{S_n}^3$ (n, m = x, y, z). The term of $B_0{S_{\mathrm{m}}}^3$ is required for some cases with high symmetry such as distorted tetrahedral or octahedral symmetry and high spin multiplicity. In the strong exchange-coupling limit, the isotropic exchange interaction term, $(-2J_{\mathrm{AB}})\mathbf{S}_{\mathrm{A}}\cdot\mathbf{S}_{\mathrm{B}}$ dominates and the other terms are considered to be perturbation ones. The z-component of $\mathbf{S} = \mathbf{S}_{\mathrm{A}} + \mathbf{S}_{\mathrm{B}}$ and $\mathbf{S}^2$ commutes with $(-2J_{\mathrm{AB}})\mathbf{S}_{\mathrm{A}}\cdot\mathbf{S}_{\mathrm{B}}$, giving the common eigenstate belonging to $(-2J_{\mathrm{AB}})\mathbf{S}_{\mathrm{A}}\cdot\mathbf{S}_{\mathrm{B}}$ and to $\mathbf{S}^2$ and S_{z}. The resultant spin quantum number S is given as $|\, S_{\mathrm{A}} - S_{\mathrm{B}}\,| \le S \le S_{\mathrm{A}} + S_{\mathrm{B}}$, and the corresponding eigenenergy, $E(S)$ is as follows;

$$E\,(S) = -J_{\mathrm{AB}}\,[S\,(S+1) - S_{\mathrm{A}}\,(S_{\mathrm{A}}+1) - S_{\mathrm{B}}\,(S_{\mathrm{B}}+1)] \quad (3.3)$$

with $|\, S_{\mathrm{A}} - S_{\mathrm{B}}\,| \le S \le S_{\mathrm{A}} + S_{\mathrm{B}}$.

In the strong exchange-coupling limit, no ESR transition occurs between different spin multiplicity states, giving superimposed fine-structure spectra with weights of Boltzmann distributions at a given temperature. It is to be noted that particular relationships of resonance fields and transition probabilities between the different spin states hold when superimposed fine-structure spectra appear from the same molecular magnetic origins. For example, the transition probabilities inherent in the quintet and triplet states arising from an $S_{\mathrm{A}} = S_{\mathrm{B}} = 1$ coupled system with an equivalent $\boldsymbol{D}_{\alpha}$, assuming $J \gg |\, D_{\mathrm{S}}\,|$, strongly depend on the ratio of $|D_{\mathrm{S}}|/h\nu$, where D_{S} stands for the fine-structure constant for the quintet or triplet state and $h\nu$ is the microwave transition energy. For the experimental condition of the ratio much smaller than unity, the transition probability for the $|\, S = 1;\, M_S = \pm 1\rangle \iff |\, S = 1;\, M_S = 0\,\rangle$ allowed transitions becomes, to first order, one half of that for the $|\, S = 2;\, M_S = \pm 2\rangle \iff |\, S = 2;\, M_S = \pm 1\,\rangle$ transitions. This is one of the reasons why a thermally accessible triplet state originating in intramolecularly interacting triplet-triplet systems has been difficult to identify experimentally in

Table 3.1 Formulas for the coefficients, c, c_+, and c_- for a given set of S_A and S_B[a]

$c = \{S_A(S_A+1) - S_B(S_B+1)\}/S(S+1)$
$c_+ = [3\{S_A(S_A+1) - S_B(S_B+1)\}^2 + S(S+1)\{3S(S+1) - 3$ $-2S_A(S_A+1)\}]/(2S+3)(2S-1)S(S+1)$
$c_- = [4S(S+1)\{S_A(S_A+1) - S_B(S_B+1)\} - 3\{S_A(S_A+1)$ $-S_B(S_B+1)\}]/(2S+3)(2S-1)S(S+1)$

[a]The coefficients are taken to be zero for spin-singlet states ($S = 0$), and also the coefficients should be zero for the vanishing denominator

non-oriented media such as organic glasses. In general, high-field/high-frequency resonance conditions are most favorable for identifying experimentally the different spin states from the same magnetic origin. The fact that the resulting resonance fields and transition probabilities from the different spin states in exchange-coupled systems are interrelated has been overlooked in the documentation so far except for a few cases [12]. The interrelation is crucially important for comprehensive analyses of the electronic structures of molecular exchange-coupled systems based on their fine-structure spectra.

Fine-structure spectra due to any spin state with a well-defined spin quantum number S whose energy is given by Eq. (3.3) are described by the resultant spin Hamiltonian, $\hat{H}_S{}^{spin}$ as follows;

$$\hat{H}_S{}^{spin} = \beta \mathbf{B}_0 \cdot \boldsymbol{g}_S \cdot \mathbf{S} + \mathbf{S} \cdot \boldsymbol{D}_S \cdot \mathbf{S} + \sum\nolimits_k \mathbf{I}^k \cdot \boldsymbol{A}_S^k \cdot \mathbf{S} \tag{3.4}$$

where the similar neglect of tensor terms as in Eq. (3.2) is made. Intrinsic relationships between a set of spin Hamiltonian parameters, $\boldsymbol{g}_S$, $\boldsymbol{D}_S$, $\boldsymbol{A}_S{}^k$ and those of the A and B components, $\boldsymbol{g}_\alpha$, $\boldsymbol{D}_\alpha$, $\boldsymbol{A}_\alpha{}^k$ (α = A, B) are acquired by invoking Wigner-Eckart theorem with irreducible tensor operators and using Clebsch-Gordon coefficients as follows [1f, 2f, 13];

$$\begin{aligned}\hat{H}_S{}^{spin} = {} & \beta[\mathbf{B}_0 \cdot (1/2)\left(\boldsymbol{g}_+ + c\boldsymbol{g}_-\right) \cdot \mathbf{S}] + \mathbf{S} \cdot (1/2)\left[(1-c_+)\boldsymbol{D}_{AB} + c_+ \boldsymbol{D}_+ \right. \\ & \left. + c_- D_-\right] \cdot \mathbf{S} + \sum\nolimits_k \mathbf{I}^k \cdot (1/2)\left[(1+c)\boldsymbol{A}_A{}^k + (1-c)\boldsymbol{A}_B{}^k\right] \cdot \mathbf{S} \\ & - J_{AB}\left[S(S+1) - S_A(S_A+1) - S_B(S_B+1)\right]\end{aligned} \tag{3.5}$$

where the term of $\boldsymbol{d}_{AB} \cdot \boldsymbol{S}_A \times \boldsymbol{S}_B$ is neglected. The set of the coefficients, c, c_+, and c_-, are expressed as functions of S, S_A, and S_B only. Formulas for the functions are given in Table 3.1 [1f, 2f]. The relationships between the resultant tensors in the resultant spin Hamiltonian and those in the component spin Hamiltonians are given by

$$\boldsymbol{g}_S = c_1 \boldsymbol{g}_A + c_2 \boldsymbol{g}_B \qquad (\boldsymbol{g}_\pm = \boldsymbol{g}_A \pm \boldsymbol{g}_B) \tag{3.6a}$$

$$\boldsymbol{D}_S = d_1 \boldsymbol{D}_A + d_2 \boldsymbol{D}_B + d_{12} \boldsymbol{D}_{AB} \quad (\boldsymbol{D}_\pm = \boldsymbol{D}_A \pm \boldsymbol{D}_B) \tag{3.6b}$$

$$\boldsymbol{A}_S{}^{k} = c_1 \boldsymbol{A}_A{}^{k} + c_2 \boldsymbol{A}_B{}^{k} \tag{3.6c}$$

$$c_1 = (1 + c)/2, \quad c_2 = (1 - c)/2$$

$$d_1 = (c_+ + c_-)/2, \quad d_2 = (c_+ - c_-)/2, \quad d_{12} = (1 - c_+)/2$$

All the relationships above are given in terms of tensor-based expressions in their own coordinate systems. There have been seen many documentations which commit errors in the expressions and the understanding of the relationships. Thus, it is worthwhile noting that unitary transformation procedures are required for theoretical calculations of the resulting tensors from the component tensors [12]. For example, a given component tensor $\boldsymbol{D}_i$ in a convenient reference frame (e. g., a common coordinate-axis system such as a molecular principal-axis system) is given by

$$\boldsymbol{D}_i = {}^{t}\mathbf{U}_i \cdot \boldsymbol{D}_i^{d} \cdot \mathbf{U}_i \qquad (i = A, B, AB) \tag{3.7}$$

where $\boldsymbol{D}_i{}^{d}$ denotes the given component tensor in the diagonal (principal axis and local molecular) frame and $\mathbf{U}_i$ is a rotation (unitary) matrix in which the three rows are constructed by the three set of the corresponding direction cosines for the three principal values of $\boldsymbol{D}_i{}^{d}$, and ${}^{t}\mathbf{U}_i$ stands for the transposed matrix of $\mathbf{U}_i$. During this procedure, the local molecular structure relevant to $\boldsymbol{D}_i{}^{d}$, theoretically or empirically, should be known. The resultant $\boldsymbol{D}_S$ (e.g., Eq. (3.6b)) in terms of the convenient reference frame is diagonalized to give $\boldsymbol{D}_S{}^{d}$, i.e., the principal values and corresponding direction cosines of $\boldsymbol{D}_S$ in the reference frame. In order to produce theory-based spectral simulations, all the resultant theoretical tensors are transformed to the field-based coordinate axes defined by both $\boldsymbol{B}_0$ and $\boldsymbol{B}_1$ (microwave oscillating field).

In the weak exchange-coupling limit and for intermediate exchange-coupling cases, general and group-theoretical treatments have been made also by Bencini and Gatteschi [1f], and analytical expressions for the spin Hamiltonian parameters are given in their book together with examples of ESR spectra. Extended applications of the above approach to three- or four-spin exchange-coupled systems in the strong coupling limit are feasible. In the case of intermediate exchange coupling, a remarkable change in fine-structure ESR spectra takes place due to spin quantum mixing between interrelated spin states. The changes depend on the ratio of $|D_S/2J|$ and the group-theoretical symmetry of the systems under study. Figure 3.1 exemplifies a quantum spin mixing occurring in an exchange-coupled triplet pair, showing typical fine-structure ESR spectra at K-band (∼25 GHz) calculated for the static magnetic field $\boldsymbol{B}_0$ along a given direction. For symmetry arguments, $\boldsymbol{D}_A = \boldsymbol{D}_B$ is assumed in the calculation [14]. As the spin quantum mixing with $|2J|$ comparable to $|D_S|$ grows, new ESR transitions arise with intensity borrowing and a considerable amount of shifting of the resonance fields occurs. In the case of complete mixing, the characteristic spectral features arising from the quintet and triplet states disappear, giving the appearance of only two triplet-state fine-structure spectra. They are not independent, but interrelated. In this example, a singlet-quintet complete mixing takes place due to the group-theoretical symmetry

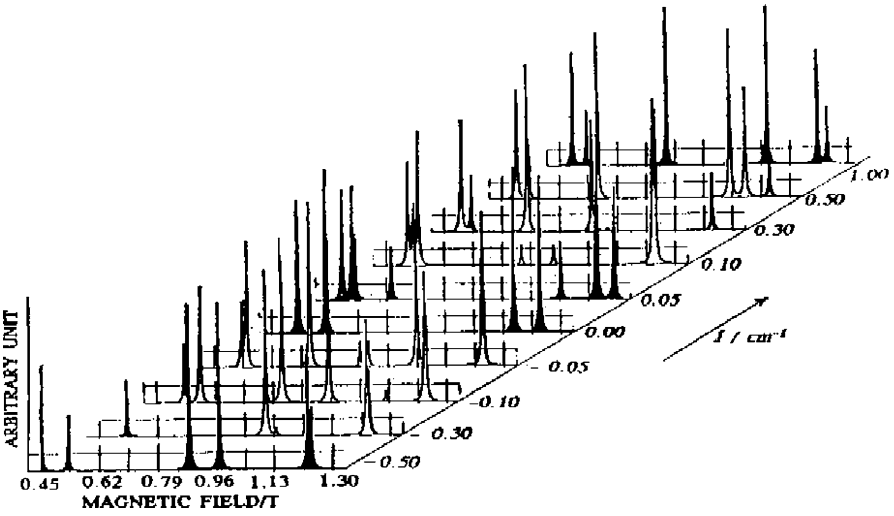

Fig. 3.1 Fine-structure ESR transitions from an exchange-coupled triplet pair undergoing spin quantum mixing. A K-band microwave frequency is assumed with the fine-structure constants comparable to $|2J|$

requirement for a pair of equivalent $S_i = 1$ spins (i = A, B), while the resultant triplet state is isolated because of symmetry requirements. The permutation symmetry for Bose ($S_i = 1$) particles is symmetric, preventing the mixing between the triplet and the other spin multiplicities. Thus, remarkable spectral changes are anticipated when complete spin quantum mixing occurs with a nearly vanishing exchange coupling. In conventional X-band ESR spectroscopy, the transition probabilities which gain intensity owing to the high-field resonance conditions in high-frequency ESR spectroscopy are reduced a great deal. As a result, the characteristics of intensity distributions in the high-field approximation are weakened. In this sense, the practical advantages of X-band ESR spectroscopy are limited for the cases of spin quantum mixing. High-field/high-frequency ESR spectroscopy is desirable for the detection of spin quantum mixing in terms of the transition probability of intermediate spin states. For these reasons, molecular designs for the fine-tuning of on-and-off quantum spin mixing with spin-mediated devices are the current topics of molecular spin science. Effects of the quantum mixing in hetero-spin systems are shown more remarkably for molecular exchange-coupled systems [15]. Under favorable conditions, the relative signs of the fine-structure constants for the resultant spin states can be determined.

Referred to the higher-order terms of fine-structure tensors in spin Hamiltonians, Eqs. (3.2) and (3.4), the group-theoretical arguments apparently allow the inclusion of them for molecular high spins of relatively low molecular symmetry ($S = 2, 3$). Indeed, for even high-spin hydrocarbons in the electronic ground state the inclusion may yield apparent better agreement between observed fine-structure spectra and simulated ones, where different spin-state species gave complicated superimposed fine-structure spectra [16]. Nevertheless, additionally derived spin Hamiltonian

parameters cannot give a rationale for such high-spin hydrocarbons with small spin-orbit couplings of carbon atoms. The obtained result has been misleading in terms of the physical meaning of the derived terms. A refined set of spin Hamiltonian parameters has produced much better agreement between the observed spectra and simulated ones by invoking similar spectral simulation methods without incorporating the higher-order, quartic terms [17]. Due care is necessary to incorporate the higher-order fine-structure terms in spin Hamiltonians for genuinely organic high-spin systems to avoid artifacts and over-parameterization in spectral simulations.

3.2.2 *Appearance of Off-Principal-Axis Lines in Fine-Structure Spectra in Molecular High Spin Systems*

One of the salient features appearing in the fine-structure spectra due to high spin systems is the appearance of off-principal-axis absorption peaks, called extra lines (or off-axis extra lines), in fine-structure ESR spectroscopy for randomly oriented media. Extra lines inevitably appear when high spin systems have sizable fine-structure constants compared with the magnitude of the microwave excitation energy. In general, lineshapes of forbidden transition peaks are anomalous, compared with those of the allowed ones. This is because the angular dependence (anisotropy) of forbidden transitions is constrained and thus undergoes angular anomaly, which corresponds to stationary points with $\mathbf{B}_0$ pointing off the principal axis of the fine-structure tensor. As described above, a typical example is $B_{\min}$ appearing in the fine-structure spectra from triplet states in non-oriented media. The $B_{\min}$ anomaly underlies the stationary behavior of the extra lines from high spins ($S > 1$) [10b, 11]. Appearance of off-axis extra lines is general for anisotropic ESR spectroscopy, and physical origins of "hyperfine-structure" extra lines have been elucidated by several authors [1g, 18]. The hyperfine-structure extra lines originate in large anisotropic g- and hyperfine tensors.

The first extensive study of fine-structure extra lines has been made in terms of higher-order (second- and third-order) perturbation treatments, giving general conditions and formulas for the appearance of extra lines for arbitrary high spins as well as recipes for the analyses of fine-structure extra lines [11]. The formulas in the literature [11] also enable us to identify off-principal-axis orientations within the frame work of the perturbation theory. In order to complete the analyses of all the fine-structure stationary peaks including extra lines, it is desirable to invoke exact numerical diagonalization approaches which execute the calculation of resonance fields, transition probabilities and their angular dependence with high accuracy. Such a good example is illustrated in Fig. 3.2, where a quartet ground state from *m*-phenylenebis(phenyl-methylene) monoanion in an organic glass is shown. High spin states with odd spin quantum numbers show strong characteristic peaks of extra lines from the $M_S = -1/2 \iff M_S = +1/2$ transition, as illustrated in Fig. 2.2.

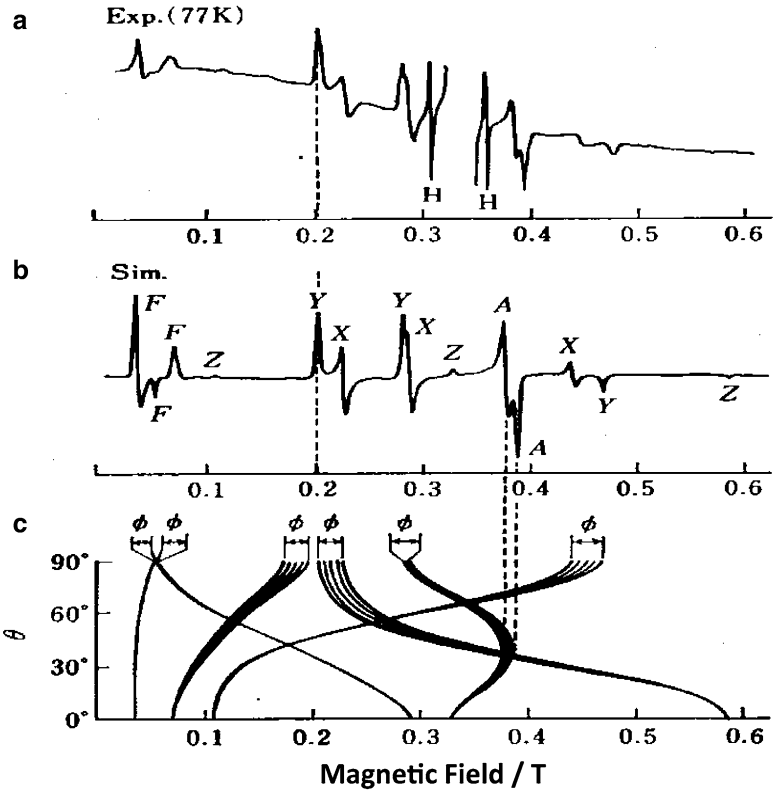

Fig. 3.2 Appearance of extra lines in fine-structure ESR spectroscopy from random orientation; Fine-structure spectra from *m*-phenylenebis(phenylmethylene) monoanion in the quartet ground state [19]. (**a**) Observed spectrum; H's denote the absorption lines due to hydrogen atom. (**b**) Simulated one; X, Y and Z denote the absorption lines corresponding to the canonical orientations. F's denote the lines from $\Delta M_S = \pm 2$ and ± 3 forbidden transitions. A's denote the extra lines

The inevitable occurrence of the angular anomaly corresponding to this transition arises from the disappearance of the first-order fine-structure term in the resonance field in terms of perturbation theory. High-field/high-frequency ESR spectroscopy affords to simplify fine-structure spectra, weakening the importance of extra line analyses for spin multiplicities of odd numbers. Nevertheless, the simplification is hampered by the anisotropic nature intrinsic to molecular systems with both even spin multiplicities and sizable fine-structure constants.

For smaller fine-structure constants, first-order perturbation treatments have been invoked for the sake of simplicity in order to extract fine-structure constants and *g*-values. It has turned out that in most of the documented first-order-perturbation analyses for molecular high spins in the ground state, where π-π spin-spin interactions dominate in the contribution to the fine-structure parameters the appearance

conditions for extra lines from those high spins are not fulfilled. During the simulation procedure, readers are recommended to check the appearance conditions by substituting any trial fine-structure parameters and the microwave frequency employed into the formulas given in the literature [11]. Whether or not extra lines appear also depends on the line width of the single ESR transition used for the simulation. If the difference in resonance fields between extra lines and principal-axis lines is comparable to or smaller than the line width, the extra line will not be distinctly observed. Instead, an asymmetry of the line shape or an intensity anomaly will be appreciable.

3.2.3 Theoretical Spectral Simulation of Molecular High-Spin Clusters: Direct Comparison Between Theoretical Simulations and Observed Spectra of a Triplet-State Cluster

This section gives a theoretical spectral simulation approach to molecular high-spin clusters, exemplifying a direct comparison of simulated fine-structure spectra with the observed one from a novel exchange-coupled triplet-state molecule, calix[4]arene-based biradical with two nitroxide spin sites [20]. The system is composed of two NO-based radical centers within the molecule. Thus, spectral simulations require the incorporation of hyperfine tensors due to two nitrogen atoms. The crystal and molecular structures of the exchange-coupled triplet molecule are not known, but the X-ray crystal structure analysis of the corresponding precursor of a new nitroxide-based biradical has been made. The local molecular structures of the two nitroxides have attracted attention. With the help of theoretical spectral simulations, the molecular geometry of the biradical of the two-site spin exchange-coupling can be evaluated, as given below.

For the exchange-coupled system under study, we adopt spin Hamiltonians as follows;

$$\hat{\mathrm{H}} = \hat{\mathrm{H}}_1 + \hat{\mathrm{H}}_2 + \hat{\mathrm{H}}_{12} \tag{3.8}$$

$$\hat{\mathrm{H}}_1 = \beta \mathbf{B}_0 \cdot \boldsymbol{g}_1 \cdot \mathbf{S}_1 + \mathbf{I}_1 \cdot \boldsymbol{A}_1 \cdot \mathbf{S}_1 \tag{3.9}$$

$$\hat{\mathrm{H}}_2 = \beta \mathbf{B}_0 \cdot \boldsymbol{g}_2 \cdot \boldsymbol{S}_2 + \mathbf{I}_2 \cdot \boldsymbol{A}_2 \cdot \mathbf{S}_2 \tag{3.10}$$

$$\hat{\mathrm{H}}_{12} = \mathbf{S}_1 \cdot \boldsymbol{J}_{12} \cdot \mathbf{S}_2 \tag{3.11}$$

where $\boldsymbol{g}_\mathrm{i}$, $\boldsymbol{A}_\mathrm{i}$ (i =1, 2) and $\boldsymbol{J}_{12}$ stand for the g tensor, hyperfine coupling tensor for the i-th nitroxide site and the exchange coupling tensor, respectively. Here an anisotropic exchange coupling interaction is assumed for theoretical arguments.

In the case of biradicals where the interacting spins are sufficiently far from each other, magnetic dipole-dipole interactions dominate the exchange interaction. The present two-nitroxide-based biradical is of this type. The classical magnetic dipole-dipole interaction between two spins is given by

$$J_{12} = \frac{\mu_0}{4\pi}\left[\frac{\boldsymbol{\mu}_{e1}\cdot\boldsymbol{\mu}_{e2}}{r^3} - \frac{3(\boldsymbol{\mu}_{e1}\cdot r)(r\cdot\boldsymbol{\mu}_{e2})}{r^5}\right] = \frac{\boldsymbol{\mu}_0}{4\pi}\beta^2\left[\frac{\boldsymbol{g}_1\cdot\boldsymbol{g}_2}{r^3} - \frac{3(\boldsymbol{g}_1\cdot r)(r\cdot\boldsymbol{g}_2)}{r^5}\right] \tag{3.12}$$

with $\boldsymbol{\mu}_{ei} = -\beta\boldsymbol{g}_i\cdot\mathbf{S}_i$, noting $\beta = \mu_B$ throughout this section. This equation indicates that the interacting tensor based on the classical magnetic dipolar interaction depends on both the anisotropy of the g tensor of the two spins and the distance between the spins.

Relationships between the anisotropic g tensors reflect the molecular geometry of the biradical. $\boldsymbol{J}_{12}$ is a dyadic, and it can be decomposed into the sum of a scalar product, a symmetric traceless tensor and an antisymmetric tensor. Then, $\hat{\mathrm{H}}_{12}$ can be rewritten as

$$\hat{\mathrm{H}}_{12} = \mathbf{S}_1\cdot\boldsymbol{J}_{12}\cdot\mathbf{S}_2 = J_{12}\,\mathbf{S}_1\cdot\mathbf{S}_2 + \mathbf{S}_1\cdot\boldsymbol{D}_{12}\cdot\mathbf{S}_2 + \boldsymbol{d}_{12}\cdot\mathbf{S}_1\times\mathbf{S}_2 \tag{3.13}$$

where J_{12} is a scalar, $\boldsymbol{D}_{12}$ is the symmetric traceless tensor, and $\boldsymbol{d}_{12}$ is a polar vector which is constructed by the off-diagonal elements of the antisymmetric tensor part of $\boldsymbol{J}_{12}$. Each term is termed an isotropic, anisotropic, and antisymmetric spin-spin interaction, respectively. Relationships between $\boldsymbol{J}_{12}$ and the decomposed terms are given by the following equations,

$$J_{12} = (1/3)\,\mathrm{Tr}\,(\boldsymbol{J}_{12}) \tag{3.14}$$

$$\boldsymbol{D}_{12} = (1/2)\left(\boldsymbol{J}_{12} + {}^t\boldsymbol{J}_{12}\right) - J_{12} \tag{3.15}$$

$$d_{12,x} = (1/2)\left(\boldsymbol{J}_{12} - {}^t\boldsymbol{J}_{12}\right)_{yz},\ d_{12,y} = (1/2)\left(\boldsymbol{J}_{12} - {}^t\boldsymbol{J}_{12}\right)_{zx},$$
$$d_{12,z} = (1/2)\left(\boldsymbol{J}_{12} - {}^t\boldsymbol{J}_{12}\right)_{xy} \tag{3.16}$$

where ${}^t\boldsymbol{J}_{12}$ stands for the transposed matrix of $\boldsymbol{J}_{12}$.

Considering the spin Hamiltonian parameters of the coupled spin system in terms of the coupled eigenbase of S_{1z} and S_{2z}, the exchange interaction term reflects the relative orientation of the two radical sites. The isotropic term makes the energies of all eigenstates shift, not affecting the spectrum at all in ESR spectroscopy. The antisymmetric interaction arises from a second-order term of the spin-orbit coupling in terms of perturbation treatments. The antisymmetric vector given by Eq. (3.16) is relevant to the symmetry of the coupled spin system. When the spin system has an inversion center, the vector vanishes. For most of the organic biradicals,

the antisymmetric term is safely assumed to be zero because of their small spin-orbit interaction in the ground state. Returning to the effective spin Hamiltonian approach, we recall Eqs. (3.4) and (3.5), as given below

$$\hat{\mathrm{H}}_S{}^{\mathrm{spin}} = \beta \boldsymbol{B}_0 \cdot \mathbf{g}^{\mathrm{eff}} \cdot \mathbf{S} + \mathbf{S} \cdot \boldsymbol{D}^{\mathrm{eff}} \cdot \mathbf{S} + \mathbf{I}_1 \cdot \boldsymbol{A}_1^{\mathrm{eff}} \cdot \mathbf{S} + \mathbf{I}_2 \cdot \boldsymbol{A}_2^{\mathrm{eff}} \cdot \mathbf{S} \tag{3.17}$$

with $\mathbf{S} = \mathbf{S}_1 + \mathbf{S}_2$. $\boldsymbol{g}^{\mathrm{eff}}$ denotes the effective g tensor of the exchange-coupled system with $S = 1$, and $\boldsymbol{D}^{\mathrm{eff}}$ the effective fine-structure tensor for the triplet state. $\boldsymbol{A}_1{}^{\mathrm{eff}}$ and $\boldsymbol{A}_2{}^{\mathrm{eff}}$ designate the hyperfine coupling tensors of nitrogen nuclei 1 and 2 in the effective spin framework. Exploiting Eqs. (3.6a–c) for the present case, we obtain the following relationships;

$$\boldsymbol{g}^{\mathrm{eff}} = (1/2)\, \boldsymbol{g}_1 + (1/2)\, \boldsymbol{g}_2 \tag{3.18a}$$

$$\boldsymbol{D}^{\mathrm{eff}} = (1/2)\, \boldsymbol{D}_{\mathrm{AB}} \tag{3.18b}$$

$$\boldsymbol{A}_{\mathrm{i}}^{\mathrm{eff}} = (1/2)\, \boldsymbol{A}_{\mathrm{i}} \quad (\mathrm{i} = 1, 2) \tag{3.18c}$$

It is worthwhile again noting that the relationships above in Eqs. (3.18a–c) are tensor-based and should be expressed in terms of a common reference molecular frame, as generally described in Sect. 3.2.1.

Figure 3.3 shows a fine-structure ESR spectrum of the calix[4]arene-based biradical with two nitroxide radical sites observed in an organic glass together with calculated spectra. The observed ESR spectrum consists of ESR transitions in both the target biradical and the monoradical in which hydroxyamino groups were partially oxidized. In the field range of forbidden transitions with $|\Delta M_S = 2|$, an asymmetric hyperfine structure pattern due to interactions between electron spin and two nitrogen nuclei was observed. Absorption peaks assignable to the ESR transitions due to the Z canonical orientations for a triplet state were too broad to be seen. These salient features should be reproduced by theoretical spectral simulations, giving electronic molecular structures of the novel calixarene-based biradical. The theoretical spectral simulations based on the effective spin Hamiltonian approach have successfully reproduced the observation. The obtained spin Hamiltonian parameters are summarized in Table 3.2. The observed spectral features are well interpreted by considering the anisotropic hyperfine coupling tensors of both the nitrogen nuclei. The broadened Z components are due to large hyperfine splittings of the nitrogen nuclei in the principal Z axis of the fine-structure tensor, as shown in Fig. 3.4. It shows that the two π-orbitals localized on the nitrogen nuclei point head to head each other in a σ-type bonding. The derived molecular structure agrees with the fact that the triplet state is thermally accessible. The distance between the two spin centers can also be evaluated.

Figure 3.4 shows the molecular structural dependence of the theoretically simulated spectra for the calixarene-based biradical in non-oriented media.

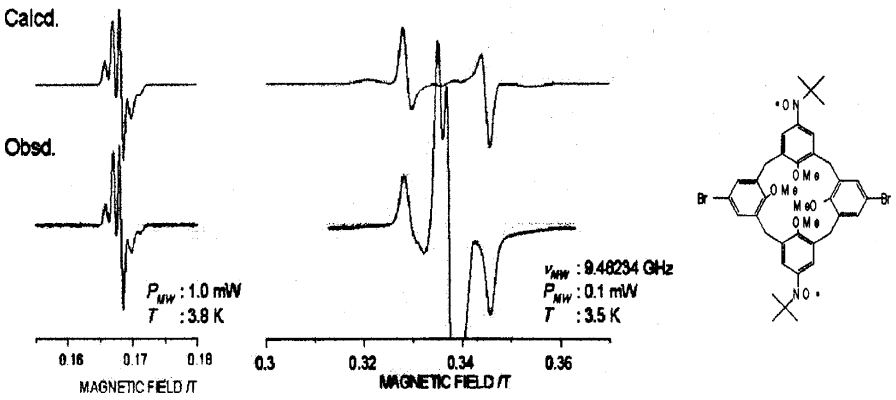

Fig. 3.3 Observed and calculated triplet-state ESR spectra from a calix[4]arene-based biradical with two nitroxide radical centers

Table 3.2 Spin Hamiltonian parameters of a calix[4]arene-based biradical ($S = 1$)

	g^{eff}	D^{eff} /cm^{-1}	$A_1{}^{\text{eff}}$ /cm^{-1}	$A_2{}^{\text{eff}}$ /cm^{-1}
XX	2.008	0.0053	0.00025	0.00025
YY	2.005	0.0053	0.00025	0.00025
ZZ	2.003	−0.0106	0.00135	0.00135

Only the principal values are given. The principal Z axis is parallel to the direction connecting the two nitroxide radical sites

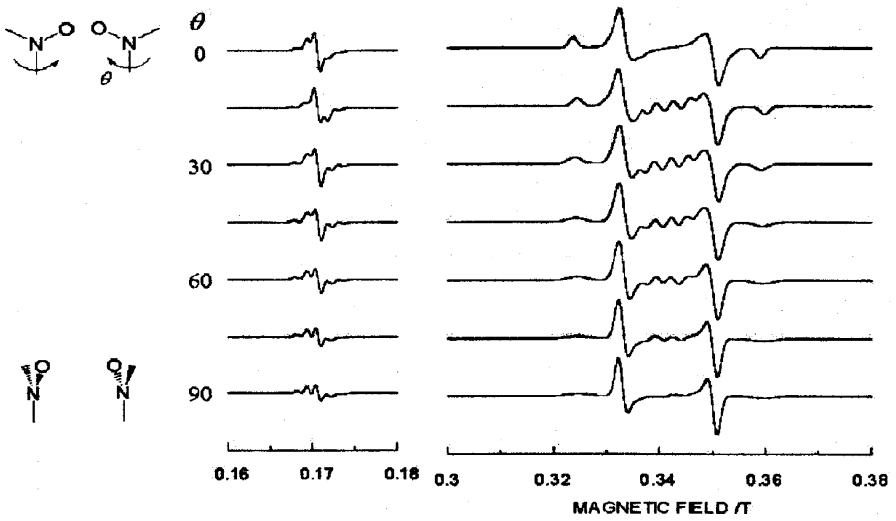

Fig. 3.4 Dependence of the fine-structure spectra on the relative orientation between the tensors in the calixarene-based biradical with the two nitroxide radical sites

When both the z axes of the nitrogen hyperfine coupling tensors are parallel to the principal Z axis of the fine-structure tensor $\boldsymbol{D}^{\mathrm{eff}}$, i.e., $\theta = \pi/2$ (see Fig. 3.4 for the definition of θ), the Z canonical peaks are broadened because of the large hyperfine splittings due to the nitrogen nuclei in that direction. In the intermediate orientations of the z axes, absorption peaks with appreciable amounts of intensity appear in the magnetic field range of $g \sim 2$. The appearance of these peaks is due to the disagreement between the principal axes of the fine-structure tensor, hyperfine coupling ones and the g tensors. The salient lineshape of the half-field transitions is also affected by the relative orientations of the tensors. Although the ESR transitions due to the partially oxidized nitroxide monoradical masked the central part of the fine-structure ESR spectrum of the biradical, the molecular structural features for this novel biradical are probable. A pure triplet-state spectrum from the biradical gives much more precise information on the molecular conformation, however [21]. In addition, the molecular structure with one hydrogen bond due to partial oxidation gives a clue to molecular magnetic functionality controlled by intramolecular hydrogen bonding [20].

Tensor-based theoretical spectral simulation approaches are also useful for extracting spin Hamiltonian parameters for molecular high-spin systems whose spin sites are composed of transition metal ions and organic high spins. A subtle issue during the simulation procedure is to evaluate the interaction term $\boldsymbol{D}_{\mathrm{AB}}$ for hybrid high-spin systems with extremely delocalized spins over the whole system or moiety. For such cases, if thermally accessible spin states with different S's are observed, $\boldsymbol{D}_{\boldsymbol{AB}}$ can be estimated under favorable conditions. Otherwise, quantum chemical computations are invoked for the estimation of $\boldsymbol{D}_{\mathrm{AB}}$ (see Chap. 8 of Volume 1). In exchange-coupled systems with sizable molecular frames, the contribution of the interacting terms in the ground or nearby excited states decreases rapidly with increasing molecular sizes. The molecular size effect, however, does not hold for electronic excited high-spin states with extreme spin delocalization, and high spin chemistry in electronic excited states of inter- and intra-molecularly exchange-coupled systems are the focus of current issues in chemistry and spin science. It is worth noting that semi-empirical tensor-based spectral simulation gives a rationale for molecular structural determination of relatively small molecular clusters such as triplet-state dimeric $(NO)_2$–$(Na^+)_x$ adsorbed in zeolites with the help of theoretical estimation for the triplet-state fine-structure tensor, in which accurate quantum chemical calculation should be invoked because of a large amount of spin densities on the nitrogen and oxygen sites [22]. The absolute sign of the principal fine-structure D-value determined experimentally (by high-field/high-frequency ESR or ENDOR experiments) gives crucial information on the molecular and electronic spin structures of the systems under study.

3.2.4 *Microscopic Spin Dynamics Underlying Magnetization Dynamics in Infinite Systems of Exchanged Couplings*

One of the crucial issues in electron magnetic resonance spectroscopy applied to "ordered" magnetic assemblages with exchange couplings is to understand their magnetization dynamics in terms of microscopic spin dynamics [23]. The magnetization dynamics has been treated by both Kubo-Tomita [24] and Mori (and Tokuyama-Mori) [25] theories in terms of spin assemblages in microscopic detail. The former theory describes the transverse relaxation by invoking a relaxation function $\phi(t)$ of a macroscopic magnetization as

$$\phi(t) = < M_x(t)\, M_x(0) > / k_B T \tag{3.19}$$

where $< M_x(t)\, M_x(0) >$ stands for a time correlation function of M_x under thermal fluctuation and therefore the symbol $\phi(t)$ describes the magnetization, classically. Isotropic exchange interactions expressed as $-\sum 2J_{ij}\mathbf{S}_i \cdot \mathbf{S}_j$ are commutable with $\mathbf{S} = \sum \mathbf{S}_i$, thus giving no contribution to the transverse relaxation. Noncommutable local magnetic fluctuations are expressed in terms of a time correlation function $\varphi(t)$ for the local magnetic field. The relaxation function $\phi(t)$ for the macroscopic magnetization can be expressed by using $\varphi(t)$. Noting that the phase memories of individual spins $\mathbf{S}_i$'s are vanishing in time of nearly $h/4J$ because of mutual exchange interactions with surrounding spins, the motion of $\mathbf{M}$, i.e., that of $\mathbf{S}$ is conserved for a long time because $\mathbf{M}$ commutes with isotropic exchange interactions. Dynamics of $\mathbf{S}_i$ can be expressed in terms of a spin-time-correlation function $\Phi(t)$ as

$$\Phi(t) = 3 < S_{xi}(t)\, S_{xi}(0) > / S(S+1) \tag{3.20}$$

In the rotating frame, the first three terms appearing in $\Phi(t)$ are approximated to be

$$\Phi(t) = \exp[-(t/\tau_e)^2/2] (t < \tau_e) \tag{3.21}$$

with $\tau_e = (h/|4J|)\{3/[2qS(S+1)]\}^{1/2}$, where J stands for an exchange integral of a pair of nearest-neighboring spins and q for the number of the nearest-neighboring spins. For a long time, $t > \tau_e$,

$$\Phi(t) \propto [S(S+1)/3]\, t^{-d/2} \tag{3.22}$$

holds, where d stands for the dimension of the spin assemblages. According to Eq. (3.22), $\Phi(t)$ decays slowly for low-dimensional spin assemblages ($d = 1, 2$), leading to the occurrence of a long transverse relaxation called a long time tail (LTT). An LTT arises from increases in the contributing weights of the zero-mode Fourier component of the wave vector in $\Phi(t)$ for smaller d. Compared with three-dimensional spin assemblages, whose spin correlations decay in times

much shorter than periods of microwave frequency $\omega_0/2\pi \sim 10$ - 10^2 GHz, free induction decays with transverse relaxations characteristic of LTT or satellite peaks due to spin dipolar interactions appear for low-dimensional organic spin assemblages in pulsed ESR experiments. In this context, high-field/high-frequency ESR spectroscopy such as W-band ESR spectroscopy is potentially capable of extending vital information on magnetization dynamics in microscopic detail. Particularly, it is worth noting that microscopic spin dynamics characteristic of low dimensionality in organic magnetics reflects the contribution of nearly-zero-mode Fourier components as T approaches T_c (or T_N). The difference in the contributions originates from the difference in temperature evolution of short-range interactions between ferromagnetics and antiferromagnetics. Pulsed-FT-based time domain ESR spectroscopy is direct and sensitive to the difference.

3.3 Spectral Simulation Based on a Hybrid Eigenfield Method and Perturbation Treatments

Electron spin resonance spectroscopy from random orientation of high-spin molecular systems gives us a variety of fine-structure spectra. It is generally tough to extract the underlying physical parameters of paramagnetic species from spectra in non-oriented media in a straightforward manner except for simple cases. Difficulties arise from the spectroscopic methodology that cw-ESR spectroscopy measures resonance with an electromagnetic irradiation field by sweeping a static magnetic field $\mathbf{B}_0$ (=$\mathbf{B}$). A spectroscopic coordinate in ESR spectra is not easy to be intuitively transformed to an energy difference between electronic spin states involved in the resonance transitions, contrary to most other spectroscopies. Because of the many types of spin Hamiltonian terms, ESR spectral simulations [26–42] are important procedures for quantitatively interpreting observed ESR spectra and extracting physically meaningful parameters with high accuracy. A failure of successful spectral simulations weakens the usefulness of random orientation ESR spectroscopy. This section is intended to introduce to readers a general and powerful procedure for simulating ESR spectra from random orientation, exemplifying fine-structure spectra. Methods given in this section are free from notorious problems of non-convergence and save computation time. The program softwares based on the present methods are available. They are written in terms of Mathematica-based and other languages [37].

In order to reproduce overall fine-structure spectra with low-field absorption peaks from forbidden transitions, the second- or higher-order perturbation treatments in terms of both Rayleigh-Schroedinger and Brillouin-Wigner types have been frequently used and all the mathematical expressions required for spectral simulations are available in analytical forms with respect to arbitrary coordinate axes as well as arbitrary spin quantum numbers [43–45]. The perturbation approach has been developed to the third-order stage in terms of fine-structure terms in

spin Hamiltonians [36]. Fourth order treatments for the analyses of fine-structure spectra in an arbitrary coordinate-axis system are also available [46]. Program packages of second-order treatments for random orientation ESR spectroscopy, including hyperfine terms, were intended to be distributed by various authors at early time [43]. Recently, a program package for ESR spectral simulations based on a second-order perturbation theory has been commercially distributed, but its efficiency has been hampered by a failure to simulate forbidden transition peaks and the forced assumption of collinearity between $\boldsymbol{g}$ and fine-structure tensors [47]. The perturbation approaches are efficient in terms of computation time and they are free from a non-convergence problem due to energy crossings, but a weakness is that they fail to reproduce low-field peaks and give out-of–phase artifact lines in conventional X-band fine-structure spectra. The appearance of such somewhat peculiar-looking lines strongly suggests a possible breakdown of the perturbation treatments. Nevertheless, it is apparent that the perturbation approach programs are useful for the cases of $|D|/h\nu \ll 1$ under the experimental conditions of X-band or high-field/high-frequency spectroscopy (K-, Q-, W- and higher bands).

The breakdown of the perturbation approaches based on general analytical expressions can be avoided by invoking exact numerical diagonilizations of spin Hamiltonian matrices, either the $n \times n$ eigenenergy matrix or the $n^2 \times n^2$ eigenfield matrix, where $n = 2S + 1$. The eigenenergy approach suffers from notorious non-convergence problems while matching $h\nu$ to the difference between the energies involved in the transitions, if the calculation involves avoided energy crossings. Particularly, this difficulty takes place in the simulation procedure for the transitions appearing in the low-field region of X-band fine-structure spectra.

On the other hand, the eigenfield approach is free from the non-convergence problem but needs much more computation time, which increases in proportion to the third power of the matrix dimension. Thus, the eigenfield approach becomes impractical when the dimension of an original eigenenergy matrix is large. An enormous amount of computation time inherent in the original eigenfield approach [34, 35] should be eliminated for the practical use of the methodology. A hybrid eigenfield approach here gives a practical solution for this problem. In addition, some important technical problems with eigenfield matrices should be solved in order to acquire physically meaningful parameters. It should be recollected that the exact analytical solutions of the eigenfield for triplet states have been derived in an arbitrary orientation of $\mathbf{B}_0$ ($= \mathbf{B}$) [48]. Not only a weakness of the eigenfield method is the sizable dimension of the $n^2 \times n^2$ eigenfield matrix, but also the method requires solving generalized eigenvalue problems, which give rise to imaginary eigenfield values. Technically, elaborate mathematical techniques are necessary during the numerical convergence procedure. There have been a commercially available program package [49] and home-made ones [37, 41] which fulfill the above requirements. The latter unites the above requirements with the shortening the computation time by invoking a methodologically hybrid method between the original eigenfield theory and conventional eigenenergy method [37, 41].

3.3.1 *Fine-Structure ESR Spectroscopy from Random Orientations in Non-oriented Media*

The effective spin Hamiltonian [27, 28] for analyses of ESR spectra is generally expressed by

$$\begin{aligned}\hat{\mathrm{H}} &= \hat{\mathrm{H}}_{\mathrm{eZ}} + \hat{\mathrm{H}}_{\mathrm{D}} + \hat{\mathrm{H}}_{\mathrm{hf}} + \hat{\mathrm{H}}_{\mathrm{nZ}} + \hat{\mathrm{H}}_{\mathrm{Q}} \\ &= \beta \mathbf{S}\cdot\boldsymbol{g}\cdot\mathbf{B} + \mathbf{S}\cdot\boldsymbol{D}\cdot\mathbf{S} + \sum [\mathbf{S}\cdot\boldsymbol{A}_{\mathrm{k}}\cdot\mathbf{I}_{\mathrm{k}} - \beta_{\mathrm{n}}\mathbf{B}\cdot\boldsymbol{g}_{\mathrm{n}}{}^{\mathrm{k}}\cdot\mathbf{I}_{\mathrm{k}} + \mathbf{I}_{\mathrm{k}}\cdot\boldsymbol{Q}_{\mathrm{k}}\cdot\mathbf{I}_{\mathrm{k}}] \end{aligned} \tag{3.23}$$

where $\hat{\mathrm{H}}_{\mathrm{eZ}}$, $\hat{\mathrm{H}}_{\mathrm{D}}$, $\hat{\mathrm{H}}_{\mathrm{hf}}$, $\hat{\mathrm{H}}_{\mathrm{nZ}}$, and $\hat{\mathrm{H}}_{\mathrm{Q}}$ stand for the electron Zeeman, fine-structure, hyperfine coupling, nuclear Zeeman, and quadrupole terms, respectively. The electron and nuclear Zeeman terms are magnetic-field dependent, and the others are independent. A single-crystal ESR spectrum, i.e., the one at a single given orientation of the magnetic field $\mathbf{B}$ ($=\mathbf{B}_0$) is constructed from resonance fields B^{res} and transition probabilities P calculated from the spin Hamiltonian for $\mathbf{B}$. Hereafter we omit the suffix 0 for the static magnetic field $\mathbf{B}_0$. When assuming an appropriate function f (B-B^{res}, $\Delta B_{1/2}$) for the ESR signal, the spectrum pattern $s(\theta,\varphi,\psi,B)$ is described by

$$s(\theta,\varphi,\psi,B) = \sum P_{\mathrm{i}}(\theta,\varphi,\psi) \times f[B - B_{\mathrm{i}}^{\mathrm{res}}(\theta,\varphi), \Delta B_{1/2}] \tag{3.24}$$

where θ, φ, and ψ stand for the Euler angles and $\Delta B_{1/2}$ for the line width at half height. Euler angles are required for the calculation of resonance fields and transition probabilities in the laboratory frame referred to both $\boldsymbol{B}$ and $\boldsymbol{B}_1$ (called Zeeman coordinate systems). When a given component tensor such as $\boldsymbol{D}_{\mathrm{i}}$ in a convenient reference frame is transformed to the laboratory frame, Euler angles are defined referred to the convenient reference frame. The summation runs over all the transitions i's. The first derivative of a normalized Gaussian or Lorentzian function is commonly applied as the function for field-swept and field-modulation scheme detection.

An overall ESR spectrum from powdered states or non-oriented media such as organic glasses is composed of the single-crystal like ESR transitions due to all the randomly oriented molecules in the laboratory frame. Thus, the overall ESR spectrum $S(B)$ from random orientation is constructed by integrating single-crystal spectrum patterns, i.e.,

$$S(B) = \int_{\theta}\int_{\varphi}\int_{\psi} s(\theta,\varphi,\psi,B)\sin\theta d\ \theta d\ \varphi d\ \psi \tag{3.25}$$

One of the most time-consuming processes in spectrum simulation is the numerical integration given in Eq. (3.25). Several methods for improving the numerical integration, such as angular grid methods, application of interpolation

techniques, statistical calculations based on random sampling, and so on, have been developed so far in order to reduce computation time in the simulation procedure [29–31]. A new method based on a 'sophe' partition and interpolation scheme has been developed by Hanson and coworkers [32, 33]. Their simulation software achieves high efficiency and accuracy for any parameters in the spin Hamiltonian by solving the eigenvalue problem with the help of homotopy. Application of homotopy is a solution that can avoid mathematical difficulties in the vicinity of anti-level crossings and looping transitions.

3.3.2 Eigenfield Method and Hybrid Eigenfield Approach as an Improved Accessible Method

One of the "tricky" manipulations in the ESR spectroscopic analysis is to convert transition frequencies obtainable from energy eigenvalue problems to external (applied) static magnetic fields satisfying the resonance condition, because current ESR spectroscopy is magnetic field-swept in contrast to ordinary spectroscopy which is frequency-swept. In the direct calculation, exact resonance fields are acquired by an iteration procedure using the numerical diagonalization of the spin Hamiltonian matrix with $\boldsymbol{B}$ included. However, we sometimes meet a problem that the iteration does not converge. In addition, even though convergence takes place within a certain accuracy, a method employed under a certain algorithm does not always assure whether calculated resonance fields are complete and exact. The eigenfield method [34–38] formulated and developed by Belford et al. and by Hatfield is free from such numerical "breakdown or pitfall". It is worth while noting that Brillouin-Wigner types of higher-order perturbation treatments require iterations for numerical convergence in contrast to Rayleigh-Schroedinger ones, but the former ones do converge quickly and give more accurate resonance fields than the latter ones [38b].

In the following, we derive the eigenfield method so that the readers can easily understand to encode programs. Since the spin Hamiltonian consists of a magnetic field dependent term $\mathbf{F}B$ and an independent term $\mathbf{G}$, we rewrite the spin Hamiltonian as given by

$$H = \mathbf{F}B + \mathbf{G} \tag{3.26}$$

The time-independent Schrödinger equation and its complex conjugate are written as follows,

$$H\,|\psi_i> = w_i\,|\,\psi_i> \tag{3.27a}$$

$$H^*\left|\psi_j^*> = w_j\right|\psi_j^*> \tag{3.27b}$$

where i denotes a particular energy eigenvalue w_i and the corresponding eigenvector $|\psi_i>$. $|\psi_i>$ and $|\psi_j^*>$ are explicitly defined in terms of a basis set $\{|\phi_n>\}$ as

$$|\psi_i> = \sum_n a_{in}|\phi_n> \tag{3.28a}$$

$$|\psi_j^*> = \sum_n a_{jn}^*|\phi_n^*> \tag{3.28b}$$

where we assume another solution denoted by j. Making the direct product space which is constructed by both $|\psi_i>$ and $|\psi_j^*>$, we can rewrite Eqs. (3.27a) and (3.27b) as

$$H \otimes \mathbf{E}|\psi_i, \psi_j^*> = \omega_i \mathbf{E} \otimes \mathbf{E}|\psi_i, \psi_j^*> \tag{3.29a}$$

$$\mathbf{E} \otimes H^*|\psi_i, \psi_j^*> = \omega_j \mathbf{E} \otimes \mathbf{E}|\psi_i, \psi_j^*> \tag{3.29b}$$

where $|\psi_i, \psi_j^*> \equiv |\psi_i> \otimes |\psi_j^*>$ and $\mathbf{E}$ is the $(2S+1)\times(2S+1)$ identity matrix. By subtracting Eq. (3.29b) from Eq. (3.29a), we obtain

$$\left(H \otimes \mathbf{E} - \mathbf{E} \otimes H^*\right)|\psi_i, \psi_j^*> = \left(\omega_i - \omega_j\right)\mathbf{E} \otimes \mathbf{E}|\psi_i, \psi_j^*> \tag{3.30}$$

The eigenvalue $(\omega_i - \omega_i)$ of Eq. (3.30) is identical to the energy difference between the $|\psi_i>$ and $|\psi_j^*>$ states. Since resonance occurs when the difference is equal to the microwave energy $h\nu$, we obtain

$$\left(H \otimes \mathbf{E} - \mathbf{E} \otimes H^*\right)|\psi_i, \psi_j^*> = h\nu \mathbf{E} \otimes \mathbf{E}|\psi_j, \psi_i^*> \tag{3.31}$$

By substituting Eq. (3.26) into Eq. (3.31), we have the following eigenfield equation which affords resonance magnetic fields (eigenfields) as generalized eigenvalues.

$$\left(h\nu\ \mathbf{E} \otimes \mathbf{E} - \mathbf{G} \otimes \mathbf{E}\ +\ \mathbf{E} \otimes^t \mathbf{G}\right)\mathbf{Z}\ =\ B(\mathbf{F} \otimes \mathbf{E} - \mathbf{E} \otimes^t \mathbf{F})\mathbf{Z} \tag{3.32}$$

where $\mathbf{Z} = |\psi_i, \psi_j^*> = \sum_{m,n} a_{im}a_{jn}^*|\phi_m, \phi_n^*>$.

By solving this eigenfield equation, we have the resonance field B as the generalized eigenvalue and corresponding eigenvector $\mathbf{Z}$. The $\mathbf{Z}$ eigenvector in the eigenfield equation is composed of a direct product of two energy eigenstates associated with a particular transition on resonance. The $\mathbf{Z}$ vector includes all the information on the corresponding transition.

The transition moment μ_{ij} between $|\psi_i>$ and $|\psi_j>$ and the corresponding transition probability is calculated according to

$$\begin{aligned}\mu_{ij} &= <\psi_j|\beta\mathbf{S}\cdot\mathbf{g}\cdot\mathbf{B}_1|\psi_i> = <\psi_j|H_1|\psi_i> \\ &= \sum_{m,n} a_{im}a_{jn}^* <\phi_n|H_1|\phi_m> \\ &= \sum_{m,n} (H_1)_{nm} \times a_{im}a_{jn}^* = \boldsymbol{\mu}\cdot\mathbf{Z}\end{aligned} \tag{3.33}$$

where H_1 is the transition moment operator and $\boldsymbol{\mu}$ is a vector composed of all the rows of H_1, as defined by

$$\boldsymbol{\mu} = \sum_{m,n} (H_1)_{mn} < \phi_m, \phi_n^* | \tag{3.34}$$

The transition probability $| \mu_{ij} |^2$, therefore, is given by

$$|\mu_{ij}|^2 = |\boldsymbol{\mu} \cdot \mathbf{Z}|^2 \tag{3.35}$$

The expectation values for S_Z of the states involved in the transition are also derived in the eigenfield formalism as follows [37]:

$$\begin{aligned} < S_Z^i > &=< \psi_i | S_Z | \psi_i > =< \psi_i, \psi_j^* | S_Z \otimes \mathbf{E} | \psi_i, \psi_j^* > \\ &= \tilde{\mathbf{Z}}^* S_Z^i \mathbf{Z} \end{aligned} \tag{3.36a}$$

$$\begin{aligned} < S_Z^j > &=< S_z^j >^* =< \psi_j^* | S_Z | \psi_j^* > =< \psi_i, \psi_j^* | \mathbf{E} \otimes S_Z | \psi_i, \psi_j^* > \\ &= \tilde{\mathbf{Z}}^* S_Z^i \mathbf{Z} \end{aligned} \tag{3.36b}$$

where $S_Z^i = S_Z \otimes \mathbf{E}$, $S_Z^i = \mathbf{E} \otimes S_Z$, and $\tilde{\mathbf{Z}}^* =< \psi_i, \psi_i^* |$.

Numerical computations and encoding programs by invoking the use of the expressions derived in this section are rather straightforward [37]. All the resonance fields and transition probabilities in the eigenfield method are directly calculated without any iteration procedure for searching the resonance field. Thus, the method eliminates the difficulties that the iteration does not converge in the vicinity of anti-level crossing and looping transitions. It is, however, necessary to completely solve the generalized eigenvalue problem of a sizable dimension compared with the energy eigenvalue problem. Although the generalized eigenvalues are calculated with enough accuracy, the calculation procedure sometimes loses a great deal in obtaining the eigenvectors in terms of accuracy even if applying the latest sophisticated program package for generalized eigenvalue problems. In order to avoid such numerical inconvenience, we have extended a hybrid approach which unites the original eigenfield method with conventional eigenenergy calculations. The approach is termed a hybrid eigenfield method. In the hybrid eigenfield method, resonance fields are acquired by the eigenfield method and the corresponding eigenvectors required for transition probabilities are calculated by numerically diagonalizing the ordinary eigenenergy spin-Hamiltonian matrices with the eigenfields substituted. The hybrid method has been successfully applied to organic and inorganic high-spin molecular systems so far [36–40]. Besides the numerical convergence problem, the hybrid method saves computation time a great deal.

3.3.3 *Exact Analytical Treatment of the Spin Hamiltonian: Exact Analytical Solutions for Fine-Structure Resonance Fields and Transition Probabilities*

3.3.3.1 General Arguments

Analytical expressions for resonance fields and transition probabilities are useful for interpreting ESR spectra in any levels, and perturbation treatments are employed for this purpose and predicting unknown spectral features. Perturbation-based analytical expressions for a given effective spin in an arbitrary direction of the static magnetic field have been documented [43–46]. Electron-nuclear multiple magnetic resonance frequencies in terms of second-order perturbation theory are also given in a general and comprehensive form [44]. This section gives "exact analytical formulae" derived from the eigenfield method. The formulae can be neither general nor for an arbitrary spin, but are particular for spin quantum numbers and spin Hamiltonian terms. Exact analytical approaches for $S \geq 3/2$ are feasible for fine-structure terms of axial symmetry [50–51]. The treatment here does not assume symmetry and is enough to be generally used in this context [37].

We start with the spin Hamiltonian for an arbitrary effective spin S as given by Eq. (3.23). We treat only the electron Zeeman and fine-structure terms, ignoring the others for simplicity. Once exact eigenvectors for the electron spin part are acquired, details such as hyperfine interactions in terms of electron magnetic resonance can be obtained with good accuracy. For an arbitrary direction of the magnetic field, we have to solve an eigenvalue problem of the $(2S+1) \times (2S+1)$ spin-Hamiltonian matrix based on Eq. (3.23) to obtain the energy eigenvalues. Then, the corresponding secular equation for the energy eigenvalues is given as a $2S+1$ degree polynomial equation of the energy. As analytical general solutions for the polynomial equations less than a quintic are available, the eigenenergy expressions for spin states less than a quintet ($S = 2$) can be derived. It was proven by two mathematicians, Ruffini in1799 and Abel in1826, that it is not possible to derive an explicit analytical solution for the general quintic equation. To obtain resonance fields for an arbitrary orientation of the magnetic field one needs to solve the eigenfield equation of the $(2S+1)^2$ dimension. As the eigenfield equation formally gives zero and negative fields, the secular equation for the resonance fields is reduced to an $S(2S+1)$ degree polynomial equation of the function of the squared resonance field B^2, as shown in Eq. (3.37). General analytical expressions for the resonance fields, therefore, do not exist for spin states higher than $S = 3/2$.

$$\begin{aligned} f &= \left[h\nu\mathbf{E}\otimes\mathbf{E} - \mathbf{G}\otimes\mathbf{E} + \mathbf{E}\otimes\mathbf{G}^* - B\left(\mathbf{F}\otimes\mathbf{E} - \mathbf{E}\otimes\mathbf{F}^*\right)\right] \\ &= \det\left[h\nu\mathbf{E}\otimes\mathbf{E} - (\mathbf{G} + B\mathbf{F})\otimes\mathbf{E} + \mathbf{E}\otimes\left(\mathbf{G}^* + B\mathbf{F}^*\right)\right] \\ &= \det\left(h\nu\mathbf{E}\otimes\mathbf{E} - \mathbf{H}\otimes\mathbf{E} + \mathbf{E}\otimes\mathbf{H}^*\right) \\ &= B^{2S+1} f_0\left(B^2\right) \end{aligned} \tag{3.37}$$

In addition, it is not easy to describe general solutions for ESR transitions derived from the spin Hamiltonian in an arbitrary orientation of the static magnetic field. Useful expressions for the analysis of powder-pattern fine-structure ESR spectra, however, are available when assuming that the principal axes of the magnetic tensors in the spin Hamiltonian coincide. The expressions allow us to reproduce the canonical peaks, i.e., the observed resonance fields corresponding to **B** along the principal axes, without time-consuming sophisticated computation, once salient features of the observed spectral patterns are characterized.

In the following argument, we assume that the principal axes of the $\boldsymbol{g}$ and $\boldsymbol{D}$ tensors coincide for convenience. This assumption is not a requirement for the present approach and can be eliminated if necessary. For noncollinear cases, additional unitary transformation procedures with respect to common references are required [2g, 10b]. In the Zeeman coordinate system where the direction of the magnetic field is taken parallel to the z axis, choosing the eigenfunctions $\{|S, M_S>\}$ of S_z as a basis set, we can rewrite the fine-structure terms of Eq. (3.23) in the following;

$$H = \beta g_{zz} S_Z + \frac{1}{2} g_1 S_- = \frac{1}{2} g_1^* S_+ + D_0 \left[S_z^2 + \frac{1}{4} (S_+ S_- + S_- S_+) \right] + \frac{1}{2} D_1 (S_Z S_- + S_- S_Z) + \frac{1}{2} D_1^* (S_Z S_+ + S_+ S_Z) + \frac{1}{4} D_2 S_-^2 + \frac{1}{4} D_2^* S_+^2$$

$$\text{with } g_1 = g_{zx} + i g_{zy},$$

$$D_0 = -D_{zz},\ D_1 = D_{zx} + i D_{zy} \quad \text{and} \quad D_2 = D_{xx} - D_{yy} + 2i D_{xy}. \tag{3.38}$$

In the case which one of the axes of the Zeeman coordinate system coincides with one of the principal axes of the $\boldsymbol{D}$ tensor, both g_1 and D_1 vanish because the $\boldsymbol{g}$ and $\boldsymbol{D}$ tensor become diagonal. Therefore, the spin Hamiltonian matrix is reducible to two sub blocks in some cases, as shown below; where n_1 and n_2 are $2S$ and $2S+1$ for half-integral spins, and $2S+1$ and $2S$ for integral spins, respectively. We can therefore reduce the matrix size of the spin Hamiltonian. Then, we do not necessarily solve the eigenvalue problem with the full-size Hamiltonian matrix, instead solving the eigenvalue problem with each

$$h = \begin{pmatrix} H_{1,1} & 0 & H_{1,3} & & & & & 0 \\ 0 & H_{2,2} & 0 & H_{2,4} & & & & \\ H_{3,1} & 0 & H_{3,3} & & \ddots & & & \\ & H_{4,2} & & \ddots & & H_{2S-S,2S} & & \\ & & \ddots & & H_{2S-1,2S-1} & 0 & H_{2S-1,2S+1} & \\ & & & H_{2S,2S-2} & 0 & H_{2S,2S} & 0 & \\ & & & & H_{2S+1,2S-1} & 0 & H_{2S+1,2S+1} & \end{pmatrix}$$

$$= \begin{pmatrix} H_{1,1} & H_{1,3} & & & & \\ H_{3,1} & \ddots & & 0 & & \\ & H_{n1,n} & & & & \\ & & H_{2,2} & & & \\ & 0 & & \ddots & H_{n2-2,n2} & \\ & & & H_{n2,n2-2} & H_{n2,n2} \end{pmatrix} = H_1 \oplus H_2 \tag{3.39}$$

block matrix. For instance, for a quintet state ($S = 2$) it is enough to solve secular equations from 2×2 and 3×3 spin Hamiltonian matrices. This reduction means that for the canonical orientations with $\mathbf{B}$ along the principal axes of the $\boldsymbol{D}$ tensor it is possible under certain conditions to obtain exact analytical expressions for energy eigenvalues even for high-spin states. The corresponding eigenfield equation is also reducible and solved by a block diagonalization. The eigenfield matrix giving the secular equation is expressed by

$$\mathrm{C} = \begin{pmatrix} \mathrm{C}_{11} & & & 0 \\ & \mathrm{C}_{12} & & \\ & & \mathrm{C}_{21} & \\ 0 & & & \mathrm{C}_{22} \end{pmatrix} = \mathrm{C}_{11} \oplus \mathrm{C}_{12} \oplus \mathrm{C}_{21} \oplus \mathrm{C}_{22}$$

$$\text{with} \quad \mathrm{C}_{ij} = h\nu \mathbf{E}_i \otimes \mathbf{E}_j - \mathbf{H}_i \otimes \mathbf{E}_j + \mathbf{E}_i \otimes \mathbf{H}_j^* \quad (i,\ j = 1, 2)\,. \tag{3.40}$$

The secular equation of the determinant of $\mathbf{C}$ is given by a polynomial in B^2. In the case of an integral spin, the total determinant is factorized into the product of four polynomials in B^2, corresponding to the determinant of each block matrix. In the case of a half-integral spin, the determinant of each block matrix is a polynomial in B, even though the total determinant is a polynomial in B^2.

For the quintet state the 4×4 block matrix due to C_{22} provides a linear equation in B^2, and all the remaining ones provide cubic equations in B^2. Thus, we can obtain the exact analytical solutions for principal-axis resonance fields. We can also calculate the transition probabilities using Eq. (3.35) when obtaining the eigenvectors of the spin Hamiltonian. However, since the simulation of the powder-pattern ESR spectrum requires integration over all the transitions arising from all the orientations distributed in three-dimensional space, the transition probability for only a particular orientation is of no crucial importance. On the other hand, it is more useful to know salient features for the canonical orientations for most cases. The above arguments give the possible expressions of the exact analytical eigenenergy and eigenfield, as summarized in Table 3.3.

Table 3.3 Possibility for analytically obtaining the eigenvalues of the spin Hamiltonian (see the text) and the ESR resonance fields

	Arbitrary Direction		Directions of principal axes	
	Eigenvalue	Resonance field	Eigenvalue	Resonance field
1/2	○	○	○	○
1	○	○	○	○
3/2	○	×	○	○
2	×	×	○	○
5/2	×	×	○	×
3	×	×	○	△
7/2	×	×	○	×
4	×	×	△	×
≥9/2	×	×	×	×

The circle, triangle, and cross denote exactly soluble, partially soluble, and insoluble, respectively

3.3.3.2 Exact Analytical Formulae for Resonance Fields by the Eigenfield Method

Exact analytical formulae for only three particular high-spin states derived by the present treatment of the eigenfield equation are given in this section, for space limitation. The other exact analytical formulae for a given S summarized in Table 3.3 are available [37, 41]. These expressions are correct for an anisotropic g value under the assumption of the collinearity between the $\boldsymbol{g}$ and $\boldsymbol{D}$ tensors. The formulae given here are their energy eigenvalues and resonance fields with the magnetic field $\mathbf{B}$ parallel to the Z principal axis of the $\boldsymbol{D}$ tensor. The formulae with $\mathbf{B}$ parallel to the X and Y axes are straightforwardly obtained by the cyclic permutation with respect to X, Y, and Z, as follows;

X → Y, Y → Z, and Z → X for the X principal-axis orientation, or
X → Z, Y → X, and Z → Y for the Y principal-axis orientation.

Throughout the present description, the fine-structure parameters D and E are defined as

$$D = (3/2)\, D_{zz},$$
$$\text{and} \quad E = (D_{XX} - D_{YY})/2 \tag{3.41}$$

The expressions above can be converted into the D- and E-based ones with the traceless relation $D_{XX} + D_{YY} + D_{ZZ} = 0$.

Since the analytically derived complete formulae for the eigenfield solution of a cubic or quartic equation are complicated, only the original cubic or quartic

equations are explicitly presented instead, for space limitation. These equations can exactly and analytically be solved using, e.g., Cardano's formula for the cubic equation or Ferrari's formula for the quartic equation without mathematical difficulty. Resonance fields for double quantum transitions are also obtained by changing the resonance condition involving $2h\nu$ as two-photon absorption processes in the expressions. In the calculation, only non-negative eigenfields are valid. The solutions given in the literature include all the forbidden transitions with **B** // Z and the cyclic permutation procedure (thus, with the other canonical orientations), predicting that in favorable cases the $\Delta M_S = \pm 2$ forbidden transitions show a marked fine-structure anisotropy in the fine-structure ESR spectra ($S \geq 3/2$) from randomly oriented media.

The exact analytical expressions for $S = 1$ and 3/2 are compact, but not given here because of space. All the other exact analytical formula for a given S larger than 3/2 are quite long, but manageable to calculate resonance fields and they are available also in electronic media [37, 41].

3.3.3.3 Parallel Microwave Polarization Excitation Spectroscopy Combined with the Hybrid Eigenfield Method

In high spin chemistry, parallel microwave polarization (parametric) excitation spectroscopy under the experimental condition of B//B_1 in X band has attracted considerable attention, recently. In high-field/high-frequency ESR experiments, parametric excitation techniques are not so important in practice as in X-band, simply because group-theoretically allowed transitions dominate in high-field/high-frequency fine-structure spectra. In conventional X-band spectroscopy, forbidden transitions from molecular high-spin systems with intermediate or sizable D values sometimes dominate in the fine-structure spectra and afford us key peaks in determining the spin Hamiltonian parameters. Exact eigenvectors obtained by the present hybrid eigenfield method reproduce enhanced "forbidden" (=allowed) transition probabilities by the use of the expressions Eqs. (3.33, 3.34, 3.35) in Sect. 3.3.2 [39, 42]. High spin systems arising from transition metal ions require the inclusion of higher-order fine-structure terms such as ${S_i}^2{S_j}^2$ or ${S_i}^3 B_0$ in interpreting powder-pattern spectra [39, 42]. The hybrid eigenfield method has been extended to lanthanoid ions. Conventional X-band parametric (parallel) excitation spectroscopy is strengthened with the help of the hybrid eigenfield method. Also, the transition moment calculated by the hybrid eigenfield method plays an essential role to unequivocally identify the transition assignment in combination with theoretical spectral simulations of pulsed-based two-dimensional electron spin transient nutation spectroscopy, which is termed transition moment spectroscopy.

3.4 Solution ESR Spectroscopy for Molecular High-Spin Systems with Exchange Interaction Comparable to Hyperfine Interactions

3.4.1 Introductory Remarks

Exchange interactions between paramagnetic centers are important for some biological molecular systems and magnetic materials. The electron-electron exchange has been studied by magnetic susceptibility measurements when the magnitude of the exchange interaction is comparable to, or larger than, the thermal energy $k_B T$ of the temperature examined in the susceptibility experiments. The exchange interactions much weaker than $k_B T$ are not detectable in conventional susceptibility measurements. This limitation can be overcome by the use of ESR spectroscopy. This section concerns the determinations of exchange interactions by solution ESR spectroscopy. In the aspect of the exchange interactions, ESR spectroscopy has been used to characterize metal-containing proteins, spin-labeled biomolecules [52, 53], and building blocks for magnetic materials. Our focus in this section is on organic polyradicals in which two or more unpaired electrons are exchange-coupled in a single molecule. As for systems in which two unpaired electrons are nonequivalent, *i.e.*, one from transition metal ions and the other from organic radicals such as nitroxides, lots of studies have been reported and textbooks and reviews are available [54–56].

Hyperfine splitting patterns for a given set of nuclear spins can be analyzed in terms of the chemical equivalence of the nuclear spins, or chemical environment in a molecule, and the hyperfine coupling constants. One can determine the electron spin density distribution from the obtained hyperfine coupling constants and elucidate the electronic spin structure of the molecule, as described in many text books [57–59]. In addition, one can detect the exchange interaction from the splitting patterns obtained in solution ESR spectroscopy when the interaction is comparable to the hyperfine coupling. The exchange interaction is usually described by the scalar product of two vector operators of electron spins $S_1 = S_2 = 1/2$, as a Heisenberg type of Hamiltonian, $H = -2J\mathbf{S}_1 \cdot \mathbf{S}_2$. The scalar parameter J represents the strength of the exchange interaction between $\mathbf{S}_1$ and $\mathbf{S}_2$. In Sect. 3.4.2, a quantum mechanical and quantum chemical description of the Heisenberg exchange interaction above is described only briefly. Section 3.4.3 exemplifies a spectral simulation for organic biradicals with two unpaired electrons which are coupled by an intramolecular exchange interaction. A large number of superficially different molecules are classified as biradicals [60, 61]. We restrict ourselves here to nitroxide-based biradicals consisting of two radical fragments since they are sufficiently stable and widely used both as spin labels and building blocks for molecule-based magnetic materials.

The spin Hamiltonian suitable for such nitroxide biradicals in solution is written as

$$H = -2J\mathbf{S}_1 \cdot \mathbf{S}_2 + g\mu_B B\left(S_1^Z + S_2^Z\right) + A\left(S_1^Z I_1^Z + S_2^Z I_2^Z\right) \tag{3.42}$$

The first term represents the Heisenberg exchange interaction with the exchange parameter J. The second and the third terms denote the electronic Zeeman and the hyperfine interaction for nitrogen nuclei, respectively. The hyperfine term in the spin Hamiltonian (3.42) does not commute with the exchange term, as demonstrated in Sect. 3.4.3. Therefore, the energy eigenvalues and the spin eigenfunctions of the spin Hamiltonian (3.42), and hence the resonance field and intensity of ^{14}N hyperfine ESR transitions, depend on the relative magnitudes of J and A. As shown below, the extreme limits of $|J| \gg |A|$ or $|J| \ll |A|$ give simple hyperfine splitting patterns in the ESR spectra reflecting the relative magnitude, while intermediate cases of $|J| \sim |A|$ give rise to complicated hyperfine splitting patterns as compared with monoradicals of $S = 1/2$ with one unpaired electron. The magnitude of hyperfine interactions $|A|$ falls within the order of 10^1 Oe (1 mK or 10^{-3} cm^{-1} for $g = 2$) for nitrogen nuclei in stable nitroxide radicals. We are able to determine the magnitude of exchange interaction in this range of energy. The hyperfine splitting patterns of biradicals are a spectroscopic "probe" for intramolecular exchange interactions. The energy eigenvalues and the resonance fields analytically obtained from the spin Hamiltonian (3.42) are given in Sect. 3.4.3 in order to allow nonexperts to simulate the ESR spectra.

Hyperfine splitting patterns reflecting the magnitude of the exchange interaction can be distorted by dynamical effects. Time-dependent perturbations affecting the ESR spectra of biradicals are only briefly discussed in Sect. 3.4.4. Finally, an application of hyperfine ESR spectroscopy to building blocks for molecule-based magnets is presented in Sect. 3.4.5. The building block molecules have characteristics of two types of intramolecular exchange interactions; one is much larger than hyperfine interactions and the other is comparable to them.

3.4.2 The Heisenberg Exchange Coupling

Coulombic energies of electrons relevant to magnetic resonance of molecules or magnetism of molecular assemblages in solid states are described by exchange interactions between electron spins. As outlined below, the spin-dependent part of the coulombic energy between electrons, which are assumed to be spatially localized on atoms or molecules, are termed "exchange interaction". The spin Hamiltonian of the exchange-coupled spins is given by $H_0 = -2J_{ij}\mathbf{S}_i \cdot \mathbf{S}_i$, where $\mathbf{S}_\mathrm{i}$ and $\mathbf{S}_\mathrm{j}$ denote vector operators of two electron spins ($S_\mathrm{i} = S_\mathrm{j} = 1/2$). The scalar parameter J_ij represents the strength of the exchange interaction between $\mathbf{S}_\mathrm{i}$ and $\mathbf{S}_\mathrm{j}$. The basic description of the exchange interaction has been given by Heisenberg [62], Dirac [63, 64], and Van Vleck [65, 66]. The spin Hamiltonian for many-body systems are written as

$$H = \sum_{i,j} -2J_{ij}\mathbf{S}_i \cdot \mathbf{S}_j . \tag{3.43}$$

The formalism based on the inner product of spin operators as given above or in Eq. (3.43) has been utilized to analyze the magnetic coupling within and between open-shell molecules. We have to recall, however, that the Heisenberg Hamiltonian above or Eq. (3.43) is phenomenological. On the theoretical side, accurate quantum chemical computations are necessary for J_{ij}. The electronic energy of the two spin system is $E_A = E_0 + K_{12}^0 - J_{12}^0$ for the triplet ($S = 1$) state and $E_A = E_0 + K_{12}^0 - J_{12}^0$ for the singlet ($S = 0$) state in usual notation. Therefore, the electronic energy is written as

$$E = E_0 + K_{12}^0 - \frac{1}{2}J_{12}^0 - 2J_{12}^0\mathbf{S}_1\ \mathbf{S}_2. \tag{3.44}$$

Omitting the constants independent of the spin variables, the Hamiltonian of the two-spin system is written as $H_{12} = -2J_{12}^0\mathbf{S}_1 \cdot \mathbf{S}_2$. H_{12} or H_0 above is customarily called the Heisenberg Hamiltonian. Expanding the description to systems of $S > 1/2$ spins and to those containing more than two spin variables [64–66], we reach the Heisenberg-Dirac-Van Vleck (HDV) Hamiltonian (3.43). The applicability of the Hamiltonian for nonorthogonal orbitals has also been established [67, 68]. It should be noted that the single parameter J_{ij} contains many nontrivial integrals other than $J_{ij}{}^0$ in general cases of many-spin systems. Furthermore, the Hamiltonian H_0 does not mean any "actual magnetic coupling" between the magnetic moments $g\mu_B\mathbf{S}_i$ and $g\mu_B\mathbf{S}_i$; it describes only in a phenomenological way the electronic or coulombic interaction between two open-shell atoms, molecules, or molecular fragments.

3.4.3 *Biradicals Composed of Two Radical Fragments with a Time-Independent Exchange Coupling*

Let us consider a simple system of two unpaired electrons in a single molecule. The system is informative to extend solution hyperfine ESR spectroscopy so as to be applicable to molecule-based magnetics. The molecule is either in a triplet or a singlet state. The energy separation between the states, the singlet-triplet energy gap, is designated by $2J$, as discussed in Sect. 3.4.2. We assume that the two radical fragments are identical, each having one nucleus of nitrogen with the nuclear spin quantum number $I = 1$. This type of two-spin systems is frequently found in nitroxide radicals which are used as spin labeling reagents and building blocks for molecule-based magnetic materials.

The spin Hamiltonian of the system is given by Eq. (3.42), as shown above. In the two terms S_i^Z and I_i^Z stand for the spin operators for the z components of the electron and nuclear spins in the ith fragment. An averaged g-factor g is adopted here in solution ESR spectroscopy. In Eq. (3.42) the hyperfine interactions are assumed to be small as compared with the electronic Zeeman interaction and nonsecular

terms of the hyperfine coupling are neglected. The parameter A denotes the isotropic hyperfine coupling constant at the nitrogen nuclei. Since the Hamiltonian (3.42) commutes with the z-component of the total electron spin, $S_{\mathrm{T}}^{Z} = S_{1}^{Z} + S_{2}^{Z}$ ($\left[H, S_{T}^{z}\right] = 0$), the Hamiltonian is set up in the ket space spanned by the set of direct products defined as

$$\mathbf{S}_{i}^{z} \left| m_{1}^{\mathrm{S}}, m_{2}^{\mathrm{S}}, m_{1}, m_{2} \right\rangle = \pm 1/2 \left| m_{1}^{\mathrm{S}}, m_{2}^{\mathrm{S}}, m_{1}, m_{2} \right\rangle, \quad (i = 1, 2), \tag{3.45}$$

where m_{i}^{S} and m_{i} are the quantum numbers for the z-components of the electron and nuclear spins in the ith fragment, respectively. The matrix representation of the spin Hamiltonian is given as

$$H = \begin{bmatrix} -\frac{J}{2} + \frac{A}{2}(m_1 + m_2) + g\mu_{\mathrm{B}}B & 0 & 0 & 0 \\ 0 & \frac{J}{2} + \frac{A}{2}(m_1 + m_2) & -J & \\ 0 & -J & \frac{J}{2} - \frac{A}{2}(m_1 + m_2) & 0 \\ 0 & 0 & 0 & -\frac{J}{2} - \frac{A}{2}(m_1 + m_2) - g\mu_B B \end{bmatrix}$$

$$\begin{matrix} |+\frac{1}{2}, +\frac{1}{2}\rangle \\ |+\frac{1}{2}, -\frac{1}{2}\rangle \\ |-\frac{1}{2}, +\frac{1}{2}\rangle \\ |-\frac{1}{2}, -\frac{1}{2}\rangle \end{matrix} \tag{3.46}$$

where the electron spin part of the basis ket $\left| m_{1}^{\mathrm{S}}, m_{2}^{\mathrm{S}} \right\rangle$ is shown in the right side of the matrix. The energy eigenvalues of the spin Hamiltonian are obtained by diagonalizing the matrix (3.46). The results are straightforward. The transition field $B\,(i \leftrightarrow j)$ and the relative transition intensity $P\,(i \leftrightarrow j)$ associated with the ith and the jth states for the allowed ESR transition with $\Delta M_S = \pm 1$ are calculated as

$$h\nu = E(i) - E(j) \equiv \Delta E\,(i \leftrightarrow j) \quad (\nu : \text{the microwave frequency}) \tag{3.47}$$

$$\delta \Delta E(i \leftrightarrow j) \equiv \Delta E(i \leftrightarrow j) - g\mu_B B \tag{3.48}$$

$$B\,(i \leftrightarrow j) = B_0 - \delta \Delta E(i \leftrightarrow j)/g\mu_B \tag{3.49}$$

$$P(i \leftrightarrow j) = \left| \left\langle i \left| S_{T}^{X} \right| j \right\rangle \right|^2 . \tag{3.50}$$

In Eq. (3.50) S_{T}^{X} denotes the spin operator of the x-component of the total electron spin, assuming the configuration of the oscillating microwave field perpendicular to the static field in conventional experiments. The central field B_0 in Eq. (3.49), $B_0 = h\nu/g\mu_B$ is the single resonance field appearing when both J and A are vanishing. We have four allowed transitions at most for each nuclear spin configuration $|m_1, m_2>$ in the two-spin system, which are listed in Table 3.4 for readers' convenience. The resonance fields $\delta \Delta E(i \leftrightarrow j)/g\mu_B$ are measured from

Table 3.4 Resonance fields $B(i \leftrightarrow j) = B_0 - \delta\Delta E\ (i \leftrightarrow j)/g\mu_B$ and relative intensities of allowed ESR transitions for the Hamiltonian (11.42)[a]

I	j	$\delta\Delta(i \leftrightarrow j)^b$	Relative intensity[b]
1	3	$-\frac{1}{2}\Delta + J + \frac{1}{2}A(m_1 + m_2)$	$\frac{1}{4} + \frac{J}{2\Delta}$
1	4	$\frac{1}{2}\Delta - J + \frac{1}{2}A\,(m_1 + m_2)$	$\frac{1}{4} + \frac{J}{2\Delta}$
2	3	$\frac{1}{2}\Delta + J + \frac{1}{2}A\,(m_1 + m_2)$	$\frac{1}{4} - \frac{J}{2\Delta}$
2	4	$-\frac{1}{2}\Delta - J + \frac{1}{2}A\,(m_1 + m_2)$	$\frac{1}{4} - \frac{J}{2\Delta}$

[a] $B_0 \equiv h\nu/g\mu_B$

[b] $\Delta = \sqrt{4J^2 + A^2(m_1 - m_2)^2}$

the central field B_0. Spectral simulations are made by applying an appropriate function such as a Lorentzian and a line width for the $4 \times (2I + 1)^2 = 36$ allowed transitions and accumulating them. The overall distribution of the intensity is simulated by weighting the transitions with the relative intensity $P(i \leftrightarrow j)$ and the Boltzmann factor, $|\exp(-E(i)/k_BT) - \exp(-E(j)/k_BT)|$.

In Fig. 3.5 are shown the simulated spectra for various ratios of $|J/A|$ as a function of the reduced magnetic field $g\mu_B(B - B_0)/|A|$. When the exchange interaction between the two unpaired electron spins is weak as compared with the hyperfine coupling ($|J/A| = 0.01$), the resultant hyperfine splitting pattern consists of three equally weighted lines with a spacing of $|A|$. This pattern is the same as that expected for an $S = 1/2$ radical with one nitrogen nucleus. The weak exchange interaction makes each electron stay at one particular $I = 1$ nucleus such that a fluid solution of the biradical with such a weak J value is equivalent to that of an $S = 1/2$ radical with a doubled concentration. In contrast, if $|J| >> |A|$ ($|J/A| = 100$ in Fig. 3.5), each electron spin interacts with the two nitrogen nuclei in the two fragments owing to the strong exchange interaction, resulting in five lines with the intensity ratio of 1:2:3:2:1 and the spacing of $|A|/2$. When the exchange interaction $|J|$ falls within the same order of magnitude as the hyperfine coupling $|A|$, the hyperfine splitting pattern is complicated as depicted in Fig. 3.5. In some favorable cases, however, one can determine the strength of a specific exchange interaction directly from the splitting patterns of an ESR spectrum. An example is found in the literature [71]. Another example by the present authors is presented in Sect. 3.4.5. It should be noted that the commutator of the Hamiltonian and the total electron spin

$$\mathbf{S}_T^2 \equiv (\mathbf{S}_1 + \mathbf{S}_2)^2 \tag{3.51}$$

$$\left[H,\ S_T^2\right] = \begin{bmatrix} 0 & 0 & 0 & 0 \\ 0 & 0 & A(m_1 - m_2) & 0 \\ 0 & -A(m_1 - m_2) & 0 & 0 \\ 0 & 0 & 0 & 0 \end{bmatrix} \tag{3.52}$$

has nonvanishing elements in the second and the third rows or columns, which correspond to the states with the z components of the total spin $M_S = 0$. This incommutability mixes the states of $M_S = 0$ with each other. The well-known spin wavefunctions for $M_S = 0$ ($S = 1, 0$) are no longer valid for $A \neq 0$.

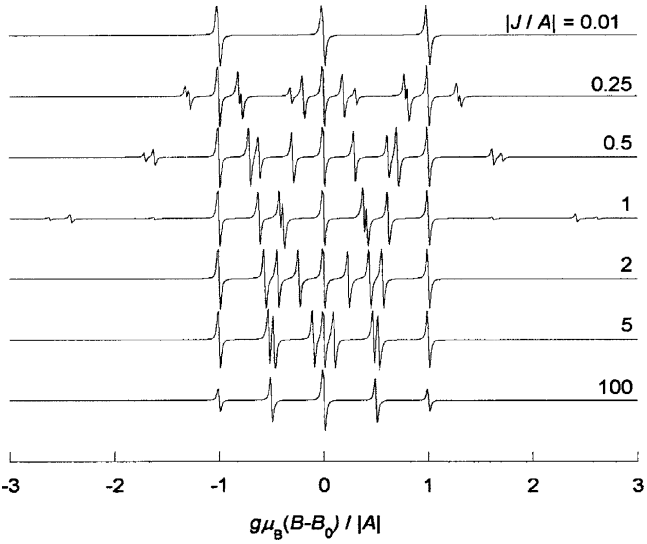

Fig. 3.5 Simulated spectra of biradicals consisting of two identical radical fragments for various ratios of $|J/A|$ as a function of the reduced magnetic field $g\mu_B(B\text{-}B_0)/|A|$. The Lorentzian lineshapes are adopted with the line width of $0.01|A|$

3.4.4 Effects of Time-Dependent Interactions

A five-line hyperfine splitting pattern with an intensity ratio of 1:2:3:2:1 is expected for biradicals with two nitrogen nuclei in the strong exchange limit $|J| >> |A|$, whereas a simple three-line pattern is found for the weak exchange limit $|J| << |A|$, as described in Sect. 3.4.3. One finds many examples of biradicals exhibiting such ESR spectra. Typical examples of nitroxide biradicals are given in the literature [69–71]. It is worth noting that these hyperfine splitting patterns reflecting the exchange interactions $|J|$ as compared with the hyperfine coupling $|A|$ are valid only when the exchange interaction $|J|$ is independent of time. When $|J|$ is modulated by time-dependent perturbations, the intensity ratio of the five-line spectra is distorted even for $|J| >> |A|$. In Fig. 3.6 is given the solution ESR spectrum of a glutarate biradical [72, 73], which contains five lines implying $|J| >> |A|$. An alternation of line widths is, however, found in the spectrum: The two lines between the central and the outermost lines are broadened with a seemingly weaker intensity. This alternation of line width is a historically important example of molecular dynamics affecting ESR spectra, which has been rationalized by Luckhurst [72, 73] on the basis of the relaxation matrix method developed first by Redfield [74–76]. The rationalization is outlined as follows: The matrix elements $R_{ii',jj'}$ of the relaxation matrix $\mathbf{R}$ are given from the matrix elements of $H'(t) = [J(t) - J_{av}]\mathbf{S}_1 \bullet \mathbf{S}_2$ [72, 73]. The time average of the exchange interaction J_{av} is expressed as $J_{av} = (\tau_a J_a + \tau_b J_b) / (\tau_a + \tau_b)$ in the simplest case, where an interconversion,

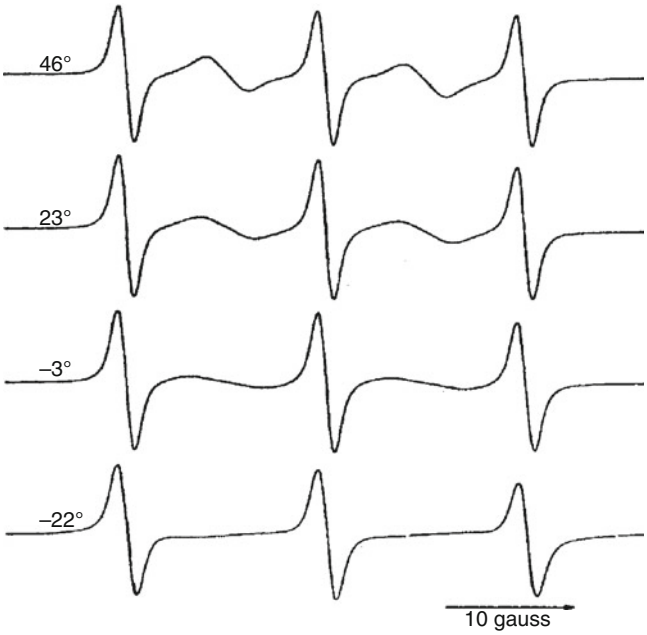

Fig. 3.6 Hyperfine spectra of a glutarate biradical. The spectra were observed at 45, 23, −3, and −22°C from top to bottom (Adapted from Ref. [73] with kind permission of © The American Chemical Society 1970)

or a jumping, is assumed to occur between two molecular conformations with the lifetimes τ_a and τ_b, and with the exchange interactions J_a, and J_b. The eigenvalue of **R** multiplied by –1 for a hyperfine transition with the nuclear quantum numbers m_1 and m_2 is

$$T_2^{-1} = \frac{A^2 (m_1 - m_2)^2}{4J_{av}^2} j\,(J_{av})\,, \tag{3.53}$$

where $j(J_{av})$ is the spectral density for the fluctuation at an angular frequency $J_{av}/\hbar$. Equation (3.53) shows that the hyperfine transitions with m_1-$m_2 = 0$ are not affected by the fluctuation of J; the outermost lines ($m_1 = m_2 = \pm 1$) and one of the overlapping central lines ($m_1 = m_2 = 0$) remain sharp. The other lines are broadened, as observed in the experimental spectra. Only the above three lines ($m_1 = m_2 = \pm 1, 0$) with an equal weight appear with the spacing of $|A|$ in the limit of extreme broadening, which are just alike those for biradicals in the weak exchange limit $|J| << |A|$ or those for monoradicals with one $I = 1$ nucleus. As for an organic triradical, a line width broadening depending on the nuclear quantum numbers m's has been reported [77]. The broadening has been explained in the same way as for the biradical [77]. Hyperfine ESR spectra reflecting dynamic phenomena of chemical importance besides the fluctuation of $|J|$ have been analyzed in the same

way as described here. Examples are *cis-trans* isomerism, restricted rotations, ring inversion, proton exchange, and ion pair formation. An extensive review [78] has been published on dynamical effects on ESR line shapes, which includes dynamic effects other than the line width alternation.

An alternative way of analyzing ESR lineshapes affected by some chemical dynamics is to use a general lineshape equation, which has been derived in terms of the density matrix theory in the Liouville representation [79–85]. Kinetics for the conformational dynamics of a symmetrical triradical has also been analyzed assuming an interconversion among conformers with strong or weak exchange interactions in isosceles and equilateral triangle symmetries [85].

3.4.5 An Application to Models for Organic Molecule Based Magnets

An application of solution hyperfine ESR spectroscopy to building blocks for molecule-based magnets is described in this section. Molecule-based magnets and other molecular functionality magnetics have received great interests in recent years. For reviews of molecule-based magnetism, see Refs. [86–92]. More than 30 crystalline ferromagnets have been discovered in genuinely organic molecule-based materials [86–92] since the discovery of the first organic ferromagnet [93–95]. Ferrimagnets have also attracted attention as one of the facile approaches to organic magnets since the first proposal by Buchachenko in 1979 [96]. Ferrimagnetic spin ordering is conventionally regarded as an antiferro-magnetic ordering of different spin quantum numbers, e.g., $S = 1$ and $S = 1/2$, giving net and bulk magnetization in the solid state. This picture has been initiated by Néel's mean field theory [97]. The concept of organic ferrimagnetics and the seemingly practical feasibility are based on the tendency for organic open-shell molecules to have antiferromagnetic intermolecular interactions in their assemblages. The antiferromagnetic interactions would bring about antiparallel spin alignment between neighboring molecules with different magnetic moments to result in a possible ordered state in the mixed crystalline assemblages. Genuinely organic ferrimagnets composed of two discrete kinds of organic open-shell molecules, however, have not been discovered yet and is a challenging issue in spin chemistry and materials science. The possibility of the occurrence of the ferrimagnetic spin alignments has been examined by the authors both by experiments and theoretical calculations in an elaborate fashion [98–106].

One of the practical difficulties in constructing molecule-based ferrimagnetics is co-crystallization of molecules with different spin quantum numbers. Generally, co-crystallization of distinct molecules in a crystal lattice gives rise to a decrease in entropy, which prevents them from packing in a structurally ordered fashion. Some purposive molecular designing is needed to overcome the separative crystallization driven by entropy. As one of such a purposive molecular designing for purely organic molecule-based ferrimagnets, the authors have proposed a strategy of "single-component ferrimagnetics" [107, 108], which is schematically shown in

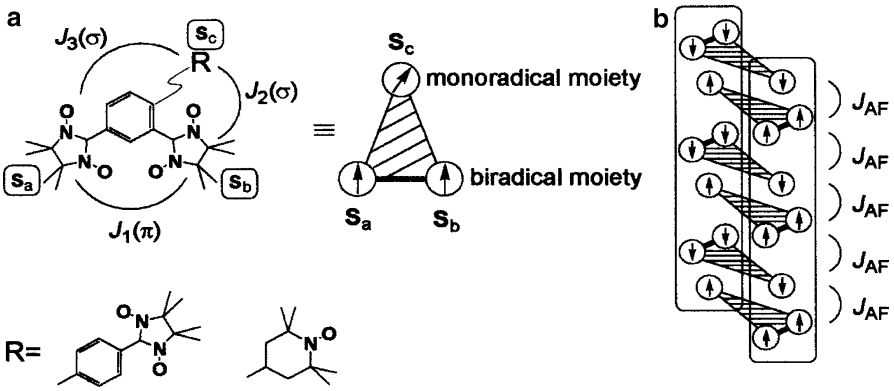

Fig. 3.7 Schematic pictures of single-component ferrimagnetics. (**a**) A triradical consisting of weakly coupled biradical and monoradical moieties. $J_1(\pi)$ denotes the intramolecular exchange interaction within the biradical moiety with the spin $\mathbf{S}_a + \mathbf{S}_b$ ($S_a = S_b = 1/2$), which is coupled with the monoradical moiety with $S_c = 1/2$ by $J_2(\sigma)$ and $J_3(\sigma)$ ($|J_2(\sigma)| \sim |J_3(\sigma)| \ll |J_1(\pi)|$). (**b**) An example of the ferrimagnetic chain based on the intermolecular antiferromagnetic interaction J_{AF} in the crystalline solid. The *rounded rectangles* represent the alternating molecular chain of the biradical and the monoradical

Fig. 3.7. When a π-biradical with an $S = 1$ ground state and a π-monoradical with $S = 1/2$ are united by σ-bonds, the π-conjugation between the biradical and the monoradical moieties should be effectively truncated in the resultant triradical. The triradical has magnetic degrees of freedom for both $S = 1$ and $S = 1/2$ in the single molecule, serving as a building block for ferrimagnets. Intermolecular π-orbital overlaps between an $S = 1$ moiety of one molecule and an $S = 1/2$ moiety of the adjacent molecule mimic molecular complexation of π-biradicals and π-monoradicals in the crystalline solid state. The chemical bonding between the biradical and the monoradical moieties within the single triradical molecule plays a role of binding only; the antiferromagnetic interactions underlying the ferrimagnetic spin alignment have a chance to undergo an *intermolecular* π-π orbital overlap of π-SOMO's of the constituent biradical and monoradical moieties. Thus, in this single-component ferrimagnetics it is important whether or not the additional intramolecular interactions through the σ-bonds $J_2(\sigma)$ and $J_3(\sigma)$ are negligible as compared with the intramolecular ferromagnetic interaction $J_1(\pi)$ in the biradical moiety. In this section, ESR spectroscopic determination of the intramolecular exchange interaction in organic triradicals is described.

The authors have designed and have synthesized triradicals **7** and **8** from benzoic acid monoradicals **9** and **10** and phenol-substituted biradical **11** (Fig. 3.8) as building blocks of "single-component ferrimagnetics". The phenol biradical **11** is known to have an intramolecular ferromagnetic interaction of $J_1(\pi)/k_B = 13$ K [104]. The experimental spectra of the triradicals **7** and **8** are shown in Figs. 3.9 and 3.10. The hyperfine splitting patterns of the triradicals are analyzed in the same way as those of biradicals in Sect. 3.4.3.

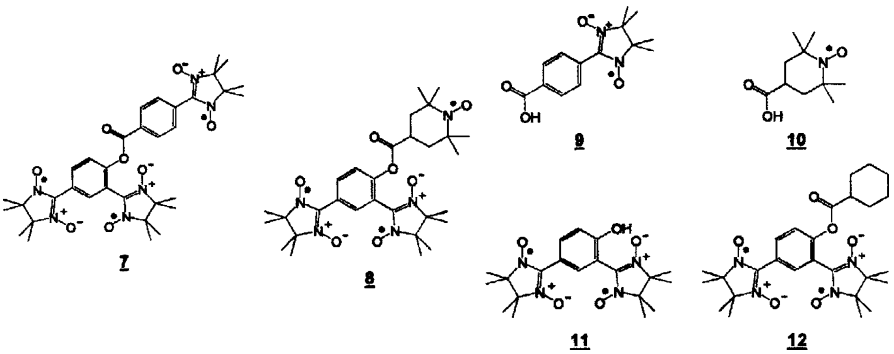

Fig. 3.8 Stable nitroxide radicals as building blocks of "single-component ferrimagnetics"

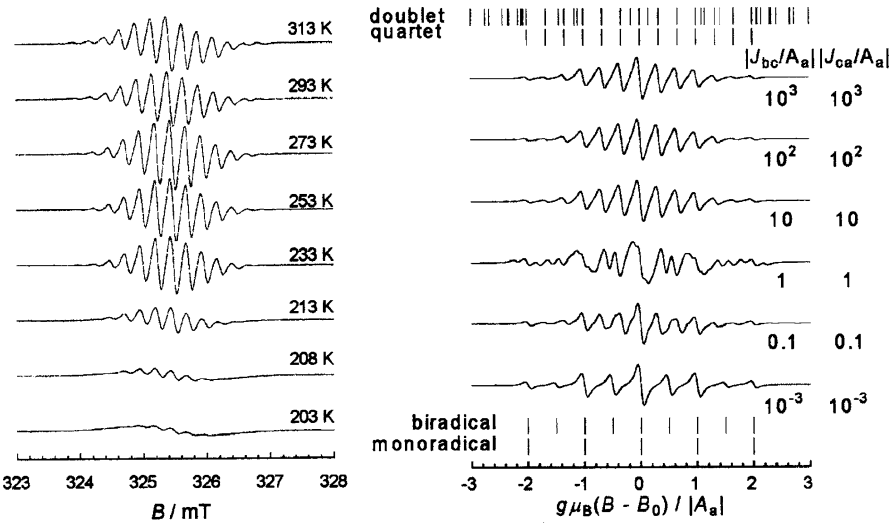

Fig. 3.9 ESR spectra of **7**. (*Left*) observed in a toluene solution. (*Right*) simulated spectra. B_0 is the central field, $B_0 = h\nu/g\mu_B$. The sticks in the upper portion indicate the resonance field for the quartet and doublet states of the triradical in the strong exchange limit ($|J_{bc}/A_a| \sim |J_{ca}/A_a| \gg 1$), while in the lower portion are shown those of the constituent biradical and monoradical in the weak exchange limit ($|J_{bc}/A_a| \sim |J_{ca}/A_a| \ll 1$). See text for the experimental conditions and the parameters employed for the simulation

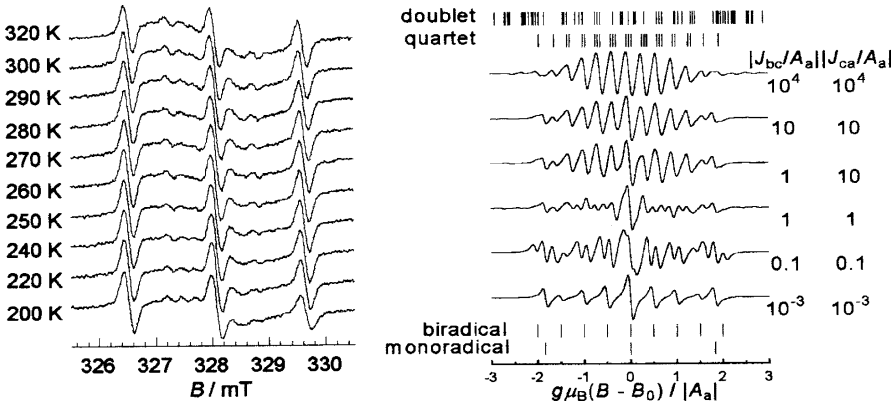

Fig. 3.10 ESR spectra of **8**. (*Left*) observed in a toluene solution. (*Right*) simulated spectra. B_0 is the central field; $B_0 = h\nu/g\mu_B$. The sticks in the *upper portion* indicate the resonance field for the quartet and doublet states of the triradical for the strong exchange limit ($|J_{bc}/A_a| \sim |J_{ca}/A_a| \gg 1$), while in the lower portion are shown those of the constituent biradical and monoradical for the weak exchange limit ($|J_{bc}/A_a| \sim |J_{ca}/A_a| \ll 1$). See text for the experimental conditions and the parameters employed for the simulation

The spin Hamiltonian for the triradicals is written as

$$H = g\mu_B B\left(S_a^z + S_b^z + S_c^z\right) - 2J_1(\pi)\mathbf{S}_a \cdot \mathbf{S}_b - 2J_2(\sigma)\mathbf{S}_b \cdot \mathbf{S}_c - 2J_3(\sigma)\mathbf{S}_c \cdot \mathbf{S}_a + A_{ab}\left(I_a^z S_a^z + I_b^z S_b^z\right) + A_c I_c^z S_c^z \tag{3.54}$$

which consists of the electronic Zeeman, the Heisenberg exchange, and the hyperfine coupling terms. The three-centered Heisenberg exchange couplings are described with the inner products of the three vector operators. This is derived [109] in the same way as that of the two-centered system described in Sect. 3.4.2. A generalized formulation of the exchange couplings for molecular systems with more than two electrons is found in the literature [110, 111]. Since the nitronyl nitroxide radical group has two nitrogen nuclei which are chemically equivalent, the nuclear spin operators in Eq. (3.54) are given by

$$I_a^z \equiv I_{a1}^z + I_{a2}^z,\ I_b^z \equiv I_{b1}^z + I_{b2}^z \tag{3.55}$$

$$I_c^z \equiv I_{c1}^z + I_{c2}^z \quad \text{(Triradical 7)} \qquad I_c^z \equiv I_{c1}^z \quad \text{(Triradical 8)} \tag{3.56}$$

The Hamiltonian is set up in the ket space spanned by the set of direct products

$$S_I^z \left|m_a^S, m_b^S, m_c^S, m\right\rangle = \pm\frac{1}{2}\left|m_a^S, m_b^S, m_c^S, m\right\rangle, \quad (\mathrm{I} = \mathrm{a},\ \mathrm{b},\ \mathrm{c}) \tag{3.57}$$

where m is the collective index of a nuclear spin configuration of

$$m = \{m_{a1}, m_{a2}, m_{b1}, m_{b2}, m_{c1}(, m_{c2})\} \tag{3.58}$$

The Hamiltonian is represented by a $2^3 \times 2^3$ matrix. The energy eigenvalues and eigenvectors can be obtained analytically. They are, however, quite complicated, hampering their practical usability. Instead, from the exact, numerical diagonalization of the spin Hamiltonian, the resonance fields and the transition probability are calculated in the same way as in Eq. (3.47) through Eq. (3.50). We have 15 allowed transitions, i.e., 15 pairs of the spin states (five within the multiplets and ten across the multiplets) with $\Delta M_S = \pm 1/2$ for one set Eq. (3.58) of nuclear configuration. We have simulated the hyperfine ESR spectra for the triradicals **7** and **8** by superposing at most $15 \times (2I \times 1)^5 = 3645$ or $15 \times (2I \times 1)^6 = 10,935$ of the transitions.

The simulated spectra for triradical **7** are shown in Fig. 3.9. In the weak exchange limit of $|J_2(\sigma)/A| << 1$ and $|J_3(\sigma)/A| << 1$, the simulated spectrum is a simple superposition of the spectrum of the biradical and that of the monoradical. The biradical spectrum consists of nine lines with equal spacings of $|A|/2$ due to five nitrogen nuclei, while the monoradical has the contribution of five lines attributable to two nitrogen nuclei. The biradical is in the strong exchange limit of $|J_{ab}/A| >> 1$. Thirteen lines with equal spacing of $|A|/3$ show up in the simulated spectra due to the strong exchange limit of $|J_2(\sigma)/A| >> 1$ and $|J_3(\sigma)/A| >> 1$. The experimental spectra of the triradical **7** are reproduced by assuming $|J_2(\sigma)/A_a| \sim |J_3(\sigma)/A_a| \geq 10$, *i.e.*, $|J_2(\sigma)|/k_B \sim |J_3(\sigma)|/k_B \geq 10$ mK for $|A|/g\mu_B = 0.75$ mT. The simulated hyperfine splitting patterns are insensitive to the difference between $|J_2(\sigma)|$ and $|J_3(\sigma)|$: The deviation of molecular symmetry from the isosceles triangle is not detectable in the strong exchange limit, $|J_2(\sigma)/A_a| \sim |J_3(\sigma)/A_a| \geq 10$. The spectral simulation gives the lower limit of the hyperfine coupling constant in triradical **7**. The exchange interactions in **7** are much larger than the hyperfine couplings. The π-conjugation through the phenyl group of the monoradical moiety in **7** is not completely truncated. An estimate for the exchange interactions $J_2(\sigma)$ and $J_3(\sigma)$ in **7** has been obtained from paramagnetic susceptibility measurements in the crystalline solid state [107]; $|J_2(\sigma)|/k_B$ and $|J_3(\sigma)|/k_B$ are in the order of 0.1 K.

The solution ESR spectra of triradical **8** are shown in Fig. 3.10. An intense triad of signals with the spacing of the ^{14}N hyperfine coupling of the TEMPO monoradical features in the spectra. The other signals between the triad decrease in intensity on lowering the temperature, as shown in the figure. The spectral simulations for **8** were carried out in the same way as **7** except that $|A_c|/g\mu_B = 1.38$ mT and $I_{c2} = 0$. The simulated spectra for $|J_2(\sigma)/A_a| = |J_3(\sigma)/A_a| = 10^{-3}$ (at the bottom on the right) that is equivalent to the simple Lorentzian ($\Delta B = 0.04$ mT) are shown in Fig. 3.10. The spectrum simulated for $|J_2(\sigma)/A_a| = |J_3(\sigma)/A_a| = 10^4$ demonstrates the strong limit of intramolecular exchange interaction. On the other hand, the simulated superposition of the spectra of the biradical and the monoradical represents the weak limit of intramolecular exchange interaction. The experimental spectra at room temperature cannot be interpreted in terms of either the strong or the weak exchange limit. Thus, the exchange interactions

between the biradical and the monoradical moieties are estimated to be of the same order of magnitude as the hyperfine couplings; $|J_{bc}/A_a| \sim |J_{ca}/A_a| \sim 1$. Satisfactory agreement between the experimental and the simulated spectra, however, is not obtained. The disagreement suggests that the fluctuation of J_{bc} and J_{ca} occurs due to conformational interconversion of the molecule **8** in solution.

Effects of molecular dynamics on ESR spectra in solution have not been studied so much for triradicals as compared with those for biradicals. ESR spectra of a triradical with three nitroxide groups containing three nitrogen nuclei have been analyzed in terms of the relaxation matrix [77] and the composite Liouville space formalism [85]. We present here an alternative perturbation treatment approach [112], assuming that the exchange interaction within the biradical moiety $|J_1(\pi)|$ is much larger than those between the biradical and the monoradical moieties $|J_2(\sigma)|$, $|J_3(\sigma)|$. This approach gives the assignment of specific signals in complicated hyperfine splitting patterns, explaining the appearance of the triad signals for **8**. Such an assignment is difficult to obtain by the exact diagonalization described above. The spin Hamiltonian (3.54) is split into two parts

$$H^{(0)} = g\mu_B B\left(S_a^z + S_b^z + S_c^z\right) - 2J_1(\pi)\mathbf{S}_a \cdot \mathbf{S}_b, \tag{3.59}$$

$$H^{(1)} = -2J_2(\sigma)\mathbf{S}_b \cdot \mathbf{S}_c - 2J_3(\sigma)\mathbf{S}_c \cdot \mathbf{S}_a + A_{ab}\left(I_a^z S_a^z + I_b^z S_b^z\right) + A_c I_c^z S_c^z \tag{3.60}$$

The unperturbed Hamiltonian (3.59) is block-diagonalized with respect to the z-component of the total electron spin M_S

$$\left(\sum_I S_I^z\right)\left|m_a^S, m_b^S, m_c^S, m^I\right\rangle = M^S\left|m_a^S, m_b^S, m_c^S, m^I\right\rangle, \quad (M_S = \pm 3/2, \pm 1/2) \tag{3.61}$$

$$\mathbf{H}^{(0)} = \left[\begin{array}{c|c|c|c} \frac{3}{2}g\mu_B B - \frac{1}{2}J_1(\pi) & \mathbf{O} & \mathbf{O} & 0 \\ \hline \mathbf{O} & \mathbf{H}_{234}^{(0)} & \mathbf{O} & \mathbf{O} \\ \hline \mathbf{O} & \mathbf{O} & \mathbf{H}_{567}^{(0)} & \mathbf{O} \\ \hline 0 & \mathbf{O} & \mathbf{O} & -\frac{3}{2}g\mu_B B - \frac{1}{2}J_1(\pi) \end{array}\right] \tag{3.62}$$

The four block submatrices correspond to $M_S = +3/2$, $+1/2$, $-1/2$, and $-3/2$. The submatrices for $M_S = \pm 1/2$ are given as follows;

$$\mathbf{H}_{234}^{(0)} = \begin{bmatrix} \frac{1}{2}g\mu_B B + \frac{1}{2}J_1(\pi) & -J_1(\pi) & 0 \\ -J_1(\pi) & \frac{1}{2}g\mu_B B + \frac{1}{2}J_1(\pi) & 0 \\ 0 & 0 & \frac{1}{2}g\mu_B B - \frac{1}{2}J_1(\pi) \end{bmatrix} \tag{3.63}$$

$$\mathbf{H}^{(0)}_{567} = \begin{bmatrix} -\frac{1}{2}g\mu_B B + \frac{1}{2}J_1(\pi) & -J_1(\pi) & 0 \\ -J_1(\pi) & -\frac{1}{2}g\mu_B B + \frac{1}{2}J_1(\pi) & 0 \\ 0 & 0 & -\frac{1}{2}g\mu_B B - \frac{1}{2}J_1(\pi) \end{bmatrix} \tag{3.64}$$

By diagonalizing the matrix (3.62), we obtain the zeroth order energy eigenvalues and the eigenvectors. The energies are listed in the literature [113]. The eight eigenvectors $\left\{\mathbf{x}_i^{(0)}\right\}$ are represented in the columns of the matrix $\mathbf{U}$;

$$\begin{aligned} \mathbf{U} &= \left[\mathbf{X}_1^{(0)}\mathbf{X}_2^{(0)}\mathbf{X}_3^{(0)}\mathbf{X}_4^{(0)}\mathbf{X}_5^{(0)}\mathbf{X}_6^{(0)}\mathbf{X}_7^{(0)}\mathbf{X}_8^{(0)}\right] \\ &= \begin{bmatrix} 1 & 0 & 0 & 0 & 0 & 0 & 0 & 0 \\ 0 & -\frac{1}{\sqrt{2}} & \frac{1}{\sqrt{3}} & -\frac{1}{\sqrt{6}} & 0 & 0 & 0 & 0 \\ 0 & \frac{1}{\sqrt{2}} & \frac{1}{\sqrt{3}} & -\frac{1}{\sqrt{6}} & 0 & 0 & 0 & 0 \\ 0 & 0 & \frac{1}{\sqrt{3}} & \frac{2}{\sqrt{6}} & 0 & 0 & 0 & 0 \\ 0 & 0 & 0 & 0 & -\frac{1}{\sqrt{2}} & \frac{1}{\sqrt{3}} & -\frac{1}{\sqrt{6}} & 0 \\ 0 & 0 & 0 & 0 & \frac{1}{\sqrt{2}} & \frac{1}{\sqrt{3}} & -\frac{1}{\sqrt{6}} & 0 \\ 0 & 0 & 0 & 0 & 0 & \frac{1}{\sqrt{3}} & \frac{2}{\sqrt{6}} & 0 \\ 0 & 0 & 0 & 0 & 0 & 0 & 0 & 1 \end{bmatrix} \end{aligned} \tag{3.65}$$

The perturbed vectors and the state energies to the first order are given as

$$\mathbf{x}_n = \mathbf{x}_n^{(0)} + \sum_{i \neq n} \frac{H^{(1)}_{in}}{E_n^{(0)} - E_i^{(0)}} \mathbf{x}_n^{(0)}, \quad E_n = E_n^{(0)} + H^{(1)}_{nm} \tag{3.66}$$

where $H^{(1)}_{in}$ is the matrix element of the first order submatrices

$$\mathbf{U}^{-1}\mathbf{H}^{(1)}\mathbf{U} = \left[\begin{array}{c|c|c|c} -J(\sigma) + \frac{1}{2}[A_b(m_a + m_b) + A_m m_c] & \mathbf{O} & \mathbf{O} & 0 \\ \hline \mathbf{O} & (\mathbf{U}^{-1}\mathbf{H}^{(1)}\mathbf{U})_{234} & \mathbf{O} & \mathbf{O} \\ \hline \mathbf{O} & \mathbf{O} & (\mathbf{U}^{-1}\mathbf{H}^{(1)}\mathbf{U})_{567} & \mathbf{O} \\ \hline 0 & \mathbf{O} & \mathbf{O} & -J(\sigma) - \frac{1}{2}[A_b(m_a + m_b) + A_m m_c] \end{array}\right] \tag{3.67}$$

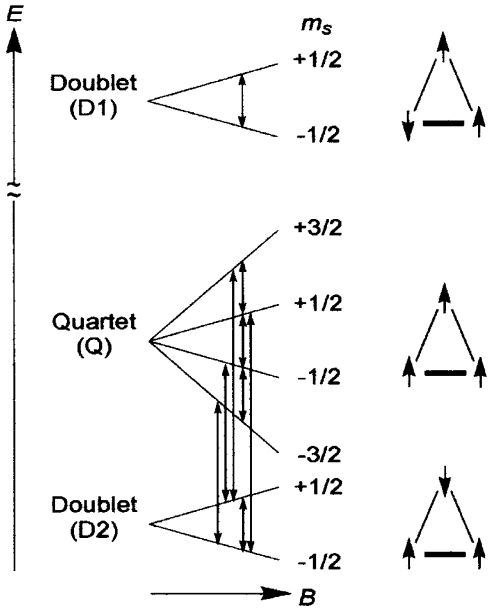

Fig. 3.11 Energy diagram for the triradicals **7** and **8**. The *arrows* indicate the allowed transitions. The hyperfine sublevels are omitted for clarity. In the *right side* are shown the schematic representations of electron spin configurations for the quartet (Q) and doublet (D1, D2) states

$$(\mathbf{U}^{-1}\mathbf{H}^{(1)}\mathbf{U})_{234} = \begin{bmatrix} \frac{1}{2}A_m m_c & \frac{1}{\sqrt{6}}A_b(m_a - m_b) & -\frac{1}{2\sqrt{3}}A_b(m_a - m_b) \\ \frac{1}{\sqrt{6}}A_b(m_a - m_b) & -J(\sigma) + \frac{1}{6}[A_b(m_a + m_b) + A_m m_c] & \frac{1}{3\sqrt{2}}[A_b(m_a + m_b) - 2A_m m_c] \\ -\frac{1}{2\sqrt{3}}A_b(m_a - m_b) & \frac{1}{3\sqrt{2}}[A_b(m_a + m_b) - 2A_m m_c] & 2J(\sigma) + \frac{1}{6}[A_b(m_a + m_b) - A_m m_c] \end{bmatrix} \tag{3.68}$$

$$(\mathrm{U}^{-1}\mathrm{H}^{(1)}\mathrm{U})_{567} = \begin{bmatrix} -\frac{1}{2}A_\mathrm{m} m_\mathrm{c} & -\frac{1}{\sqrt{6}}A_\mathrm{o}(m_\mathrm{a} - m_\mathrm{b}) & \frac{1}{2\sqrt{3}}A_\mathrm{o}(m_\mathrm{a} - m_\mathrm{b}) \\ -\frac{1}{\sqrt{6}}A_\mathrm{o}(m_\mathrm{a} - m_\mathrm{b}) & -J(\sigma) - \frac{1}{6}[A_\mathrm{o}(m_\mathrm{a} + m_\mathrm{b}) + A_\mathrm{m} m_\mathrm{c}] & -\frac{1}{3\sqrt{2}}[A_\mathrm{o}(m_\mathrm{a} + m_\mathrm{b}) - 2A_\mathrm{m} m_\mathrm{c}] \\ \frac{1}{2\sqrt{3}}A_\mathrm{o}(m_\mathrm{a} - m_\mathrm{b}) & -\frac{1}{3\sqrt{2}}[A_\mathrm{o}(m_\mathrm{a} + m_\mathrm{b}) - 2A_\mathrm{m} m_\mathrm{c}] & 2J(\sigma) - \frac{1}{6}[2A_\mathrm{o}(m_\mathrm{a} + m_\mathrm{b}) - A_\mathrm{m} m_\mathrm{c}] \end{bmatrix} \tag{3.69}$$

where the two exchange interactions $J_2(\sigma)$ and $J_3(\sigma)$ are assumed to be identical for simplicity; $J_2(\sigma) = J_3(\sigma) \equiv J(\sigma)$. The two pairs of the vectors $\{\mathbf{x}_3^{(0)}, \mathbf{x}_4^{(0)}\}$ and $\{\mathbf{x}_6^{(0)}, \mathbf{x}_7^{(0)}\}$ are degenerate in energy to the zeroth order. Diagonalizing the perturbation matrices (3.68) and (3.69) with respect to these degenerate states, the state energies $E(i)$ and vectors $\{\mathbf{x}_i\}$ to the first order are obtained. The energies are listed in the literature [112, 113]. We have 15 allowed transitions with $\Delta M_S = \pm 1/2$, as mentioned above. Since the intramolecular exchange interaction within the biradical moiety $J_1(\pi)/k_\mathrm{B} = 13$ K is much larger than all other interactions, one of the two doublet states D1 lies far apart above the other doublet (D2) and the quartet (Q) states, as depicted in Fig. 3.11. Therefore, we can exclude contribution

from allowed ESR transitions across the multiplets, i.e., those between D1 and Q or between D1 and D2. One has only nine pairs of states, five within the multiplets and four across the multiplets of Q and D2. The resonance fields $B\,(i \leftrightarrow j)$ are calculated in the same way as in Eqs. (3.47), (3.48), (3.49), (3.50) for the $S = 1/2$ radicals. In the literature [112, 113] the first-order resonance fields are given as measured from the central field B_0.

It should be noted that the resonance field $\delta\ \Delta\mathrm{E}(2 \leftrightarrow 5)/g\mu_\mathrm{B}$ is independent of the exchange interaction $J(\sigma)$ ($J_2(\sigma)$ and $J_3(\sigma)$). Thus, the transition $\Delta E(2 \leftrightarrow 5)$ is little affected by the fluctuation of the $J(\sigma)$ values. Furthermore, the hyperfine splitting of this transition is $|A_\mathrm{m}|$, which is the hyperfine coupling constant of the monoradical. The intense triad of the signals with the spacing of $|A_\mathrm{m}|$ in the observed ESR spectra is assigned to the transition of $\Delta E(2 \leftrightarrow 5)$ in D1. Resonance fields of other transitions have a contribution of $J(\sigma)$, which fluctuates in a solution. The appearance of the intense triad signals and the rest of the broadened signals indicate that the exchange interactions through the σ bondings of the ester group are quite small as compared with that within the biradical moiety:

$$J_1(\pi) \gg |J_2(\sigma)|, |J_3(\sigma)| \approx |A_\mathrm{ab}|, |A_\mathrm{c}| \tag{3.70}$$

This indicates that the triradical **8** has the potential to be building blocks of single-component organic ferrimagnets.

Some of the perturbation-based useful expressions derived in this section are given in the literature [112, 113].

3.5 High Spin Chemistry of Various Molecular Clusters: Utilization of High-Field/High-Frequency ESR and Pulsed ESR Spectroscopy

This section deals with recent documentation, focusing on important issues in terms of electron magnetic resonance spectroscopy with the emphasis of recent important progress in chemistry, materials science and physics of molecule-based high-spin clusters. Readers are recommended to refer to the monographs “EPR of Exchanged Coupled Systems” by Bencini and Gatteschi [114] (the updated version available now) and “Molecular Magnetism” by Kahn [2] for comprehensive treatises on metal-ion-based molecular high-spin multi-clusters in terms of electron magnetic resonance and materials science, respectively.

3.5.1 *Inorganic Molecule-Based Metal High-Spin Clusters Including Dinuclear Triplet-State Clusters*

In this section, recent progress on pure inorganic molecule-based metal high-spin clusters is summarized. Readers are recommended to refer to other chapters for inorganic molecule-based non-transition metal clusters with high spin multiplicities, where important chemical species such as dimeric $(NO)_2(Na^+)x$ in the triplet state adsorbed on zeolites are included.

3.5.1.1 Exchange-Coupled Dinuclear Clusters

In isolated high-spin systems composed of dinuclear clusters, the spin Hamiltonian given in Sect. 3.2.1 is generally applicable. Throughout this chapter, dinuclear clusters are termed metal-ion-based molecular bi-clusters. The total spin Hamiltonian can include all the terms and any resulting effective spin Hamiltonian can be expressed in terms of component spin Hamiltonian terms. If the component spin Hamiltonian parameters in tensor-based terms are known, experimentally or theoretically, the spin Hamiltonian parameters for the exchange-coupled dinuclear cluster can be derived, reproducing the corresponding ESR fine-structure spectrum. This procedure is phenomenological, but applicable to either homo-spin or hetero-spin molecular systems. During the spectral simulation procedure, molecular structural parameters are required for unitary transformation into desired molecular principal-axes systems. One can assume the molecular structures, theoretically, or derive them from X-ray structural analyses.

In dealing with the exchange-coupled spin systems in terms of ESR spectroscopy, a crucial point is to evaluate the interacting terms such as the exchange coupling $\boldsymbol{J}^{AB}$, the magnetic dipolar coupling $\boldsymbol{D}^{AB}$ and the asymmetric terms $\boldsymbol{d}^{AB}$ between the component spins A and B. In the approximation given in Sect. 3.2, the interacting terms can be derived from dinuclear clusters of two effective spin centers. For multi-centers, this is not the case, generally. Only for a series of well controlled molecule-based high-spin clusters, semi-empirical estimations for the interacting terms can be acquired. Otherwise, for most molecular clustering systems, quantum chemical computations which enable us to consider nearby excited electronic states with high accuracy are desirable to estimate the interacting terms, the computations for high spin systems with non-vanishing angular momenta are formidable. For most cases, the asymmetric terms are regarded to be negligible, although they are important in terms of group theoretical arguments for the systems under study. In order to understand molecular high-spin clusters in the crystalline state, it is worth noting that ESR spectroscopy should be supported with the help of magnetic susceptibility measurements of the bulk magnetic properties.

Table 3.5 Adjustable magnetic parameters for Cr(III)-Cr(III), Fe(III)-Fe(III), and Cr(III)-Fe(III) pairs

Compounds	J/cm^{-1}	G	θ/cm^{-1}	ρ/%	$N\alpha$/emu mol^{-1}
Cr-Cr[a]	−3.23	1.989			610×10^{-6}
Fe-Fe[b]	−3.84	2.00		0.5	
Cr-Fe[c]	+1.10	1.97	−0.97		547×10^{-6}

[a] $\chi_m = \chi_D + N\alpha$
[b] $\chi_m = (1 - \rho)\ \chi_D + \rho(35\, N\beta^2\, g^2/(12kT))$
[c] $\chi_m = \chi_D T/(T - \theta) + N\alpha$, where the dimer susceptibility χ_D can be obtained for any isotropic dimer

The oxalato-bridged bi-clusters (dimers) of Cu(II) have been thoroughly studied in magnetochemistry because they provide model systems to give testing grounds for theories describing magnetic interactions on a molecular orbital basis [115–117]. Focusing on other metal-based oxalato-bridged homo-spin pairs, examples are known with Ti(III) [118], Fe(III) [119, 120], and Cr(III) [121]. Also, an oxalato-bridged hetero-pair Cr(III)-Fe(III) was reported [122, 123]. The high-spin-based hetero-spin bi-cluster is particularly intriguing in terms of molecular exchange couplings, although the crystal structure was not reported. Triki et al. compared the hetero-spin pair (Cr(III)-Fe(III)) with the homo-spin ones (Cr(III)-Cr(III) and Fe(III)-Fe(III)). From the magnetic susceptibility measurements for the homo- and hetero-spin pairs, the exchange coupling parameters were obtained. In Table 3.5 are summarized their adjustable magnetic parameters in terms of bulk magnetic properties. The table shows that in the homo-spin pairs antiferromagnetic interactions between the spins were observed, while the ferromagnetic exchange interaction between the spins was observed in the hetero-spin pair. The ESR spectra for these dinuclear clusters qualitatively agree with the temperature dependence of the magnetic susceptibilities. Figure 3.12 shows the temperature-dependent ESR spectra for the Cr(III)-Cr(III), Fe(III)-Fe(III), and Cr(III)-Fe(III) pairs. In the Cr-Cr clusters, only one peak around $g = 2.00$ was observed and an asymmetric large signal around 0.2 T was observed, indicating that the feature is typical of ESR spectra for high-spin systems with large zero-field splittings. The accurate spin Hamiltonian parameters have neither been determined in terms of ESR spectroscopy and mechanisms of the exchange coupling nor interpreted yet. Possible applications of high-field/high-frequency ESR spectroscopy and parallel microwave excitation spectroscopy at liquid helium temperature are desirable to give direct information about the high-spin ground or intermediate state of the homo- and hetero-spin pairs. Particularly, pulse-based two-dimensional electron spin nutation spectroscopy with high time-resolution for dinuclear molecular bi-clusters at low temperature gives reliable spin identification in a straightforward manner. Recently, many authors have reported various types of molecule-based exchange-coupled dinuclear clusters [124–138]. For most dinuclear clusters, the exchange interaction is larger than the energy of the X-band microwave. Thus, high-field/high-frequency ESR technique is a powerful tool [139, 140].

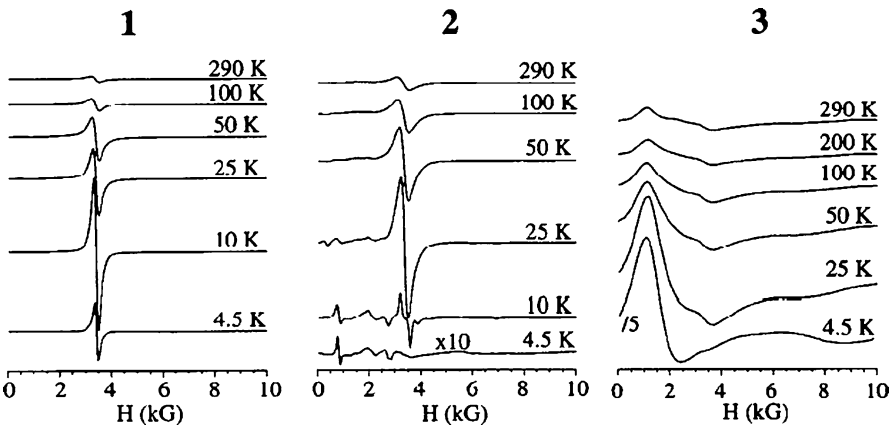

Fig. 3.12 ESR spectra of dinuclear-pair compounds in solids at various temperatures **1**: Cr-Cr, **2**: Fe-Fe, **3**: Cr-Fe (Adapted from Ref. [123] with kind permission of © The American Chemical Society 2000)

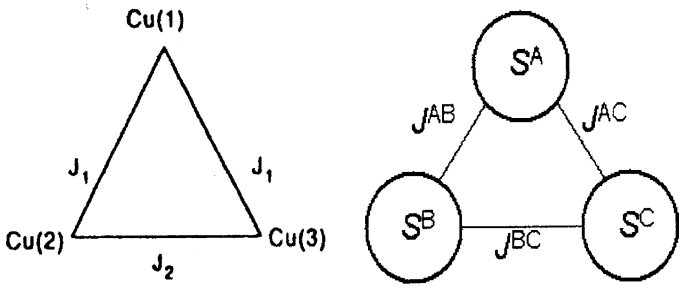

Fig. 3.13 Schematic models of the spin frustration systems for trinuclear clusters

3.5.1.2 Exchange-Coupled Trinuclear Clusters: Spin Frustration and Mixed Valence States

There has been much interest in the spin frustration of equilateral triangular tri-clusters composed of paramagnetic metal-ions. A crucial point of the spin frustration systems is the occurrence of the antiferromagnetic interaction between the spin centers. Figure 3.13 shows the schematic model of the spin frustration systems for trinuclear clusters. J^{AB}, J^{BC}, and J^{CA} denote the exchange interaction between the A-B, B-C, and C-A spin sites, respectively. The frustration systems are important issues in spin chemistry, and related structural chemistry and magnetics in quantum terms because the whole systems are not described by simple spin schemes for the ground stabilized state. In Fig. 3.14, a simplified model for trinuclear clusters is given on the left side, where the three spin sites are composed of Cu(II) ($S_i = S = 1/2$) with $J^{AB} = J^{CA} = J_1$ and $J^{BC} = J_2$, noting that exchange coupling terms in spin Hamiltonians should be expressed by coefficients $-2J_i$ or $-2J^{ij}$, i.e., $-\sum 2J^{ij}\mathbf{S}_i \cdot \mathbf{S}_j$.

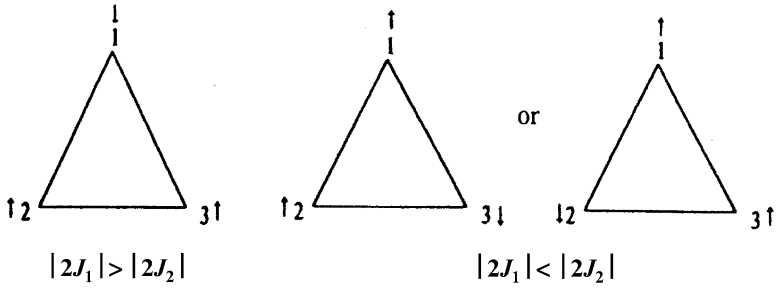

Fig. 3.14 Spin frustration modes of the ground spin state for two cases

Spin structures representing typical ground states are described for the cases of $|2J_1| \neq |2J_2|$. When the spin states are represented by $\mathbf{S} = \mathbf{S}^{A} + \mathbf{S}^{B} + \mathbf{S}^{C}$, the resulting states are two doublets and one quartet. The ground state for the isosceles three spin system is described by a ket $| S, S' >$ with the definition of the total spin $S = S_1 + S_2 + S_3$ and $S' = S_2 + S_3$. For $|2J_1| > |2J_2|$, the ground state is given by $|\ 1/2, 1>$ and for $|2J_1| < |2J_2|$, the one given by $|\ 1/2, 0>$. For both cases, the highest spin state$|\ 3/2, 1>$ is above the two doublet states by $-2(J_1/2 + J_2/4)$. For $2J_1 = 2J_2$, the two doublet states are degenerate, giving rise to trinuclear spin frustration. The spin frustration associated with vibronic interaction is expected to cause rapid spin fluctuation. Many authors have studied spin-frustration systems until quite recently [141–154].

$$|2J_1| > |2J_2| \cdot |2J_1| < |2J_2|$$

Recently, So et al. have reported ESR studies of the Cu(II)-based equilateral triangular clusters **1**: $Na_9[\beta\text{-}SiW_9O_{37}\{Cu(H_2O)\}_3]$ [155] and **2**: $K_{12}[As_2W_{18}O_{66}Cu_3(H_2O)_2]\cdot 11H_2O$ [156], revealing the possible occurrence of the trinuclear spin frustration. The crystal structure for **1** has not been reported. The presumed molecular structure for 1 and the crystal structure of 2, however, have been reported by Robert et al. [157, 158], showing that three Cu(II) ions form a nearly equilateral triangle. From the temperature dependence of the magnetic susceptibility, the antiferromagnetic exchange interactions between the Cu(II) spins ($S = 1/2$) were confirmed to occur: $2J_1 = 2J_2 = -7.8\ cm^{-1}$. The sizable magnitude of the exchange coupling indicates that through-bond exchange interactions occur. If the bridging oxygen and tungsten atoms play a role of superexchange interactions between the Cu(II) spin sites, the lowest doublet states are expected to be dynamically stabilized also by vibronic coupling or a vibrational spin-orbit one. Such spin frustration systems undergoing pseudo-rotations are expected to be ESR silent in terms of conventional ESR spectroscopy at low temperatures. They measured conventional ESR spectra of **2**, in which the crystal structure is known, in order to obtain information on the frustration effects. Fig. 3.15 shows the observed and simulated ESR fine-structure spectra for **2** at room temperature (left) and 77 K (right). A second-

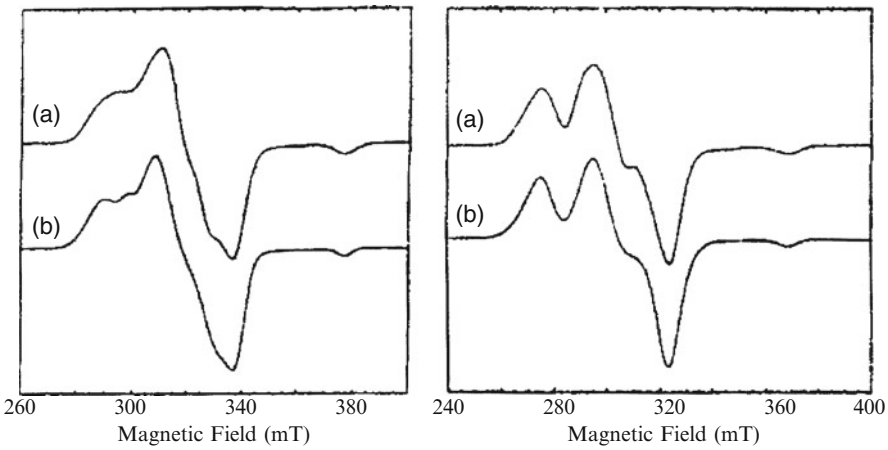

Fig. 3.15 ESR spectra observed for **2**: $K_{12}[As_2W_{18}O_{66}Cu_3\ (H_2O)_2]\cdot 11H_2O$ (polycrystalline) at room temperature (*left*) and 77 K (*right*). (**a**) And (**b**) denote the observed and simulated spectra ($S = 3/2$), respectively (Adapted from Ref. [156] with kind permission of © The Korean Chemical Society 1995)

order-perturbation-based simulation was carried out assuming axial symmetry: $S = 3/2$, $g_x = g_y = 2.226$, $g_z = 2.062$, $|D| = 0.0223\ cm^{-1}$, and $E = 0\ cm^{-1}$ at 77 K: the smaller $|D|$ value of $0.0189\ cm^{-1}$ was determined at room temperature. No doublet state was explicitly detected, indicating the occurrence of rapid spin fluctuation. In terms of tensor-based exchange-coupling analyses for the observed D values the inter-distance between the Cu(II) sites was determined to be 0.420 nm at 77 K and 0.437 nm at room temperature, suggesting the possible vibronic contraction of the nuclear distance. Also, it was indicated that the doublet-quartet energy gap is small enough to undergo thermally activated processes at room temperature in **2**. For the complete analysis, solving the puzzles of this molecular spin frustration system, high-field/high-frequency ESR spectroscopy at liquid helium temperatures is required. The relaxation anomaly due to the pseudo rotation of the trinuclear sites should be hampered at temperatures below 2 K. Another model system **1** for the triangular spin frustration was ESR silent at ambient temperature, suggesting an anomalously rapid spin relaxation occurring in the excited high-spin quartet state. In addition, the temperature dependence of the magnetic susceptibility of **1** in the range of 5–300 K has given another complicated puzzle [155], to which single-crystal high-field/high-frequency ESR spectroscopy finds a clue.

Sandwich-type triangular clusters with various transition metals were characterized by ESR spectroscopy [159]. They reveal the antiferromagnetic exchange interactions between the metals from the temperature dependence of the signal intensity of high-field/high-frequency ESR spectroscopy. Similar clusters were synthesized and studied by many authors [159–161]. However, detailed information on the electronic spin structures due to the frustration has not been clear yet. A crucial issue of the frustration systems in terms of X-band ESR spectroscopy is

the enormous line broadening due to rapid spin relaxations intrinsic to the spin degeneracy or rapid relaxation assisted by vibronic quantum spin mixing between the ground and excited spin states. For some cases of spin frustration systems, high-field/high-frequency ESR techniques have proven to be useful [149, 162–167].

Okubo *et al*. have examined a triangular-*Kagome* antiferromagnet $Cu_9X_2(cpa)_6$ by high-field/high-frequency ESR spectroscopy, where cpa and X denote carboxypentonic acid and halogen atoms (F, Cl, and Br) [162]. They have obtained the temperature dependence of the line width of the ESR spectra for the *Kagome* lattice.

McCusker et al. have reported the μ_3-oxide trinuclear mixed-valence manganese clusters of $Mn(II)Mn(III)_2O$ [168–172]. The reported structures of this type were $[Mn_3O(acetato)_6(pyr)_3]pyr$ [169], $[Mn_3O(acetato)_6(3Cl\text{-}pyr)_3]$ [170], $[Mn_3O(benzoato)_6(pyr)_2(H_2O)]1/2MeCN$ [171], and $[Mn_3O(X\text{-}benzoato)_6L_3]$ (X = 2-F, 2-Cl, 2-Br, 3-F, 3-Cl, 3-Br; L = pyridine or water) [172]. A remarkable feature of these mixed-valence clusters is the variety of their ground states. For their ESR analysis, Vincent et al. have applied a similar spin Hamiltonian of isotropic exchange-couplings used for the triangular spin frustration systems [171], given by

$$\begin{aligned} H &= -2J^{12}\mathbf{S}^1 \cdot \mathbf{S}^2 - 2J^{13}\mathbf{S}^1 \cdot \mathbf{S}^3 - 2J^{23}\mathbf{S}^2 \cdot \mathbf{S}^3 \\ &= -2J\left(\mathbf{S}^1 \cdot \mathbf{S}^2 + \mathbf{S}^1 \cdot \mathbf{S}^3\right) - 2J^*\left(\mathbf{S}^2 \cdot \mathbf{S}^3\right) \\ &= -J\left(\mathbf{S}^{T^2} - \mathbf{S}^{*^2}\right) - 2J^*\mathbf{S}^{*^2} \end{aligned} \tag{3.71}$$

where $J = J^{12} = J^{13} = J_1$, $J^* = J^{23} = J_2$, $\mathbf{S^T} = \mathbf{S^1} + \mathbf{S}^*$, and $\mathbf{S}^* = \mathbf{S^2} + \mathbf{S^3}$. McCusker *et al*. have calculated the J/J^* dependence of the energy. The energy diagram reveals that there are various spin multiplicities for the ground state of the mixed-valence μ_3-oxide trinuclear Mn cluster. Ribas et al. have shown from magnetic susceptibility measurements and ESR spectroscopy that the variety of the ground states is governed by ligands [172].

Referred to mixed-valence clusters, one of the important processes in nature occurs in the oxygen-evolving complex (OEC) of the photosystem II (PSII), where the four-electron oxidation of water to molecular oxygen is believed to be catalyzed by a cluster composed of four manganese ions. Mixed-valence homo- and hetero-trinuclear linear clusters containing the [tris(dimethylglyoximato)-metalate(II)]$^{4-}$ anions as bridging ligands have been examined. From the X-ray diffraction, magnetic susceptibility, and ESR spectra, the exchange interaction between the nuclei have been discussed [173–180]. Manganese clusters of biological importance will be only briefly dealt with in Sect. 3.6 of this chapter. Sizable organometallic triangular clusters of the transition metal $[(Cp^*)(dppe)Fe(III)\text{-}]^+$ units bridged by 1,3,5-triethynylbenzene spacers have been studied, emphasizing that triangular topology is important and the ferromagnetic coupling occurs at nanoscale distances between the metal spin carriers [181].

3.5.2 Inorganic Molecule-Based High-Spin Large Clusters Revealing Quantum Spin Tunneling: Single-Molecule Magnets

This section deals with molecule-based high-spin metallic multi-clusters which reveal apparent magnetic hysteresis associated with molecular superparamagnetic entities at low temperature. These large clusters have emerged recently and they have been the focus of the current topics in the field of molecule-based magnetism and high spin chemistry. Their microscopic details have most successfully been characterized by invoking high-field/high-frequency ESR spectroscopy.

3.5.2.1 Single-Molecule Magnets

During the last decades, a huge number of polynuclear complexes containing transition metal ions have been reported. Polynuclear complexes have a great potential as building blocks for exotic molecular materials, especially for magnetic materials with extremely high spins. The discovery that certain polynuclear metal clusters exhibit slow magnetic relaxation and quantum tunneling has opened a new area in the field of molecule-based magnetism. The relevant high spin multi-clusters are currently termed "Single-Molecule Magnets (SMMs)" [182, 183], which are isolated molecules with large spin multiplicities in the ground state spin and characterized by negative zero-field splitting parameters D's. An Mn_{25} SMM with a record of an $S = 61/2$ spin was recently realized [184]. Since lanthanide mononuclear complexes were found to exhibit slow relaxation of the magnetization at liquid nitrogen temperature [185], lanthanide-based SMMs have also emerged [183i]. SMMs may be used for new types of molecular devices such as quantum information processing systems [186, 187] where information can be handled taking advantage of quantum effects. SMMs may also be used for the storage of a large density of information in their well-defined nano-scale dimensions if they are properly fabricated. SMMs have extensively been characterized by ESR spectroscopy [188–202], providing direct information about the magnetic anisotropy and energy levels of their ground states. In the following, single-molecule magnetism and applications of ESR spectroscopy to SMMs are surveyed, emphasizing the importance of SMMs of chemical implication in terms of materials science.

3.5.2.2 Mn-Based Clusters

The first compound to exhibit SMM phenomena, "Mn_{12} cluster", was discovered by Gatteschi and co-workers in 1991 [203], although the cluster had been structurally characterized by Lis in 1980 [204]. Following the pioneering work by Gatteschi et al., a variety of SMMs based on polymetallic manganese (Mn)

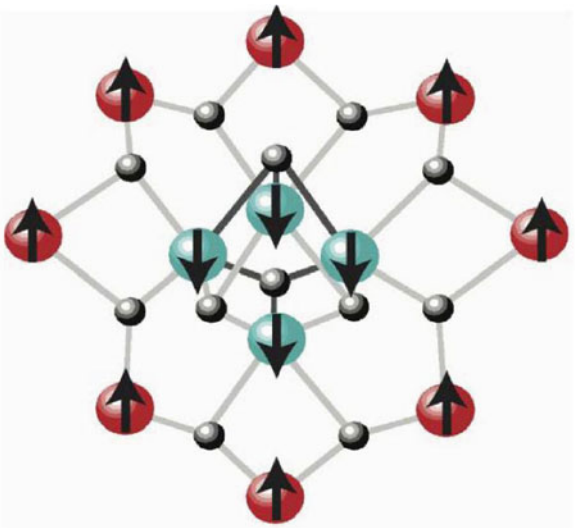

Fig. 3.16 Schematic structure of $Mn_{12}Ac$ with the suggested preferred orientation of the individual spins (Adapted from Ref. [183 g] with kind permission of © Annual Reviews 2010)

complexes have been documented so far: Mn_{84} [205], Mn_{44} [206], Mn_{30} [207]. $[Mn_{12}O_{12}(CH_3COO)_{16}(H_2O)_4]\cdot 2CH_3COOH\cdot 4\text{-}H_2O$ (abbreviated as $Mn_{12}Ac$) was the first documented SMM, which has three independent manganese ions, namely two Mn(III) and one Mn(IV). The magnetic core schematically shown in Fig. 3.16 is composed of an external ring of eight Mn(III) ions ($S = 2$) with an internal tetrahedron of four Mn(IV) ions ($S = 3/2$) [208]. A ground spin state of $S = 10$ was generated by superexchange interactions between Mn(III) and Mn(IV) ions through the oxygen bridges, which was characterized by ESR and magnetization measurements by Gatteschi et al. [203]. As shown in Fig. 3.17, the magnetic cluster exhibits a hysteresis loop below a blocking temperature of about 3 K, and also it shows slow exponential relaxation of the magnetization that obeys Eq. (3.72) down to 2.1 K. Any intermolecular interactions are considered to be negligible because the neighboring molecules are 7 Å apart at least. In addition, there was no evidence of three-dimensional magnetic order in magnetic susceptibility for frozen solutions and polymer-doped samples from specific heat measurements, and MCD spectra in solution. Therefore, it is concluded that the hysteresis loop observed for $Mn_{12}Ac$ arises from the individual isolated molecules.

In general, SMM's can be regarded as a molecular cluster exhibiting very slow relaxation of the magnetization. The slow relaxation originates in a large S value of the ground spin state and large magnetic anisotropy associated with a large negative zero-field splitting constant D. Fig. 3.18 shows a potential energy diagram for a single-molecule magnet with an electron spin S in a certain field [188], where the lowest energy level with $m = S$ in the left well corresponds to the "spin-up" state and the level with $m = -S$ in the right well corresponds to the "spin-down" state. Assuming axial symmetry, the height of the energy barrier U in zero field is given by $S^2|D|$ and $(S^2 - 1/4)|D|$ for integer and half-integer spins, respectively. In order to invert the magnetization vector from "spin-up" to "spin-down", the spin system

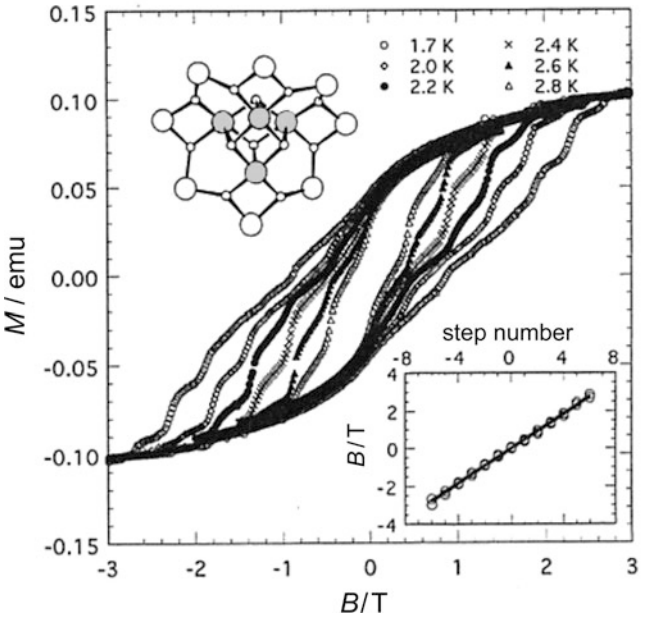

Fig. 3.17 Plots of magnetization versus magnetic field for $Mn_{12}Ac$ (field sweep rate of 67 mT/min). The inset shows plots of the magnetic fields where steps occur versus step number. Based on a least square fit, the straight line with a slope of 0.46 T has been obtained (Adapted from Ref. [213a] with kind permission of © The American Physical Society 1996)

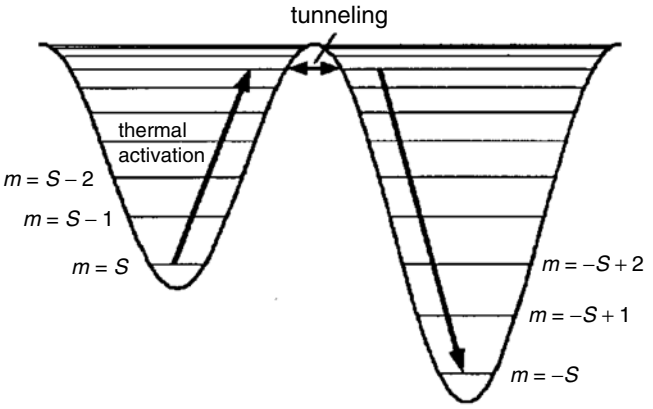

Fig. 3.18 Plot of the potential energy versus magnetization direction for an SMM with an electron spin *S*, a negative *D* value and axial symmetry in the presence of an external magnetic field (Adapted from Ref. [213a] with kind permission of © The American Physical Society 1996)

climbs over the potential energy barrier through a thermally activated process. Thus, the magnetization of SMM's relaxes slowly at sufficiently low temperature. In fact, the relaxation time of $Mn_{12}Ac$ is of the order of 2 months at 2 K [188c]. The slow magnetization relaxation results in the observation of out-of-phase AC (alternating current) magnetic susceptibility signals and magnetization hysteresis loops.

The first evidence of slow magnetic relaxation at low temperature in $Mn_{12}Ac$ was given by AC susceptibility measurements, in which the dynamic susceptibility is investigated by applying an oscillating magnetic field. The magnetic relaxation of SMMs generally follows the Arrhenius equation which governs elementary activation processes:

$$\tau = \tau_0 \exp\left(\Delta/k_B T\right) \tag{3.72}$$

where Δ and τ_0 stand for the height of the activation energy and the pre-exponential factor, respectively [209]. Both the energy barrier to reorient the magnetization (Δ/k_B) and the relaxation time (τ_0) can be determined from a simple plot of $\ln(\tau)$ versus ($1/T$). This behavior is analogous to that observed for superparamagnets. In addition, it was found that at low temperature the relaxation time is given by

$$\tau = C\frac{S^6}{\Delta^3}\exp\left(\Delta/k_B T\right) \tag{3.73}$$

where C is a constant that depends on the phonon coupling and on Δ. Consequently, it is indicated that a ground spin state with a large S value is a crucial factor to design and synthesize new SMM's.

In the principal z direction, the energies of the spin levels for $Mn_{12}Ac$ are given by

$$E\left(M_S\right) = D\left(M_S^2 - 110/3\right) + g\beta_e M_S B_Z \tag{3.74}$$

The energy levels can be schematically plotted as already shown in Fig. 3.18. In the absence of the external field, the spin sublevels $\pm M_S$ are degenerate, except $M_S = 0$ (the top of the potential energy barrier). Equation (3.74) shows that the energy barrier is related to the total spin quantum number S and zero-field splitting parameter D ($\Delta = S^2 \mid D \mid$). Because of the negative D value, the $M_S = \pm S$ levels have the lowest energy. A potential energy barrier Δ can be overcome by climbing up and down all the $(2S+1)$ energy levels, leading to the reorientation of the magnetization. The excitation of the spin from the $M_S = \pm S$ levels to the $M_S = 0$ level can be assisted by phonon absorption, as described previously. It is indicated from Eq. (3.74) that the increase in both the S and D values leads to increasing the blocking temperature of SMMs. However, it should be noted that a general criterion for the energy barrier in SMMs has been found, which demonstrated that the barrier does not increase with S as a function of S^2 [210]. In fact, a ground spin state of S = 83/2 developed in a ferromagnetically coupled mixed valent (MnII/III)

Mn_{19} aggregate did not show the SMM behavior in spite of the high ground spin state [211]. Therefore, a promising approach to realize SMMs with higher blocking temperatures is probably to concentrate on the increase in $|D|$ values. $Mn_{12}Ac$ has a blocking temperature of 2.1 K. The record blocking temperature is 4.5 K by $[Mn_6O_2(Etsao)_6(O_2CPh(Me)_2)_2(EtOH)_6]$ {Et-saoH$_2$ = 2-hydroxyphenylpropanone oxime} with an $S = 12$ ground state [212]. Many SMMs based on other 3d paramagnetic metal ions like Fe, Ni, and Co have also been reported [213], although the Mn-based cluster still holds the highest blocking temperature.

The magnetization reorientation can also occur via quantum tunneling between energy levels as shown in Fig. 3.18 when the energy levels in the two wells are in resonance. Magnetic hysteresis of $Mn_{12}Ac$ exhibited characteristic steps due to Quantum Tunneling of the Magnetization (QTM) through the energy barrier [203]. The first explicit and quantitative evidence that the quantum tunneling through the barrier as well as thermal activation over the barrier occurs in $Mn_{12}Ac$ was demonstrated by Friedman et al. [213], and several groups also confirmed such phenomena [214]. Here, the fourth order terms are neglected because of their small contribution to resonance fields. When the static field **B** is applied along the easy axis, the eigenstates of the spin Hamiltonian are given as $|S, m>$. S and m denote the total spin and the magnetic spin quantum number, respectively. When the applied field is equal to

$$B_n = -\frac{Dn}{g\beta_e} \quad (n = 0,\ 1,\ 2\cdots) \tag{3.75}$$

the eigenenergy of the $|S, m>$ state in the left well coincides with that of the $|S, -m+n>$ state in the right well. Under these conditions, the pairs of the energy levels can be quantum mechanically well admixed, resulting in the sufficiently strong coupling between the states. Therefore, the observed steps in the hysteresis loop occur at intervals of field given by $B_n = 0.4n$T. The resonance tunneling must be derived from off-diagonal terms in the spin Hamiltonian (a transverse magnetic anisotropy). This means that the spin Hamiltonian should contain a term that does not commute with S_z in order to observe QTM. $Mn_{12}Ac$, however, has tetragonal symmetry (axial symmetry), so that only the fourth-order terms, Eq. (3.76) as given below, originating from the crystal field correspond to such anisotropy:

$$\sum_{k,q} B_k^q O_k^q = B_4^0 O_4^0 + B_4^4 O_4^4 \tag{3.76}$$

where B_k^q and O_k^q represent the crystal field constants and Steven's equivalent operators, respectively. The equivalent operators in Eq. (3.76) are explicitly given below in Eqs. (3.78) and (3.79).

High-frequency electron spin resonance (HFESR) spectroscopy has been extensively applied to SMMs. Several reviews describe how HFESR has been used to study SMMs [215–218]. Since SMMs generally have large ground spin states

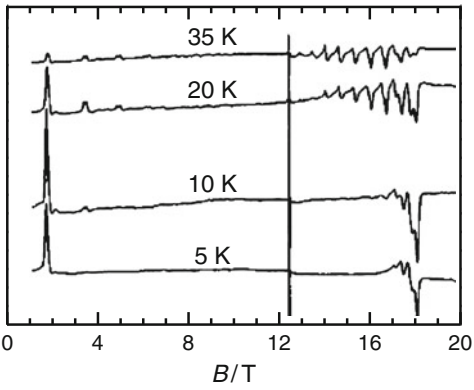

Fig. 3.19 Observed ESR spectra from a powder sample of $Mn_{12}Ac$ at low temperatures ($\nu = 525$ GHz). The narrow signal arises from DPPH used for the field calibration (Adapted from Ref. [219] with kind permission of © The American Physical Society 1997)

and relatively large D values, HFESR using higher frequencies than 100 GHz is crucial to observe ESR transitions. The first ESR study of $Mn_{12}Ac$ was reported by Gatteschi et al. on a powder sample at frequencies and applied magnetic fields in the ranges 246–525 GHz and 0–12 T, respectively [219]. The observed fine-structure ESR spectra at 525 GHz at low temperatures are shown in Fig. 3.19. The ESR spectra of $Mn_{12}Ac$ were simulated by the following spin Hamiltonian:

$$\hat{H} = \beta_e \mathbf{S} \cdot \mathbf{g} \cdot \mathbf{B} + D\left[S_z^2 - S\left(S+1\right)/3\right] + B_4^0 O_4^0 + B_4^4 O_4^4 \tag{3.77}$$

$$\mathrm{O}_4^0 = 35\mathrm{S}_z^4 + 30\mathrm{S}\left(\mathrm{S}+1\right)\mathrm{S}_z^2 + 25\mathrm{S}_z^2 - 6\mathrm{S}\left(\mathrm{S}+1\right) + 3\mathrm{S}^2\left(\mathrm{S}+1\right)^2 \tag{3.78}$$

$$\mathrm{O}_4^4 = \left(\mathrm{S}_+^4 + \mathrm{S}_-^4\right) / 2 \tag{3.79}$$

with $g_{/\!/} = 1.93$, $g_\perp = 1.96$, $D = -0.46\,\mathrm{cm}^{-1}$, $B_4^0 = -2.2 \times 10^{-5}\,\mathrm{cm}^{-1}$, and $B_4^4 = \pm 4 \times 10^{-5}\,\mathrm{cm}^{-1}$. Magnetic interactions transverse to the easy-axis of magnetization for SMMs lead to interactions between the states on either side of the barrier shown in Fig. 3.18. For $Mn_{12}Ac$, the B_4^4 term can connect sublevels on either side of the barrier to the reverse magnetization, as is necessary for QTM. Single-crystal HFESR is one of the best techniques to characterize the transverse magnetic interactions. A series of papers studying ESR spectra in single crystals of $Mn_{12}Ac$ and other SMMs have been published by several research groups [220–223]. Figure 3.20 shows angular dependent ESR spectra of $[Mn_{12}O_{12}(^t\mathrm{Bu\text{-}CH_2CO_2})_{16}(CH_3OH)_4]\cdot CH_3OH$ (abbreviated as $Mn_{12}{}^t\mathrm{BuAc}$) observed at 115 GHz [224]. Angular dependence of the resonance field could be interpreted by the spin Hamiltonian including up to the sixth-order terms given below:

$$\hat{H} = \beta_e \mathbf{S} \cdot \mathbf{g} \cdot \mathbf{B} + D\left[S_z^2 - S\left(S+1\right)/3\right] + B_4^0 O_4^0 + B_4^4 O_4^4 + B_6^0 O_6^0 + B_6^4 O_6^4 \tag{3.80}$$

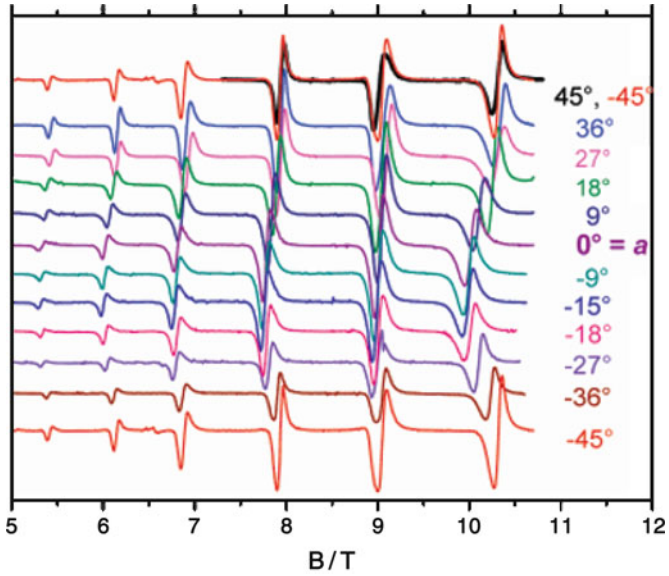

Fig. 3.20 Angular dependent HFESR spectra of Mn_{12}'BuAc observed at 5 K and 115 GHz. The external magnetic field was applied in the *ab* crystallographic plane corresponding to the hard axes of magnetization (Adapted from Ref. [224] with kind permission of The American Chemical Society 2007)

$$\begin{aligned} O_6^0 = 212S_z^6 - 315S\,(S+1)\;S_z^4 + 735S_z^4 + \\ 105S^2\,(S+1)^2\;S_z^2 - 525S\,(S+1)\,S_z^2 + 294S_z^2 - \\ 5S^3\,(S+1)^3\; + 40S^2\,(S+1)^2 - 60S\,(S+1) \end{aligned} \tag{3.81}$$

$$\begin{aligned} O_6^4 = {}^1\!/_4\,\left\{\left(11S_z^2 - S\,(S+1) - 38\right)\left(S_+^4 + S_-^4\right) + \left(S_+^4 + S_-^4\right)\right. \\ \left.\left(11S_z^2 - S\,(S+1) - 38\right)\right\} \end{aligned} \tag{3.82}$$

with $g_{//} = 2.00$, $g_\perp = 1.93$, $D = -0.459\ \mathrm{cm}^{-1}$, $B_4^0 = -2.34 \times 10^{-5}\ \mathrm{cm}^{-1}$, and $B_4^4 = 2.0 \times 10^{-5}\ \mathrm{cm}^{-1}$, $B_{6=}^0 - 1.0 \times 10^{-8}\ \mathrm{cm}^{-1}$, and $B_{6=}^4 - 1.0 \times 10^{-7}\ \mathrm{cm}^{-1}$. The nonzero sixth-order term led to a significant improvement of the fit between theory and experiment. Based on ligand field calculations, it was concluded that the fourth-order transverse anisotropy is directly connected to the tilting of the single-ion easy axes of magnetization with respect to the fourfold molecular axis of the cluster.

3.5.2.3 Quantum Coherence in SMMs

A new field of molecular spintronics is emerging, in which the concepts and the advantages of spintronics and molecular electronics are combined. Such a

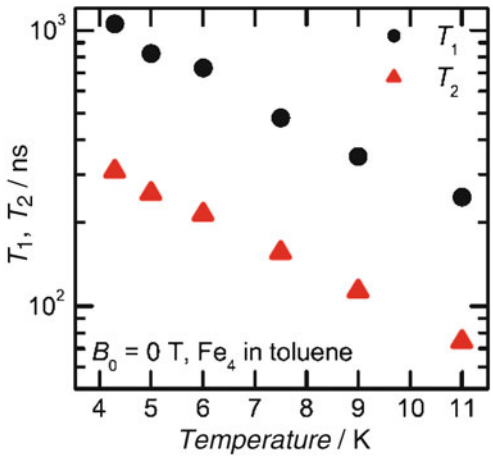

Fig. 3.21 Temperature-dependent spin-spin (T_2) and spin-lattice (T_1) relaxation times of Fe_4 in the frozen toluene solution (Adapted from Ref. [230] with kind permission of © The American Physical Society 2008)

device requires the use of one or few magnetic molecules themselves. Since the magnetization relaxation time of SMMs is extremely long at low temperature reaching years below 2 K [225], SMMs are attractive in order to realize such a device. In particular, SMMs look attractive for quantum computing due to their long coherence times [226–228]. Considerable efforts have been focused on the attempt to determine the quantum coherence times in SMMs. Intermolecular magnetic dipolar interactions usually dominate decoherence of SMMs in crystalline samples [229], which was estimated to be in the order of 10 ns. Schlegel et al. succeeded in increasing the coherence time by modifying the matrix surrounding SMMs [230]. Figure 3.21 shows temperature-dependent spin-spin (T_2) and spin-lattice (T_1) relaxation times of $[Fe_4(acac)_6(Br\text{-}mp_2)]$ (abbreviated to Fe_4) in toluene. Fe_4 in a frozen toluene solution gave the coherence time as long as $T_2 = 630 \pm 30$ ns. The dilution of Fe_4 into the frozen solution led to the limitation of decoherence due to the intermolecular interactions. A low lying excited state at 5 cm^{-1} was expected by assuming the Orbach process for the spin-lattice relaxation. Figure 3.22 displays the first demonstration of Rabi oscillations appearing in SMMs [230]. Rabi oscillations are quantum oscillations resulting from the coherent absorption and emission of photons driven by an electromagnetic wave [231]. The Rabi oscillations were recorded using a nutation pulse of length t, followed by a $\pi/2$-π pulse sequence, demonstrating clear intensity oscillations with a frequency of 17.6 ± 0.5 MHz at the zero external field and maximum microwave power.

3.5.2.4 Frequency Domain ESR

Slageren et al. have reviewed the application of frequency domain ESR to SMMs, in which microwave frequency is swept at a static magnetic field [232]. This has become possible at the high frequencies suitable for studying many SMMs, in the range from 30 GHz to 1.5 THz. Frequency domain ESR has the advantage

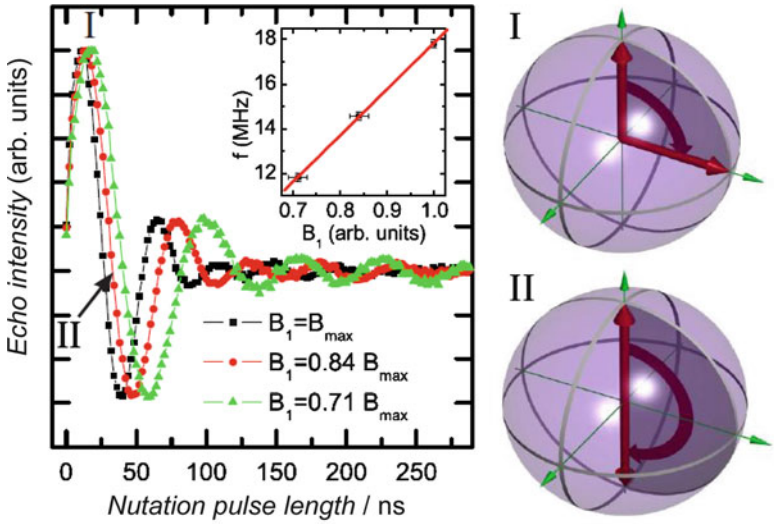

Fig. 3.22 Rabi oscillations of Fe_4 in CS_2 at 0 T. *Inset* shows the dependence of Rabi frequencies on the magnetic field strength B_1. The corresponding path on the Bloch sphere in the Rabi cycle is displayed on the *right* (Adapted from Ref. [230] with kind permission of The American Physical Society 2008)

of measuring ZFS parameters in the absence of an external field. The frequency-swept ESR applied to a SMM was for the first time studied by Muhkin's Mn_{12} in 1998 [233]. Kirchner et al. also studied the lineshapes of the ESR transitions in $(PPh)_4[Mn_{12}O_{12}(CH_3COO)_{16}(H_2O)_4]$ with an $S = 19/2$ ground state. [234] The lineshapes were Lorentzian and temperature dependent, *i.e.* the resonances are homogeneously broadened, while $Mn_{12}Ac$ shows inhomogeneously broadened Gaussian lines. The observation of homogeneous broadening is unusual for SMMs. The authors related this anomaly to the lifetimes of the excited-state M_S levels, estimating the lifetimes of ~ 50 ps from the $M_S = \pm 19/2$ to $\pm 17/2$ transition depending on temperature.

3.5.2.5 Fe Clusters

The exciting aspect of SMMs is that they are on the borderline between the classical and quantum world. Quantum phase interference is among the most interesting quantum phenomena that can be studied at the mesoscopic level in SMMs. This effect was first observed in the Fe_8 cluster [235], leading to new theoretical studies on quantum phase interference in spin systems. Very recently, Sessoli et al. also demonstrated that the quantum spin dynamics can be observed in a monolayer of oriented single-molecule magnets based on Fe_4 clusters [236]. On the gold-wired magnetic molecules, a memory effect, whose application in the field of information storage and spintronics is a long-sought goal, was observed.

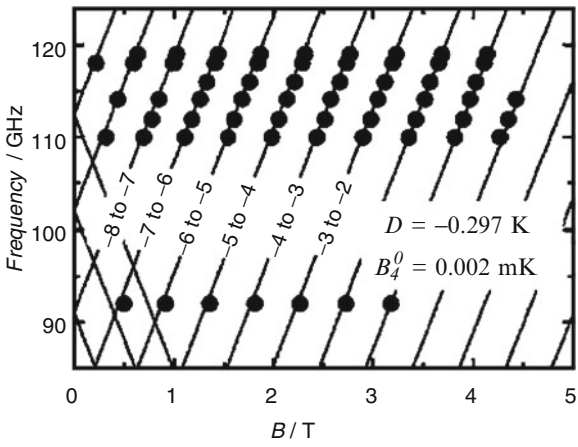

Fig. 3.23 Resonance field positions of the microwave absorption peaks at several frequencies (Adapted from Ref. [252] with kind permission of The American Physical Society 2005)

The Fe_8 cluster ($[Fe_8O_2(OH)_{12}(tacn)_6]Br_8$) with an $S = 10$ ground state is the second molecule that has been intensively investigated in the field of SMMs [237–247]. In zerofield, the giant magnetic momentum reverses via the interference of two quantum spin paths of opposite windings in the easy anisotropy (yz) plane. Based on a semi-classical description, the observed oscillations are considered as constructive or destructive interference of quantum spin phases associated with the two tunneling paths. In fact, it has been found experimentally that a magnetic field applied along the hard axis can periodically change the splitting Δ. This is the first direct observation of the topological part of the quantum spin phase (Berry phase) in magnets. The tunneling splitting Δ can be directly obtained in terms of the Landau-Zener model. The tunneling probability in this model is given by the following expression when the longitudinal field H_z is swept over the avoided level crossing at a constant rate:

$$P = 1 - \exp\left[-\frac{\pi \Delta^2}{4\hbar g \mu_B S dH/dt}\right] \tag{3.83}$$

where dH/dt is the field sweeping rates. The tunneling rate P related with the tunneling splitting Δ was obtained with the Fe_8 cluster ($[Fe_8O_2(OH)_{12}(tacn)_6]Br_8$) with the $S = 10$ ground state. This technique enables us to directly measure very small tunneling splittings of the order of 10^{-8} K, which is not accessible in terms of resonance techniques at the moment.

The Fe_8 cluster has a large zero-field splitting as shown by HFEPR/ESR [248, 249], inelastic neutron scattering [250] and far infrared spectroscopy [251]. The magnetization-detected ESR was also reported on the Fe_8 cluster. Petukhov et al. monitored the magnetization response of a single crystal of the cluster under microwave radiation as the external magnetic field was swept, using a Hall-probe magnetometer [252]. The sensitivity of the Hall-probe technique allows measurements on micron-sized single crystals. Figure 3.23 shows resonance field

Table 3.6 List of SMMs documented so far and their important magnetic parameters

Complex	S	g	D/cm^{-1}	U/K	Ref.
$[Mn_{12}O_{12}(O_2CCH2tBu)_{12}(NO_3)_4(H_2O)_4]\cdot H_2O$	10	1.92	−0.40	71.9	[255]
$[Mn_{12}O_{12}(O_2CCH_2BR)_{16}(H_2O)_4]\cdot 4CH_2C_{12}$	10	1.87	−0.38	74.8	[256]
$(NBun_4)[Mn_{12}O_{12}(O_2CPh)_{16}(H_2O)_3]$	19/2	2.00	−0.40	55.1	[257]
$[Mn_3O(O_2CCMe)_3(mpko)_3]\cdot CCl_4\cdot 3CH_2Cl_2$	6	1.92	−0.034	10.9	[258]
$[Mn_4O_3Cl(O_2CCMe)_3(dbm)_3]$	9/2	1.99	−0.35	18.7	[259]
$[Mn_4(hmp)_6(H_2O)_2(NO_3)_2](NO_3)_2\cdot 2.5H_2O$	9	1.96	−0.24	20.9	[260]
$[Mn_6O_2(Et\text{-}salox)_6\{O_2CPh(Me_2)\}_2(EtOH)_6]$	12		−0.43	86.5	[261]
$\{Mn_7O \subset [Mn_6Cl_6(L^3)_6]\}.2CHCl_3$	27/2	2.0	−0.05	10.1	[262]
$[Mn_9O_7(O_2CCMe_3)_{11}(Hpeol)(py)_3(H_2O)_2]$	17/2	1.98	−0.27	26.5	[263]
$[Mn_{21}O_{14}(OH_2)_2(O_2CMe)_{16}(hmp)_8(pic)_2(py)(H_2O)](ClO_4)$	17/2	1.8	−0.09	13.2	[264]
$[Mn_{30}O_{24}(OH)_8(O_2CCH_2C(CH_3)_3)_{32}(H_2O)_2(CH_3NO_2)_4]$	5	2.00	−0.51	14.4	[265]
$\{[Fe_8O_2(OH_2)_{12}(tacn)_6]Br_7\cdot H_2O\}Br\cdot H_2O$	10	2.00	−0.27	22.1	[266]
$[Fe4(L_{R,L})_6]\cdot 5DMF\cdot H_2O$	5	2.01	−0.34	5.9	[267]
$[Fe_9O_4(OH)_5(heia)_6(Hheia)_2]\cdot 3.5MeOH\cdot 8H_2O$	25/2	1.99	−0.07	7.6	[268]
$[CO(NCO)_2(4NOPy)_4]$	5/2	3.11	−9.94	50.4	[269]
$[Co(hmp)_4(MeOH)_4Cl_4]$	6		−3.00		[270]
$[Mn^{III}Cu^{II}Cl(5\text{-}Br\text{-}sap)_2(MeOH)]$	5/2	20.95(Cu), 1.97(Mn)	−1.81	6.2	[271]
$K[(Me_3tacn)_6MnMo_6(CN)_{18}(ClO_4)_3]$	13/2	1.57	−0.33	14.4	[272]
$[(PY_5Me_2)_4Mn_4Re(CN)_7](PF_6)$	21/2	2.00	−0.44	47.5	[273]

positions of the microwave absorption peaks at several frequencies. ESR was detected via the magnetization measurements by irradiation with microwaves at frequencies between 92 and 120 GHz, illustrating that the spectra can be transformed to determine the spin temperature of the sample. With microwave irradiation in the range from 95 to 141 GHz, Cage et al. also reported the magnetization-detected ESR of the Fe_8 single crystal using a commercial SQUID magnetometer [253, 254].

3.5.2.6 Representative Examples of Other SMMs Documented So Far and Their Important Magnetic Parameters

As expected, other clusters characterized by SMM behavior have been reported. These include Fe_4, Mn_4, Mn_{21}, Mn_{30}, Co, MnCu, and so on. Table 3.6 shows the representative examples of SMMs documented so far and their important magnetic parameters.

3.5.3 Hydrogen-Bonded Molecule-Based High-Spin Clusters

Recently, hydrogen-bonded molecule-based high-spin clusters have emerged, where a two- or three-dimensional hydrogen network plays crucial roles for constructing cooperative magnetic behavior [275]. For some cases, magnetic sites of transition metal ions are in high symmetry such as tetrahedron or octahedron, giving models for molecular magnetic assemblages with nonvanishing orbital angular momenta. In these exchange-coupled systems, isotropic Heisenberg types of exchange interactions are not enough to interpret their bulk magnetic properties. The models of well defined molecular structures are suitable for establishing molecular magnetism with sizable orbital momenta. Sophisticated theoretical treatments have also been documented recently [2f]. Fine-structure ESR spectroscopy for molecule-based exchange-coupled systems having nonvanishing orbital angular momenta has not fully been established in terms of both effective and theoretical spin Hamiltonians. In addition, fine-structure ESR spectroscopy for such molecular systems has neither been established yet. From a methodological point of view, analyses for magnetic susceptibility of molecular assemblages with sizable orbital angular momenta require reliable *g*-tensors of the systems under study as well as fine-structure tensors for the lowest and nearby excited multiplets [276]. Electron transfer phenomena assisted by proton transfer in solids, organic or inorganic, are detectable by conventional ESR spectroscopy at low temperature. For favorable cases, quantum chemical calculations help to identify vibronic origins on a microscopic scale.

Referred to roles of hydrogen bonding in high spin clusters or infinite molecular assemblages, magnetic functionality properties are modulated by changes in the bonding scheme reflecting temperature variation and the modulation effects occur in a wide range of temperature from ambient to low temperature. The functionality changes arise mainly from vibronic and rotational modulations of magnetic tensors of paramagnetic metal ions. Single-crystal high-field/high-frequency ESR spectroscopy and conventional ESR spectroscopy below 2 K and at ultra-low temperature are powerful tools for identifying such microscopic changes [277].

3.5.4 Genuinely Organic Molecule-Based High-Spin Clusters: Spin Identification by Pulse-ESR-Based Electron Spin Transient Nutation Spectroscopy

Genuinely organic high-spin molecular multi-clusters can date back to Hirota's pioneering work on alkaline-metal-ion bridged aromatic ketone-based dianions in the triplet state [278]. *Meta*-connected oligoketones have pseudo-degenerate π-LUMO's near zero-energy in units of resonance integral β, and the extended π-conjugation network of the LUMO's undergoes robust dynamic spin polarization upon reduction by excess electrons. *Meta*-connected-oligoketone-based inter-molecular high-spin clusters and their magnetic characterization have been a

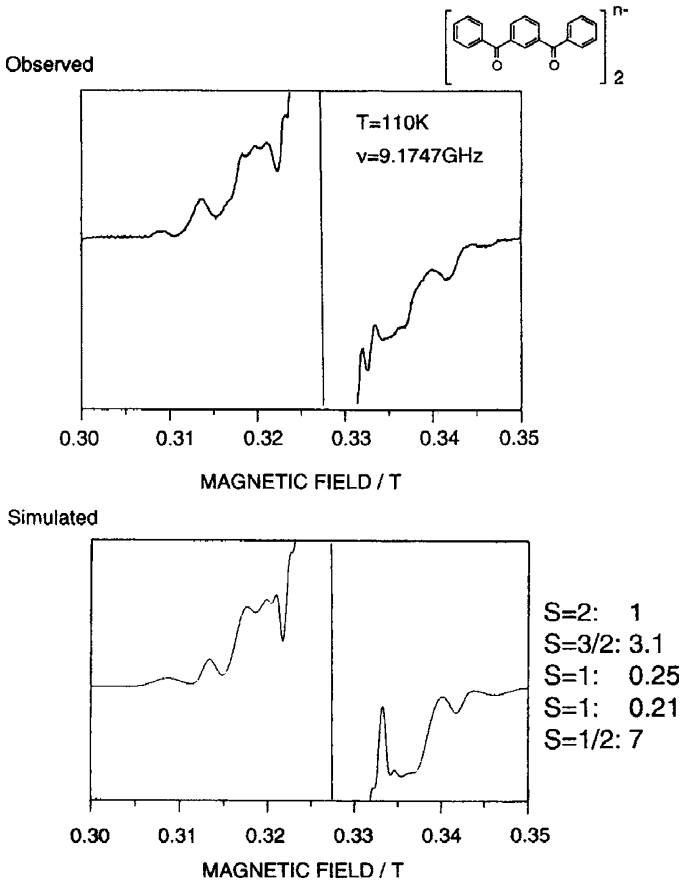

Fig. 3.24 Observed (*top*) at 110 K and simulated (*bottom*) fine-structure X-band spectra composed of inter-molecularly exchange-coupled triplet, quartet, and quintet pluri-anionic dimers derived from chemical reduction of 1,3-dizenzoylbenezene in 2-MTHF solution. The contributing weights are given on the right hand side of the simulated spectrum

long standing issue in high spin chemistry and materials science. Recently, such inter-molecular pluri-anionic high-spin clusters have been unequivocally identified by invoking pulsed ESR based 2D electron spin nutation spectroscopy applied to non-oriented media [279]. The nutation spectroscopy is a novel spectroscopy which is termed transition moment spectroscopy and also applicable to transition assignments of hyperfine allowed and forbidden spectra in a 2D representation [280]. The nutation spectroscopy applied to intramolecularly exchange-coupled high-spin systems is dealt with in the following chapter. The nutation technique is the most powerful for identifying molecular spins of the spin mixture in non-oriented media in a straightforward manner.

Figure 3.24 shows observed (top) and simulated (bottom) fine-structure ESR spectra due to various high-spin states derived from 1,3-dibenzoylbenzene upon

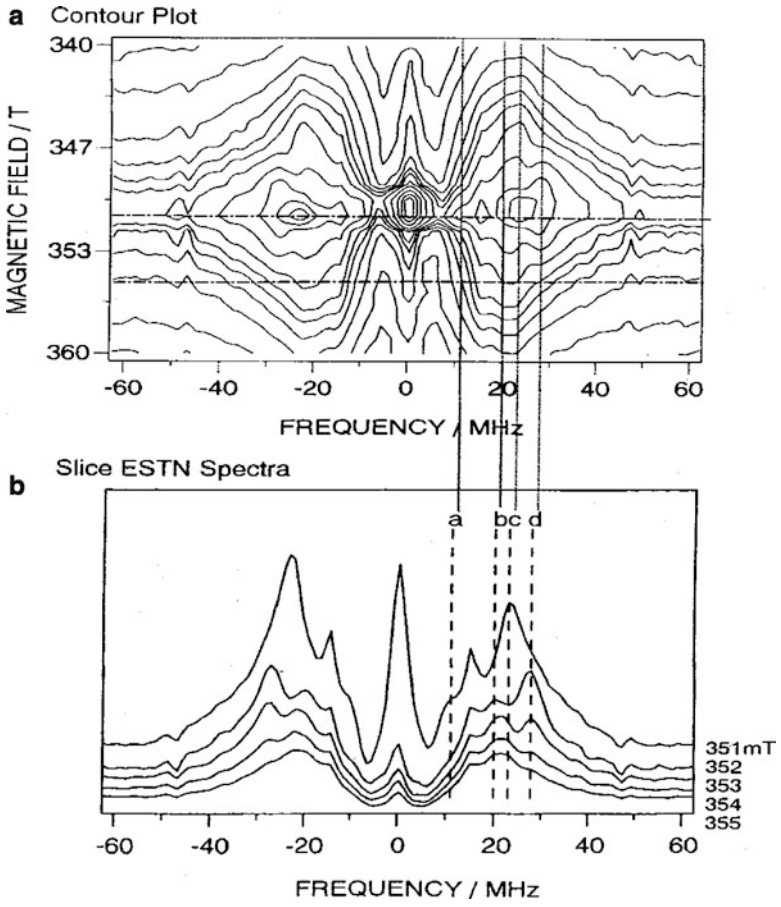

Fig. 3.25 Contour plot of nutation spectra in the 2D representation and slice spectra observed for high spin species derived from chemical reduction of 1,3-dibenzoylbenzene in 2-MTHF. The nutation frequency peaks denoted by a, b, c, and d correspond to the doublet, quartet, quartet and quintet, and quintet state, respectively. The 1 mT-step slice spectra are from 351 to 355 mT

chemical reduction in 2-MTHF solution [280]. Complete simulation has been made by evaluating their contributing weights and identifying their spin multiplicities, experimentally. Agreement between experiment and theoretical simulation is satisfactory. The observed spectrum given in Fig. 3.24 is the most complicated fine-structure assigned to a mixture of organic high spins. The experimentally derived spin Hamiltonian parameters are as follows; $g = 2.001$, $|D| = 0.00585\,\mathrm{cm}^{-1}$, $E = 0$ for $S = 2$ tetra-anionic dimer species, $g = 2.001$, $|D| = 0.0066\,\mathrm{cm}^{-1}$, $E = 0$ for $S = 3/2$ tri-anionic dimer species, and $g = 2.001$, $|D| = 0.0115\,\mathrm{cm}^{-1}$, $E = 0$ for $S = 1$ dianionic dimer species. The most crucial point to determine these spin Hamiltonian parameters with high accuracy has been to identify the contributing high spin states in the observed complex fine-structure ESR spectra. Figure 3.25 demonstrates the

usefulness of nutation spectra in the 2D representation. The nutation frequency peaks ω_a, ω_b, ω_c, ω_d denoted by a, b, c, and d in the slice spectra correspond directly to the transitions $|S = 1/2; m = +1/2 \leftrightarrow -1/2>$, $|S = 3/2; m = \pm 3/2 \leftrightarrow \pm 1/2>$, $|S = 2; m = \pm 2 \leftrightarrow \pm 1>$ and $|S = 3/2; m = +1/2 \leftrightarrow -1/2>$, and $|S = 2; m = \pm 1 \leftrightarrow 0>$ with the ratios of ω_a: ω_b: ω_c: ω_d = 1: 1.80: 2.06: 2.51. The ratios of the theoretical values are 1: $\sqrt{3}$: 2: $\sqrt{6}$ in terms of the first-order transition moment, assuming that the *g* anisotropy of the organic high-spin clusters is small. Agreement between the experimental and theoretical nutation frequency rations is satisfactory. A complete analysis of the mixture can be made only with the help of the nutation spectroscopy. The temperature dependence of the fine-structure spectra have shown that all the inter-molecular high-spin clusters are in the ground state. Throughout the tensor-based analyses for their probable molecular structures of the oligoketone-based dimeric clusters, an intramolecularly exchange-coupled 1,3-dibenzoylbenzene dianion in the triplet state has been assumed and the corresponding fine-structure constants have been predicted.

Benzoylenebenzene, decacyclene and C_{60} fullerene also give inter-molecularly exchange-coupled high-spin clusters upon chemical reduction by alkaline metal ions [281]. They are stable in polar solutions at ambient temperature. On the basis of experimental fine-structure constants, their probable molecular structures via alkaline metal ions can be determined with the help of tensor-based calculations for the fine-structure tensors, as given in Sect. 3.2. It should be noted that C_{60} fullerene upon chemical reduction gives a variety of intermolecularly exchange-coupled high-spin clusters depending on the reduction stage [282]. Both the intramolecular high-spin pluri-anionic C_{60} species and intermolecular high-spin pluri-anionic C_{60} clusters give useful models for the formation of molecular high-spin clusters in a crystalline solid of alkaline-doped C_{60} fullerene. It is worth noting that γ-ray irradiations of oligoketones in organic glasses generate solvent-containing ionic molecular clusters [283]. Neutral organic hydrocarbon-based high-spin clusters in crystalline solids are classified into two types in terms of the packing motif of the intermolecular assemblages. One is a motif of herringbone types, and the other the columnar motif. Documented molecular systems of these categories have been rare. Recently, the latter one has appeared [284], where gable *syn*-dimers of a stable neutral 1,3-diazaphenalenyl radical are stacked in a columnar motif, and the triplet state of the dimer is thermally accessible. The columnar motif has been established by elaborate molecular designs which are influential in molecular packing. In contrast, homoatomic phenalenyl radicals undergo π-dimerization in the crystal and the triplet-state dimers are stacked with the herringbone motif [285]. One-dimensional assemblies of stable "neutral" radicals in solids have been a materials challenge in quest of new molecular functionalities such as energy transport phenomena.

3.5.5 *Low-Dimensional Molecule-Based Exchange-Coupled Assemblages*

Interacting magnetic moments in the crystal experience the dipolar and exchange fields in addition to the Zeeman interaction in the presence of an applied magnetic field. A fundamental theoretical description of the electron spin resonance phenomena for exchange-coupled systems is given as

$$\begin{aligned} \mathrm{Re}(\chi) &= \mathrm{Re}(\omega \mathrm{V}/k_{\mathrm{B}}T \int < M_{\mathrm{x}}(t) M_{\mathrm{x}}(0) > \mathrm{e}^{-i\omega t} \mathrm{d}t) \\ &= \chi''(\omega) = \omega \mathrm{V}/k_{\mathrm{B}}T \int < M_{\mathrm{x}}(t) M_{\mathrm{x}}(0) > \cos \omega t \, \mathrm{d}t \end{aligned} \tag{3.84}$$

where the resonance is analyzed by using a linear response theory [286], and the symbols have the usual meanings. The intensity of the ESR-absorbed power $\int \chi''(\omega)\, \mathrm{d}\omega$ is proportional to the static susceptibility χ. A relaxation function $\phi(t) = < M_{\mathrm{x}}(t)\ M_{\mathrm{x}}(0) > / \ k_{\mathrm{B}}T$ of macroscopic magnetization is defined by a time correlation function $< M_{\mathrm{x}}(t)\ M_{\mathrm{x}}(0) >$, as given also in Sect. 3.2.4. Equation (3.84) is derived from the fluctuation-dissipation theorem. The resonance field is dominated by the molecular g-tensor, which is determined by the resonance condition of $h(\omega/2\pi) = g\beta B_0$, where B_0 stands for the strength of the static applied field $\mathbf{B_0} = B_0\mathbf{h}$ with $g^2 = \mathbf{hggh}$. The quantization axis of effective $\boldsymbol{S}$ points in the direction of the unit vector, $\mathbf{u} = \boldsymbol{g}\mathbf{h}/g$. Experimental determination of the molecular g-tensor is the most crucial part in single-crystal ESR spectroscopy for the exchange-coupled systems, and the g-tensor gives the essential magnetic nature of the intermolecular interaction with due theoretical arguments and crystallographic molecular data from X-ray measurements. This approach applies successfully to uniform molecular spin chains [287]. The approach has been applied to more complicated molecular hetero-spin ($S = 1/2$ and $S = 1$ molecular chain assemblages coupled antiferromagnetically in the crystal) systems, where two kinds of g-tensors with different magnetic behavior were observed, showing the formation of magnetic supramolecules [288].

The temperature dependence of the g-tensor gives crucial information on the evolution of inter- as well as intra-molecular magnetic interactions such as internal fields arising from demagnetization. The temperature dependences of the g-shift due to the magnetic dipolar field were studied theoretically [289] and experimentally [290]. The pioneering theoretical work by Nagata and Tazuke showed that a significant modification of the T^{-1}-dependence of the g-shift is established for magnetic short-range interactions along the chains occurring in quasi 1D Heisenberg antiferromagnets [289]. Resonance measurements give clues for the kinds of the intermolecular magnetic interactions occurring in molecular assemblages; the resonance lines of homogeneous broadening are responsible for dipolar fields, while those of narrowing are due to exchange fields. The purely dipolar broadening gives a Gaussian, while the exchange narrowing yields a Lorentzian line shapes. Departures

Table 3.7 Relations between ESR lineshapes, line widths vs. dimensions of spin systems, and the spin relaxation functions, Φ(t)

Dimension d	Relaxation function Φ(t)	Lineshape	Line width $\Delta B_{1/2}(\theta) \propto$
1	$\exp(-\Gamma t^{3/2})$	FT of Φ(t)	$(3\cos^2\theta - 1)^{4/3}$
2	$\exp(-\Gamma t \ln t)$	FT of Φ(t)	$(3\cos^2\theta - 1)^2$
3	$\exp(-\Gamma t)$	FT of Φ(t)	$(\cos^2\theta + 1)$

from Lorentzian lineshapes give rationales for the possible occurrence of additional spin-related mechanisms such as spin diffusions at high temperatures [291]. Angular variations of the lineshapes with the line width as a function of the orientation of the static magnetic field $\boldsymbol{B_0}$ for single-crystal molecular magnetic materials, under favorable conditions, yield magnetic relaxation phenomena closely related to the dimensionality of magnetic interactions [292]. The magnetic relaxations reflect spin dynamics and magnetic interactions in microscopic detail, which is based on the crystal and electronic molecular structures of the component magnetic molecules. Anomalies appearing in magnetic relaxations are vital for organic magnetics because of the low dimensionality inherent in organic molecule-based magnetic materials.

The anomalies originate in the dimension d of magnetic systems and the low symmetry of spin interactions. Related ESR phenomena are described in terms of a relaxation function for spin magnetization, $\Phi(t) = < M_+(t)M_-(0)>/<M_+M_->$ (a spin self-time-correlation function for transverse magnetization) and its Fourier transform. The time dependence of M_+ or M_- is attributed to the slow modulation due to H', which stands for two-center spin interactions such as spin dipolar ones. It should be noted that H_{ex} for intermolecular exchange interactions between molecular spins and H' undergo restrictions arising from the dimensionality of magnetic systems under study. When H' stands for spin dipolar interactions ($H' = H_{dip}$), the resonance absorption lineshapes as a function of the angle θ depend on the dimensionality of the systems, where θ denotes the angle between the direction of a one-dimensional magnetic chain and $\boldsymbol{B}_0$, or the normal axis of a two-dimensional magnetic plane and $\boldsymbol{B}_0$ in two-dimensional square-planar systems. For reduced symmetric spin systems, the appearance of additional shifts in resonance fields is predicted; the shifts are due to the topology of J-connectivity (the connectivity of intermolecular exchange interactions) when a contribution to magnetic relaxation from a long transverse relaxation, i.e., a long-time tailing (LTT) occurs.

In Table 3.7 are briefly summarized the relations between ESR lineshapes, the line widths vs. the dimensions of spin systems, and the spin relaxation functions, Φ(t). In terms of the magnitude of spin relaxations in low-dimensional magnetic systems, only cw-ESR spectroscopic studies have been documented. Recently, pulsed ESR techniques have been applied to directly identify the dimensionality of exchange-coupled molecular magnetic systems, whose relaxation times fall within the time resolution of ESR spectrometers [292].

3.6 Metal High-Spin Clusters of Biological Importance: Manganese Clusters in Photosystem II

This section briefly deals with transition-metal-ion high-spin clusters of the biologically important photosystem II (PSII), emphasizing the use of high-field/high-frequency ESR and parallel microwave excitation techniques and contrasting with synthetic molecule-based metallic clusters treated in the other sections of this chapter. A comprehensive treatise on this subject in terms of chemistry and biophysics is given in Chap. 6.

3.6.1 Oxygen-Evolving High-Spin Complexes

Most of molecular oxygen in the atmosphere has been released as a by-product of water oxidation during photosynthesis in plants and algae. The photosynthetic oxidation of water to molecular oxygen is energetically driven by light-induced charge separations in the reaction center of PSII. Water is chemically the terminal electron donor for the electron transfer processes that constitute the light reactions of plant photosynthesis. Absorption of a photon results in a charge separation between a chlorophyll molecule (P680) and a pheophytin molecule. The pheophtytin anion transfers an electron to a quinone Q_A and $P680^+$ is reduced by a tyrosine residue, Tyr_Z. Interestingly, the oxidized Tyr_z is in turn reduced by a nearby cluster of four Mn ions and one Ca ion, often called the oxygen-evolving complex (OEC) because it catalyzes the oxidation of water. The manganese cluster in OEC is conceived of including one Ca ion [293a], and abbreviated to the Mn_4Ca cluster. Ca^+ is involved in the photoactivation process of OEC, which has been demonstrated by an ESR study [293b]. Photochemical charge separation is a one-electron process while water oxidation is a concerted process involving four electrons. Joliot and Kok showed that this can be described by a cyclic process involving five redox states [293, 294], termed $S_{0–4}$ and that the presence of a number of metastable redox states can be demonstrated in chloroplasts following flash illumination. When the complex reaches the state S_4, molecular oxygen is released and the complex reverts to the S_0-state. Although many models for the oxygen-evolving process have been proposed [295–299], no consensus has yet emerged.

The S_i-states below the S_0-state are generated via reducing the Mn cluster of OEC by hydrazine and hydroxylamine, whose states are named the S_{-1}, S_{-2}, and S_{-3}-states [300–304]. The detailed structure of the Mn_4 cluster of OEC is still unknown. There is structural information obtained from X-ray spectroscopic experiments (EXAFS and XANES) and models for the structure have been developed. Extended X-ray absorption fine-structure (EXAFS) spectroscopy experiments provide evidence that in the S_1- and S_2-states the Mn_4Ca cluster contains two 0.27-nm Mn-Mn distances and one 0.33-nm Mn-Mn distance [305–307]. Possible structures of the Mn_4Ca cluster in OEC have been proposed by DeRose et al. [307]. Recently, the crystal

structure of OEC within atomic resolution has been reported by Jian-Ren Shen and co-workers in the 15th International Congress on Photosynthesis in Beijing. The detailed structure will be published soon. In this section, we review only the recent ESR results for the exchange-coupled Mn_4Ca cluster in the S_{0-3}-states of OEC in PSII. An exhaustive review and in-depth discussions of relevant controversial issues are beyond the scope of this chapter, and readers are recommended to refer to Chap. 6 by Kawamori.

3.6.2 The S_2-State of OEC in Photosystem II

The light-induced S_2 oxidation state of OEC is the most extensively characterized S state. The S_2-state is paramagnetic and gives rise to three characteristic ESR signals: (i) A multiline signal, (ii) $g = 4.1$ signal, (iii) $g = 10.6$ signals. Among them, the $g = 2$ multiline signal was first reported to provide direct evidence of the involvement of the Mn cluster [308]. The multiline ESR signal appearing near $g = 2$ is spread over about 180 mT and is made up of at least 18 lines, each separated by 8–9 mT originating from ^{55}Mn hyperfine structures [309]. Peloquin et al. reported the four effective ^{55}Mn hyperfine tensors (A_X, A_Y, A_Z) to be (−232, −232, −270), (200, 200, 250), (−311, −311, −270), (180, 180, 240) in units of MHz, which were derived from the simultaneously constrained simulations of the CW-ESR and ESE-ENDOR [310]. The multiline signal is ascribed to the ground state with $S = 1/2$. Recently, they have refined these absolute values as follows: (310, 310, 275), (235, 235, 275), (185, 185, 245), (170, 170, 240) in units of MHz, which are derived from the same simulations of the CW-ESR and ^{55} M-ENDOR at 35 GHz [293c, d]. According to the analysis of ^{55}Mn ENDOR spectrum, the oxidation states of the manganese ions in S_2 are Mn_4(III, IV, IV, IV) [293c]. Recent development of quantum chemical calculations can afford to give the hyperfine interaction constants of ^{55}Mn, ^{14}N, and ^{13}C in OEC, which are comparable with the experimental values from EPR/ESR, ENDOR and ESEEM, respectively [293e]. These computations of the EPR/ESR parameters for different structural models of OEC provide a possibility of reducing the number and types of acceptable structural models.

Figure 3.26 shows the multiline ESR signal obtained by conventional X-band and Q-band ESR spectroscopy reported by Smith *et al* [314]. The $g = 4.1$ signal reveals a broad unstructured ESR spectrum with a peak-to-peak width of 35 mT at X-band. The $g = 4.1$ signal has been assigned to arise from the Mn cluster having an $S = 5/2$ state [311, 312] or an $S = 3/2$ state [313, 314]. The $g = 4.1$ signal has been observed by Q-band ESR spectroscopy, exhibiting two partially resolved components at $g = 4.34$ and $g = 4.14$. Boussac et al. have reported that the new signals at $g = 10$ and 6 can be observed by conventional ESR spectroscopy. They are assigned to be $m_s = \pm 5/2$ and $\pm 3/2$ transitions in an $S = 5/2$ spin state [315].

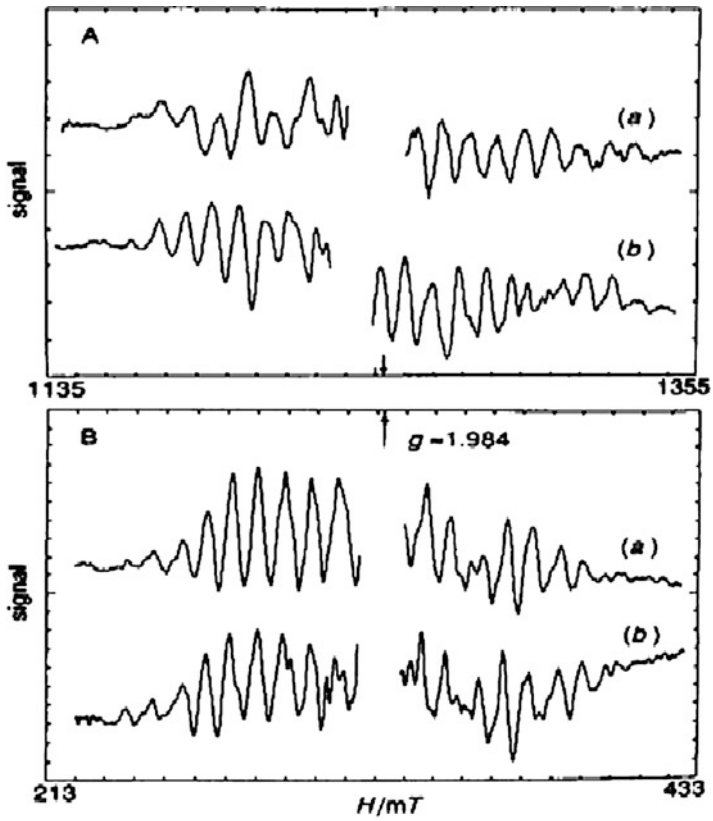

Fig. 3.26 Multiline signals from the photosystem II at (A) Q-band and (B) X-band. (a) Minus alcohol, (b) plus alcohol. Illumination temperatures: (a) 200 K, (b) 220 K. Spectrometer conditions: X-band, 9.03 GHz, 2 mT modulation amplitude, 30 mW microwave power, 100 kHz modulation frequency, temperature 8 K. Q-band, 34.650 GHz, 0.5 mT modulation amplitude, 5 mW microwave power, 100 kHz modulation frequency, temperature 8 K (Adapted from Ref. [314] with kind permission of © The Royal Society of Chemistry 1993)

3.6.3 The S_0-State of OEC in Photosystem II

Because the S_0-state is reduced by two further electrons from the S_2-state, it is expected to be an odd-electron or Kramers state observable with conventional ESR spectroscopy. The first observation of an ESR signal arising from the S_0-state was made by different methods. One is a chemical reduction with hydrazine of the S_1-state to the S_{-1}-state followed by photogeneration of the S_0-state at 273 K in the presence of DCMU (3-(3,4-dichlorophenyl)-1,1-dimethylurea), the other is a chemical reduction with hydroxylamine of the S_1-state to the S_0-state [316]. The S_0-state ESR signals have hyperfine structures similar to the multiline signal in the S_2-state except for a broader overall width [316, 317]. The splittings of the hyperfine lines are more variable (7–11 mT) than those for the S_2-state. The total spectral

breadth is in the range of 220–240 mT and the total number of peaks amounts to 24–26. The S_0 multiline signal gives rise to an asymmetry of this ESR signal, indicative of an average g value below $g = 2.0$. The temperature dependence of the S_0 multiline signal has shown that the $S = 1/2$ state responsible for the signal is an isolated ground state [318, 319]. The four effective ^{55}Mn hyperfine tensors (A_X, A_Y, A_Z) have been reported to be (320, 320, 400), (270, 270, 200), (190, 190, 280), (170, 170, 240) in units of MHz, which are derived from the simultaneously constrained simulations of the CW-ESR and ^{55} M-ENDOR at 35 GHz [293c, d]. The sign of these principal values was not determined in this study, therefore the absolute values were provided. The oxidation states of the manganese ions in S_0 were found to be Mn_4 (III, IV, IV, IV) [293c].

3.6.4 The S_1-State of OEC in Photosystem II

The S_1-state which is the one-electron reduced state from the S_2-state is paramagnetic, but the S_1-state is of even electron number and a non-Kramers ESR signal is observed in parallel-polarized ESR spectroscopy. Recently, the multiline signal for the S_1-state has been detected from the PSII particles isolated from the cyanobacterium Synechocytstis sp. PCC 6803 [320] and spinach [321], showing the parallel polarization ESR spectrum composed of a well-resolved multiline pattern centered at $g \sim 12$ with at least 18 well-resolved hyperfine lines having an average splitting of 3.2 mT. This hyperfine pattern gives unambiguous evidence for the existence of a tri- or tetra nuclear exchange-coupled paramagnetic Mn cluster in the S_1-state of OEC in PSII. Another parallel polarization ESR signal of the S_1-state of the PSII particles isolated from spinach has been also observed, which appears at an effective g value of approximately 4.8 with a peak-to-peak width of roughly 60 mT [322, 323]. It has been concluded that this parallel polarization ESR signal of the S_1-state arises from a thermally excited state with $S = 1$ which is located 2.5 K above the ground singlet state.

3.6.5 The S_3-State of OEC in Photosystem II

Finally, we discuss the ESR studies for the S_3-state that is the third one-electron oxidation state from the S_0-state of OEC in PSII. The S_3-state is expected to be an integer spin state because the S_2-state is characterized by the ESR signals from half-integer spin states. The parallel polarization ESR spectra of the S_3-state have been reported by Kawamori et al., in which the ESR signals at $g = 12$ and 8 are observed in accompaniment with their peak-to-peak widths of about 30 and 20 mT, respectively [324]. The signals have been obtained after two turnovers from the S_1-state by flash illumination and its intensity has showed the periodicity of a four flash illumination oscillation, thus the observed signals have been rationalized to originate from the S_3-state. The spectral simulation for the ESR signals of the S_3-state has

been performed by using the ordinary fine-structure spin Hamiltonian and numerical diagonalization of the spin Hamiltonian, giving $S = 1$, $D = \pm 0.435 \pm 0.005$ cm^{-1}, $E/D = -0.317 \pm 0.002$ cm^{-1}. The temperature dependence of the EPR signals at $g = 12$ and 8 has been studied, showing that the signals arise from a low-lying excited triplet state. The authors [324] have concluded that the manganese in OEC might be oxidized during the transition $S_2 \rightarrow S_3$-state. The reason is that if an organic residue such as histidine is oxidized the interaction between the Mn cluster in the S_2-state with $S = 1/2$ and $g = 2$ and the organic residue with $S = 1/2$ and $g = 2$ would have the resonance line at $g_{ob} = 2$ (g_{ob}: the observed field position) but the experimental filed position is $g_{ob} = 12$ and 8 in their work. There have been researchers who insist that the oxidized site in the S_3-state is organic residues on the basis of the study of Mn Kβ X-ray emission spectroscopy [325, 326]. The issue is the focus of the current topics in PSII.

Recently, Boussac et al. claimed that the ESR signal in the S_3-state does not arise from a spin $S = 1$, but a spin $S = 3$ [293f]. The simulated ESR spectrum of $S = 1$ with the ZFS parameters predicts a signal appearing at g $\approx$ 0.85, but not the other signals between 200 and 500 mT. The satisfactory reproduction of all the features of the ESR signals observed experimentally was achieved by the spectral simulation using spin Hamiltonian parameters $S = 3$, $|D| = 0.175$ cm^{-1} and $E/D = 0.275$. Therefore, it is suggested that the ESR spectrum in the S_3-state is associated with a high spin $S = 3$ system and not with $S = 1$.

3.7 Conclusions

Recently, organic and inorganic hybrid high-spin systems are emerging in which both organic high-spin entities and inorganic metallic sites are composed of open-shell systems and both are connected via chemical bonding. They are classified into intramolecularly exchange-coupled hybrid high-spin systems. Molecular assemblages composed of the hybrid molecular entities have attracted attention in the field of molecule-based magnetism and molecular materials spin science. The reason is that magnetic orbitals in the entities are basically composed of transition-metal-ion based localized orbitals and organic spin-delocalized SOMO's. Spin alignments in the entities are governed by orbital and topological symmetry. Thus, magnetism-based functionalities are controllable in microscopic molecular terms in the hybrid systems. Molecular design and synthetic molecular engineering for exotic materials and chemical system materials are feasible. A typical example is high-spin carbene-based paramagnetic porphyrins [Koga N, et al., personal communications]. The other examples are novel neutral radical-based metallo-oxophenalenyls with nonvanishing orbital angular momenta [327]. The above two categories are for organic moieties which are extremely spin-delocalized. For less spin-delocalized and weak spin-polarized organic parts, the concept of the hybrid high-spin systems is also applicable [328, 329]. In the former two hybrid systems, highly delocalized spins from the organic entity give robust dynamic spin polarization network, establishing strong exchange-coupled molecular

systems if transition-metal-ion sites are coordinated in such a way as dynamic spin polarization or spin delocalization mechanisms are operative. For the latter *N-tert*-butyl-*N*-aminoxyl-based manganese(II) and copper(II) complexes, asymmetric coordination of NO-based SOMO's and nitrogen sites of pyrimidines with the magnetic orbitals are elaborately performed, giving useful testing grounds for the spin alignment in the hybrid molecular systems [328, 329]. Nevertheless, the symmetry reduction and the weak spin polarization occurring in the heterocyclic linkers such as pyrimidine give ferromagnetic-antiferromagnetic competing effects. In the dimerized hybrid exchange-coupled systems, through-space orbital interactions also participate in the competition [328, 329]. Fine-structure and hyperfine-structure ESR spectroscopy plays a crucially important role to characterize novel magnetic properties in microscopic details. Ground and excited high-spin states originating in such novel hybrid molecular systems give intriguing exchange coupling schemes not documented so far. The research area is immature, but the relevant topics are important in terms of chemistry and molecular materials science. Nevertheless, the topics are not included in this chapter because of space. Genuinely organic molecule-based super high-spin intermolecular clusters appearing in the crystal edge are also an intriguing issue [330].

Also, genuinely organic molecule-based exchange-coupled systems with high spin multiplicities are only briefly exemplified in Sect. 3.5.4. There have been potentially important examples for intermolecularly exchange-coupled high-spin systems in oriented or non-oriented media. Among them, well identified chemical species are not many in terms of electronic-spin and molecular structures. In ESR terms, resonance peaks due to intermolecularly exchange-coupled organic high spins appear in the $g = 2$ region because of both small spin-orbit couplings in the ground state and apparently decreasing fine-structure constants: the decrease is due to projection factors even if the magnitude of the exchange coupling is kept constant. For these particular high-spin systems, 2D pulsed ESR-based electron spin nutation spectroscopy is the most useful in identifying chemical species and deriving spin Hamiltonian parameters. The latter procedure for quantitative evaluations of the parameters can be carried out by invoking spectral simulation of 2D nutation spectra as functions of resonance fields and transition moments in two dimensions. We emphasize that the pulse-based transition moment spectroscopy requires the accurate measurement of microwave irradiation power on resonance, which allows us to evaluate an even small zero-field splitting parameter in very weakly exchange-coupled chemical entities such as biradicals.

The nutation and transition moment spectroscopic techniques are also useful for phosphorescence fine-structure ESR spectroscopy in the lowest excited triplet state as well as in the excited high-spin multiplet states. Even extremely small fine-structure parameters due to high symmetry of the molecular systems under study can be detectable [279c, 331]. In this context, the pulse-based electron spin nutation spectroscopy equipped with only one microwave frequency is a practically useful and easy-to-access technique, while pulse-based ELlectron-electron DOuble Resonance (pulsed ELDOR) spectroscopy has been the most powerful tool to provide insights into small fine-structure parameters and exchange interactions with molecular structural variables such as typically long spin-spin distances.

Acknowledgments This work has been supported by Grants-in-Aid for Scientific Research (B, C) and Scientific Research on Innovative Areas, "Quantum Cybernetics" from MEXT, Japan. The support by JST through Core Research for Evolutional Science and Technology (CREST) project, "Implementation of Molecular Spin Quantum Computers" and the support by the Funding Program for World-Leading Innovative R&D on Science and Technology (FIRST) project on "Quantum Information Processing", JSPS, Japan are also acknowledged.

References

1. Standard and advanced textbooks. (a) Bolton JR, Wertz JE (1972) Electron paramagnetic resonance. Elementary theory and practical applications. McGraw-Hill, Inc., New York; (b) Weil JA, Bolton JR, Wertz JE (1994) Electron paramagnetic resonance. Elementary theory and practical applications. Wiley, Inc., New York; (c) Atherton NM (1993) Principles of electron spin resonance. Ellis Horwood Ltd., New York; Atherton NM (1973) Electron spin resonance theory and applications. Ellis Horwood Ltd., Chichester; (d) Pilbrow JR (1990) Transition ion electron paramagnetic resonance. Clarendon Press, Oxford; (e) Kuwata K, Itoh K (1978) Introduction to electron spin resonance. Nankou-Dou Inc., Tokyo; (f) Bencini A, Gatteschi D (1990) Electron paramagnetic resonance of exchange coupled systems. Springer, Berlin/Heidelberg; (g) Weltner W Jr (1983) Magnetic atoms and molecules. Scientific and Academic Editions, New York; (h) Date M (1978) Electron spin resonance. Baifuh-Kan, Tokyo
2. Monographs and books for molecule-based magnetism. (a) Gatteschi D, Kahn O, Miller JS (eds) (1991) Molecular magnetic materials. Kluwer, Dordrecht; (b) Kahn O (1993) Molecular magnetism. Wiley-VCH, New York; (c) Takui T (1994) Organic molecule-based magnetic materials. In: Handbook of opto-electronic organic functionality materials. Asakura Inc., Tokyo; (d) Lahti PM (ed) (1999) Magnetic properties of organic materials. Marcel Dekker Inc., New York; (e) Itoh K, Kinoshita M (eds) (2000) Molecular magnetism: new magnetic materials. Kodansha, Tokyo, Gordon & Breach, Amsterdam; (f) Boca R (1999) Theoretical foundations of molecular magnetism. Elsevier, Amsterdam. Book (f) is the most comprehensive treatise on inorganic-molecule-based magnetism from the group-theoretical side after Ref. [1f]; (g) Takui T, Sato K, Shiomi D, Itoh K (1999) Chap. 11. In Lahti PM (ed) Magnetic properties of organic materials. Marcel Dekker Inc., New York
3. (a) Shiomi D, Nishizawa M, Sato K, Takui T, Itoh K, Sakurai H, Izuoka A, Sugawara T (1997) A prerequisite for purely organic molecule-based ferrimagnetics: breakdown of simple classical pictures. J Phys Chem B 101:3342–3348; (b) Nishizawa M, Shiomi D, Sato K, Takui T, Itoh K, Sawa H, Kato R, Sakurai H, Izuoka A, Sugawara T (2000) Evidence for the breakdown of simple classical pictures of organic molecule-based ferrimagnetics: low-temperature crystal structure and single-crystal ESR studies of an organic heterospin system. J Phys Chem B 104:503–509; (c) Shiomi D, Sato K, Takui T (2000) Spin-spin correlation function and magnetic susceptibility of quantum ferrimagnetic spin chains as model for organic molecule-based ferrimagnetics. J Phys Chem B 104:1961–1965; (d) Shiomi D, Sato K, Takui T (2001) Quantum ferrimagnetism based on organic biradicals with a spin-0 ground state: Numerical calculations of molecule-based ferrimagnetic spin chains. J Phys Chem B 105:2932–2938; (e) Shiomi D, Sato K, Takui T (2002) A molecular quantum description of spin alignments in molecule-based ferrimagnets: numerical calculations of thermodynamic properties. J Phys Chem A 106:2096–2103; (f) Shiomi D, Kanaya T, Sato K, Mori M, Takeda K, Takui T (2001) Single-component molecule-based ferrimagnetics. J Am Chem Soc 123:11823–11824
4. Furukawa K, Shiomi D, Sato K, Yamano H, Takahashi H, Maeda A, Takui T (to be published)
5. Intramolecularly exchange-coupled organic high-spin systems are exclusively dealt with in the following chapter

6. Pilawa B (1999) New concepts for molecular magnets. Ann Phys (Leipzig) 8:191–254
7. (a) Drillon M, Georges R (1981) New approach for the exchange Hamiltonian of an orbitally degenerate ground-state system ($^2T_{2g}$ or $^3T_{1g}$). Phys Rev B 24:1278–1286; (b) Drillon M, Georges R (1982) Binuclear unit $(Ti_2Cl_9)^{3-}$: a new development for the exchange between orbitally unquenched ions. Phys Rev B 26:3882–3890; (c) Leuenberger B, Gudel HU (1984) Exchange interactions between orbitally degenerate ions in $Ti_2X_9{}^{3-}$ $Ti_2Cl_9{}^{3-}$, $Ti_2Br_9{}^{3-}$ – a theoretical approach. Mol Phys 51:1–20
8. (a) Borras-Almenar JJ, Clemente-Juan JM, Coronado E, Palii AV, Tsukerblat BS (2001) Magnetic exchange interaction in clusters of orbitally degenerate ions. I. Effective Hamiltonian. Chem Phys 274:131–144; (b) Borras-Almenar JJ, Clemente-Juan JM, Coronado E, Palii AV, Tsukerblat BS (2001) Magnetic exchange interaction in clusters of orbitally degenerate ions. II. Application of the irreducible tensor operator technique. Chem Phys 274:145–163; (c) Borras-Almenar JJ, Clemente-Juan JM, Coronado E, Palii AV, Tsukerblat BS (2001) Magnetic exchange interaction in a pair of orbitally degenerate ions: Magnetic anisotropy of $[Ti_2Cl_9]^{-3}$. J Chem Phys 114:1148–1164; (d) Overparamerization in the analysis of magnetic susceptibility is a crucial problem. Matsuoka H, Onishi H, Kubono K, Sato K, Shiomi D, Yokoi K, Takui T (to be published)
9. Takui T, Kita S, Ichikawa S, Teki Y, Kinoshita T, Itoh K (1989) Spin distribution of organic high-spin molecules as studied by ENDOR/TRIPLE. Mol Cryst Liq Cryst 176:67–76
10. (a) Kurreck H, Kirste B, Lubitz W (1988) Electron double resonance spectroscopy of radicals in solution; application to organic and biological chemistry. VCH, Weinheim; (b) Takui T (1993) Electron nuclear multiple resonance spectroscopy (Chap. 8.5). In: Molecular spectroscopy III, a monograph series of experimental chemistry, 4th edn., vol 8 (Chem Soc Jpn), Maruzen, Tokyo
11. Teki Y, Takui T, Itoh K (1988) General conditions for the occurrence of off-axis extra lines in powder-pattern electron-spin-resonance fine-structure. J Chem Phys 88:6134–6145
12. Itoh K (1978) Electronic-structures of aromatic-hydrocarbons with high-spin multiplicities in the electronic ground-state. Pure Appl Chem 50:1251–1259; (b) Takui T (1973) PhD, thesis. Osaka University
13. Judd BR (1998) Operator techniques in atomic spectroscopy. Princeton University Press, Princeton
14. Takui T, Itoh K (unpublished)
15. Yagi H, Teki Y, Takui T, Itoh K (unpublished)
16. Tanaka K, Sato K, Shiomi D, Takui T (to be published)
17. Tanaka K, Sato K, Shiomi D, Baumgarten M, Adam W, Takui T (to be published)
18. (a) Gersmann HM, Swalen JD (1962) Electron paramagnetic resonance spectra of copper complexes. J Chem Phys 36:3221; (b) Rollmann LD, Chan SI (1969) Quadrupole effects in electron paramagnetic resonance spectra of polycrystalline copper and cobalt complexes. J Chem Phys 50:3416–3431; (c) Ovchinnikov IV, Konstantinov VN (1978) Extra absorption peaks in EPR-spectra of systems with anisotropic g-tensor and hyperfine-structure in powders and glasses. J Magn Reson 32:179–190; (d) Itoh K, Takui T (1993) ESR in solids (Chap. 8.4). In: Molecular spectroscopy III, a monograph series of experimental chemistry, 4th edn., vol 8 (Chem Soc Jpn), Maruzen, Tokyo
19. Matsushita M, Momose T, Shida T, Teki Y, Takui T, Itoh K (1990) Novel organic ions of high-spin states – ESR detection of a monoanion of meta-phenylenebis(phenylmethylene). J Am Chem Soc 112:4700–4702
20. Wang Q, Wang JS, Li Y, Wu GS (2002) ESR studies on a new phenyl t-butyl nitroxide biradical based on calyx[4] arene. In: Kawamori A, Yamauchi J, Ohta H (eds) EPR in the 21st century: basics and applications to materials, life and earth sciences. Elsevier, Boston
21. Scaringe RP, Hodgson DJ, Hatfield WE (1978) Coupled representation matrix of pair Hamiltonian. Mol Phys 35:701–713
22. Nakazawa S, Sato K, Shiomi D, Takui T (unpublished)
23. (a) Nagata K (1972) Bussei Jap 13:149–160; (b) Nagata K (1981) Physics for random systems, Chapter 13. Bifuhkan, Tokyo

24. Kubo R, Tomita K (1954) A general theory of magnetic resonance absorption. J Phys Soc Jpn 9:888–919
25. (a) Mori H (1965) Transport collective motion and Brownian motion. Prog Theor Phys 33:423–455; (b) Mori H (1966) A continued-fraction representation of the time-correlation functions. Prog Theor Phys 34:399–416; (c) Tokuyama M, Mori H (1976) Statistical-mechanical theory of random frequency modulations and generalized Brownian motions. Prog Theor Phys 55:411–429
26. Rockenbauer A, Pilbrow J (eds) (1999) Computer simulations in EPR spectroscopy. Mol Phys Rep 26
27. Abragam A, Bleaney B (1970) Electron paramagnetic resonance of transition ions. Clarendon Press, Oxford
28. Pilbrow JR (1990) Transition ion electron paramagnetic resonance. Clarendon Press, Oxford
29. Alderman DW, Solum MS, Grant DM (1986) Methods for analyzing spectroscopic line-shapes – NMR solid powder patterns. J Chem Phys 84:3717–3725
30. Mombourquette MJ, Weil JA (1992) Simulation of magnetic-resonance powder spectra. J Magn Reson 99:37–44
31. Galindo S, Gonzáles-Tovany L (1981) Monte-Carlo simulation of electron-paramagnetic-res of polycrystalline samples. J Magn Reson 44:250–254
32. Wang D, Hanson GR (1995) A new method for simulating randomly oriented powder spectra in magnetic-resonance – the sydney-opera-house (sophe) method. J Magn Reson A 117:1–8
33. Gates KE, Griffin M, Hanson GR, Burrage K (1998) Computer simulation of magnetic resonance spectra employing homotopy. J Magn Reson 135:104–112
34. Belford GG, Belford RL, Burkhalter JF (1973) Eigenfields – practical direct calculation of resonance fields and intensities for field-swept fixed-frequency spectrometers. J Magn Reson 11:251–265
35. McGregor KT, Scaringe RP, Hatfield WE (1975) EPR calculations by eigenfield method. Mol Phys 30:1925–1933
36. Teki Y, Fujita I, Takui T, Kinoshita T, Itoh K (1994) Topology and spin alignment in a novel organic high-spin a molecule, 3,4′-bis(phenylmethylene)biphenyl, as studied by ESR and a generalized UHF hubbard calculation. J Am Chem Soc 116:11499–11505
37. Sato K (1994) Doctoral thesis. Osaka City University, Japan
38. Fukuzawa TA, Sato K, Ichimura AS, Kinoshita T, Takui T, Itoh K, Lahti PM (1996) Electronic and molecular structures of quintet bisnitrenes as studied by fine-structure ESR spectra from random orientation: All the documented ZFS constants correct? Mol Cryst Liq Cryst 278:253–260; (b) Takui T (unpublished work)
39. Matsuoka H, Sato K, Shiomi D, Kojima Y, Hirotsu K, Furuno N, Takui T (2002) CW/pulsed ESR studies on Eu^{2+}-doped $SrAl_2O_4$ phosphor. In: Kawamori A, Yamauchi J, Ohta H (eds) EPR in the 21st century: basics and applications to materials, life and earth sciences, Elsevier, Boston
40. Oda N, Nakai T, Sato K, Shiomi D, Kozaki M, Okada K, Takui T (2002) Molecular and electronic spin structures of high-spin polyphenylene-based oligonitrenes with high symmetry; a semiempirical approach to fine-structure tensors. Mol Cryst Liq Cryst 376: 501–506
41. Sato K, Takui T, Itoh K Program software package (ESR spectral simulation and exact analytical expressions based on hybrid eigenfield approach). Osaka City University: available on request
42. Matsuoka H, Sato K, Shiomi D, Takui T (2003) 2-D electron spin transient nutation spectroscopy of lanthanoid ion Eu^{2+}($^8S_{7/2}$) in a CaF_2 single crystal on the basis of FT-pulsed electron spin resonance spectroscopy: transition moment spectroscopy. Appl Magn Reson 23:517–538
43. (a) Rockenbauer A, Simon P (1973) Second-order perturbation treatment of spin Hamiltonian for low symmetry. J Magn Reson 11:217–218; (b) Iwasaki M (1974) Second-order perturbation treatment of general spin Hamiltonian in an arbitrary coordinate system. J Magn Reson 16:417–423

44. Takui T (1993) Electron nuclear multiple resonance spectroscopy (Chap. 8.5). In: Molecular spectroscopy III – a monograph series of experimental chemistry, 4th edn., vol 8 (Chem Soc Jpn), Maruzen, Tokyo
45. (a) Weil JA, Bolton JR, Wertz JE (1994) Electron paramagnetic resonance. Elementary theory and practical applications. John Wiley, New York; (b) Atherton NM (1993) Principles of electron spin resonance. Ellis Horwood Ltd., New York
46. Takui T (unpublished work)
47. Program Package, Symfonia; Bruker Analytishe Messtehnik GMBH, D-7512 Rheinstetten, FRG
48. Wasserman E, Snyder LC, Yager WA (1964) ESR of triplet states of randomly oriented molecules. J Chem Phys 41:1763–1772
49. Program Package, X'Sophe; Bruker Analytishe Messtehnik GMBH, D-7512 Rheinstetten, FRG
50. Matta ML, Sukheeja BD, Narchal ML (1973) Exact eigensolutions for Cr^{3+} ion. J Magn Reson 9:121–127
51. Sato K, Shiomi D, Takui T (unpublished work)
52. Berliner LJ (ed) (1976) Spin labeling. Academic Press, New York
53. Berliner LJ (ed) (1979) Spin labeling II. Academic Press, New York
54. Likhtenstein GI (1976) Spin labeling methods in molecular biology. Wiley Interscience, New York
55. Eaton SS, Eaton GR (1978) Metal-nitroxyl interactions.5. Interaction of spin labels with transition-metals. Coord Chem Rev 26:207–262
56. Eaton GR, Eaton SS (1988) Electron-paramagnetic-res studies of long-range intramolecular electron electron exchange interaction. Acc Chem Res 21:107–113
57. Weil JA, Bolton JR, Wertz JE (1994) Electron paramagnetic resonance elementary theory and practical applications – Chapter 6. Wiley, New York
58. Atherton NM (1993) Principles of electron spin resonance. Ellis Horwood, Chichester
59. Pake GE, Estle TL (1973) The physical principles of electron paramagnetic resonance. W.A. Benjamin, Reading
60. Salem L, Rowland C (1972) Electronic properties of diradicals. Angew Chem Int Ed Engl 11:92–111
61. Borden WT (ed) (1982) Diradicals. Wiley, New York
62. Heisenberg W (1926) Mehrkörperproblem und resonanz in der quantenmechanik. Z Phys 38:411–426
63. Dirac PAM (1926) On the theory of quantum mechanics. Proc R Soc 112A:661–677
64. Dirac PAM (1929) Quantum mechanics of many-electron systems. Proc R Soc 123A:714–733
65. Van Vleck JH (1945) On the shape of collision-broadened lines. Rev Mod Phys 17:227–236
66. Van Vleck JH (1932) The theory of electric and magnetic susceptibilities – Chapter XII. Oxford University Press, Oxford
67. Arai T (1962) Exchange interaction and Heisenbergs spin Hamiltonian. Phys Rev 126: 471–488
68. Arai T (1964) Cluster expansion in Heitler-London approach to many-electron problems. Phys Rev 134A:824–840
69. Dupeyre RM, Lemaire H, Rassat A (1965) Nitroxides.14. a stable biradical in nitroxide series. J Am Chem Soc 87:3771–3772
70. Briere R, Dupeyre RM, Lemaire H, Morat C, Rassat A, Rey P (1965) Nitroxydes 17 – biradicaux stables du type nitroxide. Bull Soc Chim France 11:3290–3297
71. Nakajima A, Ohya-Nishiguchi H, Deguchi Y (1972) Magnetic properties of some iminoxyl polyradicals.3. Exchange interaction in iminoxyl biradicals. Bull Chem Soc Jpn 45:713–716
72. Luckhurst GR (1966) Alternating linewidths. A novel relaxation process in electron resonance of biradicals. Mol Phys 10:543–550
73. Luckhurst GR, Pedulli GF (1970) Interpretation of biradical electron resonance spectra. J Am Chem Soc 92:4738–4739
74. Redfield AG (1957) On the theory of relaxation processes. IBM J Res Develop 1:19–31

75. Freed JH, Frankel GK (1963) Theory of linewidths in electron spin resonance spectra. J Chem Phys 39:326–348
76. Freed JH, Frankel GK (1964) Alternating linewidths + related phenomena in electron spin resonance spectra of nitro-substituted benzene anions. J Chem Phys 41:699–716
77. Hudson A, Luckhurst GR (1967) Electron resonance spectrum of a triradical. Mol Phys 13:409–416
78. Hudson A, Luckhurst GR (1969) Electron resonance line shapes of radicals in solution. Chem Rev 69:191–225
79. Heinzer J (1971) Fast computation of exchange-broadened isotropic ESR spectra. Mol Phys 22:167–177
80. Heinzer J (1972) QCPE No.209; Quantum Chemistry Program Exchange, Indiana University, Bloomington
81. Binsch G (1968) Direct method for calculating high-resolution nuclear magnetic resonance spectra. Mol Phys 15:469–478
82. Binsch G (1969) A unified theory of exchange effects on nuclear magnetic resonance line shapes. J Am Chem Soc 91:1304–1309
83. Kleier DA, Binsch G (1970) General theory of exchange-broadened NMR line shapes II. Exploitation of invariance properties. J Magn Reson 3:146–160
84. Sankarapandi S, Chandramouli GVR, Daul C, Manoharan PT (1993) Fast computation of dynamic EPR spectra of biradicals. J Magn Reson A 103:163–170
85. Corvaja C, DeMarchi M, Toffoletti A (1997) Conformational dynamics of triradical nitroxides as studied by EPR. Appl Magn Reson 12:1–14
86. Gatteschi D, Kahn O, Miller JS, Palacio F (eds) (1991) Molecular magnetic materials. Kluwer Academic, Dordrecht
87. Iwamura H, Miller JS (eds) (1993) Mol Cryst Liq Cryst 232:1–360; 233:1–360
88. Miller JS, Epstein AJ (eds) (1995) Mol Cryst Liq Cryst 271:1–222; 272:1–215; 273:1–217; 274:1–211
89. Itoh K, Miller JS, Takui T (eds.) (1997) Mol Cryst Liq Cryst 305:1–586; 306:1–520
90. Kahn O (ed) (1999) Mol Cryst Liq Cryst 334:1–702 and 335:1–706
91. Lahti PM (ed) (1999) Magnetic properties of organic materials. Marcel Dekker, New York
92. Itoh K, Kinoshita M (eds) (2000) Molecular magnetism. Gordon & Breach, Amsterdam (Kodansha, Tokyo)
93. Kinoshita M, Turek P, Tamura M, Nozawa K, Shiomi D, Nakazawa Y, Ishikawa M, Takahashi M, Awaga K, Inabe T, Maruyama Y (1991) An organic radical ferromagnet. Chem Lett 1225–1228
94. Tamura M, Nakazawa Y, Shiomi D, Nozawa K, Hosokoshi Y, Ishikawa M, Takahashi M, Kinoshita M (1991) Bulk ferromagnetism in the beta-phase crystal of the para-nitrophenyl nitronyl nitroxide radical. Chem Phys Lett 186:401–404
95. Nakazawa Y, Tamura M, Shirakawa N, Shiomi D, Takahashi M, Kinoshita M, Ishikawa M (1992) Low-temperature magnetic-properties of the ferromagnetic organic radical, p-nitrophenyl nitronyl nitroxide. Phys Rev B 46:8906–8914
96. Buchachenko AL (1979) Organic ferromagnets. Dokl Phys Chem 244:107–109
97. Néel L (1948) Magnetic properties of ferrites: ferrimagnetism and antiferromagnetism. Ann Phys 3:137–198
98. Shiomi D, Nishizawa M, Sato K, Takui T, Itoh K, Sakurai H, Izuoka A, Sugawara T (1997) A prerequisite for purely organic molecule-based ferrimagnetics: breakdown of simple classical pictures. J Phys Chem B 101:3342–3348
99. Nishizawa M, Shiomi D, Sato K, Takui T, Itoh K, Sawa H, Kato R, Sakurai H, Izuoka A, Sugawara T (2000) Evidence for the breakdown of simple classical pictures of organic molecule-based ferrimagnetics: low-temperature crystal structure and single-crystal ESR studies of an organic heterospin system. J Phys Chem B 104:503–509
100. Shiomi D, Sato K, Takui T (2000) Spin-spin correlation function and magnetic susceptibility of quantum ferrimagnetic spin chains as model for organic molecule-based ferrimagnetics. J Phys Chem B 104:1961–1965

101. Shiomi D, Sato K, Takui T (2001) Quantum ferrimagnetism based on organic biradicals with a spin-0 ground state: numerical calculations of molecule-based ferrimagnetic spin chains. J Phys Chem B 105:2932–2938
102. Shiomi D, Sato K, Takui T (2002) A molecular quantum description of spin alignments in molecule-based ferrimagnets: numerical calculations of thermodynamic properties. J Phys Chem A 106:2096–2103
103. Shiomi D, Nishizawa M, Kamiyama K, Hase S, Kanaya T, Sato K, Takui T (2001) Molecular design of organic ferrimagnets. Synth Met 121:1810–1811
104. Hase S, Shiomi D, Sato K, Takui T (2001) Phenol-substituted nitronyl nitroxide biradicals with a triplet (S = 1) ground state. J Mater Chem 11:756–760
105. Shiomi D, Ito K, Nishizawa M, Sato K, Takui T, Itoh K (1999) Magnetic coupling of nitronyl nitroxide-based biradical salts. Synth Met 103:2271–2272
106. Shiomi D, Nishizawa M, Kamiyama K, Hase S, Kanaya T, Sato K, Takui T (2001) Molecular design of organic ferrimagnets. Synth Met 121:1810–1811
107. Shiomi D, Kanaya T, Sato K, Mito M, Takeda K, Takui T (2001) Single-component molecule-based ferrimagnetics. J Am Chem Soc 123:11823–11824
108. Kanaya T, Shiomi D, Sato K, Takui T (2001) Single-component ferrimagnetics: triplet-doublet composite molecules as constituents of purely organic molecule-based ferrimagnets. Polyhedron 20:1397–1402
109. Shiomi D, Sato K, Takui T to be reported elsewhere
110. McWeeny R (1970) Spins in chemistry. Academic Press, New York/London
111. McWeeny R, Sutcliffe BT (1969) Methods of molecular quantum mechanics. Academic Press, New York/London
112. Kaneda C, Shiomi D, Sato K, Takui T (2003) A stable organic triradical with truncated pi-conjugation as a model for single-component organic molecule-based ferrimagnetics. Polyhedron 22:1809–1816
113. Shiomi D, Kaneda C, Sato K, Takui T (2003) Hyperfine structure of ESR spectra as a probe for Heisenberg exchange couplings in nitroxide triradicals serving as building blocks for molecule-based ferrimagnets. Appl Magn Reson 23:495–506
114. Bencini A, Gatteschi D (1990) Electron paramagnetic resonance of exchange coupled systems. Springer: Berlin
115. Hay PJ, Thibeault JC, Hoffmann R (1975) Orbital interactions in metal dimer complexes. J Am Chem Soc 97:4884–4889
116. Kahn O (1985) Dinuclear complexes with predictable magnetic-properties. Angew Chem Int Ed 24:834–850
117. Kitagawa S, Okubo T, Kawata S, Kondo M, Katada M, Kobayashi H (1995) An oxalate-linked copper(II) coordination polymer, $[Cu_2(oxalate)_2(pyrazine)_3]_n$, constructed with two different copper units: x-ray crystallographic and electronic structures. Inorg Chem 34:4790–4796
118. Drew MGB, Fowless GWA, Lewis DF (1969) Structure of mu-oxalatobis(oxalato) hexaquodititatnium(3) tetrahydrate – a pentagonal-bipyramidal titanium complex. J Chem Soc Chem D Chem Commun 876–877
119. Julve M, Kahn O (1983) Synthesis, magnetic properties and EPR of μ-oxalatotetrakis (acetylacetonato)diiron(III). Inorg Chim Acta 76:39–41
120. Feist M, Troyanov S, Kemnitz E (1996) A binuclear chloroferrate anion with octahedral metal coordination: octachloro(μ-oxalato)diferrate(III), $[(FeCl_4)_2(\mu\text{-}C_2O_4)]^{4-}$. Inorg Chem 35:3067–3068
121. Masters VM, Sharrad CA, Bernhardt PV, Gahan LR, Moubaraki B, Murray KS (1998) Synthesis, structure and magnetism of the oxalato-bridged chromium(III) complex [NBu4n]$_4$[Cr-2 (ox)$_5$]2CHCl$_3$. J Chem Soc Dalton Trans 413–416
122. Triki S, Berezovsky F, Pala JS, Gomez-Garcia CJ, Coronado E, Costuas K, Halet JF (2001) New charge transfer salts based on bis(ethylenedithio)tetrathiafulvalene (ET) and ferro- or antiferromagnetic oxalato-bridged dinuclear anions: syntheses, structures and magnetism of $ET_5[MM'(C_2O_4)(NCS)_8]$ with MM' = $Cr^{III}Fe^{III}$, $Cr^{III}Cr^{III}$. Inorg Chem 40:5127–5132

123. Triki S, Berezovsky F, Pala JS, Coronado E, Gomez-Garcia CJ, Clemente JM, Riou A, Molinie P (2000) Oxalato-bridged dinuclear complexes of Cr(III) and Fe(III): synthesis, structure, and magnetism of $[(C_2H_5)_4N]_4[MM'(ox)(NCS)_8]$ with MM'= CrCr, FeFe, and CrFe. Inorg Chem 39:3771–3776
124. Viswanathan R, Palaniandavar M, Prabakaran P, Muthiah PT (1998) Structure, spectra, and redox behavior of a μ-dimethoxo-bridged diferric complex with an asymmetric Fe_2O_2 bridge. Inorg Chem 37:3881–3884
125. Unamuno I, Gutierrez-Zorrilla JM, Luque A, Roman P, Lezama L, Calvo R, Rojo T (1998) Ion-pair charge-transfer complexes based on (o-phenylenebis(oxamato))cuprate(II) and cyclic diquaternary cations of 1,10-phenanthroline and 2,2′-bipyridine: synthesis, crystal structure, and physical properties. Inorg Chem 37:6452–6460
126. Ferrer S, van Koningsbruggen PJ, Haasnoot JG, Reedijk J, Kooijman H, Spek AL, Lezama L, Arif AM, Miller JS (1999) Dimetallic complexes derived from a novel dinucleating chelating symmetric triazole ligand; crystal structure, magnetic properties and ESR study of bis[mu-3,5-diacetylamino-1,2,4-triazolato-O′,N-1,N-2,O '']bis[(nitrato)(aqua)copper(II)]. J Chem Soc Dalton Trans 4269–4276
127. Horner O, Anxolabehere-Mallart E, Charlot MF, Tchertanov L, Guilhem J, Mattioli TA, Boussac A, Girerd JJ (1999) A new manganese dinuclear complex with phenolate ligands and a single unsupported oxo bridge. Storage of two positive charges within less than 500 mV. Relevance to photosynthesis. Inorg Chem 38:1222–1232
128. Asaji T, Wada K, Horiuchi K, Chiba T (1999) Single crystal EPR and polycrystalline 1 H NMR study of a ferromagnetically coupled dinuclear copper(II) complex in $[P(C_6H_5)_4][CuCl_3]$. Phys Chem Chem Phys 1:801–805
129. Weder JE, Hambley TW, Kennedy BJ, Lay PA, MacLachlan D, Bramley R, Delfs CD, Murray KS, Moubaraki B, Warwick B, Biffin JR, Regtop HL (1999) Anti-inflammatory dinuclear copper(II) complexes with indomethacin. synthesis, magnetism and EPR spectroscopy. Crystal structure of the N,N-dimethylformamide adduct. Inorg Chem 38:1736–1744
130. Ohtsu H, Shimazaki Y, Odani A, Yamauchi O, Mori W, Itoh S, Fukuzumi S (2000) Synthesis and characterization of imidazolate-bridged dinuclear complexes as active site models of Cu,Zn-SOD. J Am Chem Soc 122:5733–5741
131. Bernhardt PV (2001) Diverse solid-state and solution structures within a series of hexaamine dicopper(II) complexes. Inorg Chem 40:1086–1092
132. Haj MA, Quiros M, Salas JM, Dobado JA, Molina JM, Basallote MG, Manez MA (2002) Structurally different dinuclear copper(II) complexes with the same triazolopyrimidine bridging ligand. Euro J Inorg Chem 811–818
133. Theil S, Yerande R, Chikate R, Dahan F, Bousseksou A, Padhye S, Tuchagues JP (1997) Synthesis, structure, and magnetic and redox properties of linear bis-dinuclear complexes afforded by schiff base ligands containing catecholate and pyridine or imidazole groups. Inorg Chem 36:6279–6286
134. Agterberg FPW, Kluit HAJP, Driessen WL, Oevering H, Buijs W, Lakin MT, Spek AL, Reedijk J (1997) Dinuclear paddle-wheel copper(ii) carboxylates in the catalytic oxidation of carboxylic acids. Unusual polymeric chains found in the single-crystal X-ray structures of [tetrakis(μ-1-phenylcyclopropane-1-carboxylato-O,O′) bis(ethanol-O)dicopper(II)] and catena-poly [[bis(μ-diphenylacetato-O:O′)dicopper](μ3-diphenylacetato-1-O:2-O′:1′-O′)(μ3-diphenylacetato-1-O:2-O′:2′-O′)]. Inorg Chem 36:4321–4328
135. Ung VA, Thompson AMWC, Bardwell DA, Gatteschi D, Jeffery JC, McCleverty JA, Totti F, Ward MD (1997) Roles of bridging ligand topology and conformation in controlling exchange interactions between paramagnetic molybdenum fragments in dinuclear and trinuclear complexes. Inorg Chem 36:3447–3454
136. Yonemura M, Matsumura Y, Furutachi H, Ohba M, Okawa H, Fenton DE (1997) Migratory transmetalation in diphenoxo-bridged $Cu^{II}M^{II}$ complexes of a dinucleating macrocycle with $N(amine)_2O_2$ and $N(imine)_2O_2$ metal-binding sites. Inorg Chem 36:2711–2717

137. Casanova J, Alzuet G, Latorre J, Borras J (1997) Spectroscopic, magnetic, and electrochemical studies of a dimeric N-substituted-sulfanilamide copper(II) complex. X-ray and molecular structure of the Cu_2(sulfathiazolato)$_4$ complex. Inorg Chem 36:2052–2058
138. Higgs TC, Helliwell M, McInnes EJL, Mabbs FE, Harding CJ, Garner CD (1997) Synthesis, structural and magnetic characterisation of tris(1-methyl-4,5-diphenylimidazol-2-yl)methanol (L) and [{CuL(NO_3)}$_2$][NO_3]$_2$. J Chem Soc Dalton Trans 927–933
139. Knapp MJ, Krzystek J, Brunel LC, Hendrickson DN (1999) High-field EPR study of resonance-delocalized $[Fe_2(OH)_3(tmtacn)_2]^{2+}$. Inorg Chem 38:3321–3328
140. Dei A, Gatteschi D, Massa CA, Pardi LA, Poussereau S, Sorace L (2000) Spontaneous symmetry breaking in the formation of a dinuclear gadolinium semiquinonato complex: synthesis, high-field EPR studies, and magnetic properties. Chem Euro J 6:4580–4586
141. Elschenbroich C, Wolf M, Buirghaus O, Harms K, Pebler J (1999) The mono-, di-, and tri([5]trovacenyl)boranes: a study of intermetallic communication across an sp2-hybridized boron atom. Euro J Inorg Chem 2173–2185
142. Ferrer S, Haasnoot JG, Reedijk J, Muller E, Cingi MB, Lanfranchi M, Lanfredi AMM, Ribas J (2000) Trinuclear N,N-bridged copper(II) complexes involving a Cu_3OH core: [Cu_3(μ_3-OH)L3A(H_2O)$_2$]A·(H_2O)$_x$ {L = 3-acetylamino-1,2,4-triazolate; A = CF_3SO_3, NO_3, ClO_4; x = 0, 2} synthesis, X-ray structures, spectroscopy, and magnetic properties. Inorg Chem 39:1859–1867
143. Raptopoulou CP, Tangoulis V, Psycharis V (2000) Synthesis and structural, spectroscopic, and magnetic characterization of (NH_4)[Fe_3(μ_3-OH)(H_2L)$_3$(HL)$_3$] (H_3L = orotic acid) presenting two novel metal-binding modes of the orotate ligand: the case of a spin-frustrated system. Inorg Chem 39:4452–4459
144. Gomez-Garcia CJ, Coronado E, Borras-Almenar JJ (1992) Magnetic characterization of tetranuclear copper(II) and cobalt(II) exchange-coupled clusters encapsulated in heteropolyoxotungstate complexes. Study of the nature of the ground states. Inorg Chem 31:1667–1673
145. Belinsky MI (2002) Anisotropic mixing of spin levels in spin-admixed tetrameric iron-sulfur clusters with spin frustration. Chem Phys 277:271–296
146. Reynaud F, Mertz D, Celestini F, Debierre JM, Ghorayeb AM, Simon P, Stepanov A, Voiron J, Delmas C (2001) Orbital frustration at the origin of the magnetic behavior in $LiNiO_2$. Phys Rev Lett 86:3638–3641
147. Chappel E, Nunez-Regueiro MD, Chouteau G, Darie C, Delmas C, Bianchi V, Caurant D, Baffier N (2001) High magnetic field study of quasi-stoichiometric $Li_{1-x}Ni_{1+x}O_2$. Physica B 294:124–127
148. Inagaki Y, Asano T, Ajiro Y, Kawae T, Takeda K, Nojiri H, Motokawa M, Mitamura H, Goto T, Tanaka M, Matsuda K, Iwamura H (2000) High-field magnetization and high-frequency ESR study on the tetranuclear cluster composed of pi-electrons ($S = 1/2$) and d-electrons ($S = 5/2$). Mol Cryst Liq Cryst 343:433–438
149. Plass W (1997) Competing magnetic exchange interactions in tetranuclear d1 systems: synthesis, structure, and magnetochemistry of a neutral vanadium(IV) complex with a $\{(VO)_4(\mu_3\text{-}OR)_2(\mu_2\text{-}OR)_4\}^{2+}$ Core. Inorg Chem 36:2200–2205
150. Powell AK, Heath SL, Gatteschi D, Pardi L, Sessoli R, Spina G, Del Giallo F, Pieralli F (1995) Synthesis, structures, and magnetic properties of Fe_2, Fe_{17}, and Fe_{19} oxo-bridged iron clusters: the stabilization of high ground state spins by cluster aggregates. J Am Chem Soc 117:2491–2502
151. Goldberg DP, Caneschi A, Delfs CD, Sessoli R, Lippard SJ (1995) A decanuclear manganese cluster with oxo and halide bridging ligands: magnetic behavior of an $s \geq 12$ system. J Am Chem Soc 117:5789–5800
152. Delfs C, Gatteschi D, Pardi L, Sessoli R, Wieghardt K, Hanke D (1993) Magnetic properties of an octanuclear iron(III) cation. Inorg Chem 32:3099–3103
153. Jones R, Oberg S (1992) Oxygen frustration and the interstitial carbon-oxygen complex in Si. Phys Rev Lett 68:86–89

154. Hendrickson DN, Christou G, Schmitt EA, Libby E, Bashkin JS, Wang S, Tsai HL, Vincent JB, Boyd PDW (1992) Photosynthetic water oxidation center: spin frustration in distorted cubane $Mn^{IV}Mn_3{}^{III}$ model complexes. J Am Chem Soc 114:2455–2471
155. Woo HY, So H, Pope MT (1996) Trimetallo derivatives of lacunary 9-tungstosilicate heteropolyanions. 2. Isotropic nmr shifts in pyridine-type ligands coordinated to the paramagnetic 9-tungsto-3-cuprio(II)silicate anion. J Am Chem Soc 118:621–626
156. Cho YH, So HS (1995) Single-crystal EPR-spectra of $K_{12}[As_2W_{18}O_{66}Cu_3(H_2O)_2]11H_2O$, a copper(II) trimer. Bull Korean Chem Soc 16:243–247
157. Robert F, Leyrie M, Herve G (1982) Structure of potassium diaquatricuprooctadecatungstodiarsenate(III)(12-) undecahydrate. Acta Cryst B 38:358–362
158. Robert F, Teze A (1981) Structure of sodium beta-hydrogenenneatungstosilicate hydrate $Na_9(\beta\text{-}SiW_9O_{34}H)23H_2O$. Acta Cryst B 37:318–322
159. Rusu D, Craciun C, Barra AL, David L, Rusu M, Rosu C, Cozar O, Marcu G (2001) Spectroscopic and electron paramagnetic resonance behavior of trinuclear metallic clusters encapsulated in $[M_3{}^{n+}(H_2O)_x(BiW_9O_{33})_2]$((18–3n)-) heteropolyanion ($M^{n+} = (VO)^{II}$, $x = 0$ and M^{n+} = Cr-III, Mn-II, Fe-III, Co-II, Ni-II, Cu-II, $x = 3$). J Chem Soc Dalton Trans 2001:2879–2887
160. Kazansky LP, McGarvey BR (1999) NMR and EPR spectroscopies and electron density distribution in polyoxoanions. Coord Chem Rev 188:157–210
161. Clemente-Juan JM, Coronado E (1999) Magnetic clusters from polyoxometalate complexes. Coord Chem Rev 195:361–394
162. Okubo S, Ohta H, Hazuki K, Sakurai T, Kobayashi N, Hiroi Z (2001) High-field ESR study of kagome-like substance $Cu_3V_2O_7(OH)_2c2H_2O$. Physica B 294:75–78
163. Abbati GL, Brunel LC, Casalta H, Cornia A, Fabretti AC, Gatteschi D, Hassan AK, Jansen AGM, Maniero AL, Pardi L, Paulsen C, Segre U (2001) Single-ion versus dipolar origin of the magnetic anisotropy in iron(III)-oxo clusters: a case study. Chem Euro J 7:1796–1807
164. Okubo S, Hayashi M, Kimura S, Ohta H, Motokawa M, Kikuchi H, Nagasawa H (1998) Submillimeter wave ESR of triangular-kagome antiferromagnet $Cu_9X_2(cpa)_6$ (X = Cl, Br). Physica B 246:553–556
165. Mekata M, Abdulla M, Asano T, Kikuchi H, Goto T, Morishita T, Hori H (1998) Magnetic ordering in triangulated kagome lattice compound, $Cu_9Cl_2(cpa)_6nH_2O$. J Magn Magn Mater 177:731–732
166. Ohta H, Sumikawa M, Motokawa M, Kikuchi H, Nagasawa H (1996) High field ESR of kagome antiferromagnets $SrCr_xGa_{12\text{-}x}O_{19}$. J Phys Soc Jpn 65:848–852
167. Martinez B, Sandiumenge F, Rouco A, Labarta A, Rodriguezcarvajal J, Tovar M, Causa MT, Gali S, Obradors X (1992) Magnetic dilution in the strongly frustrated kagome antiferromagnet SrGa12-xCrxO19. Phys Rev B 46:10786–10792
168. McCusker JK, Jang HG, Wang S, Christou G, Hendrickson DN (1992) Ground-state variability in.mu.3-oxide trinuclear mixed-valence manganese complexes: spin frustration. Inorg Chem 31:1874–1880
169. Baikie ARE, Hursthouse MB, New DB, Thornton P (1978) Preparation, crystal-structure, and magnetic-properties of a trinuclear mixed-valence manganese carboxylate. J Chem Soc Chem Commun 1978:62–63
170. Baikie ARE, Hursthouse MB, New L, Thornton P, White RG (1980) Discrete oxidation-states and x-ray crystal-structure of the trinuclear manganese Carboxylate $[Mn_3(3\text{-}ClC_5H_4N)_3O(O_2CMe)_6]$. J Chem Soc Chem Commun 684–685
171. Vincent JB, Chang HR, Folting K, Huffman JC, Christou G, Hendrickson DN (1987) Preparation and physical properties of trinuclear oxo-centered manganese complexes of general formulation $[Mn_3O(O_2CR)_6L_3]0,+$ (R = methyl or phenyl; L = a neutral donor group) and the crystal structures of $[Mn_3O(O_2CMe)_6(pyr)_3](pyr)$ and $[Mn_3O(O_2CPh)_6(pyr)_2(H_2O)]0.5MeCN$. J Am Chem Soc 109:5703–5711

172. Ribas J, Albela B, Stoeckli-Evans H, Christou G (1997) Synthesis and magnetic properties of six new trinuclear oxo-centered manganese complexes of general formula [Mn_3O(X-benzoato)$_6$ L_3] (X = 2-F, 2-Cl, 2-Br, 3-F, 3-Cl, 3-Br; L = pyridine or water) and crystal structures of the 2-F, 3-Cl, and 3-Br complexes. Inorg Chem 36:2352–2360
173. Burdinski D, Birkelbach F, Weyhermuller T, Florke U, Haupt HJ, Lengen M, Trautwein AX, Bill E, Wieghardt K, Chaudhuri P (1998) Encapsulation by a chromium(III)-containing bicyclic ligand cage. Synthesis, structures, and physical properties of heterometal complexes $Cr^{III}MCr^{III}$ [M = (H+)2, Li(I), Mg(II), Cu(II), Ni(II), Ni(IV), Co(III), Fe(II), Fe(III), Mn(II)]. Inorg Chem 37:1009–1020
174. Birkelbach F, Florke U, Haupt HJ, Butzlaff C, Trautwein AX, Wieghardt K, Chaudhuri P (1998) Competing exchange interactions and ground-state variability: linear homo- and heterotrinuclear manganese(III, IV) complexes with tris(dimethylglyoximato)metalate(II) tetraanions as bridging ligands. Inorg Chem 37:2000–2008
175. Glaser T, Kesting F, Beissel T, Bill E, Weyhermuller T, Meyer-Klaucke W, Wieghardt K (1999) Spin-dependent delocalization in three isostructural complexes [LFeNiFeL]2+/3+/4+ (L = 1,4,7-(4-tert-Butyl-2-mercaptobenzyl)-1,4,7-triazacyclononane). Inorg Chem 38:722–732
176. Glaser T, Beissel T, Bill E, Weyhermuller T, Schunemann V, Meyer-Klaucke W, Trautwein AX, Wieghardt K (1999) Electronic structure of linear thiophenolate-bridged heterotrinuclear complexes [LFeMFeL]n + (M = Cr, Co, Fe; n = 1 − 3): localized vs delocalized models. J Am Chem Soc 121:2193–2208
177. Glaser T, Bill E, Weyhermuller T, Meyer-Klaucke W, Wieghardt K (1999) Sn(III) and Ge(III) in the thiophenolato-bridged complexes [LFeSnFeL]n + and [LFeGeFeL]n + (n = 2, 3; L = 1,4,7-(4-tert-Butyl-2-mercaptobenzyl)-1,4,7-triazacyclononane). Inorg Chem 38:2632–2642
178. van Albada GA, van Koningsbruggen PJ, Mutikainen I, Turpeinen U, Reedijk J (1999) Synthesis, structure, spectroscopy, and magnetism of unique propeller-type linear trinuclear Cu^{II} complexes with in-situ prepared formamidine ligands. Euro J Inorg Chem 12:2269–2275
179. Gutierrez L, Alzuet G, Real JA, Cano J, Borras J, Castineiras A (2000) Countercomplementarity and strong ferromagnetic coupling in a linear mixed μ-acetato, μ-hydroxo trinuclear copper(II) complex. Synthesis, structure, magnetic properties, EPR, and theoretical studies. Inorg Chem 39:3608–3614
180. Birkelbach F, Weyhermuller T, Lengen M, Gerdan M, Trautwein AX, Wieghardt K, Chaudhuri P (1997) Linear trinuclear oximato-bridged complexes Mn-III,Mn-IV;M-II;Mn-III,Mn-IV (M = Zn, Cu or Mn): synthesis, structure, redox behaviour and magnetism. J Chem Soc Dalton Trans 4529–4537
181. Weyland T, Costuas K, Mari A, Halet JF, Lapinte C (1998) [(Cp*)(dppe)Fe(III)-](+) units bridged through 1,3-diethynylbenzene and 1,3,5-triethynylbenzene spacers: ferromagnetic metal-metal exchange interaction. Organometallics 17:5569–5579
182. Aubin SMJ, Wemple MW, Adams DM, Tsai HL, Christou G, Hendrickson DN (1996) Distorted $Mn^{IV}Mn_3{}^{III}$ cubane complexes as single-molecule magnets. J Am Chem Soc 118:7746–7754
183. Recent developments in single-molecule magnetism are overviewed in the following literatures. (a) Gatteschi D, Sessoli R, Villain J (2006) Molecular nanomanet. Oxford University Press, Oxford; (b) Winpenny R (ed) (2006) Single-molecule magnets and related phenomena. Springer (c) Stamopoulos D (ed) (2008) Magnetism and superconductivity in low-dimensional systems; utilization in future applications. Nova Science Publishers, New York; (d) Sessoli R, Powell AK (2009) Strategies towards single molecule magnets based on lanthanide ions. Coord Chem Rev 253:2328–2341; (f) Murrie M, (2010) Cobalt(II) single-molecule magnets. Chem Soc Rev 39:1986–1995; (g) Friedman JR, Sarachik MP (2010) Single-molecule nanomagnets. Annu Rev Condens Matter Phys 1:109–128; (h) Cornia A, Mannini M, Sainctavitc P, Sessoli R (2011) Chemical strategies and characterization tools for the organization of single molecule magnets on surfaces. Chem Soc Rev 40:3076–3091; (i) Sorace L, Benelli C, Gatteschi D (2011) Lanthanides in molecular magnetism: old tools in a new field. Chem Soc Rev 40:3092–3104

184. Stamatatos TC, Abboud KA, Wernsdorfer W, Christou G (2007) "Spin Tweaking" of a high-spin molecule: an Mn_{25} single-molecule magnet with an S = 61/2 ground state. Angew Chem Int Ed 46:884–888
185. (a) Ishikawa N, Sugita M, Ishikawa T, Koshihara S, Kaizu Y (2003) Lanthanide double-decker complexes functioning as magnets at the single-molecular level. J Am Chem Soc 125:8694–8695; (b) Ishikawa N, Sugita M, Ishikawa T, Koshihara S, Kaizu Y (2004) Mononuclear lanthanide complexes with a long magnetization relaxation time at high temperatures: a new category of magnets at the single-molecular level. J Phys Chem B 108:11265–11271; (c) Ishikawa N, Mizuno Y, Takamatsu S, Ishikawa T, Koshihara S (2008) Effects of chemically induced contraction of a coordination polyhedron on the dynamical magnetism of bis(phthalocyaninato)disprosium, a single-4f-ionic single-molecule magnet with a kramers ground state. Inorg Chem 47:10217–10219
186. Jones A (1998) Fast searches with nuclear magnetic resonance computers. Science 280:229
187. Leuenberger MN, Loss D (2001) Quantum computing in molecular magnets. Nature 410:789–793
188. (a) Barra A, Gatteschi D, Sessoli R (1997) High-frequency EPR spectra of a molecular nanomagnet: understanding quantum tunneling of the magnetization. Phys Rev B56:8192–8198; (b) Barra AL, Caneschi A, Gatteschi D, Sessoli R (1998) Very high field EPR study of a molecular nanomagnet. J Magn Magn Mater 177–181:709–710; (c) Sessoli R, Gatteschi D, Caneschi A, Novak MA (1993) Magnetic bistability in a metal-ion cluster. Nature 365: 141–143
189. Hill S, Perenboom JAAJ, Dalal NS, Hathaway T, Stalcup T, Brooks JS (1998) high-sensitivity electron paramagnetic resonance of Mn_{12}-acetate. Phys Rev Lett 80:2453–2456
190. Awaga K, Takeda K, Inabe T (1999) Magnetic properties of molecular compounds of Mn_{12}Ph. Mol Cryst Liq Cryst 335:473–482
191. Aubin SMJ, Sun Z, Pardi L, Krzystek J, Folting K, Brunel LC, Rheingold AL, Christou G, Hendrickson DN (1999) Reduced anionic Mn_{12} molecules with half-integer ground states as single-molecule magnets. Inorg Chem 38:5329–5340
192. Barra AL, Caneschi A, Cornia A, De Biani FF, Gatteschi D, Sangregorio C, Sessoli R, Sorace L (1999) Single-molecule magnet behavior of a tetranuclear iron(III) complex. The origin of slow magnetic relaxation in iron(III) clusters. J Am Chem Soc 121:5302–5310
193. Yoo J, Brechin EK, Yamaguchi A, Nakano M, Huffman JC, Maniero AL, Brunel LC, Awaga K, Ishimoto H, Christou G, Hendrickson DN (2000) Single-molecule magnets: a new class of tetranuclear manganese magnets. Inorg Chem 39:3615–3623
194. Blinc R, Cevc P, Arcon D, Dalal NS, Achey RM (2001) Excited-state X-band EPR in a molecular cluster nanomagnet, Phys Rev B63:212401/1–212401/4
195. Kuroda-Sowa T, Lam M, Rheingold AL, Frommen C, Reiff WM, Nakano M, Yoo J, Maniero AL, Brunel LC, Christou G, Hendrickson DN (2001) Effects of paramagnetic ferrocenium cations on the magnetic properties of the anionic single-molecule magnet $[Mn_{12}O_{12}(O_2CC_6F_5)_{16}(H_2O)_4]$. Inorg Chem 40: 6469–6480
196. Artus P, Boskovic C, Yoo J, Streib WE, Brunel LC, Hnedrickson DN, Christou G (2001) Single-molecule magnets: site-specific ligand abstraction from $[Mn_{12}O_{12}(O_2CR)_{16}(H_2O)_4]$ and the preparation and properties of $[Mn_{12}O_{12}(NO_3)_4(O_2CCH_2But)_{12}(H_2O)_4]$. Inorg Chem 40:4199–4210
197. Yoo J, Yamaguchi A, Nakano M, Krzystek J, Streib WE, Brunel LC, Ishimoto H, Christou G, Hendrickson DN (2001) Mixed-valence tetranuclear manganese single-molecule magnets. Inorg Chem 40:4604–4616
198. Barra AL, Debrunner P, Gatteschi D, Schulz CE, Sessoli R (1996) Superparamagnetic-like behavior in an octanuclear iron cluster. Europhys Lett 35:133–138
199. Barra AL, Gatteschi D, Sessoli R (2000) High-frequency EPR spectra of $[Fe_8O_2(OH)_{12}(tacn)_6]Br_8$: a critical appraisal of the barrier for the reorientation of the magnetization in single-molecule magnets. Chem Eur J 6:1608–1614
200. Barra AL, Bencini F, Caneschi A, Gatteshi D, Paulsen C, Sangregorio C, Sessoli R, Sorace L (2001) Tuning the magnetic properties of the high-spin molecular cluster Fe_8. ChemPhysChem 2:523–531

201. Bouwen A, Caneschi A, Gatteschi D, Goovaerts E, Schoemaker D, Sorace L, Stefan M (2001) Single-crystal high-frequency electron paramagnetic resonance investigation of a tetranuclear iron(III) single-molecule magnet. J Phys Chem B 105:2658–2663
202. Yang EC, Kirman C, Lawrence J, Zakharov LN, Rheingold AL, Hill S, Hendrickson DN (2005) Single-molecule magnets: high-field electron paramagnetic resonance evaluation of the single-ion zero-field interaction in a $Zn_3^{II}Ni^{II}$ Complex. Inorg Chem 44:3827–3836
203. Caneschi A, Gatteschi D, Sessoli R, Barra AL, Brunel LC, Guillot M (1991) Alternating current susceptibility, high field magnetization, and millimeter band EPR evidence for a ground S = 10 state in $[Mn_{12}O_{12}(Ch_3COO)_{16}(H_2O)_4]\cdot_2 CH_3COOH_4H_2O$. J Am Chem Soc 113:5873–5874
204. Lis T (1980) Preparation, structure, and magnetic properties of a dodecanuclear mixed-valence manganese carboxylate. Acta Crystallogr B36:2042–2046
205. Tasiopoulos AJ, Vinslava A, Wernsdorfer W, Abboud KA, Christou G (2004) Giant single-molecule magnets: a $\{Mn_{84}\}$ torus and its supramolecular nanotubes. Angew Chem Int Ed 43:2117–2121
206. Moushi EE, Lampropoulos C, Wernsdorfer W, Nastopoulos V, Christou G, Tasiopoulos AJ (2010) Inducing single-molecule magnetism in a family of loop-of-loops aggregates: heterometallic $Mn_{40}Na_4$ clusters and the homometallic Mn_{44} analogue. J Am Chem Soc 132:16146–16155
207. (a) Soler M, Wernsdorfer W, Folting K, Pink M, Christou G (2004) Single-molecule magnets: a large Mn_{30} molecular nanomagnet exhibiting quantum tunneling of magnetization. J Am Chem Soc 126:2156–2165; (b) Soler M, Rumberger E, Folting K, Hendrickson DN, Christou G (2001) Synthesis, characterization and magnetic properties of $[Mn_{30}O_{24}(OH)_8(O_2CCH_2C(CH_3)_3)_{32}(H^2O)_2(CH_3NO_2)_4]$: the largest manganese carboxylate cluster. Polyhedron 20:1365–1369
208. Barra A, Gatteschi D, Sessoli R (1997) High-frequency EPR spectra of a molecular nanomagnet: understanding quantum tunneling of the magnetization. Phys Rev B56: 8192–8198
209. Sessoli R, Tsai HL, Schake AR, Wang S, Vincent JB, Folting K, Gatteschi D, Christou G, Hendrickson DN (1993) High-spin molecules: $[Mn_{12}O_{12}(O_2CR)_{16}(H_2O)_4]$. J Am Chem Soc 115:1804–1816
210. Waldmann O (2007) A criterion for the anisotropy barrier in single-molecule magnets. Inorg Chem 46 10035–10037
211. Ako AM, Hewitt IJ, Mereacre V, Cl´erac R, Wernsdorfer W, Anson CE, Powell AK (2006) A ferromagnetically coupled Mn_{19} aggregate with a record S = 83/2 ground spin state. Angew Chem Int Ed 45:4926–4929
212. Milios CJ, Vinslava A, Wernsdorfer W, Moggach S, Parsons S, Perlepes SP, Christou G, Brechin EK (2007) A record anisotropy barrier for a single-molecule magnet. J Am Chem Soc 129:2754–2755
213. (a) Friedman J, Sarchik MP, Tejada J, Ziolo R (1996) Macroscopic measurement of resonant magnetization tunneling in high-spin molecules. Phys Rev Lett 76:3830–3833; (b) Friedman J, Sarchik MP, Tejada J, Maciejewski J, Ziolo R (1996) Steps in the hysteresis loops of a high-spin molecule. J Appl Phys 79:6031–6034
214. (a) Hernandez JM, Zhang XX, Luis F, Bartolome J, Tejada J, Ziolo R (1996) Field tuning of thermally activated magnetic quantum tunnelling in Mn_{12} − Ac molecules. Europhys Lett 35:301–306; (b) Thomas L, Lionti F, Ballou R, Gatteschi D, Sessoli R, Barbara B (1996) Macroscopic quantum tunnelling of magnetization in a single crystal of nanomagnets. Nature 383:145–147; (c) Hernandez J M, Zhang XX, Luis F, Tejada J, Friedman J, Sarachik MP, Ziolo R (1997) Evidence for resonant tunneling of magnetization in Mn_{12}sacetate complex. Phys Rev B55:5858–5865
215. McInnes EJL, Spectroscopy of single-molecule magnets. Struct Bond 122:69–102
216. Gatteschi D, Caneschi A, Sessoli R, Cornia A (1996) Magnetism of large iron-oxo clusters. Chem Soc Rev 25:101–109

217. Gatteschi D, Barra AL, Caneschi A, Cornia A, Sessoli R, Sorace L, EPR of molecular nanomagnets. Coord Chem Rev 250:1514–1529
218. McInnes EJL, Piligkos S, Timco GA, Winpenny REP (2006) Studies of chromium cages and wheels. Coord Chem Rev 249:2577–2590
219. Barra A, Gatteschi D, Sessoli R (1997) High-frequency EPR spectra of a molecular nanomagnet: understanding quantum tunneling of the magnetization. Phys Rev B56: 8192–8198
220. Gatteschi D, Sessoli R (2003) Quantum tunneling of magnetization and related phenomena in molecular materials. Angew Chem Int Ed 42:268–297
221. Edwards RS, Hill S, Bhaduri S, Aliaga-Alcalde N, Bolin E, Maccagnano S, Christou G, Hendrickson DN (2003) A comparative high frequency EPR study of monomeric and dimeric Mn_4 single-molecule magnets. Polyhedron 22:1911–1916
222. Rumberger EM, Hill S, Edwards RS, Wernsdorfer W, Zakharov LN, Rheingold AL, Christou G, Hendrickson DN (2003) Search for new iron single-molecule magnets. Polyhedron 22: 1865–1870
223. Feng PL, Beedle CC, Koo C, Lawrence J, Hill S, Hendrickson DN (2008) Origin of magnetization tunneling in single-molecule magnets as determined by single-crystal high-frequency EPR. Inorg Chim Acta 361:3465–3480
224. Barra L, Caneschi A, Cornia A, Gatteschi D, Gorini L, Heiniger LP, Sessoli R, Sorace L (2007) The origin of transverse anisotropy in axially symmetric single molecule magnets. J Am Chem Soc 129:10754–10762
225. Christou G, Gatteschi D, Hendrickson DN, Sessoli R, (2000) Single-molecule magnets. MRS Bull 25:66–71
226. Leuenberger MN, Loss D (2001) Quantum computing in molecular magnets. Nature 410:789–793
227. Troiani F, Ghirri A, Affronte M, Carretta S, Santini P, Amoretti G, Piligkos S, Timco G, Winpenny REP (2005) Molecular engineering of antiferromagnetic rings for quantum computation. Phys Rev Lett 94:207208–207211
228. Lehmann J, Gaita-Ariño A, Coronado E, Loss D (2007) Spin qubits with electrically gated polyoxometalate molecules. Nature Nanotechnol 2:312–317
229. Morello A, Stamp PCE, Tupitsyn IS (2006) Pairwise decoherence in coupled spin qubit networks. Phys Rev Lett 97:207206–207209
230. Schlegel C, van Slageren J, Manoli M, Brechin EK, Dressel M (2008) Direct observation of quantum coherence in single-molecule magnets. Phys Rev Lett 101: 147203–147206
231. Rabi II (1937) Space quantization in a gyrating magnetic field. Phys Rev 51:652–654
232. van Slageren J, Vongtragool S, Gorshunov B, Mukhin AA, Karl N, Krzystek J, Telser J, Müller A, Sangregorio C, Gatteschi D, Dressel M (2003) Frequency-domain magnetic resonance spectroscopy of molecular magnetic materials. Phys Chem Chem Phys 5: 3837–3843
233. Mukhin A, Travkin VD, Zvezdin AK, Lebedev SP, Caneschi A, Gatteschi D (1998) Submillimeter spectroscopy of Mn_{12}-Ac magnetic clusters Europhys Lett 44:778–782
234. Kirchner N, van Slageren J, Brechin EK, Dressel M (2005) Frequency domain magnetic resonance spectroscopy on $[Mn_{12}]^-$ and $[Mn_9]$: zero-field splittings and lineshape analysis. Polyhedron 24:2400–2404
235. Wernsdorfer W, Sessoli R (1999) Quantum phase interference and parity effects in magnetic molecular clusters. Science 284:133–135
236. Mannini M, Pineider F, Danieli C, Totti F, Sorace L, Sainctavit Ph, Arrio MA, Otero E, Joly L, Criginski Cezar J, Cornia A, Sessoli R (2010) Quantum tunnelling of the magnetization in a monolayer of oriented single-molecule magnets. Nature 468:417–421
237. Barra AL, Debrunner P, Gatteschi D, Schulz CE, Sessoli R (1996) Superparamagnetic-like behavior in an octanuclear iron cluster. Europhys Lett 35:133–138
238. Barra AL, Gatteschi D, Sessoli R (2000) High-frequency EPR spectra of $[Fe_8O_2(OH)_{12}(tacn)_6]Br_8$: a critical appraisal of the barrier for the reorientation of the magnetization in single-molecule magnets. Chem Eur J 6:1608–1614

239. Barra AL, Bencini F, Caneschi A, Gatteshi D, Paulsen C, Sangregorio C, Sessoli R, Sorace L (2001) Tuning the magnetic properties of the high-spin molecular cluster Fe_8. ChemPhysChem 2:523–531
240. Fominaya F, Gandit P, Gaudin G, Chaussy J, Sessoli R, Sangregorio C (1999) Heat capacity anomalies in Fe_8 single crystal. J Magn Magn Mater 195:L253–L255
241. Sangregorio C, Ohm T, Paulsen C, Sessoli R, Gatteschi D (1997) Quantum tunneling of the magnetization in an iron cluster nanomagnet. Phys Rev Lett 78:4645–4648
242. Wernsdorfer W, Sessoli R (1999) Quantum phase interference and parity effects in magnetic molecular clusters. Science 284:133–135
243. Wernsdorfer W, Sessoli R, Caneschi A, Gatteschi D, Cornia A (2000) Nonadiabatic Landau-Zener tunneling in Fe_8 molecular nanomagnets. Europhys Lett 50:552–558
244. Wernsdorfer W, Chiorescu I, Sessoli R, Gatteschi D, Mailly D (2000) Quantum phase interference in magnetic molecular clusters. Physca B 284–288:1231–1232
245. Wernsdorfer W, Sessoli R, Caneschi A, Gatteschi D, Cornia A, Mailly D (2000) Landau–Zener method to study quantum phase interference of Fe_8 molecular nanomagnets. J Appl Phys 87:5481–5486
246. Sessoli R, Caneschi A, Gatteschi D, Sorace L, Cornia A, Wernssdorfer W (2001) Isotopic effect on the quantum tunneling of the magnetization of molecular nanomagnets. J Magn Magn Mater 226–230:1954–1960
247. Maccagnano S, Achey R, Negusse E, Lussier A, Mola MM, Hill S, Dalal NS (2001) Single crystal EPR determination of the spin Hamiltonian parameters for Fe_8 molecular clusters. Polyhedron 20:1441–1445
248. Barra AL, Debrunner P, Gatteschi D, Schulz E, Sessoli R (1996) Superparamagnetic-like behavior in an octanuclear iron cluster. Europhys Lett 35:133–138
249. Barra AL, Gatteschi D, Sessoli R (2000) High-frequency EPR spectra of $[Fe_8O_2(OH)_{12}(tacn)_6]Br_8$: a critical appraisal of the barrier for the reorientation of the magnetization in single-molecule magnets. Chem Eur J 6:1608–1614
250. Caciuffo R, Amoretti G, Murani A, Sessoli R, Caneschi A, Gatteschi D (1998) Neutron spectroscopy for the magnetic anisotropy of molecular clusters. Phys Rev Lett 81:4744–4747
251. Mukhin A, Gorshunov B, Dressel M, Sangregorio C, Gatteschi D (2001) Optical spectroscopy of crystal-field transitions in the molecular magnet Fe_8. Phys Rev B63:214411–214417
252. Petukhov K, Wernsdorfer W, Barra AL, Mosser V (2005) Resonant photon absorption in Fe_8 single-molecule magnets detected via magnetization measurements. Phys Rev B72:052401–052404
253. Cage B, Russek SE, Zipse D, Dalal NS (2005) Advantages of superconducting quantum interference device-detected magnetic resonance over conventional high-frequency electron paramagnetic resonance for characterization of nanomagnetic materials. J Appl Phys 97:10 M507–10M507-3
254. Cage B, Russek SE, Zipse D, North JM, Dalal NS (2005) Resonant microwave power absorption and relaxation of the energy levels of the molecular nanomagnet Fe_8 using superconducting quantum interference device-based magnetometry. Appl Phys Lett 87:082501–082503
255. Artus P, Boskovic C, Yoo J, Streib WE, Brunel LC, Hnedrickson DN, Christou G (2001) Single-molecule magnets: site-specific ligand abstraction from $[Mn_{12}O_{12}(O_2CR)_{16}(H_2O)_4]$ and the preparation and properties of $[Mn_{12}O_{12}(NO_3)_4(O_2CCH_2But)_{12}(H_2O)_4]$. Inorg Chem 40:4199–4210
256. Chakov NE, Lee SE, Harter A, Kuhns PL, Reyes AP, Hill SO, Dalal NS, Wernsdorfer W, Abboud KA, Christou G (2006) The properties of the $[Mn_{12}O_{12}(O_2CR)_{16}(H_2O)_4]$ single-molecule magnets in truly axial symmetry: $[Mn_{12}O_{12}(O_2CCH_2Br)_{16}(H_2O)_4]\cdot 4CH_2Cl_2$. J Am Chem Soc 128:6975–6989
257. Tasiopoulos AJ, Wernsdorfer W, Abboud K, Christou G (2004) A reductive-aggregation route to $[Mn_{12}O_{12}(OMe)_2(O_2CPh)_{16}(H_2O)_2]^{2-}$ single-molecule magnets related to the $[Mn_{12}]$ family Angew Chem Int Ed 43:6338–6342. (b) Tasiopoulos AJ, Wernsdorfer W, Abboud K, Christou G (2005) $[Mn_{12}O_{12}(OMe)_2(O_2CPh)_{16}(H_2O)_2]^{2-}$ single-molecule magnets and other manganese compounds from a reductive aggregation procedure. Inorg Chem 44:6324–6338

258. Stamatatos TC, Foguet-Albiol D, Stoumpos CC, Raptopoulou CP, Terzis A, Wernsdorfer W, Perlepes SP, Christou G (2005) Initial example of a triangular single-molecule magnet from ligand-induced structural distortion of a $[Mn_3{}^{III}O]^{7+}$ Complex. J Am Chem Soc 127: 15380–15381
259. Aubin SMJ, Wemple MW, Adams DM, Tsai HL, Christou G, Hendrickson DN (1996) Distorted $Mn^{IV}Mn_3{}^{III}$ cubane complexes as single-molecule magnets. J Am Chem Soc 118:7746–7754
260. Lecren L, Wernsdorfer W, Li YG, Roubeau O, Miyasaka H, Clérac R (2005) Quantum tunneling and quantum phase interference in a $[Mn_2{}^{II}Mn_2{}^{III}]$ single-molecule magnet. J Am Chem Soc 127:11311–11317
261. Milios CJ, Vinslava A, Wernsdorfer W, Moggach S, Parsons S, Perlepes SP, Christou G, Brechin EK (2007) A record anisotropy barrier for a single-molecule magnet. J Am Chem Soc 129: 2754–2755
262. Saalfrank RW, Scheurer A, Prakash R, Heinemann FW, Nakajima T, Hampel F, Leppin R, Pilawa B, Rupp H, Müller P (2007) Synthesis, redox, and magnetic properties of a neutral, mixed-valent heptanuclear manganese wheel with S = 27/2 high-spin ground state. Inorg Chem 46:1586–1592
263. Murugesu M, Wernsdorfer W, Christou G, Brechin EK (2007) New derivatives of an enneanuclear Mn SMM. Polyhedron 26:1845–1848
264. Sanudo EC, Wernsdorfer W, Abboud KA, Christou G (2004) Synthesis, structure, and magnetic properties of a Mn_{21} single-molecule magnet. Inorg Chem 43:4137–4144
265. Soler M, Wernsdorfer W, Folting K, Pink M, Christou G (2004) Single-molecule magnets: a large Mn_{30} molecular nanomagnet exhibiting quantum tunneling of magnetization. J Am Chem Soc 126:2156–2165
266. Barra AL, Debrunner P, Gatteschi D, Schulz CE, Sessoli R (1996) Superparamagnetic-like behavior in an octanuclear iron cluster. Europhys Lett 35:133–138
267. Zhu YY, Guo X, Cui C, Wang BW, Wang ZM, Gao S (2011) An enantiopure $Fe_4{}^{III}$ single-molecule magnet. Chem Commun 47:8049–8051
268. Powell GW, Lancashire HN, Brechin EK, Collison D, Heath SL, Mallah T, Wernsdorfer W (2004) Building molecular minerals: all ferric pieces of molecular magnetite. Angew Chem Int Ed 43:5772–5775
269. Kanegawa S, Karasawa S, Nakano M, Koga N (2006) Magnetic properties of 1:4 Complexes of $Co^{II}X_2$ (X = NCO^-, NCS^-, and Br^-) with 4-(n-tert-butylaminoxyl)pyridine antiferromagnets in crystalline states and single-molecule magnets in frozen solutions. Bull Chem Soc Jpn 79:1372–1382
270. Tobinaga H, Suehiro M, Ito T, Zhou G, Karasawa S, Koga N (2007) Magnetic property of 1:2 mixture of $Co(p\text{-tolsal})_2$; p-tolsal = n-p-tolylsalicylideniminato, and cyclic pentacarbene–pyridine with S = 10/2 in dilute frozen solution. Polyhedron 26:1905–1911
271. Oshio H, Nihei M, Yoshida A, Nohiri H, Nakano M, Yamaguchi A, Karaki Y, Ishimoto H (2005) A dinuclear Mn^{III}–Cu^{II} single-molecule magnet. Chem Eur J 11:843–848
272. Sokol JJ, Hee AG, Long JR (2002) A cyano-bridged single-molecule magnet: slow magnetic relaxation in a trigonal prismatic $MnMo_6(CN)_{18}$ Cluster. J Am Chem Soc 124:7656–7657
273. Freedman DE, Jenkins DM, Iavarone AT, Long JR (2008) A redox-switchable single-molecule magnet incorporating $[Re(CN)_7]^{3-}$. J Am Chem Soc 130:2884–2885
274. Bogani L, Wernsdorfer W (2008) Molecular spintronics using single-molecule magnets. Nat Mater 7:179–186
275. Sakai M, Toyada J, Mitsumi M, Nakasuji K, Furukawa K, Shiomi D, Sato K, Takui T (2001) Low-dimensional molecule-based magnets with hydrogen-bonded network. Synth Metals 121:1776–1777
276. Matsuoka H, Yoshida T, Kubono K, Sato K, Shiomi D, Furukawa K, Kato T, Yokoi K, Takui T (2003) Pseudo-octahedral high-spin Co(II) complexes with orbitally degenerate ground states as studied by SQUID and ESR spectroscopy. Synth Met 137:1213–1214
277. Sakai M, Toyada J, Furukawa K, Mitsumi M, Sato K, Shiomi D, Nakasuji K, Takui T (to be published)

278. Hirota N, Weissman SI (1964) Electronic interaction in ketyl radicals. J Am Chem Soc 86:2538–2545
279. For pulse-ESR based electron spin transient nutation spectroscopy and applications to transition assignments of fine structure ESR spectra, refer to the following chapter and also see (a) Isoya J, Kanda H, Norris JR, Tang J, Bowman MK (1990) Fourier-transform and continuous-wave EPR studies of nickel in synthetic diamond – site and spin multiplicity. Phys Rev B 41:3905–3913; (b) Astashkin AV, Schweiger A (1990) Electron-spin transient nutation – a new approach to simplify the interpretation of ESR-spectra. Chem Phys Lett 174:595–602; (c) Sato K, Shiomi D, Takui T, Itoh K, Kaneko T, Tsuchida E, Nishide H (1994) FT pulsed EPR/transient quantum spin nutation spectroscopy applied to inorganic high-spin systems and a high-spin polymer as models for organic ferromagnets. J Spectrosc Soc Jpn 43:280–291
280. For pulse-ESR based electron spin transient nutation spectroscopy applied to hyperfine fine-structure spectroscopy, see Matsuoka H, Sato K, Shiomi D, Takui T (2003) 2-D electron spin transient nutation spectroscopy of lanthanoid ion $Eu^{2+}(^8S_{7/2})$ in a CaF_2 single crystal on the basis of FT-pulsed electron spin resonance spectroscopy: transition moment spectroscopy. Appl Magn Reson 23:517–538
281. Nakazawa S, Sato K, Shiomi D, Yano M, Kinoshita T, Franco MLTMB, Lazana MCRLR, Shohoji MCBL, Itoh K, Takui T (2011) Organic polyanionic high-spin molecular clusters: topological-symmetry controlled models for organic ferromagnetic metals. Phys Chem Chem Phys 13:1424–1433; (b) Shohoji MCBL, Franco MLTMB, Lazana MCRLR, Nakazawa S, Sato K, Shiomi D, Itoh K, Takui T (to be published)
282. Nakazawa S, Sato K, Shiomi D, Franco MLTMB, Lazana MCRLR, Shohoji MCBL, Itoh K, Takui T (2008) Electronic and molecular structures of C_{60}-based polyanionic high-spin molecular clusters: direct spin identification and electron spin transient nutation spectroscopy for high-spin chemistry. Inorg Chim Acta 361:4031–4037
283. Nakamura T, Nakazawa S, Sato K, Shiomi D, Takui T, Shida T, Itoh K unpublished work
284. Morita Y, Aoki T, Fukui K, Nakazawa S, Tamaki K, Suzuki S, Fuyuhiro A, Yamamoto K, Sato K, Shiomi D, Naito A, Takui T, Nakasuji K (2002) A new trend in phenalenyl chemistry: a persistent neutral radical, 2,5,8-tri-tert-butyl-1,3-diazaphenalenyl, and the excited triplet state of the gable *syn*-dimer in the crystal of column motif. Angew Chem Int Ed 41:1793–1796
285. Goto K, Kubo T, Yamamoto K, Nakasuji K, Sato K, Shiomi D, Takui T, Kubota M, Kobayashi T, Yakushi K, Ouyang J (1999) A stable neutral hydrocarbon radical: Synthesis, crystal structure, and physical properties of 2,5,8-tri-tert-butyl-phenalenyl. J Am Chem Soc 121:1619–1620
286. Kubo R, Tomita K (1954) A general theory of magnetic resonance absorption. J Phys Soc Jpn 9:888–919
287. (a) Pilawa B, Ziegler J (1996) Spin and charge distribution in hexaperylene hexafluorophosphate, $(C_{20}H_{12})_6PF_6$. Syn Met 82:53–58; (b) Wolter A, Fasol U, Jaeppelt R, Dormann E (1996) Perylene radical cation salts with a five-eighths-filled conduction band: an ESR analysis. Phys Rev B 54:12272–12282
288. (a) Shiomi D, Nishizawa M, Sato K, Takui T, Itoh K, Sakurai H, Izuoka A, Sugawara T (1997) A prerequisite for purely organic molecule-based ferrimagnetics: breakdown of simple classical pictures. J Phys Chem B 101:3342–3348; (b) Nishizawa M, Shiomi D, Sato K, Takui T, Itoh K, Sawa H, Kato R, Sakurai H, Izuoka A, Sugawara T (2000) Evidence for the breakdown of simple classical pictures of organic molecule-based ferrimagnetics: low-temperature crystal structure and single-crystal ESR studies of an organic heterospin system. J Phys Chem B 104:503–509
289. Nagata K, Tazuke Y (1972) Short-range order effects on EPR frequencies in Heisenberg linear chain antiferromagnets. J Phys Soc Jpn 32:337–345

290. Only typical examples are cited in the following: (a) Oshima K, Okuda K, Date M (1976) g-shift in low dimensional antiferromagnets at low-temperatures. J Phys Soc Jpn 41:475–480; (b) Pilawa B, Pietrus T (1995) Magnetic-properties of the one-dimensional Heisenberg-antiferromagnet tetraphenylverdazyl. J Magn Magn Mat 150:165–174; (c) Stanger JL, Andre JJ, Turek P, Hosokoshi Y, Tamura M, Kinoshita M, Rey P, Cirujeda J, Veciana J (1997) Role of the demagnetizing field on the EPR of organic radical magnets. Phys Rev B 55:8398–8405
291. Benner H, Boucher JP (1990) In: de Jongh LJ (ed) Magnetic properties of layered transition metal compounds. Kluwer Academic, Dordrecht
292. Turek P (1993) Spin correlations in organic radical magnets. Mol Cryst Liq Cryst 232:551–567
293. (a) Latimer MJ, DeRose VJ, Mukerji I, Yachandra VK, Sauer K, Klein MP (1995) Evidence for the proximity of calcium to the manganese cluster of photosystem II – determination by x-ray-absorption spectroscopy. Biochemistry 34:10898–10909; (b) Tyryshkin AM, Watt RK, Baranov SV, Dasgupta J, Hendrich MP, Dismukes GC (2006) Spectroscopic evidence for Ca^{2+} involvement in the assembly of the Mn_4Ca cluster in the photosynthetic water-oxidizing complex. Biochemistry 45:12876–12889; (c) Kulik LV, Epel B, Lubitz W, Messinger J (2005) Mn-55 pulse ENDOR at 34 GHz of the S_0 and S_2 states of the oxygen-evolving complex in photosystem II. J Am Chem Soc 127:2392–2393; (d) Kulik LV, Epel B, Lubitz W, Messinger J (2007) Electronic structure of the Mn_4O_xCa cluster in the S_0 and S_2 states of the oxygen-evolving complex of photosystem II based on pulse Mn-55-ENDOR and EPR Spectroscopy. J Am Chem Soc 129:13421–13435; (e) Schinzel S, Schraut J, Arbuznikov AV, Siegbahn PEM, Kaupp M (2010) Density functional calculations of (55)Mn, (14)N and (13)C electron paramagnetic resonance parameters support an energetically feasible model system for the S_2 state of the oxygen-evolving complex of photosystem II. Chem A Eur J 16:10424–10438; (f) Boussac A, Sugiura M, Rutherford AW, Dorlet R (2009) Complete EPR Spectrum of the S_3-tate of the oxygen-evolving photosystem II. J Am Chem Soc 131:5050–5051; (g) Joliot P, Barbieri G, Chabaud R (1969) A new model of photochemical centers in system-2. Photochem Photobiol 10:309–329
294. Kok B, Forbush B, McGloin M (1970) Cooperation of charges in photosynthetic o2 evolution.1. a linear 4step mechanism. Photochem Photobiol 11:457–475
295. Debus RJ (1992) The manganese and calcium-ions of photosynthetic oxygen evolution. Biochim Biophys Acta 1102:269–352
296. Witt HT (1996) Primary reactions of oxygenic photosynthesis. Ber Bunsenges Phys Chem 100:1923–1942
297. Britt RD (1996) In: Ort DR Yocum (eds) Oxygenic photosynthesis – the light reactions, Kluwer, Dordrecht, pp 137–164
298. Yachandra VK, Sauer K, Klein MP (1996) Manganese cluster in photosynthesis: where plants oxidize water to dioxygen. Chem Rev 96:2927–2950
299. Saygin Ö, Witt HT (1985) Sequence of the redox changes of manganese and pattern of the changes of charges during water cleavage in photosynthesis – optical events in the UV and the red region in the presence and absence of hydroxylamine. Photobiochem Photobiophys 10:71–81
300. Beck WF, Brudvig GW (1987) Reactions of hydroxylamine with the electron-donor side of photosystem-II. Biochemistry 26:8285–8295
301. Messinger J, Renger G (1993) Generation, oxidation by the oxidized form of the tyrosine of polypeptide D2, and possible electronic configuration of the redox state-S_0, state-S_1, and state-S_2 of the water oxidase in isolated spinach thylakoids. Biochemistry 32:9379–9386
302. Riggs-Gelasco PJ, Mei R, Yocum CF, Penner-Hahn JE (1996) Reduced derivatives of the Mn cluster in the oxygen-evolving complex of photosystem II: An EXAFS study. J Am Chem Soc 118:2387–2399
303. Messinger J, Seaton G, Wydrzynski T, Wacker U, Renger G (1997) S_3 state of the water oxidase in photosystem II. Biochemistry 36:6862–6873
304. Yachandra VK, Sauer K, Klein MP (1996) Manganese cluster in photosynthesis: where plants oxidize water to dioxygen. Chem Rev 96:2927–2950

305. Schiller H, Dettmer J, Iuzzolino L, Dörner W, Meyer-Klaucke W, Solé VA, Nolting HF, Dau H (1998) Structure and orientation of the oxygen-evolving manganese complex of green algae and higher plants investigated by X-ray absorption linear dichroism spectroscopy on oriented photosystem II membrane particles. Biochemistry 37:7340–7350
306. Penner-Hahn JE (1998) In Hill HAO, Sadler PJ, Thomson AJ (eds) Metal sites in proteins and models-redox centres. Springer, Berlin, pp 1–36
307. DeRose VJ, Mukerji I, Latimer MJ, Yachandra VK, Sauer K, Klein MP (1994) Comparison of the manganese oxygen-evolving complex in photosystem-II of spinach and synechococcus sp with multinuclear manganese model compounds by X-ray-absorption spectroscopy. J Am Chem Soc 116:5239–5249
308. Dismukes GC, Siderer Y (1981) Intermediates of a polynuclear manganese center involved in photosynthetic oxidation of water. Proc Natl Acad Sci USA 78:274–278
309. Review Article; Debus RJ (1992) The manganese and calcium-ions of photosynthetic oxygen evolution. Biochim Biophys Acta 1102:269–352
310. Peloquin JM, Campbell KA, Randall DW, Evanchik MA, Pecoraro VL, Armstrong WH, Britt RD (2000) Mn-55 ENDOR of the S_2-state multiline EPR signal of photosystem II: implications on the structure of the tetranuclear Mn cluster. J Am Chem Soc 122: 10926–10942
311. Haddy A, Dunham WR, Sands RH, Aasa R (1992) Multifrequency ESR investigations into the origin of the S_2-state signal at $g = 4$ of the O_2-evolving complex. Biochim Biophys Acta 1099:25–34
312. Astashkin AV, Kodera Y, Kawamori A (1994) Pulsed EPR study of manganese g = 4.1 signal in plant photosystem-II. J Magn Reson 105:113–119
313. Hansson O, Aasa R, Vanngard T (1987) The origin of the multiline and g = 4.1 electron-paramagnetic resonance signals from the oxygen-evolving system of photosystem-II. Biophys J 51:825–832
314. Smith PJ, Åhrling KA, Pace RJ (1993) Nature of the S_2 state electron-paramagnetic-resonance signals from the oxygen-evolving complex of photosystem-II – Q-band and oriented X-band studies. J Chem Soc Faraday Trans I 89:2863–2868
315. Boussac A, Un S, Horner O, Rutherford AW (1998) High-spin states (S > = 5/2) of the photosystem II manganese complex. Biochemistry 37:4001–4007
316. Messinger J, Nugent JHA, Evans MCW (1997) Detection of an EPR multiline signal for the S-0 state in photosystem II. Biochemistry 36:11055–11060
317. Åhrling KA, Peterson S, Styring S (1997) An oscillating manganese electron paramagnetic resonance signal from the S_0 state of the oxygen evolving complex in photosystem II. Biochemistry 36:13148–13152
318. Messinger J, Robblee JH, Yu WO, Sauer K, Yachandra VK, Klein MP (1997) The S-0 state of the oxygen-evolving complex in photosystem II is paramagnetic: detection of EPR multiline signal. J Am Chem Soc 119:11349–11350
319. Åhrling KA, Peterson S, Styring S (1998) The S_0 state EPR signal from the Mn cluster in photosystem II arises from an isolated S = 1/2 ground state. Biochemistry 37:8115–8120
320. Campbell KA, Peloquin JM, Pham DP, Debus RJ, Britt RD (1998) Parallel polarization EPR detection of an S_1-state "multiline" EPR signal in photosystem II particles from Synechocystis sp. PCC 6803. J Am Chem Soc 120:447–448
321. Campbell KA, Gregor W, Pham DP, Peloquin JM, Debus RJ, Britt RD (1998) The 23 and 17 kDa extrinsic proteins of photosystem II modulate the magnetic properties of the S_1-state manganese cluster. Biochemistry 37:5039–5045
322. Dexheimer SL, Klein MP (1992) Detection of a paramagnetic intermediate in the s1-state of the photosynthetic oxygen-evolving complex. J Am Chem Soc 114:2821–2826
323. Yamauchi T, Mino H, Matsukawa T, Kawamori A, Ono T (1997) Parallel polarization electron paramagnetic resonance studies of the S_1-state manganese cluster in the photosynthetic oxygen-evolving system. Biochemistry 36:7520–7526
324. Matsukawa T, Mino H, Yoneda D, Kawamori A (1999) Dual-mode EPR study of new signals from the S_3-state of oxygen-evolving complex in photosystem II. Biochemistry 38:4072–4077

325. Ioannidis N, Petrouleas V (2000) Electron paramagnetic resonance signals from the S_3 state of the oxygen-evolving complex. A broadened radical signal induced by low-temperature near-infrared light illumination. Biochemistry 39:5246–5254
326. Messinger J, Robblee JH, Bergmann U, Fernandez C, Glatzel P, Visser H, Cinco RM, McFarlane KL, Bellacchio E, Pizarro SA, Cramer SP, Sauer K, Klein MP, Yachandra VK (2001) Absence of Mn-centered oxidation in the S-2 - > S-3 transition: implications for the mechanism of photosynthetic water oxidation. J Am Chem Soc 123:7804–7820
327. Morita Y, Suzuki S, Fukui K, Nakazawa S, Sato K, Shiomi D, Takui T, Nakasuji K (to be published)
328. (a) Ishimaru Y, Inoue K, Koga N, Iwamura H (1994) Structures and magnetic-properties of bis(hexafluoroacetylacetonato)manganese(II) ligated with n-[3- and 4-(n-tert-butyl-n-oxyaminophenyl)]imidazole. Chem Lett 1693–1696; (b) Kitano M, Ishimaru Y, Inoue K, Koga N, Iwamura H (1994) Exchange interaction in metal radical systems – chloro(meso-tetraphenylporphyrinato)chromium(III)s and (hexafluoroacetylacetonato)manganese(II) ligated with 3-(n-oxy-n-tert- and 4-(n-oxy-n-tert-butylamino)pyridines. Inorg Chem 33:6012–6019; (c) Iwamura H, Koga N (1999) The metal-dependent regiospecificity in the exchange coupling of manganese(II), copper(II), and chromium (III) ions with the aminoxyl radical attached as a substituent on the aromatic base ligands. Mol Cryst Liq Cryst 334:437–457
329. Field LM, Lahti PM, Palacio F (2002) 1:1 Complexes of 5-(4-[N-tert-butyl-N-aminoxyl]phenyl) pyrimidine with manganese(II) and copper(II) hexafluoroacetonylacetonate. J Chem Soc (Chem Commun) 2002:636–637
330. Sato K, Shiomi D, Takui T (to be published)
331. Ayabe K, Nishida S, Sato K, Ise T, Nakazawa S, Sugisaki K, Morita Y, Toyota K, Shiomi D, Kitagawa M, Takui T (2012) Pulsed electron spin nutation spectroscopy of weakly exchange-coupled biradicals: a general theoretical approach and determination of the spin dipolar interaction. Phys Chem Chem Phys 14:9137–9148

Chapter 4
Novel Applications of ESR/EPR: Quantum Computing/Quantum Information Processing

Kazunobu Sato, Shigeaki Nakazawa, Shinsuke Nishida, Robabeh D. Rahimi, Tomohiro Yoshino, Yasushi Morita, Kazuo Toyota, Daisuke Shiomi, Masahiro Kitagawa, and Takeji Takui

Abstract A qubit (quantum bit) is a quantum mechanical two-state system. The qubit can afford to give an arbitrary superposition of quantum states, and it has substantially higher complication than a classical bit. A canonical example of the qubit is the matter spin with spin-1/2. Thus, electrons with the spin quantum number 1/2, as physical qubits, have naturally been anticipated for implementing quantum computing and information processing (QC/QIP). Recently, electron spin-qubit systems in organic molecular frames such as extremely stable radicals have emerged as a hybrid spin-qubit system along with a nuclear spin-1/2 qubit, termed molecular electron-bus qubits. Indeed, molecular electron spins are the latest arrival as qubits. Among promising candidates for QC/QIP from the materials science side, the reasons why electron spin-qubits such as synthetic electron spin systems, i.e., unpaired electron spins in molecular frames, have potentialities for serving for QC/QIP are briefly described in this chapter. Issues relevant to synthetic multi-electron qubit systems are important for the implementation of qubit scalability, but are not included. Compared with NMR-based QC/QIP, pulse ESR-based QC/QIP is totally immature, simply because of the intrinsic technical restrictions and decoherence inherent in electron spins in ensemble physical systems. In terms of the linkage between QC/QIP and pulsed electron magnetic resonance as enabling

K. Sato • S. Nakazawa • S. Nishida • R.D. Rahimi • T. Yoshino • K. Toyota • D. Shiomi • T. Takui (✉)
Department of Chemistry and Molecular Materials Science, Graduate School of Science, Osaka City University, 3–3–138 Sugimoto, Sumiyoshi-ku, Osaka 558–8585, Japan
e-mail: takui@sci.osaka-cu.ac.jp

Y. Morita
Department of Chemistry, Graduate School of Science, Osaka University, 1–1 Machikaneyama, Toyonaka, Osaka 560–0043, Japan

M. Kitagawa
Department of System Innovation, Graduate School of Engineering Science, Osaka University, 1–3 Machikaneyama, Toyonaka, Osaka 560–8531, Japan

A. Lund and M. Shiotani (eds.), *EPR of Free Radicals in Solids II*, Progress in Theoretical Chemistry and Physics 25, DOI 10.1007/978-94-007-4887-3_4,

ensemble-spin manipulation technology, there are many important and emerging issues. The linkage between QC/QIP and chemistry or materials science is also important, providing insights into the quest for practically scalable spin qubits. In this chapter, we only emphasize that current pulsed electron magnetic resonance enables us to manipulate an electron spin and nuclear spin qubits in an equivalent manner. Super dense coding (SDC) experiments by the use of pulse ENDOR are introduced to understand QC ENDOR and how it differs from QC NMR based on modern nuclear spin technology. Direct observation of the spinor inherent in an electron spin, detected for the first time, will be shown in connection with the entanglement of an electron-nuclear hybrid system (the simplest electron-bus system).

4.1 Introduction

4.1.1 General Introduction

During the last decades, implementation of quantum computers, which are conceived of all the advantages of quantum computing (QC) and quantum information processing (QIP), has been the focus of the contemporary issues in quantum science and related fields [1, 2]. Among various physical systems for qubits, photon qubits have recently been utilized for quantum information communications in our ordinary life. Quantum cryptography has been used to protect Swiss Federal Election in October, 2007 against hacking into the database or accidental data corruption. Also, in October, 2010, field work on quantum communication was carried out in Tokyo. These exemplify that QC/QIP is a really emerging technology from the practical side. QC/QIP technology promises to solve problems that are intractable on currently available digital classical computers.

Quantum algorithms can reduce the CPU time for some important problems by many orders of magnitude. An important advantage of QC is the rapid parallel execution of logic operations carried out by quantum entangled (superposition) states. For example, with the same input and output, the quantum processing of given information data represents exponential speed-up for factorization by the Shor algorithm [3] and quadratic speed-up for search problems using the Grover algorithm [4]. Also, by the implementation of the quantum information algorithms such as quantum teleportation [5] and quantum super dense coding [6], some intrinsic advantages can be achieved compared with the classical information processing. From the theoretical side, quantum information processing and quantum computation have been established considerably well during the last decades [2]. A road map to the goal of building practical quantum computers (QCs) shows problems to be solved such as the establishment and possible utilization of the entangled states, the implementation of quantum simulators (digital or analog), the preparation of scalable qubits, the creation and storage of quantum data bases and the implementation of novel QC algorithms.

4.1.2 What Is Entanglement?

This Section gives a brief description of entanglement between quantum states or the entangled states, which constitute a central issue and necessary property for QC/QIP. As well known, multi-partite systems are described by density matrix formalism, which includes the statistical distribution of the multi-partite states and the superposition of the states. This implies that entangled states are primarily included in the treatment.

The superposition of the states is described by a linear combination of the eigenstates. For simplicity, we consider a bi-partite system whose parts, A and B, are simple qubits. Their eigenvalues are 0 and 1. For the two-qubit system, we have the following four basis of product states:

$$\{ |0_A 0_B>,\ |0_A 1_B>,\ |1_A 0_B>,\ |1_A 1_B> \}$$

These four basis vectors span a four-dimensional complex vector space, implying that the tensor product, i.e., the Hilbert space of the two qubits A and B is isomorphic to the four-dimensional Hilbert space of the two-qubit system. In other words, the tensor product composed of the one-qubit subspaces does not cover all the states of the four-dimensional Hilbert space. In the four-dimensional Hilbert space, another basis is available, defined as

$$|\Psi_{even}{}^{\pm}> = (\ |0_A 0_B> \pm |1_A 1_B>\ )/2^{1/2}$$

and

$$|\Psi_{odd}{}^{\pm}> = (\ |0_A 1_B> \pm |1_A 0_B>\ )/2^{1/2}$$

where the states $|\Psi_{even}{}^{\pm}>$ are the superpositions of the product states in which the qubit spins are parallel, called even parity states. The states $|\Psi_{odd}{}^{\pm}>$ are the superpositions of the odd parity states. The basis given by the four states, $|\Psi_{even}{}^{\pm}>$ and $|\Psi_{odd}{}^{\pm}>$, consists of entangled states, called the Bell basis. Thus, a state of a compound system such as AB is termed "entangled" if the state cannot be described as a single tensor product of the subsystem states. When a compound system is written by a single product, the state is unentangled or separable. The above four states are maximally entangled ones, for which the density operators for A and B are $\rho_A = \rho_B = 1/2$.

4.1.3 An Electron Spin as an Inherent Matter Spin-Qubit

In view of the implementation of QC/QIP, an electron spin itself as a matter qubit naturally given in the molecular frame has only lately appeared in the research field

of QC/QIP. An electron spin with the spin quantum number 1/2 is an inherent spin qubit, to which spinor property belongs as a result of quantum relativistic effects. The spinor is a physical quantity of quantum phase that plays an essential role in QC/QIP, but never experimentally nor explicitly observed so far in contrast to a nuclear spin-1/2. Direct observation of the spinor of an electron spin has been detected for the first time in connection with the entanglement of an electron-nuclear hybrid system (the simplest electron-bus system). Some highlighted parts of the observation will be shown in this chapter.

Recently, electron-spin qubit systems in "organic" molecular frames have emerged as a hybrid spin-qubit system with a nuclear spin-1/2 qubit [7–13], where "hybrid" designates the physical qubits composed of electron and nuclear spin-qubits. Here, the electron spin qubit plays a role of "bus", termed by M. Mehring. Physical realization of genuine electron-spin qubit based QC/QIP in the molecular frame is another issue to be tackled by synthetic chemists. This issue is closely linked to the building up of periodic one-dimensional spin assemblages, where a minimum number of unpaired electron spins are embedded in a molecular scale and in an addressable manner. The electron spins are designed to have non-equivalent *g*-tensors in the molecular frame (*g*-tensor engineering).

Among many technologically promising candidates for physical matter qubits [14–17], it is worth noting the reasons why an electron-spin qubit has been the latest arrival in the field of QC/QIP. There have been two major drawbacks of electron spin-qubits in molecular frames, when the unpaired electron spins are utilized as matter qubits. One is a few but crucial technical difficulties intrinsic to decoherence time of the electron-spin qubit, compared with nuclear spin-qubits, and the other is the difficulty in the preparation of the assemblies of the matter electron spin-qubit in terms of materials science: The decoherence time is three orders of magnitude shorter than that of nuclear spin-qubits. This is the case for both in-ensemble electron spin and single-molecule based QC. The issue of decoherence is one of the apparently intractable obstacles for the physical realization of realistic, practical electron spin-qubit based QCs. Taking advantages of long decoherence intrinsic to nuclear spin-qubits and their resonant interactions of radiofrequency pulses, as invoked by current spin manipulation technology, NMR based QC/QIP has successfully illustrated the most significant achievement in terms of implementation of quantum logic gates [2]. Recently, attempts for the quantum entanglement based on electron-nuclear spin systems as matter qubits in ensemble have emerged from the experimental side [7–13], referring to quantum information processing [9, 10, 12]. The entanglement between two 1/2-spins is essential in quantum information science. The occurrence of the entangled spin states in a crystalline solid becomes an important event in solid-state quantum computing. We have applied pulse-based electron-nuclear and electron-electron multiple magnetic resonance (EMR/ENDOR/ELDOR) techniques to molecular spin-based qubits, implementing the ensemble quantum computing in solids [7–13]. This chapter describes only some parts of our work on ENDOR based QC/QIP and important QC-ENDOR related spin techniques recently carried out by other groups, particularly by Mehring and coworkers.

The second drawback described above, i.e., the difficulty in the preparation of the assemblies of matter electron spin-qubits in molecular frames is closely relevant to an issue of the scalability of qubits for practical true QCs. Indeed, the issue is a materials challenge for chemists and in this context chemistry for QC/QIP is a new field in terms of synthetic strategy. This is an important issue for implementing realistic scalable QCs, but beyond the scope of this chapter.

Any practical QC has to fulfill DiVincenzo's five criteria [18]. Thus, in implementing molecule-based QC ENDOR, the five criteria are the starting point. Particularly, the first criterion, i.e., well defined and scalable qubits, has to be amplified: Molecular hybrid spin-qubits are chemically identified and well characterized in view of molecular and electronic-spin structures. The magnetic tensors of the targeted qubits, the g tensor for bus electrons or hyperfine/quadrupolar tensors for client nuclei, should be determined experimentally prior to the use of the defined qubits. Obviously, the anisotropic tensors are for solid-state QCs and isotropic principal values for QC/QIP in isotropic media like solution.

4.2 A Basis of Spin Manipulation Technology for QC/QIP

4.2.1 Fourier-Transform ESR/ENDOR Spectroscopy: Pulse-Based ESR/ENDOR as Enabling Spin Technology

In the preceding Section, the QC ENDOR technology has briefly been described. Referred to quantum gate operations for QC/QIP, currently there is nothing to do with CW ENDOR in view of spin-qubit manipulation technology. The matter spin qubit based QC/QIP experiments essentially involve the time evolution of relevant quantum spin states. We now come to different aspects of electron magnetic resonance technology, in other words the issues of spin manipulation in the time domain. The issues are to manipulate both electron and nuclear spins in molecular frames in terms of their time evolution and phases, which enable us to discriminate between any quantum spin states against the decoherence. The key technology is the introduction of Fourier-transform techniques to electron magnetic resonance, which makes us utilize intense pulses of MW and RF (radiofrequency) irradiations to generate a coherent superposition of the relevant spin states in ensemble. In this context, the irradiation pulses link the magnetic resonance to matter spin-qubit based QC/QIP. Macroscopic magnetic moments, as the coherent superposition, precessing at frequencies ω_k, ($k = 1$ to K) and with amplitudes A_k emit radiation that corresponds to free induction decay (FID) signals. They are coherently detected and digitized for further procedure of Fourier-transform (FT) analyses. Pulse-based ENDOR spectroscopy utilizes both MW and RF pulses, in which MW radiation signals in FID or electron spin-echo scheme after on-resonance MW excitations are monitored when pulse-based NMR events occur.

In any QC/QIP ENDOR experiments, macroscopic moments of electron and nuclear spin-qubits have to be manipulated in any desired orientations in the Bloch

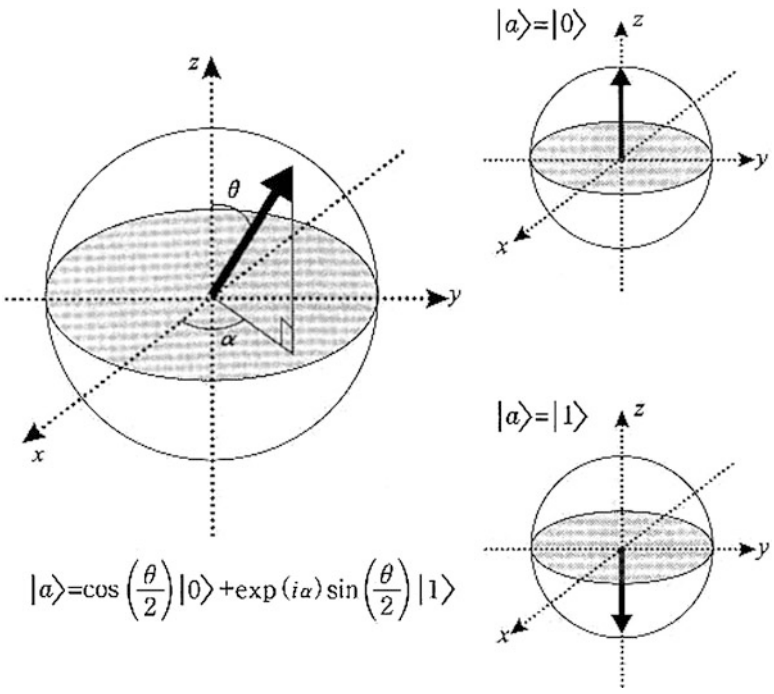

Fig. 4.1 Magnetic moments represented as qubits in the Bloch sphere. The *thick arrow* denotes the moment. The moment in the xy plane of the Bloch sphere is a superposition of the $|0>$ and $|1>$ states with equal weights

sphere, as depicted in Fig. 4.1. When the $\pi/2$ pulse along the x-axis operates on the $|0>$ state, a superposition of the $|0>$ and $|1>$ states with equal weights is generated, as depicted in Fig. 4.2 (1). Figure 4.2 (2) depicts how the direct product composed of the two superpositions is represented in the macroscopic magnetization qubit scheme for simplicity. The representation given in Fig. 4.2 (1) illustrates why the phase manipulation between the qubits is essential for QC/QIP experiments. The π pulse transforms the $|0>$ to the $|1>$ state, exemplifying the NOT-gate operation. NMR spin technology has been much advanced and matured in terms of the pulse-based spin technology, as described earlier in this Section, but in pulse-based FT electron magnetic resonance we lack essential experience of manipulating electron spins themselves due to the technical difficulties.

In order to illustrate the entanglement between an electron spin-qubit and nuclear spin-qubits, quantum phases belonging to the spin states are utilized. QC types of experiments, in which the quantum phases are controlled and manipulated, have never been carried out and are neither necessary nor useful for ordinary pulsed magnetic resonance spectroscopy. In this context, the implementation of pulse ENDOR QC/QIP may provide new aspects for electron magnetic resonance spectroscopy, as exemplified later.

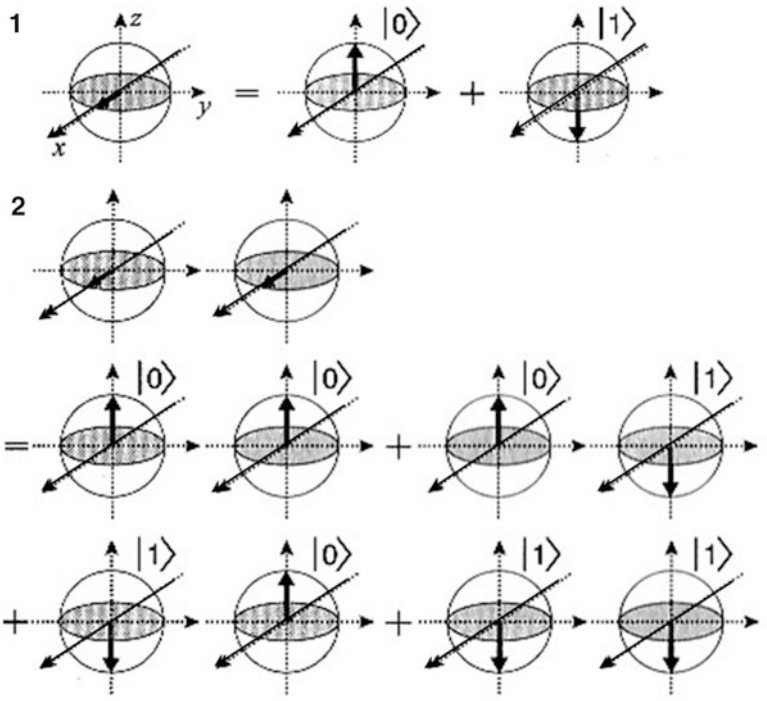

Fig. 4.2 Macroscopic magnetizations of spins in pulse-based spin manipulation technology. (1) A superposition of the $|0>$ and $|1>$ states as generated by the $\pi/2$ pulse applied along the x axis in pulsed magnetic resonance. The *thick arrow* denotes a macroscopic magnetization of spins. (2) A schematic representation of the direct product of the two superpositions in terms of the macroscopic magnetizations. In both (1) and (2), the coefficients associated to the states are omitted for clarity

4.2.2 A Basis of Spin Manipulation Technology for QC/QIP in Pulsed Electron Magnetic Resonance

Figure 4.3 shows how the single MW or RF pulses on resonance, acting on the magnetization aligning originally along the z axis, generate superpositions of the states or quantum gates. All the pulse operations are applied in the rotating frame of the oscillating irradiation field. In Fig. 4.3a, $|\psi>$ is represented by two variables, θ and ϕ. For $\theta = \pi/2$, the cases of $\phi = 0$ and $\pi/2$ generate distinguishable superspositions of the states in terms of the phase. These situations can be achieved in an on-resonance $\pi/2$ pulse irradiation along the y or x axis. Importantly, for a spin-1/2 qubit, the 2π rotation of the magnetization around the x axis does not recover the original state, but changes the sign of the phase and only the 4π rotation does, denoting the spinor property for the spin-1/2 qubit, as described in the following:

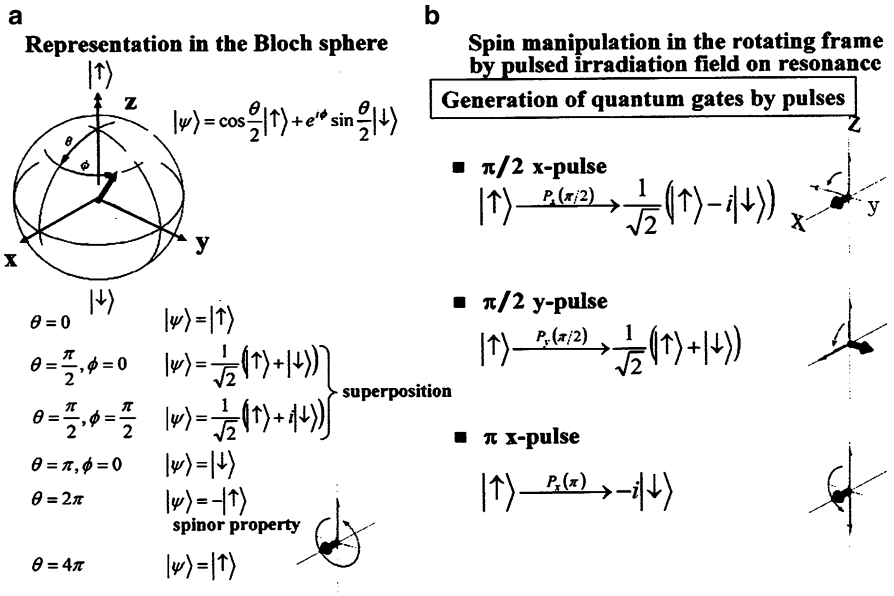

Fig. 4.3 Macroscopic magnetization represented in the Bloch sphere and the role of on-resonance pulses generating various superpositions of the states $|\uparrow>$ and $|\downarrow>$ and quantum gates. All the operations by the pulses are applied in the rotating frame of the oscillating irradiation field. The magnetization is denoted by the *thick arrow* in (**a**) and the *arrow* originally aligning along the z-axis in (**b**). It is noteworthy that for a spin-1/2 qubit the 2π rotation of the magnetization around the x-axis does not recover the original state, but the 4π rotation does, denoting the spinor property for the spin-1/2 qubit (Adapted from Ref. [48] with kind permission of © World Scientific Publishing Co. 2009)

$$R_j(\theta) = e^{(i\theta\sigma_j)/2}$$

which describes the rotation around the *j*-axis with Pauli matrices,

$$\sigma_x = \begin{pmatrix} 0 & 1 \\ 1 & 0 \end{pmatrix},\ \sigma_y = \begin{pmatrix} 0 & -i \\ i & 0 \end{pmatrix},\ \sigma_z = \begin{pmatrix} 1 & 0 \\ 0 & -1 \end{pmatrix}$$

The rotation around the x-axis is given as

$$R_x(\theta) = \mathrm{e}^{(i\theta\sigma_x/2)} = \begin{pmatrix} \cos(\theta/2) & i\sin(\theta/2) \\ i\sin(\theta/2) & \cos(\theta/2) \end{pmatrix}$$

Thus, when the spin is rotated by the angle of 2π, the spin state changes its sign:

$$R_x(2\pi) = \begin{pmatrix} -1 & 0 \\ 0 & -1 \end{pmatrix},\ R_x(2\pi)\begin{pmatrix} 1 \\ 0 \end{pmatrix} = -\begin{pmatrix} 1 \\ 0 \end{pmatrix}$$

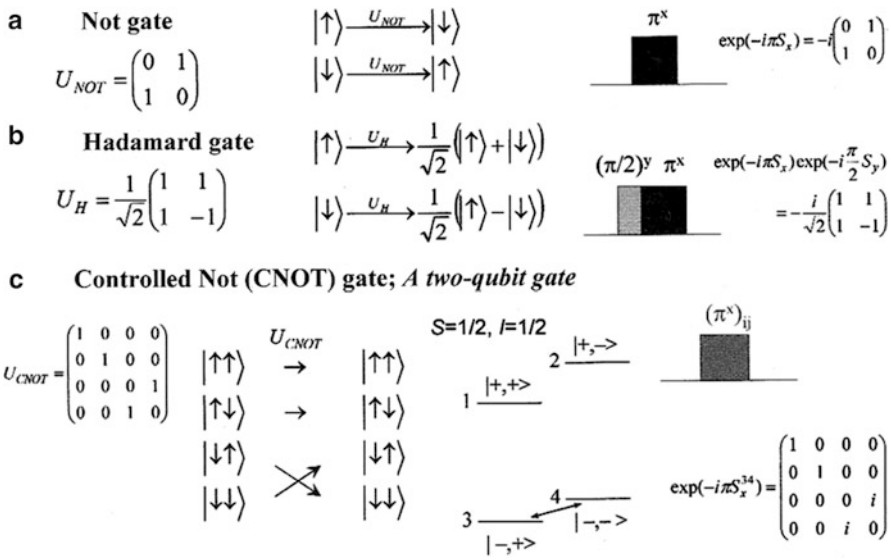

Fig. 4.4 Quantum logic gates, the transformation of the states after the operation and the corresponding electron magnetic resonance pulses. The NOT (**a**) and CNOT (**c**) gate are achieved by the operation of the corresponding single pulse. The Hadamard gate is achieved by the first π/2 pulse applied along the y axis followed by the second π pulse along the x axis. The CNOT (**c**) gate is a two-qubit one, for which the corresponding energy level diagram with the state designation is given. In (**c**), an electron-nuclear hybrid system with one electron spin-qubit and one nuclear spin-1/2 is assumed. The state $|+-\rangle$ designates $|M_s = -1/2, M_I = +1/2\rangle$ and so on (Adapted from Ref. [48] with kind permission of © World Scientific Publishing Co. 2009)

This example illustrates that the double-rotation group is not equivalent to the single-rotation one. Any half integer spin belongs to the former.

In Fig. 4.3b, the bold arrow along a particular axis denotes the axis along which the irradiation pulse is applied. All the situations depicted in Fig. 4.3 are achieved in terms of the rotating frame of the oscillating irradiation of MW or RF with the static magnetic field along the z axis. Practically, it is important to create the stable, narrow and strong pulses of good shapes in spin manipulation technology. MW high-frequency technology still suffers from technical difficulties in power, multiple-frequency production and relative phase control between the multiple frequencies.

Figure 4.4 exemplifies quantum logic gates, the transformation of the states after the operation and the corresponding magnetic resonance pulses. The Hadamard gate in Fig. 4.4b is achieved by the use of two pulses, i.e., the first π/2 pulse along the y axis followed by the second π pulse along the x axis. The Hadamard transformation is performed by a π-rotation around the particular axis π/4-rotated from the z axis in the zx plane. The operation around this particular rotation axis corresponds conventionally to the combination of the two pulses given above in pulsed electron magnetic resonance. In Fig. 4.4, the gate (c) is a controlled-not

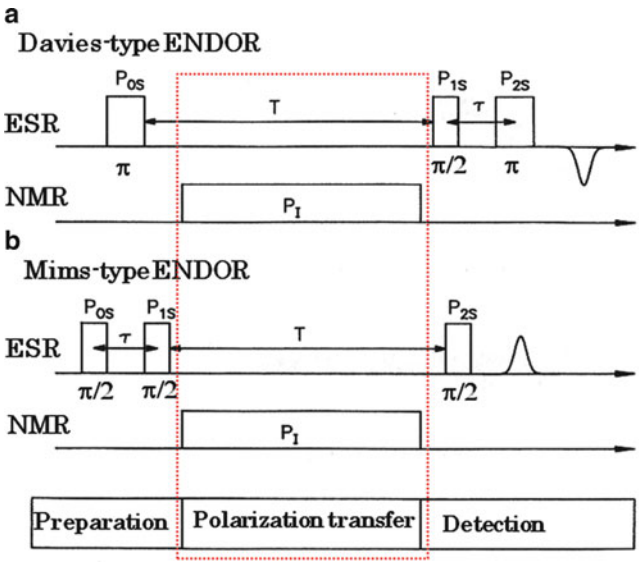

Fig. 4.5 Typical two types of Electron-Spin-Echo (ESE) detected ENDOR techniques: (**a**) Davies-type ENDOR and (**b**) Mims-type ENDOR. Their pulse sequences and timing charts are illustrated, in which MW and RF pulse irradiations are for ESR and NMR transitions, respectively. The period denoted by T is for the transfer of the polarization between particular electron-nuclear sublevels. It should be noted that any change of an ESE signal during the NMR transition driven by the RF pulse is monitored in the detection period

gate composed of two qubits, in which an electron- nuclear hybrid system with one electron spin-qubit and one nuclear spin-1/2 qubit are assumed. The corresponding CNOT gates composed of electron two qubits in molecular frames have not yet been established. The electron-nuclear spin energy level diagram and state designation are given in (c). The transition between the level 3 and 4 corresponds to the ENDOR one which converts the populations of the level 3 and 4 by a π RF pulse applied along the x-axis. Again, all the quantum operations in Fig. 4.4 are achieved in the on- resonance rotating frame of the oscillating irradiation field for electron magnetic resonance.

4.2.3 A Basis for Pulse-Based ENDOR Spin Technology: Two Types of Electron-Spin-Echo Detected ENDOR Spectroscopy

Now, we come to pulse-based ENDOR spin technology. There are typically two types of Electron-Spin-Echo (ESE) detected ENDOR techniques, i.e., Davies-type ENDOR and Mims-type ENDOR. Fig. 4.5 illustrates their pulse sequences and

timing charts, in which MW and RF pulse irradiations are for ESR and NMR transitions, respectively. NMR, i.e., ENDOR signals are detected (= monitored) by an ESE scheme. In Davies-type ENDOR, as depicted in Fig. 4.5a, P_{0S} and P_{2S} are MW π-pulses and P_{1S} is a MW π/2-pulse: P_{0S} with an irradiation strength (converted to the corresponding frequency) $\omega_1 << A$ and P_I denotes the RF pulse applied during the waiting period T. The P_{0S} pulse interchanges the populations of the level 1 and 3, as is exemplified in Fig. 4.4c. Thus on NMR resonance, 1–2 or 3–4, the population change of the level 1 resp. 3 is detected as an increase in the "ESE amplitude." The maximum effect is obtained when the sublevel population of the NMR transition 1–2 or 3–4 are inverted, i.e., for the nuclear flip angle $\theta = \omega_r t_p = \pi$, where ω_r is the effective nuclear Rabi-frequency (nutation frequency) and t_p is the RF pulse length. An ESR excitation has to be hyperfine nuclear-level selective. For QC/QIP ENDOR experiments, the hyperfine nuclear-level selective excitation by a MW pulse is essentially important for generating entanglement composed of electron-nuclear spin-qubits, as discussed in Sect. 4.3.

Figure 4.5b shows the pulse sequence and timing chart for Mims-type ENDOR spectroscopy, where the MW three-pulse ESE scheme is utilized for the preparation and detection periods. Mims-type ENDOR spectroscopy is particularly useful for studying molecular information on nuclei with small hyperfine interactions and small nuclear Zeeman splittings. In the frequency domain, the two-pulses in the preparation period produce a periodic pattern $M_{zi} = M_0 \cos(\Delta\omega_i \tau)$. The M_z-component of a spin packet "i" depends on how its precession frequency in the rotating frame ($\Delta\omega_i$) "fits" in the waiting time τ.

In the standard stimulated echo, the whole pattern refocuses at the time t after the third pulse. When the RF pulse is resonant with a transition matching to a hyperfine interaction A, the polarization transfer shifts the whole M_z pattern up and down in frequency by an amount of A. Thus, the pattern of M_z-components will be less clear (blurred) and as a result the intensity of the echo will be reduced. Only the $A = n/\pi$ ($n = 0,1.2\ldots.$) pattern is retained and the stimulated echo amplitude is unaffected. In other words, the echo amplitude will be modulated by a factor $\cos(2\pi A\tau)$.

4.3 Pulse ENDOR Based Spin Technology for QC/QIP

4.3.1 Generation of A Pseudo Pure State for Electron-Nuclear Spin-Qubit Systems by Pulse-Based ENDOR Spin Technology

Pulse-based ENDOR spectroscopy, carried out in the rotating frame of applied coherent (oscillating) irradiation fields, consists of three main operation periods, i.e., preparation, polarization transfer and detection, as illustrated at the bottom of Fig. 4.5. During the Second period mixing/evolution relevant to the spin states involved on resonance takes place. The three periods correspond to those in QC/QIP

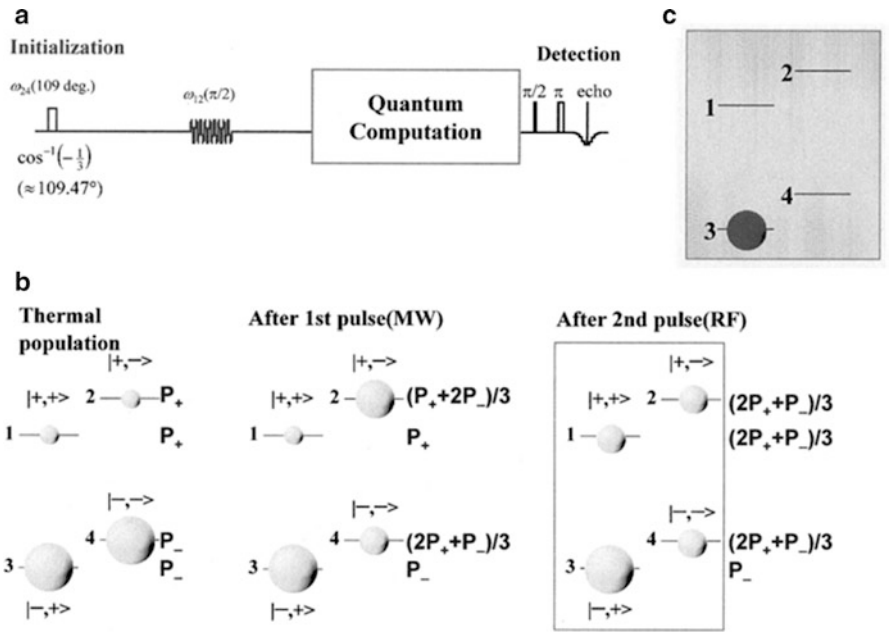

Fig. 4.6 Initialization of an electron-nuclear spin-qubit system by pulse ENDOR spin technology. (**a**) An ENDOR-based pulse sequence for preparing the initialization of an electron-nuclear system with one electron and one nuclear spin-1/2. (**b**) The change in the population among the state on each pulse operation of resonance. (**c**) Here, the level 3 is depicted as a pseudo-pure state of the electron-nuclear hybrid system (Adapted from Ref. [48] with kind permission of © World Scientific Publishing Co. 2009)

processes in time in pulse-based electron magnetic resonance experiments. The first, second and third periods correspond to initialization, manipulation/computing and readout (= detection), respectively, in pulse-EMR based QC/QIP experiments. The initialization prepares an either pure or pseudo-pure spin state necessary for executing any quantum computation. The manipulation/computing is for selective/non-selective excitation among the allowed or forbidden transitions between the spin states, or time evolution of the states involved for particular purposes. In the second period, quantum phases can be manipulated in phase-controlled interferogram experiments for QC/QIP. The readout formally includes variants of electron-spin based detection such as Hahn ESE, three-pulse stimulated echo, refocused echo and FID.

Figure 4.6 shows an ENDOR-based pulse sequence for preparing the initialization of an electron-nuclear system with one electron and one nuclear spin-1/2 (a) and the population change among the states involved on each pulse operation on resonance. The first MW pulse for selective excitation has a particular role to generate the population inversion between the level 3 and 4, assuming an equal Boltzmann distribution between the nuclear spin states in the same electron-spin M_S

sub-level. The second RF π/2-pulse equates the population between the nuclear sub-levels, 1 and 2 of the electron-spin $M_S = +1/2$ level. The two pulses of the MW and RF irradiations on resonance redistribute the populations $2P^+$ and P^- equally among the levels, 1,2 and 4, making only the level 3 more populated by $2(P^- - P^+)/3$. Here, a pseudo-pure state of the electron-nuclear hybrid system with the four spin states is generated as the level 3 after the second RF π/2 pulse in Fig. 4.6b. In Fig. 4.6a, any quantum computing with operations is followed in the second period, and the readout exemplified in a Hahn ESE scheme.

4.3.2 Generation and Identification of Quantum Entanglement between An Electron and One Nuclear Spin Qubit by Pulse-Based ENDOR Spin Technology

Quantum entanglement plays an essential role in QC/QIP. The generation of quantum entanglement between an electron and one nuclear spin-1/2 qubit in a molecular entity has for the first time been achieved by Mehring's group [7], and the establishment of the entanglement has been identified by invoking TPPI (Time-Proportional-Phase-Increment) technique, which enables us to detect quantum phases belonging to particular spin states in the hybrid system. First, following the line shown by Mehring's group, we illustrate how to generate the entangled state in an electron-nuclear spin-qubit system by the use of the pulse ENDOR technique, as given in Fig. 4.7.

In Fig. 4.7a, after the initialization of an electron-nuclear spin-qubit system, e.g., the level 3 as an initialized state (pseudo-pure state), a sequence of RF2 and MW on-resonance pulses required for generating entangled states are applied and the resulting state-transformation by the pulses are schematically given. The role of each pulse is indicated. For entangling the electron-nuclear spin states, we inevitably utilize MW pulses, which force electron spin sublevels to be involved in the entanglement process. This process technically gives rise to some difficulties in QC/QIP experiments. The levels 2 and 3 are entangled in the present pulse scheme. Figure 4.7b depicts the four spin states involved and their population changes by the pulses. The level 1 apparently is not involved during the processes. Any relaxations are not explicitly considered here. In Fig. 4.7c, the pulse sequence for establishing the entanglement between an electron and one nuclear spin-1/2 is schematically given in time. The first period is for the preparation of the pseudo-pure state, as discussed above, and the RF2 π/2-pulse and π-MW one generate a pair of the entangled states. This Second period corresponds to the manipulation of the spin-qubits involved in any quantum operation. The third period depicted as the light gray part in Fig. 4.7c is for the readout of the manipulation, which is referred to in Sects. 4.4, 4.5, 4.6, and 4.7. The third part is a highlighted one to illustrate QC/QIP experiments in terms of quantum phases. In Fig. 4.7d, are depicted quantum logic gates for generating the entanglement between one spin-qubit and another spin-qubit. Here, *S* and *I* stand for an electron and a nuclear spin-qubit.

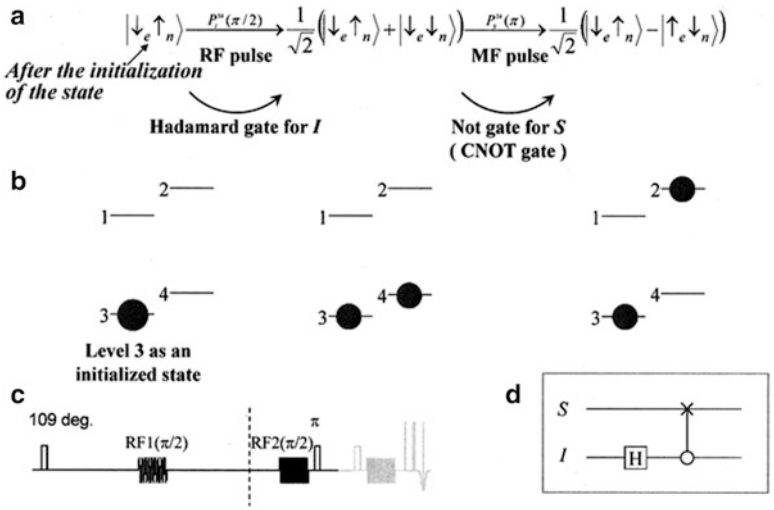

Fig. 4.7 Generation of entanglement between an electron and one nuclear spin-1/2 qubit by pulse ENDOR technique. (**a**) After the initialization of an electron-nuclear spin-qubit system, e.g., the level 3 as an initialized state (pseudo-pure state), a sequence of RF2 and MW on-resonance pulses is required for generating entangled states and resulting state-transformation by the pulses. The role of each pulse is indicated. The levels 2 and 3 are entangled in the present pulse scheme. (**b**) The four spin states involved and their population changes by the pulses. The level 1 apparently is not involved during the processes. Any relaxations are not explicitly considered. (**c**) The pulse sequence for establishing the entanglement between an electron and one nuclear spin-1/2 is given in time. The first period is for the preparation of the pseudo-pure state and the RF2 π/2-pulse and π-MW one generate a pair of the entangled states. (**d**) Quantum logic gates for generating the entanglement between one spin-qubit and another spin-qubit. Here, *S* and *I* stand for an electron and nuclear spin-qubit, respectively (Adapted from Ref. [48] with kind permission of © World Scientific Publishing Co. 2009)

In order to identify the establishment of the entanglement between an electron and one nuclear spin-1/2 qubit, TPPI technique has been introduced by Mehring et al. to pulse ENDOR technology for QC/QIP experiments, for the first time. The method introduced really convinces us of the occurrence of the entanglement between the matter spin-qubits. Basically, TPPI is a general technique to enhance spectroscopic information by increasing the number of spectral dimensions. This can be achieved by introducing a plural number of phases for the pulses, i.e. the MW and/or RF irradiations relevant to the magnetic transitions. The phase increment can be described in terms of angular frequency by time increments, and the frequency is composed of the difference between two relevant frequencies introduced in an arbitrary manner. Invoking this technique makes spectroscopic information multi-dimensional. For example, TPPI has been applied in order to allow on-resonance excitation with the spreading of n-quantum-transition spectra by $n\Delta\omega$. The phase

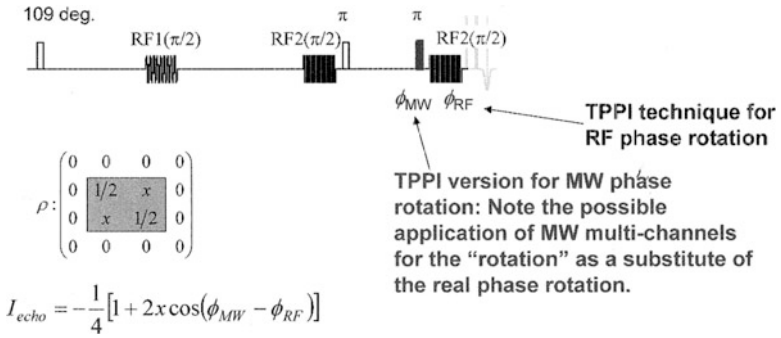

Fig. 4.8 Enabling pulse-ENDOR spin technology for identifying the establishment of the entanglement between an electron and nuclear spin-1/2 qubit. A pulse sequence enabling us to manipulate quantum phases of the matter spin-qubits is depicted schematically. There are two approaches to the phase rotations of the MW and/or RF pulse. One is a variant of the real MW phase rotation termed "MW-phase quasi-rotation," as a substitute rotation technology in the case that the real rotation of the MW pulse phase is technically difficult. In the quasi-rotation, different MW channels are utilized, achieving quasi-rotation of the MW pulse (Adapted from Ref. [48] with kind permission of © World Scientific Publishing Co. 2009)

of the pulse is shifted by $\delta\phi = \Delta\omega\delta t_1$, i.e., $\delta\phi = 2\pi\ \Delta\nu\ \delta t_1$, each time the evolution time is incremented by δt_1, thereby resolving multiple-quantum coherence in pulse-based ENDOR spectroscopy in solution as observed by Hoefer et al., for the first time [20].

Figure 4.8 shows experimental approaches to the evaluation of the quantum entanglement between the electro-nuclear hybrid system. One is a variant of the technique for rotating a MW phase in the case that the real MW rotation is not applicable, in which MW pulse channels can be utilized as a substitute "quasi-rotation" technology for the MW part. This variant has been used in our first previous experiments for identifying the occurrence of the entanglement between an electron and one nuclear spin-1/2 qubit [9, 10]. For the entangled states (the Bell states) generated by an electron and one nuclear spin-1/2 qubit, each Bell state is characterized by its own quantum phase originally composed of both the quantum numbers, M_S and M_I. Thus, the introduction of the corresponding two phases, ϕ_{MW} and ϕ_{RF} for the MW π-pulse and the RF π/2-pulse, respectively, enables us to discriminate between the Bell states. The desired phase shift can be controlled by time increment described above. Any possible quantum phase-interference between an electron and the nuclear spin-qubit in time can be experimentally acquired via interferograms transformed into the frequency domain. Examples for interferograms will be given with particular QC/QIP experiments in Sect. 4.3.4. The ESE intensity is described by an equation, as given in Fig. 4.8, depending on the difference between the two phases in the case that entanglement occurs. Otherwise, the ESE signal is constant in the time increment.

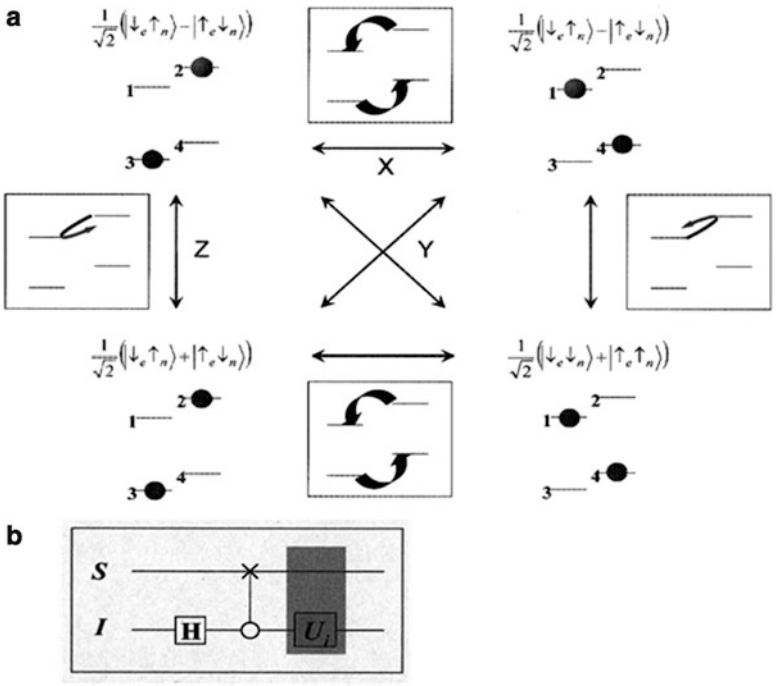

Fig. 4.9 Inter-conversion between the entangled states (the Bell states) by unitary transformations denoted by X, Y and Z, each of which corresponds to the *curved arrows* (**a**). The Z operations designate 2π rotation for a half-integral spin-qubit. The inter-conversion between the Bell states can be achieved by pulse ENDOR spin technology. (**b**) The procedures depicted in (**a**) are represented by a quantum logic gate, in which a unitary operation $\boldsymbol{U}_{\mathrm{i}}$ is applied after generating the entangled state (Adapted from Ref. [48] with kind permission of © World Scientific Publishing Co. 2009)

4.3.3 Inter-Conversion of Entangled States by Pulse ENDOR Technique

Once the entangled states between an electron and one nuclear spin-1/2 qubit are generated by a particular pulse protocol, the pulse ENDOR technique enables us to interchange them by manipulating the nuclear spin sublevels by RF pulses. The procedures for the inter-conversion between the Bell states are schematically depicted in Fig. 4.9, where attention should be paid to the difference in the phase belonging to each Bell state. Inter-conversion between the entangled states (the Bell states) can be achieved by one of the unitary transformations denoted by X, Y and Z, each of which corresponds to the curved thick arrows, as depicted in Fig. 4.9a. The Z operations designate 2π rotation for a half-integral spin-qubit. Thus, the inter-conversion between the electron-nuclear hybrid spin-qubit systems can be implemented by pulse ENDOR spin technology. In Fig. 4.9b, the procedures

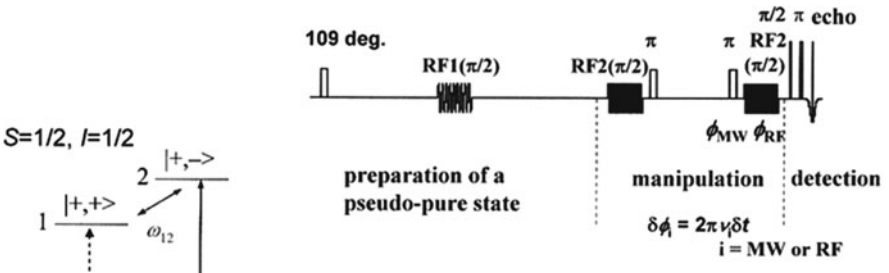

MW	RF1	RF2	Bell state	ν_{TPPI}
ω_{24}	ω_{12}	ω_{34}	$\frac{1}{\sqrt{2}}(\|-+\rangle - \|+-\rangle)$	$\nu_{MW} - \nu_{RF}$
ω_{24}	ω_{34}	ω_{12}	$\frac{1}{\sqrt{2}}(\|++\rangle + \|--\rangle)$	$\nu_{MW} + \nu_{RF}$
ω_{13}	ω_{12}	ω_{34}	$\frac{1}{\sqrt{2}}(\|++\rangle - \|--\rangle)$	$\nu_{MW} + \nu_{RF}$
ω_{13}	ω_{34}	ω_{12}	$\frac{1}{\sqrt{2}}(\|-+\rangle + \|+-\rangle)$	$\nu_{MW} - \nu_{RF}$

Fig. 4.10 TPPI detection of the entanglement between an electron and one nuclear spin-1/2 qubit by the pulse ENDOR technique. The pulse sequence for the TPPI procedure is depicted at the *top* along with the role of the three periods. The transitions are denoted by ω_{ij}. The longer *solid* and *dotted arrows* correspond to the ESR transitions. It should be noted that the two pairs among the four Bell states give the same ν_{TPPI} as seen in the table (Adapted from Ref. [48] with kind permission of © World Scientific Publishing Co. 2009)

depicted in Fig. 4.9a are represented by a quantum logic gate, in which a unitary operation $\boldsymbol{U}_i$ is applied after generating any entangled state. In Sect. 4.7, real hybrid qubit systems in molecular frames will be treated from the experimental side. Our pulse ENDOR spectrometer devoted to QC/QIP experiments operating at Q-band has been designed for the microwave phase which can be rotated at any arbitrary orientation in the three-dimensional way.

4.3.4 TPPI Detection of the Entanglement Between Electron-Nuclear Hybrid Spin-Qubits by Pulse ENDOR Technique

Figure 4.10 summarizes the TPPI detection of the entanglement between an electron and one nuclear spin-1/2 qubits by the pulse ENDOR technique. The pulse sequence for the TPPI procedure is depicted at the top along with the role of the three periods. The TPPI procedure is carried out in the second period of quantum operation/manipulation of the qubits, where the phase of the MW π-pulse and that of the RF2 π/2-pulse are controlled in time in pulse ENDOR technology. In order to manipulate genuine electron spin-qubits in contrast to the hybrid qubit

system, we have to introduce the corresponding phase control technique, say, for two electron qubits with non-equivalent g-factors in molecular frames. Current MW spin technology for QC/QIP requires two MW sources with their relative phases locked electronically. Such MW phase locking technology has never been implemented so far, nor is it necessary for ordinary pulse-based EMR/ESR spectroscopy.

The TPPI frequency denoted by ν_{TPPI} corresponds to the phase information on which an electron-nuclear sublevel is entangled with another sublevel, as exemplified in the table in Fig. 4.10. It should be noted that the two pairs among the four Bell states give the same ν_{TPPI} as seen in the table in Fig. 4.10. The transition frequencies, ω_{12} and ω_{34}, between the level 1 and 2 and the level 3 and 4, respectively, correspond to ENDOR ones. In the Bell states composed of an electron and one nuclear spin-1/2 qubit, the TPPI frequency is either the simplest combination of addition or the one of subtraction. In case the sublevels of an electronic high-spin qubit are utilized with the spin quantum number S, the M_{S} manifolds involved in the MW transitions appear explicitly in the ν_{MW}.

4.4 Implementation of Molecular-Spin Based QC/QIP by the Use of Pulse ENDOR Spin Technology

Section 4.4 deals with molecular spin-qubit based QC/QIP by the use of pulse ENDOR spin technology. A basis for the pulse ENDOR technology has been given in the preceding Sections. In this Section, we are involved in a bit extended applications of the ENDOR spin technology. Further extended applications by the use of multi-qubit systems in molecular frames such as quantum teleportation experiments, data storage processing or realistic applications of quantum algorithms are important and have been underway, noting that prior to any such QC/QIP experiments the syntheses associated with elaborate molecular designs are required. We emphasize that the field of QC/QIP is interdisciplinary over chemistry and modern materials science and that a new area in chemistry is emerging. We start answering a fundamental query "Why molecular electron spin-qubit based QC/QIP by using pulse spin technology?"

4.4.1 Why Molecular Electron Spin-Qubit Based QC/QIP by Using Pulse ENDOR Spin Technology?

A very well-known physical system for the realization of QC/QIP is based on modern pulsed NMR spectroscopy [14, 15]. In this scheme, the quantum information is stored in nuclear spins, as qubits, of particular diamagnetic molecules. Liquid-state NMR spectroscopy has been widely used for implementations of even considerably complicated quantum non-local algorithms and the experimental

outcomes apparently represent the capability of NMR as the proper physical system for QC/QIP [21–25]. Nevertheless, liquid-state NMR at ambient temperature suffers from its intrinsic low spin polarization, making the initial state in a highly mixed state, whereas the accessibility to a pure initial state is one of the major requirements for any physical qubit system to be a valid candidate for demonstrating a quantum computer [18] as discussed above in part. In order to overcome this drawback, in a conventional approach, pseudo-pure states have been introduced [26, 27] and widely used for NMR-based QC/QIP experiments. Molecular spin-qubits in ensemble exploit a similar initialization condition above a certain "critical temperature" depending on the microwave resonance energy used for selective excitation of the qubits.

4.4.2 Pseudo-Pure States and Quantum Entanglement

A pseudo-pure state is composed of two terms, one belonging to the highly mixed state of the unitary part and the other to the pure state term with a coefficient, which is related to experimental conditions. Referred to the current technology of the NMR spectroscopy at ambient temperature the corresponding value is as small as typically 10^{-5}. Since all the observables in NMR are traceless, the mixed state term is hardly detectable through the NMR processing. Weak signal intensities, however, through the other term still give some information in quantum processing. Then the whole pseudo-pure state behaves as if an initial pure state has been used for the quantum information processing.

Quantum entanglement is known as a prerequisite for any quantum non-local algorithm [28, 29]. Thermal mixed states used for NMR QC/QIP have been proved to be separable [30, 31], therefore being useless for the quantum non-local processing. Pseudo-pure states that apparently are capable of resolving the problem of the admixture of the initial state are not useful with respect to the separability of the state, since the pseudo-pure state can also be represented as a convex combination of thermal states. The entanglement is a convex function. Then, the pseudo-pure states are at least as separable as the thermal states. In this context, liquid-state NMR with low spin polarization cannot afford entanglement-based advantages of QC/QIP. In order to solve this drawback, nuclear spin polarization should be increased to the extent expected by the theoretical criteria for the existence of entanglement. The enhancement of the nuclear spin polarization has been one of the recent focuses in the field of quantum information science [32, 33].

Despite the drawbacks of QC-NMR as discussed, it is no doubt that NMR spectroscopy can be a superb physical system representing very important advantages for the realization of QCs in some crucial aspects. QC-NMR has brought reality for QC/QIP and driven the rapid progress in this field. The existence of nuclear spin-qubits with long decoherence time is a proper physical realization of qubits since the spin manipulation can easily be performed by introducing a series of many sophisticated radiofrequency pulses with relevant resonance frequencies.

In this context, to retain the advantage of the long decoherence time it is crucial to look for novel matter spin-qubit systems in which easy-to-access spin manipulations are performed. In our latest study, pulse-based Electron Nuclear DOuble Resonance (ENDOR) [34], as well as pulsed ELectron electron DOuble Resonance (ELDOR) for electron spin qubits, has been examined as novel candidates to approach quantum computers by invoking ensemble molecular entities with both electron and nuclear spins in the solid state. Since the physical system under study involves nuclear spin-qubits, pulse ENDOR spin-manipulation technology retains the main advantage inherent in NMR-based QC systems. In addition, it seems easier to overcome the drawbacks of the NMR systems for the realization of QCs because additional molecular electron spin-qubits originating in open-shell molecular entities are also incorporated in the electron spin-qubit physical systems.

Generally speaking, an ENDOR based QC event based on electron-nuclear multiple magnetic resonance spectroscopy is a much heavier experimental task compared with QC-NMR, as some crucial parts discussed above. QC-ENDOR based gate operations are different from the counterparts of QC NMR in many aspects, particularly in QC ENDOR experiments in solids. Attempts to combine the advantages of NMR and ESR spin technology are rewarded with faster gate operations with entangled spin states. It is worthwhile to notice that an elaborate total design of the QC-ENDOR experimental setup should be associated with molecular design for open-shell entities, as frequently emphasized. This is because the number of client nuclear spin-qubits, the kinds of the nuclear spin-qubits available for radiofrequency irradiation, i.e., their gyromagnetic ratios, the magnitudes of their hyperfine/fine-structure interactions and the tuning of their relaxation times of molecular open-shell entities are all crucially important in the QC-ENDOR setup. In this context, the molecular design is underlain by the current stage of pulsed microwave and radiofrequency spin technology.

4.5 Molecular Spin-Qubit ENDOR Based Quantum Computers

For any physical system as a candidate for the realization of a quantum computer, there are some fundamental criteria, known as DiVincenzo's five criteria that should be met [18]. The molecule-based ENDOR system is also expected to meet these criteria in order to be a realistic physical system for QC/QIP; see Table 4.1 for a list of the DiVincenzo's five criteria. The table also contains the corresponding properties of the ENDOR system.

In the ENDOR-based QC/QIP, molecular electron spins in addition to nuclear spins have been introduced as qubits that play the role of bus spins while the nuclear spins are client qubits. In a thermal equilibrium, the populations in the ground states of the molecular electron spins are more than 10^3 times larger than the corresponding excited states with different M_s-manifolds in the presence of a

Table 4.1 QC-ENDOR systems satisfying the conditions of the DiVincenzo's five criteria

	DiVincenzo's Criteria [18]	QC-ENDOR
Qubit	Identifiable; well characterized and scalable qubits are required.	Molecule-based electrons and nuclear spins in molecular open-shell entities, in which hyperfine couplings play an essentially important role for selective excitations of both the electron spin- and nuclear spin-qubits. Molecular designs, syntheses and identifications of spin properties are required. The scalability of client nuclear spin-qubits in electron spin bus QCs has to be solved from the synthetic viewpoint.
Initialization	Possibility to be initialized to a simple and fiduciary state.	Pseudo-pure states can be used in this context, whereas in order to avoid pseudo-pure states high polarizations of the electron spin can be coherently transferred to the nuclear spin by applying relevant pulse sequences followed by proper waiting times.
Decoherence time	Long relevant decoherence times, much longer than gate operation times are necessary.	Long decoherence times of nuclear spins and electron spin in organic radical qubits in the solid state have been available for the demonstration of quantum operations between the bi- and tri-partite qubits. Proper molecular entities with long decoherence times for multi-qubit operations are not out of reach, for which stable isotope-labeled open-shell molecules have been designed and synthesized [46]. QC-ENDOR experiments in solution also are not out of reach. An attempt to synthesize one- or two-dimensional periodic spin arrays in molecular frames such as Lloyd's model have been made from synthetic chemistry sides.
Quantum operation	A universal set of quantum gates is required.	Quantum gates between a single electron and a single nuclear spin have been demonstrated experimentally. Multi-qubit operations in terms of ENDOR spin Hamiltonians are underway. Particularly, a protocol for three-partite QC operations has been implemented [41].
Measurement	The ability of measurements on quantum qubits to obtain the result of the computation is required.	The current measurement scheme is ensemble-based, in which an individual client nuclear spin-qubit is readout via the electron bus spin-qubit. A field gradient approach for the readout is proposed. On the other hand, single electron spin detections may be available in the future by the use of STM-based electron magnetic resonance detection.

static magnetic field or of zero-field splittings, compared with QC-NMR. Therefore, with ground-state ENDOR systems, achievement of the required experimental conditions for preparing the initial state for QC/QIP seems to be substantially easier

with the current electron magnetic resonance technology. The exact and complete preparation of the pure initial state, however, requires manipulation of single molecule systems, for which electron magnetic resonance or Larmor precession detection has been considered and even the experimental equipments by the use of electric detection schemes seem to be accessible in the near future.

Any physical/molecular system for QC/QIP should be chemically stable during computational processing. Robust organic open-shell entities against long and high-power irradiations of both radiofrequency and microwave at ambient temperature have in fact been prepared, as exemplified in our own work. In addition, the corresponding decoherence time of the qubits is expected to be long enough compared with the computational or gate operational times. As a result of the existence of nuclear spin-qubits in molecular open-shell entities, there is a wide possibility to work with samples having long decoherence times. Proper samples with a long decoherence time and their synthetic procedure should be considered, in advance. In this context, open-shell metal cationic complexes with available nuclear client qubits have intrinsic advantages whereas relatively strong spin-orbit couplings hamper their decoherence time in ensemble solid states [35]. Long enough decoherence times for samples involving two qubits have been measured during the course of this work. For particular molecular entities the feasibility of the ENDOR-based QC/QIP has been examined from both the experimental and theoretical sides as is reported in the following Sections.

In QC-ENDOR, manipulation and processing on the qubits as well as the readout processing can be realized by introducing both microwave and radiofrequency pulses in an approach different from genuine NMR-based QC experiments, i.e., by ENDOR (NMR) resonant pulses on the client nuclear spin-qubits and/or by the microwave frequency resonant pulses on the electron bus spin-qubits, as exemplified in Fig. 4.11, where the state notation is modified in accordance with the later Sect. 4.7.1.

It is known that the realization of particular quantum gates being known as universal gates can be enough for the implementation of any other quantum gates [2]. One-qubit gates in addition to a non-trivial two-qubit gate, e.g. a Controlled-Not (CNOT) gate, give a universal set of quantum gates. For implementations of the quantum gates in terms of resonance concepts, it is possible to perform this task by introducing the relevant pulses. From the experimental side, for the QC-ENDOR system particular quantum gates have been demonstrated by means of the two-qubit system composed of one electron spin-qubit and one nuclear spin-qubit, as it is described in the following Section. Multi-qubit gates for molecular systems involving a larger number of qubits should be considered for relevant physical systems in terms of the particular form of the spin Hamiltonian for the corresponding sample [7–13]. Tri-partite spin-qubits experiments have for the first time been demonstrated for a separable set of two-partite entangled states in our work, as described in the following Section. There are several typical types of the quantum operations based on multi-qubit gates, depending upon spin Hamiltonians for realistic QC-ENDOR experiments: A QC-ENDOR pulse protocol for quantum teleportation differs from the counterpart of QC-NMR [35].

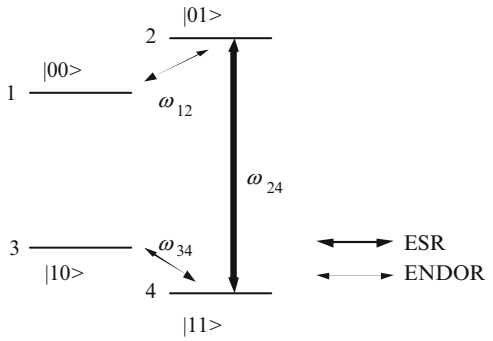

Fig. 4.11 Energy levels and corresponding ESR and ENDOR resonance transitions in the presence of a static magnetic field. Note that the nuclear sublevels correspond to the case for the system with a positive hyperfine coupling. The splittings of the nuclear sublevels are exaggerated for clarity. The definition for the level is as follows; $|00>(=|++.>)$ and $|10>(=|-+>)$ denote $|Ms=+1/2, M_I=+1/2>$ and $|Ms=-1/2, M_I=+1/2>$, respectively. Similarly, $|01>(=|+->)$ and $|11>(=|--.>)$ denote $|Ms=+1/2, M_I=-1/2>$ and $|Ms=-1/2, M_I=-1/2>$, respectively. Also, see the text for the use of the notation of the sublevels. Both the notations for the electron-nuclear sublevels are used and for later Section the Arabic numerals are used for convenience (Adapted from Ref. [48] with kind permission of © World Scientific Publishing Co. 2009)

In the ENDOR based QC, the readout or the measurements have been implemented by introducing the radiofrequency and microwave pulses on nuclear spin- and electron spin-qubits, respectively. Nevertheless, as is in a similar approach to NMR QC, the measurement scheme is ensemble-based and is rather different from exact measurements which are required for QC. This issue is still an open practical problem in terms of QC ENDOR. This is due to the fact that molecular electron spin-qubits play a special role in QC ENDOR. This role as "bus" spins is associated with the electron-spin echo detection schemes used instead of FID ones in QC NMR for the selective excitation/readout processes. As already mentioned, the present QC/QIP experiments are based on ensemble measurements, in which the initialization of pure spin states is an intractable process. In the ENDOR based QC, however, we have only proposed the single molecule system for which the measurements can be accomplished by single electron spin detection as referred to above. In this scheme, the detection sensitivity is a crucial and underlying issue.

It has been proved that for the case of pure-states, entanglement is the necessary requirement for the quantum exponential speed-up over the classical counterpart. For mixed states, the statement has still not completely been proved, but is believed to be correct. Therefore, one very important issue that should be examined for any physical system for QC/QIP is the entanglement status. Realization of the entanglement between an electron spin- and a nuclear spin-qubit has for the first time been reported in an ENDOR experiment by using the pseudo-pure states [7, 8]. So far, we have been mainly engaged in two experimental tasks for the realization of QCs by molecule-based ENDOR. One has been an attempt for the preparation of the experimental requirements for demonstrating the true entanglement between a

molecular electron spin- and a nuclear spin-qubit by the use of a simple organic radical in the single crystal and avoiding the use of pseudo-pure states. High spin polarizations on both the electron and nuclear spins are essentially required to achieve the true entanglement between the two spin-qubits in the molecular frame. Investigation of the entanglement for the ENDOR system composed of only two electron and nuclear spins gives a necessary temperature of 0.8 K in a static magnetic field for the microwave transition frequency of 95 GHz, as given by the negativity criterion [36, 37]. Whereas, if pulses can be applied for the transfer of the high spin polarization, the required temperature at the same magnetic field is nearly 5.1 K, which is well in reach with the current technology with a W-band (95 GHz) ENDOR spectrometer operating at liquid Helium temperature.

While the preparation of all the experimental requirements is in progress, the efforts still can be maintained on some other aspects of the research like the materials challenges to design and synthesize stable or scalable open-shell molecular entities suitable for QC/QIP ENDOR experiments. Novel molecular open-shell systems with stable isotope labels suitable for our purposes have been designed and synthesized [35]. Also, the critical temperature can be tuned by invoking stable high-spin molecular entities. Some of the most crucial aspects for scalable molecular electron spin-qubits are given elsewhere [35]. We emphasize that a road-map to the synthetic strategy for scalable molecular spin qubits includes a supramolecular chemistry approach to metal cationic open-shell entities with three non-equivalent *g*-tensors in a one-dimensional periodic manner. One-dimensional molecular spin arrays are termed Lloyd model. Such *g*-tensor engineering enables us to achieve selective microwave excitations for the preparation of initial spin states and for the readout procedure.

Efforts have also been made to investigate the credibility of the pulse ENDOR based QC/QIP and to develop the necessary quantum gates and the entangling unitary operations. It is clear that for acquiring the former task with the achievement of the experimental conditions for entanglement and pure states, there would be no need to have an additional experimental processing to make the pseudo-pure state.

In order to check both the credibility of the ENDOR physical system for QC/QIP and the feasibility of the molecule-based QC-ENDOR with the current technology, implementation of super dense coding (SDC) [6] has been revisited in our experiments. The pulse ENDOR technique has been applied to a molecular electron- and nuclear-spin system, i.e., the malonyl radical in the single crystal of malonic acid [38], in order to for the first time implement the SDC in the electron-nuclear spin-qubit system. Additionally, we have shown that the non-selective microwave excitation in QC-ENDOR experiments gives a set of separable states composed of the entangled states. QC experiments on tripartite spin-qubits have also been attempted, in which the quantum phases of various entangled states are monitored. In these experiments, we have chosen a multi-nuclear client organic stable radical such as diphenylnitroxide-h_{10} magnetically diluted in diamagnetic host lattices at a desired concentration.

4.6 Preparation of a Molecular Entity for QC-ENDOR: The Simplest Case

Malonyl radicals incorporated in the single crystal of malonic acid were generated by X-ray irradiation at ambient temperature as shown in Scheme 4.1. Spin Hamiltonian parameters of malonyl radical under study, as summarized in Table 4.2, have been reported by McConnell and coworkers [38]. The principal axes, *X*, *Y* and *Z* of the *g*-tensor and the hyperfine tensor of the α-proton are collinear, as depicted in Fig. 4.12. A typical echo-detected field-swept Q-band ESR spectrum of malonyl radical observed at 50 K is shown in Fig. 4.13. Pulse ENDOR measurements for the malonyl radical were performed with a Davies-type pulse sequence [39] and an observed Davies-ENDOR spectrum is shown in Fig. 4.14.

The existence of one electron spin on the carbon atom and one α−proton with a large hyperfine coupling gives two spins as the two qubits required for super dense coding (SDC). The large hyperfine interaction is primarily required to enable us to make a selective microwave excitation within the framework of the current spin technology for QC/QIP experiments. Energy levels and the corresponding resonance frequencies of the RF and MW frequencies are shown in Fig. 4.11, noting that the order of the nuclear sublevels should be reversed for the malonyl radical with the negative hyperfine coupling (see Table 4.2). Detection of the pseudo-entanglement with this system has been already reported [7] and in a different approach we demonstrate the implementation of SDC by the use of the pseudo-entangled states and pulse ENDOR spin technology.

4.6.1 Implementation of Super Dense Coding (SDC) by Pulse QC-ENDOR and Direct Detection of the Spinor of a Spin-1/2 Proton and Electron

Super dense coding (SDC) introduced by Bennett and Wiesner [6] is a non-local quantum algorithm in which two classical bits of information are transformed from

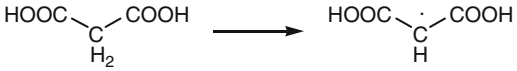

Scheme 4.1 Generation of malonyl radical from malonyl acid in the single crystal by X-or γ-ray irradiation

Table 4.2 The spin Hamiltonian parameters of malonyl radical

	Principal g-values			$^{\alpha}$A /MHz		
S	*xx*	*yy*	*zz*	xx	yy	zz
1/2	*2.0026*	*2.0035*	*2.0033*	−61	−91	−29

The corresponding principal axes are depicted in Fig. 4.12

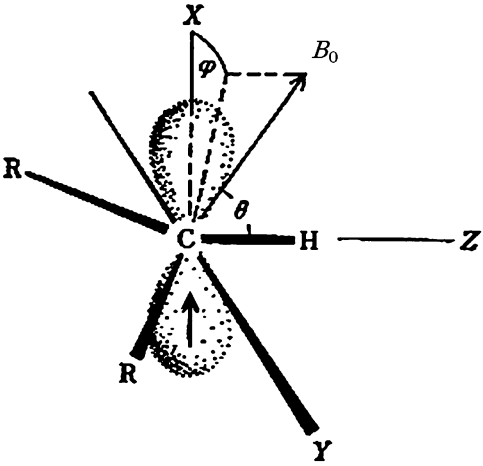

Fig. 4.12 The principal axes of the magnetic tensors in malonyl radical. The principal axes of the g-tensor and the hyperfine tensor of the α-proton are collinear. The principal Z axis is along the C-H bond and the X axis parallel to the symmetry axis of the pπ-orbital at the carbon site

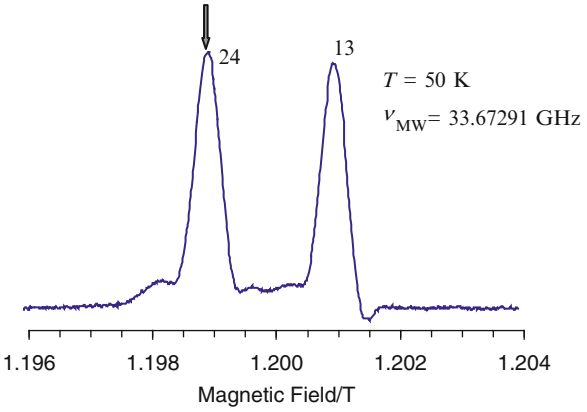

Fig. 4.13 A typical ESE-detected field-swept Q-band ESR spectrum of malonyl radical in the single crystal of malonic acid observed at 50 K. The numbers at the peaks denote the ESR allowed transition assignments (see the energy diagram in Fig. 4.11)

Alice to Bob by sending only a single qubit, as depicted in Fig. 4.15. SDC is the simplest example of the application of entanglement to communication. The scheme of SDC is based on the fact that the entangled initial states have been shared between two involved parties, i.e., Alice and Bob. The efficiency of the scheme is two times improved, compared with the classical counterpart, since maximum one bit of information can be transferred through a single use of an information channel referring to Fig. 4.15.

Simply, SDC can be explained as follows. Let two qubits, which are originally entangled with each other, be shared between the two involved parties, Alice and Bob. Alice encodes the qubit by applying her desired unitary transformation out of the four choices of the unitary operations {I, X, Y, Z}, where I denotes the identity, and then she sends the encoded qubit to Bob, who has been initially given a qubit entangled with the Alice's one. After receiving the encoded qubit from Alice, Bob carries out the appropriate unitary transformations, that is, Bob makes

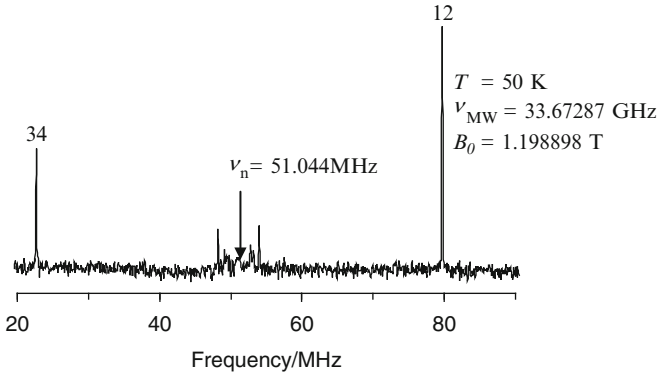

Fig. 4.14 A Davies-type pulsed Q-band ENDOR spectrum from malonyl radical with the magnetic field set as indicated by the *arrow* in Fig. 4.13. A selective MW pulse for the preparation and non-selective MW pulses for the detection were applied. The numbers indicate the ENDOR transitions (see Fig. 4.11) due to the α-proton of malonyl radical with a negative hyperfine coupling. The appearance of the only strong peaks designated by 12 and 34 in the ENDOR spectrum indicates that the crystal dominantly contain malonyl radical. The alignment is relatively easy for selective nuclear-spin excitations with this system [38]

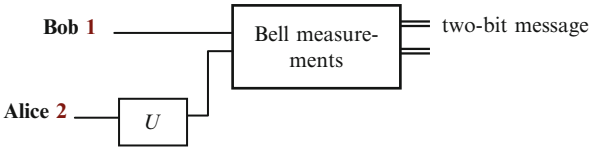

Fig. 4.15 Scheme for super dense coding (SDC). U denotes a unitary transformation (see the text for details)

measurements in the Bell basis (see Table 4.4) on both of the qubits and obtains the two classical bits. The result of the measurement makes Bob know what the Alice's choice has been in the encoding part. Therefore, he extracts the information on the Alice's choice, which means a two-bit message has been transferred by sending only a single qubit. It is important to note that SDC is not possible in classical terms since any classical bits have well-defined values prior to the measurements.

Concepts for the ENDOR-based experimental setup for two-qubit SDC are depicted in Fig. 4.16, in which S and I denote the electron-spin part and the nuclear-spin one. Figure 4.16 shows one of the quantum circuits implementing SDC. The quantum circuit for SDC consists of Hadamard, denoted by H in Fig. 4.16, and controlled NOT (CNOT) gates. U_i stands for one of the unitary transformations which has been encoded by one of the two parties, say Alice. In Fig. 4.16, an alternative unitary operation performed by the Bob side is depicted in the dotted box. From the experimental side, the choice of encoding is important, exemplified in the later Sect. 4.7.2. Also, from the technical viewpoint, both the encoding procedures may not be possible in pulse ENDOR spin technology. The first Hadamard and CNOT gates generate an entangled state between the electron and nuclear spin-qubits. Following the unitary transformation, the CNOT and Hadamard gates

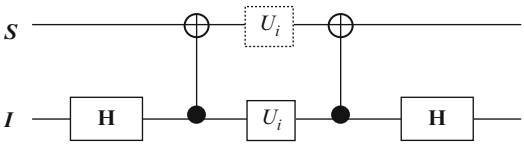

Fig. 4.16 Quantum circuit implementing super dense coding (SDC). U_i denotes a unitary transformation. U_i can be carried out also by the *S* side instead of the *I* side

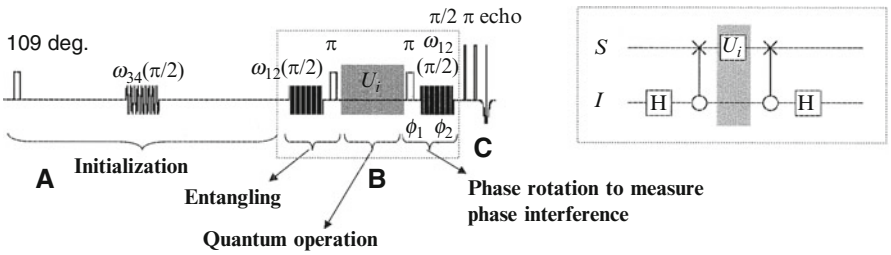

Fig. 4.17 A pulse sequence for implementation of super dense coding (SDC) by pulse ENDOR spin technology. The sequence is composed of the three periods: **A** preparation period for the initialization, **B** manipulation period for any quantum operations including entangling procedure, quantum phase rotations by the use of TPPI technique, or additional unitary operations denoted by U_i, U_i can be performed on the *I* side. **C** detection period for the readout of the results obtained by QC/QIP operations

back-transform the entangled state in order to extract the encoding results. Except for a phase factor which does not affect any signal, selective π/2 and π pulses are available for the Hadamard gate for a single qubit and for the CNOT gate as a two-qubit operation in pulsed magnetic resonance spectroscopy, respectively.

Super dense coding has been implemented using some quantum physical systems including NMR [14]. This chapter gives the first report on the implementation of SDC by ENDOR spin technology. However, the main idea is only to test the ENDOR system for QIP rather than the total implementation of SDC, giving a testing ground for QC/QIP to molecular-spin based ENDOR. One has to argue the ENDOR case for being truly realizable in manipulating the entangled state and not just by a "pseudo-entanglement". In our experiments, the initial states have been prepared as pseudo-pure ones in a similar approach as reported by Mehring's group [7, 8].

The pulse sequence used for the implementation of SDC with our ENDOR experiments is represented in Fig. 4.17. As generally discussed in the preceding Sections, there are three main parts of the sequences, i.e., A; the preparation of the pseudo-pure states, B; the manipulation of spin-qubits for quantum operations and finally C; the detection according to the customs in magnetic resonance spectroscopy. In the ENDOR experiment described in Fig. 4.17, the readout is simply carried out by an electron-spin Hahn echo detection scheme.

Table 4.3 The unitary operations and corresponding pulse sequences for encoding in the SDC experiments

U	Angular dependent RF pulses for encoding	Detected angular dependent echo intensity
I		$-\frac{1}{4}[1+\cos(\phi_1-\phi_2)]$
X	$P_x^{34}(\pi)P_x^{12}(\pi)$	$\frac{1}{16}[-3\cos\theta-\cos\phi-4\cos\frac{\theta}{2}\cos\frac{\phi}{2}(\phi_1-\phi_2)]$
Y	$P_x^{34}(2\pi)P_x^{34}(\theta)P_x^{12}(\phi)$	$\frac{1}{16}[-3\cos\theta-\cos\phi+4\cos\frac{\theta}{2}\cos\frac{\phi}{2}\ \cos(\phi_1-\phi_2)]$
Z	$P_x^{34}(\theta)$	$\frac{1}{16}[-1-3\cos\theta-4\cos\frac{\theta}{2}\ \cos(\phi_1-\phi_2)]$

Table 4.4 Angular dependence of the intensities of the electron spin echo in the SDC experiments

U	Initial state	Necessary operation	Required pulses	Encoded State
I	$\frac{\|++\rangle+\|--\rangle}{\sqrt{2}}$			$\frac{\|++\rangle+\|--\rangle}{\sqrt{2}}$
X	$\frac{\|++\rangle+\|--\rangle}{\sqrt{2}}$	$\exp(-i\pi I_x)$	$P_x^{34}(\pi)P_x^{12}(\pi)$	$\frac{\|+-\rangle+\|-+\rangle}{\sqrt{2}}$
Y	$\frac{\|++\rangle+\|--\rangle}{\sqrt{2}}$	$\exp(-i\pi I_y)$	$P_x^{34}(2\pi)P_x^{34}(\pi)P_x^{12}(\pi)$	$\frac{\|+-\rangle-\|-+\rangle}{\sqrt{2}}$
Z	$\frac{\|++\rangle+\|--\rangle}{\sqrt{2}}$	$\exp(-i\pi I_z)$	$P_x^{34}(2\pi)$	$\frac{\|++\rangle-\|--\rangle}{\sqrt{2}}$

The encoding pulse is defined by the angles θ and ϕ

In contrast to the preparation period in ordinary magnetic resonance spectroscopy, the left part labeled by "A" is for the preparation of the pseudo-pure state required as initialization for quantum operations or computing. Two pulses on the electron and nuclear spins with additional waiting times in order to make the off diagonal term of the density matrix vanishing are required for acquiring the pseudo-pure state. The first two pulses in the central part of the sequence are for the entangling and the last two pulses are for the detection of the entanglement, as reported by Mehring's group [7, 8]. Two phases of Φ_1 and Φ_2 for the pulses in the detection part are required for discriminating the entangled states from the simple superposition states. In the central part between the entangling and the detection of the entanglement, labeled by B2 ($= U_i$), one of the qubits, the electron spin-qubit (or the client nuclear spin) in our experiments, is encoded by randomly applying one of the four pulses of {I, X, Y, Z}. The necessary pulses for the encoding are described in Table 4.3.

Finally, there are pulses for the detection by an electron-spin Hahn echo signal, as carried out in the detection period denoted by C in Fig. 4.17. For the measurement part, the situation has been modified for some detection considerations. In this study, we have used the electron spin echo detection. The echo intensities have been detected for different angular dependencies of the pulses in the encoding part. As a result, there are four sets of angular dependencies for the RF pulses which have been used for encoding, as given in Table 4.4.

4.6.2 *Direct Detection of the Spinor for an Electron Spin by the Use of QC/QIP Technology*

In QC-ENDOR, unitary operations are realized by some particular pulse operations with their controlled phases and polarizations. Phase manipulations are crucial in the molecular-spin based ENDOR experiments for QC/QIP. Table 4.4 shows the angular dependence of the electro-spin-echo intensities in the detection part, depending also on experimental conditions for the measurements. In the SDC experiments, the detected echo intensities incorporate the terms characteristic of a 4π period, as shown in Table 4.4. This 4π period originates from the spinor nature intrinsic to spin-1/2, but it never explicitly appears under ordinary experimental conditions. The very entanglement condition realizes the experimental appearance of the spinor nature. We have detected this salient behavior of the intensities as the function of the RF pulse length, exemplifying the case for $U_i = X$ as given in Fig. 4.18, in which the phase manipulation was carried out for the client nuclear spin-1/2. Thus, the spinor observed in Fig. 4.18 is due to the client α-proton. In contrast to the 2π period of the population, the observed 4π period originates from the spinor property [20]. The spinor of the proton spin appears under such a particular experimental condition as the proton spin is entangled with the electron spin via the selective microwave excitation. The sign difference appearing between Fig. 4.18 and Table 4.4 is due to the difference between the experimental setup. The spinor behavior for non-selective microwave excitations is of interest in terms of the phase manipulation.

In Fig. 4.18, the spinor nature appears in one of the Bell states $(|-+>+|+->)/2^{1/2}$ at the origin of time. At 20 μs corresponding to the angle $\theta = 2\pi$, the original state is converted to $(-|-+>+|+->)/2^{1/2}$ but not transformed back to the original state due to the spinor nature of the nuclear spin-1/2. The observed ESE intensity is well reproduced by the theoretical function of the angle θ, as shown in the dotted curve in Fig. 4.18. The salient features of the ESE intensity appearing in this SDC experiment give a direct evidence of the spinor nature of the proton spin. This is the first direct evidence in which the spinor nature appears in QC/QIP experiments. Noticeably, the spinor of an electron as a physical quantity has never directly been illustrated so far, whereas the spinor is unequivocally established from the theoretical side. Thus, any direct detection of the spinor is a challenging issue from the experimental side. A QC/QIP-based experimental version for the spinor of an electron will be described in the following Sect. 4.7.4. In addition, it is noteworthy that the spinor nature of spin-1/2 is intrinsically quantum mechanical and of double-group property to be treated in group theory. For spectroscopic purposes, the spinor nature of protons has been utilized in pulse ENDOR spectroscopy by Hoefer and Mehring for the first time, implementing spinor-ENDOR spectroscopy to achieve an enormous amount of sensitivity enhancement in detecting proton ENDOR transitions [20].

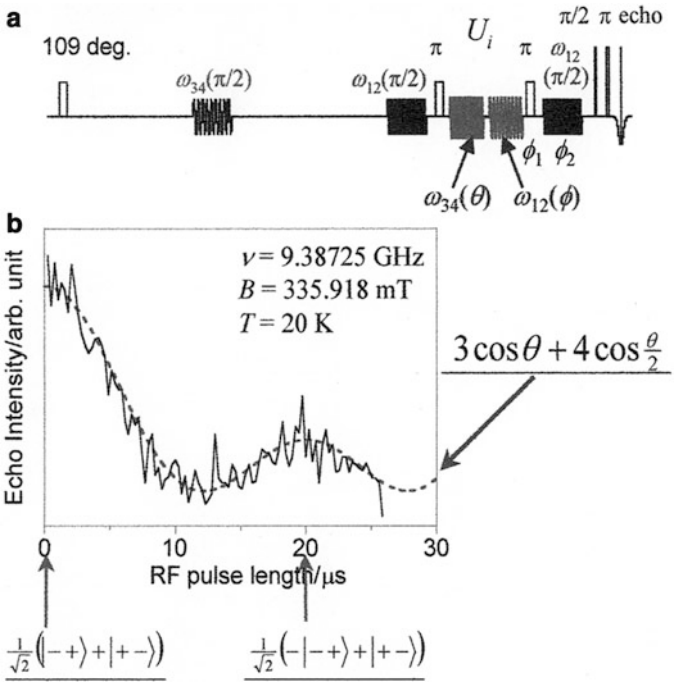

Fig. 4.18 Spinor of the spin-1/2 proton of malonyl radical in the single crystal detected in the SDC experiments by pulse ENDOR spin technology. (**a**) A pulse sequence protocol for the phase manipulation of the nuclear spin-qubit, i.e., manipulating the nuclear spin-1/2 qubit by invoking variable angles, θ and ϕ. (**b**) 4π Periodic dependence of the electron spin echo readout as a function of the RF pulse length. Microwave frequency: $\nu = 9.38725$ GHz. Static magnetic field set for ENDOR: $B = 335.918$ mT. Temperature: $T = 20$ K. The phase angles, ϕ_1 and ϕ_2 stand for the MW pulse and the RF pulse, respectively, during the TPPI procedure. The phase angles are composed of two virtual frequencies introduced in the TPPI procedure (Adapted from Ref. [48] with kind permission of © World Scientific Publishing Co. 2009)

4.6.3 TPPI Detection and Inter-Conversion of the Bell States by Pulse ENDOR

A pulse sequence applied for the QC-ENDOR experiments has already been given in Fig. 4.18. The first microwave and second RF pulses are applied to make the pseudo-pure state described above. Some waiting times between the first and second pulses and between the second and third pulses are required to diminish any coherence generated by the supplied pulses. After making the pseudo-pure state, we apply further microwave and RF pulses in order to manipulate electron and nuclear spin-qubits. This procedure belongs to quantum operations. When applying

a microwave π-pulse following an RF π/2 pulse, we can generate a quantum entangled state which is one of the Bell states and the most important event in the QC experiments. By changing the combination of the microwave and RF pulses with different resonance conditions, different Bell states can be constructed. In order to detect the entangled states and to make the establishment of the entanglement clear from "conventional" or ordinary superposition states, we employ time proportional phase increment (TPPI) technique mainly for the nuclear spin during our QC/QIP experiments.

As it is intractable to perform the TPPI technique for electron spin-qubits because of difficulties with currently available microwave technology, the phase rotation with four different pulse channels (x, y, -x and -y) for microwave has been applied in our experiments. The TPPI version of microwave technology devoted to QC/QIP, mimicking the paradigm of NMR, is underway, and only some parts of the latest innovation are described in this chapter.

The TPPI technique in pulse ENDOR spectroscopy is known for the separation of multiple quantum coherences [20]. On the other hand, we have used the scheme in a way that it can give global information on the state of the electron and nuclear spins in terms of quantum phases inherent in spin-qubits.

This is for resolving the restriction of ENDOR spectroscopy that any measurement can only be done via electron spin echo signals. Especially, for the case that information on the state of entanglement is required, the TPPI technique is an essential part which allows us to differentiate the entangled states from the simple "conventional" superposition states. The TPPI procedure is one of the highlighted parts in QC/QIP experiments. The dynamical parts of the electron spin echo signals as functions of the TPPI procedure give the time structure of the entanglement, which is useful for QC/QIP experiments for multi-partite spin-qubits. An essential part of the trick used in the TPPI technique applied for novel ELDOR spectroscopy has only partly been described in this chapter, and the technique is applicable to increase the number of dimensions by using virtual frequencies in any of the pulse-based spectroscopic measurements.

Figure 4.19 shows that the TPPI-detected phase spectra from the malonyl radical in the single crystal of malonic acid unequivocally discriminate the entangled Bell states composed of one electron spin- and one nuclear spin-qubit. The phase spectra illustrated in Fig. 4.19 have been achieved in a Q-band pulse ENDOR spectrometer in which both the MW and RF pulses can be rotated in any desired orientation. The phases ϕ_1 and ϕ_2 in Figs. 4.17 and 4.18 correspond to ν_{MW} and ν_{RF}, respectively, for the phase rotation as given in Figs. 4.8 and 4.10. Combination signals between ν_{MW} and ν_{RF}, which are due to the entangled states between an electron spin and one proton nuclear spin, were observed, indicating that the corresponding entangled Bell states are discriminated in terms of the quantum phase. The appearance of ν_{MW} or ν_{RF} is due to the imperfections of the TPPI procedure. The line widths of the phase spectra reflect decay times appearing in the time-domain interferograms.

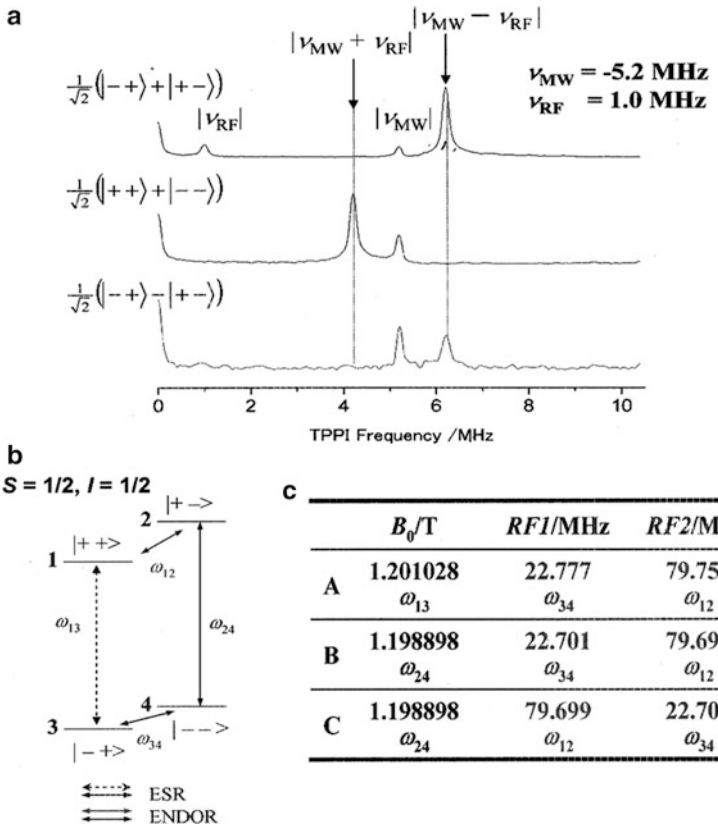

c

	B_0/T	*RF1*/MHz	*RF2*/MHz
A	1.201028	22.777	79.757
	ω_{13}	ω_{34}	ω_{12}
B	1.198898	22.701	79.699
	ω_{24}	ω_{34}	ω_{12}
C	1.198898	79.699	22.701
	ω_{24}	ω_{12}	ω_{34}

Fig. 4.19 Phase spectra of malonyl radical observed by Q-band pulsed ENDOR technique with the TPPI detection. Combination signals between ν_{MW} and ν_{RF}, which are due to the entangled states between an electron spin and one proton nuclear spin, were observed. $|-+>$, $|+->$, $|++>$ and $|-->$ denote the four entangled Bell states composed of one electron spin-qubit and one nuclear spin-qubit. See the caption of Fig. 4.1 for the notations of $|-+>$, $|+->$, $|++>$ and $|-->$. ϕ_1 and ϕ_2 in Figs. 4.17 and 4.18 correspond to ν_{MW} and ν_{RF} for the phase rotation, respectively. Also, see Fig. 4.10. (**c**) Gives the ESR resonance fields and ENDOR resonance frequencies which are depicted in (**b**) (Adapted from Ref. [48] with kind permission of © World Scientific Publishing Co. 2009)

4.6.4 The First Direct Detection of Spinor of an Electron Spin-Qubit by Quantum Phase Manipulation

Another measurement was carried out in order to examine the quantum spin entangled states. If the pulses generate the entangled states, they are expected to show the 4π periodicity originating from the spinor property. In Fig. 4.18, the

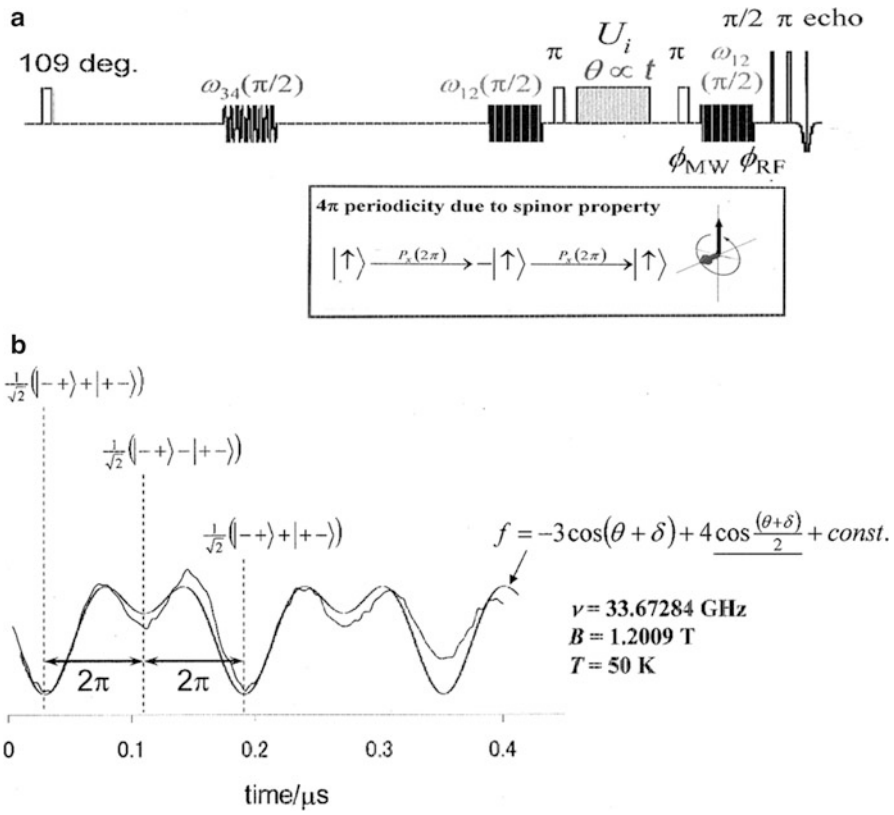

Fig. 4.20 4π-Spinor behavior due to electron spin-1/2 appeared in the electron-spin echo intensity when applying a selective microwave pulse. (**a**) The pulse sequence which generates the time evolution of the electron-nuclear spin entangled state illustrating the electron-spin spinor in a straightforward manner. U_i denotes the quantum operation of the MW excitation pulse length as a function of time t. (**b**) The Hahn ESE intensity was readout after the operations as a function of the MW pulse duration time t. The *curves* in *thin* and *thick black* denote the experimental and theoretical one, respectively. The former shows a relaxation effect due to decoherence during the experiment (Adapted from Ref. [48] with kind permission of © World Scientific Publishing Co. 2009)

TPPI-based phase manipulation was made on the client nuclear qubit spin-1/2 by rotating ϕ_2 with an X-band pulse ENDOR spectrometer. Recently, we have designed and set up a novel Q-band pulse EMR-based QC/QIP apparatus. Figure 4.20 shows a protocol for the MW/RF pulse sequence for the spinor behavior of an electron spin-qubit in the electron-nuclear spin entangled state and a readout time-domain spectrum as a function of the microwave pulse length applied to the entangled state, observed by invoking the phase rotation of ϕ_1, i.e., microwave TPPI operated

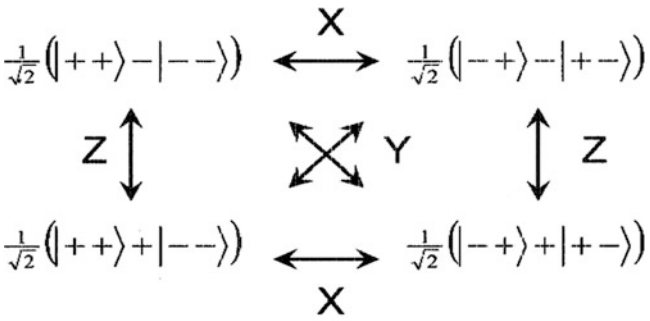

Fig. 4.21 Inter-conversion between the four Bell (entangled) states composed of the two spin-1/2 qubit system. X, Y and Z denote the quantum transformations converting the one Bell state to another

on the electron spin-qubit in the malonyl radical system. Figure 4.20a shows the pulse sequence that generates the time evolution of the electron-nuclear spin entangled state illustrating the electron-spin spinor in a straightforward manner. U_{i} denotes the quantum operation of the MW excitation pulse length as a function of time t. Figure 4.20b clearly shows that the echo-signal intensity oscillates with a 4π periodicity. The 4π periodicity does not appear in usual magnetic resonance experiments because of the inherence of the quantum phase property. In order to observe the periodicity, it is necessary to make an interferometric experiment for at least a two-spin system. The findings of the periodicity support the generation of the entangled states in an alternative way. When applying a microwave 2π pulse in this experiment, the spin manipulation corresponds to interconversion between the entangled states, *e.g.*

$$(|{+}{+}\rangle - |{-}{-}\rangle)\Big/\sqrt{2} \overset{2\pi}{\longleftrightarrow} (|{+}{+}\rangle + |{-}{-}\rangle)\Big/\sqrt{2}.$$

It is shown that the spin manipulation is successfully performed by the pulse ENDOR technique. In our QC/QIP experiments, it is also possible to operate the nuclear spin using the RF pulse. When applying the RF pulse for the generated entangled state instead of the microwave pulse, the spinor behavior due to the nuclear spin-1/2 appeared directly, as illustrated in Fig. 4.18. It is indicated that application of the microwave and RF pulses enables us to manipulate the electron-nuclear spin-qubit system, and the pulse ENDOR technique is available for performing the fundamental quantum computation in the molecular spin system. We emphasize that the direct detection of the spinor from an electron spin-qubit has for the first time been achieved only by building the entangled state involving the electron qubit. A schematic picture of the inter-conversion between the entangled states in the electron-nuclear bipartite system is given with the corresponding quantum operations in Fig. 4.21.

4.7 Tripartite Electron-Spin Nuclear-Qubits Experiments; Identification of Separable States Decomposed into Bipartite Entanglement

The first electron-involved tripartite QC experiment, in which one electron bus spin and two client nuclear spins participate, was carried out under the condition of non-selective microwave excitation. In this experiment, we also demonstrate the appearance of the entanglement between an electron spin and two nuclear spins, nitrogen and proton nuclei in the pseudo-pure state of stable non-deuterated diphenylnitroxide (DPNO-h_{10}) diluted in the lattice of diamagnetic benzophenone-h_{10} crystals, as is given in Fig. 4.22. DPNO-h_{10}, which is a typical organic radical, is multi-nuclear client spin-qubits of protons and extremely stable in the benzophenone lattice under the exposure of strong MW and RF irradiations. The α-protons of the phenyl rings are capable of nuclear client qubits in the solid state, simply because of the anisotropic nature of the proton hyperfine coupling. All the magnetic tensors of DPNO-h_{10} have experimentally been determined by CW-ENDOR/ESR spectroscopy prior to use as molecular-spin qubits [40, 41]. In order to precisely determine the magnetic tensors including the g-tensor, appropriate isotope labeling has been achieved. The perdeuterated benzophenone-d_{10} host lattice was chosen to reduce the line width of the ESR transitions, the spectral density due to the protons of neighboring host molecules in pulse ENDOR spectra and to suppress dephasing effects arising from the protons of neighboring and surrounding host benzophenone molecules.

The phase spectra belonging to the entangled states in the electron-nuclear spin-qubit system of DPNO-h_{10} have been obtained by using the TPPI technique. As described above, the microwave excitation in the ESE-detected ESR spectrum are not selective in this particular QC/QIP experiment, because the DPNO-h_{10} we used does not give highly resolved hyperfine splittings due to many protons in any orientations of the static magnetic field. Thus, the ^{14}N nucleus spin-qubit is apparently involved in the ESR transition, but not in the entanglement process and only one client proton is entangled with an electron bus qubit. Figure 4.23 shows

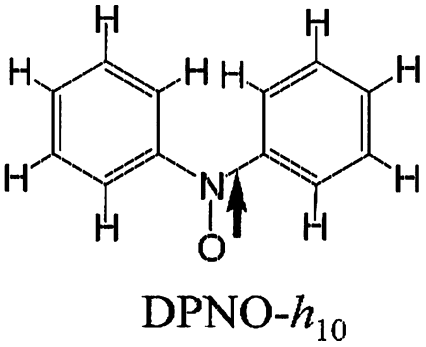

Fig. 4.22 Stable non-deuterated diphenyl nitroxide (DPNO-h_{10}) with multi-nuclear spin-qubits. DPNO-h_{10} is diluted in diamagnetic benzophenone-d_{10} crystals at any desired concentration

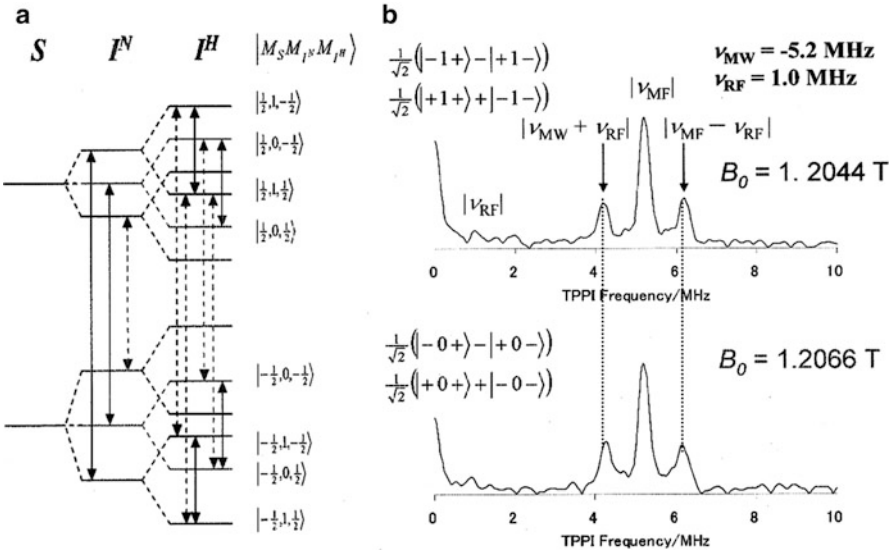

Fig. 4.23 Phase spectra obtained from the tripartite "apparent entanglement" in DONO-h_{10} magnetically diluted in the diamagnetic benzophenone-d_{10} lattice. (**a**) Energy diagram of the tripartite spin-qubits under study in DPNO-h_{10}. The MW excitations and ENDOR transitions involved in the tripartite experiments are denoted by the *arrows*. The *longest arrow* denoting the ESR allowed transition corresponds to the ESE peak appearing in the lowest field ($B_0 = 1.2044$ T). The *middle one* corresponds to the peak at $B_0 = 1.2066$ T. (**b**) Phase spectrum of DPNO-h_{10} observed by Q-band pulsed ENDOR technique with the TPPI detection. Phase frequency values, ν_1 and ν_2 are shown in the corner of this figure. The appearance of both these combination frequencies, i.e., $\nu_1 + \nu_2$ and $\nu_1 - \nu_2$, is experimental evidence for the occurrence of the superposition of the two entangled states (Adapted from Ref. [48] with kind permission of © World Scientific Publishing Co. 2009)

the separable tripartite-states that can be decomposed into a pair of the bipartite-entangled states. In the tripartite QC/QIP experiments, the partially-resolved proton ENDOR peaks were selected.

The entangled states established here involve those in which only the two particles, *i.e.*, an electron spin and one of the two proton nuclei are entangled. Seemingly, the Q-band pulse ENDOR-based phase interferogram measurements involve tripartite particles, but the event in terms of entanglement is bipartite. The nitrogen nuclear states play only a role of "the electron sublevels"; the initialization of the pseudo-pure state was established to start our QC experiments. In our three-qubit experiment, unresolved hyperfine splittings due to the protons were excited by the ^{14}N-hyperfine selective microwave irradiation, as denoted by the broken lines in Fig. 4.23a. In this context, the microwave excitation was not completely selective in terms of the proton nuclear spin states, nevertheless the experiments are still appealing because the double bipartite pseudo-entanglement between an electron and one nucleus-1/2 qubit was for the first time realized by means of

pulse ENDOR applied to the real three-qubit physical systems. True tripartite-entanglement can be realized by the use of partially deuterated DPNO properly oriented in the benzophenone lattice [42]. Such electron-bus qubit systems give us a chance to achieve such quantum teleportation experiments as electron spin-qubits in molecular-spin levels are involved in [42]. The physical aspects in terms of QC/QIP in molecular-spin qubits with nuclear client qubits are different from those in NMR-based quantum teleportation. Detailed QC/QIP experiments on molecular-spin quantum teleportation will be given elsewhere with the full analysis of electronic and molecular structures of DPNO-h_{10} from both the experimental and theoretical sides.

4.8 Conclusions and Outlook

Electron bus spin-qubits with nuclear client spin-qubits in molecular frames have been candidates for QC/QIP appearing recently among a variety of physical systems in quantum information science. In terms of hidden qubits in molecular frames, molecular chirality associated with the circularly polarized optical nature is available. Molecular electron-spin based qubits are only in the cradle and are thus challenging materials targets in quantum information science and related fields. There are a wide variety of interactions, as utilized for quantum operations or hybridization with other micro-or macroscopic qubits, between spin qubits in molecular frames, and their modes and magnitudes can be designed in terms of rapidly developing sophisticated quantum chemistry [45]. The utilization of ground-state triplet molecules with sizable zerofield splitting constants, which enables us to couple the ensemble triplets with superconducting macroscopic qubits at low temperature, is emerging. Molecular materials that are capable of giving testing grounds for QC/QIP experiments or theoretical considerations can be synthesized in many cases. Because of space, we have only introduced Lloyd's theoretical model and its variant of electron spin-qubit version for scalable QCs. Synthetic efforts for the prototypical examples of such scalable QCs have been made by invoking sophisticated supramolecular chemistry. In this context, novel functionality molecular entities have appeared, encouraging us to develop novel pulse-based MW spin manipulation technology. In particular, the time resolution associated with manipulating the electron spin-qubits in ensemble is crucial, in addition to the multi-frequency capabilities with coherency. In this context, spin manipulation technology itself for electron spin-qubits in any molecular frames is in the cradle and very immature. Electrical detection of magnetic resonance for single molecular spin-qubit systems is also an important issue, which is associated with two-dimensional array versions of Lloyd model in view of the materials challenge in chemistry and materials science. Field gradient technology applicable to periodic assemblies of molecular electron spins is still limited in terms of space resolution, which is directly associated with addressability of scalable qubits.

This chapter dealt with pulse-ENDOR based QC/QIP experiments, omitting detailed or general descriptions, with rich science behind, of eigenenergies or resonance eigenfields involved in magnetic spin transitions. We have omitted significant pulse technology dealing with decoherency in molecular frames, such as the bang-bang pulse method by Morton et al. [11] and the first important experimental results of the density-matrix based tomography for the electron-nuclear entangled states achieved for the C_{60} system including ^{15}N nucleus ($S = 3/2$, $I = 1/2$) [13].

The QC/QIP experiments on molecular spin-qubits described in this chapter are based on electron-nuclear magnetic resonance methods for all the QC processes in ensemble solids. Some advantages of the use of the organic molecular spin-qubits are described referring to both NMR QC and the current pulse MW spin technology. The heart of our matter-spin-qubit based QC/QIP experiments is the quantum-phase manipulation technology for the entanglement between molecular electro-spin and client nuclear spin-qubits. The spin-qubit manipulation technology for quantum gate operations in this work is based on time-proportional-phase-increment (TPPI) technique, enabling us to discriminate between the quantum phases of the Bell entangled states. Pulse ENDOR based QC/QIP experiments for super dense coding (SDC) have for the first time been carried out by the use of stable malonyl radical as matter spin-qubits. The TPPI technique has illustrated the establishment of quantum entanglement between electron- and nuclear-spin states and mutual interconvesion between the Bell states. Interestingly, the electron-spin 4π-periodicity in quantum phase has been explicitly observed in the QC experiments for the first time, illustrating the electron-spin spinor nature from the experimental side. A basis for the tripartite QC experiments involving electron and nuclear spin-qubits has also been given for the first time. This chapter refers to another important topic of relevance in molecular spin-qubit based QC/QIP experiments, describing that the pulsed coherent-dual ELDOR for QC/QIP has for the first time been implemented by invoking a novel microwave coherent-dual phase-rotation technique. Thus, applications of the coherent-dual ELDOR to molecular electron spin-qubit systems are anticipated, emphasizing the need for designing the molecular two electron-qubits systems appropriate for QC/QIP. g- And/or hyperfine A-tensor engineering approaches are required in materials challenge for preparing the two- and multi-electron-qubits systems.

The chapter implies that general requisites for scalable true electron spin-qubits systems such as 1D periodic robust spin structures, the electron spin-qubit variant of Lloyd model, in addition to DiVincenzo's five criteria, are necessary in terms of synthetic strategy. In order to implement real QCs and QIP systems, the scalability of qubits is essential. In this context, the synthetic feasibility for the scalability of particularly chosen ligands is essentially important. According to the requisites, double- or triple-stranded helicates embedding open-shell metal cations are suggested instead of organic molecular spin-qubits [35, 46, 47]. The reasons why weakly exchange-coupled electron spin-qubits such as organic multi-radicals are suitable for present-stage QC/QIP are emphasized in terms of the currently available microwave spin technology. Nevertheless, this is only a temporal limitation.

Acknowledgments This work has been supported by Grants-in-Aid for Scientific Research (B) and Scientific Research on Innovative Areas, "Quantum Cybernetics" from MEXT, Japan. The support by JST through Core Research for Evolutional Science and Technology (CREST) project, "Implementation of Molecular Spin Quantum Computers" and the support by the Funding Program for World-Leading Innovative R&D on Science and Technology (FIRST) project on "Quantum Information Processing", JSPS, Japan are also acknowledged.

References

1. Feynman RP (1982) Simulating physics with computers. Int J Theor Phys 21:467–488: *ibid*. (1985) Quantum mechanical computers. Opt News 11:11–20
2. Nielsen MA, Chuang IL (2000) Quantum computation and quantum information. Cambridge University Press, Cambridge
3. Shor PW (1994) In: Proceedings, 35th annual symposium on foundations of computer science, IEEE Computer Society Press, New York, pp 124–134
4. Grover LK (1997) Quantum mechanics helps in searching for a needle in a haystack. Phys Rev Lett 79:325–328
5. Bennett CH, Brassard G., Crepeau C, Jozsa R, Peres A, Wootters W (1993) Teleporting an unknown quantum state via dual classical and Einstein-Podolsky-Rosen channels. Phys Rev Lett 70:1895–1899
6. Bennett CH, Wiesner SJ (1992) Communication via one-particle and 2-particle operators on Einstein-Podolsky-Rosen states. Phys Rev Lett 69:2881–2884
7. Mehring M, Mende J, Scherer W (2003) Entanglement between an electron and a nuclear spin 1/2. Phys Rev Lett 90:153001
8. Mehring M, Scherer W, Weidinger A (2004) Pseudoentanglement of spin states in the multilevel N-15@C-60 system. Phys Rev Lett 93:206603
9. Rahimi R, Sato K, Furukawa K, Toyota K, Shiomi D, Nakamura T, Kitagawa M, Takui T (2004) Pulsed ENDOR-based quantum information processing. In: Soo C, Zhang WM (eds) Proceedings of the 1st Asia-Pacific conference on quantum information science, World Scientific Publishing Co. Pte. Ltd., Singapore
10. Rahimi R, Sato K, Furukawa K, Toyota K, Shiomi D, Nakamura T, Kitagawa M, Takui T (2005) Pulsed ENDOR-based quantum information processing. Int J Quantum Inf 3:197–204
11. Morton JJL, Tyryshkin A, Ardavan A, Benjamin S, Porfyrakis K, Lyon SA, Briggs GAD (2006) Bang-bang control of fullerene qubits using ultrafast phase gates. Nat Phys 2:40–43
12. Sato K, Rahimi R, Nishida S, Toyota K, Shiomi D, Morita Y, Ueda A, Suzuki S, Furukawa K, Nakamura T, Kitagawa M, Makasuji K, Nakahara M, Hara H, Carl P, Hoefer P, Takui T (2007) Implementation of molecular spin quantum computing by pulsed ENDOR technique: direct observation of quantum entanglement and spinor. Physica E 40:363–366
13. Scherer W, Mehring M (2008) Entangled electron and nuclear spin states in $^{15}N@C_{60}$: density matrix tomography. J Chem Phys 128:052305
14. Jones JA, Mosca M, Hansen RH (1998) Implementation of a quantum search algorithm on a quantum computer. Nature 393:344–346
15. Chuang IL, Vandersypen LMK, Zhou X, Leung DW, Lloyd S (1998) Experimental realization of a quantum algorithm. Nature 393:143–146
16. Chuang IL, Yamamoto Y (1995) Simple quantum computer. Phys Rev A 52:3489–3496
17. Cirac JI, Zoller P (1995) Quantum computations with cold trapped ions. Phys Rev Lett 74:4091–4094
18. Divincenzo DP (1997) Topics in quantum computers. In: Sohn L, Kouwenhoven L, Schon G (eds) Mesoscopic electron transport (vol 345, NATO ASI Series E), Kluwer, Dordrecht (Cond_mat/9612126)
19. Nakazawa S, Sato K, Takui T et al., unpublished work

20. Mehring M, Hoefer P, Grupp A (1986) Bloch-Siegert shift, Rabi oscillation, and spinor behavior in pulsed electron-nuclear double-resonance experiments. Phys Rev A 33:3523–3526
21. Chuang IL, Gershenfeld N, Kubinec M (1998) Experimental implementation of fast quantum searching. Phys Rev Lett 18:3408–3411
22. Chuang IL, Vandersypen LMK, Zhou X, Leung DW, Lloyd S (1998) Experimental realization of a quantum algorithm. Nature 393:143–146
23. Nielsen MA, Knill E, Laflamme R (1998) Complete quantum teleportation using nuclear magnetic resonance. Nature 396:52–55
24. Vandersypen LMK, Steffen M, Breytra G, Yannoni CS, Sherwood MH, Chuang I.L (2001) Experimental realization of Shor's quantum factoring algorithm using nuclear magnetic resonance. Nature 414:883–887
25. Fang X, Zhu X, Feng M, Mao X, Du F (2000) Experimental implementation of dense coding using nuclear magnetic resonance. Phys Rev A 61:022307
26. Cory DG., Fahmy AF, Havel TF (1997) Ensemble quantum computing by NMR spectroscopy. Proc Natl Acad Sci USA 94:1634–1639
27. Gershenfeld N, Chuang IL (1997) Bulk spin-resonance quantum computation. Science 275:350–356
28. Ekert A, Jozsa R (1998) Quantum algorithms: entanglement-enhanced information processing. Philos Trans R Soc Lond A 356:1769–1781
29. Linden N, Popescu S (2001) Good dynamics versus bad kinematics: is entanglement needed for quantum computation? Phys Rev Lett 87:047901
30. Zyczkowski K, Horodecki P, Sanpera A, Lewenstein M (1998) Volume of the set of separable states. Phys Rev A 58:883–892
31. Braunstein SL, Caves SM, Jozsa R, Linden N, Popescu S, Schack R (1999) Separability of very noisy mixed states and implications for NMR quantum computing. Phys Rev Lett 83: 1054–1057
32. Anwar MS, Blazina D, Carteret H, Duckett SB, Halstead TK, Jones JA, Kozak CM, Taylor RJK (2004) Preparing high purity initial states for nuclear magnetic resonance quantum computing. Phys Rev Lett 93:040501
33. Anwar MS, Jones JA, Blazina D, Duckett SB, Carteret HA (2004) Implementation of NMR quantum computation with parahydrogen-derived high-purity quantum states. Phys Rev A 70:032324
34. Feher G (1956) Observation of nuclear magnetic resonances via the electron spin resonance line. Phys Rev 103:834–835; (b) Mims WB (1965) Pulsed ENDOR experiments. Proc R Soc Lond 283:452–457; (c) Grupp A, Mehring M (1990) Pulsed ENDOR spectroscopy in solids. In: Kevan L, Bowman MK (eds) Modern pulsed and continuous-wave electron spin resonance. Wiley, New York
35. Morita Y, Yakiyama Y, Murata T, Ise T, Hashizume D, Shiomi D, Sato K, Kitgawa M, Takui T, Nakasuji K (2010) Triple-stranded metallo-helicates addressable as Lloyd's electron spin qubits. J Am Chem Soc 132:6944–6946
36. Peres A (1996) Separability criterion for density matrices. Phys Rev Lett **77**:1413–1415
37. Horodecki M, Horodecki P, Horodecki R (1996) Separability of mixed states: necessary and sufficient conditions. Phys Lett A 223:1–8
38. McConnell HM, Heller C, Cole T, Fessenden RW (1960) Radiation damage in organic crystals.1. $CH(COOH)_2$ in malonic acid. J Am Chem Soc 82:766–775
39. Davies ER (1974) New pulse ENDOR technique. Phys Lett A 47:1–2
40. Rahimi R, Sato K, Nishida S, Morita Y, Kitagawa M, Takui T, et al., to be published
41. Yoshino T, Nishida S, Nakazawa S, Rahimi R, Sato K, Morita Y, Kitagawa M, Takui T, et al (2011) ESR and ^{1}H-, ^{19}F-ENDOR/TRIPLE study of fluorinated diphenylnitroxides as synthetic bus spin-qubit radicals with client qubits in solution. J Phys Chem Lett 2:449–453
42. Nakazawa S, Sato K, Yoshino T, Morita Y, Takui T et al., to be submitted
43. Lloyd S (1995) Quantum-mechanical computers. Sci Am 273:140–145
44. Lloyd S (1993) A potentially realizable quantum computer. Science 261:1569–1571

45. Sugisaki K, Toyota K, Sato K, Shiomi D, Kitagawa M, Takui T (2009) Ab initio calculations of spin-orbit contribution to the zero-field splitting tensors of nπ* excited states by the CASSCF method with MRMP2 energy correction. Chem Phys Lett 477:369–373; (b) Sugisaki K, Toyota K, Sato K, Shiomi D, Kitagawa M, Takui T (2010) Spin-orbit contributions in high-spin nitrenes/carbenes: a hybrid CASSCF/MRMP2 study of zero-field splitting tensors. ChemPhysChem 11:3146–3151; (c) Sugisaki K, Toyota K, Sato K, Shiomi D, Kitagawa M, Takui T (2011) Ab initio and DFT studies of the spin-orbit and spin-spin contributions to the zero-field splitting tensors of triplet nitrenes with aryl scaffolds. Phys Chem Chem Phys 13:6939–6949
46. Sato K, Nakazawa S, Rahimi R, Ise T, Nishida S, Yoshino T, Mori N, Toyota K, Shiomi D, Yakiyama Y, Morita Y, Kitagawa M, Nakasuji K, Nakahara M, Hara H, Carl P, Höfer P, Takui T (2009) Molecular electron-spin quantum computers and quantum information processing: pulse-based electron magnetic resonance spin technology applied to matter spin-qubits. J Mater Chem 19:3739–3754
47. Morita Y, Yakiyama Y, Nakazawa S, Murata T, Ise T, Hashizume D, Shiomi D, Sato K, Kitagawa M, Nakasuji K, Takui T (2010) Triple-stranded metallo-helicates addressable as Lloyd's electron spin qubits. J Am Chem Soc 132:6944–6946
48. Sato K, Nakazawa S, Rahimi RD, Nishida S, Ise T, Shiomi D, Toyota K, Morita Y, Kitagawa M, Carl P, Hoefer P, Takui T (2009) Quantum computing using pulse-based electron-nuclear double resonance (ENDOR): molecular spin qubits. In: Nakahara M, Ota Y, Rahimi R, Kondo Y, Tada-Umezaki M (eds) Molecular realizations of quantum computing 2007: Kinki university series on quantum computing, vol. 2. World Scientific Publishing Co. Pte. Ltd., Singapore

Chapter 5
High Spin Molecules Directed Towards Molecular Magnets

Martin Baumgarten

Abstract EPR has often been used to define spin states of high spin molecules. This chapter outlines some meaningful considerations for the classification of interacting radicals and the determination of their ground state spin multiplicity. Then a review on different classes of high spin molecules follows, sorted by their spin state, summarizing the application of EPR in that domain.

5.1 Introduction

Molecular magnetism is a part of material science chemistry, which strongly developed over the last 30 years. It may be viewed as a frontier research among inorganic and organic structures and their hybrid solids. Milestones include the detection of bulk ferromagnetism in the molecular complex of decamethylferrocene-tetracyanoethylene $Fe^{III}(C_5(CH_3)_5)_2$ in 1987 by Miller and Epstein [1] and the first pure organic ferromagnet of *p*-nitrophenyl-nitronylnitroxide in 1991 by Kinoshita [2]. Besides the use of inorganic metal complexes for molecular magnets large efforts went into the controlled synthesis of new stable organic high spin moieties and their in depth characterization. Therefore, by now a huge number of organic bi- and oligo-radicals of very different nature concerning their radical sites and the connectivity between them are available. Some of them are fairly old and are known since the beginning of the last century: ones like the Schlenk hydrocarbon [3] and Tschitschibabin's [4] or Yang's [5] and Coppinger's [6] biradicals (Fig. 5.1). Many more were just added over the last 20 years and most of them were synthesized and characterized or trapped as intermediates to clarify their electronic structure and ground state spin multiplicity. This has been performed especially in

M. Baumgarten (✉)
Max Planck Institute for Polymer Research, Ackermannweg 10, D-55128 Mainz, Germany
e-mail: martin.baumgarten@mpip-mainz.mpg.de

A. Lund and M. Shiotani (eds.), *EPR of Free Radicals in Solids II*, Progress in Theoretical Chemistry and Physics 25, DOI 10.1007/978-94-007-4887-3_5,

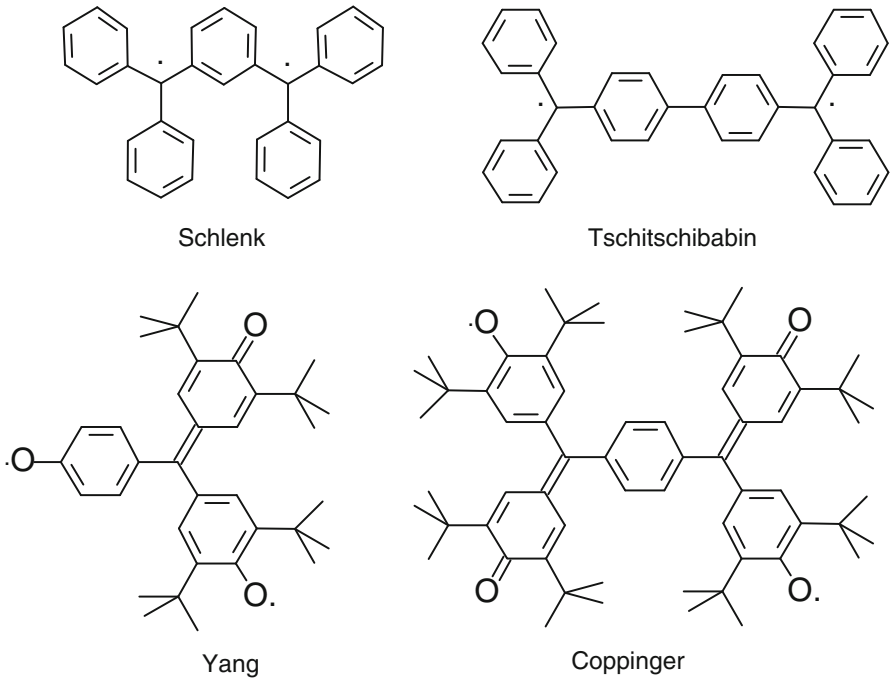

Fig. 5.1 Some classical biradicals

order to gain further insight into the factors controlling spin alignment and their possible use as building blocks for organic materials with magnetic ordering.

Triplet state molecules, on the other hand, also play an important role as intermediates in bio-organics and bio-physics. In order to define the basic structure of this chapter we may first consider the classification of bi- and oligoradicals (see Fig. 5.2 for the energy levels of two spin systems in a magnetic field). While a monoradical is just represented by the spin up/spin down energy levels which lose their degeneracy in a magnetic field, a biradical can be described in many different ways, e.g. if there is a large distance ($d \geq 1$ nm) and no conjugation between the radical sites the exchange coupling J is zero and the biradical may either be presented as two independent monoradicals or as an equilibrium mixture of a triplet and a singlet state (Fig. 5.2b, c).

If we deal with the excited states of neutral organic precursors as aromatic compounds, then the lowest triplet often is below the lowest photoexcited singlet state and can be accessed by intersystem crossing from the latter. Such highly activated triplet states will not be considered in this review, although it might be an intriguing task to find even higher than triplet spin multiplicities after photoexcitation, e.g. by considering two phenyl bridged naphthalenes, where a quintet state may become accessible.

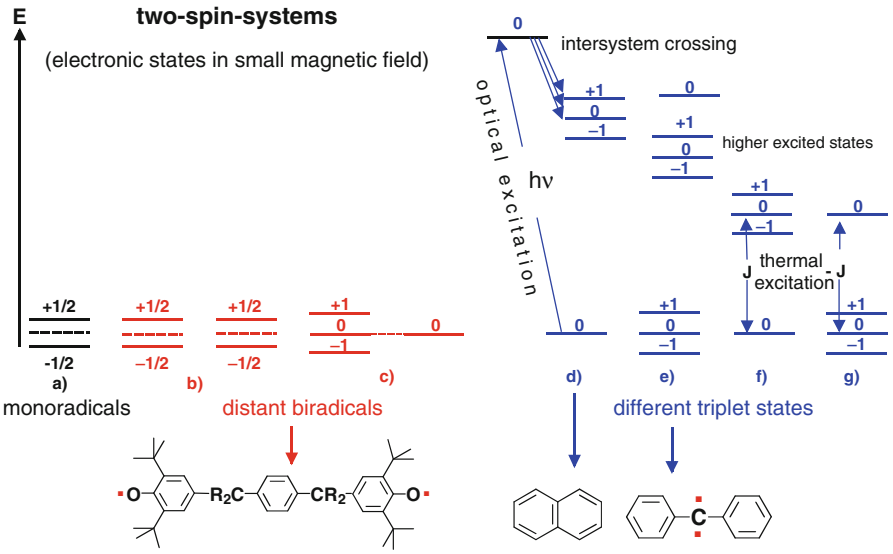

Fig. 5.2 Different kinds of the biradicals and their energetic states compared to (*a*) monoradical, (*b*) or (*c*) biradical with distant radical centers (*d*) photoexcited triplet state, (*e*) ground state triplet, and (*f*) ground state singlet with thermally accessible triplet, and (*g*) ground state triplet with thermally accessible singlet [7]

In this vein it was demonstrated that quartet and quintet states are amenable upon photoexcitation of a 9,10-diphenyl-anthracene **1** situated between one or two stable nitronylnitroxide **1a** or oxo-verdazyl radicals **1b** [8, 9].

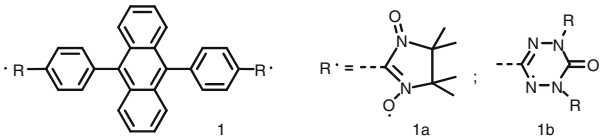

In the discussion we can delineate three cases in order of decreasing high-spin stability: (i) a triplet ground state where no thermal activation to the excited states is possible under ambient laboratory conditions (Fig. 5.2e); (ii) a ground-state triplet with thermally accessible singlet state, and (iii) thermally activated triplet state above a singlet ground state. While biradicals at large distance connected through saturated spacers may easily be classified as (b) or (c) and photo excited triplet states (d) are rarely long lived stable species, the last three groups (Fig. 5.2e, f, g) deserve more intimate characterization in order to define their ground state spin multiplicity unambiguously. This also holds for even higher spin states in discrete molecules and the method of choice to do that certainly is EPR spectroscopy.

5.2 Determination of the Spin States and Ground State Multiplicities of High Spin Molecules

Over the last decade EPR has often been applied to identify many ambiguous spin states in high spin molecules and for characterizing new molecules. This was performed in order to fully understand the conditions and prerequisites for obtaining high spin molecules or parallel spin alignment in extended polymers with radical sites in the main or side chain with linear, branched, dendritic, or hyperbranched extensions. The basis for these approaches was the clean experimental elucidation of the spin states of the molecular building blocks by EPR spectroscopic methods and their theoretical understandings. Continuous wave X-band EPR and sometimes ENDOR studies have most often been employed, besides the use of high field high frequency and FT-pulsed EPR techniques. The latter especially transient nutation experiments developed fast during the last 10 to 15 years [10–12].

The basic parameters for characterization of more than one unpaired electron are the electron electron spin-spin interactions H_{SS}, consisting of the isotropic exchange J and the dipolar exchange described by tensor **D**. The latter are also referred to as fine structure or zero field splitting (ZFS) parameters. The spin Hamiltonian H_{spin} for describing high spin molecules is then expressed by Eq. (5.1), including further the electron spin orbit and electronic Zeeman $(H_{LS}+H_{ZE}) = \beta\, \boldsymbol{B} \bullet \mathbf{g} \bullet \boldsymbol{S}$ and the hyperfine interaction $H_{SI} = \boldsymbol{S} \bullet \mathbf{A} \bullet \boldsymbol{I}$, while higher order terms for nuclear Zeeman $H_{nZ} = -g_n\beta_n \boldsymbol{I} \bullet \boldsymbol{B}$ and quadrupolar interactions $H_Q = \boldsymbol{I} \bullet \mathbf{P} \bullet \boldsymbol{I}$ are often neglected.

$$\begin{aligned} H_{spin} =& H_{LS} + H_{ZE} + H_{SS} + H_{SI}\left[+H_{nZ} + H_Q + \cdots\right] = \\ =& \beta\, \mathbf{B} \bullet \mathbf{g} \bullet \mathbf{S} + \mathbf{S} \bullet \mathbf{D} \bullet \mathbf{S} + J\, \mathbf{S} \bullet \mathbf{S} + \mathbf{S} \bullet \mathbf{A} \bullet \mathbf{I} \\ & \times \left[-g_n\beta_n \mathbf{I} \bullet \mathbf{B} + \mathbf{I} \bullet \mathbf{P} \bullet \mathbf{I} + \cdots\right] \end{aligned} \tag{5.1}$$

In solid state EPR the dipolar exchange (ZFS) is dominating, while the isotropic exchange J contributes a common constant to the energy of each high spin state. Since **D** is traceless, the fine structure is usually described by two energetic parameters D and E, which are $D = 3D_z/2$ and $E = (D_x - D_y)/2$, expressed in cm^{-1} as $D' = D/hc$ and $E' = E/hc$ or in magnetic field units $D' = D/g_e\beta$ and $E' = E/g_e\beta$. The EPR spectral analyses for isolated triplet state molecules are well established and described in standard textbooks [13].

For high spin molecules usually it is assumed that the g anisotropy is small and that the zero field splitting $|\mathbf{D}|$ is not larger than the microwave transition energy (high field approximation), but exceeds the hyperfine interaction, which can then be considered as perturbation.

$$H_{spin} = \beta\, \mathbf{B} \bullet \mathbf{g} \bullet \mathbf{S} + D\left(S_Z^2 - \frac{S\,(S+1)}{3}\right) + E\left(S_X^2 - S_Y^2\right) \tag{5.2}$$

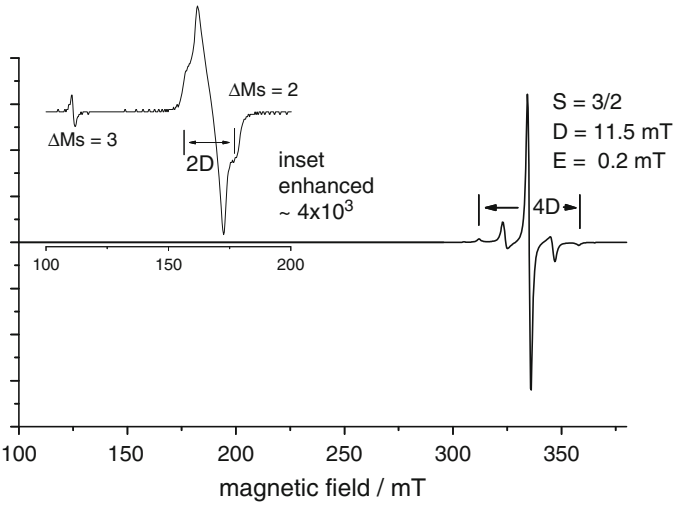

Fig. 5.3 Simulated X-band EPR spectrum for S=3/2 with $D' = 0.01075\ cm^{-1}$, $E' = 0.00019\ cm^{-1}$, and g = 2.003 at 9.4 GHz. ($B_{res} = 335$ mT)

This approximation has been encountered most widely in bridged bi- and oligoradicals leading to the "typical" high spin patterns with a maximum of $2S \times 3$ allowed fine structure transitions ($\Delta m_S = 1$). In addition $\Delta m_S = 2$ and sometimes $\Delta m_S = 3$ forbidden transitions can be observed. One should note that the relative intensities of the $\Delta m_S = 1$, $\Delta m_S = 2$, and $\Delta m_S = 3$ transition obey the ratio $1:(D'/Bo)^2:(D'/Bo)^4$, respectively. A typical spectral simulation for a quartet state (S = 3/2) at X-band is shown in Fig. 5.3.

Very complex patterns and additional absorption lines have been identified and analysed for high spin molecules with very large zero field splittings (e.g. carbenes and nitrenes) where $H_{SS} \geq H_{ZE}$. Such spectra were a true puzzle in the early 1960s, when Wassermann et al. reported [14] about new powder spectra for *m*-phenylene bridged dicarbenes and dinitrenes. They could not be explained until 1967 [15], when Itoh [16] submitted a single crystal study on *m*-phenylene-bis(phenyl-methylene) **2**.

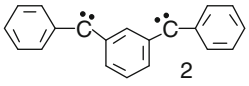

2

The breakdown of the perturbation approach in cases of very large zero field splitting parameters $|D| \geq h\nu$ was pointed out carefully by Takui et al. [17] leading to off axis extra absorption peaks. Those can be simulated by direct diagonalization of the spin Hamiltonian but not directly extracted from the observed spectra, which led to spurious documentation on spin-quintet dinitrenes.

If these measurements, on the other hand, would be performed in W-band at 94 GHz, where the high field approximation still holds, they will give the "usual"

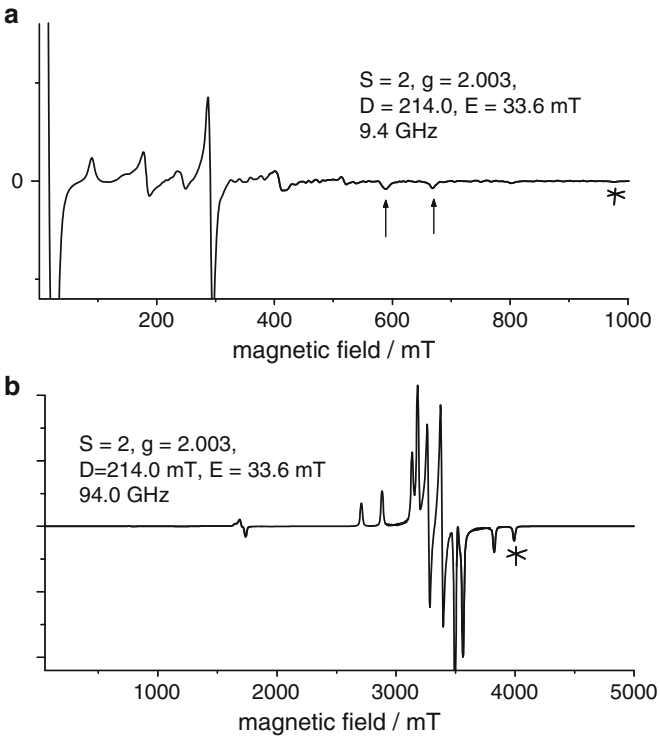

Fig. 5.4 Simulated EPR spectra at X-band (**a**) and at W-band (**b**) for very large ZFS parameters $D' = 0.200\ cm^{-1}$, $E' = 0.0314\ cm^{-1}$. The *star marks* highest z-field component, the *sharp arrows* some extra absorption lines

pattern for a $S = 2$ spin state (Fig. 5.4a, b). The standard cw EPR application is limited to discrete spin systems since with increasing number of spins the number of allowed transitions grows rapidly, producing high spectral density in the center with extremely weak intensity of the outermost signals. This was found already for a hexaradical in a septet state [18] and can be further demonstrated for an $S = 5$ state with $D' = 0.0060\ cm^{-1}$ and $E' = 0.0002\ cm^{-1}$ (Fig. 5.5).

Another problem in determining the fine structures by EPR may occur when they are smaller or equal to the hyperfine splitting. In some cases with well defined hyperfine couplings as in phosphinyl radicals ($^{31}P\ A_{\parallel} = 850$ MHz, $A_{iso} = 297$ MHz while $D' = 260$ MHz), shown by Janssen et al. [19], the well resolved transitions can still be fully analysed. Otherwise this situation may lead to unresolved EPR spectra in the $\Delta m_S = 1$ region but also to weak signals for the $\Delta m_S = 2$ transition due to small D′-value. In such cases high resolution ENDOR experiments can be very helpful to analyze hyperfine and sometimes exchange interaction.

The ENDOR studies have been applied for the identification of multispin states in solution and in rigid media [20, 21], but hardly for the identification of the ground state multiplicity itself. However, additional information on the hyperfine coupling

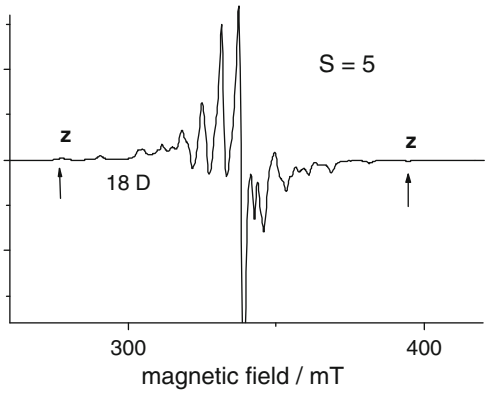

Fig. 5.5 EPR spectrum for S = 5, D = 0.0060 and E = 0.0002 cm^{-1} at 9.4 GHz and g = 2.00. The outermost z components are separated by 18 D

scheme and thus spin density distribution can be obtained. If the absolute signs of the hyperfine coupling constants are determined, e.g. from isotopic labeling and triple resonance, the sign and the size of the isotropic exchange coupling J and of the dipolar ZFS component D' can be deduced as well [21].

Other hurdles may be faced in large molecular or polymeric spin systems where the observed spectra are often composed of mixtures of different spin states and also conformers rendering the analysis very difficult. New FT-EPR methods based on transient nutation therefore seem to be very promising for elucidating such spin states [10, 11]. The transient nutation spectroscopy provides an extremely high resolution for spin multiplicities and magnitudes of ZFS parameters. It is based on the precession or nutation of the magnitization vector $\boldsymbol{M}$ around the effective magnetic field $\boldsymbol{B}_{eff}$ summed by the static field $\boldsymbol{B}_o$ and the microwave field $\boldsymbol{B}_1$ described in the rotating frame. In the rotating frame under microwave irradiation this precession is no longer the Larmor frequency as in the laboratory frame but called "transient nutation", since the signal is observed for a finite time only after turning on the microwave radiation until a steady state is reached. When the excitation pulse is turned off, $\boldsymbol{M}$ undergoes the free induction decay (FID). The effective nutation frequency ω_{eff} for a doublet spin S = 1/2 with an isotropic g value is described in the rotating frame ω_{rot} as typical Larmor precession $\omega_s = g\beta_e B_o/\hbar$ and the additional precession about the microwave field $\omega_1 = g_1\beta_e B_1/\hbar$ (here g_1 is related to the laboratory frame as described by equation 3.4.17 in Ref. [11]).

$$\omega_{eff} = \left[(\omega_s - \omega_{rot})^2 + \omega_1^2\right]^{1/2} \tag{5.3}$$

In the resonant case $\omega_s = \omega_{rot}$ and $\omega_{eff} = \omega_1$. That is the resonant magnetization nutates with ω_1 around the rotating x-axis, whereas the off resonance magnetization nutates with frequency ω_{eff} around the effective field vector, which is deflected from the z-axis by the angle θ. The description of the spin nutation about the effective field follows the Hamiltonian including their spin states.

$$H = H_0 + H_1 = (\omega_s - \omega_{rot})\ S_Z + \omega_1 S_X \tag{5.4}$$

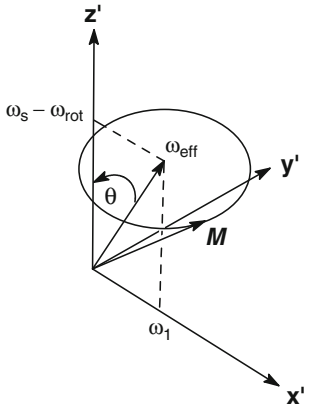

Fig. 5.6 Nutation of the magnetization vector ***M*** in the rotating frame

In case of high spin molecules the nutation frequency is directly depending on the contributing spin states (Fig. 5.6). The transition amplitudes depend on the spin quantum number S. If the microwave radiation excites only a single transition in the weak extreme limit, the nutation frequency for the transition between the two states characterized by the magnetic quantum numbers m_s and m_s+1 is given by ω_{nut}:

$$\omega_{nut}\,(m_S, m_S + 1) = \omega_1\,(S\,(S+1) - m_S\,(m_S+1))^{1/2} \tag{5.5}$$

where ω_1 includes the microwave B_1 field (see Eq. 5.4) which can be determined separately in a calibration experiment for a standard as DPPH, where $g = g_1 = 2.0037$. If the microwave excitation is not transition sensitive, as in strong microwave field limit where all transitions are excited, a nutation of the magnetization along ω_1 is observed, which is independent of the spin states ($\omega_{nut} \sim \omega_1$). For the intermediate situations the interpretation of the spectra may be more or less complicated. The various limits are well described by Takui et al. [10, 22]. Finally the Nutation experiments can be conducted by either observing the FID or the electron spin echo, and the latter has most often been applied for characterizing high spin molecules [10, 11, 22].

In order to define the ground state spin multiplicities and to separate them from thermally activated ones, the most usual characterization is to follow the temperature dependent variation of signal intensities of the given spin state. Especially for the standard cw-techniques, complications in the ground state determination for the bi- and oligoradicals may arise from overlapping signal contamination of other spin states, and very different saturation effects. Therefore these measurements should be checked for reversibility, temperature errors, and saturation effects, which become most important at lowest accessible temperature range. A deviation from linear dependence of signal intensity versus square root of microwave power showing the saturation effect may easily be implied upon lowering the temperature.

If the intensity changes linearly with the temperature ($I_*T = \text{const}$) the behavior is Curie like (Fig. 5.7a) and the exchange interaction is either large or small.

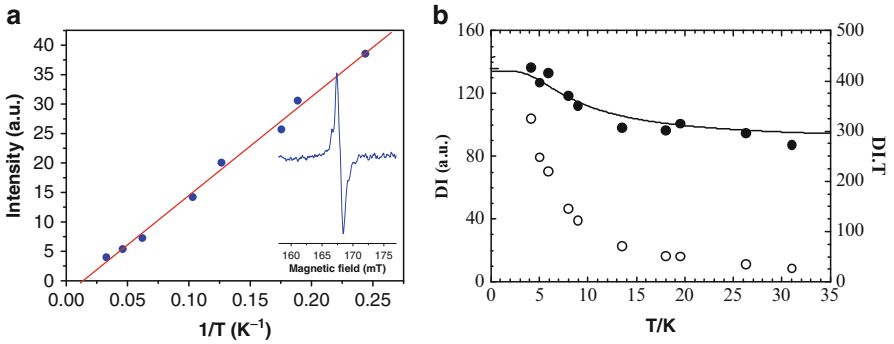

Fig. 5.7 Curie plot (**a**) and double integrated intensity (DI) or DI*T vs. T (**b**) for a triplet ground state biradical with thermally excited singlet state (Partially adopted from Ref. [23] with kind permission of © Wiley-VCH 2004)

For thermally activated triplet states with mediate exchange coupling the signal intensity will reach a maximum allowing easy extraction of the antiferromagnetic exchange interaction. For ground state triplet states with thermally excited singlet states the I*T should increase by one third upon full occupation of the triplet state (Fig. 5.7b) [23], where the transition temperature directly implies the exchange interaction through the Bleaney-Bowers equation 5.6 [24] with their standard meanings.

$$\chi_{EPR} \sim \left[\left(\frac{2Ng^2\beta_c^2}{3k_bT}\right) \times \left(\frac{1}{3} + \exp\left(\frac{-2J}{k_bT}\right)\right)\right] \tag{5.6}$$

The activation energy for experimental determination is usually limited to the temperature range 2–350 K (~4–700 cal/mol) or even lower due to the thermal stability of the radicals or their matrix.

Besides experimental techniques for determining ground state spin multiplicities, where also magnetic susceptibility measurements have been applied, many molecular systems were considered theoretically in order to obtain a deeper understanding of the spin exchange and further confirmation of the multiplicity. Such quantum chemical studies on high spin states also enable the prediction of ground state spin multiplicities for molecules so far unknown as a guiding design.

Discrepancies between experimental results and theoretical predictions have spurred more accurate characterisation of already known or the synthesis of novel high spin candidates. A number of high spin molecules have been designed from standard radicals attached to coupling units (CU) providing spin exchange by topological or geometrical control. Thus in the following paragraph we will pass through the common rules and exceptions, in order to get a more complete picture on the molecular level. Since this book focuses on EPR spectroscopy and its application, we will sort this chapter by the spin states and not by the type of

radicals. A few exceptions may be apologized, for very closely related molecules. Research has been focused mainly on bi-, tri-, and tetra-radicals, while even higher spin states have only been dealt with in a few cases.

Since the number of biradicals is huge we have to limit this outline to a choice of importance. For a more complete overview on all available organic high spin molecules and extended molecular based magnets further textbooks and review articles may be considered [25–34].

5.3 Biradicals – The Triplet State

The most often used approach for high spin molecules is the control of through bond exchange in conjugated molecules leading to so called non-Kekulé structures as in *m*-xylene (1,3-dimethylene-benzene), where no double bond between the unpaired electrons can be formed. In difference thereto, the *para* and *ortho* derivatives usually undergo spin pairing to the more stable quinoid structures in the Kekulé forms (Fig. 5.8).

The number of non bonding MO's (NBMO's) and thus the number of unpaired electrons S can easily be predicted by the rules of Longuet Higgins [35] [nNBMO = (N-2T); S = 0.5 (N-2T) with N number of π-centers and T number of double bonds] or according to the rule of Ovchinnikov [36] based on spin polarisation, by substracting the number of starred and unstarred π-centers S = 0.5 ($n^* - n^o$). The spin polarisation is thus used to explain high spin ground states for Schlenk's and Yang's biradicals, but low spin ground state for Tschitschibabins and Coppingers biradicals (Fig. 5.1).

The *m*-phenylene as coupling unit (**CU**) to connect radical sites has therefore been used in many high spin molecules with common radical sites as given in Fig. 5.9. Some of them are very stable and can be handled even in solution at room or higher temperatures (**NN**, **IN**). Others are moisture and air sensitive as the ketyl anion or aromatic radical anions and cations. The usual nitrenes and carbenes are very reactive and only stable below 100 K. Over the last years a major breakthrough was made with triplet carbenes being stable up to room temperatures. They could be synthesized with halides in the *o*-phenyl-positions close to the

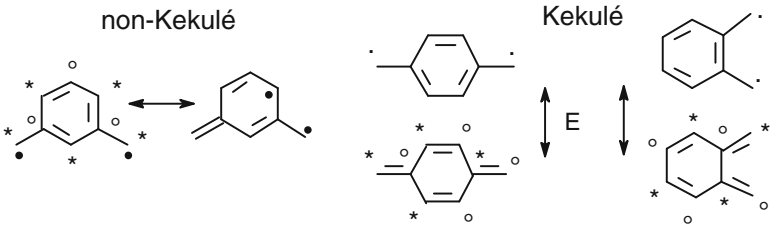

Fig. 5.8 Non-Kekulé vs. Kekulé structures

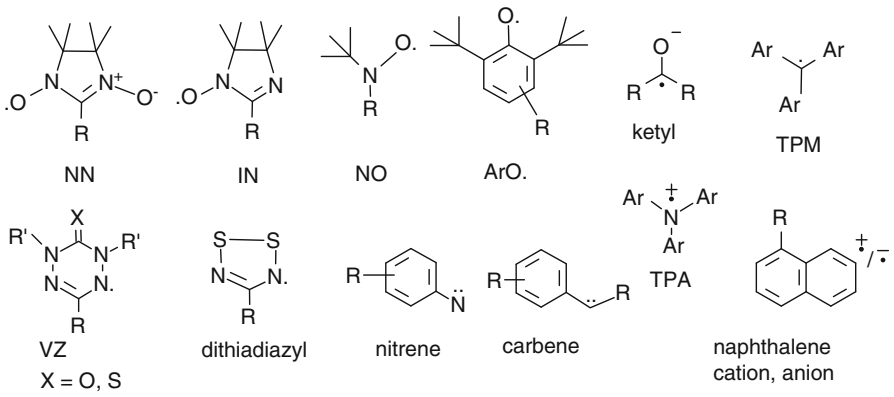

Fig. 5.9 Common radical sites, nitronyl nitroxide **NN**, iminonitroxide **IN**, *tert.-but.*-nitroxide **NO**, phenoxide **ArO**, ketyl radicals, triphenylmethyl **TPM**, verdazyl **VZ**, dithiadiazyl, nitrenes, carbenes, triphenylamin cation **TPA** or aromatic radical cation and anions like naphthalene

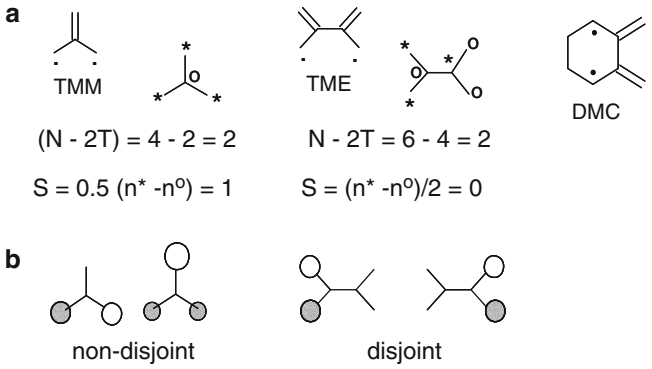

Fig. 5.10 (**a**) Structure and spin state of **TMM**, **TME**, and **DMC**, (**b**) the NBMO's of **TMM** and **TME**

carbene as perchlorodiphenylcarbene, 2,2′,4,4′,6,6′-hexachlorodiphenyl-carbene, or 2,2′,6,6′-tetrabromo-4,4′-di*tert*-butyldiphenylcarbene [12, 37, 38] Fig. 3.9.

In the 1990's there were already known several exceptions of high spin states in non-Kekulé hydrocarbon structures, which were then addressed as *Violations of Hund's Rule in non-Kekulé Hydrocarbons* [39]. It was shown and predicted earlier by Borden [40, 41] that another classification of non-Kekulé molecules is very important, e.g. the separation of molecules into those possessing non-disjoint and those possessing disjoint non-bonding MO's (Fig. 5.10). Most easily it can be demonstrated by comparing trimethylenemethane (**TMM**) and tetramethyleneethane (**TME**). In **TMM** the NBMOs are distributed over the whole molecule (non-disjoint) while in **TME** and in the more rigid 2,3-dimethylenecyclohexane-1,4-diyl (**DMC**) the NBMOs are localized on two subparts as separate moieties (disjoint). Thus spin polarization already predicts ground state singlets for **TME** and **DMC**.

Experimentally Dowd et al. could access all 3 molecules above in frozen matrices [42–44] showing similar biradical behavior concerning their EPR fine structure with ZFS's of $D' = 0.024\ cm^{-1}$ (**TMM**), and $D' = 0.025\ cm^{-1}$ (**TME**) and $D' = 0.024\ cm^{-1}$ (**DMC**). Although irradiations for nitrogen extrusion of the precursors were performed at 10 K, Curie like temperature dependence of EPR signal intensities was only plotted down to 20, 15, and 16 K, respectively, suggesting ground spin triplets for all three of them. While for **TMM** there were no doubts about, the ground spin multiplicities of **TME** and **DMC** were heavily discussed for quite some time, and many further theoretical calculations with different geometries and basis sets resulted in contradictory descriptions of **TME** and **DMC** [45–49]. In 1996 Iwamura's group [50, 51] unambiguously evidenced that the ground state for **DMC** and **TME** is singlet, nearly degenerate with a thermally excited triplet above 10 K. The final experiments was even more important, since there exists a large number of similar biradicals and substituted derivatives which can be grouped into the "families" of **TMM** and **TME** possessing the same spin interaction core [51–54].

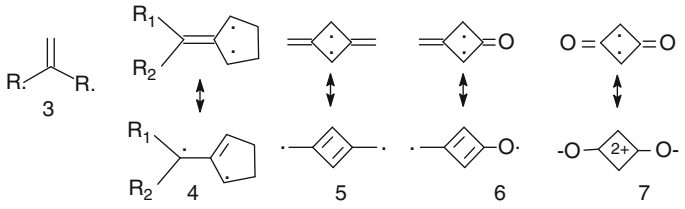

The "**TMM** family" has been widely tested for all kinds of radicals attached to 1,1′-ethenyl (**3**) [54, 55]. It comprises also cyclic structures like dihydropentafulvenes **4** and cyclobutenes **5–7**. Different symmetric and asymmetric substitutions R_1,R_2 have been used for **4** and for all of them the ground state was triplet [52, 56]. Just the ZFS values were largest for electron donating groups like methoxy, while electron acceptors or extension of the π-system leads to a decrease of the zero field splitting. Only for the cyclobutadion-diyl **7**, no biradical could be found and a singlet state is predicted [56], also argued from the strong contribution of dipolar resonance structures, as shown below.

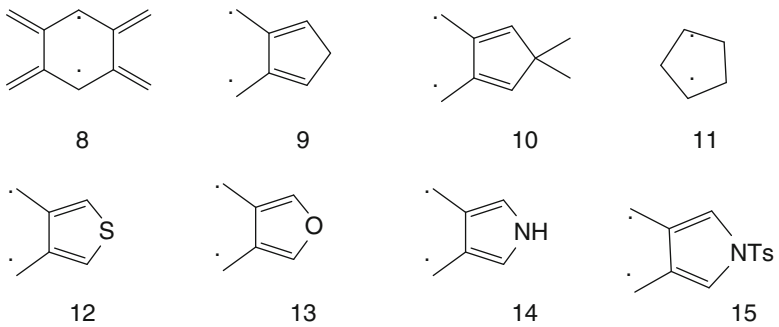

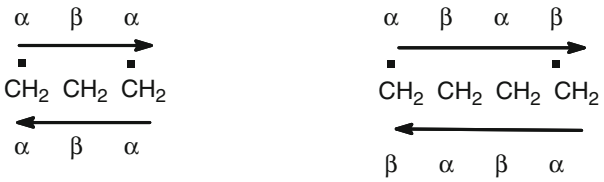

Fig. 5.11 Spin polarisation through methylene and ethylene

Within the "**TME** family" as for **TME** itself, there occurred many ambiguous papers, while theory predicts singlet ground states for them, even more in the cyclic planarized forms. For **8–10** at first triplet states were assumed [57, 58], then Berson studied the tetramethylenebenzene **8** in more detail demonstrating ground state singlet [59]. Therefore it must be assumed that also cyclopentadienes **9** and **10** should be further requested. Closely related is the cyclopentane-1,3-diyl **11** where a triplet ground state has been established [60].

But the singlet triplet splitting should be small, since the two competing pathways through σ bond yield opposite signed spin polarization presented by α and β spin (or spin up and spin down) as given schematically in Fig. 5.11.

The heteroatomic substitution in the five membered ring systems leading to dimethylenethiophene **12**, dimethylenefuran **13**, and dimethylenepyrrol **14**, destabilizes the triplet state to such an extent that all of them are biradical singlets, even without thermal activation of the triplet state. Partially zwitterionic forms must be considered [61]. One exception seems the tosylated pyrrole **15** where a stable triplet was reported with thermally activated components of only 19 cal/mol [62]. This exception was explained with long lived spin isomerism and shown to be dependent on the excitation wavelength for nitrogen extraction leading to different species.

Also several exceptions for *meta*-phenylene bridging without high spin ground state multiplicities have been found in the 1990s. While for a typical *meta*-phenyl bridged bisnitroxide **16** the triplet state was witnessed [63], in case of the trismethylated bisnitroxide **17** two isomers were found in their singlet state and the triplet excitation was reported to be in the range $2J/k = -(66 - 81)$ K [64]. This was also the first case where it could be shown that a corresponding *para*-phenylene bridged biradical is more stable triplet with $2J/k = -35$ K or ca 70 cal/mol than its meta form [65].

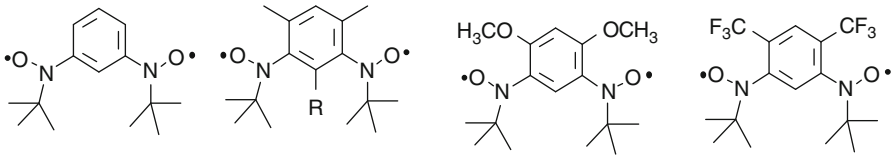

A very similar finding of thermally excited triplet bisnitroxides was reported by Iwamura [66] using methoxy groups neighboring the nitroxides **18** and yielded $2J/k = -7.0$ K for a diluted sample in solid PVC, where the intermolecular exchange is negligible, and −73.8 K for a crystalline material, where strong antiferromagnetic intermolecular interactions are enclosed. Thus not surprisingly also the three spins in a trisnitroxide with one more nitroxide radical between the methoxy groups are coupled antiferromagnetically to a doublet ground state [67].

The reason for this unusual singlet ground states of **17** and **18** was further discussed by Borden [68]. On the basis of ab initio calculations considering twisted radical sites, singlet states for angles of torsion between 70 and 90° were unequivocally predicted. A surprise was found for a bis-trifluormethyl derivative **19** reported by Rajca et al. [69] demonstrating that rapid cooling of the biradical leads to a singlet state, which slowly converts to its ground state triplet. Different temperature dependent conformer preferences were assumed to be responsible for the observed changes.

Other exceptions of *m*-phenylene acting as ferromagnetic CU's when strong steric hindrances are involved were manifested by the diphenothiazine and diphenoxazine dication derivatives [70, 71]. The zero field splittings of the biradical *para*-, *meta*-, and *ortho*- derivatives (**20–25**) formed in sulfuric acid nicely reflected their distance dependence with $D' = 0.0043$, 0.0060, and 0.0204 cm^{-1} (**20–22**) corresponding to $r \sim 0.84$, 0.76, and 0.50 nm, respectively. This dipolar approach with $D' \sim 3g_e^2\beta_e^2/4r^3$ estimation can be refined for distributed spin densities in delocalised biradicals, as well. The above finding is one of the very rare cases, where *o*-phenylene bridging gave EPR active species, what is based on the strong twisting and stabilization of the dication through the sulfonate counterion. In case of the phenoxazines the ZFS components are slightly larger, due to the higher spin density on the connecting nitrogens and lower charge on the oxygen compared to sulfur in phenothiazines. The temperature dependence indicated a singlet ground state for **21** with $2J/k_b = -28$ cal/mol and here again more stable triplet states with Curie like behavior were identified for the corresponding *p*-phenylene bridged biradicals **20**.

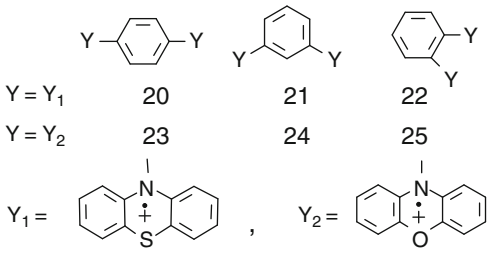

In principle strict orthogonal alignment of radicals may also open a way to high spin ground states (geometrical vs. topological approach) [26]. In an early approach this was tested by Veciana et al. [72] with the perchlorobiphenyl-dication **26**, where the large chloro-substituents lead to a strong twisting of the biphenyl unit and also decrease the oxidation potential. But later it was shown that the biradical had singlet ground state. Since bianthryl **27** is aligned perpendicularly and can be oxidized with

$SbCl_5$ to the biradical dication ($D' = 0.00225\ cm^{-1}$) or reduced with alkali metal to the biradical dianion ($D' = 0.00177\ cm^{-1}$), also oligo(anthrylenes) **27–29** and the corresponding polymer were studied for this purpose [73]. Temperature dependent studies of the zero field splittings (zfs) in the frozen solution EPR spectra evidenced that the charged oligo(9,10-anthrylenes)

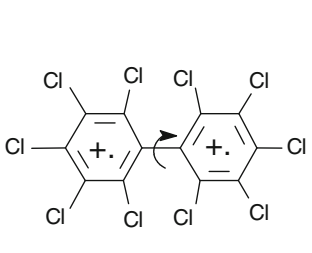

26

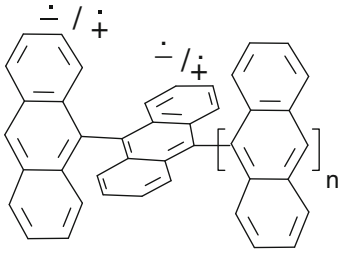

27 n=0
28 n = 1
29 n = 2

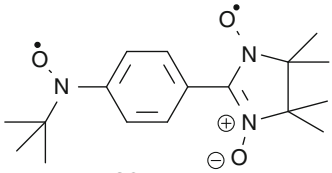

30

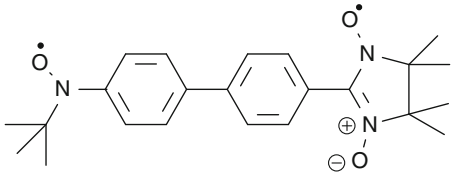

31

27–29 persist in low spin ground states. The low temperature measurements of the bianthryl dianion additionally revealed that the average orthogonal alignment is lost upon lowering the temperature, with a clear orthorhombicity of the zero field splitting parameters $D' = 0.00182\ cm^{-1}$ and $E' = 0.0010\ cm^{-1}$ at 20 K which correlates to an angle θ of 81° derived from the two extremes $E_{min} = 0$ ($\theta = 90°$) and $E_{max} = D/3$ ($\theta = 0°$). Also in other asymmetric biaryles with strong to orthogonal hindrance only thermally activated triplet states were found [74].

Another possibility to overcome the standard topological rule was excellently demonstrated by Iwamura and Inoue [75, 76] using asymmetric radical sites in **30**, **31**. Then spin polarisation explains to stable triplet ground state biradicals with strong intramolecular ferromagnetic coupling.

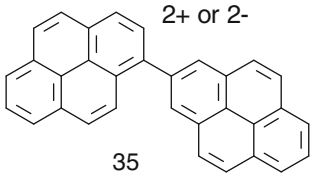

35

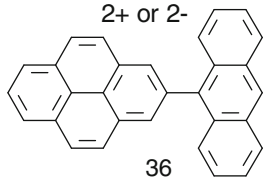

36

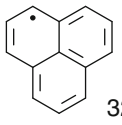

32

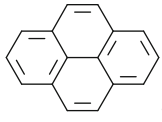

33

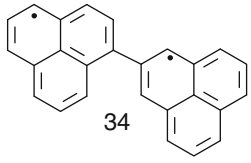

34

In a similar way the topological rules for exchange coupling may be overcome upon use of delocalized radicals and radical ions [77, 78]. A necessary property is large sign-alternating spin densities along the periphery, well known for the neutral phenalenyl- (**32**) and pyrenyl (**33**) cation or anion radicals. Bridging through so called antiferromagnetic CU's as single bond, 1,2-ethenyl, or *p*-phenylene will then lead to high spin formation if the radical ions are connected through positions of opposite signed spin densities. While the bridged 1,2′-biphenalene **34** was just considered as model theoretically [77] the 1,2′-bipyrene **35** and 2-(9-anthryl)-pyrene **36** [78] should also form high spin ground state entities and were synthesized and charged to their biradical dianion [79].

A third opportunity to obtain high spin molecules besides topology and geometry, is based on high symmetry. It has long been established for molecules having threefold or higher symmetry, that they possess doubly degenerate HOMO's or LUMO's which can be charged, leading to triplet biradicals. Classical examples are the pentadienyl cation **37** [80] and some cations of substituted derivatives [81, 82] as well as the benzene dianion **38** [83], so called antiaromatic annulenes. The perphenyl substituted derivatives **37**, **38**, on the other hand, yielded singlet ground states or paramagnetic contributions only [84, 85]. For hexaphenylbenzene **38** even a one step dehydrocyclization to hexabenzocoronene **46** is well established [86].

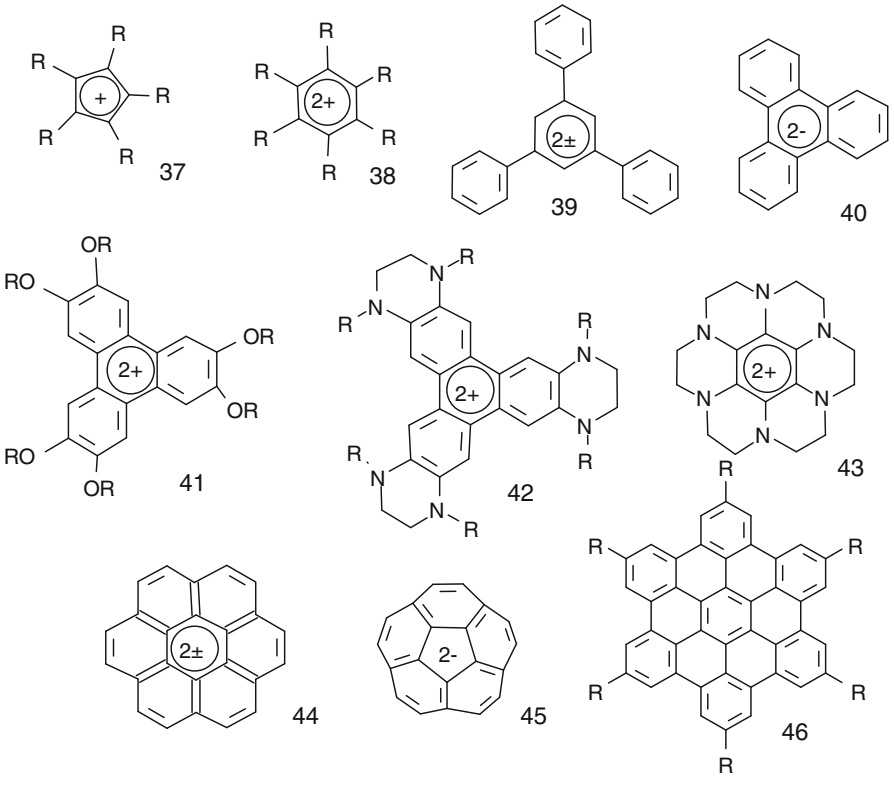

Therefore also 1,3,5-triphenylbenzene **39** dianion and dication [87], triphenylene dianion **40** [88], and the dication of donor substituted derivatives **41** [89], **42** [90] yield triplet ground states. Suitable derivatives with lowered reduction/oxidation potentials as **42** [91] and hexaazahydrocoronene **43** [92] were also deemed as building blocks for organic magnets by Breslow [93–95] in alternating donor acceptor stacks, in line with McConnell model II [96]. For **43** more detailed studies revealed the singlet ground state [97–98] which was also found for the dianion ($D' = 0.054\ cm^{-1}$, $\Delta E_{ST} = 2.3$ kcal/mol) [99] and dication ($D' = 0.0591\ cm^{-1}$, $\Delta E_{ST} = 1.4$ kcal/mol) [100] of coronene **44**. Due to Jahn-Teller distortions also other fused hydrocarbons like corannulene **45** [101] and hexabenzocoronene **46**,[99] [102] loose their high symmetry upon charging, yielding singlet ground state dianions. For **46**, however the thermal activation of the triplet state is extremely small, nearly degenerate with the singlet ($\Delta E_{st} = 15$ cal/mol). For higher charged molecules the use of an additional independent methods besides EPR spectroscopy to characterize the charging process like optical absorption or potentially controlled generation has shown to be very powerful in many occasions. The latter holds also for the reduction of (C_{60})fullerene which even possesses threefold degenerate LUMO's in the neutral form. Only for the dianion of C_{60} new large thermally excited ZFS components were measured, being lost upon trianion formation, where the transition from mono- to di- and trianion was additionally evidenced by absorption spectroscopy [103] and potentiometric control [104]. Without such control in higher concentrated samples even triradicals and higher spin states were found [105], while the single crystal study of the trianion supported its doublet state [106].

5.4 Triradicals – The Quartet State

Many triradicals have been evidenced by EPR spectroscopy, since the early work by Brickmann und Kothe [107] on a triradical in the quartet state **47** and the full analysis of its powder spectra [108]. At first glance some ambiguities from cw-EPR spectral analysis may easily occur, since the ZFS in the $\Delta m_S = 1$ region itself can be very similar to a mixture from mono- and biradicals. Additional information then come from the possible identification of a $\Delta m_S = 3$ forbidden transition and splittings of the size of D' in the $\Delta m_S = 2$ region (e.g. Fig. 5.3) [73, 109]. Further hints

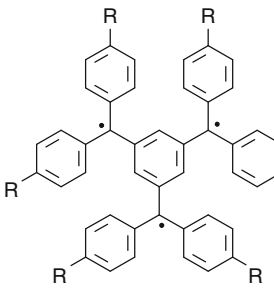

47 R = phenyl
48 R = H

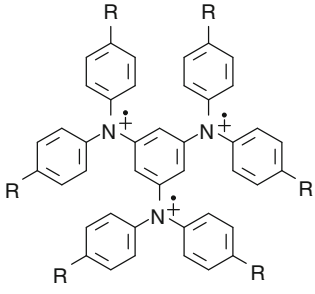

49 R = H, 50 R = OCH_3

can be derived in cases of stepwise formation upon charging and control of the relative signal intensities as well as by comparison with similarly structured triradicals.

In 1992 a triradical trication of trisphenylaminobenzene (**49**) was reported [110], but the ZFS components were very small ($D = 0.0012\ cm^{-1}$), and the 5 line solution spectrum for three equivalent nitrogens unexplained. This forced Blackstock [111] to fully characterize the charging of the hexa-anisyl (**50** $R = OCH_3$) derivative. The electron donating methoxy groups certainly support the trication formation, where cyclic voltammetry at low temperature (−78 °C) yielded 3 reversible oxidation waves. The liquid solution EPR spectrum of the trication showed 10 lines for strong exchange coupled nitrogens. In frozen state a typical spectrum of a quartet was found (5 lines) with $D' = 0.0046\ cm^{-1}$. This value is very close to the one given for the isoelectronic hexaphenyl-trimethylenebenzene **48** [112] ($D' = 0.0049\ cm^{-1}$) and further supported the correct quartet state assignment. Thus it was assumed that in the earlier report some dimerization might have occurred, which can easily be found for triphenylamines and triphenylmethylenes [113]. The ground state quartet of **50** was further evidenced by 2D-ESTN spectroscopy [114], where in a well defined trication no hint of contributing excited doublet states was found.

The problems of dimerization can also be overcome in extended oligo(*m*-*p*-N-phenylaniline)s **51–56** reported by Janssen et al. [115–117]. They indicated quartet ground state for all of them, but certainly with much smaller ZFS ($D' = 0.0026$, $0.0029\ cm^{-1}$ **51**, **52**) than for **50** due to the larger spin delocalisation. As seen from the D' values, the exchange of each phenyl group by a donating methyl substituent still does not strengthen much dipolar interactions.

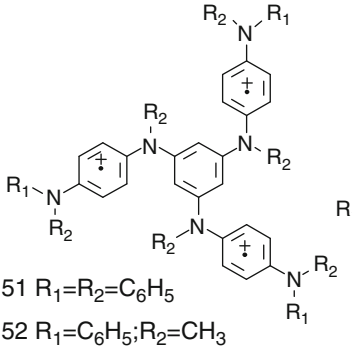

51 $R_1=R_2=C_6H_5$

52 $R_1=C_6H_5;R_2=CH_3$

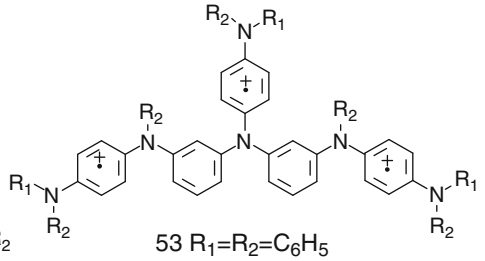

53 $R_1=R_2=C_6H_5$

54 $R_1=C_6H_5;R_2=CH_3$

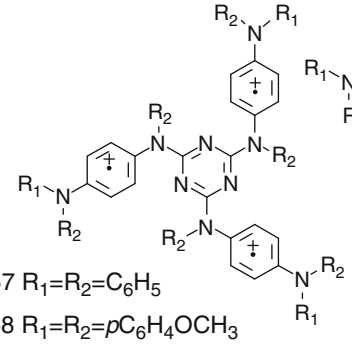

57 $R_1=R_2=C_6H_5$

58 $R_1=R_2=pC_6H_4OCH_3$

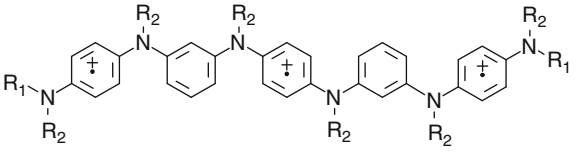

55 $R_1=R_2=C_6H_5$

56 $R_1=C_6H_5;R_2=CH_3$

Comparable triradicals with triazine skeleton obtained by Blackstock [118], on the other hand, were found to deviate from Curie like behavior at low temperatures, and a low spin ground state was assumed. This is somewhat in contrast to other reports, claiming the disubstituted 1,3-triazines or trisubstituted 1,3,5-triazines to be a more favourable CU than substituted 1,3- or 1,3,5-benzenes [119, 120]. The s-triazine skeleton was also shown to support high spin ground states for dinitrenes [121].

Many more stable quartet triradicals were reported, synthesized by attaching radical sites to topologically controlled positions of a π-network. Only a few will be discussed here focusing on EPR studies. Several triradicals with nitroxides as spin carrying units have been synthesized extensively by Iwamura et al. [122–125]. Herein the quartet states were proven for the phenylene bridging between the radical sites in **59–61**. They have also been established as valuable stable building blocks for molecular magnets upon further ligation with metal complexes through the nitroxide unit [126]. This is inherently combined with the need of very clean oligo-radicals (100%).

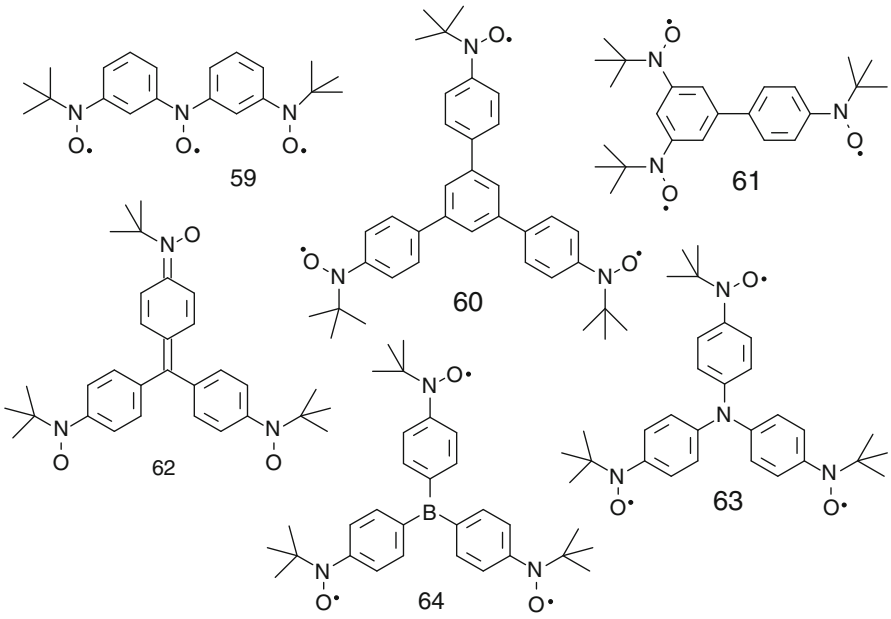

If a methylenyl center is used as in **62** a triplet ground state results, while for a central amine in **63** or a borane in **64** only doublet ground states were found [127, 128]. This was reasoned by electron excess in case of the amine leading to superexchange between two spin sites, and by electron deficiency in borane, stabilizing degenerate doublet states below the quartet.

Similarly, many nitronyl-nitroxides (**NN**) and iminonitroxides (**IN**) have been attached to aromatic cores and used also in mixtures with nitroxide radicals and as

building blocks for molecular magnets [129]. Typical examples are the 1,3,5-tris-NN-benzene (**65**) by Shiomi et al. [130] and the tris-NN-diphenylacetylene **66** by Turek et al. [131].

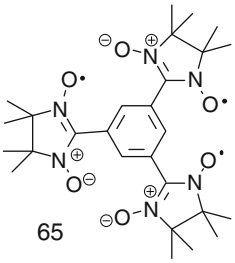

65

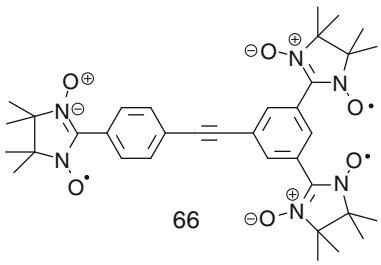

66

While many publications just treated symmetrical radical sites with a 1,3,5-phenylene bridging, Matsuchita and Itoh et al. [132] tried to charge dicarbenes to the monoanion **67** and monocation **68**. First some deviation from Curie type behavior in the very low temperature range ~5 K was reported, but since there was no obvious reason for spin frustration of the quartet state, the work was redone carefully also with ^{13}C labelling of the methylene [133]. The quartet ground state was evidenced thereby for both, **67** and **68** [133, 134].

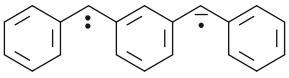

67

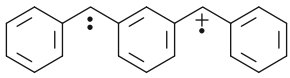

68

Several other triradicals in the quartet state were also obtained by using mixtures of different radical sites – so called "heterospin molecules" – and modified topology as for instance nitrenes in combination with **NN** or nitroxides [135–136]. Although a quinoid structure can be formed in **69** it remains a non-Kekulé form with 3 unpaired electrons and quartet ground state. The ZFS value ($D' = 0.277\ cm^{-1}$, $E' \sim 0$) is smaller than for the *m*-isomer **70** ($D' = 0.347\ cm^{-1}$, $E' = 0.0045\ cm^{-1}$) which was found to be a general criterion for a range of different radicals, e.g. the nitroxide **71** ($D' = 0.336\ cm^{-1}$, $E' = 0.0045\ cm^{-1}$) yields nearly identical ZFS components as the NN **70**. This similarity for the ZFS still makes sense although **70** actually should be low spin ground state judged from the topology (it was only reported at 77 K) while **71** should have high spin ground state.

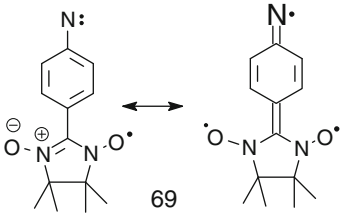

69

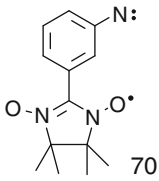

70

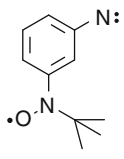

71

The features of the nitrenes coupled with **NN** or nitroxide radicals are structurally very close to those found earlier by Matsuda and Iwamura [137, 138] for carbenes

mixed with **NN 72** (D = 0.113 cm^{-1}, E = 0.006 cm^{-1}) or *t*-butyl nitroxide **73** (D′ = 0.118–0.125 cm^{-1}, E′ = 0.006 cm^{-1}). As in the case of phenyl carbenes, conformational isomers occur again and the spin is partially delocalised towards the outer phenyl ring reducing the direct exchange interaction.

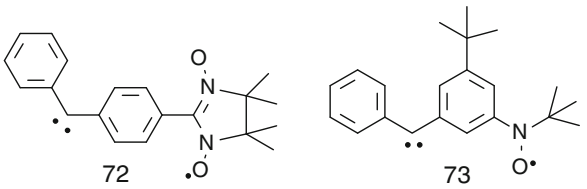

As shown for the trisnitroxide **59** one diphenyl-nitroxide can also be used as bridging unit between radical sites. This was extended to bis-NN **74**, bis-IN **75** and their mixed structure **76** [139]. Here the EPR spectra yielded no resolved ZFS components, only a strong central signal and some shoulders, together with non resolved $\Delta m_S = 2$ signal. The magnetic measurements further proved the quartet state and were fitted with nearly twice as large exchange coupling for the bis-NN **74** (J = 231 cm^{-1}) than for bis-IN **75** (J = 127 cm^{-1}). For the asymmetric **76** an even more complex analysis yielded one very strong and a weak interaction. The elucidation of these effects on a cleanly separated sample seems worthwhile, since **NN** can easily be contaminated with **IN** upon sample preparation.

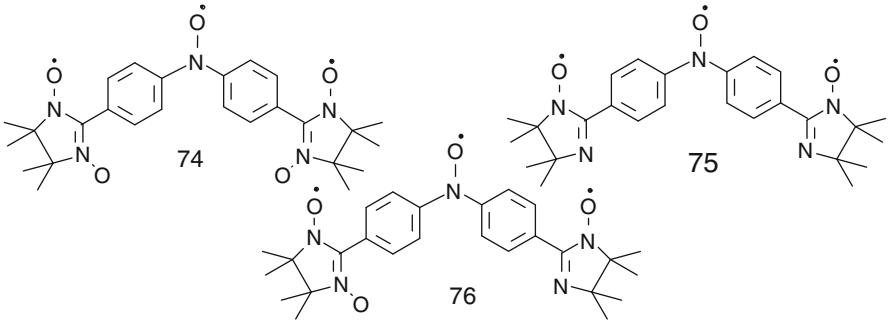

Sugawara demonstrated that the attachment of two **NN** units to thianthrene in **77**, **78** regardless of the substitution position in 2,7 or 2,8 lead to quartet ground states upon one electron oxidation of the thianthrene [140].

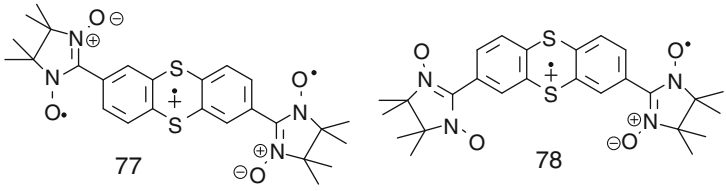

The ZFS components also are nearly identical for both isomers D′ = 0.012(5), E′ = 0.0009 cm^{-1}. The independence of the topology was reasoned by equally

signed spin densities on the 7 and 8 position of the thianthrene cation. Several other redox switchable high spin molecules based on stable radicals and easily oxidized π-systems like tetrathiafulvalenes or triarylamines have been prepared by Sugawara et al. [141, 142].

5.5 Tetraradicals – The Quintet State

Many tetraradicals in the quintet state have been evidenced by EPR. Classical examples are the *m*-phenylene bridged dicarbenes and dinitrenes mentioned in the introduction and a 3,6-dimethyleneanthracenediyl-1,7-dioxy **80** in its quintet state [14–17, 143]. The carbenes and nitrenes have been applied as spin sources with many different CU's.

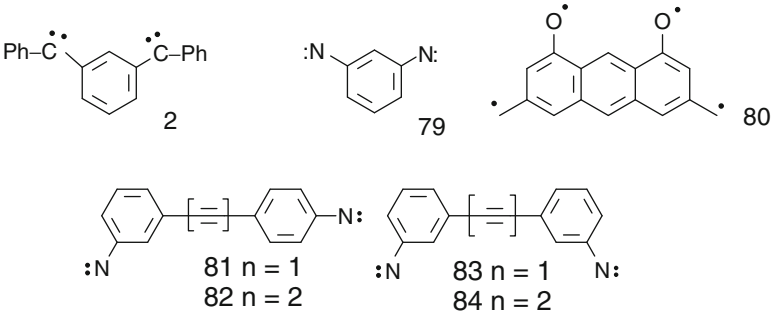

In 1991 Iwamura [144] evidenced that quintet spectra are formed for the diphenylacetylene and diphenyldiacetylene dinitrenes **81–84**. But stable ground state entities resulted from the *m*,*p*′ isomers **81**, **82**, only. The quintet *m*,*m*′-isomers **83**, **84** gave maximum intensity at 50 and 28 K, according to antiferromagnetic exchange with $J \sim -30$ (**83**) and $J \sim -14$ cal/mol (**84**), respectively. The exchange couplings were derived from the fit of the intensity of the quintet state by assuming standard thermal excitation with $\Delta E_{Quin\text{-}S} = 6\,J$ and accounting for the intermediate triplet state $\Delta E_{S\text{-}T} = 2\,J$.

$$I \bullet T \sim \left[\exp\left(\frac{6J}{RT}\right) \Big/ \left(1 + 3\exp\left(\frac{2J}{RT}\right) + 5\exp\left(\frac{2J}{RT}\right)\right)\right] \tag{5.7}$$

From the ZFS ($D' = 0.169\ cm^{-1}$, $E' = 0.040\ cm^{-1}$) it was concluded that the Z-isomers should be preferred. The overall result is similar to the reports of ground state singlets for the dicarbene **85** [145] and ground state quintet for **86** [146]. Several years before it had been shown that a *meta-para* linkage at a stilbene unit yields quintet ground states for **87** [147].

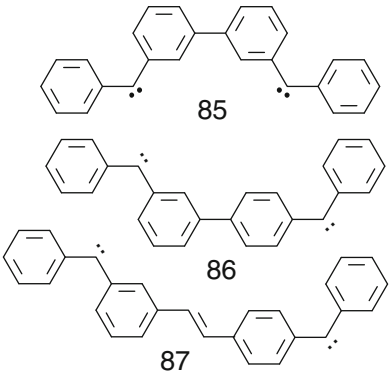

Further diphenyldinitrenes with 1,1-ethenyl [148, 149] or carbonyl [149] bridges were also studied for obtaining deeper insight into the spin coupling mechanism. The *p*,*p*′-isomers **88**, **91** were shown to be the only one to form ground state quintets, while for the *m*,*m*′- and *m*,*p*′-isomers **89**, **90** thermally activated quintet states were defined.

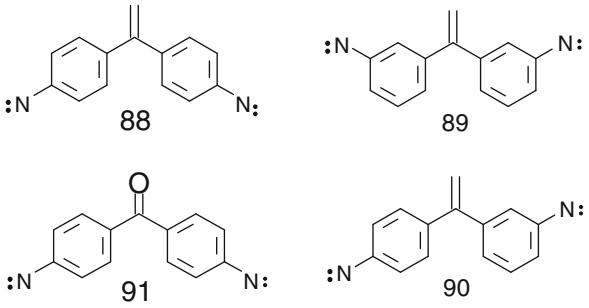

Spin polarization accounts for the low spin state of the *m*,*p*′-isomer **90**, but it does not in case of the *m*,*m*′-isomer **89**. This isomeric structure was concluded by Iwamura to be explained as a "doubly-disjoint" dinitrene on basis of Borden's classification [40, 41]. A comparison with nitroxide spin centers instead of nitrenes at the same positions shown above, yielded the same signs for the exchange interaction, even though the dinitroxides lead to weaker spin polarization into the bridging units. Based on the nitrene results and Itoh's model [150] for weakly interacting triplets, the ZFS D_q of a quintet was estimated from the two triplets D_t from centers a and b (Eq. 5.8). Lahti [151, 152] proposed a vector model to explain the angular dependence of the ZFS in bridged dinitrenes. Thereby it clearly came out that a decent approximation is obtained but that it is still limited to planarized spin centers and π-network [152]. Overall the topology determines the ground state multiplicity as long as no large geometrical demands (strong torsions) occur.

$$D_q = \frac{\left(D_t^a + D_t^b\right)}{6} + \frac{D_t^{ab}}{3} \tag{5.8}$$

In an elegant work using the **TMM**-approach with 2-alkylidene-1,3-cyclopentanediyl, Dougherty [153] tested the spin interaction through various spacers **92–95**. Even saturated CU's as cyclobutanediyl, cyclopentanediyl, and adamantyl were included. For each system Kekulé forms can be drawn towards the inner/outer units, indicating the bridging of triplets directly connected to the spacer. In **92** different substituents R were applied, demonstrating the ability to control the interaction. For R = methyl still sufficient coupling to the quintet was found, but not for R = *tert.*-butyl, where only triplets could be measured, presumably since the biradicals are twisted out of conjugation and become separated moieties.

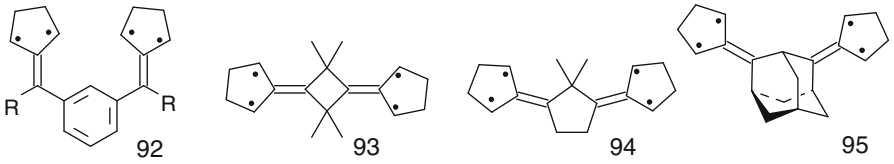

93 and **94** were shown to possess quintet ground states, with $D' = 0.021$ and 0.018 cm^{-1}, respectively. For **94** thermally activated triplet components appeared around 40 K in the temperature dependent study, suggesting a small quintet triplet gap $\Delta E_{QT} = 200$ cal/mol ($\Delta E_{QT} = 4J$, $J = 50$ cal/mol). For the adamantane derivative **95** containing a 1,3-cyclohexanediyl fragment, no quintet was found upon photolysis of the diaza-precursor. This showed that the interaction between the triplet sites depends sensitively on the through bond coupling, the bond angle, and the distance.

Heterocycles have been considered further as substitutes for benzene, e.g. the aforementioned triazine [121] and pyridine [154–157]. Dougherty [154] described stable quintet ground state for all three pyridine isomers **96–98**. Only small changes in D' were found for the neutral tetraradicals and as assumed from model calculations, **96** is closest to **92**, since the nitrogen is substituted in a so called "inactive" position (unstarred). Additional formation of the pyridinium cation by protonation led to singlet ground state for the 2,6-isomer **99** as predicted, but surprisingly not for the protonated 2,4-isomer **98**, where also an active position is involved.

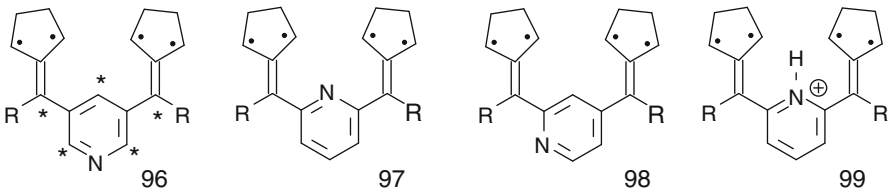

Using phenyl carbenes as radical sites, other authors [155] suggested that only 3,5-pyridine bridging should yield high spin quintet states, while for the 2,6- and 2,4-pyridine bridging, the disturbance of active sites by heteroatomic substitution should lead to ground state singlets. This is somewhat contradictory to other reports where the 2,6-pyridine bridging is well acknowledged for high spin formation

[156, 157]. Also Lahti et al. [158] tested the interaction of di- and trinitrenes through 2,6-, and 2,4-, and 2,4,6-substituted pyridines. They further supported the finding of high spin ground states by ab initio and DFT calculations with 6-31 G* basis sets. The pyridine seems thus to act very similar to benzene as coupling unit.

Rajca [159] synthesized and characterized many oligoarylmethanes which were used to get further control of spin interaction but also directed towards use in larger arrays, where a defect on one spin site would not hinder interaction between the others. One of these examples is the cyclic tetraradical **100**, which has been used as a core or a building block in many other polyradicals. The ZFS components of **100** ($D' = 0.0033\ cm^{-1}$) are only slightly larger than those for the branched tetraradical **101** [160].

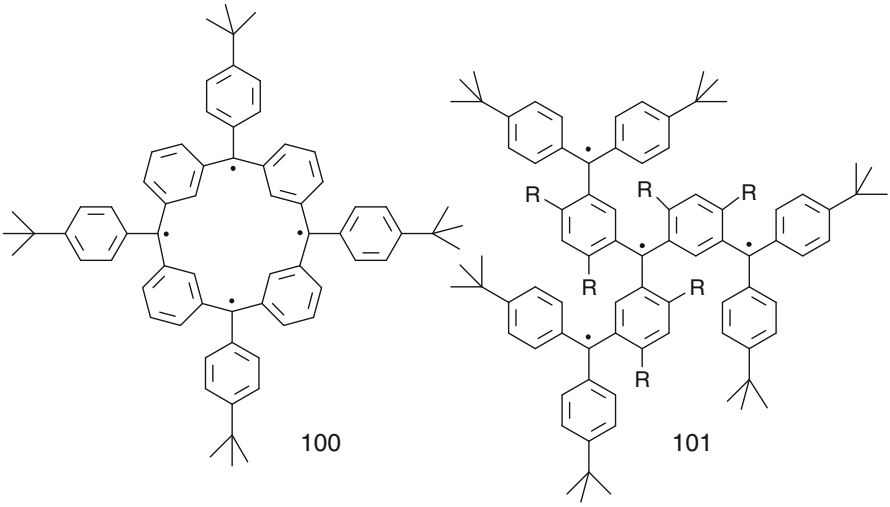

100 101

A small central peak was attributed to half integral spin (S = 1/2, 3/2) impurities estimated to contribute less than 10%. No thermally excited low spin components were envisaged up to 80 K, which become a problem for the even further extended high spin states.

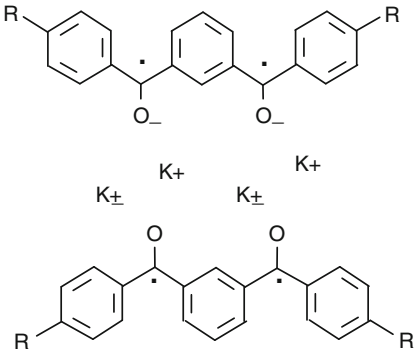

102

In a very different approach well defined tetraradical formation could be proven for diketyl radical dimerization through alkaline metal bridging [161, 162]. Based on very early examples of triplet formation in benzophenone anions [163] dibenzoylketones **102** were shown to persist in their quintet ground state.

5.6 Higher Spin States, S ≥ 5/2

Just a handful of papers are dealing with spin state detection by EPR of even higher spin multiplicities than the quintet, with the majority of reports for the heptet state. Two pentaradicals with S = 5/2 state based on **NO** as in **103** [164] and arylmethyl **104** [160] radical sites of very similar structure have been identified. They were found in their sextet ground state from temperature dependent studies. As expected from further spin delocalisation into the outer aryl units in **104** the ZFS parameters are smaller (D′ = 0.0027 cm, E′ = 0.0009) than for the oligonitroxide **133** (D′ = 0.0039, E′ = 0.0013 cm^{-1}).

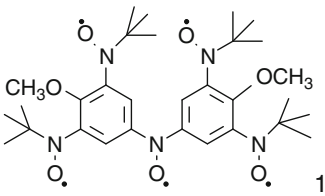

103

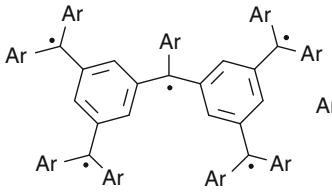

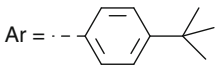

104

The heptet state was considered most often, since it is accessible through threefold 1,3,5-benzene substitution with S = 1 radical units. The first prepared hexaradical of this type was a tricarbene reported in 1973 [165] soon after the understanding of the dicarbene spectra. Further preparations on extended linear carbenes **105**, **106** followed. They were studied by single crystal EPR spectroscopy and shown to persist in S = 4 and S = 5 state [166, 167]. The oligocarbenes are much more difficult to characterize in powders, since the number of possible conformers increases, all giving rise to somewhat different ZFS parameters.

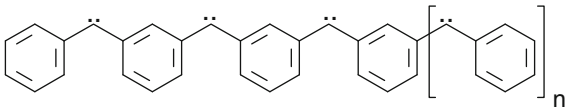

105 n = 1, 106 n = 2

Adam et al. [18] reported the hexaradical **107** based on the 1,3-cyclopentanediyl unit as a spin carrier. It was shown that nitrogen extrusion takes place in a stepwise fashion, leading to a triplet, a quintet and finally a heptet ground state. The intermediately formed bi- and tetraradicals were identical to the ones found earlier **108**, **109** [168]. The difficulty in analysing the hexaradical was its incomplete

formation (yield ~ 35%). Although the identification of the ZFS components of D′ = 0.00907 cm^{-1} and a small E′ = 0.000187 cm^{-1} was possible [18, 169] such molecules can not be considered as building blocks for organic magnets, since incomplete formation is a major problem in all extended organic high spin systems.

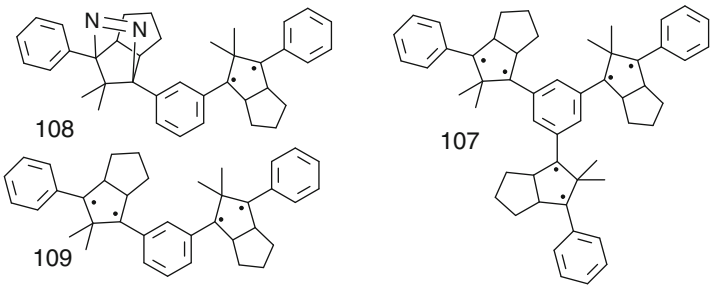

In the early 1990s Rajca [170] synthesized and characterized by cw-EPR spectroscopy star shaped polyarylmethylradicals **110**, **111** achieving S = 7/2 (D′ = 0.00163, E ~ 0) and S = 5 (D′ = 0.0012, E ~ 0), which could still be resolved due to high symmetry (E ~ 0) and quite clean preparations of the spin states with only small contributions from lower spin moieties.

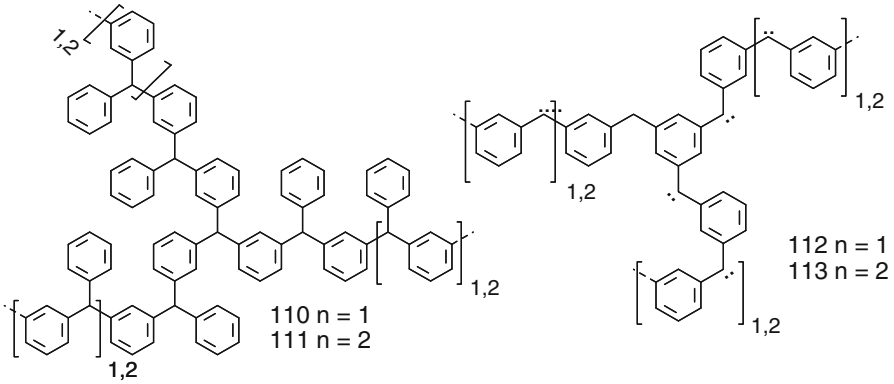

Similar carbene structures with S = 6 (**112**) and S = 9 (**113**) were reported [171, 172], which at that time have been the highest spin states from organic high spin molecules. While EPR spectroscopy was used for many of the above described radicals this method so far was only applied up to S = 6.

The comparison of different hexacarbenes was made including cyclic and further branched derivatives **114–116** [173, 174]. Different fine structures were observed and shown to follow Curie behaviour but no complete analysis of the complex spectra was given. A critical behaviour was found for the further extended branched nonacarbenes **116**, which did not yield the anticipated S = 18/2 spin state, but S = 7. Subsequent sample analysis indicated a loss of two active centers most probably due to chemical bond formation between the outer carbenes which should be spin allowed [174].

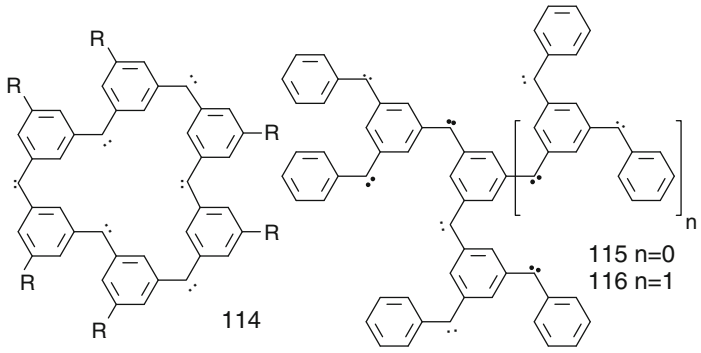

Since such unsubstituted carbenes generally suffer from high reactivity and destruction at ambient temperatures new halide substituted derivatives, as mentioned for the radical sites, are very promising. An example for such an extended stable hexaradical **117** was described by Tomioka et al. [12].

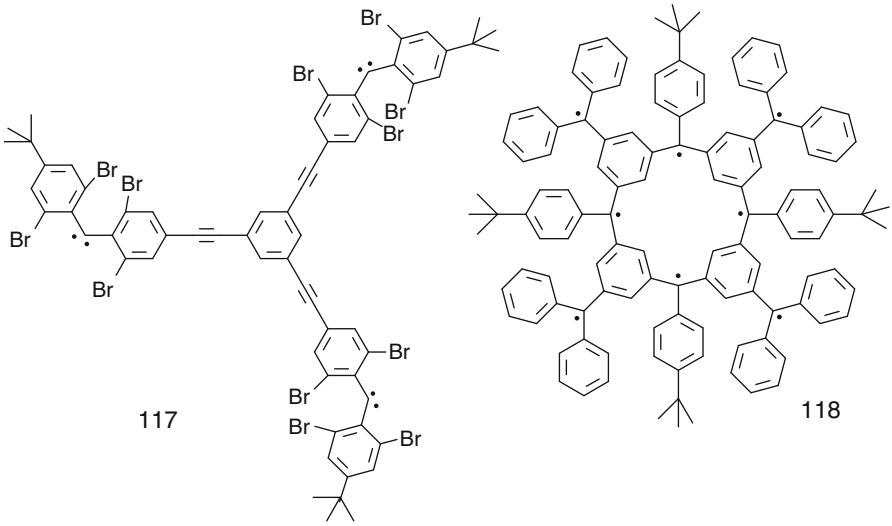

Upon the search of stable building blocks with very high spin, Rajca extended manifold the structures of polyarylmethyl radicals [160, 175]. One major goal was to establish substructures where even a defect does not hinder the interaction between all remaining spins. He achieved that perfectly using calix[4]arene rings like **118**. For such well defined molecules full cw-EPR spectral analysis became possible. For **118** the ZFS components were determined to be $D' = 0.00127\ cm^{-1}$, $E' \sim 0$.

Some remarkable resolutions of high spin states in polymers by 2D-ESTN were achieved, where standard cw-EPR just showed a single broad line [10, 22, 176] High spin components in the polymer **119** were identified as having S = 1/2–4 from their different nutation frequencies. Many more polyradicals like **120**, **121** with phenoxy, nitroxy and other radical sources attached under topological control

to conjugated linear polymer chains or to star shaped, dendritic or hyperbranched structures were still published in the 1990s [176–183]. The overall problem as in many other polymeric materials is the complete conversion of all active precursors to the radical sites without defects or a "soft" polymerisation with the radicals as shown nicely by Miura et al. [182]. Therefore usually only relatively low spin concentrations of 0.2–0.9 per repeat unit are found, displayed by an average of discrete S states, and no ferromagnetic domains are formed.

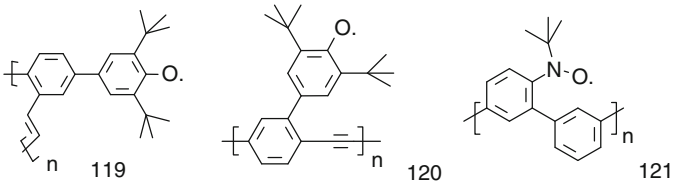

So far the only way towards very high spin pure organic molecules and polymers is based on Rajca's extension [184, 185] of ladder type and star-branched polymers with multiple pathways of spin interacting moieties. Intriguing example are the ladder type structures **122** (S = 12.4/2 measured instead of S = 14) and the cyclic

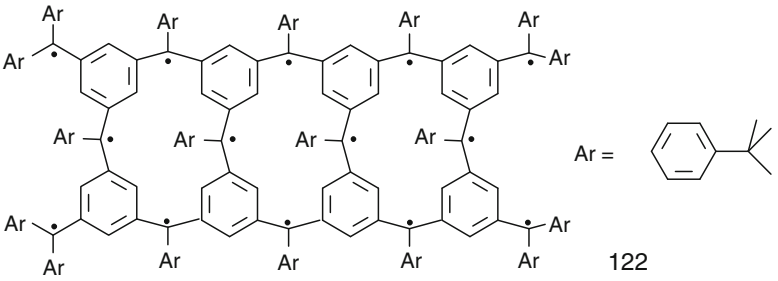

branched molecule **123** (S = 10 measured instead of S = 12) which have further been extended to polymers accessing high spin states of S = 50, 100, or even several 1,000 s [186]. However EPR does no longer represent a useful technique for the identification of such spin states.

5.7 Conclusion and Outlook

The highest spin states in organic molecules determined by EPR spectroscopy so far do not exceed the S = 6 state and it remains an open question whether even with new developed and extended pulsed techniques they could be identified. Therefore, the inherent usefulness of the EPR methods seems to be based on identification of oligoradicals and their ground state multiplicities. Manifold applications of magnetic susceptibility measurements have shown to be useful and superior for identification of real high spin states (S > 10/2) or magnetic probes and can be used in addition.

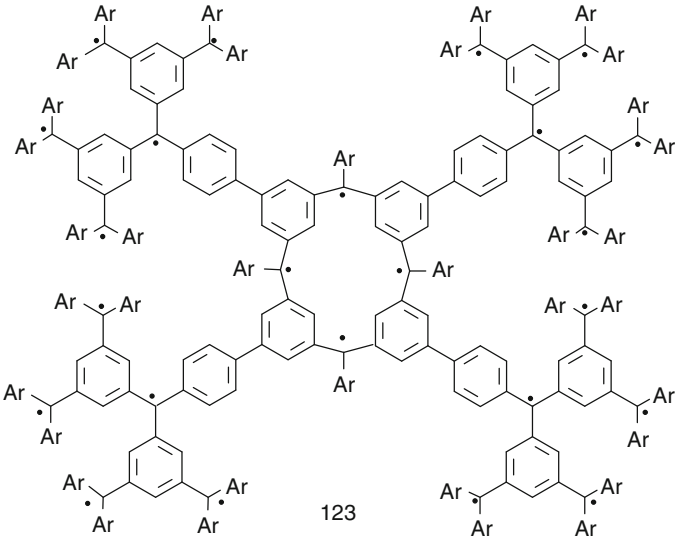

123

From the outlines above it should be clear that application of EPR to high spin molecules is very fruitful and an important characterization. As mentioned in the introduction most of the work is directed towards organic magnets. Although it is already an intellectual task to add new building blocks of high spin ground state molecules by design, magnetic ordering desires bulk spin alignment. In order to use the molecules further as building blocks for organic magnets, the molecules in their high spin state should be well defined and very clean, not contaminated partially by lower spin states. Since 1991 a large progress has been made and many more examples of organic ferromagnets became available. Earlier reported ones were shown to be unreproducible most probably due to impurities, especially those from ill defined polymers. Some of the newly developed organic ferromagnets are based on stable organic mono- or biradicals and their 3-dimensional ordering. For instance after the nitrophenyl-NN **124** ordering at 0.7 K [2], Chiarelli and Rassat [187] showed an organic ferromagnet **125** with a ferromagnetic transition temperature of Tc = 1.48 K and Banister et al. [188] succeeded in the alignment of a dithiadiazolyl derivative **126** with a much higher Tc = 36 K.

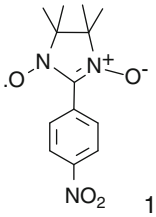

124

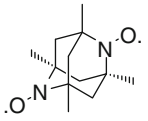

125

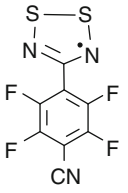

126

Also pure organic (C_{60}) fullerene charge transfer compounds have been found to exhibit ferromagnetic ordering besides high superconductivity. Already in 1991

Wudl et al. [189] realized a C_{60}/TDAE complex with Tc = 16 K and prompted further studies to understand this phenomenon from pure S = ½ spin systems [190].

Inorganic organic hybrid solids have shown to become very promising and resulted in magnetic ordering at much higher temperatures than for pure organic molecules. For instance Gatteschi mixed hexafluoroacetylacetonato-Mn(II) with NN and found magnetic transition at Tc < 8 K [191]. This approach was further used extensively with NO and NN radicals as mentioned earlier [125, 126].

Certainly the inorganic complexes prepared by Verdaguer [192] based on iron exchange in Prussian blue by V and Cr (V[Cr(CN)6], Tc = 315 K) and those of Miller [193] complexing vanadocene with tetracyanoethylene under loss of the benzenes $(V(TCNE)_x(CH_2Cl_2)_y$, Tc ~ 400 K) resulted so far in even higher Tc's. However the organic and inorganic/organic hybrid solids based on organic high spin molecules are still a very promising field of material science research and many more interesting results are anticipated from them in the near future.

Acknowledgments The author thanks his former PhD students, postdocs, and colleagues Prof. Anela Ivanova, Dr. Giorgio Zoppellaro, Prof. Chandrasekar Rajadurai, Prof. Ahmed Geies, and Dr. Stoyan Karabunarliev (Houston) for proof reading and the DFG and MPG for continuous financial support. He is indebted to Prof. Hiizu Iwamura for a workshop entitled *Organic Structures and Properties* during the first Gordon Conference in Fukuoka, Japan in 1996.

References

1. Chittapeddi S, Cromack KR, Miller JS, Epstein A (1987) Ferromagnetism in molecular decamethylferrocenium tetracyanoethenide (DMEFC TCNE). Phys Rev Lett 58:2695–2698
2. Tamura M, Nakazawa Y, Shiomi D, Nozawa K, Hoosokoshi Y, Ishikawa M, Takahashi M Kinoshita M (1991) Bulk ferromagnetism in the beta-phase crystal of the *para*–nitrophenyl nitronyl nitroxide radical. Chem Phys Lett 186:401–404
3. Schlenk W, Brauns M (1915) Some bis-triaryl-methyle [Triarylmethyle XV]. Ber Dtsch Chem Ges 48:716–728
4. Tschitschibabin AE (1907) Some phenylate derivates of p, p ditoyl. Ber Dtsch Chem Ges 40:1810–1819
5. Yang NC, Castro AJ (1960) Synthesis of a stable biradical. J Am Chem Soc 82:6208–6208
6. Coppinger GM (1962) A stable phenoxy radical inert to oxygen. Tetrahedron 18:61–63
7. Scheffler K, Stegmann HB (1970) Elektronenspinresonanz. Springer, Heidelberg
8. Teki Y, Miyamoto S, Iimura K, Nakatsuji M (2000) Intramolecular spin alignment utilizing the excited molecular field between the triplet (S = 1) excited state and the dangling stable radicals (S = 1/2) as studied by time-resolved electron spin resonance: observation of the excited quartet (S = 3/2) and quintet (S = 2) states on the purely organic pi-conjugated spin systems. J Am Chem Soc 122:984–985
9. Teki Y, Nakatsuji M, Miura, Y (2002) Excited high spin states of novel pi conjugated verdazyl radicals: photoinduced spin alignment utilizing the excited molecular field. Mol Phys 100:1385–1394
10. Takui T (2000) Characterization of molecular magnetism. In: Itoh K, Kinoshita M (eds) Molecular magnetism. Kodansha (Gordon and Breach), Tokyo
11. Schweiger A, Jeschke G (2001) Principles of pulse electron paramagnetic resonance. Oxford University Press, Oxford
12. Tomioka H, Hattori M, Hirai K, Sato K, Shiomi D, Takui T, Itoh K (1998) Persistent high-spin polycarbene: generation of polybrominated 1,3,5-tris-2,4-(phenylcarbeno)phenyl ethynyl

benzene (S = 3) and spin identification by two-dimensional electron spin transient nutation spectroscopy. J Am Chem Soc 120:1106–1107
13. Weil JA, Bolton JR, Wertz JE (1994) Electron paramagnetic resonance. Wiley, New York
14. Trozzolo AM, Murray RW, Smolinsky G, Yager WA, Wassermann E (1963) EPR of dicarbene and dinitrene derivatives. J Am Chem Soc 85:2526–2527
15. Wassermann E, Murray RW, Yager WA, Trozzolo AM, Smolinsky G (1967) Quintet ground states of m-dicarbene and m-dinitrene compounds. J Am Chem Soc 89:5076–5077
16. Itoh K (1967) Electron spin resonance of an aromatic hydrocarbon in its quintet ground state. Chem Phys Lett 1:235–238
17. Teki Y, Takui T, Itoh K (1988) General conditions for the occurrence of off-axis extra lines in powder-pattern electron-spin-resonance fine-structure. J Chem Phys 88:6134–6145
18. Adam W, Baumgarten M, Maas W (2000) A hydrocarbon hexaradical with three localized 1,3-cyclopentanediyl triplet diradicals linked by 1,3,5-trimethylenebenzene as ferromagnetic coupler: synthesis of the azoalkane precursor, photochemical generation of the polyradical, and EPR characterization of its septet-spin ground state. J Am Chem Soc 122:6735–6738
19. Wienk MM, Janssen RAJ (1996) Triplet-state phosphinyl diradicals. Chem Commun 16:1919–1920
20. Kirste B, vanWilligen H, Kurreck H, Möbius K, Plato M, Biehl R (1978) Endor of organic triplet-state and quartet-state in liquid solutions and in rigid media. J Am Chem Soc 100:7505–7513
21. Kurreck H, Kirste B, Lubitz W (1988) Electron nuclear double resonance spectroscopy of radicals in solution. Weinheim
22. Takui T, Sato K, Shiomi D, Itoh K (1999) Continuous wave ESR and Fourier transform-pulsed electron spin transient nutation spectroscopy. In: Lahti PM (ed) Magnetic properties of organic materials. Marcel Decker, New York
23. Zoppellaro G, Geies A, Enkelmann V, Baumgarten M (2004) 2,6-Bis(pyrazolyl)pyridine functionalised with two nitronylnitroxide and iminonitroxide radicals. Eur J Org Chem 2367–2374
24. Bleaney B, Bowers K (1952) Anomalous paramagnetism of copper acetate. Proc. R. Soc., London A214:451–456
25. Iwamura H (1990) High-spin organic molecules and spin alignment in organic molecular assemblies. Adv Phys Org Chem 26:179–253
26. O Kahn (1993) Molecular magnets. VCH, Weinheim
27. Miller JS, Epstein AJ (1994) Organic and organometallic molecular magnetic materials - designer magnets. Angew Chem 106:399–415
28. Lahti PM (1999) Magnetic properties of organic materials. Marcel Decker, New York
29. Itoh K, Kinoshita M (2000) Molecular magnetism. Kodansha (Gordon and Breach), Tokyo
30. Miller JS, Drillon M (2001–2003) Magnetism, molecules to materials, vols I–IV. Wiley-VCH
31. Veciana J (2001) π-Electron magnetism. From molecules to materials. Structure & bonding Vol 100., Springer
32. Rajca A (1994) Organic diradicals and polyradicals – from spin coupling to magnetism Chem Rev 94:871–893
33. Nau WM (1997) Organic tri- and tetraradicals with high-spin or low-spin states. Angew Chem Int Ed Engl 36:2445–2448
34. Crayston JA, Devine JN, Walton JC (2000) Conceptual and synthetic strategies for the preparation of organic magnets. Tetrahedron 56:7829–7857
35. Longuet-Higgins HC (1950) Molecular orbital calculations of porphine and tetrahydroporphine. J Chem Phys 18:1174–1181
36. Ovchinnikov AA (1978) Multiplicity of ground-state of large alternant organic molecules with conjugated bonds Theor Chim Acta 47:297–304
37. Tomioka H, Hirai K, Fujii C (1992) Flash-photolysis of highly hindered diarylcarbenes – optical-absorption spectrum and reaction-kinetics of 2,2′,4,4′,6,6′-hexachlorodiphenylcarbene. Acta Chem Scand 46:680–682

38. Tomioka H, Hattori M, Hirai K (1996) Anomalous effects of para substituents on the stability of sterically congested triplet diarylcarbenes. The first triplet carbene surviving over minutes under normal conditions. J Am Chem Soc 118:8723–8724
39. Borden WT, Iwamura H, Berson JA (1994) Violations of Hunds rule in non-Kekulé hydrocarbons–theoretical prediction and experimental verification. Acc Chem Res 27:109–116
40. Borden WT, Davidson ER (1977) Effects of electron repulsion in conjugated hydrocarbon diradicals. J Am Chem Soc 99:4587–4594
41. Borden WT (1982) Diradicals. Wiley, New York
42. Dowd P, Sachdev K (1967) Trimethylenemethane from photolysis of 3-methylenecyclobutanone. J Am Chem Soc 89:715–716
43. Dowd P, Chang W, Paik YH (1986) Tetramethyleneethane, a ground-state triplet. J Am Chem Soc 108:7416–7417
44. Dowd P, Chang W, Paik YH (1987) The 2,3-dimethylenecyclohexa-1,3-diene diradical is a ground-state triplet. J Am Chem Soc 109:5284–5285
45. Du P, Borden WT (1987) Abinitio calculations predict a singlet ground-state for tetramethyleneethane. J Am Chem Soc 109:930–931
46. Prasad BLV, Rhadhakrishnan TP (1992) Dependence of spin coupling in non-Kekulé molecules on the pi-electron network. J Phys Chem 9232–9235
47. Nachtigall P, Jordan KD (1992) Theoretical study of the low-lying triplet and singlet-states of diradicals: tetramethyleneethane J Am Chem Soc 114:4743–4747
48. Pranata J (1992) Spin preferences of conjugated polyradicals – the disjoint NBMO analysis. J Am Chem Soc 114:10537–10541
49. Nachtigall P, Jordan KD (1993) Theoretical study of the low-lying triplet and singlet states of tetramethyleneethane – prediction of triplet below singlet-state at the triplet equilibrium geometry. J Am Chem Soc 115:270–271
50. Matsuda K, Iwamura H (1997) Singlet and triplet states are degenerate in 2,3-dimethylenecyclohexane-1,4-diyl. J Am Chem Soc 119:7412–7413
51. Matsuda K, Iwamura H (1998) Demonstration of the degeneracy of the singlet and triplet states in 2,3-dimethylenecyclohexane-1,4-diyl by measurement of its magnetic properties. J Chem Soc Perkin II 1023–1026
52. Platz MS, McBride JM, Little RD, Harrison JJ, Shaw A, Potter SE, Berson JA (1976) Triplet ground-states of trimethylenemethanes. J Am Chem Soc 98:5725–5726
53. Berson JA (1982) Capturable diradicals of the trimethylenemethane series. In: Borden WT (ed) Diradicals. Wiley
54. Shultz DA (1999) Conformational exchange modulation in trimethylenemethane-type biradicals. In: Lahti PM (ed) Magnetic properties of organic materials. Marcel Decker, New York
55. Shultz DA, Boal AK, Farmer GT (1997) The biradical, bis(3,5-di-tert-butyl-4-phenoxyl)methyleneadamantane, exhibits matrix-dependent EPR spectra suggesting rotamer bistability with differential exchange coupling. J Am Chem Soc 119: 3846–3847
56. Rule M, Matlin AR, Seeger DE, Hilinski EF, Dougherty DA, Berson JA (1982) Non-Kekulé molecules derived conceptually by heteroatom for carbon substitution in alternant hydrocarbons- m-quinomethane and m-naphthoquinomethane. Tetrahedron 38:787–798
57. Roth WR, Langer R, Bartmann M, Stevermann B, Maier G, Reisenauer HP, Sustmann R, Müller W (1987) The diradical 2,3,5,6-tetramethylene-1,4-caclohexanediyl (1,2,4,5-tetramethylenebenzene. Angew Chem Int Ed 26:256–258
58. Roth WR, Kowalzik U, Meier G, Reisenauer HP, Sustmann R, Müller M (1987) 2,2-Dimethyl-4,5-dimethylene-1,3-cyclopentanediyl. Angew Chem Int Ed 26:1285–1287
59. Reynolds JH, Berson JA, Kumashiro KK, Duchamp JC, Zilm K, Rubello A, Vogel P (1992) A kinetically stable singlet-state of 1,2,4,5-tetramethylenebenzene. J Am Chem Soc 114:763–764
60. Buchwalter SL, Closs GL (1979) Electron-spin resonance and CIDNP studies on 1,3-cyclopentadiyls – localized 1,3 carbon biradical system with a triplet ground-state – tunneling in carbon-carbon bond formation. J Am Chem Soc 101:4688–4694

61. Berson JA (1997) A new class of non-Kekulé molecules with tunable singlet-triplet energy spacings. Acc Chem Res 30:238–144
62. Bush LC, Heath RB, Feng XW, Wang PA, Maksimovic L, Song AI, Chung WS, Berinstain AB, Scaiano AB, Berson JA (1997) Tuning the singlet-triplet energy gap in a non-Kekule series by designed structural variation the singlet states of N-substituted-3,4-dimethylenepyrrole biradicals. J Am Chem Soc 119:1406–1415
63. Calder A, Forrester AR, James PG, Luckhurst GR (1969) Nitroxide radicals: V N,N'-di-t-butyl-m-phenylenebinitroxide a stable triplet. J Am Chem Soc 91:3724–3725
64. Dvolaitzki M, Chiarelli R, Rassat A (1992) Stable N,N'-di-t-butyl-meta-phenylene-bisnitroxides – unexpected ground state singlets. Angew Chem Int Ed Engl 31:180–181
65. Chiarelli R, Gambarelli S, Rassat A (1997) Exchange interactions in nitroxide biradicals. Mol Cryst Liq Cryst 305:455–478
66. Kanno F, Inoue K, Koga N, Iwamura H (1993) 4,6-Dimethoxy-1,3-phenylylenebis(N-tert-butyl nitroxide) with a singlet ground-state – formal violation of a rule that m-phenylene serves as a robust ferromagnetic coupling unit. J Am Chem Soc 115:847–850
67. Fang S, Lee MS, Hrovat DA, Borden WT (1995) Ab-initio calculations show why m-phenylene is not always a ferromagnetic coupler. J Am Chem Soc 117:6727–6731
68. Fujita F, Tanaka M, Suemune H, Koga N, Matsuda K, Iwamura H (1996) Antiferromagnetic exchange interaction among the three spins placed in an isosceles triangular configuration in 2,4-dimethoxy-1,3,5-benzenetriyltris(N-tert-butyl nitroxide). J Am Chem Soc 118:9347–9351
69. Rajca A, Lu K, Rajca S, Ross CR (1999) Singlet-triplet bistability in a 1,3-phenylene-based bis(aminoxyl) diradical. Chem Commun 1249–1250
70. Okada K, Imakura T, Oda M, Baumgarten M (1996) 10,10''-(m- and p-phenylene)diphenothiazine dications: violation of a topology rule in heterocyclic high-spin pi-systems. J Am Chem Soc 118:3047–3048
71. Friedrich J (1997) Elektronische Eigenschaften ausgewählter konjugierter Kohlenwasserstoffe und heteroaromatischer Systeme. PhD, thesis Mainz
72. Veciana J, Vidal J, Jullian N (1989) Is the orthogonality of partially filled orbitals in a regular chain a proper strategy towards high-spin molecules. Mol Cryst Liq Cryst 176:443–449
73. Müller U, Baumgarten M (1995) Novel oligo(9,10-anthrylene)s – models for Electron-transfer and high-spin formation. J Am Chem Soc 117:5840–5850
74. Baumgarten M, Gherghel L, Friedrich J, Jurczok M, Rettig W (2000) Electronic decoupling in ground and excited states of asymmetric biaryls. J Phys Chem 104:1130–1140
75. Inoue K, Iwamura H (1995) 2-P-(N-tert-butyl-N-oxyamino)phenyl-4,4,5,5-tetramethyl-4,5-dihydroimidazol-3-oxide-1-oxyl, a stable diradical with a triplet ground-state Angew Chem Int Ed 34:927–928
76. Kumagai H, Hosokoshi Y, Markosyan AS, Inoue K (2001) Synthesis, structure and magnetic properties of bis(hexafluoroacetylacetonato)Mn(II) complex with a novel triplet organic radical, 4-N-tert-butylaminoxyl-4''-nitronylnitroxylbiphenyl. Polyhedron 20:1329–1333
77. Karabunarliev S, Baumgarten M (1999) Reverting the effect of magnetic couplers in bridged di- and polyradicals. Chem Phys 244:35–47
78. Karabunarliev S, Baumgarten M (2000) Using antiferromagnetic couplers for high-spin ground states in ion radicals. Chem Phys 254239–247
79. Harfmann C (1996) PhD thesis. Ludwig Maximilian Univ Munich
80. Saunders M, Berger R, Jaffe A, McBride JM, ONeill J, Breslow R, Hoffmann JM, Perchonock C, Wassermann E, Hutton RS, Kuck VJ (1973) Unsubstituted cyclopentadienyl cation, a ground-state triplet. J Am Chem Soc 95:3017–3018
81. Breslow R, Hill R, Wassermann E (1964) Pentachlorocyclopentadienyl cation ground-state triplet. J Am Chem Soc 86:5349–5350
82. Breslow R, Chang HW, Hill R, Wassermann E (1967) Stable triplet states of some cyclopentadienyl cations. J Am Chem Soc 89:1112–1113
83. Wassermann E, Hutton RS, Kuck VJ, Chandross EA (1974) Dipositive ion of hexachlorobenzene- ground-state triplet. J Am Chem Soc 96:1965–1966

84. Breslow R, Chang HW, Yager WA (1963) A stable triplet of pentaphenylcyclopentadienyl cation. J Am Chem Soc 85:2033–2034
85. Broser W, Kurreck H, Siegele P (1967) Ueber substituierte pentaphenyl-cyclopentadienyl-Verbindungen und tetracyclone. 3 Symmetrische cyclopentadienyl Kationen mit nachweisbaren Triplettzuständen. Chem Ber 100:788–794
86. Halleux A, Martin RH, King GSD (1958) Synthese dans la serie des derives polycycliques aromatique hautement condenses- hexabenzo-1,12–2,3–4,5–6,7–8,9–10,11-coronene, le tetrabenzo-4,5–6,7–11,12–13,14-peropyrene et le tetrabenzo-1,2–3,4–8,9–10,11-bisanthene. Helv Chim Acta 41:1177–1183
87. Jesse RE, Biloen P, Prins R, van Voorst JDW, Hoijtink GJ (1963) Hydrocarbon ions with triplet ground states. Mol Phys 6:633–635
88. van Willigen H, van Broekhaven JAM, de Boer E (1967) An ESR study of mono and dinegative ions of triphenylene. Evidence for Jahn-Teller instability of triplet dianion. Mol Phys 12:533–548
89. Bechgaard K, Parker VD (1972) Monocations, dications, and trications of hexamethoxytriphenylene- novel anodic trimerization. J Am Chem Soc 94:4749–4750
90. Breslow R, Jaun B, Kluttz RQ, Xia CZ (1982) Ground-state pi-electron triplet molecules of potential use in the synthesis of organic ferromagnets. Tetrahedron 38:863–867
91. LePage TG, Breslow R (1987) Charge-transfer complexes as potential organic ferromagnets. J Am Chem Soc109:6412–6421
92. Breslow R, Maslak P, Thomaides JS (1984) Synthesis of the hexaaminobenzene derivative hexaazaoctadecahydrocoronene (HOC) and related cations. J Am Chem Soc 106:6453–6454
93. Breslow R (1985) Approaches to organic ferromagnets. Mol Cryst Liq Cryst 125:261–267; (1989) 4 N pi-electron triplet species and their potential use in organic ferromagnets. ibid 176:199–210
94. Breslow R (1999) Antiaromatic triplet ground state molecules. In Lahti PM (ed) Magnetic properties of organic materials. Marcel Decker, New York
95. Thomaides JS, Maslak P, Breslow R (1988) Electron-rich hexasubstituted benzene-derivatives and their oxidized cation radicals with potential triplet ground-states and polycations. J Am Chem Soc 110:3970–3979
96. Hoffman BM, Gamble FR, McConell HM (1967) Interactions between molecules and superconductors. J Am Chem Soc 89:27–30
97. Miller JS, Dixon DA, Calabrese JC (1988) Crystal-structure of hexaazaoctadecahydrocoronene dication [HAOC]2+, a singlet benzene dication. Science 240:1185–1188
98. Dixon DA, Calabrese JC, Harlow RL, Miller JS (1989) The structure of the tetracation of hexaazaoctadecahydrocoronene, a simple substituted benzene. Angew Chem Int Ed 28:92–94
99. Glasbeek M, van Voorst JDW, Hoijtink GJ (1966) Coronene dinegative ion. A thermally excitet triplet state. J Chem Phys 45:1852–1853
100. Krusic P J, Wassermann E (1991) Coronene dication – a thermally accessible triplet. J Am Chem Soc 113:2322–2323
101. Baumgarten M, Gherghel L, Wagner M, Weitz A, Rabinovitz M, Cheng PC, Scott LT (1995) Corannulene reduction – spectroscopic detection of all anionic oxidation states. J Am Chem Soc 117:6254–6257
102. Gherghel L, Brandt JD, Baumgarten M, Müllen K (1999) Exceptional triplet and quartet states in highly charged hexabenzocoronenes. J Am Chem Soc 121:8104–8105
103. Baumgarten M, Gügel A, Gherghel L (1993) EPR and optical-absorption spectra of reduced buckminsterfullerene. Adv Mater 5:458–461
104. Friedrich J, Baumgarten M (1997) Development and application of a new electrochemical cell allowing EPR/ENDOR and NIR measurements. Appl Magn Res 13:393–403
105. Shohoji MCBL, Franco MLTMB, Lazana MCRLR, Nakazawa S, Sato K, Shiomi D, Takui T (2000) Electronic quartet and triplet states of polyanionic C-60 fullerene and their anomalous spin relaxation as studied by cw-ESR/2D-Electron spin transient nutation spectroscopy. J Am Chem Soc122:2962–2963

106. Fässler TF, Hoffmann R, Hoffmann S, Wörle M (2000) Triple-decker type coordination of a fullerene trianion in [K([18]crown-6)](3)[eta(6),eta(6)-C-60](eta(3)-C6H5CH3)(2) - Single crystal structure and magnetic properties. Angew Chem Int Ed 39:2091–2094
107. Kothe G, Ohmes E, Brickmann J, Zimmermann H (1971) 1,3,5-Benzenetriyltri[di(para-biphenyl)methyl], a radical having a quartet ground state that dimerizes by entropy bonding. Angew Chem Int Ed 10:938–940
108. Brickmann J, Kothe G (1973) ESR of quartet states of randomly oriented molecules – calculation of line shape and detection of zero-field splitting. J Chem Phys 59:2807–2814
109. Rajca, A, Utamapanya, S (1993) Poly(arylmethyl) quartet triradicals and quintet tetraradicals. J Am Chem Soc 115:2396–2401 166 double!
110. Yoshizawa K, Chano A, Ito A, Tanaka K, Yamabe T, Fujita H, Yamauchi J, Shiro M (1992) ESR of the cationic triradical of 1,3,5-tris(diphenylamino)benzene. J Am Chem Soc 114:5994–5998
111. Stickley KR, Blackstock SC (1994) Triplet dication and quartet trication of a triaminobenzene. J Am Chem Soc 116:11576–11577
112. Dollish FR, Hall WK (1965) On interaction of triphenylamine with iodine and with silica-alumina catalysts. J Phys Chem 69:2127–2129
113. Wilker W, Kothe G, Zimmermann H (1975) 1,3,5-Benzenetris(diphenylmethyl)–tetramers and quartet state. Chem Berichte 108:2124–2136
114. Sato K, Yano M, Furuichi M, Shiomi D, Takui T, Abe K, Itoh K, Higuchi A, Katsuma K, Shirota Y (1997) Polycationic high-spin states of one- and two-dimensional (diarylamino)benzenes, prototypical model units for purely organic ferromagnetic metals as studied by pulsed ESR/electron spin transient nutation spectroscopy. J Am Chem Soc 119:6607–6613
115. Wienk MM, Janssen RAJ (1997) High-spin cation radicals of meta-para aniline oligomers. J Am Chem Soc 119:4492–4501
116. Wienk MM, Janssen RJA (1997) High-spin m-p-aniline oligo(cation radical)s. Synth Met 85:1725–1726
117. Struik MP (2001) High spin through bond and space. PhD thesis, Eindhoven
118. Selby T D, Stickley KR, Blackstock SC (2000) Triamino-s-triazine triradical trications. An experimental study of triazine as a magnetic coupling unit. Org Lett 2:171–174
119. Zhang J P, Baumgarten M (1997) Using triazine as coupling unit for intra and intermolecular ferromagnetic coupling. Chem Phys 214:291–299
120. Zhang JP, Wang RS, Wang LX, Baumgarten M (1999) Using triazine as coupling unit for intramolecular ferromagnetic coupling of multiradicals. Chem Phys 246:209–215
121. Nakai T, Sato K, Shiomi D, Takui T, Itoh K, Kazaki M, Okada K (1999) ESR study of high-spin nitrenes with s-triazine skeleton. Synth Met 102:2265–2266
122. Ishida T, Iwamura H (1991) Bis[3-tert-butyl-5-(N-oxy-tert-butylamino)phenylo] nitroxidein a quartet ground-state – a prototype for persistent high-spin poly poly[(oxyimino)-1,3-phenylenes]. J Am Chem Soc 113:4238–4241
123. Kanno F, Inoue K, Koga N, Iwamura H (1993) Persistent 1,3,5-benzenetriyltris(N-tert-butylnitroxide) and its analogs with quartet ground-states – intramolecular triangular exchange coupling among 3 nitroxide radical centers. J Phys Chem 97:13267–13272
124. Inoue K, Iwamura H (1994)Ferromagnetic and ferrimagnetic ordering in a 2-D network formed by manganese(II) and 1,3,5-tris[P(N-tert-butyl-N-oxyamino)phenyl]benzene. J Am Chem Soc 116:3173–3174
125. Inoue K, Iwamura H (1996) Spontaneous magnetization in a 2:3 complex formed by 3,4′,5-tris(N-oxy-tert-butylamino)biphenyl and manganese(II) bis(hexafluoroacetyl-acetonate). Adv Mater 8:73–76
126. Inoue K (2001) Metal aminoxyl-based molecular magnets. Struct Bonding 100:61–91
127. Itoh T, Matsuda K, Iwamura H (1999) A triphenylamine derivative with three p-(N-tert-butyl-N-oxylamino)phenyl radical units and yet a doublet ground state. Angew Chem 38:1791–1793

128. Itoh T, Matsuda K, Iwamura H, Hori K (2000) Tris[p-(N-oxyl-N-tert-butylamino)phenyl] amine, -methyl, and -borane have doublet, triplet, and doublet ground states, respectively. J Am Chem Soc 122:2567–2576
129. Nakatsuji S, Anzai H (1997) Recent progress in the development of organomagnetic materials based on neutral nitroxide radicals and charge transfer complexes derived from nitroxide radicals. J Mater Chem 7:2161–2174
130. Shiomi D, Tamura M, Sawa H, Kato R, Kinoshita M (1993) Novel magnetic interactions in organic polyradical crystals based on nitronyl nitroxide. Synt Met 56:3279–3284
131. Catala L, Turek P, LeMoigne J, De Cian A, Kyritsakas N (2000) Synthesis of nitronyl- and imino-nitroxide-triradicals interconnected by phenyl ethynyl spacer. Tetrahedron Lett 41:1015–1018
132. Matsuchita M, Momose T, Shida T, Teki Y, Takui T, Itoh K (1990) Novel organic ions of high-spin states- ESR detection of a monoanion of meta-phenylenebis(phenylmethylene). J Am Chem Soc 112:4700–4702
133. Matsuchita M, Nakamura T, Momose T, Shida T, Teki Y, Takui T, Kinoshita M, Itoh K, (1992) Novel organic ions of high-spin states 2 Determination of the spin multiplicity of the ground-state and H-1-ENDOR study of the monoanion of meta-phenylenebis(phenylmethane). J Am Chem Soc 114:7470–7475
134. Matsuchita M, Nakamura T, Momose T, Shida T, Teki Y, Takui T, Kinoshita M, Itoh K (1993) Novel organic ions of high-spin states 3 ESR and H-1 ENDOR studies of a monocation of m-phenylenebis(phenylmethylene). Bull Chem Soc Jpn 1:1333–1342
135. Lahti PM, Esat B, Walton R (1998) 2-(4 '-nitrenophenyl)-4,4,5,5-tetramethyl-4,5-dihydro-1 H-imidazole-3-oxide-1-oxyl: Photogeneration of a quartet state organic molecule with both localized and delocalized spins. J Am Chem Soc 120:5122–5123
136. Lahti PM, Esat B, Liao Y, Serwinski P, Lan J, Walton R (2001) Heterospin organic molecules: nitrene-radical linkages Polyhedron 20:1647–1652
137. Matsuda K, Iwamura H (1996) Synthesis and EPR characterisation of [3-(N-ylooxy-tert-butylamino)-5-tert-butylphenyl]phenylcarbene with a quartet ground state. Chem Commun 1131–1132
138. Matsuda K, Iwamura H (1997) Syntheses and ESR characterizations of diphenylcarbenes carrying t-butyl nitroxide and nitronyl nitroxide radicals as substituents and having quartet ground states. Mol Cryst Liq Cryst 306:89–94
139. Tanaka M, Matsuda K, Itoh T, Iwamura H (1998) Syntheses and magnetic properties of stable organic triradicals with quartet ground states consisting of different nitroxide radicals. J Am Chem Soc 120:7168–7173
140. Izuoka A, Hiraishi M, Abe T, Sugawara T, Sato K, Takui T (2000) Spin alignment in singly oxidized spin-polarized diradical donor: Thianthrene bis(nitronyl nitroxide). J Am Chem Soc 122:3234–3235
141. Kumai R, Matsushita M, Izuoka A, Sugawara T (1994) Intramolecular exchange in a novel cross-conjugated spin system composed of pi-ion radical and nitronyl nitroxide. J Am Chem Soc 116:4523–4524
142. Sugawara T, Izuoka A (1997) Molecular magnetism: Present and future. Mol Cryst Liq Cryst 305 41–54
143. Seeger DA, Berson J A (1983) Quintet ground-state of a non-Kekulé tetraredical, 3,6-dimethyleneanthracenediyl-1,7-dioxy. J Am Chem Soc 105:5144–5146
144. Murata S, Iwamura H (1991) Magnetic interaction between the triplet centers in ethynylenebis(phenylnitrenes) and 1,3-butadiyne-1,4-diylbis(phenylnitrenes). J Am Chem Soc 113:5547–5556
145. Teki Y, Takui T, Itoh K (1987) Spin alignment in organic high-spin molecules- a Heisenberg Hamiltonian approach. Chem Phys Lett 142:181–186
146. Teki Y, Fujita I, Takui T, Kinoshita T, Itoh K (1994) Topoly and spin alignment in a novel organic high-spin molecule 3,4'′-bis(phenylmethylene)biphenyl, as studied by ESR and a generalized UHF Hubbard calculation. J Am Chem Soc 116:11499–11505

147. Murata S, Sugawara T, Iwamura H (1987) Magnetic interaction of diphenylcarbene units linked with an ethylenic double-bond. J Am Chem Soc 109:1266–1267
148. Matsumoto T, Ishida T, Koga N, Iwamura H (1992) Intramolecular magnetic coupling between 2-nitrene or 2-nitroxide units through 1,1-diphenylethylene chromophores – isomeric dinitrenes and dinitroxides related in connectivity to trimethylenemethane, tetramethyleneethane, and pentamethylenepropane. J Am Chem Soc 114:9952–9959
149. Ling C, Minato M, Lahti PM, van Willigen H, (1992) Models for intramolecular exchange in organic pi-conjugated open-shell systems – a comparison of 1,1-ethenediyl and carbonyl linked bis(arylnitrenes). J Am Chem Soc 114:9959–9969
150. Itoh K (1978) Electronic structures of aromatic hydrocarbons with high spin multiplicities in the electronic ground state. Pure Appl Chem 50:1251–1259
151. Kalgutkar KS, Lahti PM (1997) Rigid geometry bis(arylnitrenes) as definitive tests for angular dependence of zero-field splitting in high spin molecules. J Am Chem Soc 119:4771–4772
152. Lahti PM (1999) An integrated approach to organic-based molecular magnetic materials. In: Lahti PM (ed) Magnetic properties of organic materials. Marcel Dekker, New York
153. Jacobs SJ, Shultz DA, Jain R, Novak J, Dougherty DA (1993) Evaluation of potential ferromagnetic coupling units – the bis(TMM) approach to high-spin organic molecules. J Am Chem Soc 115:1744–1753
154. West AP, Silvermann SK, Dougherty DA (1996) Do high-spin topology rules apply to charged polyradicals? Theoretical and experimental evaluation of pyridiniums as magnetic coupling units. J Am Chem Soc 118:1452–1463
155. Bae JY, Yano M, Sato K, Shiomi D, Takui T, Kinoshita T, Abe K, Itoh K, Hong D (1999) Spin alignment in high-spin carbenes of heteroatomic pi-conjugation. Synth Met 103:2261–2262
156. Shiomi D, Ito K, Nishizawa M, Hase S, Sato K, Takui T, Itoh K (1999) Charged nitronyl nitroxide biradicals as building blocks for molecular ferrimagnetics. Mol Cryst Liq Cryst 334:99–108
157. Ziessel R, Ulrich G, Lawson R C, Echegoyen L (1999) Oligopyridine bis(nitronyl nitroxides): Synthesis, structures, electrochemical, magnetic and electronic properties. J Mater Chem 9:1435–1448
158. Chapyshev SV, Walton R, Sanborn JA, Lahti PM (2000) Quintet and septet state systems based on pyridylnitrenes: Effects of substitution on open-shell high-spin states. J Am Chem Soc 122:1580–1588
159. Rajca A, Utamapanya S (1993) Toward organic-synthesis of a magnetic particle- dendritic polyradicals with 15 and 31 centers for unpaired electrons. J Am Chem Soc 115:10688–10694
160. Rajca A, Rajca S (1995) Novel high-spin molecules- pi-conjugated polyradical polyanions – ferromagnetic spin coupling and electron localization. J Am Chem Soc 117:9172–9179
161. Baumgarten M (1995) Novel oligoradicals and high spin formation. Mol Cryst Liqu Cryst 272:331–338
162. Baumgarten M, Gherghel L, Wehrmeister T (1997) Novel high-spin states in reduced dibenzoylbenzenes. Chem Phys Lett 267:175–179
163. Hirota N, Weissman SI (1962) Spin-spin interaction in dimers of free radicals. Mol Phys 5:537–538
164. Fujita J, Matsuoka Y, Matsuo K, Tanaka M, Akita T, Koga N, Iwamura H (1997) Molecular structure and magnetic properties of N,N-bis{4-methoxy-3,5-bis(N-tert-butyl-N-oxyamino)phenyl)}aminoxyl An approach to a stable and high-spin pentaradical. Chem Commun 2393–2394
165. Takui, T, Itoh, K (1973) Detection of an aromatic hydrocarbon in its septet electronic ground state by electron spin resonance. Chem Phys Lett 19:120–124
166. Teki Y, Takui T, Itoh K, Iwamura H, Kobayashi K (1983) Design, preparation, and electron-spin-resonance detection of a ground-state nonet hydrocarbon as a model for one-dimensional organic ferromagnets. J Am Chem Soc 105:3722–3723

167. Fujita I, Teki Y, Takui T, Kinoshita T, Itoh K, Miko F, Sawaki Y, Iwamura H, Izuoka A, Sugawara T (1990) Design, preparation, and electron-spin-resonance detection of a ground-state undecet (S = 5) hydrocarbon. J Am Chem Soc 112:4074–4075
168. Adam W, van Barneveld C, Bottle SE, Engert H, Hanson G, Harrer HM, Heim C, Nau WM, Wang D (1996) EPR characterization of the quintet state for a hydrocarbon tetraradical with two localized 1,3-cyclopentanediyl biradicals linked by meta-phenylene as a ferromagnetic coupler. J Am Chem Soc 118:3974–3975
169. Adam W, Maas W (2000) EPR spectral determination of electronic substituent effects on the D values of hydrocarbon polyradicals (quintet and septet spin states) composed of localized 1,3-cyclopentanediyl spin-carrying units linked by 1,3-di- and 1,3,5-trimethylenebenzene ferromagnetic couplers. J Org Chem 65:7650–7655
170. Rajca A, Utamapanya S, Thayumanavan S (1992) Poly(arylmethyl) octet (S = 7/2) heptaradical and undecet (S = 5) decaradical. J Am Chem Soc 114:1884–1885
171. Nakamura N, Inoue K, Iwamura H, Fujioka T, Sawaki Y (1992) Synthesis and characterization of a branched-chain hexacarbene in a tridecet ground-state – an approach to superparamagnetc polycarbenes. J Am Chem Soc 114:1484–1485
172. Nakamura N, Inoue K, Iwamura H (1993) A branched-chain nonacarbene with a nonadecet ground-state- a step nearer to superparamagnetic polycarbenes. Angew Chem Int Ed **32:**872–874
173. Matsuda K, Nakamura N, Takahashi K, Inoue K, Koga N, Iwamura H (1995) Design, synthesis, and characterization of 3 kinds of pi-cross conjugated hexacarbenes with high spin (S = 6) ground states. J Am Chem Soc 117:5550–5560
174. Matsuda K, Nakamura N, Inoue K, Koga N, Iwamura H (1996) Design and synthesis of a ''starburst''-type nonadiazo compound and magnetic characterization of its photoproduct. Chem Eur J 2:259
175. Rajca A, Rajca S, Desai S (1995) Macrocyclic pi-conjugated carbopolyanions and polyradicals based upon calix[4]arene and calix[3]arene rings. J Am Chem Soc 117:806–817
176. Takui T, Sato K, Shiomi D, Itoh K, Kaneko T, Tsuchida E, Nishide H (1996) FT pulsed ESR/electron spin transient nutation (ESTN) spectroscopy applied to high-spin systems in solids; Direct evidence of a topologically controlled high-spin polymer as models for quasi 1D organic ferro- and superpara-magnets. Mol Cryst Liq Cryst 279:155–178
177. Nishide H, Miyasaka M, Tsuchida E (1998) High-spin polyphenoxyls attached to star-shaped poly(phenyleneninylene)s. J Org Chem 63:7399
178. Nishide H, Miyasaka M, Tsuchida E (1998) Average octet radical polymer: A stable polyphenoxyl with star-shaped pi conjugation. Angew Chem Int Ed 37:2400–2402
179. Nishide H, Kaneko T (1999) Pendant and π-conjugated organic polyradicals. In: Lahti PM (ed) Magnetic properties of organic materials. Marcel Decker, New York
180. Nishide H, Maeda T, Oyaizu K, Tsuchida E (1999) High-spin polyphenoxyl based on poly(1,4-phenyleneethynylene). J Org Chem 64:7129–7134
181. Miura Y (1999) Synthesis and properties of organic conjugated polyradicals. In: Lahti PM (ed) Magnetic properties of organic materials. Marcel Decker, New York
182. Miura Y, Issiki T, Ushitani Y, Teki Y, Itoh K (1996) Synthesis and magnetic behaviour of polyradical: poly(1,3-phenyleneethynylene) with pi-toporegulated pendant stable aminoxyl and imino N-oxide-aminoxyl radicals. J Mater Chem 6:1745–1750
183. Oka H, Tamura T, Miura Y, Teki Y (1999) Synthesis and magnetic behaviour of poly(1,3-phenylene)-based polyradical carrying N-tert-butylaminoxyl radicals. J Mater Chem 9:1227–1232
184. Rajca A, Lu K, Rajca S (1997) High-spin polyarylmethyl polyradical: fragment of a macrocyclic 2-strand based upon calix[4]arene rings. J Am Chem Soc 119:10335–10345
185. Rajca A, Rajca S, Wongsriratanakul J (1999) Very high-spin organic polymer: pi-conjugated hydrocarbon network with average spin of S > = 40. J Am Chem Soc 121:6308–6309
186. Rajca A, Wongsriratanakul J, Rajca S (2001) Magnetic ordering in an organic polymer. Science 294:1503–1505

187. Chiarelli R, Novak MA, Rassat A, Tholence JL (1993) A ferromagnetic transition at 1.48 K in an organic nitroxide. Nature 363:147–149
188. Banister AJ, Bricklebank N, Lavender I, Rawson JM, Gregory CI, Tannner BK, Clegg W, Egglewood MRJ, Palacio F (1996) Spontaneous magnetization in a sulfur-nitrogen radical at 36 K. Angew Chem Int Ed 35:2533–2535.
189. Allemand PM, Khemani KC, Koch A, Wudl F, Holczer K. Donovan S, Gruner G, Thompson JD (1991) Organic molecular soft ferromagnetism in a fullerene C60. Science 253:301–303.
190. Narymbetov B, Omerzu A, Kabanov V, Tokumoto M, Kobayashi H, Mihailovic D (2002) C_{60} molecular configurations leading to ferromagnetic exchange interactions in TDAE*C_{60} Phys Sol State 44:437–440
191. Caneschi A, Gatteschi D, Laugier J, Rey P, Sessoli R, Zanchini C (1988) Preparation, crystal structure and magnetic properties of an oligonuclear complex with 12 coupled spins and an S = 12 Ground State. J Am Chem Soc 110:2795–2799
192. Ferlay S, Mallah T, Ouahes R, Veillet P, Verdaguer M (1995) A room-temperature organometallic magnet based on Prussian blue. Nature 378:701–703
193. Manriquez JM, Yee GT, McLean RS, Epstein AJ,. Miller JS (1991) A room temperature molecular/organic-based magnet. Science 252:1415–1417

Chapter 6
Electron Transfer and Structure of Plant Photosystem II

Asako Kawamori

Abstract Electron transfer and structure of plant photosystem II were studied by advanced EPR techniques. Pulsed EPR, pulsed electron electron double resonance (PELDOR), and spin polarized radical pair ESEEM were applied to determine the distance between radical pairs of electron transfer components. These methods can detect accurately the dipolar interaction between a pair of radicals, from which the distance is derived. The determined distances and their orientations were compared with recently observed X-ray data. EPR of the manganese cluster in water oxidizing complexes in photosystem II were discussed with respect of their functions.

6.1 Introduction

6.1.1 Primary Photochemistry in Photosynthesis

EPR of a plant photosystem was first observed by Commoner et al. [1] in the 1950s, when the pigment P700 was bleached during illumination of chloroplast suspension. A second overlapping signal was observed, even if the chloroplasts were kept in the dark. At the same time these two signals were denoted as Signal I and II, respectively. Signal I was identified to oxidized P700, the oxidized form of Chlorophyll *a*. The origin of Signal II was found to be tyrosine radical by site specific deuteration [2] in 1987, 30 years later the first discovery of EPR signals in the plant.

The primary event of photosynthesis starts with light absorption followed by electron transfer from the donor to the acceptor, where NADPH stores chemical reductants to synthesize carbohydrate. Various photosystems from bacteria to higher

A. Kawamori (✉)
AGAPE Kabutoyama Institute of Medicine, Nishinomiya, Japan
e-mail: kawamori-a@tulip.sannet.ne.jp

A. Lund and M. Shiotani (eds.), *EPR of Free Radicals in Solids II*, Progress in Theoretical Chemistry and Physics 25, DOI 10.1007/978-94-007-4887-3_6,

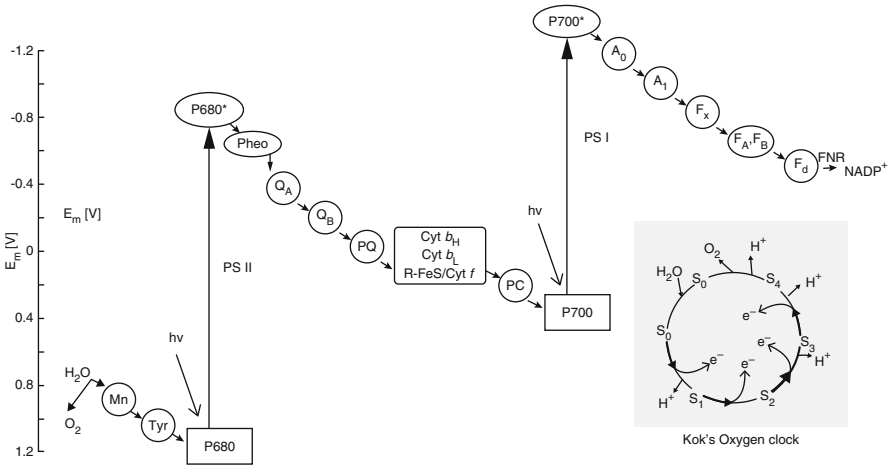

Fig. 6.1 Electron transport pathways of plants, so-called Z-scheme. Excitation by two quanta makes an electron to flow from water to $NADP^+$, nicotinamide adenine nucleotide phosphate. Membrane bound electron transfer protein cofactors Mn to Q_B belong to PSII, while P700, to F_A and F_B, iron sulphur centers, do to PS I. PQ, plastoquinone pool, Cytochrome bf complexes and PC, plastocyanin are the mobile proteins between PS II and PS I. E_m is the potential of the transport electron. In the *right below* Kok's S-sate transition of water oxidizing complex are shown

plants have developed during four billion year history of life on earth. The ancestors of the first bacterial systems are rather simple and were studied in the early 1970s. The reaction center is bacteriochlorophyll *a* that was found to be a dimer as demonstrated using the ENDOR techniques by Feher et al. [3] The crystal structure of *Rps.viridis* was analyzed by Deisenhofer et al. [4] in 1985.

In higher plants and cyanobacteria there are two photosystems; photosystem I (PS I) and photosystem II (PS II). The donor is water, which is different from that in sulfur bacteria with their donor, hydrogen sulfide. To oxidize water a strong oxidant is necessary. Therefore, two photosystems co-operate to oxidize the water by absorbing two light quanta with wavelength 700 and 680 nm, respectively at one time and to evolve one oxygen four times absorption are necessary. The overall reaction usually expressed by a Z-scheme as shown in Fig. 6.1. X-ray analysis of the crystal structure of PS I in a cyanobacterium *Synechococcus elongatus* was first reported in 1992 by Witt et al. [5] with 6 Å resolution. The electron transfer path from P700 to the final iron sulfur center A and B has been analyzed at 2.5 Å resolution [6]. Finally, in 2000 [7, 8], the PS II single crystals capable of water oxidation were grown and the structure was analyzed with 3.8 Å resolution in 2001 [9]. Further development in X-ray analysis of the crystal structure of PS II were pursued by three groups [10–12] and reached to the resolution of 3 Å [12].

EPR techniques have been used as microscopic monitors for function of photosynthesis such as oxygen evolving activity and for structural studies to measure dipolar interaction between radicals. In this chapter the structure and function of PS

II as determined by EPR methods are described, especially the unique characteristics related to water oxidations. To study photosynthesis, not only both cw EPR and pulsed techniques, but also ENDOR, ODMR etc., have been used. Other spectroscopic techniques employed are FTIR, optical absorption, fluorescence, EXAFS, and XANES, which will be referenced where necessary.

Sample preparation is an important factor in studying photosynthesis. Chloroplasts from various plants were the objects of the earlier investigations. Isolation of PSI and PS II particles was implemented later in order to discriminate various functions. Biochemical treatments were found to change functions. Physical preparations such as control of illumination, temperature and trapping are also important for obtaining appropriate sample condition.

Photosynthesis is a complicated phenomenon which depends on the concerted action of a number of enzymes and proteins. A number of studies on PS II have described the techniques required to obtain information about the important functions [13, 14]. Some recent advances such as single crystal growth, X-ray analysis and EPR of PS II during the last two decades are summarized in the chapter by Wydrzinsky and Satoh [14].

6.1.2 *Charge Separation and Electron Transfer in Plant Photosystem*

Light illumination includes excitation of P680 reaction center of chlorophyll *a* followed by electron transfer to pheophytin within hundreds of picoseconds and then to the first electron acceptor quinone, plastoquione, within microsecond [15]. Oxidized $P680^+$ is reduced by tyrosine Z (Y_Z) in 10–500 ns at physiological temperature. Oxidized $Y_Z^{\bullet}$ is reduced by water oxidizing complexes containing four manganese atoms. The electron on the primary quinine Q_A is transferred to the secondary quinone Q_B and then to the plastoquinone pool. The photosystem I accepts the electron from photosystem II after excitation as shown in Fig. 6.1.

A purified PS II reaction center is composed of D1, D2 and Cytochrome *b559* protein subunits. However, photosynthetic function cannot be realized without water in these systems. The function of water oxidase was discovered by flash illumination during oxygen evolution measurements in which the oxygen yield oscillated with a period of four.

The corresponding states were named as S-states or oxygen clocks by Kok et al. [16] as shown in the right below in Fig. 6.1. The S-state cycles from S_0 to S_4 by absorption of four light quanta.

Figure 6.2 shows the electron transfer chain derived from the crystal structure data [10]. The acceptor side of the structure is similar to that of purple bacterial reaction center. The donor side was quite different from it. The water oxidase is a quite unique enzyme of higher plants for which crystallization has been difficult

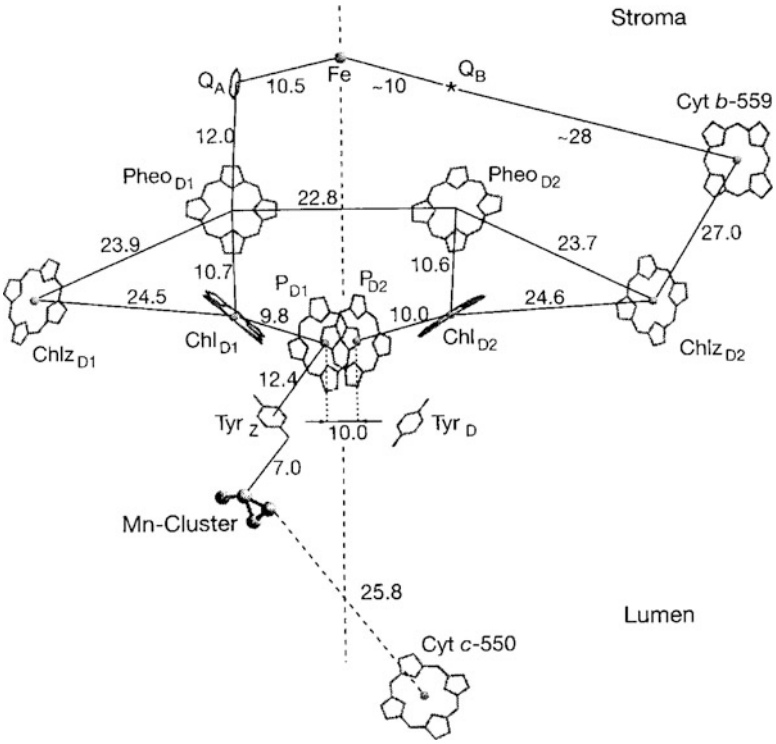

Fig. 6.2 The *side view* of the configuration of cofactors in PS II determined by X-ray analysis. The unit of distance is in Å. P_{D1} and P_{D2} are the reaction center chlorophyll molecules with the separation between Mg atoms 10 Å. The crystal c-axis is along the line from the center of P680 to Fe atoms. Cyt c-550 belongs to the extrinsic protein specific to cyanobacteria in the place of 23 kD protein in spinach (Taken from Ref. [10])

until recently. Single crystals of active PS II include water oxidizing complexes (WOC) with some extrinsic proteins and several other subunits.

In 2001, X-ray analysis of single crystals of cyanobacteria *Synechococcus elongatus* was reported [9]. The resolution was 3.9 Å and a number of the chlorophylls and the Mn-cluster were identified. However, the positions of tyrosine and quinones were not accurately determined because of their small molecular sizes. On the other hand, the distance between radical species has been determined with the accuracy of 1 Å by spin polarized ESEEM and pulsed ELDOR.

The electron transfer rate in biological systems has been thoroughly studied by Marcus and Sutin [17]. The knowledge of the distance and its direction between electron transfer components are essential for understanding the electron transfer mechanism. EPR techniques to determine distances are expected to yield more detailed structural information.

6.1.3 Electron Transfer Components in Photosystem II

Figure 6.2 shows the electron transfer pathway and its components studied by EPR and optical absorption depicted from the crystal structure data [10]. The chlorophyll function is important because a number of chlorophylls serve as antennas for energy transfer and a specific pair act as the reaction center for electron transfer.

6.1.3.1 Chlorophylls

P680

There are six chlorophyll molecules in the purified reaction center complex, two of them are the reaction center chlorophyll dimer called P680, two others are monomer chlorophylls situated between P680 and pheophytin. The last two are rather separated from P680 and one of them is believed to facilitate the side electron transfer pathway from Cytochrome *b559* (Cyt b_{559}) to P680. The re-reduction kinetics of oxidized P680 has been studied optically by observation of the decay rate at the 820 nm absorption which has a short life time. The life time was found to be dependent on pH and temperature. At low temperatures below 200 K donation of electron from tyrosine Z (Y_Z) was inhibited. The life time was determined by charge recombination with primary acceptor quinone to be about 3 ms [18].

When the primary acceptor quinone has been reduced, P680 triplet state is formed. The triplet state EPR was observed during illumination at low temperature by Rutherford et al. [19] in 1986. This triplet state configuration was found to be different from that in bacterial system [20]. The triplet state EPR signal has a large zero field splitting comparable to that in a monomer chlorophyll. FTIR study [21] also proved that the triplet electrons reside on one of the accessory chlorophylls near by.

The reaction center in a bacterial system is composed of dimer bacteriochlorophyll molecules, each one belonging to L and M proteins, separated by 8 Å between Mg atoms in the porphyrin rings [22]. The Mg atoms in P680 are separated by 10 Å. The EPR signal of the oxidized P680 is difficult to obtain because of its short life time. However, the signal of oxidized P680 has been observed transiently by several workers [23–25] at low temperatures.

Chlorophyll Z

The radical signal appears usually in an inhibited system such as by illumination at temperatures below 200 K. The line width is about 1.1 mT peak to peak, characteristic of a monomer chlorophyll radical. A side electron transfer path has been proposed from Cyt b_{559} through P680 to Q_A by Thomson and Brudvig [26]. As D1 and D2 proteins are located in C_2 symmetry, there should be two chlorophylls

with each belonging to D1 and D2. Only one is active in donating an electron to the oxidized $P680^+$ when Cyt b_{559} has been oxidized. Chlorophyll Z is named by an analogy with tyrosine Z and is suggested to be located on D1 protein [27]. Recent X-ray analysis has revealed two chlorophylls corresponding to Chlorophyll Z and Chlorophyll D that belong to D1 and D2 polypeptides, respectively. However, X-ray analysis cannot discriminate which chlorophyll is active.

6.1.3.2 Tyrosines Y_D and Y_Z

In photosystem II (PS II) particles, deuterated tyrosine was introduced, resulting in a narrowing of the line shape of Sig. II [2]. The stable radical signal in PS II called Sig. II_s, was recognized as tyrosine D (Y_D), in which s means slow or stable. This radical is located on the D2 protein, and has been well studied during the past 30 years.

The other radicals induced by illumination could be detected transiently and called Sig. II_f (fast) [28] and Sig. II_{vf} (very fast) [29] according to their life times, as the signals had the same line shapes as Sig II_s. They have been ascribed to another tyrosine Z (Y_Z) on the D1 protein, since the proof by isotopic labeling of cyanobacterial PS II was performed [30]. The WOC supplies an electron to $Y_Z^\bullet$ in microsecond to 100 ns (Sig II_{vf}). When the four manganese are depleted, the life time of $Y_Z^\bullet$ becomes longer because of slow electron donation by back reaction from the acceptor side and the EPR signal (Sig. II_f) is visible during illumination.

6.1.3.3 Plastoquinone Q_A

In photosystems, bacterial and plant PS II the acceptor side includes a non-heme iron between the primary and the secondary quinones. EPR signals of Q_A cannot be observed except for low temperature below 15 K due to broadening by exchange coupling with the ferrous iron. When this iron is depleted or substituted by zinc, a sharp typical radical signal with the line width of 0.9 mT is observed in reduced condition. The signal has been studied by ENDOR by McMillan et al. [31]. The study provided the knowledge of hyperfine coupling and hydrogen bonding with surroundings.

6.1.3.4 Cytochrome *b559* (Cyt b_{559})

Oxidized cytochrome *b559* can be observed at low temperatures over a wide range of applied magnetic field from $g_z = 2.9$ to $g_x = 1.5$ [32]. These g-values manifest low potential and high potential forms of Cyt b_{559} depending on biological systems. In oriented membranes the signal position and intensity depend on magnetic field direction. The g_y direction is along the membrane normal as observed in the oriented membranes [33]. The role of this cofactor has not yet been clarified because it works

only at an inhibited state. The axis of the heme plane of Cyt b_{559} connects α and β subunits and is suggested to be on the acceptor side by Stewart and Brudvig [34] which the recent crystal structure analysis has also shown [10].

6.1.3.5 Mn-Cluster in Water Oxidizing Complex

The water oxidizing complex (WOC) includes four manganese atoms that accumulate oxidizing equivalents by four light quanta and each state has been named S_0 to S_4 by Kok's S-state or oxygen clock as shown in Fig. 6.1 [16]. The manganese signal was first discovered at 5 K by Dismukes and Siderer [35] in 1980. The signal was very similar to that in a model Mn(III)-Mn(IV) compound [36] in which the EPR signal consists of 16 lines separated by about 8 mT over the field range of 180 mT centered at $g = 2$. The spectrum was interpreted by antiferromagnetic coupled dimer with the resultant spin $S = S_1 + S_2 = 1/2$ ($S_1 = 2$ and $S_2 = 3/2$). The signal was induced by one flash illumination and its intensity oscillated with Kok's S-state by further flashes. The first maximum was induced by 1 flash and then decreased by 2, 3 and 4 flashes. The second maximum appeared on the fifth flash. Therefore, the signal assigned to the S_2-state, because the S_1 state has been known to be most stable in the dark. This signal can be observed by illumination at 200 K and has been used as a monitor for S_2-state formation after biochemical treatment such as depletion of extrinsic proteins or Ca^{2+}.

A $g = 4.1$ signal was observed after illumination at 140 K [37]. Elimination of cofactors Ca^{2+} and Cl^- in WOC resulted in inactivation of oxygen evolution. Similar $g = 4.1$ signals were observed for PS II samples after Cl^- depletion by acetate treatment and by illumination at physiological temperature as reviewed by Britt [38].

An S_1-state signal observed by parallel polarization EPR below 5 K in a dark adapted PS II sample was reported Dexheimer and Klein [39] in 1992. Its resonance field was at $g = 4.9$ with the width about 60 mT. By simulation they assigned the signal $S = 1$ and zero field splitting D of 0.14 cm^{-1}. However, nobody could reproduce this signal during the following several years. In 1997 Yamauchi et al. [40] reproduced this signal and assigned it to the excited triplet state $S = 1$ separated from the ground singlet state by 2.5 K based on its temperature dependence.

A similar multiline signal was reported in 1997 on biochemically reduced S_0-state by Messinger et al. [41] or after 3 flashes of illumination by Åhring et al. [42]. The signal was very similar to the observed in the S_2-state. The difference was the number of lines and the overall width was also larger. Saturation behavior in S_0 and S_2-states was also different. The S_0-state signal was observable only with addition of 2–3% methanol. This signal has been ascribed to antiferromagnetic coupling between Mn(III) and Mn(II) with the resultant spin $S = 1/2$.

S_3-state signal were observed with a dual mode cavity by Matsukawa et al. [43]. This signal was also suggested to arise from one of excited states based on the temperature dependence of the signal intensity and assigned tentatively $S = 1$ state separated by about 3.6 K from the ground singlet state. Compared to the S_2-state

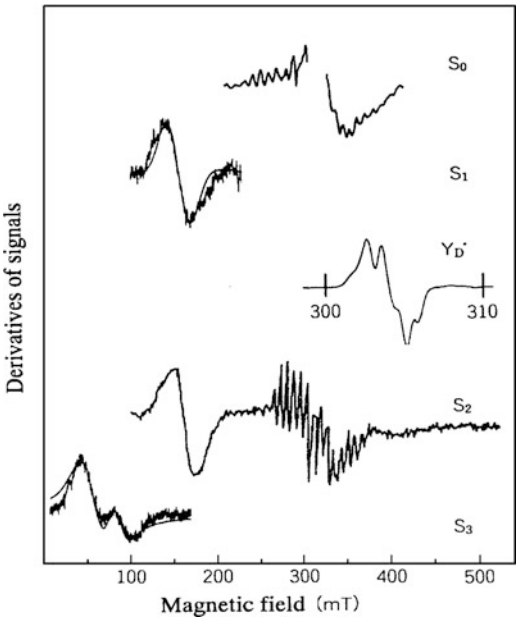

Fig. 6.3 EPR signals of Mn-cluster observed in S_0- to S_3-states and $Y_D^{\bullet}$ radical in the oxygen evolving PS II particles. The signals for S_1 and S_3 were observed by parallel mode in which *smooth lines* show simulations. The Other signals were observed by ordinary perpendicular mode

and S_0-states that have spin 1/2, the S_1 and S_3 states are difficult to observe by EPR, because the spin numbers are integers and zero field splitting is usually comparable or larger than the microwave frequency.

At present all the Kok's S-state signals except for the S_4-state have been observed in the oxygen evolving photosystem II. The S_4-state is only a transient state and cannot be trapped. Instead, the S_0-state could be observed as a ground state. In Fig. 6.3 typical manganese signals are shown for the S_0- to S_3- states together with stable radical signal of $Y_D^{\bullet}$. From the EPR and EXAFS studies a model structure called dimer of dimers has been presented for the Mn-cluster by Yachandra et al. [44]. Most of the electron transport components in Fig. 6.2a have been studied by EPR. Some typical experiments will be described in later sections.

6.2 Methods Applied to Photosynthesis

6.2.1 Distance Determination

6.2.1.1 Spin Lattice Relaxation Measurement

One of the popular methods to derive the distance between paramagnetic species is spin lattice relaxation time measurements. In PS II, we observe usually a radical

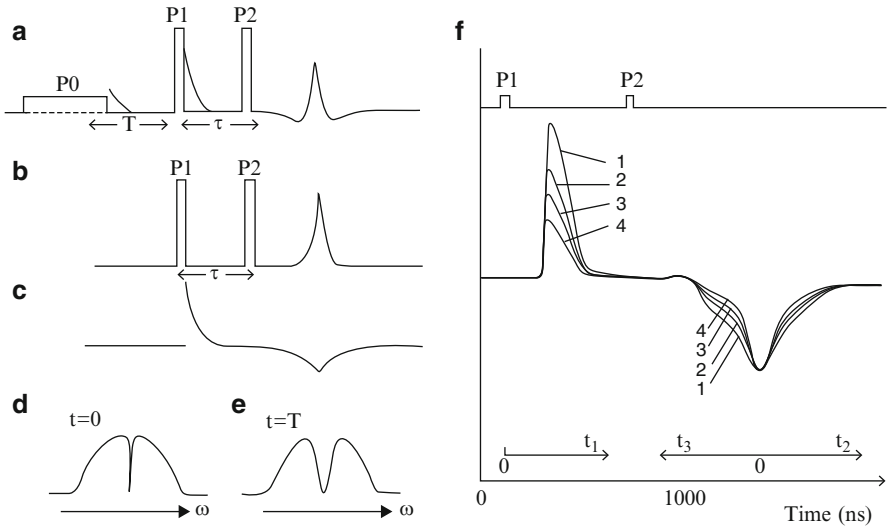

Fig. 6.4 A method of hole burning and detection of the hole broadening. (**a**) The echo signal after P2 pulse is precede by a hole-burning pulse P0. (**b**) The echo signal without P0 pulse. (**c**) Subtraction of (**b**) from (**a**) produces the time domain hole shape at time T after P0. (**d**) A hole burned and (**e**) broadened after time T by spectral diffusion and relaxation by relaxers as shown by frequency domain. (**f**) Variation of hole shapes in time domain with increasing time T as observed in coal sample

tyrosine D ($Y_D^{\bullet}$), while the non-heme iron and manganese are strong relaxers that affect relaxation of the radical called relaxee. The relaxation rate is given by:

$$1/T_1 = \text{const.}/r^6[\tau_c/(1 + \omega_0^2\tau_c^2)] \tag{6.1}$$

where τ_c is the correlation time of the relaxer and "const." is related to the magnetic moment of the relaxer.

We usually do not know about the correlation time. Instead, by observing temperature dependence, the maximum point of $1/T_1$ at $\omega_0\tau_c \sim 1$ can be obtained. Then we derive the distance between the relaxee and relaxer according to the formula const./$r^6 = 1/T_1/\tau_c$. This method was applied by Hirsh et al. [45] to calculate the distance of Y_D from the non-heme iron.

6.2.1.2 Selective Hole Burning

This method was proposed by Dzuba et al. [46] to measure the distribution of radicals in coal and was applied to photosystem II later. The pulse sequence consists of a long period of the first $\pi/2$ or π-pulse to make a hole into a part of a broad line and of ordinary strong detection $\pi/2$-π pulse to observe the electron spin echo (ESE) of the whole line as shown in Fig. 6.4a.

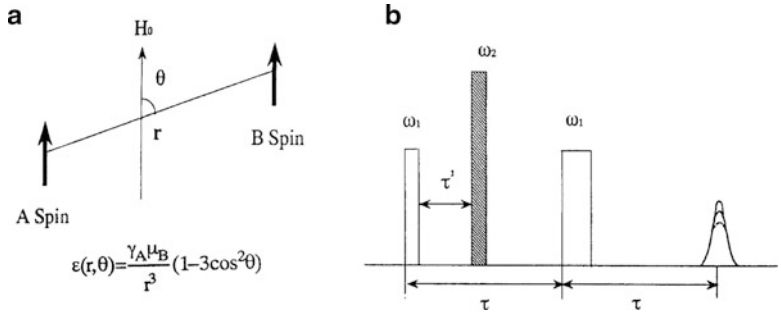

Fig. 6.5 A pulse sequence to detect magnetic dipole interaction by PELDOR. (**a**) Two interacting spins A and B. (**b**) Three pulse sequence; the first π/2 and third π pulses form the ESE signal of A spins and the second pulse turns the orientation of spins B

Let us consider a pair of interacting spins A and B shown in Fig. 6.5a. The ESE signal of the spin A is observed using a pulse sequence shown in Fig. 6.4b. In this pulsed sequence the second π/2 and the third π pulses separated by the time interval t from the ESE signal with the amplitude determined by the transverse relaxation time T_2:

$$V(2t) \propto \exp(-t/T_2) \tag{6.2}$$

The spin B produces an extra dipolar field on the spin A in addition to the applied magnetic field H_0 as shown by:

$$\Delta H = \mu_B / r^3 (3\cos^2\theta - 1) m_S \tag{6.3}$$

where m_S is the projection of the spin B on the applied field direction. The extra field usually varies with space and time in a random way contributing to the EPR line width and to the phase memory time $T_M \sim T_2$ in ESE.

By varying the time of detection T after the hole burning we can observe the broadening of the hole as a result of spin relaxation of the relaxer due to change of m_S. We do not have to know the spin relaxation of the relaxer. However, the spin relaxation time should be in an appropriate range to make the dipole interaction between the interacting paramagnetic species observable as indicated in Kodera et al. [47] and Hara et al. [48]. After a time T, the echo shape can be given by the following formula for $S = 1/2$ of B spin:

$$f_T(t) = 0.5(1 + \exp(-T/T_1)) + 0.5(1 - \exp(-T/T_1))\cos(\varepsilon(r,\theta)t) \tag{6.4}$$

where $\varepsilon(r,\theta) = \gamma_A \mu_B (3\cos^2\theta\text{-}1)/r^3$ is the dipolar interaction constant from which we can derive the distance r.

6.2.1.3 Pulsed Electron-Electron Double Resonance (PELDOR)

Two-dimensional ELDOR was introduced by Freed [49] to investigate spin labeled system. In photosystems, the concentrations of radicals are not enough to apply it and instead two frequencies can be employed [50].

Let us consider a pair of interaction spins A and B shown in Fig. 6.5a. The electron spin echo (ESE) signal of the spin A is observed using a pulse sequence shown in Fig. 6.5b. In this pulse sequence the first $\pi/2$ and third π pulses, separated by the time interval τ, form the ESE signal with the amplitude determined by the transverse relaxation time T_2 in Eq. (6.2).

The spin B produces an extra dipolar field on the spin A in addition to the applied magnetic field H_0 as shown by Eq. (6.3), where m_S is the projection of the spin B on the applied field direction. The extra field usually varies with space and time in a random way contributing to the EPR line width and to the phase memory time $T_M \sim T_2$ in ESE. When the second pulse is applied to the spin B at the time τ' to turn the B spin (i.e. to change m_S), the sudden change of the extra field given by Eq. (6.4) produces a periodic change in the echo height of $V(2\tau)$ depending on τ' as shown in Fig. 6.5b.

$$V(\tau') \propto -p[1 - \cos(\Delta\omega\tau')], \quad \text{with } \Delta\omega = \varepsilon(r, \theta) \tag{6.5}$$

Where p is a portion of B spins turned by the second pulse that will be not important for analysis.

For a randomly oriented system, $V(\tau')$ should be averaged over the orientations θ:

$$V(\tau') \propto < \cos(\Delta\omega\tau') >_\theta \propto \int \cos(\Delta\omega\tau') \sin\theta \, d\theta \tag{6.6}$$

In an oriented membrane system the same integral should be multiplied by a Gaussian distribution function $\exp[-\delta\theta^2/2 < \Delta\theta^2>]$ in which $\delta\theta$ is deviation of the membrane normal from their average, and $< \Delta\theta^2 >$ is a mean square deviation.

When the signals of A and B spins overlap each other, the same resonance frequency can be applied to excitation and detection which is called '2 + 1' pulse sequence as described for $Y_Z^\bullet$ and $Y_D^\bullet$ radical pairs in Sect. (6.4.1).

6.2.1.4 ESEEM of Spin Polarized Radical Pairs

The spin polarized radical pair ESEEM for $P700^+A_1^-$ in Photosystem I (PS I) was observed by Moënne-Loccoz et al. [51] in 1994. Dzuba et al. [52] observed the similar ESEEM for $P860^+Q_A^-$ in a bacterial reaction center and derived the distance between the pair from the obtained frequency corresponding to the dipolar interaction. In Fig. 6.6, the principle of spin polarized ESEEM is shown. As the state has 100% polarized spins, strong temperature independent signal intensity is usually observed. In the later Sect. (6.4.2), ESEEM of $P700^+$-A_1^- in PS I and $P680^+$ Q_A^- in PS II will be described.

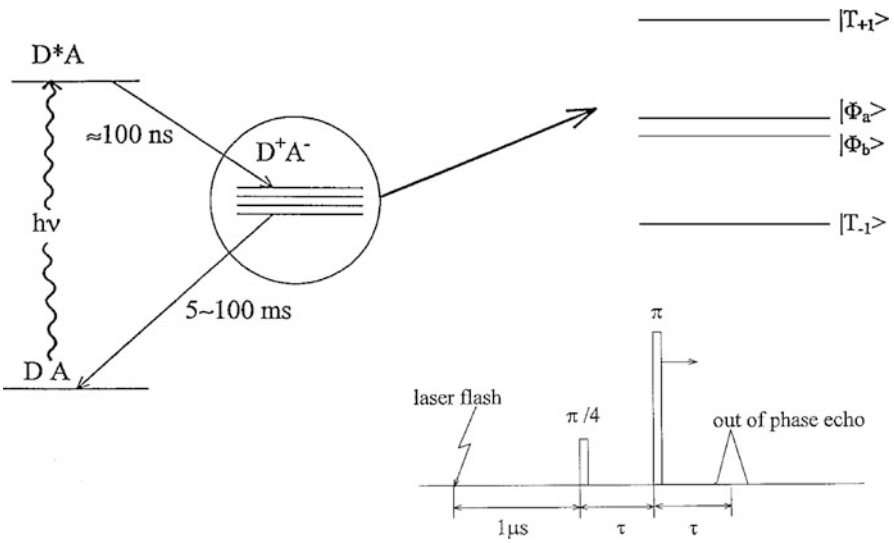

Fig. 6.6 Spin polarized radical pair state induced by laser flash. The radical pair state is a mixed state of T_0 and S with the resultant spin along x direction varying with time τ

6.2.2 Other Methods

6.2.2.1 Dual Mode EPR

EPR signals of paramagnetic ions with an integer spin have been difficult to observe because of large zero field splitting and large linewidth induced by anisotropic interaction. Forbidden transitions can be observed with *rf*-field parallel to the static magnetic field, detecting $\Delta m_S = 0$ transition induced by the matrix element S_z. The transition often appears at about half the resonance field with less line width. The *rf*-field can be applied to a dual mode cavity in TE_{012} mode while an ordinary perpendicular mode can be observed by tuning to TE_{102} mode with a slightly different frequency. In PS II only a parallel mode signal was observed for the S_1-state of WOC. Both parallel and perpendicular modes were observed for the S_3-state and shown in the later Sect. (6.4.5).

6.2.2.2 Time Resolved EPR

In photochemical reactions, electron transfer occurs rapidly, and time resolved optical absorption has been used to detect intermediate states. Some intermediate states such as triplet states of reaction centers of photosynthetic bacteria [52, 53] and PS I [51] have been studied by transient EPR for the systems with acceptor quinone reduced. Dipolar interaction between the electrons was analyzed and from the orientation dependence of the signal, the triplet electron was suggested to reside on the reaction center chlorophylls in these two systems.

The oxidized reaction center chlorolphylls were usually observed by cw EPR method for the bacterial and PS I systems during illumination. On the other hand in PS II the signal of oxidized $P680^{+}$ could be observed only by the time resolved method at low temperatures [24, 25] where spin-lattice relaxation times were investigated.

6.2.2.3 High Frequency EPR

High frequency EPR has been developed in the field of solid state physics in the last two decades and applied to photosystems recently. The equipments for W-band (95 GHz) are now available from Bruker Biospin company. A 250 GHz system has been employed to observe tyrosine radicals in PS II and others as referenced in Doret et al. [54].

6.2.2.4 ENDOR

CW and pulsed ENDOR methods have been described in detail by Brustolon in Chapter 2. The use of these methods is very convenient to study electron spin distribution and to get structural information of the cofactor molecules, tyrosines, quinones and manganese clusters, related to their functions.

6.2.2.5 Optically Detected Magnetic Resonance (ODMR)

Most of the works on ODMR have been developed by Hoff's group on triplet states of bacterial reaction centers [55]. The detection system was optical absorption or fluorescence depending on the relaxation of the relevant levels of the energy state where electron spin resonance occurred. This method has proven useful for investigating intermediate states of primary electron transfer processes, because the life times are generally too short to detect transient microwave absorption or emission. In PS II, the triplet state P680 was studied by absorption detected magnetic resonance (ADMR) [56].

6.2.2.6 ESEEM Applied to Study the Molecular Structure of Radicals

Electron Spin Echo Envelope Modulation (ESEEM) is a popular method for studying electron distributions on atoms in a molecule and chemical bonding. It has been described in detail in the book Dikanov and Tsvetkov [57]. In photosystem II most of the radicals show proton ESEEM by two-pulse but these are not useful for analyzing the state. However, by replacing the hydrogen in water by deuteron, deuteron ESEEM has been observed, which has shown information about coordination numbers around the Mn-cluster [58]. Three pulse ESEEM of nitrogen has been applied to investigate coupling of amino acids with quinone binding on the acceptor side as shown in Sect. 6.4.3 [59].

6.3 Sample Preparations

6.3.1 Oxygen Evolving PS II Membranes

Oxygen evolving PS II membranes (about 400 μmol O_2/mg Chl/h) were prepared from market spinach by the method of Kuwabara & Murata [60] or BBY [61] and suspended in a MES buffer (at pH 6.5) with Chlorophyll concentration 3–15 mg depending on the experiment with 50% glycerol added as a cryoprotectant. The membranes were stored in 77 K until use.

6.3.2 Oriented Membranes

PS II membranes were painted on mylar sheets and were dried under 90% humidity [33]. The distribution of the orientation may be from 15° to 20° as defined by root mean square deviation. The sample sheets were cut into the strips 3×20 mm^2, and a bundle of piled five and six sheets was inserted into quartz tube with inner diameter of 4 mm.

6.3.3 Single Crystals

Single crystals of PS II from cyanobacteria were prepared at Max Volmer Institute and Ruhr University for *Synechococcus eleongatus* [6, 7], and Institute of Physical Chemical Research in Harima (RIKEN) for *Synechococcus vulcanus* [8]. The space group belongs to orthorhombic $P2_12_12_1$ with unit cell dimension $130 \times 227 \times 308$ Å^3 [10]. The local C_2-rotaion axis is along to the membrane normal. The sizes of crystals were too small to be studied by X-band EPR and only tyrosine D was investigated with W-band spectrometer. Later the manganese multiline in the S_2-state was investigated with W-band after few years of X-ray analysis.

6.3.4 Biochemical Treatment

Of the various treatments to inhibit oxygen evolution, two methods will be described. All handling was carried out under dim green light except for Tris-treatment.

6.3.4.1 Tris-Treatment

PS II membranes were suspended in Tris buffer at pH 8.7 and incubated under room light with gentle stirring for 30 min at 4°C [62]. The suspension was centrifuged and

the precipitates were washed with an ordinary MES buffer at pH 6.5. This treatment eliminates all manganese and three extrinsic proteins on the donor side, making the $Y_Z^{\bullet}$ radical visible by CW EPR because quick donation of electron is inhibited.

6.3.4.2 Ca^{2+}-Depletion

Oxygen evolving PS II membranes were treated with citric acid at pH 3.0 as described in Ono and Inoue [63]. The treated membranes were suspended in MES buffer at pH 6.5 without Ca^{2+} and exhibited no appreciable oxygen evolution. However, addition of 10–20 mM $CaCl_2$ restored the oxygen evolution reversibly [64].

6.3.5 Site-Directed Isotope Labeling and Mutagenesis

In 1988 a wild type of *Synechocystis* 6803 with Y_D was deuterated. EPR of the deuterated PS II show no resolved hyperfine structure as shown by Barry and Babcock [2]. Until then the entity of Signal II_s had been considered to be plastoquinone. In the 1990s site-directed mutagenesis has often been carried out and EPR for mutants of various algae has become important for discriminating physiological functions. In this chapter a mutant of *chlamydomonas reinhardtii* lacking Y_D 160 will be investigated to show the distance from $Y_Z^{\bullet}$ radical without interference from $Y_D^{\bullet}$ signal [65].

6.3.6 Physical Treatment

6.3.6.1 Illumination

To induce charge separation, illumination of PS II samples with appropriate intensity and wavelength is essential. About a 500 W tungsten halogen lamp or a 150 W lamp with an optical fiber is required for continuous illumination, while the second harmonics of pulse Nd-YAG laser with 532 nm wavelength is used for pulse irradiation for time resolved experiments. Illumination of oxygen evolving PS II samples at 200 K produces the S_2-state of WOC at high yield. On the other hand, all S-states except for S_4 can be produced by flash illumination by laser or Xenon pulse light.

6.3.6.2 Trapping

Below 243 K, electron transfer from the primary Q_A to the secondary acceptor quinone Q_B is inhibited. Trapping below 200 K is necessary to produce radicals such as $Y_Z^{\bullet}$ and Q_A^{-} immediately after illumination above 253 K or to stabilize generally a charge separated state $D^{+}A^{-}$.

6.3.6.3 Cryoprotectant

To assure complete illumination or to protect proteins from freezing by water, 20–70% glycerol is often used.

6.4 Studied Components

6.4.1 Tyrosines Y_D and Y_Z

6.4.1.1 The Distance Between Y_D and Y_Z Studied by '2 + 1' Pulse Method

Astashkin et al. [66] applied '2 + 1' pulses sequence for the first time to photosystem II to determine the distance between Y_D and Y_Z. $Y_Z^{\bullet}$ radical was trapped at 77 K immediately after illumination for 20 s at 253 K. The distance was determined to be 29.7 ± 0.3 Å from the observed time profiles for the radical pair $Y_D^{\bullet}$-$Y_Z^{\bullet}$ in non-oriented membranes.

Figure 6.7 (left) shows the cw EPR spectra observed for trapped $Y_D^{\bullet}$-$Y_Z^{\bullet}$ radical pair for 0° and 90° orientations, respectively, in the oriented membranes [67].

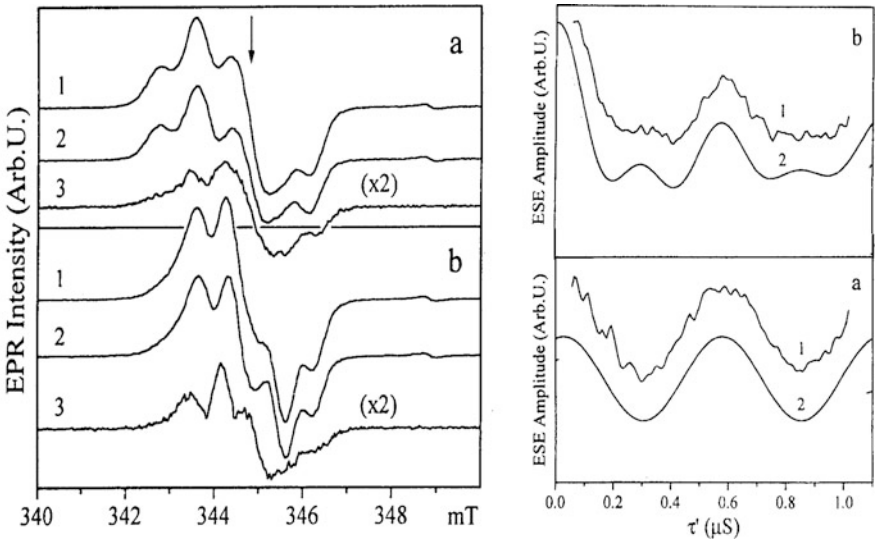

Fig. 6.7 '2 + 1' Pulse sequence applied to $Y_D^{\bullet}$-$Y_Z^{\bullet}$ pair. (*Left*) CW EPR observed in oriented membranes. The membrane normal parallel (*a*) and Perpendicular (*b*) to the magnetic field. Trace 1 shows an overlapping $Y_D^{\bullet}$ and $Y_Z^{\bullet}$ signal, and trace 2, the $Y_D^{\bullet}$ signal after dark adaptation at 0°C. Trace 3 shows $Y_Z^{\bullet}$ signal obtained by subtraction of trace 2 from 1. (*Right*) '2 + 1' time profiles for 0° (*a*) and 90° (*b*) orientation of the membrane normal relative to the field direction. *Lines* marked by 2 show simulation for the vector Y_Z-Y_D orientation of 80° from the membrane normal ***n***

As the line shapes are different for these angles, $Y_D^{\bullet}$ EPR is used for setting orientation conveniently. By applying '2 + 1' pulse a doubled frequency was observed 90° in Fig. 6.7b on the right. This suggests the distance vector is approximately along the membrane plane. By simulation the best fit orientation was determined to be 80° or 100°.

6.4.1.2 Molecular Environments of Y_D and Y_Z Studied by cw and Pulsed ENDOR

All of photosynthetic reaction enters have C_2 symmetrical arrangements of polypeptides, whereas their functions are asymmetric. D1 and D2 hetero-dimers form the photosynthetic reaction center. Two redox active tyrosine residues, Y_Z 161 in D1 and Y_D 160 in D2 polypeptides are identical. However, they have quite different functional roles. Y_Z is the secondary donor and donates an electron to $P680^+$, while Y_D is an auxiliary donor, when it has been reduced. Above pH 6.5, these radicals show similar EPR line shapes with the hyperfine couplings due to equivalent ring protons and one of the β-methylene protons. Matrix ENDOR shows the different relaxation rates of both radicals in the proteins, i.e. Y_Z located in the hydrophilic site compared to Y_D [62]. However, below pH 6.5 the EPR line shape of the $Y_Z^{\bullet}$ radical changes dramatically, while that of the $Y_D^{\bullet}$ radical doesn't. The $Y_Z^{\bullet}$ radical at low pH shows EPR/ENDOR line shapes characteristic for a cation radical [68] as shown in Fig. 6.8. In the isolated solution, the dissociation of the proton in the tyrosine molecule is considerably low ($pK_a = -2$). Therefore, the relationship between the function of the local structure in the protein and the alteration of Y_Z radical depending on pH remains an unresolved problem.

6.4.1.3 High Frequency EPR Applied to Determine Molecular Orientation

A high-frequency (94 GHz) study using the single crystals of PS II from *Synechococcus elongatus* gave accurate *g*-values deduced from the angular variation of $Y_D^{\bullet}$ signals show in Fig. 6.9 [69]. Molecular axes and *g*-axes are shown in Fig. 6.10a. The derived orientation of the Y_D molecule is shown in Fig. 6.10b. For spinach, high-frequency spectra were observed at 250 GHz in oriented membranes by Doret et al. [54]. The angle α in the crystal *c*-axis might be inclined relative to the membrane normal. It should be noted that Y_D axis is directed differently in cyanobacteria and higher plants.

6.4.1.4 Distance of Y_D and P680 from the Non-heme Iron

Measurement of a bacterial reaction center has been carried out to investigate the applicability of the selective hole burning method for a system where the distance from X-ray data and the magnetic susceptibility data of the non-heme iron on the

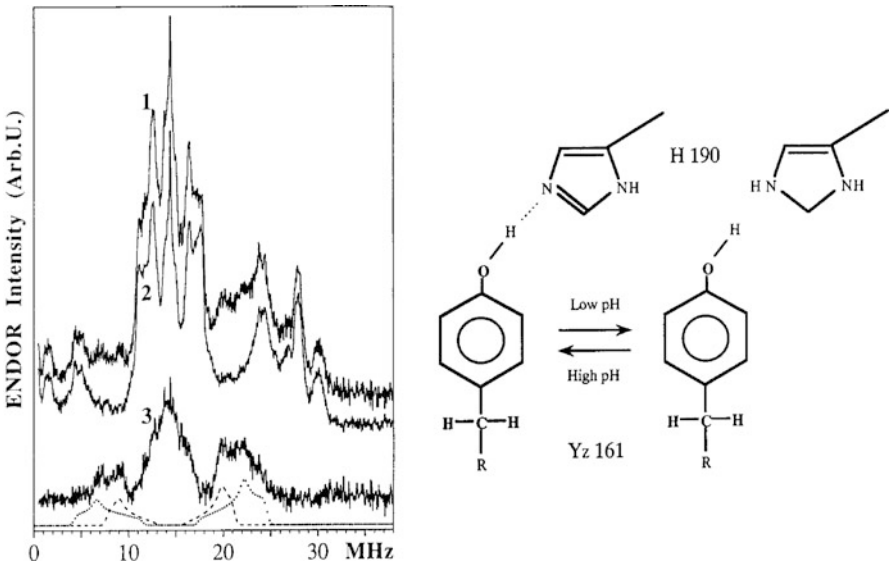

Fig. 6.8 Pulsed ENDOR spectra of tyrosine radicals. (*Left*) Pulsed ENDOR spectra observed at pH 5.5 in the Mn-depleted PS II. The sample was illuminated at 253 K and rapidly frozen to 77 K (trace 1), dark adapted for 30 min at 273 K (trace 2). Subtraction spectrum trace 2 from trace 1 (trace 3). Traces 2 and 3 show the pulsed ENDOR spectra of $Y_D^{\bullet}$ and $Y_Z^{\bullet}$ radicals, respectively. (*Right*) A proposed model for proton coupling to explain the EPR and ENDOR line shapes of $Y_Z^{\bullet}$ radical at low pH

acceptor are available [70]. According to Eq. (6.4) in section 6.2 the echo shape depends on T and varies with temperature because of variation of T_1 of the relaxer. Furthermore, the echo shape is a function of spin number, and Eq. (6.4) should be that expressed by a general value of S.

Temperature variation of the echo shape after the hole burning of oxidized $P860^+$ in *Rb. Sphaeroides R26* is shown in Fig. 6.11a. From the curve for 40 K, where the value of S was 2 and T/T_1 was considered to be approximately infinite, the distance was determined to be 27 Å. This value is the same as that obtained by X-ray diffraction [71]. In Photosystem II, where the acceptor side was considered to be analogous with the purple bacterial system, the effect of hole burning could not be observed at temperatures higher than 10 K because of $S = 2$ spin state are not populated enough and the assumption $S = 2$ is not applicable for this temperature. The effective spin number $S_{\text{eff}} = 0.8$ and the same zero-field splitting as that for the bacterial reaction center were assumed. The obtained value of $r = 42 \pm 2$ Å is close to the value for Y_D-Q_A obtained by the '2 + 1' method [72]. This value can be considered to be more reliable than the value of 38 ± 5 Å obtained based on the spin lattice relaxation of $Y_D^{\bullet}$ because of no assumption for the T_1 value [45]. Measurement of a bacterial reaction center has been carried out to investigate the applicability of the selective hole burning method for a system where the distance from X-ray data and the magnetic susceptibility data of the non-heme iron on the

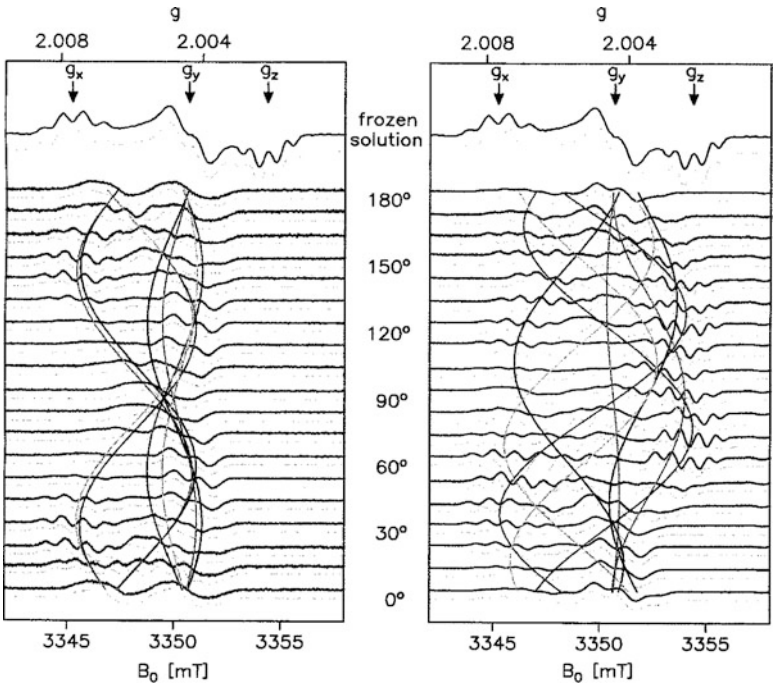

Fig. 6.9 W-band EPR spectra of $Y_D^{\bullet}$ in frozen solution and single crystals of PS II from *S. elongatus*. (*Left*) Crystal rotated approximately about the crystallographic a axis. (*Right*) Arbitrary rotation axis. *Dim shaded lines* show simulations and *curved lines* indicate the calculated angular dependence of the effective g value of $Y_D^{\bullet}$ residue in the unit cell. Simulation parameters: $g_{x/y/z} = 2.00767/2.00438/2.00219$, and $A_{x/y/z}(3/5) = -26.2/-8/-19.5$ MHz (Taken and modified from Hofbauer et al. [69])

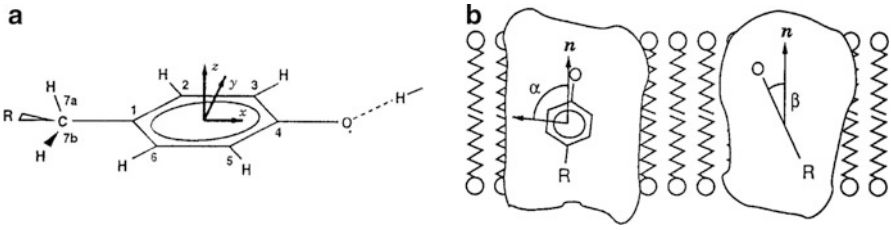

Fig. 6.10 (**a**) Tyrosine radical with numbering scheme and orientation of ***g*** tensor principal axes. (**b**) Orientation of the phenoxyl group of $Y_D^{\bullet}$ in PSII from *S. elongatus* with respect to the membrane normal (parallel to the C_2 symmetry axis) as derived from the single crystal EPR spectra. The angle $\acute{\alpha} = 84°$ is between the g_y direction and the membrane normal $\boldsymbol{n}$; $\beta = 26°$ is the phenoxyl ring plane with respect to $\boldsymbol{n}$

acceptor are available [70]. According to Eq. (6.4) in Sect. 6.2 the echo shape depends on T and varies with temperature because of variation of T_1 of the relaxer. Furthermore, the echo shape is a function of spin number, and Eq. (6.4) should be that expressed by a general value of S.

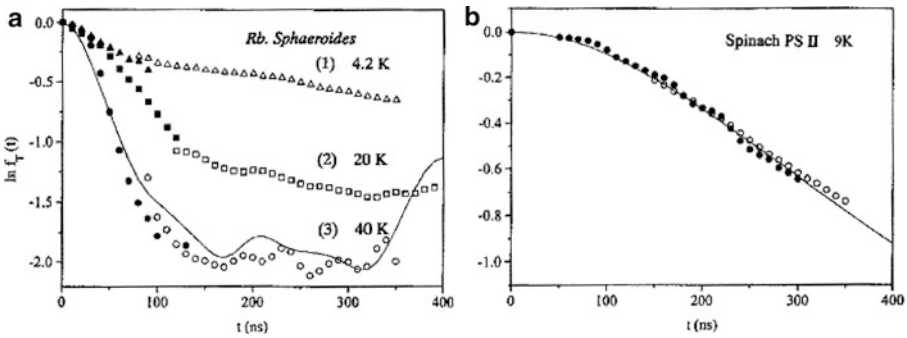

Fig. 6.11 Temperature dependence of the burned hole shapes of $P860^+$ and Y_D after $T = 260$ μs. The hole shapes observed by ESE (*closed circles*) and FID (*open circles*) (**a**) in the *left* for bacteria and (**b**) in the *right* for Y_D in PS II

6.4.2 Chlorophylls

Chlorophyll Triplet State

A triplet state signal similar to that in a bacterial reaction center was first observed in PS II during illumination at a reduced condition of Q_A by Rutherford et al. [19] as shown in Fig. 6.12. The triplet state was produced by a radical pair mechanism from $P680^+Pheo^-$. The pattern is interpreted as *aeeaae* (*a*; absorption and *e*; emission). The deduced *D* value was 0.290 cm^{-1} that is similar to the value obtained from monomeric chlorophyll. The angular dependence of the ESR spectra in oriented membranes showed that the ring plane of the triplet of $^3P680$ was tilted by 30° from the membrane plane [21]. This result suggests that the $^3P680$ may be assigned not to P680 RC but to the monomer chlorophyll near by.

ESEEM of Spin Polarized Radical Pairs: $P700^+A_1^-$ and $P680^+Q_A^-$

Figure 6.13 shows the 2 pulse ESEEM observed by out of phase detection in PS I oriented core particles 1 μs after laser excitation [74]. The period of oscillation for the magnetic field direction parallel to the membrane normal *n* is approximately twice that for the perpendicular direction. The distance was determined by analysis of ESEEM for non-oriented membranes to 25.6 Å [75, 76]. The angle of the distance vector from the *n*-axis was determined to be 24 ± 4°. In the single crystal of *Synechococcus elongatus*, the angle was determined to be 27 ± 5° [77]. Both values are identical within the experimental error. The accuracy in distance of 0.3 Å is much higher than that by X-ray analysis.

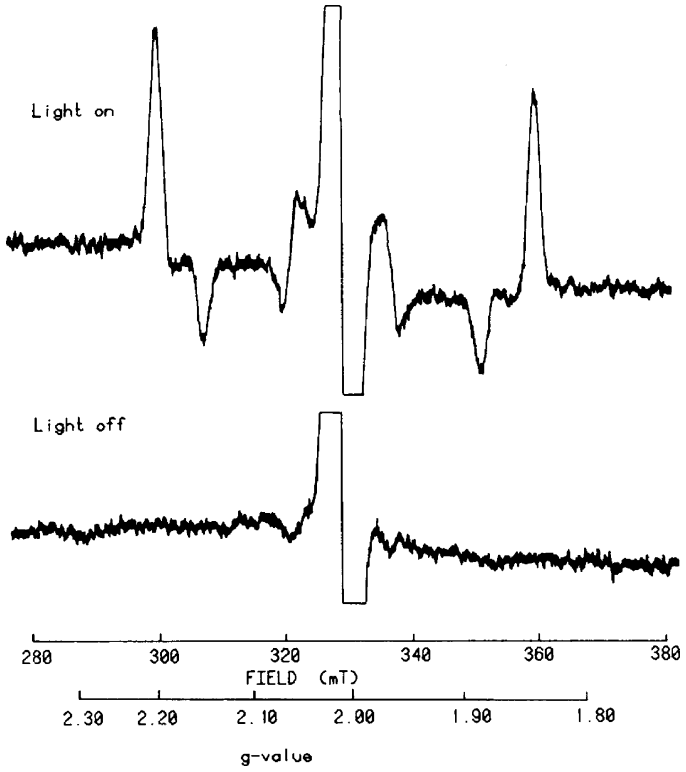

Fig. 6.12 Spectra of ^{3}P680 state. The effect of illumination at 3–5 K on the EPR spectrum of PS II particles. The sample was poised at an Eh of −7 mV

The same method has been applied to $P680^+Q_A^-$ radical pairs in PS II by Zech et al. [78] and Hara et al. [79] and the distance of 27.4 Å was obtained. The angle of 21 ± 5° was determined in the oriented membranes [73].

Temperature Dependence of Microwave Saturation of Oxidized $P680^+$

The oxidized $P680^+$ has only a short life time in oxygen evolving PS II particles at physiological temperatures and cannot be observed even by time resolved EPR. However, at temperatures below 200 K, $P680^+$ can be re-reduced by the primary acceptor quinone on a millisecond time scale and EPR signals have been observed. The line width was about 0.9 mT, which was a little narrower than that of monomer chlorophyll. The temperature dependence of microwave saturation of the peak height of the $P680^+$ signal in PS II in the S_2-state was investigated between 77 and 200 K [25]. The Mn-cluster in the S_2-state was the relaxer to $P680^+$ that was found to be most effective at about 90 K. By applying the Carr-Purcell method, the T_2 value was found to be 0.7 μs. The distance P680 from the Mn-cluster was determined to be 21–25 Å.

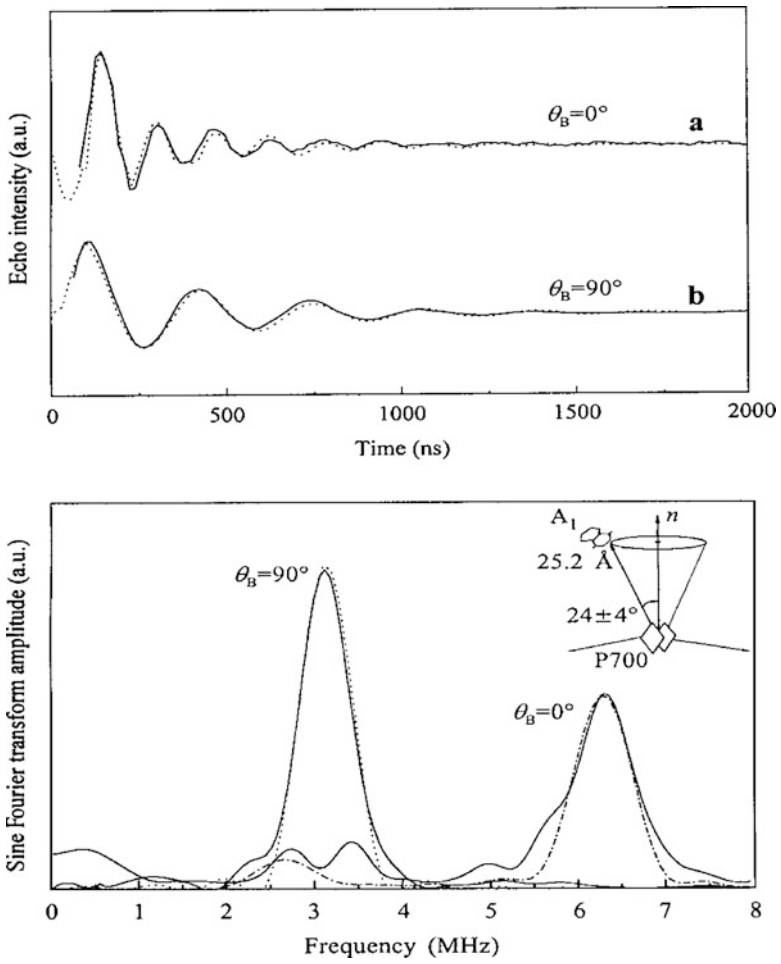

Fig. 6.13 Spin polarized radical pair ESEEM of $P700^+A_1^-$ in oriented PS I. Time profiles (*upper*) and Fourier transforms (*lower*) for orientations 0° and 90° respectively

Chlorophyll Z (Chl_Z)

At temperatures below 200 K, the normal electron transfer pathway is inhibited. A side path from Cyt b_{559} through Chl_Z to $P680^+$ was suggested by Thomson et al. [26], though the position of Chl_Z was not clarified. For the case where Cyt b_{559} was pre-oxidized, the $Chl_Z{}^+Q_A{}^-$ radical pairs were stabilized. Since $P680^+Q_A{}^-$ recombination on side path was inhibited, the transient $P680^+$ signal decreased. This is another reason why $P680^+$ EPR signal is not easily observed.

Stewart et al. [27] proposed that Chl_Z is situated on the D1 protein. X-ray analysis identified two accessory chlorophylls corresponding to this function. However, X-ray data cannot yield information about function.

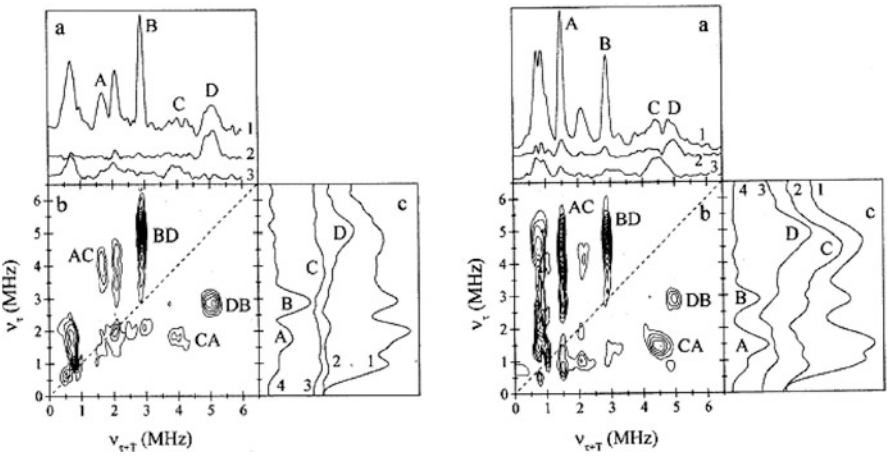

Fig. 6.14 2D spectrum of simulated ESEEM of Q_A^- in CN-treated (1) and Zn^{2+} substituted (2) PS II (b), and its projections on $\nu_{\tau-T}$ (a) and ν_τ (c). Traces 1, 2, and 3 in panel (a) are the projections of whole 2D spectra and of cross peaks DB and CA, respectively. Traces 1,2, 3 and 4 in panel (c) are the projections of the whole 2D spectra of BD and AC, and the region containing cross peaks DB and CA, respectively

The distance between Y_D and Chl_Z was determined to be 29.4 Å [72]. Furthermore, the orientation of the Y_D-Chl_Z vector was determined to be 50 ± 5° relative to the membrane normal based on the time profile of '2 + 1' pulse sequence in the oriented membrane [79]. However, PELDOR was not observed for the Y_Z-Chl_Z pair in Y_D-less mutant of *Chlamydomonas reinhardtii*, suggesting a distance greater than 50 Å between them [65]. Therefore, the active Chl_Z was determined to be on D2 protein based on the present study.

6.4.3 *ESEEM and Two-Dimensional Study of Q_A^-*

The non-heme iron connecting Q_A and Q_B can be eliminated or replaced by zinc. In such PS II, we can observe Q_A^- signals at $g = 2.0046$ position with a peak to peak width 0.9 mT. The magnetic exchange coupling with the ferrous iron can be eliminated by cyanide treatment [80] or in an alkaline buffer of pH 11 [81]. However, these treatments produce different coupling of the iron with surrounding amino acids. Three cyanides coordinate with iron instead of three histidine molecules and also result in the diamagnetic state of the ferrous ion that decouples the exchange with Q_A^-.

The chemical environment of Q_A^- was studied by Astashkin et al. [82] by 2D ESEEM as shown in Fig. 6.14 where the authors compared the two states for zinc-substituted and cyanide-treated PS II. Little change was observed for the Q_A site in

both preparations. Two nitrogen nuclei were found to contribute to the spectra in both. One of these nitrogens is, probably, an amino nitrogen in the imidazole ring of histidine 214 of D2 protein. The other nitrogen has been assigned to the peptide group of alanine 261 of the D2 protein [82, 83].

6.4.4 Cytochrome b559 (Cyt b_{559})

The oxidized Cytochrome *b*559 can be observed at low temperatures over a wide field range from $g = 2.9$ to $g = 1.5$. g-Values depend on, so called low potential and high potential forms [27]. In oriented membranes the signal position and intensity depend on the magnetic field direction. PELDOR was detected at the $g = 1.988$ position with the partner of primary acceptor quinone Q_A^- ($g = 2.005$) by Kuroiwa et al. [84]. As PELDOR was observed only for the contribution from some selective orientations of Cyt b_{559}, angular selection was taken into simulation. Assuming that g_y-axis is directed along the membrane normal, the distance between Cyt b_{559} and Q_A was determined to be 40 ± 5 Å and its orientation relative to the n-axis, to be $80 \pm 5°$. The distance was determined by X-ray to be more than 45 Å.

6.4.5 Mn-Cluster in Water Oxidizing Complex (WOC)

Since discovery of the manganese multiline signal in the S_2-state, a number of works have been carried out to elucidate the mechanism of water oxidation and the structure of the Mn cluster [85, 38]. It has been known since 1980s that the water oxidizing system includes four manganese, calcium, chloride and three extrinsic proteins in higher plants, because PS II particles deficient of any of these cofactors lose oxygen evolving activity. Among the electron transfer components in PS II, the structure and function of the Mn cluster are most poorly understood at present. EPR signals for all Kok's S_0 to S_3-states have been observed. However, the mechanism to produce these signals has not yet been clarified. Some theoretical consideration for the signal source has been done and the hyperfine structure has been ascribed to magnetic coupling between four manganeses [86, 87]. Several studies of manganese model compounds and theoretical analysis to elucidate exchange coupling schemes of the Mn-cluster have also been reported as reviewed by Pecoraro and Hsieh [88]. Figure 6.15 shows the side view of the structure of WOC in cyanobacterial PSII deduced from X-ray analysis by Loll et al. [12].

6.4.5.1 The S_3-State Signal Observed by a Dual Mode EPR

S_3-state signals in the oriented membrane were first observed at 5 K using dual modes (parallel and perpendicular) by Matsukawa et al. [43] in the 240 K

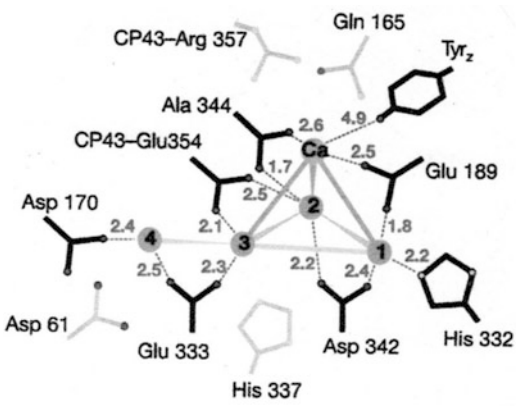

Fig. 6.15 Schematic view of the Mn_4Ca cluster presented by Loll et al. [12]. The numbers 1–4 shows manganese atoms (The figure is adapted with permission from Nature Publishing Group)

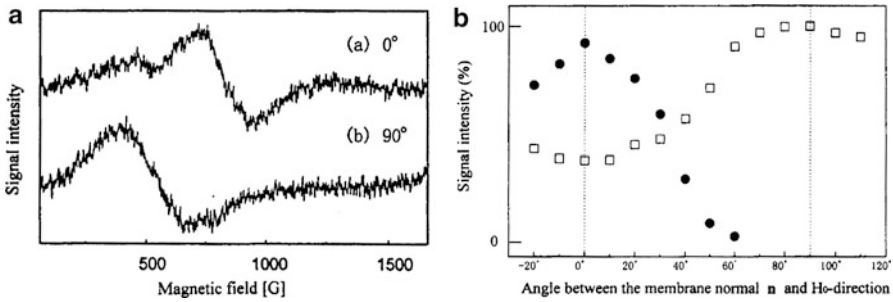

Fig. 6.16 The S_3-state signal observed in oriented membranes. (*Left*) (*a*) ***n*** along the magnetic field and (*b*) perpendicular to it. (*Right*) Angular dependence of intensity shown by *closed circles* for (*a*) and *open circles* for (*b*)

illuminated or by two flash illumination. The signals obtained for with the field parallel and perpendicular to the membrane normal are shown in Fig. 6.16.

Neglecting the intra-dipolar interaction, the value of *D* may be related to the dipole interaction between the spins on the two manganese atoms as suggested by the Mn-Mn direction between the central two atoms (1 and 3 as presented in Fig. 6.15). In the S_1-state the orientation of the *D*-axis was suggested to be perpendicular to the *n* axis [89]. The change in the *D*-axis with S-state advancement may be due to change in the spin distribution induced by oxidation of manganese.

6.4.5.2 The S_2-State Mn Multiline Observed at W-Band

The S_2-state was trapped after illumination of a single crystal of *Thermosynechococcus vulcanus* at 6 K [90]. Angular variation of the multiline signal around the *a*-axis and another different axis was observed. The axis of rotation has been determined by angular variation of $Y_D^{\cdot}$ radical at the S_1-state as shown in Fig. 6.9. The spectra

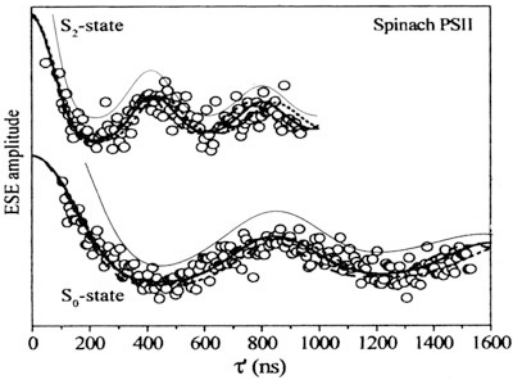

Fig. 6.17 PELDOR signals for the Mn-cluster in the S_2-state (*above*) and S_0-state (*below*). The partner is Y_D radical. The *full lines* show the simulation for the distance 27 and 34 Å respectively. The *broken lines* show simulations with ±0.5 Å

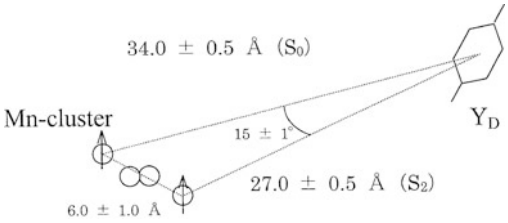

Fig. 6.18 The positions of spin centres of the S_2 and S_0 state Mn-cluster shown by *arrows* based on the approximation of a point dipole of the Mn_4-cluster

were well resolved and g-anisotropy has been determined to be $g_x = 1.988$, $g_y = 1.981$, $g_z = 1.965$. The principal values suggested an approximate axial symmetry around Mn (III) ion in the cluster.

6.4.5.3 Distances of Spin Centers of Mn-Cluster in S_0 and S_2 States

The PELDOR method has been used to measure the distance between the S_2-state manganese cluster and tyrosine D (Y_D)and its relative orientation with respect to the membranes. The distance was found to be 27.3 Å [91] and the orientation of the distance vector was 70° from the membrane normal [67]. Recently we applied the method to the system of the Mn-cluster in the S_0-state and $Y_D^{\bullet}$ radical [92] that was prepared by reduction of the PS II membranes with NH_2OH. The PELDOR signal is shown in Fig. 6.17 in comparison with that for the S_2-state. Figure 6.18 shows the obtained distances and orientations of distance vectors based on a point dipole approximation.

This result supports the conclusion that the change of position in the spin center of the manganese is accompanied by oxidation of WOC due to the change in the exchange coupling scheme of the four manganese complex. As there are magnetic exchange coupling between these manganese atoms, the spin projection on the four manganese should be taken into consideration to get more precise distances as shown in the work on a three 3Fe-S center by Elssasser et al. [94].

Table 6.1 The values of spin projections m_{Si} and valences on each Mn atom

	Mn(1)	Mn(2)	Mn(3)	Mn(4)
S_2-state	1.705 (III)	−0.99 (IV)	−1.0 (IV)	1.275(IV)
S_0-state	−1.8(III)	2.0(III)	−1.1(IV)	1.9 (III)

For S_2-state the values are given by Peloquin et al. [94] and for S_0-state tentative values are assigned

Table 6.2 The derived values of distances along crystalline axes (*a, b, c*) from Y_D-Mn_i with $i = 1$–4 in unit of Å taken from Lolls et al. [12] (2005)

i	*a*	*b*	*c*	*r*	*θ*(°)
Mn1	22.52	−5.332	18.03	29.34	128
Mn2	24.71	−5.476	19.51	31.96	128
Mn3	25.23	−7.075	17.39	31.45	124
Mn4	25.60	−7.694	14.23	30.28	118

The values of θ show the direction of distance vector from the crystalline *c*-axis

In X-ray data shown in Fig. 6.2 the size of the Mn-cluster is about 5^3 Å^3. Point dipolar interaction should be considered for each pair of Y_D-Mn_i with *i* from 1 to 4, as following. It is interesting to remark the change of spin center about 15° is comparable to the difference of Mn_i-Y_D vector direction studied by X-ray.

Dipolar field at the Y_D position Eq. (6.3) should be summed over 4 manganese:

$$\Delta H(\theta_B) = \sum_{i=1,4} P_i (3\cos^2\theta_i - 1)/r_1^3 \tag{6.7}$$

where r_i the distance between Y_D and the *i*-th manganese and $P_i = \mu_B m_{Si}$. (m_{Si} is the projection of the *i*-th manganese spin on the applied field direction. The Y_D molecule is small about 2^3 Å^3 and the spin center is assumed to be on the molecular center.

Peloquin et al. [94] derived spin projection based on Pulsed ENDOR. For simplicity, the anisotropy in projection is approximated by an isotropic projection.

$$P_{iso} = [P_{\|} + 2P_{\perp}]/3 \tag{6.8}$$

The valence for each Mn(III)Mn(IV)$_3$ has been suggested for S_2-state by EXAFS study [44]. The valence Mn(III)$_3$Mn(IV) was suggested by Kulik et al. [95] based on Q-band pulsed ENDOR. Using the spin projection given in Table 6.1, which has been given by Eq. (6.5) using pulsed ENDOR data for the S_2-state. r_i and θ_i for Y_D-Mn distance and its direction were derived based on X-ray analysis [12]. The ELDOR profiles are well fitted on the experimental data. Spin distribution tentatively assigned using ENDOR data [94] on the manganese atoms as shown in Fig. 6.15.

On the electronic state of Mn_4-cluster, Kulik et al. proposed several model of hyperfine constant distribution for S_0 and S_2 based on their ENDOR data measured at Q-band that is different from ours given in Tables 6.1 and 6.2. Therefore, it will be

Table 6.3 Derived distances and their directions of the electron transfer components in PS II studied by EPR

Paraamagnetic pairs	Distance (Å) EPR	Distance (Å) X-ray*	Angle (°) from n-axis	EPR mehtods
P680 – Q_A	27.4 ± 0.3 [76, 79]	(26_{D1}, 28_{D2})	21 ± 5 [73]	Spin polarized ESEEM
Y_D – Q_A	38.5 ± 0.8 [72]	40	28 ± 5 [97]	'2 + 1'
Y_Z – Q_A	34.0 ± 1.0 [65, 98]	34.2		PELDOR
Y_D – Y_Z	29.5 ± 0.5 [66]	29.2	80 ± 2 [67]	'2 + 1'
Y_D – Chl_Z	29.4 ± 0.5 [72]	26.8_{D2}	50 ± 5 [79]	'2 + 1'
Y_D – $Mn_4(S_2)$	27.1 ± 0.2 [47, 93]	30.3	70 ± 2 [67]	PELDOR
Q_A-Cyt b_{559}	40 ± 3 [84]	47.8	78 ± 5 [84]	PELDOR
Y_D-non heme Fe	38–42 [45, 48, 99]	37.6		Selective hole burning & saturaiton
P680 - $Mn_4(S_2)$	21 ± 4 [25]	18.2		Time resolved saturation

Distances and angles were determined by EPR with reference numbers. *The distances were calculated from PDB entry 1FE1 (Zouni et al. [9])

difficult to derive the correct distribution of spin densities over the four Manganese atoms.

The problem is that the crystal data were derived from X-ray analysis of a cyanobacterium. Our PELDOR data were taken for spinach PS II. Recent result on PELDOR of *T. vulcanus* has shown the distances are a little different from those of spinach PS II within the order of 3 Å. PELDOR data of cyanobacteria and further refining of crystal structure data will be necessary.

6.5 Structure of PS II: Comparison with X-Ray Analysis

So far we have obtained the distance and its orientation independently for each pair of paramagnetic species. PELDOR on three spin systems has been undertaken to determine relative positions of electron transfer components more accurately [96]. Results for the $Y_Z^{\bullet}$-$Y_D^{\bullet}$-Q_A^{-} system has been reported. The recorded PELDOR profile fits well with the simulation for known distances, 29 Å of Y_Z-Y_D [66], and 39 Å [72] of Y_D-Q_A and by assuming 34 Å for Y_Z-Q_A that is coincident with the obtained distance from Y_D-less mutant of *C. reinhardtii* [65] and *S. elongatus* [99]. The method was applied to $Y_D^{\bullet}$-Q_A-Chl_Z^{+} system to find the unknown distance between Q_A and Chl_Z. The derived distance was 34 Å [98].

The EPR study were pursuit mostly on spinach PS II. X-ray data could be obtained for cyanobacteria. The question is that the structures are the same for both systems. Recently we are measuring the ELDOR on cyanobacterium *T. vulcanus* that has been analyzed by X-ray [10]. The results were obtained for Y_Z-Y_D systems which are a little different for both systems.

Table 6.3 depicts distances and their orientations relative to the membrane normal (crystal *c*-axis) obtained from EPR. Accurate values for distances were obtained

by ESEEM and PELDOR. Other EPR methods give only approximate values comparable to the resolution of X-ray analysis 3 Å.

The distance from P680 to Q_A coincides. That from P680 to the Mn cluster seem to be consistent each other. The distance from Cyt b_{559} to Q_A obtained EPR is much shorter than that by X-ray data. However, the value depends on the assumed EPR line width in simulation because angular selection has been taken into account. The values of distances for Y_D and Y_Z to P680 and to the Mn-cluster by X-ray seem to be coincident with EPR results within the resolution of 3 Å for X-ray.

The coincidence in the distances derived from X-ray data and EPR were fairly good except for those related to Cyt b_{559}. The distances related small molecules were also coincident with those derived from EPR data. These distances obtained by EPR provide information of the active electron transfer components that could not be determined by other methods. The derived distances from X-ray data for cyanobacteria seem not to be the same for spinaches. Further refinement of X-ray analysis with 1.9 A resolution has been recently reported by Umena et al. [100]. EPR study of cyanobacteria should be necessary to compare with X-ray data.

References

1. Commoner B, Heise JJ, Townsend J (1956) Light-induced paramagnetism in chloroplasts. Proc Natl Acad Sci USA 42:710–718
2. Barry BA, Babcock GT (1987) Tyrosine radicals are involved in the photosynthetic oxygen evolving system. Proc Natl Acad Sci USA 84:7099–7103
3. Feher G, Hoff AJ, Isaacson RA, Ackerson LC (1975) ENDOR experiments on chlorophyll and bacteriochlorophyll in vitro and in photosynthetic unit. Ann NY Acad Sci 244:260–280
4. Deisenhofer J, Epp O, Miki K, Huber R, Michel H (1985). Structure of the protein subunits in phtotosynthetic reaction centers of the *Rhodopseudomonas viridis* at 3 Å. Nature 318:618–624
5. Witt HT, Krauss N, Hindrichs W, Witt I, Fromme P, Saenger W (1992) Three-dimensional crystals of photosystem I from *Synechococcus sp*. and X-ray structure analysis at 6 Å resolution. In: Murata N (ed) Research in photosynthesis, Proceedings of the International 9th Congress Photosynthesis. Kluwer Academic, Dordrecht, p 521
6. Jordan P, Fromme P, Klukas O, Witt HT, Saenger W, Krauss N (2001) Three-dimensional structure of cyanobacterial Photosystem I at 2.5 Å resolution. Nature 411:909–917
7. Zouni A, Jordan R, Schlodder E, Fromme P, Witt HT (2000) First Photosystem II crystals capable of water oxidation. Biochim Biophys Acta 1457:103–105
8. Shen J-R, Kamiya N (2000) Crystallization and the crystal properties of the oxygen-evolving Photosystem II from *Synechococcus vulcanus*. Biochemistry 39:14739–14744
9. Zouni A, Witt J, Kern J, Fromme P, Krauß W, Saenger W, Orth P (2001) Crystal structure of Photosystem II from *Synechococcus elongatus* at 3.8 Å resolution. Nature 409:739–743
10. Kamiya N, Shen J-R (2003) Crystal structure of oxygen evolving Photosystem II from *Thermo synechococcus vulcanus* at 3.7-Å resolution. Proc Natl Acad Sci USA 100:98–103
11. Ferreira KN, Iverson TM, Maghlaoui K, Barber J, Iwata S (2004) Architecture of the photosynthetic oxygen evolving center. Science 303:1831–1838
12. Loll B, Kern J, Saenjer W, Zouni A, Biesiadka J (2005) Towards complete cofactor arrangement in the 3.0 Å resolution structure of Photosystem II. Nature 438:1040–1044
13. Ort DR, Yocum CF (1996) Oxygenic photosynthesis: the light reactions. Kluwer Academic Publishers, Dordrecht

14. Wydrzynski TJ, Satoh K (2005) Photosystem II; the light-driven water: plastoquinone oxidoreductase. Springer, Dordrecht
15. Diner BA, Babcock GT (1996) Structure, dynamics, and energy conversion efficiency in Photosystem II. In: Ort DR, Yocum CF (eds) Oxygenic photosynthesis: the light reactions. Kluwer Academic Publishers, Dordrecht, p 213
16. Kok B, Forbush B, McGloin M (1970) Cooperation of charges in photosynthetic O_2 evolution. 1. Photochem Photobiol 11:456–475
17. Marcus RA, Sutin N (1985) Electron transfer in chemistry and biology. Biochim Biophys Acta 811:265–322
18. Nugent JHA, Evans MCW, Diner BA (1982) Characteristics of the Photosystem II reaction II. Electron Donors. Biochim Biophys Acta 682:106–114
19. Rutherford AW, Paterson DR, Mullet JE (1981) A light-induced spin polarized triplet detected by EPR in Photosystem II reaction centers. Biochim Biophys Acta 635:205–214
20. Thurnauer MC, Katz JJ, Norris JR (1975) The triplet state in bacterial photosynthesis: possible mechanisms of the primary photo-act. Proc Natl Acad Sci USA 72:3270–3274
21. Noguchi T, Tomo T, Inoue Y (2001) Triplet formation on a monomeric chlorophyll in the Photosystem II reaction center as studied by time resolved infrared spectroscopy. Biochemistry 40:2176–2185
22. Allen JP, Feher G, Yeates TO, Komiya H, Rees DC (1987) Structure of the reaction center from Rhodobacter sphaeroides R-26: the cofactors. Proc Natl Acad Sci USA 84:5730–5734
23. Bock CH, Gerken S, Stehlik D, Witt HT (1988) Time resolved EPR on ON Photosystem II particles after irreversible and reversible inhibition of water cleavage with high concentration of acetate. FEBS Lett 227:141–146
24. Hoganson CW, Babcock GT (1989) Redox cofactor interactions in Photosystem II: electron spin resonance spectrum of $P680^+$ is broadened in the presence of $Y_Z{}^{++}$. Biochemistry 28:1448–1454
25. Kodera Y, Takura K, Kawamori A (1992) Distance of P680 from the manganese complex in Photosystem II studied by time resolved EPR. Biochim Biophys Acta 1101:23–32
26. Thomson LK, Brudvig GT (1988) Cytochrome *b*-559 may function to protect Photosystem II from photoinhibition. Biochemistry 27:6653–6658
27. Stewart DH, Cua A, Chisolm DA, Diner BA, Pocian DF, Brudvig GW (1998) Biochemistry 37:10040–10046. Identification of Histidine 118 in the D1 polypeptide of Photosystem II as the Axial Ligand to Chlorophyll Z
28. Babcock GT, Sauer K (1975) A rapid, light-induced transient in electron paramagnetic resonance signal II activated upon inhibition of photosynthetic oxygen evolution. Biochim Biophys Acta 376:315–328
29. Babcock GT, Sauer K (1975) The rapid component of electron paramagnetic resonance signal II: a candidate for physiological donor to Photosystem II in Spinach chloroplasts. Biochim Biophys Acta 376:329–344
30. Boerner RJ, Barry BA, (1993) Isotopic labeling and EPR spectroscopy show that a tyrosine residue is a terminal electron donor, Z, in manganese-depleted Photosystem II preparations. J Biol Chem 268:17151–17154
31. MacMillan M, Lendzian FH, Renger G, Lubitz W (1995) EPR and ENDOR investigation of the primary electron acceptor radical anion $Q_A{}^{-\bullet}$ in iron-depleted Photosystem II membrane fragments. Biochemistry 34:8144–8156
32. Miller A-F, Brudvig GW (1991) A guide to electron spin resonance spectroscopy of Photosystem II membranes. Biochim Biophys Acta 1056:1–18
33. Rutherford AW (1985) Orientation of EPR signals arising from components in Photosystem II membranes. Biochim Biophys Acta 807:189–201
34. Stewart DH, Brudvig GW (1998) Cytochrome b559 of Photosystem II. Biochim Biophys Acta 1367:63–87
35. Dismukes GC, Siderer Y (1981) Intermediates of a polynuclear manganese center involved in photosynthetic oxidation of water. Proc Natl Acad Sci USA 78:248–274

36. Cooper SR, Dismukes GC, Klein MP, Calvin M (1978) Mixed valence interactions in di-oxo bridged manganese complexes. electron paramagnetic resonance and magnetic susceptibility studies. J Am Chem Soc 100:7248–7252
37. De Paula JC, Innes JB, Brudvig GW (1985) Electron transfer in Photosystem II at cryogenic temperatures. Biochemistry 24:8114–8120
38. Britt RD (1996) Oxygen evolution. In: Ort DR, Yocum CF (eds) Oxygenic photosynthesis: the light reactions. Kluwer Academic Publishers, Dordrecht, p 137
39. Dexheimer SL, Klein MP (1992) Detection of a paramagnetic intermediate in the photosynthetic oxygen-evolving complex. J Am Chem Soc 114:2821–2826
40. Yamauchi T, Mino H, Matsukawa T, Kawamori A, Ono T-A (1997) Parallel polarization electron paramagnetic resonance studies of the S_1-state manganese cluster in the photosynthetic oxygen-evolving system. Biochemistry 36:7520–7526
41. Messinger J, Nugent JHA, Evans MCW (1997) Detection of an EPR multiline signal for the S_0* state in Photosystem II. Biochemistry 36:11055–11060
42. Ahrling KA, Peterson S, Styring S (1997) An oscillating manganese electron paramagnetic resonance signal from the S_0 state of oxygen evolving complex in Photosystem II. Biochemistry 36:13148–13152
43. Matsukawa T, Mino H, Yoneda D, Kawamori A (1999) Dual-mode EPR study of new signals from the S_3-state of oxygen-evolving complex in Photosystem II. Biochemistry 38:4072–4077
44. Yachandra VK, Derose VJ, Latimer MJ, Mukerji I, Sauer K, Klein MP (1993) Where plants make oxygen: a structural model for the photosynthetic oxygen-evolving manganese cluster. Science 260:675–679
45. Hirsh DJ, Beck JB, Brudvig GW (1992) Using saturation-recovery EPR to measure distances in proteins: applications to Photosystem II. Biochemistry 31:532–541
46. Dzuba SA, Kawamori A (1996) Selective hole burning in EPR: spectral diffusion and dipolar broadening. Concepts Mag Reson 8:49–61
47. Kodera Y, Dzuba SA, Hara H, Kawamori A (1994) Distances from tyrosine D^+ to the manganese cluster and the acceptor iron in Photosystem II as determined by selective hole burning in EPR spectra. Biochim Biophys Acta 1186:91–99
48. Hara H, Kawamori A (1997) A selective hole burning method applied to determine distances between paramagnetic species in photosystems. Appl Magn Reson 13:241–257
49. Freed JH (2000) New technologies in electron spin resonance. Ann Rev Phys Chem 51:655–689
50. Milov AD, Ponomalrev AB, Tsvetkov YD (1984) Electron-electron double resonance in electron spin echo: model biradical systems and the sensitized photolysis of decalin. Chem Phys Lett 110:67–72
51. Moënne-Loccoz P, Heathcote P, Maclachalan DJ, Berry MC, Davis IH, Evans MCW (1994) Biochemistry 33:10037–10042. Path of Electron Transferrin Photosysten I: Direct Evidence of Forward Electron Transfer feom A_1 to Fe-S_X
52. Dzuba SA, Gast P, Hoff AJ (1995) Chem Phys Lett 236:595–602. ESEEM study of spin-spin interactions in spin-polarized $P^+Q_A^-$ pairs in the photosynthetic purplebacterium *Rhodobacter Sphaeroides* R26
53. Hoff AJ, Gast P, Romijin JC (1977) Time-resolved ESR and chemically induced dynamic electron polarization of the primary reaction in a reaction center particle of *Rhodopseudomonas Sphaeroides* wild type at low temperature. FEBS Lett 73:185–189
54. Dolet PA, Rutherford AW, Un S (2000) Orientation of tyrosyl D, pheophytin anion, and semiqionone $Q_A^{-\bullet}$ radicals in Photosystem II determined by high-field electron paramagnetic resonance. Biochemistry 39:7826–7834
55. Hoff A J (1996) In: Amesz J, Hoff AJ (eds) Biophysical technique in photosynthesis. Kluwer Academic, Dordrecht, p 277
56. van der Vos R, van Leeuwen PJ, Braun P, Hoff AJ (1992) Analysis of optical absorbance spectra of D1-D2-cytochrome b-559 complexes by absorbance-detected magnetic resonance. Structural properties of P680. Biochim Biophys Acta 1140:184–198

57. Dikanov SA, Tsvetkov YD (1992) Electron Spin Echo Envelope Moduration (ESEEM) spectroscopy. CRC Press, Boca Raton
58. Force DA, Randall DW, Lorigan GA, Clemens KL, Britt RD (1998) ESEEM studies of alcohol binding to the manganese cluster of the oxygen evolving complex of Photosystem II. J Am Chem Soc 120:13321–13333
59. Astashkin AV, Kawamori A, Kodera Y, Kuroiwa S, Akabori K (1995) An electron spin echo envelope modulation study of the primary acceptor quinone in Zn-substituted plant Photosystem II. J Chem Phys 102:5583–5588
60. Kuwabara T, Murata N (1982) Inactivation of photosynthetic oxygen evolution and concomitant release of three polypeptides in the Photosystem II particles of Spinach chloroplasts. Plant Cell Physiol 23:533–539
61. Berthold DA, Babcock GT, Yocum CF (1981) A highly resolved, oxygen evolving Photosystem II preparation from spinach thyrakoid membranes. EPR and electron transport properties. FEBS Lett 134:231–234
62. Mino H, Kawamori A (1994) Microenvironments of tyrosine D^+ and tyrosine Z^+ in Photosystem II studied by proton matrix ENDOR. Biochim Biophys Acta 1185:213–220
63. Ono T-A, Izawa S, Inoue Y (1992) Structural and functional modulation of the manganese cluster in Ca^{2+}-depleted Photosystem II induced by binding of the 24-kilodalton extrinsic protein. Biochemistry 31:7648–7655
64. Ono T-A, Inoue Y (1989) Removal of Ca by pH 3.0 treatment inhibits S_2 to S_3 transition in photosynthetic oxygen evolution system. Biochim Biophys Acta 973:443–449
65. Kawamori A, Katsuta N, Mino H, Ishii A, Minagawa J, Ono T-A (2002) Positions of Q_A and Chl_Z Relative to Tyrosine Y_Z and Y_D in Photosystem II studied by pulsed EPR. J Biol Phys 28:413–426
66. Astashkin AV, Kodera Y, Kawamori A (1994) Distance between Tyrosine Z^+ and D^+ in plant Photosystem II as determined by pulsed EPR. Biochim Biophys Acta 1187:89–93
67. Astashkin AV, Hara H, Kawmori A (1998) The pulsed electron-electron double resonance and '2 + 1' electron spin echo study of the oriented oxygen-evolving and Mn-depleted preparations of Photosystem II. J Chem Phys 108:3805–3812
68. Mino H, Astashkin AV, Kawamori A (1997) An EPR and pulsed ENDOR study of the structure of tyrosine Z in tris-treated Photosystem II. Spectrochim Acta A53:1465–1483
69. Hofbauer W, Zouni A, Bittl R, Kern RJ, Orth P, Lendzian F, Fromme P, Witt HT, Lubitz W (2001) Photosystem II single crystals studied by EPR spectroscopy at 94 GHz: the tyrosine radical $Y_D^{\bullet}$. Proc Natl Acad Sci USA 98:6623–6628
70. Butler WF, Calvo R, Fredkin DR, Isaacson RA, Okamura MY, Feher G (1984) The electronic structure of Fe^{2+} in reaction centers from *Rhopseudomonas Sphaeroides* III. EPR measurement of the reduced acceptor complex. Biophys J 45:948–973
71. Yeates TO, Komiya H, Rees DC, Allens JP, Feher G (1987) Structure of the reaction center from Rhodobacter sphaeroides R-26: membrane-protein interactions. Proc Natl Acad Sci USA 84:6438–6442
72. Shigemori K, Hara H, Kawamori A, Akabori K (1998) Determination of distances from tyrosine D to Q_A and chlorophyll Z in Photosystem II studied by '2 + 1' Pulsed EPR. Biochim Biophys Acta 1363:187–198
73. Yoshii T, Hara H, Kawamori A, Akabori K, Iwaki M, Itoh S (1999) ESEEM study of the location of spin-polarized chlorophyll-quinone radical pair in membrane-oriented Spinach Photosystem I and II complexes. Appl Magn Reson 16:565–580
74. Dzuba SA, Hara H, Kawamori A, Iwaki M, Itoh S, Tsvetkov Yu D (1997) Electron spin echo of spin-polarised radical pairs in Intact and quinone-reconstituted plant Photosystem I reaction centres. Chem Phys Lett 264:238–244
75. Bittl R, Zech SG (1997) Pulsed EPR study of spin-coupled radical pairs in photosynthetic reaction centers. J Phys Chem B101:1429–1436
76. Bittl R, Zech S G, Fromme P, Witt H T, Lubitz W (1997) Pulsed EPR structure analysis of Photosystem I single crystals: localization of the phylloquinone acceptor. Biochemistry 36:12001–12004

77. Zech SG, Kurreck J, Eckart H-J, Renger G, Lubitz W, Bittl R (1997) Pulsed EPR measurement of the distance between $P_{680}^{+\bullet}$ and $Q_A^{-\bullet}$ in Photosystem II. FEBS Lett 414:454–456
78. Hara H, Dzuba S A, Kawamori A, Akabori K, Tomo T, Satoh K, Iwaki M, Itoh S (1997) The distance between P680 and Q_A in Photosystem II determined by ESEEM spectroscopy. Biochim Biophys Acta 1322:77–85
79. Tonaka M, Kawamori A, Hara H, Astashkin A V (2000) Three-dimensional structure of electron transfer components in Photosystem II: '2 + 1' ESE of chlorophyll Z and tyrosine D. Appl Magn Reson 19:141–150
80. Sanakis Y, Petrouleas V, Diner B (1994) Cyanide binding at the non-heme Fe^{2+} of the iron-quinone complex of Photosystem II: at high concentration, cyanide converts the Fe^{2+} from High (S = 2) to Low (S = 0) Spin. Biochemistry 33:9922–9928
81. Deligiannakis Y, Boussac A, Rutherford AW (1995) ESEEM study of the plastoquinone anion radical ($Q_A^{\bullet-}$) in ^{14} N- and ^{15} N-labeled Photosystem II treated with $CN^{\bullet-}$. Biochemistry 34:16030–16038
82. Astashkin AV, Hara H, Kuroiwa S, Kawamori A, Akabori K (1998) A comparative electron spin echo envelope modulation study of the primary electron acceptor quinone in Zn-substituted and cyanide-treated preparations of Photosystem II. J Chem Phys 108:10143–10151
83. Astashkin AV, Kawamori A, Kodera Y, Kuroiwa S, Akabori K (1995) An electron spin echo envelope modulation study of the primary acceptor quinone in Zn-substituted plant Photosystem II. J Chem Phys 102:5583–5588
84. Kuroiwa S, Tonaka M, Kawamori A, Akabori K (2000) The position of cytochrome b_{559} relative to Q_A in Photosystem I studied by Electron-Electron Double Resonance (ELDOR). Biochim Biophys Acta 1460:330–337
85. Debus RJ (1992) The manganese a d calcium ions of photosynthetic oxygen evolution. Biochim Biophys Acta 1102:269–352
86. Zheng M, Dismukes GC (1996) Orbital configuration of the valence electrons, ligand fields symmetry, and manganese oxidation states of photosynthetic water oxidizing complex: Analysis of the S_2 state multiline EPR signals. Inorg Chem 35:3307–3319
87. Hasegawa K, Kusunoki M, Inoue Y, Ono T-A (1998) simulation of S2-Sate multiline EPR signal in oriented Photosystem II membranes: structural implications for the manganese cluster in an oxygen-evolving complex. Biochemistry 37:9457–9465
88. Pecorao VL, Hsieh W-U (2000) In: Sigel A, Sigel H (eds) Manganese and its role in biological processes: metal ions in biological systems, vol 37. Mrcell Decker, New York, p 429
89. Matsukawa T, Kawamori A, Mino H (1999) Electron paramagnetic resonance study of the magnetic structure of the S_1-state in oriented oxygen evolving Photosystem II membranes. Spectrochim Acta A55:895–901
90. Matsuoka H, Furukawa K, Kato T, Mino H, Shen, J-R Kawamori A (2006) g-Anisotropy of the S_2-state manganese cluster in single crystals of cyanobacterial Photosystem II studied by W-band Electron Paramagnetic Resonance Spectroscopy. J Phys Chem B110:13242–13247
91. Hara H, Kawamori A, Astashkin A V, Ono T-A (1996) The distances from tyrosine D to redox-active components on the donor side of Photosystem II determined by Pulsed Electron-Electron Double Resonance. Biochim Biophys Acta 1276:140–146
92. Arao S, Yamada S, Kawamori A, Shen J-R, Ionnidis N, Petrouleas V (2002) EPR studies of manganese spin centers in the even number oxidation states of water oxidizing complex of Photosystem II. In: Kawamori A, Yamauchi J, Ohta H (eds) EPR in the 21st Century: basics and applications to material, life and earth sciences. Elsevier, Amsterdam, pp 466–470
93. Elsasser C, Brecht M, Bittl R (2002) Pulsed electron-electron double resonance on multinuclear metal center: assignment of spin projection factors based on the dipole interaction. J Am Chem Soc 124:12606–12611
94. Peloquin JM, Cambell KA, Randall DW, Evanchic MA, Pecoraro VL, Armstrong WH, Britt RD (2000) ^{55}Mn ENDOR of the S_2-state Multiline EPR Signal of Photosystem II: implications on the structure of tetranuclear Mn Cluster. J Am Chem Soc 122:10926–10942

95. Kulik LV, Epel B, Lubitz W, Messinger J (2007) Electronic structure of the Mn_4O_xCa cluster in the S_0 and S_2 states of the oxygen-evolving complex of Photosystem II based on Pulse ^{55}Mn-ENDORand EPR spectroscopy. J Am Chem Soc 129:13421–13435
96. Kawamori A, Katsuta N, Hara H (2003) Structural analysis of three spin systems of Photosystem II by PERDOR. Appl Magn Reson 23:557–569
97. Shigemori K, Hara H, Kawamori A, Akabori K (1998) Determination of distances from tyrosine D to Q_A and chlorophyll Z in Photosystem II studied by '2 + 1' pulsed EPR. Biochim Biophys Acta 1363:187–198
98. Zech SG, Kurreck J, Eckert H-J, Renger G, Lubitz W, Bittl R (1999) Determination of the distance between $Y_Z^{ox\bullet}$ and $Q_A^{\bullet}$ in Photosystem II by pulsed EPR spectroscopy on light-induced radical pairs. FEBS Lett 442:79–82
99. Un S, Brunel L-C, Brill TM, Zimmerman J-L, Rutherford AW (1994) Angular orientation of the stable tyrosyl radical within Photosystem II by high field 245-GHz electron paramagnetic resonance. Proc Natl Acad Sci USA 91:5262–5266
100. Umena Y, Kawakami K, Shen J-R, Kamiya N (2011) Crystal structure of oxygen-evolving photosystem II at a resolution of 1.9 A. Nature 473:55–61

Chapter 7
Applications of EPR in the Environmental Sciences

Christopher J. Rhodes

Abstract Free radicals may be used as molecular probes of porous media and reactive surfaces, either as relatively stable species (nitroxides) studied by conventional EPR, or transient radicals formed by the addition of muonium (a radioactive hydrogen atom with a positive muon as its nucleus) to unsaturated sorbed precursor molecules and studied by the collective methods of MuSR (μSR). Porous solid materials, representative of those found in the environment, specifically: clays, porous carbon, silica-gel, zeolites, ice, and asbestos materials have been thus studied and motional correlation times and activation energies for reorientation of molecular radicals on their surfaces determined. The results are interpreted in terms of sorption within the pores and the interaction with specific surface sites in these materials. Direct measurements by EPR of radicals sampled directly from the atmosphere are mentioned, and the role of radical species in the toxicity of silica, coal and asbestos particles is discussed.

7.1 Introduction

Heterogeneous processes play a significant role in environmental chemistry [1] and in toxicology [1]. Free radicals, moreover, are central in Nature, particularly in living organisms, and consequently, current activity in researching into these species is enormous [1]. Mainly, this is because it is widely held, and in large measure through the agency of EPR measurements, that radicals provide both the cause and mediation of many diseases, and indeed of the ageing process itself. The generally reactive character of radicals and unpaired-electron species *per se* (including metal ions, which can participate in redox processes) further underpins

C.J. Rhodes (✉)
Fresh-lands Environmental Actions, 88 Star Road, Caversham, Berkshire RG4 5BE, UK
e-mail: cjrhodes@fresh-lands.com

A. Lund and M. Shiotani (eds.), *EPR of Free Radicals in Solids II*, Progress in Theoretical Chemistry and Physics 25, DOI 10.1007/978-94-007-4887-3_7,

much of chemistry, and it is largely on the findings from simpler chemical systems that much of current biochemical thinking is based. The underlying free radical chemistry impacts further on a variety of environmental subjects – especially in the role of pollutants in atmospheric phenomena [2], such as ozone-loss, global warming and acid-rain production. Furthermore, since the atmosphere is in direct contact and exchange with the surface of the Earth – with the soil, the plants which grow within and upon it (biosphere), the rocks and mountains (lithosphere), and the rivers, seas and oceans (hydrosphere) – the chemistry of the atmosphere takes on a wider role [1]. Remarkably, EPR can provide insight into many of these phenomena too, both through its use in the investigation of model systems, and more directly as an analytical technique.

Until quite recently, the majority of processes occurring in the atmosphere were viewed as purely reactions between gas-molecules [2], but it is now thought that many of them may in fact occur on the surfaces of suspended particles. The energy required for the activation of molecules in the atmosphere is provided by ultra-violet light. The essential chemistry in the troposphere is oxidation, a scene in which hydroxyl radicals are principal players, since they can intercept the molecules of volatile organic compounds (VOCs), converting them to free radicals [2]. The oxidation of organic compounds in the atmosphere leads both to an increased burden of greenhouse gas (CO_2) and to the formation of carbonaceous aerosol, thus contributing a solid surface on which further oxidation can occur. We have suggested previously [3] that the surfaces of solid particles might provide the "third-body", often invoked in atmospheric chemistry [2] as a sink for the excess energy released when chemical bonds are formed, enabling molecular transformations to occur. There are few methods available to study reactive radicals adsorbed on surfaces; Electron Paramagnetic Resonance (EPR) mostly lacks the sensitivity that is required for reactive radicals under reactive conditions - *especially* on surfaces - and so we have imported from the suite of techniques known as "MuSR or μSR" [4, 5], in which radicals are labelled with *muonium* - a radioactive hydrogen atom with a positive muon as its nucleus. These methods are tremendously sensitive, in part because they use *single-particle counting*; specifically, we have employed transverse-field muon spin rotation (TF-MuSR) and longitudinal-field muon spin-relaxation (LF-MuSRx) in these investigations, which are described below. Our particular motivation is to determine the reorientational diffusion of radicals derived from VOCs, sorbed on silica, clay, zeolite, carbon and ice surfaces, representative of those present in the atmosphere [2].

7.2 Methods

The positive muon (μ^+), the radioactive nucleus of muonium, is relatively short-lived, having a *mean lifetime* of 2.2×10^{-6} s. This corresponds to a *half life* of 1.52×10^{-6} s, and a *radioactive decay constant* of 0.455×10^{6} s^{-1}, thus setting a "microsecond" timescale over which kinetic processes may be studied using muons.

The decay of the muon produces a positron e^+ (Eq. 7.1) plus two neutrinos; it is, of course, the positrons which are counted.

$$\mu^+ \rightarrow \ e^+ + \upsilon_e + \upsilon_\mu \tag{7.1}$$

$$\pi^+ \rightarrow \mu^+ + \upsilon_\mu \tag{7.2}$$

$$\mu^+ + e^- \rightarrow Mu \cdot \tag{7.3}$$

Although they occur naturally as a consequence of cosmic radiation striking the nuclei of light atoms (*e.g.* O_2, N_2) in the atmosphere, muons are needed in high fluxes for research purposes. Thus they are produced using a particle accelerator, by which means a beam of energised protons is caused to impinge on a beryllium or a carbon target. Among the products of the ensuing nuclear reactions are pions (binding components of nuclei), which decay on a nanosecond timescale to form muons (Eq. 7.2).

Muonium atoms (μ^+e^-; Mu) may be formed *in situ* in a range of liquid, solid and gas phase samples, according to (Eq. 7.3), where e^- is a radiolytic electron. Muonium is equivalent to a normal protium atom (p^+e^-) and indeed shows the chemical properties of a *light* hydrogen atom (Mu has a mass 1/9 that of a protium atom); so if the sample contains unsaturated organic molecules, Mu can undergo an addition reaction. The method is highly specific for the study of free radicals, of which many types may be so formed. Some examples are indicated in [Eqs. (7.4, 7.5, 7.6)]:

$$R_2C = CR_2 + Mu \cdot \ \rightarrow \ R_2C \cdot (Mu)\, CR_2 \tag{7.4}$$

$$R_2C = CR - CR = CR_2 + Mu \cdot \rightarrow R_2C(Mu) - CR \cdot - CR = CR_2 \tag{7.5}$$

$$R2C = O + Mu \cdot \ \rightarrow \ R2C \cdot - OMu \tag{7.6}$$

7.2.1 *Transverse-Field Muon Spin Rotation Spectroscopy (TF-MuSR; TF-μSR) [4, 5]*

Though the process outlined above may be viewed in analogy with other isotopic labelling techniques, information equivalent to that obtainable from magnetic resonance experiments [6] is also available, because spectroscopic (hyperfine) magnetic interactions (couplings) are revealed by their influence on the positron count rate in designated detectors. Using high magnetic fields, applied transverse (at 90°) to the muon beam direction, the Transverse-Field Muon Spin Rotation (TF-MuSR) technique characterises each radical by a single pair of lines, which represent the $-1/2$, $+1/2$ m_s electron spin combination with the muon (m_μ) spin states. These

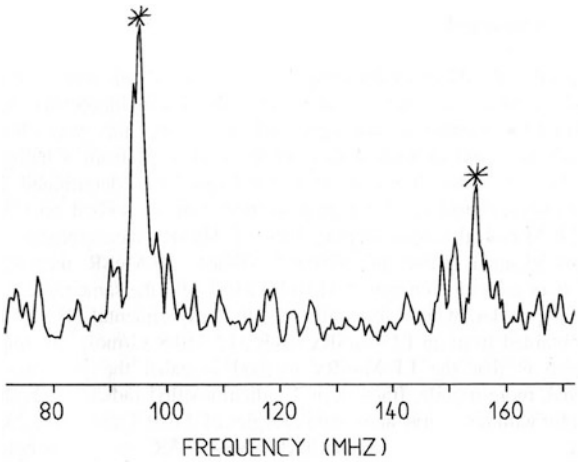

Fig. 7.1 TF-MuSR spectrum recorded at 255 K from $MuCH_2CCl_2^{\cdot}$ radicals sorbed in kaolin (see text) (From Ref. [73])

occur at the precession frequencies from muons which experience the sum of the applied and (−1/2, +1/2 m_s) hyperfine magnetic fields. A classical picture is of the muon spin *rotating* around the axis of the applied magnetic field; rather as the spin of a similar magnetic nucleus, following a 90° *pulse* of radiofrequency radiation in an "FT-NMR" experiment [7]. The muon-electron hyperfine coupling constant is obtained from the difference between the high (υ_2) and low (υ_1) frequencies for each radical: $A_\mu = \upsilon_2 - \upsilon_1$. As the coupling increases, for a given magnetic field, the frequency υ_2 increases, while concomitantly that ν_1 first decreases, reaches zero and then increases once more, due to a sign change in the transition; the coupling is now obtained from the sum of the frequencies: $A_\mu = \upsilon_1 - (-\upsilon_2)$. A representative example [3] of an *actual* such *TF-MuSR* spectrum is that of *1,1-dichloroethyl* radicals ($MuCH_2CCl_2^{\cdot}$), derived from 1,1-dichloroethene sorbed in kaolin (Fig. 7.1). Given that *single-particle counting* methods are employed, and the muon spins are nearly 100% polarised (as compared with the Boltzmann factor, on which EPR and NMR depend), techniques involving muons are extremely sensitive (one *single* molecular radical is detected at a time by TF-MuSR).

7.2.2 Longitudinal-Field Muon Spin Relaxation (LF-MuSRx)

This is a relatively new technique, but shows promise in the study of the re-orientational rates of radicals sorbed in porous materials, which so far include: zeolites [8–10], activated carbon [11–13], clays [3, 14], silica gel [3, 15] and a highly dispersed ice-surface [15]. Though it does not (certainly in its present simple form) approach the level of detail regarding determining molecular reorientation that is possible with (Avoided Level Crossing) ALC-MuSR [16, 17], the method does provide a relatively direct estimate of motional correlation times and so of

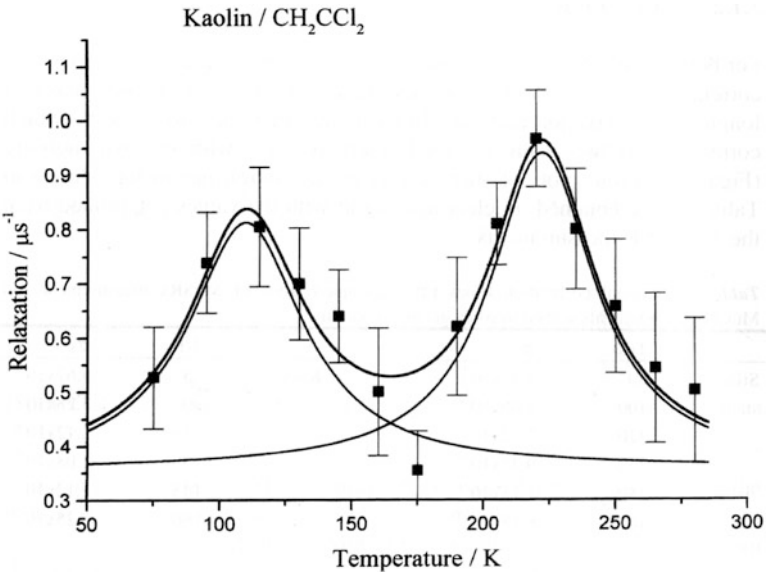

Fig. 7.2 LF-MuSR plot of relaxation rate ($\lambda/\mu s^{-1}$) vs. temperature (K) for $MuCH_2CCl_2^{\cdot}$ radicals sorbed in kaolin (From Ref. [73])

the activation energy associated with a particular kind of motional process. The underlying theory appears fairly well understood [18, 19], and other applications have been found in determining the intramolecular dynamics of radicals formed by muonium addition to Ph_4X (X = C, Si, Ge, Pb) [20, 21], and to metallocenes and benzene-metal π-complexes [20, 21], in which the muon acts as a spin-probe of torsional motion of the phenyl groups or of the overall motion of the cyclopentadienyl or benzene ring about the metal atom. Similar torsional dynamics have been measured in samples of solid dipeptides [22], oleoyl esters [23] and polymers [24]. The restricted overall molecular reorientation of the muonium adduct of the C_{60} fullerene was also measured using LF-MuSRx [25].

The physical basis of the method is one of resonance. In general, when the frequency of a particular molecular motion approaches that of the dominant spectral transition (ω) in the muon-electron coupled system [18, 19, 25], there is an increase in the relaxation rate (λ) of the muon spins, as measured in a longitudinal magnetic field (LF). This reaches a maximum when the frequencies are equal. Different motional regimes may be identified, and in some cases two maxima are measured (*e.g.* Fig. 7.2), which may reflect two distinct sorbed fractions, each with its own motional characterists (τ) may be estimated from the LF-relaxation rates (λ), *via* (Eq. 7.7):

$$\lambda = (2\pi\delta A)^2 \cdot \tau/(1 + \omega^2\tau^2) \tag{7.7}$$

In (Eq. 7.7), δA reflects the modulation in the hyperfine frequency during the motional event, which relaxes the muon spin; ω is often assumed as the frequency of the $<1| \longleftrightarrow |2>$ transition, since it is strongly induced by the mechanism of motional partial averaging of the anisotropic (dipolar) muon hyperfine coupling, as the radical tumbles [18, 19, 25]. Since $\lambda = 1/T_1$, the maximum in the relaxation rate corresponds to a "T_1 minimum" familiar [6, 7] in NMR and ESR spectroscopy. Simple estimates of activation parameters, *viz* inverse-frequency factors (τ_∞) and activation energies (E_a), for internal motion in molecules and for their overall motion in sorbed states, may be made by measuring the muon spin relaxation rate (λ) as a function of temperature. The activation terms (τ_∞) and (E_a) are obtained by fitting the τ values, determined over a particular temperature range, to (Eq. 7.8).

$$\tau = \tau_\infty \exp\left(E_a/RT\right) \tag{7.8}$$

7.2.2.1 Additional Relaxation Effects

A number of influences might cause relaxation of the muon spin. At the outset, we note that there will be contributions from transitions other than that between the $<1| \longleftrightarrow |2>$ levels; but since this particular transition is strongly induced through the dipolar modulation mechanism which is a feature of molecular reorientation, it is convenient to assume that its frequency is ω, especially for reorientation on a surface. The choice of frequency will affect the values obtained for the motional correlation times (τ), and hence the inverse-frequency factor, (τ_∞) defined in (Eq. 7.8), but not the activation energy (E_a). Therefore, a plot of $-\ln\tau$ *vs.* 1/T should provide a meaningful activation energy when a single motional mode is dominant.

Other than the effect of molecular reorientation, the degrees of freedom available to a rigid molecule like cyclohexadienyl are unlikely to affect significantly the muon spin relaxation rate (λ). This is not necessarily true in more flexible structures, which are fairly common in radicals derived by muonium addition to the molecules of VOCs: *e.g.* ring-inversion, out-of-plane vibrations of a bound muon, and rotation (or torsion) of $MuCH_2$-groups all modulate the coupling of the muon and may cause its relaxation. Paramagnetic centres in the host material are also potential contributors to (λ).

In the series of cation-exchanged zeolite X samples containing benzene, we used the inverse-frequency factors (τ_∞) to calculate activation entropies ($\Delta S^{\neq}$), from transition-state theory; we believe that a self-consistent set of data is thus provided for the rigid cyclohexadienyl radical in this medium, reflective of the varying nature of the cation. For the reasons mentioned above, we have less confidence in this procedure for some of the less-rigid radicals, when we have confined our discussion mainly to the activation energies.

7.3 Zeolites and Clay Surfaces

Until only recently atmospheric processes were viewed as being purely gas-phase reactions [2], but it is now thought that atmospheric aerosols, clouds and dust particles can provide surfaces on which reactions can occur with great efficiency [26]. Indeed, the presence of a background atmospheric dust load, evenly spread through the atmosphere, has been established [27]. The quantity of atmospheric dust blown skywards by the desert winds is thought to amount to perhaps *5–10 billion tonnes* annually [28]. Clay particles, particularly, are a major component of airborne dust, and both clay-minerals and zeolites feature centrally in pollution control and remediation strategies [32]; additionally, the catalytic properties of zeolites [29, 30] and clays [31] are well established. We believe that such properties of sorption and catalysis by zeolites and clays are likely to influence the environmental impact of VOCs [33]. Indeed, a number of catalytic applications have been found for montmorillonite [31], which are in many respects similar to those for zeolites, and it seems highly probable that clays as airborne materials might contribute in the outcome of atmospheric pollution chemistry.

A growing body of evidence implicates organic free radicals as intermediates in many reactions catalysed by these materials [29–31, 34]; however, free radicals are mostly highly reactive and have normally only a fleeting existence. EPR is a principal means for the detection and identification of radicals, but since they are present only in low concentrations, and often have fairly complex spectra, surface-sorbed radicals are generally thus undetectable. Some success *has* been found in using ESR to detect radicals on surfaces, but such measurements are limited to low temperatures [30], since under catalytically relevant conditions, the spectral signature of the radicals is rapidly lost through their diffusion and consequent termination reactions; the extreme sensitivity of MuSR has a profound advantage in such studies. The first example of a TF-MuSR study of a free radical (1,1,2-trimethylallyl) sorbed on a surface (fumed silica) was reported about 25 years ago [35]. Later, TF-MuSR was used to provide the first detection *by any method* of a reactive radical (cyclohexadienyl) in a zeolite (NaX) *at ambient temperature* [36], and was shortly extended [37] to other hydrocarbon radicals sorbed both in NaX, and in another zeolite, Na-mordenite.

All these studies show that sorption on a solid surface causes pronounced line-broadening: this is because the dipolar coupling between the muon and the unpaired electron is not fully averaged-out in a radical whose tumbling-rate is slowed by its interaction with a surface [35–37]. The linewidth is proportional to the time the molecule takes to reorient, nominally termed the "rotational correlation time" (τ). It is possible to extract this quantity from the linewidths of a series of TF-MuSR spectra measured as a function of temperature, and to estimate a frequency factor and an activation energy for the motional process, using an expression similar to the (Eq. 7.8). However, LF-MuSRx measurements may be made down to temperatures at which the corresponding TF-MuSR spectral lines become too broad for reliable analysis.

7.3.1 1,1-Dichloroethyl Radicals Sorbed in Clay and in Silica-Gel

To assess the possibility of detecting radiolabelled radicals sorbed on a clay-mineral surface, a study was made of 1,1-dichloroethyl radicals ($MuCH_2CCl_2^{\cdot}$) sorbed in silica-gel and in kaolin [3]; this was chosen to exemplify the kind of radical that might be derived from a halogenated VOC. An activation energy of 10.6 ± 1.4 kJ/mol was determined for the reorientational diffusion of 1,1-dichloroethyl radicals sorbed on silica gel using TF-MuSR; this was supported by LF-MuSRx measurements, which gave an identical value of 10.9 ± 0.7 kJ/mol. TF-MuSR measurements provided an activation energy of 11.0 ± 1.3 kJ/mol for the same radical sorbed in kaolin powder, which also agrees, within experimental error, with the value obtained from an LF-MuSRx study (12.3 ± 0.8 kJ/mol). An important difference is that the LF-MuSRx method revealed the presence of an additional, more mobile, fraction of 1,1-dichloroethyl radicals in both silica and kaolin with respective activation energies of 2.6 ± 0.4 and 2.4 ± 0.2 kJ/mol: no such second fraction was detected by TF-MuSR. As shown below, an explanation may be provided by considering the particular details of the two methods.

7.3.1.1 TF-MuSR

The major advantage of the TF-MuSR method [4, 5] is that it allows an identification of radicals formed in a given system (so long as they are formed within the timescale set by the muonium hyperfine frequency, *ca* 10^{-9} to 10^{-10} s) on the basis of the muon-hyperfine coupling. In Fig. 7.1 is shown the spectrum recorded at 255 K from a sample of 1,1-dichloroethene sorbed in kaolin, revealing a clear pair of signals from a single radical species; the isotropic muon-electron hyperfine coupling constant is 246 MHz. Since there are two possible sites for addition, leading to either radicals of type $MuCH_2CCl_2^{\cdot}$ or $MuCCl_2CH_2^{\cdot}$, we then appeal to ESR data for the corresponding proton-equivalent radicals $HCH_2CCl_2^{\cdot}$ and $HCCl_2CH_2^{\cdot}$, in order to make comparisons. The latter radical is apparently unknown, but a coupling of 19.7 G was reported for the $CH_3CCl_2^{\cdot}$ radical [38]: by scaling this value with the muon/proton magnetic moment ratio (3.1833) and converting to MHz, a coupling of 176 MHz is obtained; however, β-muon couplings are always larger than those of the protons in the corresponding radicals, generally by a factor of *ca.* 1.4 [39], and so the $MuCH_2CCl_2^{\cdot}$ radical is strongly implicated.

As in a previous TF-MuSR study of radicals sorbed in zeolites [37], the motional correlation times (τ) were determined from the temperature dependent linewidths (λ) in the $MuCH_2CCl_2^{\cdot}$ radical; the results are shown in Table 7.1.

Arrhenius type plots of $-\ln\tau$ vs. 1/T were made, according to (Eq. 7.8), so arriving at the values shown in the Table 7.3 which permit comparison between the activation parameters obtained from the TF-MuSR and LF-MuSRx measurements.

Table 7.1 Muon coupling constants (A) and motional correlation times (τ) for $MuCH_2CCl_2^{\cdot}$ radicals sorbed in silica and in kaolin, as determined from TF-MuSR measurements [3]

	T/K	A/MHz	τ/s
Silica Gel.	255	243.9	5.64×10^{-9}
	265	242.4	5.21×10^{-9}
	275	240.8	4.46×10^{-9}
	285	239.3	3.33×10^{-9}
	295	237.9	2.98×10^{-9}
Kaolin	255	244.0	5.57×10^{-9}
	265	242.6	5.14×10^{-9}
	275	241.0	4.38×10^{-9}
	285	240.4	3.38×10^{-9}
	295	238.3	2.85×10^{-9}

Table 7.2 Motional correlation times (τ) determined from LF-MuSRx measurements on $MuCH_2CCl_2^{\cdot}$ radicals sorbed in silica gel and in kaolin [3]

	T/K	τ/s		T/K	τ/s
Silica	80	4.97×10^{-9}	**Kaolin**	75	5.67×10^{-9}
	100	3.66×10^{-9}		90	3.28×10^{-9}
	120	2.12×10^{-9}		115	2.12×10^{-9}
	135	9.35×10^{-10}		130	1.08×10^{-9}
	150	1.15×10^{-9}		145	1.12×10^{-9}
	165	6.18×10^{-10}		160	8.25×10^{-10}
	180	1.36×10^{-8}		190	6.06×10^{-9}
	195	8.90×10^{-9}		205	3.96×10^{-9}
	210	5.67×10^{-9}		220	2.12×10^{-9}
	225	3.82×10^{-9}		235	1.60×10^{-9}
	240	2.67×10^{-9}		250	8.27×10^{-10}
	255	2.12×10^{-9}		265	6.39×10^{-10}
	270	1.60×10^{-9}		280	5.97×10^{-10}

Table 7.3 Motional activation parameters measured for $MuCH_2CCl_2^{\cdot}$ radicals sorbed in silica gel and in kaolin, using LF-MuSRx and TF-MuSR methods [3]

	E_a/(kJ/mol)	τ_∞/s
Silica gel	10.9 ± 0.7(LF)	$(1.10.3) \times 10^{-11}$
	10.6 ± 1.4(TF)	$(4.0 \pm 1.8) \times 10^{-11}$
	2.6 ± 0.4(LF)	$(1.2 \pm 0.4) \times 10^{-10}$
Kaolin	12.3 ± 0.8(LF)	$(1.6 \pm 0.5) \times 10^{-12}$
	11.0 ± 1.3(TF)	$(3.3 \pm 1.4) \times 10^{-11}$
	2.4 ± 0.2(LF)	$(1.5 \pm 0.3) \times 10^{-10}$

7.3.1.2 *LF-MuSRx*

For both samples of 1,1-dichloroethene (in silica gel and in kaolin) motional correlation times (τ) were also determined (Table 7.2) from the measured longitudinal relaxation rates (λ). In each case, there are two maxima which correspond to two distinct sorbed fractions, each with its own mobility (Fig. 7.2). From plots of $-\ln\tau$ vs. 1/T, the activation parameters shown in Table 7.3 were obtained, in clear agreement with the values determined from the TF-MuSR measurements.

7.3.1.3 Comparison Between TF-MuSR and LF-MuSRx Measurements

The correlation times listed in Tables 7.1 and 7.2 are in reassuring agreement as determined by the two methods, and are very similar for both the silica and the kaolin samples. As already commented on, the major difference is that a fraction with a completely separate mobility is detected by the LF-MuSRx method (Fig. 7.2), but is not evident in the TF-MuSR spectra (Fig. 7.1). This fraction was measured in the LF spectra in the temperature range 75–165 K, which is much lower than that used for the TF measurements (255–295 K); however, extrapolation of the correlation times to this higher temperature range indicates a mobility some 4–5× greater than that of the fraction which is actually being measured. Since this would correspond to a relatively sharp signal superimposed on a broader one, it should be quite evident, particularly at the lowest temperature used for the TF measurements (255 K), where the differential line-broadening between the two fractions would be greatest; however there is nothing.

The relaxation times T_1 and T_2 correspond strictly to the two experimental arrangements [4, 5], since the muon beam is 100% spin polarised (i.e. all the spins are aligned along the beam direction) with respect to the applied magnetic field, and so LF-MuSR and TF-MuSR measure separately these *longitudinal* and *transverse* components. The LF relaxation rate corresponds to muon spin-flips directly, along the beam direction, and measures the spin-lattice interaction, hence the appearance of Fig. 7.2, which corresponds to "T_1 minima" in conventional magnetic resonance [6, 7], sensing the motional frequency – the minimum occurring when motional and transition frequencies are matched; the TF measurement is also sensitive to relaxation caused by motional processes, but also to additional processes such as chemical reactions [4, 5]. In fact, the good agreement between the correlation times and activation parameters obtained from both types of measurement *indicates that factors extraneous to those of molecular reorientation are of little importance*; therefore, the lack of observation of the more mobile fraction by TF-MuSR cannot be explained in terms of differential T_1/T_2 relaxation effects.

We conclude that the explanation is actually kinetic, and refers to the rate of formation of radicals from 1,1-dichloroethene sorbed in different concentrations, in separate regions of each sorbant. In order to observe the TF-MuSR spectrum of a radical, it must be formed on a timescale set by the muonium hyperfine frequency (4.5 GHz), i.e. 10^{-9} to 10^{-10} s [4, 5], which is close to the diffusion controlled limit for reactions of atomic muonium [40]. Therefore, for dilute fractions, the muonium may not be able to add fast enough for the resulting radical to be observed. In LF experiments, there is no such restriction other than that the radical must be formed within the lifetime of the muon itself, (2.2×10^{-6} s), and so radicals can, in principle, be detected even in concentrations 100–1,000× lower than is possible in a TF experiment. Thus, the major fraction detected in LF-MuSRx corresponds to the (only) fraction detected by TF-MuSR, the more mobile fraction in the LF spectra being from a minor, more weakly sorbed, component of 1,1-dichloroethene. *Direct evidence that this is the case is provided by our observation that it could be*

readily pumped from the cell – leaving the major, less mobile component – in accord with the low activation energy for its molecular reorientation (and diffusion), which indicates weak adsorption.

One possibility is that the minor fraction is located in a "fluid" type state; however, this should require a loading of the organic sorbate in excess of that equivalent to monolayer coverage. Using standard atomic radii [41], we deduce that the surface area of one 1,1-dichloroethene molecule is 36 A^2, and so 14 mmol would cover an area of 3.04×10^{23} A^2, which is far greater than the surface area of the kaolin but is only 83% that of the silica sorbant. Therefore, on the basis of the BET surface areas determined by dinitrogen adsorption, the existence of a putative fluid fraction is entirely reasonable in kaolin, but not in silica; nonetheless, the similarities in activation parameters measured in both sorptive media would suggest its common nature, and we stress that the adsorption behaviour of dinitrogen may differ from that of 1,1-dichloroethene.

We believe that the actual surface adsorption is weak because there are fewer OH groups present in the external surface regions. Therefore, the radicals can easily break-free from the surface via a "sticking" collision with one or more 1,1-dichloroethene molecules. When a stronger surface (-HO) bond has to be broken simultaneously, the overall loss of entropy is correspondingly less since the initial, adsorbed, state of the radical is more restricted (ordered); this also accords with the large $\Delta G^{\neq}$ values, which are dominated by the enthalpies. Given the similarities between all parameters for each fraction in both silica gel and kaolin, we conclude that the sorptive properties of these materials are actually very similar.

It has been proposed [42, 43] that, in the absence of viscous friction, the inverse-frequency factor for the reorientation time should approach that of a classical free rotator: $\tau_{FR} = 2\pi(I/81kT)^{1/2}$. Assuming standard bond lengths and atomic masses for the $MuCH_2CCl_2^{\cdot}$ radical, $I = 3.93 \times 10^{-45}$ kg m^2, which gives 7.45×10^{-13} s at 250 K and 1.08×10^{-12} s at 120 K. These values are in agreement by a factor of 3 or 8 for the more strongly bound fraction in kaolin or silica, respectively, but are in excess of 70× faster for the weakly sorbed component, indicating that it is behaving as a viscous liquid. This may by taken with the large, negative activation entropies to indicate greater molecular association in the reorientation step.

7.3.2 Zeolites

7.3.2.1 LF-MuSRx Measurements of Cyclohexadienyl Radicals Sorbed in Cation-Exchanged Zeolite X

A study [8, 9] was reported of benzene sorbed in cation-exchanged (Li^+, Na^+, K^+, Mg^{2+}, Ca^{2+}, Sr^{2+}, Ba^{2+}) zeolite X and (Na^+) zeolite A, as is now discussed in some detail. Zeolite X has the essential structure of naturally occurring faujasite, which is a three-dimensional internal channel system with supercages: the supercages are some 13A in diameter, with access windows of 7.4A in cross-section,

Table 7.4 Activation parameters and effective Muon hyperfine anisotropies for reorientation of benzene in cation exchanged zeolite X and in other hosts [9]

Medium	E_a/(kJ/mol)	τ_∞/s	δA/MHz
LiX(18 wt% C_6H_6)	9.1 ± 1.1	(1.4 ± 0.4) × 10^{-12}	5.7
NaX(18 wt% C_6H_6)	6.9 ± 0.7	(5.3 ± 1.4) × 10^{-12}	4.7
KX(18 wt% C_6H_6)	4.0 ± 0.5	(6.1 ± 2.1) × 10^{-11}	5.9
KX(40 wt% C_6H_6)	12.9 ± 1.5	(1.0 ± 0.3) × 10^{-12}	5.4
4A(18 wt% C_6H_6)	12.7 ± 1.3	(2.7 ± 1.1) × 10^{-13}	5.0
MgX(18 wt% C_6H_6)	7.7 ± 0.8	(1.6 ± 0.6) × 10^{-12}	5.5
CaX(18 wt% C_6H_6)	6.9 ± 0.6	(3.7 ± 0.7) × 10^{-12}	4.8
	12.4 ± 1.3	(3.5 ± 1.5) × 10^{-13}	4.2
SrX(18 wt% C_6H_6)	6.4 ± 0.7	(8.1 ± 3.7) × 10^{-12}	5.9
	12.8 ± 1.4	(3.6 ± 1.1) × 10^{-13}	4.6
BaX(18 wt% C_6H_6)	12.0 ± 1.1	(5.4 ± 2.7) × 10^{-13}	5.1
	12.3 ± 1.4	(1.1 ± 0.5) × 10^{-12}	4.4
Carbon Pores d >20A	5.9 ± 0.5	(6.2 ± 2.2) × 10^{-12}	5.9
Bulk Benzene	6.6 ± 0.5	(2.4 ± 0.7) × 10^{-11}	4.7

and there are 8 cages per unit cell [44]. The access windows readily admit molecules as small as benzene (kinematic diameter 5.5A) into the zeolite micropores. In contrast, the pore system of zeolite A consists of a cubic array of relatively large (*ca.* 11.2A free diameter) cages, interconnected through 8-membered oxygen windows of only 4.3A diameter [44], and so this structure admits only molecules with very small cross-sections, and definitely excludes benzene. Changing the nature of the counter-cation changes the diffusivity of molecules in zeolite A by relatively blocking or unblocking the already restrictive window sites; this is less important in zeolite X (and in faujasites generally) [44, 45], but changes in the mobility of adsorbates and in their enthalpies of adsorption have been found, for instance in Na^+, K^+, Cs^+ exchanged zeolite X [48]. The aim of the study [8, 9] was to determine the influence of the exchange cation on the reorientational mobility of cyclohexadienyl radicals in zeolite X.

While the analysis of the relaxation data is fairly straightforward for LiX, NaX, KX, MgX and 4A, at 18 wt% benzene loading, since there is in each case a single maximum, the situation for the other zeolites is more complex. At a 40 wt% loading in KX, the data clearly describe two well displaced maxima, and this also pertains in CaX, even at 18 wt% of benzene; for SrX and BaX the data are more ambiguous, since it is possible to fit each case either as a single or as two components. The abrupt and clear difference in behaviour of CaX from the group 1 series does, however, point to a potentially differing influence of the dipositive ions on the sorption of benzene into the micropores of zeolite X, and this is supported by the fitting-curves obtained, which each indicate the presence of two benzene components. On this basis, two sets of activation parameters are determined, as shown in Table 7.4. The data show that each member of the group 2 series, other then MgX, contains an additional, more restricted fraction, with similar activation parameters to those

Table 7.5 For benzene sorbed in cation exchanged zeolite X, free energies (kJ/mol), enthalpies (kJ/mol), entropies (J/mol/K) of activation and entropy of activation terms at mid-temperature range (kJ/mol) for each series [9]

	$\Delta G^{\neq}$	$\Delta H^{\neq}$	$\Delta S^{\neq}$	$T\Delta S^{\neq}$
LiX(18 wt% C_6H_6)	10.7(1.5)	7.9(1.1)	−20.1(3.0)	−2.8(0.4)
NaX(18 wt% C_6H_6)	10.5(1.1)	5.7(0.7)	−31.7(2.6)	−4.8(0.4)
KX(18 wt% C_6H_6)	10.3(0.9)	2.8(0.5)	−51.7(3.0)	−7.5(0.4)
KX(40 wt% C_6H_6)	15.5(2.0)	11.2(1.5)	−20.6(2.4)	−4.3(0.5)
MgX(18 wt% C_6H_6)	9.4(1.3)	6.6(0.8)	−20.8(3.9)	−2.8(0.5)
CaX(18 wt% C_6H_6)	9.7(1.0)	5.7(0.6)	−28.2(3.2)	−4.0(0.4)
	13.2(1.7)	5.7(0.6)	−10.6(2.1)	−2.3(0.4)
SrX(18 wt% C_6H_6)	10.3(1.2)	5.2(0.7)	−35.0(3.1)	−5.1(0.5)
	12.9(1.8)	10.9(1.4)	−11.0(2.3)	−2.0(0.4)
BaX(18 wt% C_6H_6)	13.1(1.8)	10.5(0.9)	−14.0(3.8)	−2.5(0.7)
	15.0(2.0)	11.2(2.0)	−21.2(3.1)	−4.4(0.6)
4A(18 wt% C_6H_6)	12.6(2.1)	11.2(1.3)	−8.2(4.3)	−1.4(0.8)
Carbon pores d >20A	8.9(0.9)	4.8(0.5)	−31.8(3.0)	−4.1(0.4)
Bulk benzene	14.3(1.1)	5.0(0.5)	−46.6(3.0)	−9.3(0.6)

found in the heavily loaded KX and in the intrinsically pore-restricted 4A zeolites. The TF-MuSR method was used previously to study the effect of substrate (benzene) loading on the mobility of cyclohexadienyl radicals therefrom formed in NaX [47]: the results show that only for loadings above 50 wt% is a clear "fluid-like" phase observed; even at 50% loading, the lines remained broad, indicating considerable restriction in molecular reorientation. According to nitrogen adsorption data [29], the zeolite is at twice its fully saturated level; however, the nitrogen BET measures bulk diffusion phenomena. At the molecular level, which is probed by MuSR, reorientational motion is apparently impeded even under such conditions of bulk saturation.

We note that the values of δA are in the range 4.2–5.9 MHz, which is consistent with the major reorientational motion occurring about the ring plane axis, since the nature of the hyperfine anisotropy in the muonated cyclohexadienyl radical requires a variation of 5.6 MHz during a step of this kind, assuming a 90° "jump" [12, 48].

7.3.3 Energetics for Reorientation of Cyclohexadienyl Radicals in Cation-Exchanged Zeolite X

Transition-state theory was used to determine free energies ($\Delta G^{\neq}$), enthalpies ($\Delta H^{\neq}$) and entropies ($\Delta S^{\neq}$) of activation for cyclohexadienyl radicals (and by inference, benzene molecules) sorbed in the range of group 1 and group 2 cation exchanged zeolite X. The results are shown in Table 7.5 along with those determined for benzene in zeolite 4A, in the large pores (d > 20A) of porous carbon and in bulk benzene, and from which some apparent trends emerge. For the group 1 series (LiX, NaX, KX), all at 18 wt% loading of benzene, $\Delta G^{\neq}$ has an almost

common value of *ca.* 10 kJ/mol, but the relative contribution made to it by $\Delta H^{\neq}$ and $T\Delta S^{\neq}$ varies, with the entropy term becoming increasingly dominant as the cation radius increases ($r_{K+} > r_{Na+} > r_{Li+}$). This reflects the decreasing importance of cyclohexadienyl/benzene-cation interactions, since the $\Delta H^{\neq}$ value falls from 7.9 kJ/mol in LiX to only 2.8 kJ/mol in KX, and is in order with previous measurements of the isosteric enthalpies of adsorption of benzene in Na^+, K^+, Cs^+ exchanged zeolite X [46]. In both NaX and KX, the motional process is dominated by the entropy change, and in fact, the values for $\Delta H^{\neq}$ and $\Delta S^{\neq}$ are quite similar to those determined for bulk benzene and for benzene sorbed in large-pores in activated carbon [12]. Thus, we conclude that the activation process, which causes the molecular motion we are measuring, is dominated by interactions/collisions between almost free benzene molecules, certainly in NaX and in KX. In all cases, $\Delta S^{\neq}$ is negative, and it has been argued that this represents a "sticking" collision between the cyclohexadienyl radical and one or more benzene molecules in the activation step [3, 8, 9], since reorientation of an effectively *isolated* molecule is expected to show a near zero $\Delta S^{\neq}$ [49]; such a collision is expected to lose degrees of freedom from the initial state of the molecule.

In the case of benzene sorbed in LiX, the large $\Delta H^{\neq}$ indicates far stronger associations with cations, and so it is reasonable that the initial state is more "ordered"; therefore, the overall loss of degrees of freedom in making the "sticking" collision with other benzene molecules is accordingly reduced, hence the less negative $\Delta S^{\neq}$ value. In support of this explanation, the parameters $\Delta H^{\neq}$ and $\Delta S^{\neq}$ are in clear interdependence in the series LiX → KX, so reflecting the relative "ordering" in the initial state compared with the activated state.

The $\Delta H^{\neq}$ and $\Delta S^{\neq}$ parameters for the fraction of lower E_a in the series MgX → BaX indicate a similar situation: MgX appears much like LiX, and we would expect strong interactions between cyclohexadienyl radicals/benzene molecules and both Li^+ and Mg^{2+} cations, as we found for cation-$PhCH^{\cdot}$-$OMu^{\cdot}$ radical complexes in these zeolites [50]; an interdependency of $\Delta H^{\neq}$ and $\Delta S^{\neq}$ is apparent for benzene molecules sorbed in CaX and in SrX, implying their relatively weakening association with Ca^{2+} and Sr^{2+} cations, and that achieving the activated motional state in CaX is similar to doing so in bulk benzene. As in the series LiX → KX, it is expected that the cyclohexadienyl radicals/benzene molecules will associate (bind) less strongly with the larger cations, simply because the positive charge *density* is reduced; however BaX contains no equivalent mobile component. This observation does not fit the above model.

Some insight, both to this apparent anomaly and the motional behaviour of benzene molecules in the pores of zeolite X, generally, may be provided by a comparison with the activation parameters for bulk benzene [12]; the exchange cations can be considered mainly to act in perturbing the essential ordering of a small cluster of benzene molecules, located in one supercage. We note that the series of group 2 cation exchanged zeolites contain only half the number of cations that the group 1 series does, and having a greater positive charge, they are expected to associate more strongly with the zeolite framework, so leaving a greater "volume" *centred* in the cage, into which benzene molecules can be accommodated. Although,

the supercages are filled with benzene molecules, the overall cage geometry will limit the possibilities for their mutual orientation, compared with the bulk material.

In CaX and SrX, the $\Delta H^{\neq}$ values are slightly reduced, being similar to that found in bulk benzene [12], but the ΔS parameters are nearly identical. This supports our notion of a motional behaviour which is that of a small number (*ca.* 6–8) of benzene molecules clustered in the zeolite X supercage [44], interacting very weakly with the Ca^{2+} or Sr^{2+} cations, and is equivalent to the molecular reorientation occurring in the bulk material. The relaxations which are measured, we believe to represent an *average* molecular motion, or at least a *distribution* of mobilities, since at any instant, some molecules may be coordinated with cations while others remain free, and presumably characteristic activation parameters apply for each situation.

At high loadings (40 wt%) of benzene in KX, a second fraction is identified, to which is provided a more restricted molecular environment. Since this loading represents more than twice the saturation capacity of the supercages, the excess benzene must be located elsewhere, and it appears reasonable that it is resident on the external surface and in the extragranular voids: this idea is favoured by the near identity of the E_a and τ_∞ parameters, and consequently those of $\Delta H^{\neq}$, $\Delta S^{\neq}$ and $\Delta G^{\neq}$, found with an 18 wt% loading of benzene in 4A zeolite. The small access pores [44, 45] in 4A (4.1 A) definitely exclude benzene molecules, given their kinematic diameter of 5.5 A, which have no alternative than to occupy (external) non-cage sites.

The motional processes pertinent to benzene molecules in these non-cage regions are dominated by their enthalpies of activation; the relatively less negative $\Delta S^{\neq}$ values implying a relatively *ordered* initial state. This seems strange, as one might envisage the benzene molecules either lying flat on the granular surface, or forming clusters in the extragranular voids, and these arrangements surely would behave much as the benzene molecules sorbed on the walls of large carbon pores or in bulk benzene, respectively; yet these latter have significantly reduced motional activation enthalpies, and more negative $\Delta S^{\neq}$ values for their molecular reorientation. We make, therefore, the following suggestion, which is that the benzene molecules become "trapped" in pockets (niches) proximate to the external surface, which normally provide initial access for molecules into the zeolite grain; in KX, saturation of the inner structure (pores) of the grain prevents these "external" molecules making further inroads to the supercages/channel system, while in 4A, the intrinsic internal dimensions of the zeolite provide a physical barrier to them. Such "trapping" of the benzene molecules in the near-surface niches would tend to *order* them relative to the bulk material, so resulting in a less negative entropy change in their reorientation processes.

7.3.4 Cyclohexadienyl and 2,5-Dimethylcyclohexadienyl Radicals in ZSM5, Silicalite and Mordenite

We have also used LF-MuSRx to investigate the sorption and mobility of cyclohexadienyl radicals and 2,5-dimethylcyclohexadienyl radicals (derived from benzene and

from *p*-xylene) in Li-X, in Na-ZSM5, in silicalite and in Na-mordenite zeolites [10]. Unlike the faujasites (zeolites X and Y) which contain cages, ZSM5/silicalite and mordenite both contain only channels [44], though the channel-intersection in ZSM-5/silicalite can be considered to provide a "supercage" with a diameter of *ca.* 9 A. For cyclohexadienyl radicals/benzene adsorbed in Na-ZSM5, silicalite and Na-mordenite, a fraction was detected with a common reorientational activation energy in the region of *ca.* 5 kJ mol^{-1}; however, in all cases there appeared a second fraction with an activation energy of *ca* 12 kJ mol^{-1}. [In Li-X only a single fraction was observed with $E_a = 8.1$ kJ mol^{-1}, from benzene molecules adsorbed in supercages]. Given that high loadings of benzene, beyond the saturation capacities of the zeolites were employed, we believe the two distinct motional distributions represent the channel intersection and channel/external-surface niche locations in ZSM5/silicalite, the latter having the higher activation energy. An extraneous fraction may also be present (possibly as a film coating the zeolite grains), which probably also contributes to the detected *ca* 5 kJ mol^{-1} component in which, as at the channel-intersections, the motion tends toward bulk behaviour. Mordenite has only a single accessible channel structure and is hence devoid of the relatively unrestricting channel intersecting pores that are present in ZSM5/silicalite. However, the channels are wider (*ca* 7 A diameter) and we may ascribe therefore, the *ca* 5 kJ mol^{-1} fraction to the formation of benzene clusters within these channels that exhibit bulk-type behaviour, while we assign, in analogy with the results for ZSM5/silicalite, the *ca* 12 kJ mol^{-1} fraction to molecules adsorbed in niches on the external surface. It is thought that the essential difference between the two activation energies is that the *ca* 5 kJ mol^{-1} processes involve molecular motion within clusters of benzene molecules with properties similar to the bulk phase (6.6 kJ mol^{-1} was measured in pure benzene), while those characterised at *ca* 12 kJ mol^{-1} reflect single benzene molecules or small, ordered molecular clusters interacting with a zeolite surface. The results for 2,5-dimethylcyclohexadienyl radicals (derived from *p*-xylene) are rather similar, but indicate slightly reduced activation energies. This is probably because more limited molecular excursions are permitted for these larger molecules within the various zeolite media than for benzene, where free rotation is allowed. These conclusions are in accord with those drawn from ^{2}H-quadrupole-NMR measurements [51–53]. The larger mesitylene molecules can penetrate zeolite X and (more slowly) mordenite, but are excluded from the internal pores of ZSM5/silicalite. Thus, in the latter case, the derived energy terms must reflect bulk conditions for the material adsorbed on and around the external surfaces of the grains.

7.3.5 PhCH˙-OMu Radicals Sorbed in Zeolite X

It was shown that electron withdrawing substituents act to reduce the isotropic muon coupling in PhCH˙-OMu radicals [50, 54]. The question then arose, of whether association between the aromatic ring and a cation exchanged into the

Table 7.6 Activation energies (E_a) as determined for the muonium adduct radicals formed from benzaldehyde, PhCH·-OMu, sorbed in cation exchanged zeolite X, according to Eq. 7.8, showing two distinct motional regimes [55]

Zeolite	(E_a)/kJ/mol	(E_a)/kJ/mol
LiX	3.4 ± 0.4	11.4 ± 1.7
NaX	4.2 ± 0.5	11.0 ± 0.7
KX	2.1 ± 0.4	8.0 ± 0.7
MgX	–	12.2 ± 1.4
CaX	3.1 ± 0.2	8.3 ± 0.5
SrX	3.1 ± 0.0	6.2 ± 0.9
BaX	3.1 ± 0.3	13.6 ± 1.2
$C_{(s)}$	2.9 ± 0.3	11.5 ± 0.4

zeolite might provide a similar electron withdrawing influence. To explore this possibility, benzaldehyde was sorbed into a series of cation-exchanged zeolite X samples. Changes in the isotropic muon couplings were indeed found, which accord with the formation of such π-complexes: in each series, Li^+, Na^+, K^+ and Mg^{2+}, Ca^{2+}, Sr^{2+}, Ba^{2+}, the strength of this complexation was found to decrease with the increasing radius of the cation, the coupling being smallest for Li^+ and Mg^{2+} cations [50]. While representing an advance in the study of molecular sorption by zeolites, the effect noted is indirect, being one of perturbation on the π-electrons of the radical, and does not determine the influence of the cation on the reorientational motion of the sorbed species. Nonetheless, logic would suggest that such motion might be impeded, and increasingly so, by complexation of increasing strength. This was investigated, and the reorientational activation energies for PhCH·-OMu radicals sorbed in cation-exchanged zeolite X were measured using LF-MuSRx [55].

In all cases, other than MgX, two clear maxima were identified. These correspond to PhCH·-OMu radicals confined in two distinct motional regimes. The nearly common activation energy of *ca* 3 kJ/mol (Table 7.6) measured for the *low-temperature range* among all the samples is striking, and since it is the same as that attributed to benzaldehyde sorbed in the larger pores of porous carbon [11] – i.e. in an effectively *bulk* phase – we believe that some proportion of the benzaldehyde is also sorbed as bulk in zeolite X. This fraction could not be detected positively in MgX. In contrast, the activation energies measured in the *higher temperature range* vary appreciably according to which exchange-cation is present. In both series, $Li^+ \rightarrow K^+$ and $Mg^{2+} \rightarrow Sr^{2+}$, the activation energy (E_a) falls as the cation radius increases, in accord with the reduced polarising-power and hence weaker π-complexation to the cation, as was inferred from the change in the isotropic muon couplings measured in these samples. The relatively large E_a value measured in BaX is anomalous, and can be ascribed to a fraction excluded from the supercages by large Ba^{2+} cations which obstruct their access windows. A similar result for benzene sorbed in BaX has been alluded to, *vide supra*.

7.4 Carbon Particles

In the lower atmosphere the higher concentration of oxygen makes very significant contributions to its chemistry, and so the troposphere is dominated by oxidation reactions, mediated largely by ˙OH radicals. The plant kingdom emits enormous quantities of hydrocarbons into the atmosphere, especially terpenes from forests. Indeed the "Blue Ridge Mountains of Virginia", sung about in the 1937 film "Way Out West" by the famous comic duo, Laurel and Hardy, appear blue behind the haze caused by the tropospheric oxidation of pinenes and other terpenes [2]. There are also anthropogenic sources. The oxidation of these and many other organic compounds (VOCs) increases the atmospheric burden of greenhouse gases (CO_2) but also leads to the formation of carbonaceous aerosol in the atmosphere [1, 2]. Thus they may be self-promoting in providing a solid surface on which further oxidations of VOCs could occur, involving organic radicals as intermediates. We have tried to explore the utility of MuSR methods in studying the reorientational diffusion of radicals derived from VOCs sorbed in porous carbon, as a simple model of a carbon-rich surface [11, 12]. Benzene was chosen since it is forms a relatively rigid cyclohexadienyl radical, and should give reliable activation entropies as well as energies and enthalpies, it is also a significant VOC in the atmosphere, as is toluene, partly from human activities; benzaldehyde is a principal oxidation product of toluene in the troposphere [2].

7.4.1 Benzene Sorbed in Porous Carbon

When benzene is sorbed in porous carbon [12], the resulting LF-MuSRx plot describes two maxima, peaking at *ca* 125 K and *ca* 200 K. Using (Eq. 7.7) motional correlation times (τ) were extracted from the λ values, and were plotted *vs.* 1/T according to (Eq. 7.8), with its typical Arrhenius form. From the linear plots taken over the two temperature ranges, the thermodynamic activation parameters listed in Table 7.7 were obtained. We have suggested [12] that the anomalous $\Delta S^{\neq}$ value of +52.3 J/mol/K reflects benzene molecules sorbed in the smaller ($d < 10$ A) micropores of porous carbon, and which undergo rapid collisions with the pore walls; its positive sign was proposed to represent the acquisition of degrees of freedom as such initially confined molecules escape into more spacious pores. We imagine the effect on a benzene molecule as it squeezes-out through a narrow access window (slit) in the small pore, as being akin to an elastic disk, held in the hand, whose edges are suddenly compressed: the disk is thus propelled rapidly, gaining both translational and reorientational freedom. It literally "pops-out" from the small pores into more spacious regions.

That no such *positive* $\Delta S^{\neq}$ value is found for toluene or benzaldehyde (*vide infra*) strongly implies that these molecules are unable to penetrate the very small carbon pores (i.e. those toward the low-end of the 4–20 A range, which designates the "micropore" region). This accords with our view [12] that the access holes to

Table 7.7 Free energies (kJ/mol), enthalpies (kJ/mol), entropies (J/mol/K) of activation and entropy of activation terms at mid-temperature range (kJ/mol) for each series of benzene, toluene and benzaldehyde sorbed in porous carbon [11]

Substrate	$\Delta G^{\neq}$	$\Delta H^{\neq}$	$\Delta S^{\neq}$	$T\Delta S^{\neq}$
Low-temperature ranges				
Benzene (100–160 K)	8.9 ± 0.9	4.8 ± 0.5	-31.8 ± 3.0	-4.1 ± 0.4
Toluene (85–140 K)	8.5 ± 0.7	1.5 ± 0.4	-55.7 ± 2.5	-7.0 ± 0.3
Benzaldehyde (85–140 K)	11.4 ± 0.6	1.8 ± 0.3	-76.4 ± 2.0	-9.6 ± 0.3
Higher-temperature ranges.				
Benzene (175–235 K)	13.4 ± 2.8	24.1 ± 2.3	$+52.3 \pm 2.4$	$+10.7 \pm 0.5$
Toluene (160–220 K)	13.2 ± 1.2	4.3 ± 0.7	-47.0 ± 2.5	-8.9 ± 0.5
Benzaldehyde (160–220 K)	17.4 ± 0.7	9.9 ± 0.4	-39.5 ± 1.7	-7.5 ± 0.3

the micropores are very narrow, and only just admit the molecules of unsubstituted benzene; we suggest that increasing the molecular dimension by even a CH_3 or CHO substituent is sufficient to discourage admission of the substrate. The second fraction, measured for sorbed benzene, presents activation parameters which are all very similar to those measured in bulk-benzene, which is reasonable if it is resident in the meso- and macro-pores of the carbon structure (i.e. those of dimension, $20 > d < 10{,}000$ A). Benzene sorbed in porous silica [43] was shown to behave rather like bulk benzene, although a range of melting temperatures was inferred, according to the differing sizes of molecular clusters that had formed within the distribution of pore-sizes present in porous silica. We note that the distributions of pore sizes in activated carbons [44, 56] show clear maxima, both in the micropore and macropore regions, with a relatively smaller mesopore fraction, and that the majority of the (high) surface area in the material used in this study (*ca* 1,600 m^2/g) lies within its micropores. The loading used corresponds to a nominal 30–40% coverage of the carbon surface for the three substrates.

In our previous studies of sorbed radicals using LF-MuSRx [3, 8–13;13, 55], we ascribed *negative* $\Delta S^{\neq}$ values to reorientational events that were not those of *single* molecules, but rather involved "sticking-collisions" between molecules, so increasing the molecular "ordering" as the activated state for the process is achieved. We believe this is the situation for benzene, toluene and benzaldehyde sorbed in porous carbon. The latter two cases are now considered specifically.

7.4.2 Toluene Sorbed in Porous Carbon

Toluene reveals two maxima in the LF-MuSRx plot, which we would normally attribute to two types of sorbed fraction. We have already discounted that toluene molecules manage to penetrate the very small micropores, since both $\Delta S^{\neq}$ values are negative. From Table 7.7 it is clear that the fraction characterised by the very small activation energy is dominated by its activation entropy, $\Delta H^{\neq}$ being close to zero (1.5 ± 0.4 kJ/mol). The alternative toluene distribution has a very similar $\Delta H^{\neq}$

to that of "bulk" *benzene* [12], but its $\Delta G^{\neq}$ value is enhanced by the more negative $\Delta S^{\neq}$ term, which again dominates over $\Delta H^{\neq}$. That toluene should require a more specific molecular ordering between its molecules for reorientation to occur than benzene does is not surprising, given the presence of the methyl group. Some mutual orientations of toluene molecules will be sterically less favourable than those which minimise eclipsing of methyl groups between molecules; hence a greater "ordering" is achieved in the activated state. This is reflected in the more negative $\Delta S^{\neq}$ values than apply for benzene.

The lower symmetry of toluene molecules may also change the particular nature of the molecular reorientation. From the change in the muon hyperfine anisotropy (δA) which occurs during the reorientation of "bulk" benzene molecules in porous carbon, we deduced [12] that the most probable mechanism was a process involving "90° jumps" about the molecular axis. In toluene, three isomeric radicals are expected, according to *transverse-field* (TF-MuSR) measurements on liquid toluene [57], formed by Mu addition at the 2-, 3- and 4-positions (the *ipso* isomer was not detected in the TF study). We are reminded also of a study of anisole (methoxybenzene) sorbed on silica surfaces [58], made using the *Avoided Level Crossing* (ALC)-MuSR method. The results from this study show that the 2- and 3-Mu adducts of anisole have similar activation energies, close to *ca* 10 kJ/mol and similar to the value for the Mu adduct of benzene sorbed on 7 nm silica grains, while the 4-Mu adduct of anisole shows a near-zero activation energy. This result leaves us to speculate that rather than having two distinct fractions of toluene sorbed in porous carbon, there is a mainly bulk phase present in the meso- and macro-pores, but that the different radical isomers themselves exhibit differential motional behaviour. In view of the prior result for anisole, we make the tentative suggestion that it is the 4-Mu adduct of toluene which has the lowest E_a (2.5 ± 0.4 kJ/mol), while the 2- and 3-Mu adducts display a mean value of *ca* 6 kJ/mol, similar to that for benzene [12].

Despite the difference in E_a, the relaxation maxima yield nearly identical δA values, in the region of 7–8 MHz, which is close to that expected (*ca* 6 MHz) for cyclohexadienyl radicals undergoing a 90° jump motion about the ring-plane axis [12, 48]: the apparent increase in δA, even though there is some spin-delocalisation onto the methyl group (as shown by the fall [57] in the isotropic muon hyperfine coupling from that in the benzene-Mu adduct, cyclohexadienyl radical) suggests that the reorientational motion of methyl-substituted cyclohexadienyl radicals is more complex; accordingly, the entropy requirements appear greater too (*ca* −50 J/mol/K *c.f.* −30 J/mol/K for unsubstituted cyclohexadienyl radicals) too, suggesting that a more ordered activated state occurs.

7.4.3 Benzaldehyde Sorbed in Porous Carbon

TF-MuSR studies have shown that Mu addition to benzaldehyde forms dominantly the radical $PhCH^{\cdot}$-OMu, with only relatively minor amounts of the

ring-adducts [50, 54]: we assume, therefore, that the measured relaxation stems mainly from the molecular reorientation of this radical species. Previously, we discovered that the isotropic muon coupling in PhCH˙-OMu. is sensitive both to effects of its medium and to temperature, and have used the value measured in solution in cyclohexane in our calculation of the transition frequency (ω), since this was the most weakly perturbing medium found [50, 54]. Proceeding as described earlier, motional correlation times (τ) were estimated and Arrhenius-type plots were made for both temperature ranges. Clearly, the τ values are smaller by a factor of *ca* 10 than those determined for toluene in the fraction exhibiting a nearly identical activation energy (*ca* 3 kJ/mol), and we envisage that "hydrogen-bonding" effects involving the muon in PhCH˙-OMu are important (the viscosity [59] of PhCHO is only *ca* twice that of toluene, but that of $PhCH_2OH$ is greater by a factor of *ca* 10, encouraging the view that "H-bonding" effects will be influential in such a system). Indeed, the very large and negative $\Delta S^{\neq}$ value of −76 J/mol/K estimated for benzaldehyde (Table 7.7) indicates that an appreciable molecular ordering is achieved in the activated state, consistent with "H(Mu)-bond" formation; we are cautious about the absolute value, however (see Sect. 7.2.2.1). Since the process is dominated by the entropy, it appears that critical molecular orientations are required to form the "Mu-bond"; $\Delta H^{\neq}$ *being close to zero*.

The δA values for both benzaldehyde fractions are smaller than those found for benzene or toluene sorbed in porous carbon. This is surprising since the muon hyperfine anisotropy is expected to be larger in PhCH˙-OMu. than in cyclohexadienyl type radicals. In a single crystal study of related Ph_2C˙-OMu radicals [60], formed by Mu addition to benzophenone, dipolar couplings of approximately −15, −6, +21 MHz were determined; in comparison with which, values of *ca* 2 MHz for δA indicate that the type of reorientational motion for sorbed PhCH˙-OMu radicals can only involve fairly small-angle jumps, whose amplitude is limited by such Mu-bonding as proposed earlier. In contrast, Me_2C˙-OMu radicals apparently undergo extensive averaging of the muon hyperfine anisotropy, as sorbed in the zeolite NaX at 298 K [61].

The larger E_a measured for benzaldehyde over the higher temperature range (160–220 K) most likely represents the motion of effectively "isolated" PhCH˙-OMu molecules on the carbon surface, in contrast to the "clusters" that are envisaged to account for the lower temperature fraction. This explanation follows those advanced previously by us to account for the similar behaviour shown by benzene sorbed in cation-exchanged zeolite X samples [9] and by 1,1-dichloroethene sorbed in silica and in kaolin [3]. We note that the $\Delta S^{\neq}$ values are very similar for all such "isolated" molecules, and are more positive (i.e. less negative) than is found in molecular clusters. The apparent small-angle jumps indicate that there is Mu-bonding to the carbon surface, which is normally fairly rich in oxygen-containing functional groups [56].

7.4.4 Viscosity Effects for Toluene and Benzaldehyde Sorbed in Carbon

Using standard bond lengths, bond angles and atomic masses, we have estimated the moment of inertia for benzaldehyde ($I = 2.1 \times 10^{-45}$ kg m^2) and for toluene ($I = 1.8 \times 10^{-45}$ kg m^2). These values were used to estimate the reorientation time for a free rotor [42, 43], $\tau_{FR} = 2\pi(I/81kT)^{1/2}$, for both benzaldehyde and toluene. Since the inverse-frequency factor (τ_∞) is expected to approach τ_{FR}, in the absence of *viscous friction* [42, 43], the ratio τ_∞/τ_{FR} provides an indication of the effective viscosity for a given sorbed fraction [9]. The greatest departure from the predicted τ_{FR} value is found for the fraction of sorbed benzaldehyde which we believe to be in a sorbed cluster-phase; this accords with a substantial viscosity as measured by PhCH$^{\cdot}$-OMu radicals which are Mu-bonded within this sorbed medium. Lesser viscosities are apparent for the "isolated" PhCH$^{\cdot}$-OMu. radicals, despite their higher reorientational activation energy, and for all benzene and toluene fractions. [The highly accelerated motion of benzene molecules sorbed in small carbon micropores was discussed previously [12].

Another check on the viscosity of sorbed molecules is provided by comparing the motional correlation time (τ) measured at (or extrapolated to) 300 K (τ_{300}) with that expected for molecules present in the corresponding organic liquids [9]. For such non-viscous liquids as benzene and toluene, typical τ values are close to 5×10^{-12} s [49]; a value of *ca* 10^{-11} s is probably more appropriate for benzaldehyde since its bulk viscosity is higher [59]. Once again, the actual τ_{300} values are far greater than those expected, demonstrating that molecules when sorbed in porous carbon experience an effective viscous impedance to their reorientation compared with a liquid sample; this is consistent with the general finding that pore-confinement often provides a resistance to molecular motion [44].

7.4.5 Terpenes Sorbed in Activated Carbon

Terpenes, especially the pinenes, are a principal component of naturally emitted (biogenic) hydrocarbons in the atmosphere [2]. Using LF-MuSRx, we have attempted to investigate the formation of radicals from a variety of terpenes and their interaction with a porous carbon material [13]. The results for α-pinene and β-pinene are representative of this study. Addition of Mu to either pinene isomer will yield very similar radicals, differing only in the relative position of the muon and a proton. It might be expected, therefore, that their reorientational dynamics would also be very similar. Both samples reveal two distinct motional regimes, corresponding to radicals located at different sorption sites within the carbon micropores. The activation parameters are shown in Table 7.8 and it is clear that they are identical within error for both fractions for both isomers. From our LF-MuSRx results for benzene sorbed in activated carbon [12] we propose that the fraction of lower

Table 7.8 Activation parameters measured for α-pinene and β-pinene sorbed in activated carbon powder

	$\tau_\infty{}^{-1}/s^{-1}$	E_a/kJ mol^{-1}	$\tau_\infty{}^{-1}/s^{-1}$	E_a/kJ mol^{-1}
α-Pinene	$(8.1 \pm 2.4) \times 10^{11}$	6.0 ± 0.3	$(4.8 \pm 1.3) \times 10^{12}$	13.1 ± 1.7
β-Pinene	$(4.5 \pm 1.1) \times 10^{11}$	6.6 ± 0.9	$(8.1 \pm 2.5) \times 10^{12}$	16.0 ± 1.2

activation energy corresponds to molecules that occupy the meso- and macro- pores (i.e. those of dimensions >20 A), while the fraction at higher activation energy is sorbed within the micropores (4–20 A). However, the inverse-frequency factors indicate there is little increase in freedom (entropy) for the pinene derived radicals, as they escape from the small pores, in contrast with that which is apparent for benzene (*vide supra*). This may be because the larger pinene molecules are denied access to the very small (<10 A) pores, but occupy those which are somewhat larger in their size distribution.

We stress that the radical derived by muonium addition to α-pinene has a quite rigid structure, which lends confidence that the experiment is measuring true reorientation events, and the identical results for β-pinene provide no indication that the rotation of the $MuCH_2$-group in its radical is contributing appreciably to the muon spin relaxation process. Furthermore, we have estimated, using EPR spectroscopy, the spin concentration in the unloaded porous carbon to be *ca* one unpaired electron per 10,000 carbon atoms, which we do not believe will influence the muon spin relaxation unduly.

7.5 Ongoing Further Studies of Environmentally Relevant Surfaces Using LF-MuSRx

7.5.1 Clays

One example – of 1,1-dichloroethyl radicals sorbed in kaolin - has already been mentioned [3]. We have recently undertaken preliminary experiments using LF-MuSRx to distinguish between the effects of sorption of radicals in kaolin and in montmorillonite. These are fundamentally different sorbent materials, and are characterised by specific surface areas in the region of 40 m^2/g and up to 800 m^2/g, respectively, in consequence of a relatively rigid arrangement of aluminosilicate sheets for kaolin, but a more flexible structure in montmorillonite, whose layers are able to separate at the behest of molecular sorption to expose a far more extensive surface [31, 45]. Indeed, a number of catalytic applications have been found for montmorillonite [31], which are in many respects similar to those for zeolites, and it seems reasonable that clays as airborne materials might contribute in the outcome of atmospheric pollution chemistry.

The probe radicals were $MuCH(Cl)CCl_2^{\cdot}$ and $Me_2C^{\cdot}$-OMu, chosen to represent reactive intermediates in atmospheric halocarbon photolysis and in tropospheric hydrocarbon oxidation [1, 2]. Two sorbed fractions could be identified for both radicals in both types of clay: $MuCH(Cl)CCl_2^{\cdot}$ revealed activation energies of 4.6 and 8.5 kJ/mol in kaolin and of 1.9 and 10.5 kJ/mol in montmorillonite; the values measured for $Me_2C^{\cdot}$-OMu were not greatly different, at 1.9 and 7.4 kJ/mol in kaolin and 2.7 and 9.3 kJ/mol in montmorillonite. In analogy with some of the more detailed examples already discussed, the low-energy fraction can probably be ascribed to a sorbed essentially *liquid* fraction in all cases, in analogy with measurements of $MuCH_2Cl_2^{\cdot}$ sorbed in both kaolin and silica [3] and for $PhCH^{\cdot}$-OMu sorbed in porous carbon [11] and in zeolite X [55] (all *ca* 2–3 kJ/mol); the other fractions are attributed to isolated surface-sorbed radicals. The activation energy for the surface sorbed fraction is rather greater in montmorillonite than in kaolin for both $MuCH(Cl)CCl_2^{\cdot}$ and $Me_2C^{\cdot}$-OMu, which might be explained in terms of a lateral penetration between the layers of montmorillonite by both $CHCl=CCl_2$ and $Me_2C=O$ substrates, and hence an association between the resulting probe radicals and cations present in the clay.

7.5.2 Ice

Ice surfaces, prepared at low temperatures, have been used to model tropospheric clouds; however, on annealing above *ca* 200 K, an abrupt reduction in the surface-area occurs, although there is little change in density or particle size [62]. We have attempted some exploratory measurements on an ice-surface. In order to maintain a high surface area throughout sample measurements made over a wide temperature range, an ice surface was prepared by deposition of water from the vapour-phase into silica gel cooled to 195 K: the resulting bimolecular "ice" layer had a surface-area of *ca* 300 m^2/g. A subsequent monolayer coverage each of benzene and α-pinene was sorbed in separate samples, also at 195 K. LF-MuSRx measurements were made in the temperature range 90–300 K; both α-pinene and benzene showed a fraction with an activation energy to surface reorientation of 10 kJ/mol, but the sorbed benzene sample contained an additional fraction with an activation energy of 25 kJ/mol. Since the latter is manifest in the region of the melting-point of normal ice, it is tempting to ascribe the underlying dynamic process as involving a melting process of the ice component; however, the effect was not observed from sorbed α-pinene, and more likely represents benzene molecules which are trapped in localised "pockets" of the ice surface. In support of this, we recall that a nearly identical activation energy was measured from benzene in the small pores of porous carbon [12]. We note that the enthalpy of fusion of ice is only about one quarter of this value, at *ca* 6 kJ/mol [59], which further supports the view that a melting-phase-transition is not being measured.

7.6 Summary of MuSR Results

In all cases discussed, a good straight-line plot of $-\ln\tau$ *vs.* 1/T was obtained, according to (Eq. 7.8), which encourages our confidence that a single dominant activation process is involved. When we have been able to compare results obtained using both TF-MuSR and LF-MuSRx for a given system, (e.g. 1,1-dichloroethyl radicals sorbed in silica-gel and in kaolin, and benzene sorbed in porous carbon), the agreement is excellent, and strongly suggests that the process being measured is indeed a molecular reorientation.

Of further significance are the results obtained for α-pinene and β-pinene sorbed in porous carbon. The radical formed from β-pinene has a rotating $MuCH_2$-group, whereas the muonium atom is bound in an essentially "fixed" position by addition to α-pinene. Nonetheless, both E_a and τ_∞^{-1} values are identical, within experimental error (Table 7.8), for both motional regimes (sorbed fractions). Since the unloaded porous carbon samples reveal only a low concentration of paramagnetic sites (*ca* one unpaired electron per 10,000 carbon atoms) we do not believe they influence the muon relaxation rate to any great extent. Therefore, the model of molecular reorientation is also supported in the pinene/carbon samples.

A contribution to (λ) in the $Me_2C^{\cdot}$-OMu radical, formed in the solid, liquid and gas-phases of acetone, was attributed to the "out-of-plane" oscillation of the O-Mu bond, and this may also apply to the $PhCH^{\cdot}$-OMu radical. However, the only *difference* between the samples of benzaldehyde sorbed in cation-exchanged zeolite X is the type of cation which is present. The activation energies (Table 7.6) are found to decrease as the cation radius increases in each series $Li^+ > K^+$ and $Mg^{2+} > Sr^{2+}$. This accords with the formation of increasingly weak π-complexes between the $PhCH^{\cdot}$-OMu radicals and the exchange-cations, as deduced previously from changes in the isotropic muon hyperfine couplings measured in these samples. Once again, the results are more readily explained by a dominant reorientational process rather than one of intramolecular dynamics.

The results show that a diversity of VOCs can be converted into radicals bearing the muonium radiolabel, and so may be investigated on a wide range of solid surfaces, representative of the various particles present in the atmosphere.

7.7 EPR Measurement of Peroxyl Radicals and Nitrate Radicals Sampled from Air in a Cryogenic Ice-Matrix

Organic peroxyl radicals ($RO_2^{\cdot}$) are the main chain-carriers in the atmospheric oxidation of hydrocarbons. They are formed during the daytime by reactions between ·OH radicals and hydrocarbons and CO, and at night by reactions between hydrocarbons and "nitrate" radicals ($\cdot NO_3$), and from reactions of the Criegee intermediate produced by the interaction between alkenes and ozone [2]. The night-time

chemistry of $\cdot NO_3$ is as follows: $\cdot NO_3$ radicals are produced by the reaction between ozone and $\cdot NO_2$, then a rapid equilibrium is established between $\cdot NO_3$, $\cdot NO_2$ and N_2O_5. Both $\cdot NO_3$ and N_2O_5 can be removed by reaction with *hydrometeors* (literally, falling objects composed of water; *precipitation* consists of a stream of hydrometeors, in the form of droplets or ice crystals). This leads to the formation of dissolved $\cdot NO_3$, a process which provides a night-time sink for atmospheric NO_x. In addition, $\cdot NO_3$ radicals undergo addition reactions with alkenes present in the atmosphere, followed by addition of oxygen, to form β-nitratoalkylperoxyl radicals ($O_2NO\text{-}CR_2\text{-}CR_2\text{-}OO^{\cdot}$). $\cdot NO_3$ also reacts with aldehydes to yield $RO_2^{\cdot}$ radicals and nitric acid, while reactions of $RO_2^{\cdot}$ with $\cdot NO_3$ lead to the formation of alkoxy ($RO\cdot$) radicals (Eq. 7.9). Hence, the $\cdot NO_3$ radical can play a similar role as does NO during daytime [2], namely by initiating chain reactions that lead to the formation of $HO_2^{\cdot}$ and ·OH radicals at night (Eqs. 7.10 and 7.11). In (Eq. 7.10), the radical $RO\cdot$ is in fact one of type $RCH_2\text{-}O^{\cdot}$ which transfers a hydrogen atom to O_2, forming $HO_2^{\cdot}$:

$$RO_2^{\cdot} + \cdot NO_3 \rightarrow RO\cdot + \cdot NO_2 + O_2 \tag{7.9}$$

$$RO\cdot + O_2 \rightarrow RCHO + HO_2^{\cdot} \tag{7.10}$$

$$HO_2^{\cdot} + \cdot NO_3 \rightarrow \cdot OH + \cdot NO_2 + O_2 \tag{7.11}$$

Measurements of these radicals have been made in the troposphere by sampling air at the top of a mountain (Schauinsland, in Southern Germany, using a matrix-isolation apparatus [63]. The radicals were trapped from 8l of air, with an efficiency of >95%, in a D_2O matrix at 77 K over a period of 30 min. The samples were then transported, frozen in liquid nitrogen, to a laboratory at ground level for EPR measurements. The EPR spectra were analysed using a numerical procedure which fits the individual spectra of each radical component, and provides a measure of their concentrations: the detection limit is 5 parts-per-trillion-by-volume (pptv) for $HO_2^{\cdot}$, $RO_2^{\cdot}$ and $\cdot NO_2$, and 3 pptv for $\cdot NO_3$ due to its narrower EPR linewidth. From a typical EPR spectrum, recorded from one experiment, the uppermost trace (A) is the original spectrum, and is dominated by $\cdot NO_2$, at a concentration of 0.65 parts-per-billion-by-volume (ppbv); subtraction of the $\cdot NO_2$ signal (B) yields the residual signal shown in (C), which matches closely the structure of the $\cdot NO_3$ reference spectrum (D): a simultaneous fit of the reference spectra of $\cdot NO_3$, $HO_2^{\cdot}$ and various peroxyl radicals yielded a concentration of $\cdot NO_3$ at 9.5 pptv, whereas the total amount of peroxyl radicals was less than 1 pptv.

The $\cdot NO_3$ levels were always found to be quite low, e.g. <10 pptv. The concentrations of peroxyl radicals varied between almost 40 pptv and values below the detection limit of 5 pptv. The $HO_2^{\cdot}$ concentration was mainly also at or below the 5 pptv detection limit [63]. The EPR method is, of course, specific for free radicals, and can form part of an overall sampling strategy in which other analytical methods

are employed to analyse hydrocarbon and other trace gas components from the atmosphere, to provide an overall view and a test of atmospheric chemical kinetic models [2].

7.8 EPR Studies of the Toxicity of Solid Particles: Silica, Asbestos, Coal-Dust

There is current concern over the toxicity of various minerals, especially asbestos caused by their inhalation, leading to lung diseases, including specific types of cancer, although their precise mode of action remains uncertain; however, as shown in the examples below, there is evidence from spin-trapping studies that these materials can initiate free radical formation, and so might precipitate lipid peroxidation of the pulmonary cell membranes [1, 64]. In crocidolite asbestos [65], it is known that iron is present and that it can reduce O_2 and participate in Fenton-type reactions. Because of the importance of these reactions in crocidolite-induced toxicity, studies have been made, on three different types of crocidolite fibres, to determine the factors which control the activity of iron in catalysing the two reactions. Results show that the total concentration of iron in crocidolite fibres is not an appropriate parameter for characterising the activity of this mineral, which seems rather to be controlled by the valency and the location of the iron in the lattice, and also by its availability for mobilization from these minerals.

Following this is a study of crocidolite which has been "detoxified" [66]. The fibres were treated with ferric oxide salts to form a metal-micelle polymer surface coating which prevented physiological reactions with the mineral. This detoxified crocidolite was tested for its ability to produce ·OH radicals from H_2O_2. It was found that the intensity of the DMPO-OH radical adduct signal was indeed reduced from that obtained from the native crocidolite fibres. Similar experiments showed that the ability of the detoxified crocidolite to reduce oxygen was also decreased compared with the native mineral. The availability of ferrous iron present in the two crocidolite fibres to catalyse the above reactions was investigated with the chelating agent ferrozine. The results indicate that ferrozine was able to remove fewer ferrous ions from detoxified crocidolite than the native form; moreover, Mossbauer spectroscopy shows that the detoxification process results in both bulk and surface changes in the co-ordination chemistry of the detoxified sample. The detoxification process also introduces a surface coating comprising ferric ions which shield near-surface ferrous ions and consequently reduces the Fenton-type reactivity of the fibres. On the subject of "detoxification" of crocidolite, the same group [67] report the treatment of crocidolite fibres with microwave radiation at different temperatures: this reduced the Fe^{2+}/Fe^{3+} ratio, according to Mossbauer measurements, and produced a concomitant decrease in the ability of the fibres to peroxidize linoleic acid.

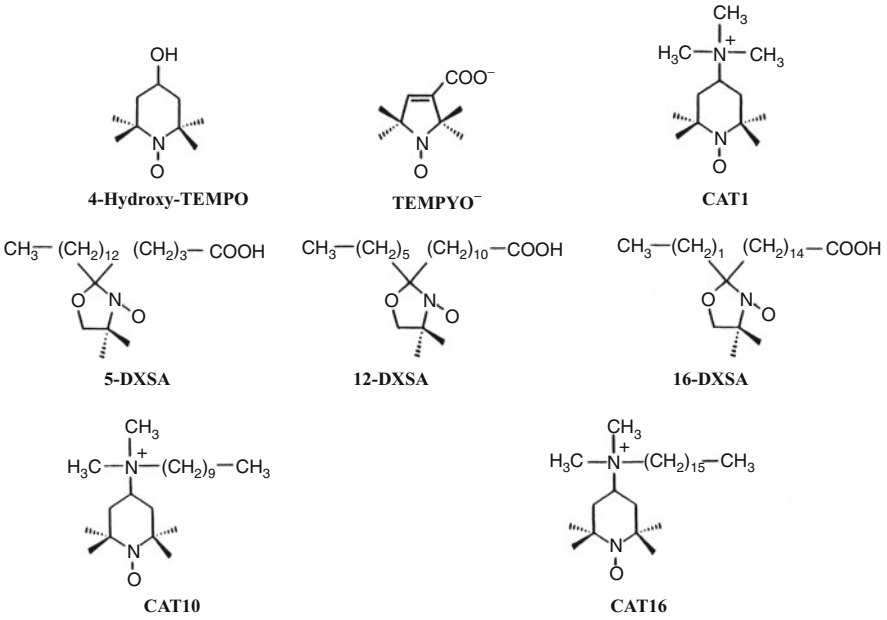

Scheme 7.1 Structures of the nitroxide spin-probes discussed in the text (Adapted from Ref. [69] with kind permission of American Chemical Society, 1996)

At least one *in vivo* study has been made of the toxicity of asbestos, using a spin-trapping technique [68]. 180 day-old rats were instilled intratracheally with either 500 μg of crocidolite or saline; 24 h later, histologic examination of the lungs revealed a neutrophilic inflammatory response. EPR examination of the chloroform extract from lungs exposed to asbestos showed a spectrum consistent with a carbon-centred radical adduct while those spectra from lungs instilled with saline revealed a far weaker spectrum. The adducts are nearly identical with ethyl and pentyl radical adducts, providing evidence of in vivo lipid peroxidation resulting from asbestos exposure [68], The adsorption of neutral and charged nitroxides from their solutions onto asbestos fibres was investigated using EPR, some of which contained an hydrophobic chain attached to the nitroxide group while in others it was absent. The four different asbestos fibres studied were chrysotile (which belongs to the serpentine group), and anthophyllite, amosite, and crocidolite (all of which belong to the amphibole group). It was found that the "chain-free" nitroxides (Scheme 7.1) 4-hydroxy-TEMPO and $TEMPYO^{-}$, being neutral and negatively charged respectively, were barely adsorbed by the positively charged chrysotile surface (<10%), while the positively charged nitroxide CAT1 (Scheme 7.1) was better adsorbed to the extent of 25% by the negatively charged anthophyllite fibres. As expected, a reduction in the rotational correlation time was observed by interection of the spin-probe with the asbestos surface. The presence of the hydrophobic chain attached to the nitroxide group encouraged the formation of surface aggregates

and led to a string enhancement of surface adsorption. The doxylstearic acids were preferentially adsorbed by chrysotile to the extent of 80% an effect that was enhanced as the solvent polarity increased and as the chain length between the carboxylic and the doxyl groups increased. The positively charged surfactants (Scheme 7.1) CAT10 and CAT16 were adsorbed preferentially by anthophyllite fibres. Amosite fibres showed poor adsorption, whereas the EPR spectra from crocidolite samples were scarcely detectable, because of spin – spin interactions between the adsorbed radicals and paramagnetic surface metal ions. The close proximity of the surface adsorption sites favoured a high local concentration of radicals adsorbed on the chrysotile fibres, while in contrast low-packed surface aggregates were formed at the anthophyllite surface, since the interacting sites were rather more widely dispersed [69].

Another report shows that the ·OH-generating potential of coal dust correlates positively with the surface iron content of the coal dust [70]. Two other papers describe results for the inhibition of quartz-induced lipid peroxidation. In one [71], an alkaloid used in China to treat the lesions of silicosis, is tested for its antioxidant activity: it is found that tetrandrine reacts efficiently with ·OH radicals generated by the reaction of freshly fractured quartz particles with an aqueous medium, and also scavenged O_2^- radicals produced from xanthine/xanthine oxidase. A significant inhibition of linoleic acid peroxidation by freshly fractured quartz particles was also found. Taurine-based compounds were similarly investigated [72]: it was discovered that hypotaurine, but not taurine, caused a significant reduction in silica-induced peroxidation, again using linoleic acid as a model lipid.

Acknowledgments I thank my former colleagues, Ivan Reid, Tim Dintinger, Harry Morris, Chantal Hinds, Estelle Butcher, Chris Scott, Ulrich Zimmerman, Steve Cox, Brian Webster and Jas Jayasooriya either for their actual participation in the experiments described, or for their helpful thoughts or both. I further acknowledge financial support from the Leverhulme Trust, the Paul Scherrer Institute, the European Union, the Engineering and Physical Sciences Research Council (EPSRC) of the United Kingdom, Unilever Research and The Royal Society of Chemistry (for a J.W.T. Jones Travelling Fellowship).

References

1. Rhodes CJ (2011) Electron spin resonance, part 1: a diagnostic method in the biomedical sciences. Sci Prog 94:16–96
2. Finlayson-Pitts BJ, Pitts JN Jr. (2000) Chemistry of the upper and lower atmosphere. Academic Press, London
3. Rhodes CJ, Dintinger TC, Reid ID, Scott CA (2000) Mobility of dichloroethyl radicals sorbed in kaolin and in silica. Magn Reson Chem 38:281–287
4. Walker DC (1983) Muon and muonium chemistry. Cambridge University Press, Cambridge
5. Roduner E (1988) The positive muon as a probe in free radical chemistry. Lecture Notes in Chemistry. Springer, Heidelberg
6. Carrington A, McLachlan AD (1979) Introduction to magnetic resonance. Chapman and Hall, London
7. Harris RK (1983) Nuclear magnetic resonance spectroscopy. Pitman, Melbourne

8. Rhodes CJ, Dintinger TC, Scott CA (2000) Rates of motion for free radicals in zeolites as directly measured by longitudinal field muon spin relaxation. Magn Reson Chem 38:62–65
9. Rhodes CJ, Dintinger TC, Scott CA (2000) Sorption of benzene in cation-exchanged zeolite X, as measured by longitudinal field muon spin relaxation (LF-MuSRx). Magn Reson Chem 38:729–737
10. Rhodes CJ, Dintinger TC (2011) Radiolabelling measurements of free radicals derived from aromatic volatile organic compounds (VOCs) adsorbed in zeolite nanomaterials to and above saturation loadings. Prog React Kinet Mech 36: in press
11. Rhodes CJ, Reid ID (2002) A radiolabelling study of radicals derived from benzene, toluene and benzaldehyde sorbed in model environmental carbon. Spectrochim Acta A 58:1209–1217
12. Rhodes CJ, Dintinger TC, Reid ID, Scott CA (2000) Spin-labelling studies of benzene sorbed in carbon particles using muonium: a molecular view of sorption by environmental carbons. Magn Reson Chem 38:S58-S64
13. Rhodes CJ (2006) Radiolabelling measurements of radicals derived from terpenoid volatile organic compounds (VOCs) adsorbed in porous carbon. Prog React Kinet Mech 31:159–188
14. Rhodes CJ, Reid ID, Zimmermann U unpublished results.
15. Rhodes CJ, Reid ID, Zimmermann U (2002) Muonium addition to DMPO and PBN sorbed in silica-gel. Chem Comm 1092–1093
16. Roduner E (1993) Polarized positive muons probing free radicals – a variant of magnetic resonance. Chem Soc Rev 22:337–346
17. Roduner E, Schwager M, Shelley M (1995) Muon spin resonance of radicals on surfaces. In: Lund A, Rhodes CJ (eds) Radicals on surfaces. Kluwer, Dordrecht
18. Cox SFJ (1998) Muon spin relaxation studies of interstitial and molecular motion. Solid State Nucl Magn Reson 11:103–121
19. Cox SFJ, Sivia DS (1997) Spin-lattice relaxation in hyperfine-coupled systems: applications to interstitial diffusion and molecular dynamics. Appl Magn Reson 12:213–226
20. Jayasooriya UA, Stride JA, Aston GM, Hopkins GA, Cox SFJ, Cottrell SP, Scott CA (1997) Muon spin relaxation as a probe of molecular dynamics of organometallic compounds. Hyperfine Interact 106:27–32
21. Jayasooriya UA, Aston GM,Stride JA (1997) Molecular dynamics of organometallic compounds using muSR. Appl Magn Reson 13:165–171
22. Rhodes CJ, Dintinger TC, Morris H, Scott CA (2002) Molecular motion in some radiolabelled dipeptides: a muon spin relaxation study. Magn Reson Chem 40:421–423
23. Clayden NJ, Jayasooriya UA, Cottrell SP (1999) Dynamics of dioleoyl phosphatidylcholine by muon spin relaxation. Phys Chem Chem Phys 1:4379–4382
24. Clayden NJ, Jayasooriya UA, Stride JA, King P (2000) Dynamics of polyurethane elastomers by muon spin relaxation. Polymer 41:3455–3461
25. Christides C, Cox SFJ, David WIF, Macrae RM, Prasides K (1993) C-60 molecular dynamics studied by muon spin relaxation. J Chim Phys 90:663–669
26. Van Dingenen R, Jensen NR, Hjorth J, Raes F (1994) Peroxynitrite formation during the daytime oxidation of dimethylsulfide – its role as a reservoir species for aerosol. J Atmos Chem 18:211–237
27. Wuebbles DJ (1983) Chlorocarbon emission scenarios – potential impact on stratospheric ozone. J Geophys Res 88:1433–1443
28. Tegen I, Fung I (1994) Modeling of mineral dust in the atmosphere – sources, transport and optical thickness. J Geophys Res 99:22897–22914
29. Townsend RP (1980) Properties and applications of zeolites. Chemical Society, London
30. Lund A, Rhodes CJ (1985) Radicals on surfaces. Kluwer, Dordrecht
31. Laszlo P (1987) Chemical reactions in clays. Science 233:1473–1477
32. Jacobs PH, Forstner U (1999) Concept of subaqueous capping of contaminated sediments with active barrier systems (ABS) using natural and modified zeolites. Water Res 33:2083–2087
33. Hester RH, Harrison RM (1995) Volatile organic compounds in the atmosphere. Royal Society of Chemistry, Cambridge

34. Clarke JKA, Darcy R, Hegarty BF, O'Donoghue E, Amir-Ebrahimi V, Rooney JJ (1986) Free radicals in dimethyl ether on H-ZSM-5 zeolite – a novel dimension of heterogeneous catalysis. J Chem Soc Chem Commun 425–436
35. Heming M,.Roduner E (1987) Formation and dynamics of a SiO_2 adsorbed radical absorbed by muon spin rotation. Surf Sci 189:535–542 (1987)
36. Rhodes CJ, Roduner E, Reid ID (1993) First direct observation of neutral radicals in a zeolite at ambient temperature. J Chem Soc Chem Commun 512–513
37. Rhodes CJ, Butcher EC, Morris H, Reid ID (1995) Mobility of radicals in zeolite catalysts: molecular motion studied by muon spectroscopy. Magn Reson Chem 33:S134-S146
38. Kochi JK (1975) Configurations and conformations of transient alkyl radicals in solution by electron spin resonance spectroscopy. Adv Free Rad Chem 5:189–317
39. Rhodes CJ, Symons MCR (1988) The formation of β-muonium-substituted cyclopentyl and cycloheptyl radicals, and the significance of the A'_μ/A_H isotope ration in relation to the conformations of muonium-substituted alkyl radicals. J Chem Soc Faraday Trans 1(84): 1187–1194
40. Walker DC (1998) Kinetic isotope effects in solution reactions of muonium atoms as H-isotopes. J Chem Soc Faraday Trans 94:1–9
41. Huheey JE (1978) Inorganic chemistry, principles of structure and reactivity. Harper & Row, New York
42. Tyrrell HJV, Harris KR (1984) Diffusion in liquids. Butterworths, London
43. Roduner E, Shwager M, Tregenna-Piggott P, Dilger H, Shelley M, Reid ID (1995) Dynamics of the cyclohexadienyl radical adsorbed in porous silica and NaZSM5. Ber Bunsenges Phys Chem 99:1338–1342
44. Karger J, Ruthven DM (1992) Diffusion in zeolites - and other microporous solids. Wiley, New York
45. Barrer RM (1978) Zeolites and clay minerals. Academic Press, London
46. Hepp MA, Ramamurthy V, Corbin DR, Dybowski C (1992) ^{2}H NMR invetigations of ion molecule interactions of aromatics included in zeolites. J Phys Chem 96:2629–2632
47. Rhodes CJ, Hinds CS, Reid ID, unpublished results
48. Roduner E (1990) Radical reorientation dynamics studied by positive-muon avoided level-crossing resonance. Hyperfine Ineract 65:857–871
49. Harrison SR, Pilkington PS, Sutcliffe LH (1984) Electron spin resonance spectroscopy, stability and spin-probe properties of dithiazolyl, dithiadiazolyl, benzodithiazolyl and disulfenimidyl free radicals. J Chem Soc Faraday Trans1 80:669–689
50. Rhodes CJ, Hinds CS, Reid ID (1996) Muonium adduct of benzaldehyde: a novel probe of cation-molecule interactions in zeolite catalysts and of solvation and electronic substituent effects. J Chem Soc Faraday Trans 92: 4265–4269
51. Nagy JB, Derouane EG, Resing HA, Ray Miller G (1983) Motions of ortho-xylenes and para-xylenes in ZSM-5 catalyst – ^{13}C nuclear magnetic resonance. J Phys Chem 87:833–837
52. Eckman RR, Vega AJ (1986) Deuterium solid-state NMR study of the dynamics of molecules adsorbed by zeolites. J Phys Chem 90:4679–4683
53. Kustanovich I, Fraenkel D, Luz Z, Vega S (1988) Dynamic properties of p-xylene adsorbed on Na-ZSM-5 by deuterium and proton magic angle sample spinning NMR. J Phys Chem 92:4134–4141
54. Rhodes CJ, Reid ID,Jackson RA (1997) Muonium adducts of benzaldehyde: structural correlation with nitroxides. Hyperfine Interact 106:193–201
55. Rhodes CJ (2006) Studies of radio-labelled free-radicals derived from a VOC (volatile organic compound), benzaldehyde, adsorbed in cation-exchanged zeolite X. Prog React Kinet Mech 31:139–158
56. Bansal RC, Donnet JB, Stoeckli F (1988) Active carbon. Marcel Dekker, Inc., New York
57. Roduner E, Brinkman GA, Louwrier PWF (1982) Muonium substituted organic free radicals in liquids – muon electron hyperfine coupling-constants and the selectivity of formation of methyl-substituted and fluorine-substituted cyclohexadienyl-type radicals. Chem Phys 73: 117–130

58. Reid ID, Azuma T, Roduner, E (1990) Probing the behaviour of surface-adsorbed free radicals using ALC-MuSR. Hyperfine Interact 65**:**879–889
59. West RC (1985) CRC handbook of chemistry and physics, 66th edn. CRC Press, Boca Raton
60. Aston GM, Stride JA, Jayasooriya UA, Reid ID (1997) The hyperfine coupling tensors of muonated radicals in single-crystal benzophenone. Hyperfine Interact 106:157–162
61. Rhodes CJ, Webster BC (1993) First observation of muoxyisopropyl radicals in a zeolite: Me_2COMu in NaX. J Chem Soc Faraday Trans 1283–1284
62. Keyser LF, Leu MT (1993) Surface-areas and porosities of ice-films used to simulate stratospheric clouds. J Colloid Interface Sci 155:137–145
63. Mihelcic D, Musgen, DKP, Patz HW, Volz-Thomas A (1993) Simultaneous measurements of peroxy and nitrate radicals at Schauinsland. J Atm Chem 16:313–335
64. Rhodes CJ (2000) Toxicology of the human environment - the critical role of free radicals. Taylor & Francis, London
65. Gulumian, M., Bhoolia, DJ, Theodorou, P, Rollin, HB, Pollak H, and Vanwyk JA.(1993) Parameters which determine the activity of the transition-metal iron in crocidolite asbestos – ESR, Mossbauer spectroscopic and iron mobilization studies. South Afr J Sci 89:405–409
66. Gulumian, M, et al. (1993) ESR and Mossbauer studies on detoxified crocidolite – mechanism of reduced toxicity. J Inorg Biochem 50:133–143
67. Gulumian M, Nkosibomvu ZL, Channa K, Pollak H (1997) Can microwave radiation at high temperatures reduce the toxicity of fibrous crocidolite asbestos? Env Health Perspec 105: 1041–1044
68. Ghio AJ, Kadiiska MB, Xiang QH, Mason RP (1998) In vivo evidence of free radical formation after asbestos instillation: an ESR spin trapping investigation. Free Rad Biol Med 24:11–17
69. Ottaviani MF, Venturi F (1996) Physicochemical study on the adsorption properties of asbestos. 1. EPR study on the sdsorption of organic radicals. J Phys Chem 100:265–273
70. Dalal, NS, Newman J, Pack D, Leonard S, Vallyathan V (1995) Hydroxyl radical generation by coal-mine dust – possible implication to coal-workers pneumoconiosis (CWP). Free Rad Biol Med 18: 11–20
71. Shi XL et al (1995) Antioxidant activity of tetrandrine and its inhibition of quartz-induced lipid-peroxidation. J Toxicol Environ Health 46:233–248
72. Shi XL, Flynn DC, Porter DW, Leonard SS., Vallyathan V, Castranova V (1997) Efficacy of taurine based compounds as hydroxyl radical scavengers in silica induced peroxidation. Ann Clin Lab Sci 27:365–374
73. Chen WM (2003) In: Lund A, Shiotani M (eds) EPR of free radicals in solids, trends in methods and applications. Kluwer Academic Publishers, Dordrecht

Chapter 8
Some Recent Developments of EPR Dosimetry

Nicola D. Yordanov, Veselka Gancheva, and Yordanka Karakirova

Abstract In the last three decades EPR spectrometry has expanded significantly in the field of practical applications. This is mainly due to its high sensitivity (10^{12}–10^{13} molecules, which means 10^{-11} to 10^{-12} M) and selectivity (it can discover "needle in hayrick"). Moreover, it is a non-destructive technique and in some cases samples may be kept as documents for future inspection. The aim of the present chapter is to highlight the current status, as well as the near future trends in development of Solid State /EPR dosimetry. The main subjects considered are the recent developments in SS/EPR dosimetry in standard and emergency accidental cases, identification of irradiated foodstuffs as well as new approaches to the extension of the period of identification by EPR.

8.1 Introduction

Despite the fact that EPR was discovered in 1944 [1] and that very intensive studies and development of the method have been done since then with regard to theoretical, methodical and instrumentation aspects, its technique has not been widely used for practical purposes. One of the main reasons for not exploiting such advantages as high selectivity, sensitivity and non-destructive analysis is the expensive, heavy, and sophisticated equipment required. On the other hand ionising radiation is used in the last few decades for many practical applications as for sterilization of medical and pharmaceutical products because of its ability to kill pathogenic microorganisms [2],

N.D. Yordanov (✉) • V. Gancheva • Y. Karakirova
National Center of EPR Spectroscopy, Institute of Catalysis, Bulgarian Academy of Sciences, 1113 Sofia, Bulgaria
e-mail: ndyepr@bas.bg

A. Lund and M. Shiotani (eds.), *EPR of Free Radicals in Solids II*, Progress in Theoretical Chemistry and Physics 25, DOI 10.1007/978-94-007-4887-3_8,

conservation of foodstuff products [3], modification of polymers [4] and so on. This increased application of ionising radiation needs reliable dosimetry systems which must fulfil some criteria: easy to use, fast to measure and low cost. The high energy radiation generates paramagnetic defects of free radicals in the matter which may be recorded by EPR. Nowadays, there are many different dosimetric methods for this purpose and among them EPR is the only method characterized by a simple and time saving procedure of dose estimation. Some methodical aspects for quantitative estimations were not well developed [5, 6] mainly because EPR spectrometry is not a calibrated method. However, some new approaches were recently developed to overcome these problems. It is possible to calibrate any EPR spectrometer and thus to compare the results obtained by different laboratories. Up to now, there are only four internationally recognised applications, all connected with the effects induced in the solid state by high-energy radiation. One of them is alanine/EPR dosimetry, which gives the possibility to estimate the absorbed dose of high-energy radiation by the alanine dosimeter [7–12]. The other three provide procedures for identification of irradiated foodstuffs containing cellulose [13], bone [14] and crystalline sugar [15]. There are many books and specialised meeting proceedings devoted to EPR. But the difficulties of its practical application are not, or very rarely, included in them although many authors are working to increase the applicability of these methods. Such problems are discussed only in a few specials reviews, books and meetings [16–22].

The aim of the present chapter is to highlight the present state, as well as the near future trends in the development of Solid State/EPR dosimetry. Three main subjects are considered – recent developments in SS/EPR dosimetry in standard applications, in emergency situations after an accident, as well as new approaches for the extension of the identification period of irradiated foodstuffs by EPR.

8.2 Principles of EPR Dosimetry as a Method for Estimation of the Absorbed Dose and for Post Radiation Processing Detection

EPR spectroscopy is a physical method which can be defined as the resonance absorption of microwave power by unpaired electron spins in the presence of a magnetic field. The objects of investigation with EPR are the paramagnetic species – thus in fact making it possible to record “a needle in a hayrick” because all other materials are not EPR active. On the other hand high energy radiation produces free (unpaired) electrons in matter some of which may be trapped by impurities as well as by inherent defects. They are usually very stable and can be accumulated with time. These unpaired electrons in organic or inorganic substances can be detected with EPR.

8.2.1 Formation of Paramagnetic Centres Upon Irradiation

The action of ionising radiation on matter primary yields charged particles (molecular ions and electrons) and excited molecules. In solid inorganic materials the liberated free electrons may be trapped by the crystal lattice whereas in solutions the solvent is also under irradiation and thus plays an important role in the overall process. In solid organic compounds, to which the present chapter is devoted, the primary active particles are transformed into free radicals and some final products of radiolysis.

In organic materials the free radicals can be generated by high energy irradiation as a result of the following reactions:

$$RH \rightarrow R^{\cdot} + H^{\cdot} \tag{8.1}$$

$$RH \rightarrow RH^{+} + e^{-} \tag{8.2}$$

$$RH^{+} + RH \rightarrow R^{\cdot} + RH_2^{+} \tag{8.3}$$

In other case free radicals may be produced by dissociation of excited molecules:

$$R' - R'' \rightarrow (R' - R'')^{\cdot} \rightarrow R'^{\cdot} + R''^{\cdot} \tag{8.4}$$

The stability of the free radicals depends on the state of the matter. The life-time of radiation induced free radicals is very short in liquids and solutions mainly due to Brown motion, whereas it can reach hundreds and thousands of years in solids.

8.2.2 Life-Time and Yield of Paramagnetic Centres ("G-Value") of a Given Irradiated Material: Minimal Detectable Absorbed Dose of Radiation by EPR

There are two main characteristics of the free radicals generated by ionising radiation of matter, which are important for dosimetric purposes:

- the life-time of the free radicals;
- the radiation sensitivity of the material i.e. the number of stable free radicals produced by the absorbed radiation per 100 eV which is the so called "G-value" of the matter.

The lifetime of the obtained free radicals of different materials varies over a very broad time scale – some of them recombine within a few milliseconds whereas others are stable for periods of several hundreds or thousands of years. The life-time depends on many factors such as the structure of the final free radicals, their ability to recombine in the solid state as well as on the conditions of their storage

(temperature, humidity, exposure to UV light, presence of O_2 etc.). Radiation sensitive materials for dosimeters should have the longest possible life-time. For example, free radicals of α-alanine are extremely stable in the solid state whereas β-alanine free radicals are not [23].

The other parameter, the G-value of the matter, gives information about the number of detected free radicals obtained by absorption of 100 eV ionising energy. G is equal to 1 if the number of free radicals produced by the absorbed dose of 1 Gy is 6.3×10^{16}/kg [17]. The G-value is specific for the material under investigation and its magnitude is usually determined for γ-radiation. The G-value data for alanine determined by different authors varies from 1.4 to 5 [24–30]. There is no explanation about the differences in the literature and it is assumed that radiation interacts directly with alanine molecules only. However, some factors not considered up to now may affect this interaction as, for example, the influence of the nature of binding materials and/or ingredients on the sensitivity of alanine/EPR dosimeters. These materials could be assumed to play a sensitising or an inhibiting role on the yield of paramagnetic centres by other processes. Another reason for the high dispersion of alanine G-value may be connected with the EPR technique. The problem is that until recently the quantitative aspects of EPR spectrometry were not well developed [5, 6]. Nowadays, there is some progress in this direction but it is not certain that quantitative EPR measurements give comparable results. At best, semi-quantitative or comparative EPR studies using reference standards are commonly accepted.

For heavy particles the G-value depends on particle identity, on their energy (LET) and typically is lower in comparison with gamma-rays. This is because whereas paramagnetic centres created by gamma-rays are randomly spread in the volume of the solid matter, the heavy particles make tracks in them with a very high number of closely situated paramagnetic species. This high density of paramagnetic species provides spin-spin interaction which facilitates recombination processes. On the other hand the liberated free electrons may interact with other molecules thus giving additional free radicals. For example the G-value of alanine estimated for fast neutrons is between 0.4 and 0.65 [31, 32]. In order to increase the EPR response (G-value) some authors add boric acid to the alanine pellet [33–36]. The method is based on the production of additional alanine free radicals caused by gamma-particles. The gamma particles are coming from the neutron capture ${}^{10}_{5}\mathrm{B}$ (n, gamma) ${}^{7}_{3}\mathrm{Li}$ reaction. It is reported [33, 34] that in this case the G-value is strongly dependent on the alanine/boric acid ratio. Increase in the EPR response between 20 and 40 times is observed.

The minimum detectable number of spins by the EPR spectrometer depends on its sensitivity, which for a commercial apparatus is ca. 10^{11} spins/mT. This value is valid for a point sample with dielectric constant $\varepsilon = 1$, situated in the middle of the EPR cavity with respect to the sample axis. The sensitivity profile of the EPR cavity is known [37] to have a bell shape along the sample axis with a maximum in the centre of the cavity, falling off to zero at the upper and bottom walls. However, real samples have finite dimensions and the spectrometer sensitivity depends on many other factors. These cannot be calculated, but recording of 5×10^{11} spins/mT in

one scan at a signal/noise ratio 2:1 can be considered as realistic. If we assume a 10 mm length and ca. 0.2 g weight of a dosimeter positioned in the centre of the cavity, irradiated with 1 Gy and $G = 1$, the expected number of spins is calculated to be ca. $0.2 \times 6.3 \times 10^{13}$ spins/mT $= 1.26 \times 10^{13}$ spins/mT. However, the spectral response, as for any spectral method is given by the area under the absorption line. Since the first derivative of the absorption line is used in EPR, the response (R) is given as the product of peak-to-peak intensity (I_R) and the square of the line width (ΔH) of the first derivative spectrum, i.e. $R \sim I_R\ (\Delta H)^2$. The line width of most of the radiation sensitive materials known up to now is at least 1 mT. Having this in mind, we can expect to obtain with $G = 1$ an EPR response of ca. 0.5 Gy radiation dose (at $\varepsilon = 1$). However, because for many materials $G > 1$ we can record even lower doses with one scan. Using spectra accumulation, the spectrometer sensitivity could be improved with increasing number of accumulated scans (n), whereas in the same time the intensity of the noise decreases with square root ($\sqrt{n}$). At present, it is assumed that for a radiation sensitive material with low dielectric constant an absorbed dose of 0.05 Gy could be detected without any difficulty.

8.3 Solid State/EPR Dosimeters

8.3.1 Earlier Studies

In 1962 Bradshow et al. [38] used for the first time α-alanine as a radiation detector. Thus, they opened the possibility to use alanine as a dosimetric material. Regulla and Defner [39] and other groups carried out intensive studies on this property of alanine. Alanine can be considered to be the best studied material in the field of Solid State/EPR dosimetry and at present it is formally accepted by IAEA [7–10], NIST [11] and NPL [12] (the abbreviations IAEA, NIST and NPL stand for International Atomic Energy Agency (Vienna, Austria), National Institute for Standards and Technology (USA) and National Physical Laboratory (UK)) as a secondary reference and transfer dosimeter for high (industrial) dose irradiation. The main advantages of the alanine dosimeter are the following:

- linear (within ±3%) EPR response in a wide range of doses - from 10 up to 5×10^4 Gy [40];
- high stability of the radiation induced free radicals under normal conditions;
- similarity to biological systems;
- simple and rapid data interpretation;
- no sample treatment before EPR measurement of the signal;
- cheap radiation detector that could be kept as a document.

The alanine dosimeter is currently produced in the form of pellets, rods, films and cables with different binding materials. However, there are various sources of uncertainties in the evaluation of absorbed dose, the main one being the necessity to

calibrate each EPR spectrometer and each batch of dosimeters before use. There is currently one method for estimation of absorbed dose in alanine/EPR dosimetry. According to this procedure each laboratory should have available for everyday calibration purposes a set of standards prepared from the same alanine dosimeter batches as those under study. These standards have to be irradiated in advance with known doses. Using these standards the EPR spectrometer is calibrated by preparing a calibration graph of the EPR intensity versus absorbed dose ($I_{\mathbf{alanine}}/D$) before measurement of an unknown sample. During the calibration and during all following measurements the EPR instrument's settings (P_{MW}, H_{mod}) must remain unchanged. (This calibration graph may be used only for the batch of dosimeters, EPR spectrometer and cavity used in the calibration. A different calibration graph will be valid for another spectrometer, cavity and/or other dosimeter batch.) Finally, the intensity of the EPR signal of the unknown sample is compared with the graph.

This procedure has several obvious disadvantages connected with the general problems of quantitative EPR measurements:

- the consecutive procedure which is used for dose estimation is not as precise as the simultaneous [5];
- every laboratory should have for everyday use a set of standards for every type (or batch) of dosimeters in use. Even with the use of similar standards, the results obtained in a given laboratory are typically not comparable with the results of other laboratories or other spectrometers in the same laboratory.

In order to overcome these disadvantages some authors have recently inserted a reference EPR standard permanently in the EPR spectrometer cavity and have simultaneously recorded the signals of alanine and standard [41–44]. The following parts of the procedure described above remain unchanged. In principle, simultaneous recording of EPR spectra of reference and unknown sample gives much better results [5] and the reproducibility and accuracy of the reading are increased. However, it is only valid for a given cavity and spectrometer. The results obtained with other cavities, spectrometers and settings, or laboratories remain still different. Having in mind these problems IAEA and NIST have offered dosimeters by mail-transfer service called "International Dose Assurance Service (IDAS)" [9, 12, 45, 46]. The overall procedure includes distribution of dosimeters by these organizations to the customers, which are sent back after irradiation for dose estimations and users receive the results. In this case the problem of calibration of EPR spectrometers is avoided. However, the procedure is concentrated in only a few laboratories and takes considerable time after the irradiation. The IDAS procedure is not for everyday use. It is only used for periodical calibrations or re-calibration of the irradiation units and after some reconstruction or changes in them.

A new generation of dosimeters, called "self-calibrated", was proposed [47–49]. Each pellet of these dosimeters incorporates radiation sensitive material, a quantity of EPR active substance and binding material. The incorporated EPR active substance acts as an internal standard permanently present in the dosimeter pellet and its signal is recorded together with the signal of the radiation sensitive material. In this way, the procedure for dose evaluation includes irradiation and simultaneous

recording of the EPR signals for both EPR active substances (standard and radiation sensitive material) in one pellet, the results do not depend on:

- the type of EPR cavity;
- the positioning of dosimeter pellet in it;
- the spectrometer used.

This is because the reading of this type of dosimeter is not a measurement of the intensity of the EPR line of the radiation sensitive material (I_{RS}), in our case the central line of alanine, but is given as the ratio of I_{RS} versus the EPR intensity of the internal standard (I_{ST}). The calibration of the ratio (I_{RS}/I_{ST}) for dose estimation may be directly obtained by one of the following two ways chosen by the operator, which may:

- irradiate in advance one or two self-calibrated dosimeters with a known dose (D, in Gy), estimate (I_{RS}/I_{ST})/D and find the ratio (I_{RS}/I_{ST}) per Gy, called "calibration coefficient" of the used dosimeter;
- ask the producer of alanine self-calibrated dosimeters to supply him with the dosimeter calibration coefficient.

Since the self-calibrated dosimeter may be kept as a document and its calibration constant (I_{RS}/I_{ST})/D as well as its response (I_{RS}/I_{ST}) are stored, it can be checked at any time without constructing a calibration graph in advance.

The materials used as the internal standard in the self-calibrated dosimeters have to satisfy some important requirements such as:

- to be EPR active before and after irradiation;
- to have radiation independent EPR response;
- to have easily and unambiguously distinguished EPR lines from alanine lines.

Mn^{2+} magnetically diluted in MgO has been used for this purpose because studies have shown [50] that after γ-irradiation (at room temperature) with doses up to 10^5 Gy the host lattice (MgO) is EPR silent. In addition no changes have been found in the intensity and other EPR parameters of the Mn^{2+} spectrum after γ-irradiation of an Mn^{2+}/MgO sample with doses up to 100 kGy. Mn^{2+} lines are narrow, easily and unambiguously distinguishable from those of the radiation sensitive material. The response of the described dosimeters for γ-rays in the range of absorbed dose from 100–50,000 Gy exhibits excellent linearity and reproducibility [47, 48].

Figure 8.1 shows the full EPR spectrum of the new self-calibrated alanine dosimeter. As seen from Fig. 8.1 it contains the six EPR lines of Mn^{2+} and those of alanine appear in the central part of the Mn^{2+} spectrum. Each of the following four Mn^{2+} lines (1, 2 or 5, 6) may be used for dose estimation.

Small portable fully computer controlled and cheap EPR spectrometers were commercially offered in the last two decades [40, 51–58]. The use of these spectrometers as dosimeter readers is a very attractive idea and the self-calibrated dosimeters were especially developed for them. These spectrometers are operating with a permanent magnet and magnetic field sweep is limited to 15–20 mT. The EPR

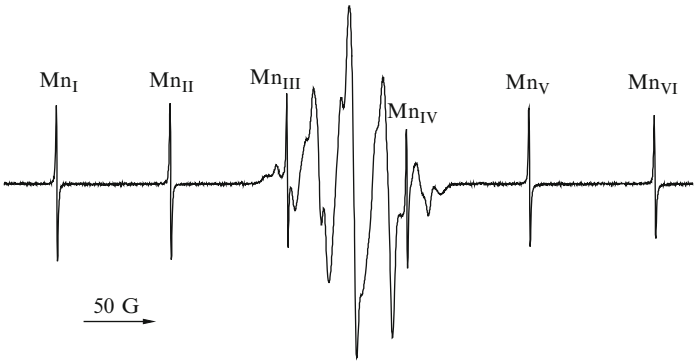

Fig. 8.1 EPR spectrum of irradiated self-calibrated alanine dosimeter (Adapted from Ref. [47] with kind permission of © Springer 1999)

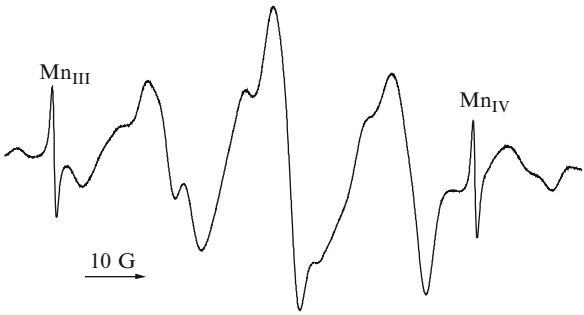

Fig. 8.2 Typical EPR spectrum for the new generation of alanine/EPR dosimeter

spectrum of the self-calibrated alanine dosimeter measured with them exhibits only part of its full spectrum including the alanine spectrum and two of the Mn^{2+} lines (3rd and 4th lines of Mn^{2+}) situated on both sides of the alanine spectrum (Fig. 8.2). The central alanine line, which is used for measurements, is not disturbed, but the 3rd and 4th lines of Mn^{2+} overlap with alanine wing lines. Recent attempts show that this effect can be overcome and very precise results can be obtained by considering the ratio ($I_{alanine}/I_{Standard}$) [47], where $I_{Standard} = (I_3 + I_4)/2$, and I_3, I_4 are the 3rd and 4th lines of Mn^{2+}).

Because after irradiation self-calibrated dosimeters contain two EPR active substances, the EPR instrumental setting parameters and conditions for simultaneous recording of undistorted spectra of both substances become important. The studies in this direction [48] have shown that an undistorted spectrum of both substances could be obtained if microwave power is less than 1 mW and modulation amplitude is less than 0.5 mT. Using these parameters it is possible to perform intercomparison with data obtained by other instruments or laboratories. Higher sensitivity can be achieved by consecutive recording of two separate spectra in the same pellet – that

of Mn^{2+} using the above parameters in order to reach a basis for the calibration and after that the alanine free radical using increased spectrometer gain, modulation amplitude and microwave power. All these parameters have to be calibrated in advance.

The advantages of the self-calibrated dosimeters were demonstrated during an International intercomparison trial [48] in which six laboratories from Europe were supplied with these dosimeters and asked to:

- irradiate them with a known dose;
- record the EPR response using the above EPR instrumental settings ($P < 1$ mW, $H_{mod} < 0.5$ mT) on their spectrometers (without any restriction in respect to the used cavities);
- estimate the ratio ($I_{alanine}/I_{Standard}$);
- report the obtained results.

The results of two international trials obtained by several laboratories and different spectrometers equipped with different EPR cavities were of extremely high precision for such international comparison trials – statistical processing of all independent measurements showed a standard deviation of 0.3% [48, 59]. All this confirms the advantages and flexibility of the self-calibrated SS/EPR dosimeters because they may be used without any limitations with respect to spectrometer and operator experience.

Dosimeters of this type are usable for calibration of the source of radiation itself as well as for everyday routine use and it is not necessary to calibrate the spectrometer before every reading. Moreover, they can be used several times because each new absorbed dose is added to the previous and can be recorded with only one scan. They may be kept as documents and re-examined at any time with only one recording of the spectrum. And finally, they work with equal accuracy for all kinds of EPR spectrometers.

Another attempt to improve the accuracy of absorbed dose estimations has been proposed by Internet calibration service for the radiation processing industry [60, private communication]. The Internet-based transfer calibration service is developed by NIST, in collaboration with Bruker Biospin. It is designed especially for alanine pellets and film shaped dosimeters. The special feature of the EPR reader is the permanently installed reference standard (ruby) in its cavity. The absorbed dose calibration is performed by two different sets of pre-irradiated dosimeters - one for pellets and the other for film shaped dosimeters (*vide supra*). Thus all calibrations and measurements are performed using the reference standard. The server, with which the readers are connected, keeps in memory the data from all of them and in this way the estimations become comparable. This is similar to the IDAS procedure. The difference is in the simultaneous recording of the reference standard with pre-irradiated dosimeters or with unknown sample and the presentation of results not as $I_{alanine}/D$ but as a ratio $I_{alanine}/I_{Standard})/D$ (*vide supra*). In this way the accuracy of the estimations of the different readers is increased. This sub-procedure has some disadvantages because the customers have to:

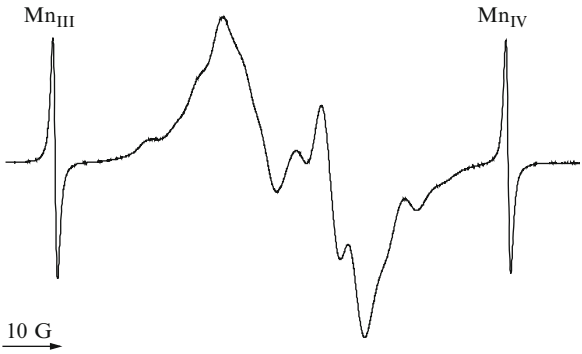

Fig. 8.3 EPR spectrum of irradiated self-calibrated sugar dosimeter (Adapted from Ref. [61] with kind permission of © Elsevier 2002)

- subscribe to the NIST service;
- use only certain types of dosimeters and pre-irradiated standards recommended by NIST;
- obtain new EPR readers from a given producer;
- pay for each dose point.

Another problem is that this procedure will be usable in only some countries but not yet all over the world. And finally, it could result in some kind of monopoly in this area.

Up to that moment SS/EPR dosimeters have received wide application for high dose radiation. Alanine/EPR dosimeters are very successfully used for estimation of γ-ray doses in the region of 50–100,000 Gy. The published data, reviewed above, suggest increased accuracy of dose measurement and acceptable intercomparison of the results.

During the last two decades a new self-calibrated dosimeter was constructed containing sugar [61] as radiation sensitive material. The EPR spectrum of this radiation sensitive material (Fig. 8.3) has narrower spectral with thus avoiding overlapping with the Mn^{2+} lines.

Sugar is widely used as dosimetric material in accidental EPR dosimetry. It is characterized by the absence of background signal before irradiation, and an easy preparation of dosimeters without any need of preliminary treatment [62–67]. Furthermore, another advantage is that sugar is a tissue equivalent material, easily found at accident sites and provides a stable and dose dependent signal, which is linear in a wide dose range. In view of this, the EPR spectrum of sugar, generated by gamma rays (63, 64, 68, 71–75) as well as by heavy particle irradiation [77–82] has been investigated by many scientists [64–66, 68–70]. The identical EPR spectra obtained after gamma- or heavy particle irradiation of sucrose suggest the formation of the same radiation induced stable free radicals. The EPR response of sucrose was found to be linear to the changes of absorbed dose radiation and logarithmical to LET [79, 81, 82]. The above studies and also the stable radiation generated of the free radicals suggest it as a very promising material for dosimetric purposes.

8.3.2 Recent Developments in the Independent Calibration of SS/EPR Dosimeters Using UV Spectroscopy

As mentioned, high energy radiation generates in the organic matter free radicals, which are trapped in the solid matrix or recombine to give new diamagnetic species with different properties, as color, for example. The solid state effects are stable with the time and can be used for dose estimation using for example solid state electron spectroscopy (SS/ES). In most cases radiation induced color disappears upon dissolution of the solid material, but this is not the case with sugar. The studies [61] show that the absorption at 267 nm appearing in irradiated sugar, linearly depends after its dissolution in water on the absorbed dose of high energy radiation [61, 74]. It was also found that the absorption maximum is time dependent and the UV absorption slowly increases with *ca*. 20% in the first 10 days after dissolution to reach a steady value. The same increase is reached after 1 h heating of the water solution at 70°C [73]. Studies [73] show that the UV response coefficient of 1% sucrose solution in 1 cm sample cell is 0.0055/kGy. Since the resolution of the absorbance axis of the used spectrophotometer is 0.03, with a sample cell of 5 cm and solution concentration up to 20%, the detection limit of the absorbed dose gamma rays may be around 55 Gy. The correlation between EPR of irradiated solid sucrose and UV response of its water solution shows excellent linearity. It opens a new possibility using UV spectrometry of water solution of irradiated sucrose to calibrate the SS/EPR sugar dosimeter. Moreover, it may be used for calibration of any SS/EPR dosimeter containing other radiation sensitive materials, say alanine. For this purpose these dosimeters should be simultaneously irradiated with sucrose. The procedure then includes dissolution of sucrose in water, 1 h heating at 70°C and recording its UV absorption at 267 nm against non-irradiated sample. The actual irradiation dose is estimated using the UV dose response and the obtained value is correlated with the intensity of the EPR spectrum of the SS/EPR dosimeter irradiated with the same dose [5].

8.3.3 Recent Developments in the SS/EPR Dosimeters by Irradiation of Heavy Particles

When ionizing heavy particles hit the matter, its molecules are excited, ionizated, free radicals and secondary electrons (delta rays) are produced. Different types of ionizing radiations have different track structures when passing through the material [76]. While primary generated free radicals are situated close to each other in the track of the particle and recombine, secondary electrons are mainly thought to produce free radicals at the target sites. There are several studies investigating sucrose, irradiated with heavy particles [77–84]. The obtained results show that EPR spectra generated in solid sucrose after irradiation with heavy ions are identical with those generated by gamma-rays, thus suggesting the same nature of the radiation-induced free radicals in them. Linear dependence of EPR intensity of

irradiated solid sucrose is found as a function of absorbed dose of heavy particles. It is also found that the EPR response of sucrose and alanine show a linear energy transfer (LET) dependence as well as particle dependence. [78, 79, 81]. Free radical yields in the irradiated samples decrease with increasing LET value of the heavy ion. It is noted that the number of alanine molecules were ∼3.8 times higher than that of sucrose [85].

A difference in the EPR response of sucrose irradiated with heavy ions was found for different ions with practically equal LET, which can be explained with the weight of the ions, but in all cases it is lower than that obtained for gamma rays [83, 84]. The linear response of the UV band intensity of aqueous solution of solid sucrose irradiated with heavy ions is higher than that irradiated with gamma rays. The linear dependence between UV and EPR spectral data for a given irradiating particle and LET opens a new simple way for calibration of the latter. However, more additional data are necessary to justify this possibility [82–84].

8.4 Trends in the Future Studies on SS/EPR Dosimetries

The following directions could be expected to develop in the near future connected with:

- increasing the sensitivity of the method and especially for the low doses (0.5–10 Gy) used in human radiation therapy;
- searching for alternatives to alanine and sucrose as a radiation sensitive material;
- increasing the EPR response of the radiation sensitive material with respect to high-LET radiation such as protons, neutrons, α- and β-rays as well as different heavy particles;
- obtaining of calibration coefficients for irradiation with various heavy particles;
- expanding the application of UV spectrometry or other methods in order to calibrate the EPR.

8.4.1 Estimations of Low Absorbed Dose Used in the Human Radiation Therapy by SS/EPR Dosimetry

Use of the alanine/EPR dosimeter was reported for the first time in 1984 for estimations of absorbed doses below 10 Gy [86] and there are several papers on this topic after that time [87–90]. Because the irradiation of humans must be carefully controlled, measurements must be very precise and the applicability of alanine is under question for estimation of low dose.

Although alanine is a very suitable radiation sensitive material it has some disadvantages particularly for low dose dosimetry:

- Only its central line is used for dosimetric purposes. As mentioned before, the alanine EPR spectrum consists of five quasi-isotropic lines with intensity

distribution 1:4:6:4:1. Using only the central line for dosimetric purposes we employ the fraction 6/16 of its radiation induced EPR response. On the other hand integration of the full EPR spectrum in order to get full EPR response is connected with some uncertainties because the spectrometer gain is high at low doses thus giving rise to noise and base line drift;

- Very often a background signal appears from alanine itself and from the binding material, as a result of high temperature and/or pressure treatment during the preparation of the dosimeters or from the spectrometer. Because the induced EPR response of alanine dosimeters is weak at low doses and overlaps with this background signal of the dosimeter [91, 92], computer-aided procedures for subtraction of the background signal from alanine response are used [39] to find the neat EPR response. Nevertheless, all stated problems still remain. Subtracting of the background signal is also connected with some uncertainties, especially at low doses.

8.4.2 Searching for New Radiation Sensitive Materials

There are several very promising studies on new radiation sensitive materials, for example on various type of saccharides [93], acetates, phosphates and lactates [94–96], ammonium tartarate [97, 98], anhydrous $MgSO_4$ [99, 100], alkaline-earth metal dithionates, $MeS_2O_6.xH_2O$, [101–103], Li_2CO_3 and $CaSO_4$ [104], etc. Recent investigations have shown that some of them are two to three times more sensitive than alanine [105]. At equal EPR spectrometer settings the increased sensitivity is attributed mainly to a more suitable EPR spectrum with narrow lines and small (or absent) hyperfine splitting [105]. It may be expected that screening of other materials will improve the sensitivity of SS/EPR dosimetry towards low ($D \leq 10$ Gy) absorbed doses.

Studies on some additives assuming the role of sensitizers for the radiation sensitive materials can also be considered as a promising direction for future studies.

Dosimeters devoted principally to industrial purposes have to be cheap. However, this is not the case for dosimeters used for estimation of low doses (0.5–10 Gy). Because of the application of some expensive radiation sensitive materials for the measurement of absorbed doses used in radiation therapy, approaches for their regeneration after a given cycle of irradiation can be considered as a promising direction for future work.

8.4.3 Instrumentation

Up to now EPR spectrometers or readers working in X-band were used for dosimetric purposes. These spectrometers have high sensitivity, depending on the dielectric constant of the sample, and are relatively expensive. The diameter of the

dosimeter species used in these spectrometers is limited to maximum 5 mm. If they are in the form of pellets their length is between 3 and 10 mm, or if they have a rod shape the length is maximally 40 mm. The third option, film shaped dosimeters, have a width of maximum 5–6 mm and thickness less than 0.5 mm. Keeping in mind these limitations it may be assumed that other EPR spectrometers (or readers) working at lower frequency for example S- or L-band (3 or 1 GHz) will be more useful. Such spectrometers are cheaper and not so heavy because the magnetic field (obtained by iron magnet and/or with only Helmholtz coils) at which they work is lower, and this makes them portable. The loss of sensitivity, compared to the X-band, may be compensated by the increased sample dimensions, and especially of the dosimeter diameter.

8.5 Identification of Radiation Processing of Foodstuffs by EPR

Radiation processing was advocated for sterilising of arterial [106] and bone grafts [107] in the beginning of 1950. In the next 20–30 years its application was extended to foodstuffs and now it is considered as a clean, inexpensive and effective method for sterilisation. However, recombination processes of the free radicals formed in the food during irradiation generate new, unknown chemical substances with unknown effects with regard to human health. For this reason, radiation processing, import and export of irradiated foodstuffs is forbidden in some countries. It is worthwhile noting that currently there is no evidence of any hazard for living organisms consuming irradiated foodstuffs. However, the simple fact of the presence of unknown substances in the irradiated foodstuffs justifies the necessity for control of radiation processing. Reviews [108–110], as well as books [21, 22] describing different methods used for identification of irradiated foodstuffs have been published. Finally, after many studies, the European Community Bureau of Reference concerted action [111] led to protocols, which were adopted in 1996 by the European Committee of Normalisation and published in the beginning of 1997 [13, 14, 112–114]. Three of these Protocols [13, 14, 15] use EPR, the first one for cellulose, the second for bone containing foodstuffs and third for foods containing crystalline sugar. Following these Protocols the problem which has to be solved by EPR is on a qualitative level – whether an appropriate food sample has been irradiated or not. In the case of samples containing hard tissues qualitative estimation of the absorbed dose of γ-rays by EPR is unambiguous because the radiation generated signals are extremely stable with time. Moreover, it is possible to estimate the magnitude of the absorbed dose by the methods applied in post-irradiation dosimetry (*vide infra*). However this is not the case with cellulose containing foodstuffs because radiation generated EPR signals can be recorded only during a limited period of time. In view of this, some new approaches were recently developed for extension of the identification period of irradiated cellulose containing foodstuffs by EPR.

Fig. 8.4 EPR spectrum of sea shell of the family of *Ostrea SP* recorded before irradiation

8.5.1 Detection of Irradiated Foods Containing Hard Tissues

The hard tissues are bio-minerals consisting of inorganic and organic part. The inorganic part of bones and teeth contains hydroxyapatite. The structure of hydroxyapatite, $Ca_{10}(PO_4)_6(OH)_2$, may be changed by replacing its cation and/or anion by other ions. For example Ca^{2+} can be replaced by Mg^{2+}, Fe^{2+} Mn^{2+}, Sr^{2+}, etc., $PO_4{}^{3-}$ by divalent $CO_3{}^{2-}$ or $SO_4{}^{2-}$ and OH^- by $CO_2{}^-$, monovalent anions or even neutral H_2O. Shells contain $CaCO_3$ as a mineral part in which Ca^{2+} can be replaced by other ions (*vide supra)* and $CO_3{}^{2-}$ by $SO_3{}^{2-}$. The organic part of bones is the collagene and that of shells is conchiolin. Teeth consist of enamel, dentine and cement. Enamel contains mainly hydroxyapatite and a few percents of organic material.

Thus, impurities sometimes appearing in hard tissues may have an effect on the formation of paramagnetic species upon irradiation and increase or decrease of the EPR response due to their presence cannot be excluded. In most cases before irradiation there are no observable EPR signals in hard tissues such as meat bones [115–117] and sea shell [118–121], egg [121–124] and snail [125] shells. However, there are some exceptions, like the EPR spectrum in Fig. 8.4 of a sea shell from the family *Ostrea SP* recorded before irradiation with significant contamination of Mn^{2+} ions [121] which does not interfere with the radiation induced EPR signal. (It is worth noting that there is no internationally accepted protocol for identification of previous radiation treatment of molluscs and shell containing foods.)

After irradiation of bone an anisotropic EPR signal with $g_{\parallel} = 1.996$ and $g_{\perp} = 2.002$ appears due to radiation induced $CO_2{}^-$ free radicals [14, 115–117]. The signal is stable if the bone is kept cold, dried or boiled [117]. The bone EPR signal exhibits some angular dependence with respect to the positioning of the sample towards the magnetic field (Fig. 8.5) [117] but its presence in the bone piece is unambiguous evidence of previous radiation treatment of the meat.

The EPR signals appearing after irradiation of fish bones are not stable. They disappear shortly after the radiation processing [126].

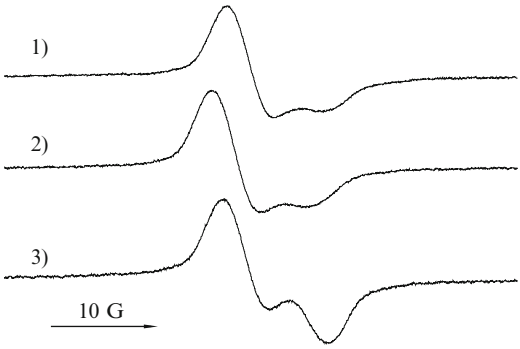

Fig. 8.5 EPR spectra of irradiated bone: *1* without any treatment, *2* dried and *3* boiled and dried (D = 8 kGy) (Adapted from Ref. [117] with kind permission of © Elsevier 1998)

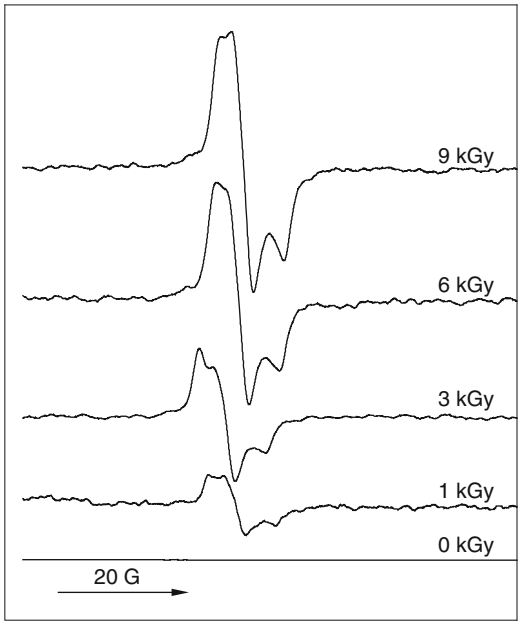

Fig. 8.6 A typical set of EPR spectra of sea snails before and after irradiation

In calcified tissues of molluscs, snails (Fig. 8.6) and eggshells (Fig. 8.7), the radiation induced EPR signal is complex, suggesting three different EPR active species. They are characterised by the following parameters: $g_1 = 2.0055$, $g_2 = 2.003$, $g_3 = 2.002$, $g_z = 1.996$ [121–125]. These EPR signals are attributed to SO_2^- (isotropic signal with $g = 2.0055$ [127]) and SO_3^- (isotropic with $g = 2.003$ [127, 128] and anisotropic with $g_z = 1.996$, $g_1 = 2.002$ and $g_2 = 2.000$ [129, 130]) free radicals [131] and have long lifetimes. The presence of such EPR signals is considered as unambiguous evidence for previous radiation treatment.

It is worth noting that EPR has a big advantage in identification of previously irradiated foods containing hard tissues since there is no need of special procedures for sample preparation, one measurement takes only 30 min and it is unambiguous.

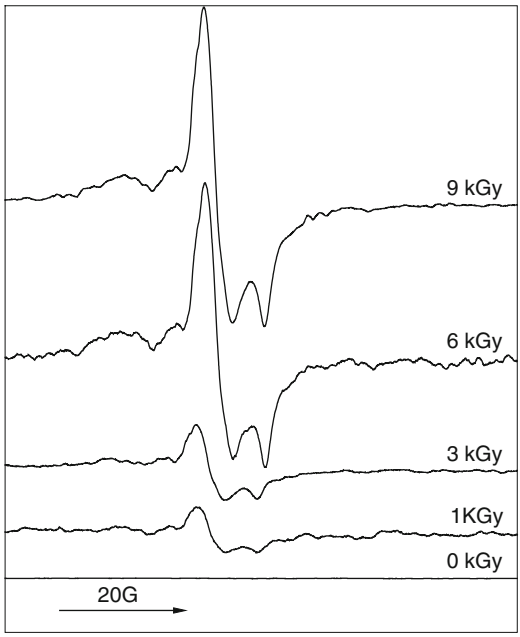

Fig. 8.7 A set of EPR spectra of egg shells before and after irradiation with doses between 1 and 9 kGy

The recommended alternative method, gas chromatography [112–114], is not useful in routine practice because it is complicated, time consuming (it needs c.a. 72 h) and expensive [117].

8.5.2 Detection of Irradiated Cellulose Containing Foods

Before irradiation, cellulose containing food samples exhibit only a weak EPR signal with $g = 2.0050 \pm 0.0005$ and line width of ca. 0.6 mT (Fig. 8.8 (1)) [132, 133]. After irradiation there is a significant increase in the amplitude of this signal with simultaneous appearance of a pair of weak lines on both sides (Fig. 8.8 (2)).

These two satellite lines [13], attributed to cellulose free radicals generated by radiation [13, 132], are considered to be unambiguous evidence of previous radiation processing. However, the applicability of this procedure is strongly limited by the lifetime of the radiation-induced free radicals. The main problem is that the satellite lines are relatively weak and disappear within a few weeks or months depending on storage conditions [133, 134]. Therefore, after this period EPR cannot give any information about the radiation history of the sample under investigation. In such case thermoluminescence analysis has to be used but it is not suitable for routine use because it is a time-consuming procedure – one measurement needs 72 h including one additional irradiation of the sample [135], which complicates the problem.

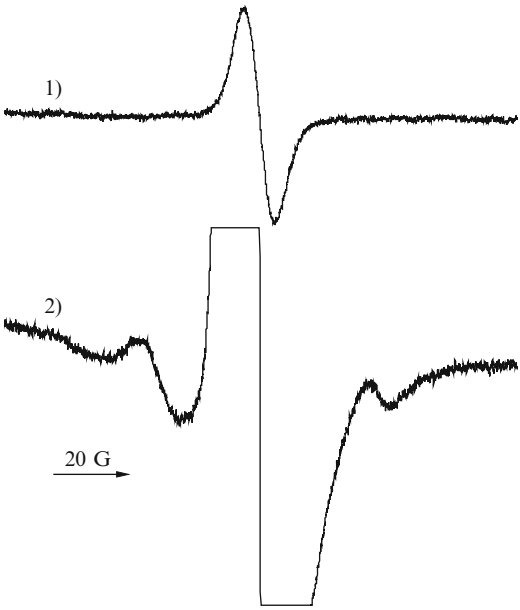

Fig. 8.8 EPR spectra of cellulose containing food: *1* before and *2* after irradiation (Adapted from Ref. [135] with kind permission of © Elsevier 1998)

8.5.3 New Approach for Extension the Period for Identification of Irradiated Cellulose Containing Foodstuffs

To overcome the time limit problem a new approach for extending the period of identification of irradiated cellulose containing foodstuffs using EPR was recently published [133]. It considers the intensity of the central line ($g = 2.0050$) which strongly increases after irradiation and remains enormously high for much longer periods of time than both radiation induced satellite lines. According to this approach, after the disappearance of the satellite lines, the sample is inserted into a special EPR quartz sample tube containing in the bottom a finger filled with Mn^{2+}/MgO [50, 133] used as a reference standard (Fig. 8.9) and the EPR spectrum is recorded.

The intensity of the central line (I_{SA}) of the foodstuff is compared with that of a given Mn^{2+} line (I_{ST}) thus obtaining the ratio (I_{SA}/I_{ST}). Then the sample tube with the material under investigation is transferred to a standard laboratory drying unit equipped with a high precision ($\pm 0.1°$) thermometer and is heated for 1 h at 60°C. After the sample has reached room temperature the EPR spectrum is recorded again and the ratio of the intensities of the same lines (I_{SA}/I_{ST}) are compared. For previously irradiated samples there is ca. 50–70% decrease of the ratio I_{SA}/I_{ST} and for non-irradiated samples the decrease of the ratio I_{SA}/I_{ST} is ca. 10–20% (Fig. 8.10). Therefore, more than 40–50% decrease of the ratio I_{SA}/I_{ST} after the described procedure is unambiguous evidence of previous radiation treatment of the sample under investigation. In this way the period of identification can be increased ca. 2–3 times.

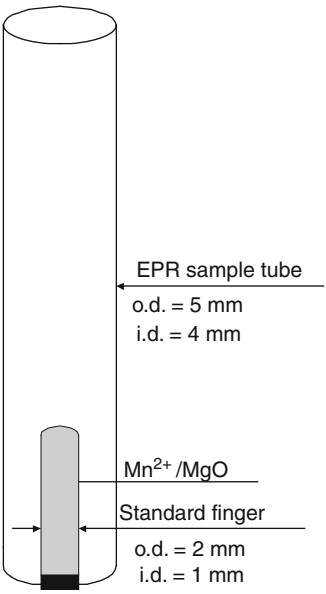

Fig. 8.9 Sketch of the EPR tube used for the simultaneous recording and processing of herb samples (Adapted from Ref. [133] with kind permission of © Elsevier 2000)

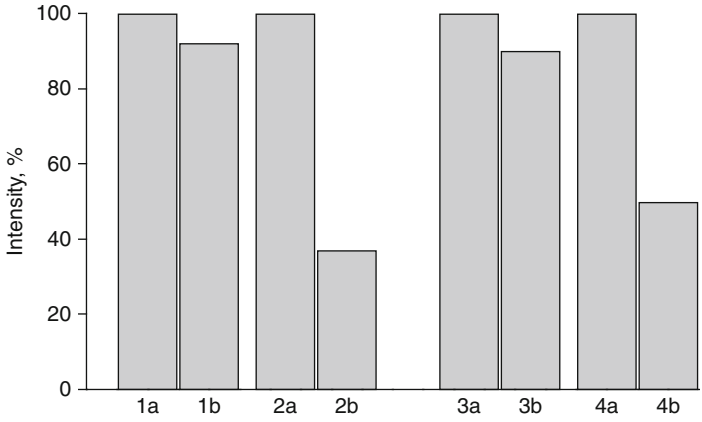

Fig. 8.10 Ratio of intensity of the sample vs. the intensity of Mn^{2+} (1) non-irradiated white pepper, (2) irradiated white pepper, (3) non-irradiated hot paprika, (4) irradiated hot paprika, (a) before and (b) after heating (Adapted from Ref. [133] with kind permission of © Elsevier 2000)

The described method [133, 134] is very easily performed but it is worth noting that it is strongly dependent on the conditions under which the samples of the foodstuff under study are kept after the radiation processing. The most critical factors are the humidity and temperature of the room in which they are stored and also the packing material – paper, polyethylene, etc. In spite of this disadvantage

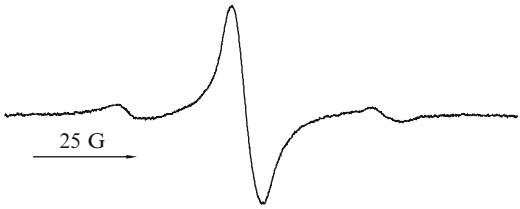

Fig. 8.11 EPR spectra of shelled fruit 1 year after irradiation (Adapted from Ref. [134] with kind permission of © Elsevier 2000)

the recommendation is first to use the EPR procedure and only if the results are not clear to use thermoluminescence.

In the case of fruits having a shell or containing pits the characteristic radiation induced EPR signal (Fig. 8.11) remains unchanged for more than 1 year [134].

8.6 Detection of Pharmaceuticals Sterilized by High Energy Radiation

In the last years ionizing radiation has attracted increasing interest as a method for sterilization of medical devices as well as for improvement of the hygienic quality of pharmaceuticals [136–139]. The major advantage of radio sterilization is that it is carried out in their final packing and keeps them sterile until their use. It is a preferable method, especially in the case of heat-sensitive drugs. On the other hand, apart from the microbiological aspect of sterilization by irradiation the problems with the radiolytic products and their pharmacological and toxicological action should be considered. According to the regulations of the European Community the radiation treatment of drugs is accepted only in cases when no toxicological hazard is possible [140]. At the moment the maximal allowable dose in the case of medical devices and drug sterilization is 25 kGy. To prevent the unauthorized and uncontrolled use of radiation processing a suitable method for distinguishing between irradiated and non-irradiated drugs is needed. The studies performed on some irradiated drugs have shown the applicability of EPR spectroscopy as a method for detection.

Intensive studies on the ionizing radiation effect on cephalosporins have been done, because of their susceptibility to degradation and their sensitivity to irradiation [141–144]. On the other hand cephalosporins are thermosensitive and can be regarded as potential candidates for non-authorized radiation treatment.

Investigation on cephradine has shown the non-feasibility of radiation sterilisation of this substance because of the formation of foreign products and long-lived free radicals [144]. In the case of radiation treated powder samples of cefuroxime and cefotaxime a composite EPR signal which is a superposition of a singlet and a weak multiplet, mostly hidden by the singlet, has been detected [143]. The different dependence of the singlet and multiplet lines on the microwave power suggests the presence of two different paramagnetic centres. The studies on the fading of the

radiation induced free radicals have shown that they are more stable in cefotaxime than in cefuroxime. After 150 days of storage at low temperature and darkness the fading of the intensity of the singlet line is 30% for cefotaxime and 70% for cefuroxime.

Extended studies on the effect of radiosterilization on ceftazidime carried out at 4.2–295 K have been done using EPR. Three types of free radicals were detected. The first one giving a septet signal in the EPR spectrum and decaying at 230 K has been attributed to the $\bullet C(CH_3)_2COOH$ radical. The second one with a triplet spectrum and decay at 293 K has been assigned to the iminoxyl radical (>C=N—O•). The third one presents a broad singlet line and remains unchanged at 295 K [139]. It was also found that the yields of free radicals in irradiated ceftazidime increase linearly with dose of irradiation up to 10 kGy both at 77 and 295 K. Half of the free radicals giving the broad singlet line decay upon storage at 277 K after 50 days. Nevertheless, after 160 days of storage at the same conditions it is still possible to observe the broad singlet EPR spectrum of irradiated ceftazidime [141].

The EPR spectrum of irradiated ampicilin consists of a broad doublet signal [142]. The shape of the spectra of ampicilin irradiated with 12.5 kGy does not change upon storage at 277 K for 140 days but the intensity of the lines decreases to ca. 60% of the initial intensity recorded immediately after the irradiation. The radical yield measured just after the irradiation at 295 K increases linearly with dose up to 12.5 kGy and slightly deviates from linearity above 12.5 kGy.

The initial results started an extensive study on a large number of irradiated antibiotics belonging to the group of cephalosporins [145]. Radiation induced EPR signals have been detected for 12 out of 13 cephalosporines irradiated with a 25 kGy dose. Only in the case of non-irradiated cefaclor a weak signal of the same shape as in the irradiated one has been recorded. The studies on the fading of the EPR signal have shown that the stability of the created free radicals in all investigated samples is comparable to the shelf life of the antibiotics when stored under the proper conditions.

Recently an EPR study on five antibiotics belonging to the groups of cephalosporins and penicillins has been carried out [146]. The influence of irradiation and storage conditions on the concentration of the radiation induced free radicals has been investigated. The samples irradiated at 77 K as well as at room temperature have shown complex EPR spectra. The influence of different factors such as: radiation dose, microwave power, temperature and storage time vary from one EPR signal to another indicating the presence of mixture of radicals in every irradiated antibiotic.

EPR spectroscopy has also been applied to study the effect of gamma rays on three nitronimidazoles [147]. The nonirradiated samples did not show any signal. After irradiation with gamma rays at a dose of 25 kGy stable paramagnetic centers were detected only in ornidazole and metronidazole samples. The intensity and the shape for both substances were similar. It was found that a significant portion of the created free radicals decayed in several days after irradiation, whereas 35 and 10%

of the initial radicals respectively in metronidazole and ornidazole could be detected after 135 days of storage.

High performance liquid chromatography (HPLC) and EPR spectrometry have been used to study the degradation of theodrenaline after gamma radiation treatment [148]. The effect of storage on the free radical concentration was studied.

Free radicals induced in drugs and excipients by radiation and mechanical treatments have been studied by EPR [149]. Special attention is focused on the use of this method as well as other methods such as thermoluminescence and gas chromatography as proof of radiation treatment of drugs.

Different substances belonging to the groups of cytostatic, anti-carcinogenic, blood circulation regulating and other drugs have been investigated before and after irradiation with high-energy irradiation. Weak EPR signals were detected in 3 of 15 non-irradiated polycrystalline samples. The EPR measurements have shown that the radiation induced radicals in all examined drugs can be detected after 4 and 8 weeks of storage. The authors also made some suggestions about the structure of the observed radical species [150].

8.7 Emergency Dosimetry

Nuclear technologies were developed during the World War II but the risk of their use was recognised many years before. Now they are considered safe and secure operations. Many different dosimetric techniques have been developed and used for control purposes during normal work as well as in the cases of accidents. The characteristic feature of an accident is that the dose of ionising radiation absorbed by the victims is unknown and as a rule it is over the limits of the personal monitors used every day at normal conditions. In these cases the method of EPR dosimetry may be, and is, helpful for reconstruction of the absorbed dose.

The commonly accepted procedure for estimation of the absorbed dose by EPR in the cases of post-radiation dosimetry is the method of the "additional"dose. It is based on the assumption that the EPR response is zero before irradiation [17, 151]. The procedure is as follows: The EPR response (R_x) due to the unknown, accidental, radiation dose (D_x) absorbed by the sample is measured at the beginning. After that, without any changes or treatments, the sample is additionally irradiated several (j) times with some well known doses (ΔD_j, $x \leq j \leq i$) and after every irradiation the new EPR response ($R_j = R_x + \Sigma \Delta R_j$) is estimated. Then, the obtained data points, D_x and all ΔD_j, are plotted on the abscissa axis in Gy, starting with D_x, in such a way that every incremental difference ($\Delta D_{j+1} - \Delta D_j$) may be used for calibration of the abscissa. The corresponding magnitudes of the EPR response, $R_j = R_x + \Sigma \Delta R_j$ at each data point D_x and ΔD_j, are plotted on the ordinate in arbitrary units (Fig. 8.12).

Initially it is not known where the origin of the co-ordinate system $R = f(D)$ is positioned. The extrapolation of the data points of R to the zero ordinate (using the least-square fitting method) gives the origin of the co-ordinate system $R = f(D)$. Finally, the difference between it and the point marked with D_x gives the

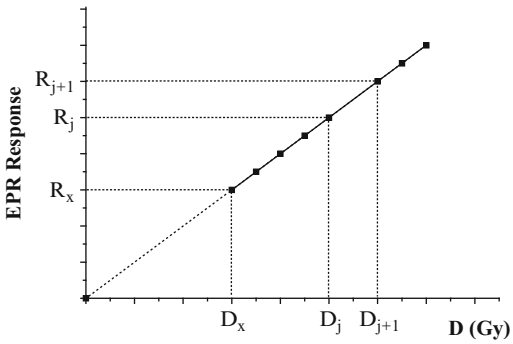

Fig. 8.12 Graph representing the method of "additional" dose, used in post-radiation dosimetry

magnitude of accidental radiation dose D_x. In general, there are two types of such reconstruction graphs – linear or approximately linear at the beginning and with saturation at high doses. This is the reason that the number of data points for the additional irradiations (j) must be between 5 and 10.

The application of EPR for accidental irradiation, especially for X- or gamma rays, was proposed for the first time in 1965 [115, 116]. After that many studies were reported mainly on the survivors of the A-bomb radiation at Hiroshima and Nagasaki by using the EPR response of shell buttons, tooth enamel and quartz grains [17]. Other accidents, with a local character, were also investigated using EPR [152, 153].

In 1986 the Chernobyl disaster appeared and after that other local accidents were also described in the literature (for example [154–158]). It was a turning point for the acceleration of emergency dosimetry. Thus after Chernobyl the application of EPR in the field of emergency dosimetry became extremely useful. Now there are numerous investigations devoted to the emergency EPR dosimetry. Many different materials as tooth enamel [17, 159–162], bones [163] shell buttons [17, 164, 165], clothing [165–168], some fabrics [165–167], fingernails and hair [165,166, 169–172], pharmaceuticals [17, 152, 166], sugar [64–66, 166], quartz grains in the rocks or house building materials [17, 173–175], etc. have been tested as EPR post-radiation dosimeters. All these materials have potential use in emergency cases but among them shell buttons, sugar and tooth enamel exhibit long-lived radiation induced EPR signals. For clothing the radiation induced EPR signal disappears very shortly after irradiation, whereas the EPR response of fingernails in addition to being short lived is dependent on the particle size [171, 172]. Recently most of the studies are concerned mainly with tooth enamel. This is because the studies have shown that tooth enamel is the only living tissue which retains indefinitely its radiation history, and EPR can record a radiation signal down to 10 cGy. Moreover, the EPR active defects in tooth enamel from the extracted teeth exhibit extremely long life-times calculated to be up to 10^7 years [176] and may be used as personal cumulative radiation dosimeter for the staff working at nuclear facilities. Thus, tooth enamel has been used for estimation of the radiation doses from individuals exposed to A-bomb radiation at Hiroshima and Nagasaki [17], in the Chernobyl accident [17, 177–180],

at the uranium processing plant Mayak in the USSR [181] and in the Ural region [182]. Extracted and irradiated *in vitro* bone (grafts) has a long life-time of the radiation induced EPR signal, but after implantation in living organisms the signal disappears within a few months [183]. Usually the investigations of the accidental cases are performed immediately after it happened. So, the bone EPR dosimetry is fully usable (the problem is only that it is invasive). Recently such an effect was also reported for the tooth EPR response [184]. In addition, sugar samples collected from different places around the accident site have been used for dose examination at Chernobyl [185] and the JCO uranium facility in Japan [155].

The problem of dose estimation by using tooth enamel appears to be complicated [186]. There are several reasons for this – the EPR signal of an irradiated tooth consists of two main overlapping components, that of enamel (CO_2^- radical with $g_z = 1.9975$ and $g_\perp = 2.0018$) and a background signal ($g = 2.0045$) which is due to the organic part of the tooth [177]. The enamel exhibits crystalline structure [187] and for EPR studies it is necessary that it be crushed in very small particles in order to avoid an angular dependence of the signal. A complicating factor is that the EPR response depends on the mechanical treatment before investigation [190, 191]. Several different procedures have been tested to obtain the true radiation induced signal - computer subtraction [190, 191], microwave saturation of the background signal [192], and chemical treatment [193, 194]. Recently, review articles have appeared [195–197] and results from an organised intercomparison trial were reported [198, 199]. They both indicate some progress but some problems still remain. And finally all studies performed on bone and teeth are *in vitro* i.e. the samples have to be extracted from the living human body.

8.7.1 In Vivo Emergency EPR Dosimetry

Recently, estimations of the absorbed dose ***in vivo***, i.e. without extracting the teeth from the patient, was carried out using the recently developed portable EPR reader operating at X band (10 GHz.) [17, 200–202]. Its specific features are:

- special, new type of cavity permitting contact of the front tooth with it;
- special configuration of the magnet.

This method is very attractive but has some disadvantages:

- due to the fact that the measurements are *in vivo* additional re-irradiation cannot be used in order to obtain the real EPR dose response;
- a calibration graph cannot be prepared;
- the tooth anisotropy must be taken into consideration.

Despite all these considerations this is currently the most promising method for estimation of the absorbed dose *in vivo*. Instead of the “method of additional dose” it is possible to use a calibration graph prepared on the basis of wide collection of data *in vitro*. In this case dose measurements over 0.5 Gy can be performed with sufficient accuracy. Thus, we look forward to future developments in this field.

More recently [203] a low frequency EPR spectrometer operating in the L-band (1.2 GHz) was reported to be useful for *in vivo* measurement of the absorbed dose by a tooth. It is estimated that the current low limit for detecting radiation doses in human teeth *in vivo* is 0.5–1.0 Gy. This is sufficient for identification of a person who has been exposed to life threatening dose of ionising radiation.

8.8 Conclusions

The present paper describes some of the recent developments in the field of EPR dosimetry. Such studies are very promising and can be expected to extend to many other subjects in the future. It is worth noting that prospects for SS/EPR dosimetry in the future are good even if the dream of "Green" movements in the world to close all facilities operating with radioactive materials (nuclear power stations, irradiation facilities, etc.) is realised since the waste radioactive materials will remain along with the need of EPR dosimetry for control purposes. In addition, there are still no alternatives to radiation therapy which will continue to serve the health needs of a large number of people.

References

1. Zavoisky E (1945) Relaxation of liquid solutions for perpendicular fields. J Phys USSR 9:211–216
2. ISO 11137–1 (2006) Sterilization of health care products – radiation – Part 1: requirements for development, validation and routine control of a sterilization process for medical devices
3. WHO, FAO (1988) Evaluation of certain veterinary drug residues in food. Thirty-second report of the Joint FAO/WHO Expert Committee on Food Additives. WHO Technical Report Series, p 763
4. Drobny JG (2003) Radiation technology for polymers. CRC Press, New York
5. Yordanov ND (1994) Quantitative EPR spectrometry – "state of the art". Appl Mag Res 6:241–257
6. Yordanov ND, Ivanova M (1994) The present state of quantitative EPR spectrometry: the results from an international experiment. Appl Mag Res 6:333–340
7. Mehta K (1998) Report of the second research co-ordination meeting (RCM) for the co-ordination research project (CRP E2 40 06) on characterisation and evaluation of high-dose dosimetry techniques for quality assurance in radiation processing. SSDL Newsletter No. 39, IAEA, Vienna 19
8. Mehta K (1998) High-dose dosimetry programme of the IAEA. In: "Techniques for high dose dosimetry in industry, agriculture and medicine", Extended Synopses of Symposium held in Vienna, November 2–5 paper # IAEA-SM-356/R2
9. Mehta K, Girzikowski R (1996) Alanine-ESR dosimetry for radiotherapy. IAEA Exp Appl Radiat Isot 47:1189–1192
10. Mehta K, Girzikowsky R (1999) IAEA reference dosimeter: alanine-ESR. In: "Techniques for high dose dosimetry in industry, agriculture and medicine", Proc Symp, IAEA-TECDOC-1070, p 299

11. Desrosiers M et al (1998) Alanine dosimetry at the NIST, Intl. Conf. Biodosimetry and 5th Intl. Sym. ESR Dosimetry and Applications, Moscow/Obninsk, Russia, June 22 Final Programme and Book of Abstracts, p 149
12. Sharpe PHG, Sephton JP (1999) Alanine dosimetry at NPL – the development of a mailed reference dosimetry service at radiotherapy dose level, in techniques for high dose dosimetry in industry, agriculture and medicine. Proc Symp, IAEA-TECDOC-1070, p 299
13. EN Protocol EN 1787 (1997) Determination of irradiated food containing cellulose: analysis by EPR
14. EN Protocol EN 1786 (1997) Detection of irradiated food containing bone: analysis by electron paramagnetic resonance
15. EN Protocol EN 13708 (2001) Detection of irradiated food containing **c**rystalline sugar: analysis by EPR
16. Ikeya M (ed) (1985) EPR dating and dosimetry. Ionics Publ., Tokyo
17. Ikeya M (1993) New applications of electron paramagnetic resonance, dating, dosimetry and microscopy. World Scientific, Singapore
18. Regulla DF (1999) EPR dosimetry – present and future. In: Techniques for high dose dosimetry in industry, agriculture and medicine, Proc Symp, IAEA-TECDOC-1070, p 171
19. International Conference on "EPR Dosimetry", organized regulary in different countries. Usually their Proceedings appear in Appl. Radiat Isot
20. International Workshops on "Electron Magnetic Resonance of Disordered Systems" (EMARDIS). Meetings organised biannually by the Bulgarian EPR Society. The first two Proceedings appear as a separate books published by World Sci Publ next two in Appl Mag Res and remaining seven in Spec Chim Acta (B)
21. Johnson DE, Stevenson MH (eds) (1990) Food irradiation and the chemist. Royal Society of Chemistry, London
22. McMurray CH, Stewart EM Gray R, Pearce J (eds) (1996) Detection methods for irradiated foods. Current Status. Royal Society of Chemistry, London
23. Prydz S, Henriksen T (1961) Radiation induced free radicals in alanine and some related amino acids. Electron spin resonance studies. Acta Chem Scand 15:791–802
24. Henrikson T, Sanner T, Pihl A (1963) Secondary Processes in proteins irradiated in the dry state. Radiat Res 18:147–162
25. Panta PP, Strzelczak-Burlinska G, Tomasinski Z (1989) ESR/L-alanine system as a proposed standard dosimeter for electron-beam irradiations. Appl Radiat Isot 40:971–975
26. Regulla DF, Defner U (1982) Dosimetry by ESR spectroscopy of alanine. Appl Radiat Isot 33:1101–1114
27. Nakagawa K, Eaton SS, Eaton GR (1993) Electron spin relaxation times of irradiated alanine. Appl Radiat Isot 44:73–76
28. Stuglik Z, Sadlo J (1996) A response of L-alpha-alanine and standard bone powder on 3.4 MeV/amu 59Co ion beam. Appl Radiat Isot 47:1219–1222
29. Rotblat J, Simmeons JA (1963) Dose-response relationship in the yield of radiation induced free radicals in amino acids. Phys Med Biol 7:489–497
30. Koehnlein W, Muller A (1962) Absolute yield measurements of radiation-produced radicals by electron spin resonance. Phys Med Biol 6:599–604
31. Katsamura K, Tabata Y (1985) In: Ikeya M (ed) EPR dating and dosimetry. Ionics, Tokyo, p 415
32. Katsumura Y, Tabata Y, Srguchi T, Morishita N, Kojima T (1986) Fast neutron irradiation effects-III. Sensitivity of alanine systems for fast neutron having an energy of 1 MeV. Radiat Phys Chem 28:337–341
33. Galindo S, Urena-Nunez F (1993) EPR signal enhancement of alanine irradiated with thermal neutrons. Radiat Res 133:387–389
34. Ciesielski B, Wielopolski L (1995) The effects of boron on the electron paramagnetic resonance spectra of alanine irradiated with thermal neutrones. Radiat Res 144:59–63
35. Uena-Nunez F, Galindo S, Azorin J (1998) An alanine-boron compound for thermal neutron fluence measurements. Part I synthesis and development. Appl Radiat Isot 49:1657–1664

36. Uena-Nunez F, Galindo S,Azorin J (1999) An alanine-boron compound for thermal neutron fluence measurements. Part 2: EPR response. Appl Radiat Isot 50:763–777
37. Yordanov ND, Genova B (1997) Analysis of some non-linear effects in quantitative electron paramagnetic resonance spectrometry. Non-linear effects due to the use of cavities with TE_{102} and TM_{110} modes. Analyt Chim Acta 353:99–103
38. Bradshaw WW, Cadena DG, Crawford GW, Spetzler HA, (1962) The use of alanine as a solid dosimeter. Radiat Res 17:11–21
39. Regulla DF, Deffner U (1982) Dosimetry by ESP spectroscopy of alanine. Int J Appl Radiat Isot 33:1101–1114
40. Kojima T, Haruyama Y, Tachibana H, Tanaka R, Okamoto J, Hara H, Yamamoto Y (1993) Development of portable ESR spectrometer as a reader for alanine dosimeters. Appl Radiat Isot 44:361–365
41. Hasskell EH, Hayes RB, Kenner GH (1998) A high sensitivity EPR technique for alanine dosimetry. Radiat Prot Dosim 77:43–49
42. Hayes RB, Haskell EH, Wieser A, Romanyukha AA, Hardy BL, Barrus FK (2000) Assessment of an alanine EPR dosimetry technique with enhanced precision and accuracy. Nucl Instrum Methods Phys Res A:453–461
43. Nagy V (2000) Accuracy consideration in EPR dosimetry. Appl Radiat Isot 52:1039–1050
44. Nagy V, Sleptchonok OF, Desrosiers MF, Weber RT, Heiss AH (2000) Advancements in accuracy of the alanine EPR dosimetry system Part III: usefulness of an adjacent reference sample. Radiat Phys Chem 59:429–441
45. Nam WJ, Regulla DF (1989) The significance of the international dose assurance service for radiation processing. Appl Radiat Isot 40:953–955
46. Mehta K (1999) High dose dosimetry programme of the Agency. In: Techniques for high dose dosimetry in industry, agriculture and medicine, Proc Symp, IAEA-TECDOC-1070, p 11
47. Yordanov ND, Gancheva V, Pelova VA (1999) Studies on some materials suitable for use as internal standards in high energy EPR dosimetry. J Radioanal Nuclear Chem 240:619–622
48. Yordanov ND, Gancheva V (2000) Some physico-technical aspects of the new generation of self-calibrated alanine/EPR dosimeter and results from the international intercomparison trial. J Radioanalyt Nuclear Chem 245:323–328
49. BG Pat. (1997) #344Y1
50. Yordanov ND, Gancheva V, Pelova VA (1999) Studies on some materials suitable for use as internal standards in high energy EPR dosimetry. J Radioanal Nuclear Chem 240:619–622
51. Lyniov VN (1991) In: Yordanov ND (ed) Electron magnetic resonance of disordered systems. World Scientific, Singapore, p 53
52. Maier D, Schmalbein D (1993) A dedicated EPR analizer for dosimetry. Appl Radiat Isot 44:345–350
53. Maier D (1994) BRUKER Rep 140:22–23
54. Ikeya M, Furusawa M (1989) A portable spectrometer for ESR microscopy, dosimetry and dating. Appl Radiat Isot 40:845–850
55. Kojima T, Tanaka R (1989), Polymer-alanine dosimeter and compact reader. Appl Radiat Isot 40:851–857
56. Nakanishi A, Sagawara N, Furuse A (1993) Portable ESR spectrometer with Neomax (Nd, Fe, B) permanent magnet circuit. Appl Radiat Isot 44:357–360
57. Herrling T, Groth N, Klein F, Rehberg J (2000) Electron paramagnetic resonance for everybody – MICROspec-X – a new class of electron paramagnetic resonance spectrometer.Spectrochim Acta (A) 56:417–421
58. Yamanaka C, Ikeya M, Meguro K, Nakanashi A (1991) A portable ESR spectrometer using Nd-Fe-B permanent magnets. Radiat Meas 18:279–282
59. Gancheva V, Yordanov N, Callens F, Vanhaelewyn G, Raffy J, Bortolin E, Onori S, Malinen E, Sagstuen E, Fabisiak S, Peimel-Stuglik Z (2008) An international intercomparison on "self-calibrated" alanine EPR dosimeters. Radiat Phys and Chem 77(3):357–364
60. Nagy V, Desrosoers MF (2001) Private communication

61. Yordanov ND, Gancheva V, Georgieva E (2002) EPR and UV spectroscopic study of table sugar as a high-dose dosimeter. Radiat Phys Chem 65:269–276
62. Kai A, Ikeya M, Miki T (1990) ESR accident dosimetry using medicine tablets coated with sugar. Radiat Protect Dos 34:307–310
63. Nakajima T, Ohtsuki T (1990) Dosimetry for radiation emergencies: Radiation-induced free radicals in sugar of various countries and the effect of pulverizing on the ESR signal. Appl Radiat Isot 41:359–365
64. Nakajima T (1988) Sugar as an emergency populace dosimeter for radiation accidents. Health Phys 55:951–955
65. Nakajima T (1994) Estimation of absorbed dose to evacuees at pripyat-city using ESR measurements of sugar and exposure rate calculations. Appl Radiat and Isot 45(1):113–120.
66. Nakajima T (1995) ESR of Sugar as a personnel monitor for radiation emergencies. Appl Radiat Isot 46:819–825
67. Gutierrez A, Azorin J (1993) Lyoluminescence and electron spin resonance of commercial sugar in accident dosimetry. J Nucl Sci 30:137–140.
68. Trivedi A, Greenstock CL (1993) Use of sugars and other samples for ESR emergency dosimetry. Appl Radiat and Isot 44:85–90
69. Yordanov N, Gancheva V, Georgieva E (2002) EPR and UV spectroscopic study of table sugar as a high-dose dosimeter. Radiat Phys Chem 65:269–276.
70. Yordanov N, Gancheva V, Georgieva E (2002) Advanced EPR applied to biosciences. Kwansei Gaikun University, Japan, p 128
71. Flores C, Cabrera E, Calderon T, Munoz E, Adem E, Hernan-dez J, Boldu J, Ovalle P, Murrieta H (2000) Appl Radiat Isot 52:1229–1234
72. Yordanov N and Georgieva E (2004) EPR and spectral study of gamma irradiated white and burned sugar, fructose and glucose. Spectrochim Acta Part A 60:1307–1314
73. Yordanov N, Karakirova Y (2007) Sugar/UV spectrophotometric system for high-energy dosimetry (0.055–160 kGy) Radiat Meas 42:121–122
74. Yordanov N, Karakirova Y (2007) EPR of gamma irradiated solid sucrose and UV spectra of its solution. An attempt for calibration of solid state/EPR dosimetry. Radiat Meas 42:347–351
75. Nakajima T (1989) Possibility of retrospective dosimetry for persons accidentally exposed to ionizing radiation using electron spin resonance of sugar and mother-of-pearl. Brit J Radiol 62:148–153
76. LaVerne JA (2000) Track effects of heavy ions in liquid water. Radiat Res 153:487–496
77. Nakagawa K (2000) Effect of heavy ion irradiation on sucrose. Chem Lett 29(4):422–423
78. Nakagawa K, Nishio T (2000) Electron Paramagnetic Resonance Investigation of sucrose irradiation with heavy ions. Radiat Res 153:835–839
79. Nakagawa K, Sato Y (2002) Effects of heavy ion irradiation on sucrose: an implication of EPR dosimeter for cosmic rays. Adv ESR Appl 18:253–257
80. Nakagawa K, Sato Y, (2004) ESR investigation of sucrose radicals produced by particle irradiation. Spectrochim Acta Part A 60:1315–1318
81. Nakagawa K, Sato Y (2005) Investigation of heavy-ion-induced sucrose radicals by Electron paramagnetic resonance. Radiat Res 164:336–338
82. Karakirova Y, Lund E, Yordanov N (2008) EPR and UV investigation of sucrose irradiated with nitrogen ions and gamma-rays. Radiat Meas 43:1337–1342
83. Karakirova Y, Nakagawa K, Yordanov N (2010) EPR and UV spectroscopic investigations of sucrose irradiated with heavy-ion particles. Radiat Meas 45:10–14
84. Karakirova Y, Yordanov N (2010) EPR and UV spectrometry investigation of sucrose irradiated with carbon particles. Radiat Meas 45:831–835
85. Nakagawa K, Ikota N, Anzai K (2008) Sucrose radical-production cross-section regarding heavy-ion irradiation. Spectrochim Acta Part A 69:1384–1387
86. Bartolotta A, Indovina FL, Onori S, Rosati A (1984) Dosimetry for Cobalt-60 gamma rays with alanine. Radiat Prot Dosim 9:277–281
87. Bugay O, Bartchuk V, Kolesnik S, Mazin M, Gaponenko H (1998) Techniques for high dose dosimetry in industry, agriculture and medicine. Proc Symposium held in Vienna, November 2–5, p 191

88. Sharpe PHG, Rajendran K, Sephton JP (1996) Progress towards an alanine/ESR therapy level reference dosimetry service at NPL. Appl Radiat Isot 47:1171–1175
89. Sharpe PHG, Sephton JP (1998) Techniques for high dose dosimetry in industry, agriculture and medicine. Proc Symposium held in Vienna, November 2–5, p 183
90. Chen F, Covas DT, Baffa O, (2001) Dosimetry of blood irradiation using an alanine/ESR Dosimeter. Appl Radiat Isot 55:13–16
91. Bugai O, Bartchuk V, Kolesnik S, Mazin M, Gaponenko H (1999) Alanine EPR dosimetry of therapeutic irradiators. In: Techniques for high dose dosimetry in industry, agriculture and medicine. Proc Symp, IAEA-TECDOC-1070, p 191
92. Sharpe PHG, Sephton JP (1999) Alanine dosimetry at NPL – the development of a mailed reference dosimetry service at radiotherapy dose level. In: Techniques for high dose dosimetry in industry, agriculture and medicine, Proc Symp, IAEA-TECDOC-1070, p 299
93. Karakirova Y, Yordanov ND, DeCooman H, Vrielinck H, Callens F (2010) Dosimetric characteristics of different types of saccharides: an EPR and UV spectrometric study. Radiat Phys Chem 79(5):654–659
94. Hassan GM, Ikeya M, Toyoda S (1998) Lithium lactate as an ESR dosimeter. Appl Radiat Isot 49:823–828
95. Hassan GM, Ikeya M (2000) Metal ion-organic compound for high sensitive ESR dosimetry. Appl Radiat Isot 52:1247–1254
96. Ikeya M, Hassan GM, Sasaoka H, Kinoshita Y, Takaki S, Yamanaka C (2000) Strategy for finding new materials for ESR dosimeters. Appl Radiat Isot 52:1209–1215
97. Olson SK, Bagherian S, Lund E, Alm Carlsson G, Lund A (1999) Ammonium tartrate as an ESR dosimeter material. Appl Radiat Isot 50:955–965
98. Olson S, Lund E, Lund A (2000) Development of ammonium tartrate as an ESR dosimeter material for clinical purposes. Appl Radiat Isot 52:1235–1241
99. Keizer PN, Morton JR, Preston KF (1991) Electron paramagnetic resonance radiation dosimetry: possible inorganic alternatives to the EPR/alanine dosimeter. J Chem Soc, Faraday Trans 87:3147
100. Morton JR, Ahlers FJ, Schneider CCJ (1993) ESR dosimetry with magnesium sulphate. Radiat Prot Dosim 47:263–266
101. Bogushevich SE, Makatin V, Potapovich AK, Ugolev I (1991) Production of SO3 ion-radicals in barium dithionate exposed to ionizing radiation. Zhurn Prikl Spektrosk 55:613–618
102. Bogushevich SE, Ugolev II, Potapovich AK (1996) Formation of ion-radicals SO_3 – in ionizing irradiation of barium dithionate. Zh Prikl Spektrosk 63:258–263
103. Bogushevich SE, Ugolev II (2000) Inorganic EPR dosimeter for medical radiology. Appl Radiat Isot 52:1217–1219
104. Murali S, Natarajan V, Venkataramani R, Pusharja, Sastry MD (2001) ESR dosimetry using inorganic materials: a case study of Li2CO3 and CaSO4:Dy as prospective dosimeters. Appl Radiat Isot 55:253–258
105. Lund A, Olson S, Bonora M, Lund E (2002) New materials for ESR dosimetry. Spectrochim Acta (A) 58:1301–1311
106. Meeker IA, Gross RE (1951) Sterilization of frozen arterial grafts by high-voltage cathode-ray irradiation. Surgery 30:19–28
107. Turner TC, Bassett CAL, Pate JW, Sawyer PN (1956) Ster-ilization of preserved *bone* grafts by high voltage cathode irradiation. J Bone Joint Surg 38A:862–884
108. Dood NJF, Swallow AJ, Ley FJ (1985) Use of ESR to identify irradiated food. Radiat Phys Chem 26:451–453
109. Delincee H, Ehermann DAE (1989) Recent advances in the identification of irradiated food. Radiat Phys Chem 34:877–890
110. Boegl KW (1989) Identification of irradiated foods – methods, development and concepts. Appl Radiat Isot 40:1203–1210
111. Raffi J, Delinecee H, Marchioni E, Hasselmann C, Sjoberg A, Leonardi M, Kent M, Bogl K-W, Schreiber G, Stevenson MH, Meier W (1994) CEC, BCR, Luxemburg, (EUR 15261 EN)

112. CEN Protocol EN 1784. Detection of irradiated food containing fat: gas chromatography(GC) analysis of hydrocarbons
113. CEN Protocol EN 1785. Detection of irradiated food containing fat: gas chromatography(GC) analysis of 2-alkylcyclobutanones
114. CEN Protocol EN 1788. Detection of irradiated food containing silicate materials: analyzis by thermoluminescence, TL
115. Swartz HM (1965) Long lived Electron spin resonances in rats irradiated at room temperature. Radiat Res 24:579–586
116. Brady JM, Aarestad NO, Swartz HM (1968) In vivo dosimetry by electron spin resonance spectroscopy. Health Phys 15:43–47
117. Yordanov ND, Gancheva V, Tarandjiiska R, Velkova R, Kulieva L, Damyanova B, Popov S (1998) Comparative investigation of irradiated meat by the methods of electron paramagnetic resonance and gas chromatography. Spectrochim Acta (A) 54:2421–2426
118. Raffi J, Stocker P (1996) Electron paramagnetic resonance detection of irradiated foodstuffs. Appl Magn Res 10:357–373
119. Stewart EM (1996) The application of ESR spectroscopy for the identification of irradiated crustacean. Appl Magn Res 10:375–393
120. Ziegelmann B, Boegel KW, Schreiber ND (1999) TL and ESR signals of mollusc shells – correlations and suitability for the detection of irradiated foods. Radiat Phys Chem 54:413–423
121. Yordanov ND, Mladenova B (2000) EPR studies on gamma-irradiated foodstuffs containing hard tissues. Bull Chem Technol Macedonia 19:171–176
122. Desrosiers MF (1991) Estimation of the absorbed dose in radiation processed food-2. Test of the EPR response function by an exponential fitting analysis. Appl Radiat Isot 42:617–619
123. Regulla DF, Goekus HY, Vogenauer A, Wisser A (1994) Retrospective dosimetry based on egg shells. Appl Radiat Isot 45:371–373
124. Corredor C, Diaz J, Diaz JM, Farach HA, Poole CP (1995) ESR experiments with egg shells of chickens. J Appl Magn Res 9:309–317
125. Yordanov ND, Mladenova B, (2001) EPR studies on γ-irradiated snails hard tissue. Radiat Phys Chem 60:191–193
126. Abdel-Rehim F, Bester AA, Al-Kahtan HA, Abu-Tarboush HM (1997) The use of electron spin resonance spectroscopy for the detection of irradiated mackerel. Appl Radiat Isot 48:241–245
127. Barabas M (1992) The nature of the paramagnetic centres at 2.0057 and 2.0031 in marine carbonates. Nuclear Tracks 20:453–464
128. Kai A, Miki T, Ikeya M (1992) Electron spin resonance of sulfite radicals in irradiated calcite and aragonite. Radiat Phys Chem 40:469–476
129. Katzenger O, Debuyst R, DeCanniere P, Dejehet F, Aper D, Barabas M (1989) Temperature experiments on mollusc samples: an approach to ESR signal identification. Appl Radiat Isot 40:1113–1118
130. Desrosiers M et al (1998) Alanine dosimetry at the NIST. In: International Conference on Biodosimetry and 5th International Symposium on ESR Dosimetry and Applications, Moscow/Obninsk, Russia, June 22 Final Programme and Book of Abstracts, p 185
131. Atkins PW, Horsefield A, Symons MCR (1964) Oxides and oxyions of the non-metals. Part VII. $SO2^{-}$ and ClO2 J Chem Soc 5220–5225
132. Raffi J, Angel JPL (1989) Electron spin resonance identification of irradiated fruits. Radiat Phys Chem 34:891–894
133. Yordanov ND, Gancheva V (2000) A new approach for extension of the identification period of irradiated cellulose-containing foodstuffs by EPR spectroscopy. Appl Radiat Isot 52:195–198
134. Raffi J, Yordanov ND, Chabane S, Douifi L, Gancheva V, Ivanova S (2000) Identification of irradiation treatment of aromatic herbs, spices and fruits by electron paramagnetic resonance and thermoluminescence.Spectrochim Acta (A) 56:409–416

135. Yordanov ND, Gancheva V, Radicheva M, Hristova B, Guelev M, Penchev O (1998) Comparative identification of irradiated herbs by the methods of electron paramagnetic resonance and thermoluminescence. Spectrochim Acta (A) 54:2413–2419
136. Bögl W (1985) Radiation sterilization of pharmaceuticals- chemical changes and consequences. Radiat Phys Chem 25:425–435
137. Jacobs GP (1985) A review: Radiation sterilization of pharmaceuticals. Radiat Phys Chem 26:133–142
138. Gopal NGS, Patel KM, Sharma G, Bhalla HL, Wills A, Hilmy N (1988) Guide for radiation sterilization of pharmaceuticals and decontamination of raw materials. Radiat Phys Chem 32:619–622
139. Zeegers F, Crucq AS, Gibella M, Tilquin B (1993) Radiolyse et radiosterilisation des medicaments. J Chim Phys 90:1029–1040
140. Commission of the European Communities (1992) CPMP working party on quality of medicinal products. Ionizing irradiation in the manufacture of medicinal products. III Suppl. N.2
141. Miyazaki T, Kaneko T, Yoshimura T, Crucq A-S, Tilquin B (1994) Electron spin resonance study of radiosterilization of antibiotics: ceftazidime. J Pharm Sci 83:68–71
142. Miyazaki T, Arai J, Kaneko T, Yamamoto K, Gibella M, Tilquin B (1994) Estimation of irradiation dose of radiosterilized antibiotics by electron spin resonance: ampicillin. J Pharm Sci 83:1643–1644
143. Ciranni Signoretti E, Valvo L, Fattibene P, Onori S, Pantaloni M (1994) Gamma Radiation Induced Effects on Cefuroxime and Cefotaxime. Investigation on Degradation and Syn-Anti Isomerization. Drug Dev Ind Pharm 20:2493–2508
144. Signoretti EC, Onori S, Valvo L, Fattibene P, Savella AL, DeSena C, Alimonti S (1993) Ionizing radiation induced effects on cephradine. Influence of sample moisture content, irradiation dose and storage conditions. Drug Dev Ind Pharm 19:1693–1708
145. Onori S, Pantaloni M, Fattibene P, Signoretti EC, Valvo L, Santucci M (1996) ESR Identification of Irradiated Antibiotics: Cephalosporins. App. Radiat Isot 47:1569–1572
146. Gibella M, Crucq A-S, Tilquin B, Stocker P, Lesgards G, Raffi J (2000) Electron spin resonance studies of some irradiated pharmaceuticals. Radiat Phys Chem 58:69–76
147. Duroux JL, Basly JP, Penicaut B, Bernard M (1996) ESR spectroscopy applied to the study of drugs radiosterilization: Case of three nitroimidazoles. Appl Radiat Isot 47:1565–1568
148. Basly JP, Longy I, Bernard M (1997) Influence of radiation treatment on theodrenaline: ESR and HPLC study. Int J Pharm 152:201–206
149. Raffi J, Gelly S, Barral L, Burger F, Piccerelle P, Prinderre P, Baron M, Chamayou A (2002) Electron paramagnetic resonance of radicals induced in drugs and excipients by radiation or mechanical treatments. Spectrochim Acta (A) 58:1313–1320
150. Ambroz HB, Kornacka EM, Marciniec B, Ogrodowczyk M, Przybytniak GK (2000) EPR study of free radicals in some drugs γ-irradiated in the solid state. Radiat Phys Chem 58:357–366
151. Gruen R (1989) Die ESR-Altersbestimmungs-methode. Springer, Berlin
152. Sagstuen E, Theisen H, Henriksen T (1983) Dosimetry by ESR spectroscopy following a radiation accident. Health Phys 45:961–968
153. Regulla DF, Deffner U (1989) Dose estimation by ESR spectroscopy at a fatal radiation accident. Appl Radiat Isot 40:1039–1043
154. Desrosiers MF (1991) In vivo assessment of radiation exposure. Health Phys 61:859–861
155. Shiraishi K, Kimura S, Yonehara H, Takada J, Ishikawa M, Igarashi Y, Aoyama M, Komura K, Nakajima T (2000) Survey of external dose around the JCO facility using sugar samples and ESR method. Adv EPR Appl 16:9–14
156. Schauer DA, Coursey BM, Dick CE, Mclaughlin WL, Puhl JM, Desrosiers MF, Jacobson AD (1993) A radiation accident at an industrial accelerator facility. Health Phys 65:131–140
157. Rossi AM, Wafcheck CC, De Jesus EE, Pelegrini F (2000) Electron spin resonance dosimetry of teeth of Goiania radiation accident victims. Appl Rad Isot 52:1297–1303

158. Hütt G, Brodski L, Polyakov V (1996) Gamma-ray dose assessment after the 1994 radiation accident in Kiisa (Estonia): preliminary results. Appl Radiat Isot 47:1329–1336
159. Pass B, Aldrich JE (1985) Dental enamel as an in vivo radiation dosimeter. Med Phys 12:305–307
160. Aldrich JE, Pass B (1986) Dental enamel as an i*n vivo* radiation dosemeter: separation of the diagnostic X ray dose from the dose due to natural sources. Radiat Prot Dosim 17:175–179
161. Ikeya M, Miyajima J, Okajima S (1984) ESR dosimetry for atomic bomb survivors using shell buttons and tooth enamel. Jpn J Appl Phys 23:697–699
162. Hoshi M, Sawada S, Ikeya M (1985) ESR dating and dosimetry. Ionica, Tokyo, p 407
163. Stachowich W, Michalik J, Dziedzia-Goclawska A, Ostrowski R (1974) Evaluation of absorbed dose of gamma and X-ray radiation using bone tissue as a dosimeter. Nucleonika 19:845–850
164. Nakajima T (1987) External dose to a Japanese tourist from the Chernobyl reactor accident. Health Phys 53:405–407
165. Nakajima T (1982) The use of organic substances as emergency dosimeters. Int J Appl Radiat Isot 33:1077–1084
166. Delgano G, McClymond JD (1989) Evaluation of ESR as a radiation accident dosimetry technique. Appl Radiat Isot 40:1013–1020
167. Kamenopoulou V, Barthe J, Hickman C, Portal G (1986) Accidental gamma irradiation dosimetry using clothing. Radiat Prot Dosim 17:185–188
168. Chumak V, Sholom S, Pasalskaya L (1999) Application of high precision EPR dosimetry with teeth for reconstruction of doses to Chernobyl populations. Radiat Prot Dosim 84:515–520
169. Barthe J, Kamenopoulou V, Cattoire B, Portal G (1989) Dose evaluation from textile fibers: a post-determination of initial ESR signal. Appl Radiat Isot 40:1029–1033
170. Chandra H, Symons MCR (1987) Sulphur radicals formed by cutting alpha-keratin. Nature 328:833–834
171. Kudinski R, Kudinska J, Buckmaster HA (1994) The decay constant for irradiated human hair using EPR spectroscopy. Appl Radiat Isot 45:645–650
172. Symons MCR, Chandra H, Wyatt JL (1995) Electron paramagnetic resonance spectra of irradiated fingernails: a possible measure of accidental exposure. Radiat Prot Dosim 58:11–15
173. Cope BC, Hopegood L, Latham RJ, Linford RG, Reilly JD, Symons MCR, Taiwo FA (1998) Studies of equid hoof horn material by EPR spectroscopy. J Mater Chem 8:43–45
174. Usatyi AF, Verein NV (1996) EPR-based dosimetry of large dimensional radiation fields (Chernobyl experience and new approaches). Appl Radiat Isot 47:1351–1356
175. Goeksu HY, Wieser A, Stoneham D, Bailiff IK, Figel M (1996) EPR, OSL, TL and spectral studies of porcelain. Appl Radiat Isot 47:1369–1374
176. Brik A, Baraboy V, Atamanenko O, Shevchenko Yu, Brik V (2000) Metabolism in tooth enamel and reliability of retrospective dosimetry. Appl Rad Isot 52:1305–1310
177. Hennig GJ, Herr W, Weber E, Xirotiris NI (1981) ESR-dating of the fossil hominid cranium from Petralona Cave, Greece. Nature 292:533–536
178. Ishii H, Ikeya M, Okano S (1990) ESR dosimetry of teeth of residents close to Chernobyl reactor accident. J Nucl Sci Technol 27:1153–1155
179. Gualtieri G, Colacicchi S, Sgattoni R, Giannoni M (2001) The Chernobyl accident: EPR dosimetry on dental enamel of children. Appl Radiat Isot 55:71–79
180. Serezhenkov A, Domracheva EV, Klavezal GA, Kulikov SM, Kuznetsov A, Mordvintcev PI, Sukhovskaya LI, Schklovsky-Kordi NE, Vanin AF, Voevodskaya NV, Vorobev AI (1992) Radiation dosimetry for residents of the Chernobyl region: a comparison of cytogenetic and electron spin resonance methods. Radiat Prot Dosim 42:33–36
181. Romanyukha A, Regulla D, Vasilenko E, Wieser A (1994) South Ural nuclear workers: comparison of individual doses from retrospective EPR dosimetry and operational personal monitoring. Appl Radiat Isot 45:1195–1199
182. Romanyukha A, Ignatev EA, Degteva MO, Kozheurov VP, Wieser A, Jacob P (1996) Radiation doses from Ural region. Nature 381:199–200

183. Ginsbourg SF, Babushkina TA, Basova LB, Klimova TP (1996) ESR-spectroscopy of building materials as a dosimetry technique. Appl Radiat Isot 47:1381–1383
184. Slager T, Zucker MJ, Reilly EB (1964) The persistence of electron spin resonance in bone grafts sterilized by ionizing radiation. Radiat Res 22:556–563
185. Nakajima T, Ohtsuki T, Likhariov I (1991) Tentative dose estimation in house at Pripyat-City on Chernobyl accident with sugar. J Nucl Sci Technol 28:71–73
186. Ostriwski K, Dziedzic-Gostawska A, Stachowich W (1980) In: Pryor W (ed) Free radicals in biology, vol 4. Academic Press, New York, p 321
187. Cevch P, Schara M, Ravnic C (1972) Electron paramagnetic resonance study of irradiated tooth enamel. Radiat Res 51:581–589
188. Desrosiers MF, Simic MG, Eichmiller FC, Johnston AD, Bowen RL (1989) Mechanically-induced generation of radicals in tooth enamel. Appl Radiat Isot 40:1195–1197
189. Aragno D, Fattibene P (2001) Mechanically induced EPR signals in tooth enamel. Appl Radiat Isot 55:375–381
190. Ikeya M, Miyajima J, Okajima S (1984) ESR dosimetry for atomic bomb survivors using shell buttons and tooth enamel. Jap J Appl Phys 23:L697–L699
191. Haskell EH, Haves RB, Kenner GH, Wieser A, Aragno D, Fattibene P, Onori (1999) Achievable precision and accuracy in EPR dosimetry of tooth enamel. Radiat Protect Dosim 84:527–535
192. Ignatiev EA, Romanyucha AA, Koshta AA, Wieser A (1996) Selective saturation method for EPR dosimetry with tooth enamel. Appl Radiat Isot 47:333–337
193. Wieser A, Haskell E, Kenner G, Bruenger F (1994) EPR dosimetry of bone gains accuracy by isolation of calcified tissue. Appl Radiat Isot 45:525–526
194. Ivannikov AL, Tikunov DD, Skovortsov VG, Stepanenko VL, Khomichyonok VV, Khamidova LG, Skiripnik DD, Bozadjiev LL, Hoshi M (2001) Elimination of the background signal in tooth enamel samples for EPR-dosimetry by means of physical-chemical treatment. Appl Radiat Isot 55:701–705
195. Wieser A, Onori S, Aragano D, Fattibene P, Romanyukha A, Ignatiev E, Koshta A, Skvortzov V, Ivannikov A, Stepenko V, Chumak V, Shalom S, Hayes R, Kenner G (2000) Comparison of sample preparation and signal evaluation methods for EPR analysis of tooth enamel. Appl Rad Isot 52:1059–1064
196. Romanyukha A, Desrosiers MF, Regulla DF (2000) Current issues on EPR dose reconstruction in tooth enamel. Appl Rad Isot 52:265–1273
197. Desrosiers M, Schauer DA (2001) Electron paramagnetic resonance (EPR) biodosimetry. Nucl Instrum Methods Phys Res (B) 184:219–228
198. Wieser A, Mehta K, Amira S, Agano D, Bercea S, Brik A, Bugai A, Callens F, Chumak V, Ciesielski B, Debuyst R, Dubrovsky S, Duliu OO, Fattibene P, Haskell H, Hayes RB, Ignatiov EA, Ivannikov A, Kirilov V, Nakamura N, Nather, Nowak J, Onori S, Pass B, Pivovarov S, Romanyukha A, Scherbina O, Shames AI, Sholom S, Skvortsov V, Stepanenko V, Tikhonov DD, Toyoda S (2000) The second international intercomparison on EPR tooth dosimetry. Radiat Meas 32:549–557
199. Vanhaelewyn G, Amira S, Debuyst R, Callens F, Glorieux Th, Leloup G, Thierens H (2001) A critical discussion of the 2nd intercomparison on electron paramagnetic resonance dosimetry with tooth enamel. Radiat Meas 33:417–426
200. Ikeya M, Ishii H (1989) Atomic bomb and accident dosimetry with ESR: natural rocks and human tooth in-vivo spectrometer. Appl Radiat Isot 40 1021–1027
201. Ishii H, Ikeya M (1990) An electron spin resonance system for in-vivo human tooth dosimetry. Jap J Appl Phys 29:871–875
202. Ikeya M, Yamamoto M, Ishii H (1994) Nondestructive measurement of large objects with electron paramagnetic resonance: pottery, sculpture and jewel ornament. Rev Sci Instrum 65:3670–3673
203. Miyake M, Liu KJ, Walczak T, Swartz HM (2000) In-vivo EPR dosimetry of accidental exposures to radiation: experimental results indicating the feasibility of practical use in human subjects. Appl Radiat Isot 52:1031

Chapter 9
Optically Detected Magnetic Resonance of Defects in Semiconductors

Weimin M. Chen

Abstract This chapter provides an overview of the optically detected magnetic resonance (ODMR) technique. The principle and methods of a variety of the ODMR technique, namely ODMR by different ways of optical detection, ODMR in zero field or in the presence of an external magnetic field, cw- and time-resolved ODMR, will be described. The ability of the ODMR technique to provide important information on physical properties of defects in semiconductors, such as chemical identification, electronic and geometric structure, related carrier recombination, etc., will be demonstrated. Recent progress, trends and prospects in achieving high spectral, time and spatial resolution of the ODMR techniques will also be outlined.

9.1 Introduction

The optically detected magnetic resonance (ODMR) technique is a combination of electron spin resonance (ESR) and photoluminescence (PL). Since its first application for the excited state of mercury atoms in 1952 [1], ODMR has been extensively employed to investigate excited states of solids in particular in retrieving detailed microscopic information on defects as well as recombination processes in semiconductors [2–6]. With recent rapid developments in semiconductor thin films and nanostructures, ODMR has attracted increasing attention as the traditional ESR technique has failed to meet the challenge of a significantly decreasing number of spins in the newly emerging materials.

In this chapter we shall provide an overview of the physics, methods, capabilities and limitations of the ODMR technique, which will hopefully be found helpful for the readers who are interested to employ ODMR in studies of various materials.

W.M. Chen (✉)
Department of Physics, Chemistry and Biology, Linköping University,
S-581 83 Linköping, Sweden
e-mail: wmc@ifm.liu.se

A. Lund and M. Shiotani (eds.), *EPR of Free Radicals in Solids II*, Progress in Theoretical Chemistry and Physics 25, DOI 10.1007/978-94-007-4887-3_9,

It is therefore not intended to provide a complete survey of the literature and the research field. The chapter will be organized in the following way. A background and methods of the ODMR technique will be given in Sects. 9.2 and 9.3. Examples of successful applications of the ODMR technique will be presented in Sect. 9.4, to demonstrate the ability of the ODMR technique in retrieving detailed electronic and microscopic information on defects. The chosen examples are from our own work, i.e. the S-Cu complex in silicon and the non-radiative defects in Si/SiGe epitaxial films and quantum structures. Recent developments and trends for high spectral, time and spatial resolution of the magnetic resonance techniques will be outlined in Sect. 9.5.

9.2 Background of the ODMR Technique

9.2.1 What Is ODMR

The spin resonance part of the ODMR technique, such as the Zeeman splitting and the spin resonance selection rule, is identical to ESR. The essential difference between the conventional ESR and the ODMR technique is the detection scheme (Fig. 9.1).

In the presence of an external magnetic field **B**, the angular momentum of the electron spin (assuming an effective spin $S = 1/2$) will be quantized along the magnetic field giving rise to two magnetic sublevels ($M_S = -1/2, +1/2$). The energy separation between these two levels scales with the field strength, described by an electronic Zeeman term in the spin Hamiltonian treatment. When this separation

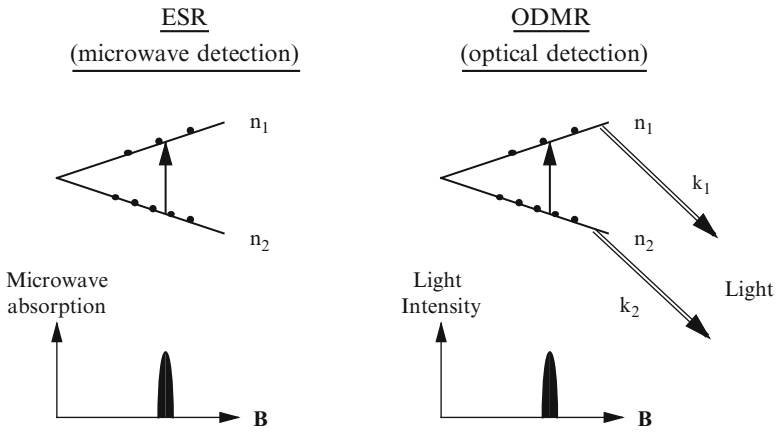

Fig. 9.1 Difference between ESR and ODMR. k_i and n_i denote the radiative decay rate and population of the spin sublevel i

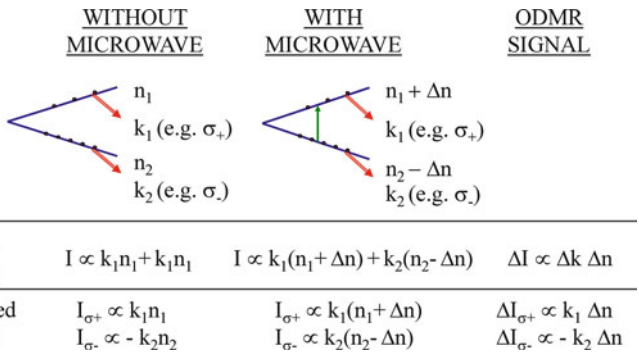

Fig. 9.2 Principle of the ODMR signals obtained by monitoring total intensity or polarization of emitting light. Δn corresponds to the population change induced by the spin resonance

coincides with the energy of the applied microwave photons, a spin resonance transition can occur by either absorbing or emitting the microwave photons. In the traditional ESR experiments, the resulting change of the microwave power is detected [7, 8]. In ODMR, a change induced by spin resonance in optical response, either in emission or in absorption, is monitored instead of the microwave power change (Fig. 9.1). (Only the ODMR technique via optical emission will be discussed in this chapter, but not via optical absorption. For the latter the reader is referred to Ref. [9]).

In Fig. 9.2 schematic pictures are displayed to describe the principle of the ODMR signal. As it can be seen, the microwave induced spin transitions can now be sensitively detected by their resulting changes in the total PL intensity ΔI or polarizations ($\Delta I_{\sigma+}$ or $\Delta I_{\sigma-}$ for examples) of the electric-dipole allowed optical transitions that give rise to the light emission, provided that the radiative decay rates or the senses of light polarization of the involved sublevels are different.

9.2.2 *Spin Hamiltonian Analysis*

Energies of magnetic sublevels revealed from ODMR studies can be analyzed by the spin Hamiltonian description [7–10], which is identical to that for analysis of ESR data,

$$H = \mu_B \mathbf{S}\bullet\mathbf{g}\bullet\mathbf{B} + \mathbf{S}\bullet\mathbf{D}\bullet\mathbf{S} + \sum \mathrm{S}\bullet\mathrm{A_i}\bullet\mathrm{I_i} \tag{9.1}$$

Here μ_B is the Bohr magneton. **S** and $\mathbf{I_i}$ represent the effective electronic spin and the nuclear spin of the defect or ligand atom *i*. **g** is the g-tensor. **D** and $\mathbf{A_i}$ are the fine-structure and hyperfine-structure (HF) tensors. The first term describes the usual linear term of electronic Zeeman splitting. The second term in Eq. (9.1) introduces a fine structure (i.e. zero-field splitting) only for $S > 1/2$, but not for $S = 1/2$ except

an identical shift in energy of both spin sublevels. The third term in Eq. (9.1) for the hyperfine structure has no effect if $I_i = 0$. The nuclear Zeeman term and other higher order terms have not been included in Eq. (9.1) due to their negligible effects in most cases of ESR and ODMR investigations.

The **g**-tensor should be isotropic and has the principal value of 2.0023 for a free electron in free space. For electrons (either free or bound at a defect) in a semiconductor crystal, **g** should be a tensor reflecting anisotropy of the crystal lattice and a defect. In other words, it reflects the local symmetry of the defect. The deviation of the **g**-tensor from the free electron g-value in the material is largely contributed by orbital angular momentum, e.g. via spin-orbit interaction if orbital angular momentum is initially quenched [8].

On the other hand, anisotropy of the **D**-tensor can be attributed to both spin-orbit interaction and magnetic dipole-dipole interaction [8, 10], of which both are a function of defect symmetry. When the contribution from the spin-orbit interaction is negligible, the magnetic dipole-dipole interaction can sometimes provide useful insight on the separation of the localized magnetic dipoles (spins). In a favorable case of a paired defect, the separation between the defect atoms forming the pair can be estimated [8].

The hyperfine structure is extremely valuable for a positive chemical identification of a defect, since the nuclear spin number I_i and the natural abundance of the isotope *i* are unique for each element in the periodic table. The value and the anisotropy of the A_i-tensor provide detailed information on the localization and the character of the electronic wavefunction of the defect.

The information on a defect gained from the spin Hamiltonian analysis of ODMR data is therefore the same as that from ESR and is summarized below:

- symmetry
- chemical identification
- local geometric arrangement
- electronic structure.

9.2.3 Why ODMR

Though the ESR technique has in the last half century played an indispensable role in identification of defects in bulk semiconductors and in determining their electronic and spin properties [9, 11], the importance of the traditional ESR technique in characterization of modern epitaxial layers and nanostructures has so far been undermined by its limited sensitivity as the volume of the materials and thus the total number of spins decreases significantly.

The main limitations of the otherwise powerful ESR technique are:

- paramagnetic ground state required
- no information on carrier recombination
- low sensitivity due to microwave detection.

The first limitation can be overcome if another charge state of the same defect can be reached by changing the Fermi level position, e.g. by doping with shallow impurities. Fortunately, the most important defects in semiconductors are either electrically or optically active by introducing energy levels within the forbidden bandgap. The presence of a defect level within the bandgap implies that a charge transition can occur when the Fermi level moves across the defect level. The first limitation can also be bypassed by performing ESR under non-equilibrium conditions such as under optical excitation, so-called photo-ESR. Non-equilibrium population of spin-active states is usually very low, however, as the spin system tends to return to its thermal equilibrium ground state, which has largely limited the success of the photo-ESR technique.

To remove the second limitation requires a direct probe of carrier recombination processes. This can also be fulfilled for example via optical excitation and detection by monitoring photoluminescence. The last limitation of a low sensitivity (thus volume demanding) has been the main reason preventing ESR from a wide application in semiconductor epitaxial layers, layered and quantum structures. Optical detection apparently provides a solution to the problem due to (a) the fact that PL transitions are electric-dipole allowed thus much more intense and easier to detect as compared to the magnetic-dipole allowed microwave transitions, and (b) the availability of sensitive optical detectors in the visible and near-infrared spectral region as compared to the microwave range.

All these limitations imposed on the ESR technique call for a solution by the optical detection method, namely the optically detected magnetic resonance technique.

ODMR has in this context emerged to be the technique of choice, which combines highly sensitive optical spectroscopies with the microscopically informative ESR technique. Apart from the capabilities shared with the ESR technique as to providing the electronic and microscopic information of defects, the ODMR technique offers new features much needed for applications in modern semiconductor thin films and nanostructures. These include

- high sensitivity due to
  - electric-dipole optical transition
  - sensitive optical detectors

  suitable for thin, layered and quantum structures
- high selectivity due to
  - spectral resolution and direct probe of corresponding optical transitions

  suitable for studies of carrier recombination processes
- high energy resolution ($\sim 10^{-7}$ eV) as compared to that of photoluminescence (typically 10^{-4} eV)
  - excited states and non-equilibrium conditions
  - new possibilities for complementary optical spectroscopies.

The main limitations of the ODMR technique can be summarized as follows:

- light emission required
- paramagnetic excited states
- spectral broadening due to lifetime effect, etc.
- not quantitative (e.g. in defect concentration)

9.3 Varieties of the ODMR Technique

In the past a variety of the ODMR technique has been explored in terms of various ways of optical detection, with or without applying an external magnetic field, cw or time-resolved spectroscopy. Below we shall give a brief account of these variations of the ODMR technique.

9.3.1 ODMR by Monitoring Total PL Intensity and Polarization

If two spin states involved in a spin transition have different radiative decay rates, a spin resonance transition leads to a net change of their total PL intensity. The so-obtained ODMR signal is proportional to the product of the difference in their radiative decay rates and the population change induced by the spin resonance transition (see Figs. 9.2 and 9.3). The vast majority of the ODMR studies reported to date have employed this type of the ODMR technique.

When the radiative decay rates are the same for the involved spin levels, the ODMR signal by monitoring total PL intensity vanishes. It is, however, still possible to observe an ODMR signal by monitoring a specific polarization or the difference of the two polarizations if the two spin levels emit light of different polarizations (Figs. 9.2 and 9.4). This is usually a more sensitive way of optical detection as compared to the above method of detecting total PL intensity.

9.3.2 ODMR in Zero Field and in Applied Magnetic Fields

In most of ODMR studies reported to date, a sweeping external magnetic field is applied to tune Zeeman splitting of spin sublevels into resonance with the energy of the microwave photons of a fixed frequency, in the same way as a conventional ESR experiment does. In a zero field ODMR experiment [12–14], on the other hand, the energy of the microwave photons is tuned by sweeping the frequency of the microwave field to match zero-field splitting of the spin multiplet (e.g. a spin triplet as shown in Fig. 9.5).

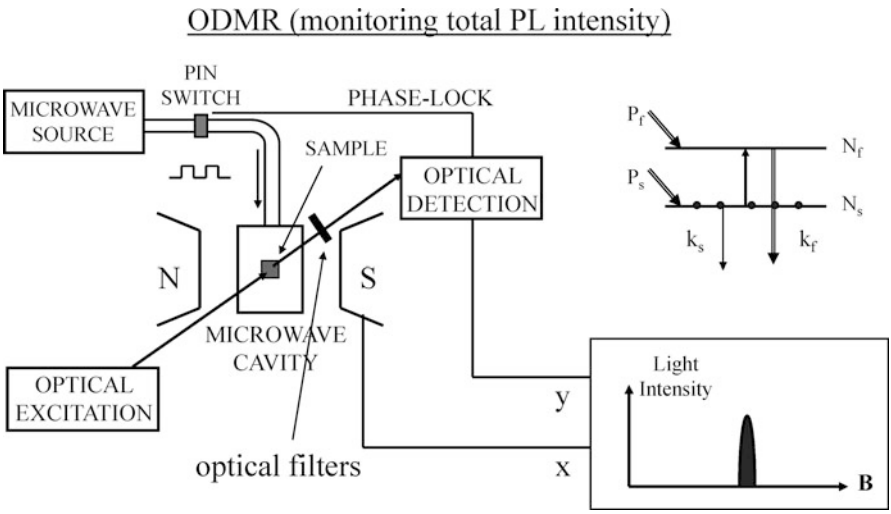

Fig. 9.3 Schematic picture of the ODMR technique by monitoring total PL intensity. P, N, and k denote the populating, population and radiative decay rate of the corresponding spin level. The subscript f and s refer to the spin levels with a faster and slower decay rate, respectively. S and N represent the poles of an external magnet

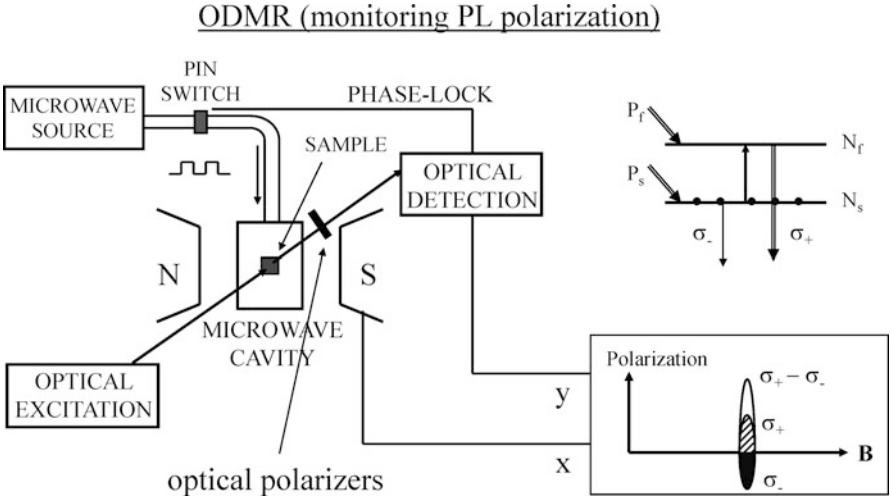

Fig. 9.4 Schematic picture of the ODMR technique, by monitoring a specific light polarization or the difference of the two polarizations

The main advantages of the zero field ODMR are as follows:

- the hyperfine interaction is quenched up to the second order since $< T_u|H_{HF}|T_u > = 0$, where T_u denotes the eigenstate of the sublevel u of the spin triplet (Fig. 9.5). This leads to a narrower ODMR linewidth as compared

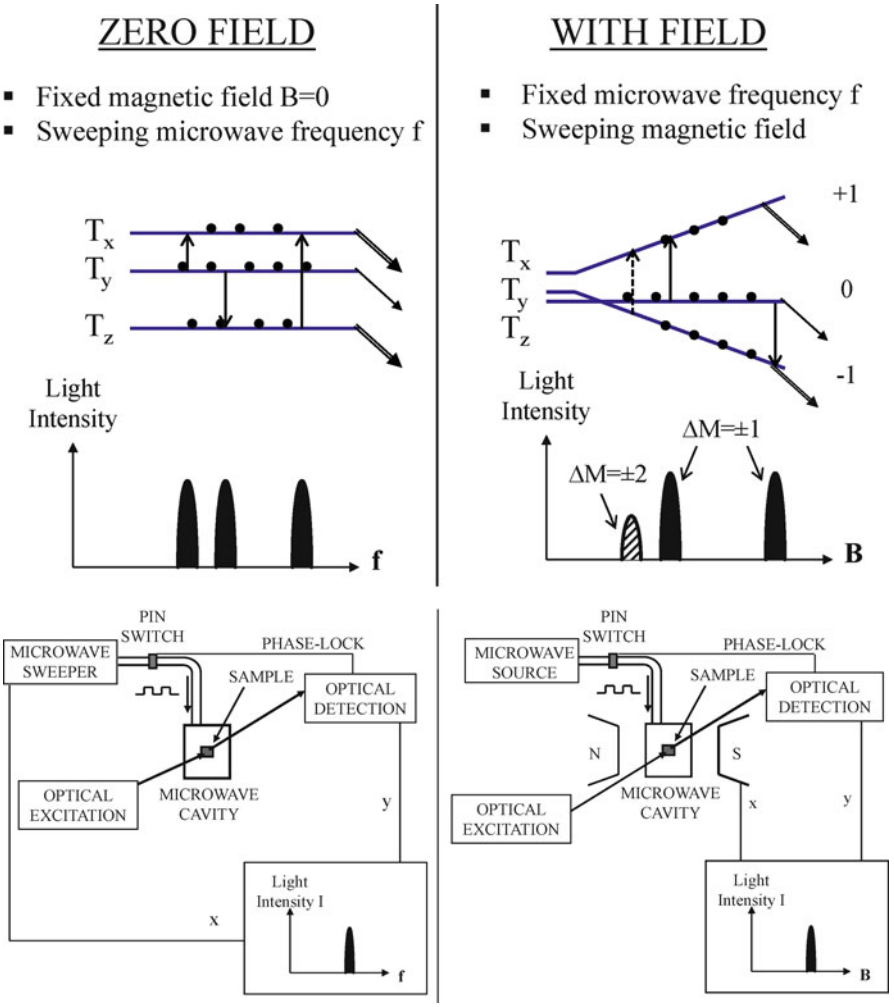

Fig. 9.5 Principle and setup of the ODMR technique in zero field and in an applied magnetic field

to that in the presence of a magnetic field [13] and gives a better chance to resolve the quadrupole interaction, which contains important information about the nuclear spin of a defect atom (thus toward a positive identification) [14] and the electric field gradient near the defect.

- a stronger ODMR signal is expected due to the orientational degeneracy.
- no external magnetic field is required.
- relatively simple states due to the absence of mixing of states by an external magnetic field.

Though the zero-field ODMR can infer the highest symmetry allowed for the defect from the resolved level degeneracy, it is not possible to definitely determine the symmetry of a defect. For that one has to resort to the ODMR technique in an applied magnetic field. It is also rather difficult to obtain a microwave resonant cavity that is tunable in frequency and can be synchronized with the sweeping frequency of the microwave source.

9.3.3 CW and Time-Resolved ODMR

In a cw ODMR experiment, an ODMR signal is obtained in a time-integrated manner. Typically, a cw optical excitation is employed to elevate a defect to its excited state from which spin dependent recombination can be studied by ODMR. To enhance the ODMR signal, an on-and-off microwave modulation or a magnetic field modulation has often been applied to allow sensitive lock-in detection of the microwave-induced change in the optical emission intensity, see Fig. 9.6. The so-obtained ODMR signal intensity can be estimated from an analysis of rather simple rate equations under steady-state conditions [15].

In a time-resolved ODMR experiment, on the other hand, a pulsed optical excitation (usually by a laser pulse) is used and the transient decay of the excited spin states is monitored. A microwave pulse applied some time after the laser pulse will change the population of the sublevels brought into resonance by the microwave field. If the radiative decay rates are different between these two sublevels, this will lead to a change in PL intensity – often called by microwave induced delayed phosphorescence (MIDP) [16] (see Fig. 9.7).

Useful dynamical properties of the defect excited states can be obtained by MIDP such as populating rates, total decay rates, relative radiative decay rates, etc., provided that spin-lattice relaxation rates are slow compared to the decay rates. To ensure that this condition applies, MIDP experiments are usually carried out at the lowest temperature possible. The method to obtain the dynamical properties of a defect excited state will be presented below in Sect. 9.4.1.2 in connection with the example case of ODMR applications.

9.4 Applications of the ODMR Technique

Below we shall present some examples to demonstrate the capability of the ODMR technique in retrieving useful information on physical properties of defects in semiconductors. We will show that ODMR can not only be directly applied to studies of radiative defects but also be employed to indirectly study nonradiative defects by monitoring radiative recombination processes of other competing defects.

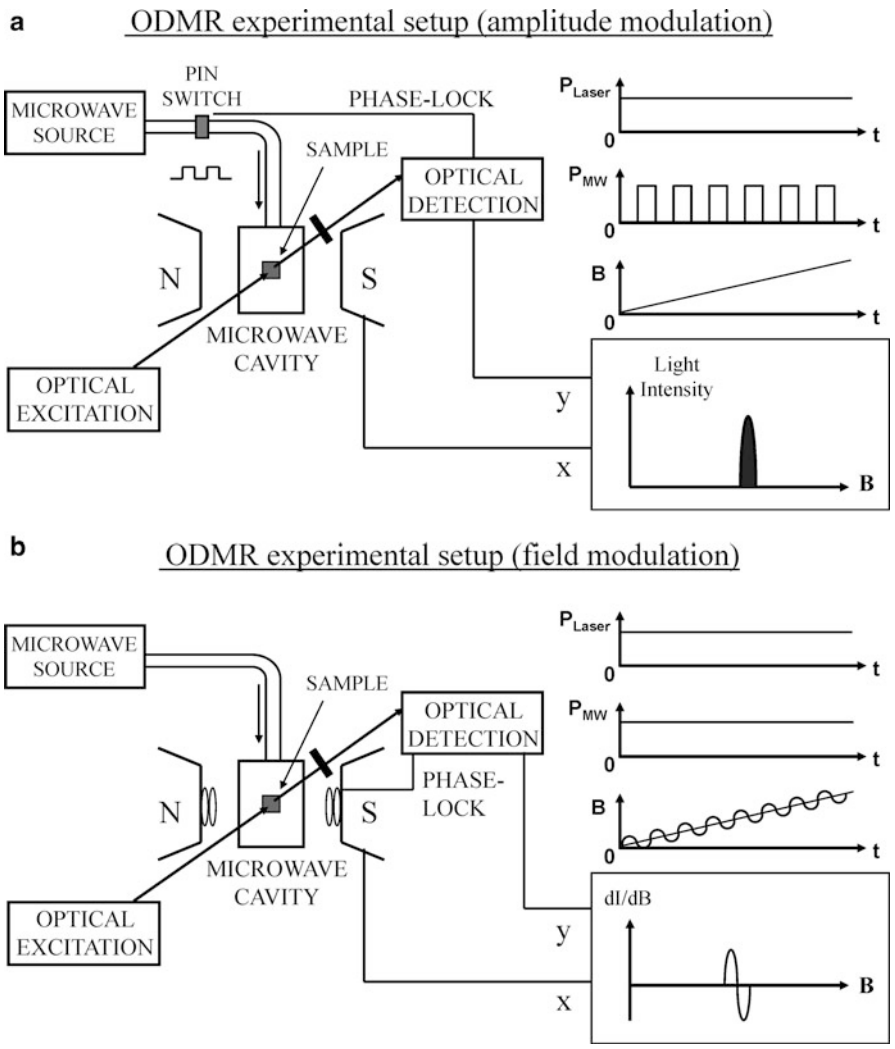

Fig. 9.6 Simple pictures of the cw ODMR experimental setup, (**a**) with an on-and-off microwave modulation, and (**b**) with a magnetic field modulation

9.4.1 Radiative Defects: Example by the S-Cu Complex in Silicon

As an example of successful applications of the ODMR technique for radiative defects in semiconductors, we present below ODMR results from the S-Cu complex defect in silicon [14, 17, 18]. The stable configuration of this defect gives rise to the zero-phonon PL line at 0.968 eV ($S_A{}^0$) at low temperature [18], originating from the photo-excited spin triplet state of the bound exciton at the defect, Figs. 9.8 and 9.9.

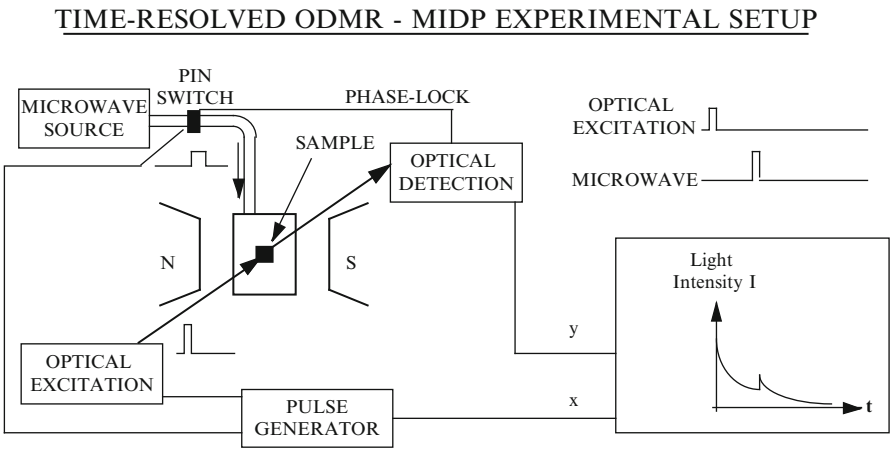

Fig. 9.7 Principle and setup of the time-resolved ODMR technique – MIDP

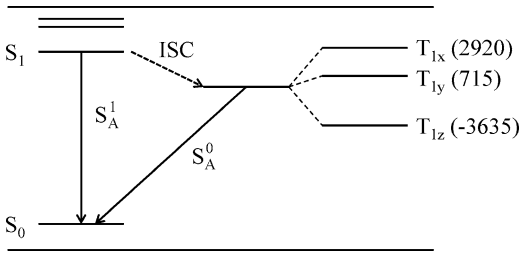

Fig. 9.8 The electronic level scheme of the S-Cu defect in silicon. *Solid* and *broken arrows* represent the radiative and nonradiative transitions, respectively. The zero-field splitting parameters are indicated in MHz (From Ref. [17])

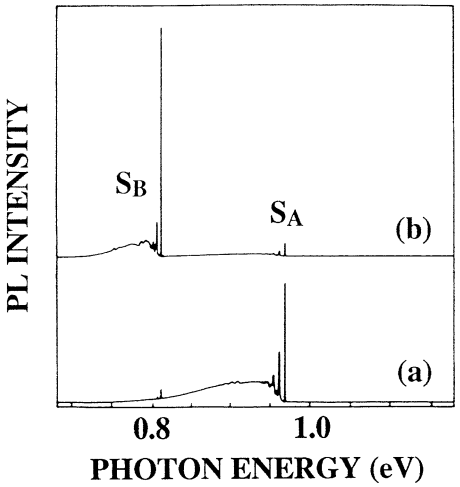

Fig. 9.9 PL spectrum of the S-Cu defect in silicon obtained at 4.2 K (From Ref. [18])

With increasing temperature the PL line at 0.9771 eV ($S_A{}^1$) arising from the singlet excited state becomes dominating. The zero-phonon PL line at 0.812 eV ($S_B{}^0$) arises from the triplet excited state of the same defect in its metastable configuration [14, 17, 18], but will not be discussed further here.

9.4.1.1 CW Zero-Field ODMR

Due to the presence of a Cu atom in the defect with a nuclear spin I = 3/2 for both isotopes (^{63}Cu, I = 3/2, $g_n = 1.484$, $Q = -0.356 \times 10^{-43}$ C cm^2, natural abundance 69.1% and ^{65}Cu, I = 3/2, $g_n = 1.588$, $Q = -0.312 \times 10^{-43}$ C cm^2, natural abundance 30.9%), the electronic structure of the spin triplet (S = 1) excited state of the S-Cu defect including interactions with the nuclear spins is rather complicated. By neglecting the difference in the nuclear g_n values and quadrupole moments of the two Cu isotopes, the following spin Hamiltonian was used to describe the interaction between the electron spin S = 1 and a single nuclear spin I = 3/2:

$$H = H_{ss} + H_Q + H_{HF} = \mathbf{S{\bullet}D{\bullet}S{+}I{\bullet}P{\bullet}I{+}S{\bullet}A{\bullet}I} \tag{9.2}$$

Here the first term describes the zero-field splitting of the electron spin induced by the spin-orbit interaction and spin-spin interactions. In its principal axes system, denoted by x,y,z, H_{ss} can be written as

$$H_{ss} = D_{zz}S_z^2 + D_{yy}S_y^2 + D_{xx}S_x^2 \tag{9.3}$$

H_{ss} is diagonal on the basis of the triplet function T_z, T_y, and T_x. These functions are linear combinations of the eigenfunctions of the S_z operator:

$$\begin{aligned} T_x &= \frac{1}{\sqrt{2}}(|{+}1\rangle - |{-}1\rangle), \\ T_y &= \frac{i}{\sqrt{2}}(|{+}1\rangle + |{-}1\rangle), \\ T_z &= |0\rangle\,. \end{aligned} \tag{9.4}$$

The functions have the property

$$\begin{aligned} S_x T_y &= -S_y T_x = i\,T_z, \\ S_u T_u &= 0, u = x, y, z. \end{aligned} \tag{9.5}$$

The result is that matrix elements of the type $< T_u|H_{HF}|T_u > = 0$ and the hyperfine interaction reduces to a second-order effect.

The second term H_Q of Eq. (9.2) represents the quadrupole splitting of the spin states of the I = 3/2 nucleus. Its principal axis system x′, y′, z′ is determined by the electric field gradient at the nucleus and H_Q can be written as

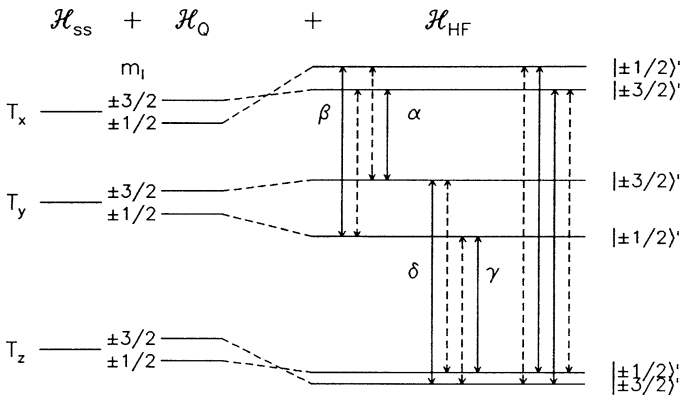

Fig. 9.10 The calculated positions of the spin triplet sublevels of the S-Cu defect in Si from Eq. (9.2). The allowed and "forbidden" spin transitions are indicated by the *solid* and *broken vertical arrows*, respectively. α, β, γ, and δ transitions give rise to the ODMR signals shown in Fig. 9.12 (From Ref. [14])

$$H_Q = P_{z'z'} I_{z'}^2 + P_{y'y'} I_{y'}^2 + P_{x'x'} I_{x'}^2$$
$$= \frac{1}{2} P_{z'z'} \left[3I_{z'}^2 - I(I+1) + \eta \left(I_{x'}^2 - I_{y'}^2 \right) \right] \tag{9.6}$$

with

$$\eta = \frac{P_{x'x'} - P_{y'y'}}{P_{z'z'}} \quad (0 < \eta < 1).$$

The last term H_{HF} describes the central hyperfine interaction between the electron spin and the nuclear spin. Since no indication was found of an anisotropy of **A** we assume that H_{HF} can be written as

$$H_{HF} = A(S_x I_x + S_y I_y + S_z I_z). \tag{9.7}$$

The calculated positions of the triplet sublevels with the aid of the spin Hamiltonian are shown in Fig. 9.10 [14]. The allowed and "forbidden" spin transitions are indicated by the solid and broken vertical arrows, respectively. Due to the mixing of states induced by the hyperfine interaction, the formerly forbidden electron spin transitions become partially allowed and can be observed at high microwave power. The experimentally obtained ODMR signals arising from the transitions T_y-T_z (4.3 GHz) and T_x-T_z (6.5 GHz) are shown in Fig. 9.11. The effect of microwave power on the ODMR spectra can be understood as being due to the relative increase of the intensities of the forbidden transitions due to saturation of the allowed ones with increasing microwave power.

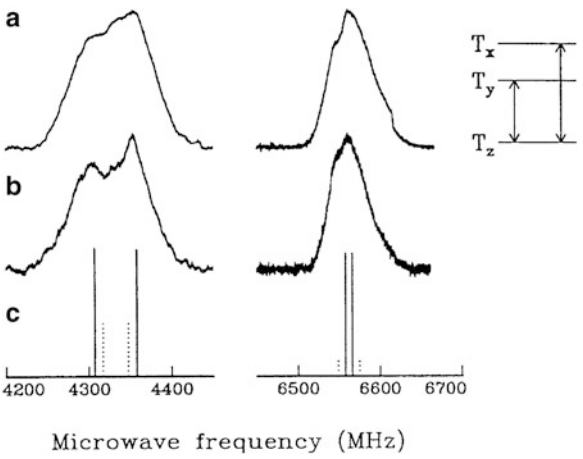

Fig. 9.11 (**a**) and (**b**) The T_y-T_z and T_x-T_z ODMR transitions of the S_A spin triplet of the S-Cu defect in Si at high (200 mW) and low (10 mW) microwave power. (**c**) The calculated positions for the forbidden (*dashed lines*) and allowed (*solid lines*) transitions as obtained from the spin Hamiltonian Eq. (9.2). The length of the sticks indicates the relative values of the transition probabilities (From Ref. [14])

The cw zero-field ODMR performed in a similar way has failed to detect the T_x-T_y (2.2 GHz) transition, however, because the two sublevels involved have the same radiative decay rate (supported by the time-resolved ODMR results of the same defect to be discussed below). This difficulty was successfully overcome by employing a double resonance technique. Here we first pump the T_y–T_z transition with cw microwaves at a fixed frequency. When using a saturating microwave power the populations of the two levels are equalized and become $(N_y + N_z)/2$. To make the T_x–T_y transition visible we subsequently scan a saturating amplitude modulated microwave field through the T_x-T_y resonance region and detect again synchronously in the PL intensity. This second microwave field will change the population of T_x, T_y and T_z to $(N_x + N_y + N_z)/3$. Since the radiative decay rate of T_z is different from T_x and T_y, this will lead to a change in PL intensity. The results are shown in Fig. 9.12. The double-resonance ODMR allowed us to prove that the T_x–T_y and the T_y–T_z transitions consist of two components as expected for the involvement of a Cu atom with a nuclear spin I = 3/2. The double-resonance ODMR also allowed us to determine the linewidth of the transitions to be about 50 MHz, considerable smaller than the linewidth of 700 MHz (25 mT) observed in the X-band ODMR experiments in applied magnetic fields [18]. This reduction of the ODMR linewidth is caused by the quenching of the hyperfine interaction in first order in zero magnetic field. The obtained spin Hamiltonian parameters are given in Table 9.1.

9.4.1.2 Time-Resolved Zero-Field ODMR

The MIDP method allows us to determine the total decay rates k_i (I = x, y, and z), the relative radiative decay rates $k_i{}^r$, and the relative populating rates P_i of the spin triplet excited state [17]. In the MIDP experiment a laser flash, with a short pulse duration compared to the decay times, is applied to excite the defect from the ground state S_0 to the singlet excited state S_1. The resulting populations of the triplet sublevels N_x, N_y and N_z are proportional to their populating rates P_x, P_y and P_z. The

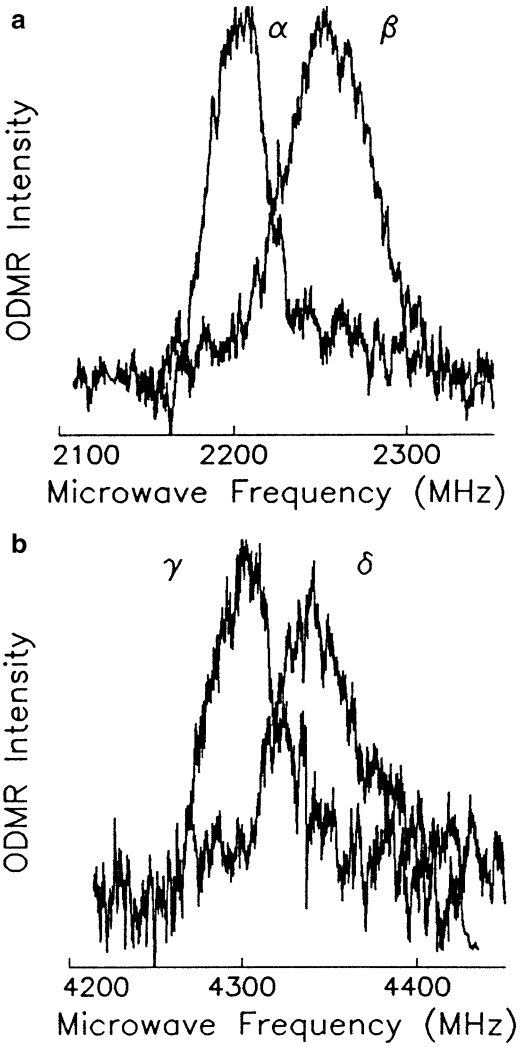

Fig. 9.12 The double-resonance ODMR transitions of the S_A spin triplet of the S-Cu defect in Si. (**a**) Transitions α and β are obtained by fixing the frequency of the first cw microwave field at 4,350- and 4,300-MHz, respectively, while scanning amplitude modulated second microwaves in the 2.2-GHz region. (**b**) Transitions γ and δ are obtained by fixing the frequency of the first cw microwave field at 2,260- and 2,200-MHz, respectively, while scanning amplitude modulated second microwaves in the 4.3-GHz region (From Ref. [14])

Table 9.1 The set of parameters from the best fit of the spin Hamiltonian Eq. (9.2) to the experimental data

D_{xx} (MHz)	D_{yy} (MHz)	D_{zz} (MHz)	A (MHz)	$P_{z'z'}$ (MHz)	η
–2,905	–705	3,610	175	10–20	0–1

From Ref. [14]

decay of the $S_A{}^0$ PL intensity from the triplet to the ground state S_0 as a function of time is given by

$$I_{PL}(t) = c \sum_{i=x,y,z} k_i^r N_i e^{-k_i t}, \tag{9.8}$$

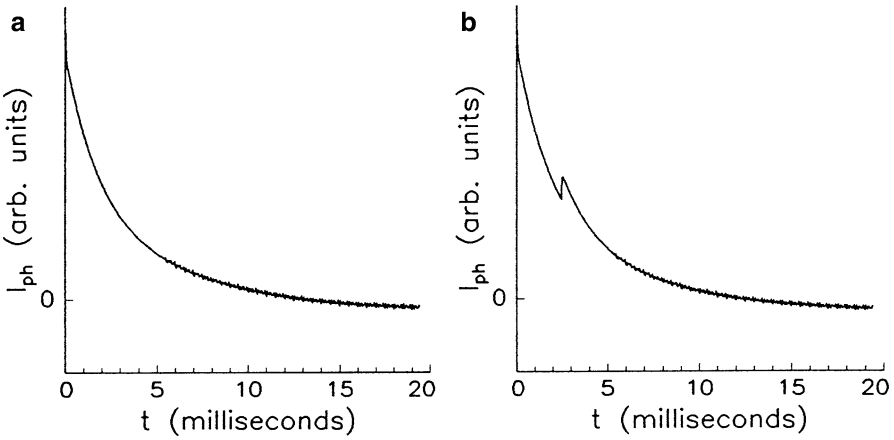

Fig. 9.13 The decay of the $S_A{}^0$ PL of the S-Cu defect in Si (**a**) without and (**b**) with the application of a microwave pulse at 6,555 MHz, resonant with the T_x-T_z transition at $t_d = 2.5$ ms. The PL is selectively excited by a pulse laser at 977.1 meV into the excited singlet state S_1. T = 1.2 K (From Ref. [17])

where c is a constant depending on the experimental conditions. At a time t_d after the laser flash a microwave pulse, resonant with, for example, the T_x-T_z transition at 6,555 MHz is applied. The pulse length is chosen to be short compared to the lifetimes $k_x{}^{-1}$ and $k_z{}^{-1}$, so that the total population of T_x and T_z is approximately constant during the microwave pulse. A typical result of this experiment is shown in Fig. 9.13. The evolution of the PL intensity following the microwave pulse is then

$$I_{PL}(t) = cN_y(t_d)k_y^r e^{-k_y(t-t_d)} + c\left[N_x(t_d) - f\Delta N_{x-z}(t_d)\right]k_x^r e^{-k_x(t-t_d)} + c\left[N_z(t_d) + f\Delta N_{x-z}(t_d)\right]k_z^r e^{-k_z(t-t_d)}, \quad (9.9)$$

where $\Delta N_{x-z}(t_d) = N_x(t_d) - N_z(t_d)$.

The factor f in Eq. (9.9) represents the effect of the transfer of population between T_x and T_z induced by the resonant microwaves. The MIDP signal is obtained from the difference of the PL decay with and without microwaves, respectively. The result of this subtraction for $t_d = 2.5$ ms is shown in Fig. 9.14. The evolution of this signal is described by the difference of Eqs. (9.9) and (9.8) for $t \geq t_d$.

$$I_{MIDP}(t) = cf\left[N_x(t_d) - N_z(t_d)\right] \times \left[k_z^r e^{-k_z(t-t_d)} - k_x^r e^{-k_x(t-t_d)}\right]. \quad (9.10)$$

From this equation it follows that the MIDP signal can be fitted to a biexponential function with time constants that represent the decay rates of the two sublevels connected by the microwave field. The ratio of the prefactors of the two exponentials

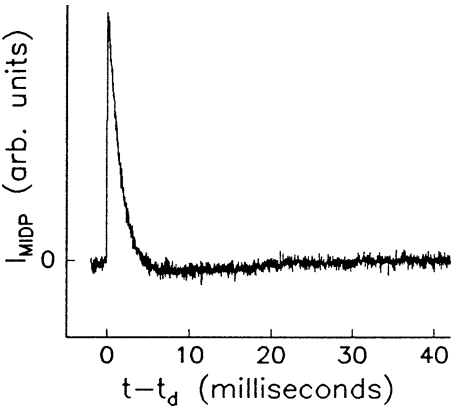

Fig. 9.14 The MIDP signal – the difference of the PL decay curves with and without the application of a microwave pulse resonant with the T_x-T_z transition at 6,555 MHz. T = 1.2 K (From Ref. [17])

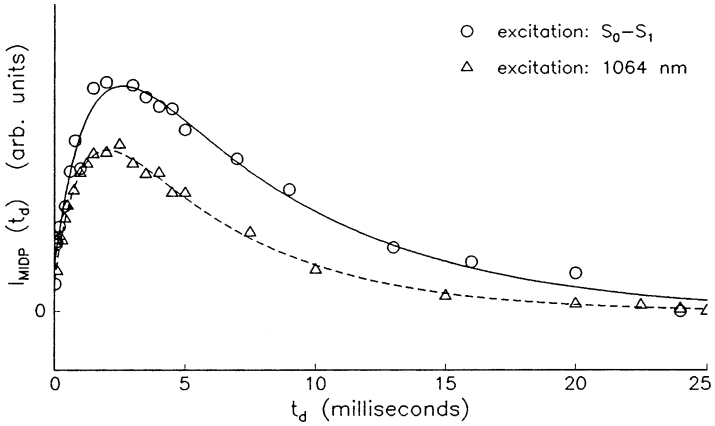

Fig. 9.15 The maximum amplitude of the MIDP signal, upon a microwave pulse at 6,555 MHz saturating the T_x-T_z transition, as a function of t_d. The signals have been obtained either following selective excitation at 977.1 meV into the S_1 excited state or following excitation at 1,164 meV (1,064 nm) over the band gap of Si. The *drawn lines* represent a fit to Eq. (9.11). T = 1.2 K (From Ref. [17])

yields the relative radiative decay rates $k_x{}^r$ and $k_z{}^r$. The maximum amplitude of the MIDP signal at $t = t_d$ as a function of t_d is described by the following relation:

$$I_{MIDP}(t_d) = cf(k_z^r - k_x^r)\left[N_x(0)e^{-k_x t_d} - N_z(0)e^{-k_z t_d}\right]. \tag{9.11}$$

In this way one again finds a decay curve which is described by a biexponential function with k_x and k_z as the time constants (Fig. 9.15). Here the ratio of the prefactors yields the relative populations at $t_d = 0$ and thus the relative populating rates of the two sublevels involved in the microwave transition. A similar set of experiments on the T_y-T_z transition at 4,350 MHz yields $k_y{}^r$, $k_z{}^r$, k_y, k_z, P_y *and* P_z. They are summarized in Table 9.2.

Table 9.2 The decay rates k_i, the relative radiative decay rates k_i^r, and the relative populating rates P_i of the first excited triplet state T_1 of the S-Cu defect in Si in zero field. T = 1.2 K

	k_i	k_i^r	P_i
T_x	$(0.11 \pm 0.02) \times 10^3$	1.0 ± 0.2	1.0 ± 0.15
T_y	$(0.11 \pm 0.02) \times 10^3$	1.0 ± 0.2	1.0 ± 0.15
T_z	$(0.56 \pm 0.08) \times 10^3$	4.0 ± 1.0	1.0 ± 0.15

From Ref. [17]

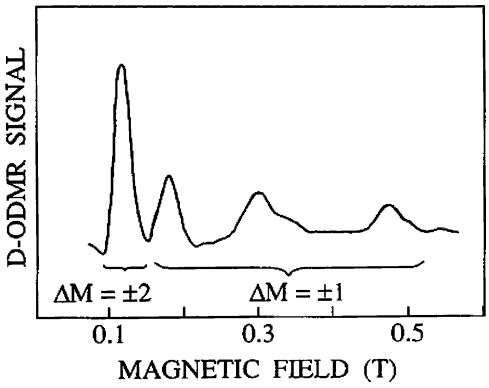

Fig. 9.16 A typical ODMR spectrum from the S_A spin triplet of the S-Cu defect in Si, at 4 K and 9.24 GHz (From Ref. [18])

9.4.1.3 CW ODMR in Magnetic Fields

In the X-band ODMR experiments, the microwave frequency is fixed at 9.24 GHz while sweeping magnetic field. At certain field positions, the Zeeman splitting of the triplet sublevels can be brought into resonance with the microwave photon energy causing a spin resonance transition between the involved sublevels. If these sublevels have different radiative decay rates, such a spin transition can be detected optically leading to an ODMR signal. A typical ODMR spectrum obtained by the quasi-cw delayed ODMR technique [19] is shown in Fig. 9.16, where both the allowed $\Delta M = \pm 1$ and the forbidden $\Delta M = \pm 2$ transitions are observed. The observation of the forbidden transitions is attributed to large mixing of states by the strong fine-structure and hyperfine interactions of the defect. From the angular dependence study of the ODMR signals, the principal defect axes x, y, z can be determined and the defect symmetry is concluded to be monoclinic-I [18].

9.4.2 Nonradiative Defects: Examples by the Vacancy-Oxygen Complex and the P-Donor in MBE-Si/SiGe

The scope of the ODMR applications actually reaches beyond radiative defects and recombination channels. The ODMR technique is also sensitive to strong

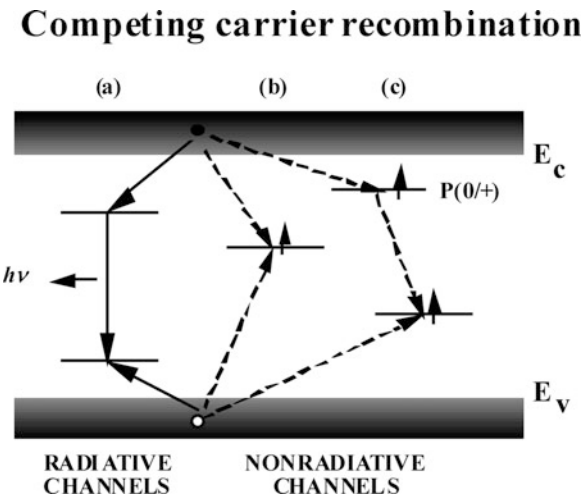

Fig. 9.17 Principle for ODMR studies of nonradiative defects. Spin-resonance enhanced carrier recombination via non-radiative channels [(**b**) by a single nonradiative defect and (**c**) by nonradiative inter-center charge transfer] reduces the number of carriers available for radiative recombination channel (**a**), leading to a corresponding decrease in PL intensity

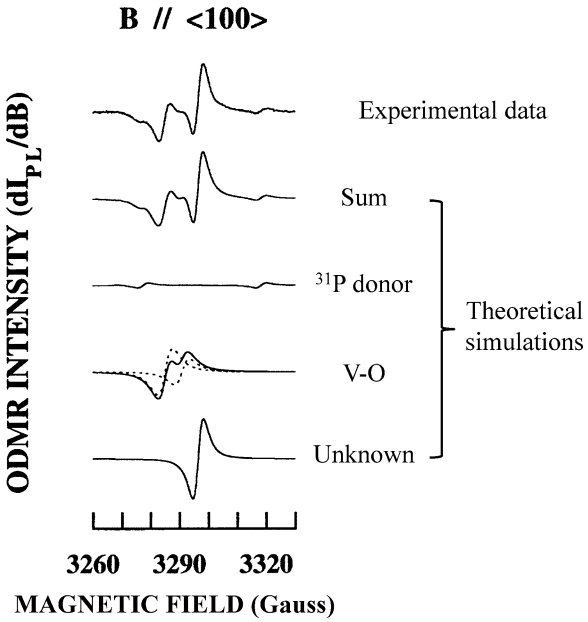

Fig. 9.18 The *top curve* shows an ODMR spectrum from MBE-Si grown at 420°C, taken at 9.23 GHz. From the analysis, three nonradiative defects (the P donor, the V-O complex and an unknown defect) were revealed and their corresponding ODMR spectra could be deconvoluted. The derivative lineshape is due to the field modulation in the ODMR experiments (From Ref. [23])

nonradiative recombination channels and defects, via their competition in carrier recombination. This provides the framework for the optical detection of nonradiative defects [20], as also illustrated in Fig. 9.17.

Figure 9.18 shows an ODMR spectrum observed via deep PL bands in a wide spectral range 0.7–1.05 eV occurring in Si epitaxial layers and Si/SiGe quantum well structures grown by molecular beam epitaxy (MBE) at low temperatures [21–25]. Even though the origins of various PL bands are known to be different, the

same ODMR spectrum could be obtained since the nonradiative defects undergoing the spin resonance transitions compete with all the radiative defects in carrier recombination. From detailed analysis of the ODMR data, two of the nonradiative defects were identified to be the shallow P donor and the deep vacancy-oxygen (V-O) complex [23]. While a deep center like the V-O complex is largely expected to act as a recombination center, the similar observation for the P donor is rather surprising as its traditional role should be an electron trap. The physical mechanism has in the past been shown in bulk Si as being due to efficient charge transfer from the P donor to other efficient recombination centers (Fig. 9.17c) [26]. The introduction of the V-O defect in the as-grown material was facilitated by a low surface adatom mobility and a substrate bias during potential-enhanced growth in combination with a low oxygen desorption from the surface at the low growth temperatures. Fortunately, the V-O defect is known from earlier studies in bulk Si to be readily annealed out at 500°C. A similar postgrowth annealing treatment can thus be expected to remove this nonradiative defect, leading to an improvement in the optical properties of the structures. This has indeed been experimentally demonstrated where a significant improvement has been achieved in thermal quenching behavior of the PL emissions by annealing [24, 25]. This gives a good example on the feedback from the knowledge gained from the ODMR investigations to the defect engineering.

9.5 Recent Developments and Trends

Substantial effort has been made over the past years in instrumentation developments of spin resonance techniques. It has mainly been directed to the following three fronts: high spectral resolution, better time resolution and high spatial resolution. The first two fronts have now been met with the commercialization of the W-band (95-GHz) and mm-wave (263 GHz) ESR spectrometer and the pulsed ESR spectrometer in both X-band (9-GHz) and W-band. The W-band system offers ten times better in spectral resolution as compared to that of the commonly used X-band system [4]. The best time resolution available in the commercial spectrometers is about 20 ns at present. High frequency (>95 GHz) ODMR has been developed in several research labs worldwide.

The quest for unprecedented spatial resolution has been made through various approaches. The first approach utilizes selective optical excitation by single-frequency laser to single out a single spin system from the inhomogeneously broadened spectral line of an ensemble under only a slight fluctuation in local potential. This approach has been shown to be rather successful for molecular systems, where ODMR from a single molecule has been reported [27, 28]. Though the single-spin ODMR was achieved by improved spectral resolution rather than by spatial resolution, it has demonstrated the ability of the ODMR technique for single-spin detection. The second approach applied submicron optical apertures made by a metal mask patterned directly on samples with electron-beam lithographic

technique, so that only few spins are monitored. By this approach, single quantum dots in GaAs/AlGaAs semiconductor quantum structures were studied by optically detected nuclear magnetic resonance (OD-NMR) reaching a lateral spatial resolution of about 10 nm [29]. Similarly, confocal optical microscopy in combination with ODMR has recently shown great success in manipulating spins of a single defect, e.g. the N-V center in diamond, promising for applications in solid-state quantum computation [30]. The third approach for high spatial resolution of spin resonance is based on local probe microscopies. The most remarkable progress in this aspect has been the magnetic resonance force microscopy (MRFM) [31, 32], which has been demonstrated the capability of single spin detection. It also offers possibilities for three-dimensional imaging. The best spatial resolution achieved so far is still far from atomic scale, though. No local probe ODMR has been reported so far. The most recent years have witnessed a sharp increase of the interest towards this issue among scientific communities of various disciplines, driven by e.g. growing interest in the emerging fields of spintronics and quantum computation, and surely this trend will continue to grow.

Acknowledgments I am grateful to many colleagues for their valuable collaboration and contributions in connection to the work presented in this chapter, in particular J. Schmidt, A.M. Frens, M.T. Bennebroek, M.E. Braat, I.A. Buyanova, B. Monemar, A. Henry, E. Janzén, W.X. Ni, and G.V. Hansson. The financial support by the Swedish Research Council is also greatly appreciated.

References

1. Brossel J, Bitter F (1952) A new "double resonance" method for investigating atomic energy levels. Application to Hg $^3P_1^*$. Phys Rev 86:308–316
2. Cavenett BC (1981) Optically detected magnetic resonance (O.D.M.R.) investigations of recombination processes in semiconductors. Adv Phys **30**:475
3. Davies JJ (1988) Optically-detected magnetic resonance studies of II–VI compounds. J Cryst Growth 86:599–608
4. Chen WM, Monemar B, Frens AM, Bennebroek MT, Schmidt J (1994) Magnetic resonance techniques for excited state spectroscopy of defects in silicon. Mat Sci Forum 143–147: 1345–1352
5. Kennedy TA, Glaser ER (1998) Magnetic resonance of epitaxial layers detected by photoluminescence. Semicond Semimet 51A:93–136
6. Chen WM (2000) Applications of optically detected magnetic resonance in semiconductor layered structures. Thin Solid Films 364:45–52
7. Slichter CP (1990) Principles of magnetic resonance. Springer Ser in Solid State Sci, vol 1. Springer, Berlin
8. Abragam A, Bleaney B (1970) Electron paramagnetic resonance of transition ions. Clarendon, Oxford
9. Spaeth J-M, Niklas JR, Bartram RH (1992) Structural analysis of point defects in solids. Springer, New York
10. Chen WM, Monemar B, Godlewski M (1989) Magneto-optical characterization of isoelectronic complex defects in semiconductors. Defects Diffusion Forum 62–63:133–144
11. Watkins GD (1998) EPR and ENDOR studies of defects in semiconductors. Semicond Semimet 51A:1–43

12. Salib EH, Cavenett BC (1984) Zero-field optically detected magnetic resonance (ZF-ODMR) in semiconductors. J Phys C17:L251–255
13. Schmidt J, van der Waals JH (1969) The structure of the zero-field transitions of phosphorescent quinoxaline. Chem Phys Lett 3:546–549
14. Frens AM, Bennebroek MT, Schmidt J, Chen WM, Monemar B (1992) Zero-field optical detection of magnetic resonance on a metastable sulfur-pair-related defect in silicon: Evidence for a Cu constituent. Phys Rev B46:12316–12322
15. Morigaki K (1983) Optically detected magnetic resonance in amorphous semiconductors. Jap J Appl Phys 22:375–388
16. Schmidt J, Antheunis DA, van der Waals JH (1971) The dynamics of populating and depopulating the phosphorescent triplet state as studied by microwave induced delayed phosphorescence. Mol Phys 22:1–17
17. Frens AM, Braat ME, Schmidt J, Chen WM, Monemar B (1995) Transfer mechanism between pseudodonor excited singlet and triplet states of the S-Cu complex defect in silicon. Phys Rev B52:8848–8853
18. Chen WM, Singh M, Monemar B, Henry A, Janzén E, Frens AM, Bennebroek MT, J. Schmidt J (1994) S-Cu-related metastable complex defect in Si by optical detection of magnetic resonance. Phys Rev B50:7365–7370
19. Chen WM, Monemar B (1990) Delayed optical detection of magnetic resonance for defects in Si and GaAs. J Appl Phys 68:2506–2509
20. Chen WM, Monemar B (1991) Role of free carriers in the application of optically detected magnetic resonance for studies of defects in silicon. Appl Phys A53:130–135
21. Buyanova IA, Chen WM, Henry A, Ni WX, Hansson GV, Monemar B (1995) Properties of deep photoluminescence bands in SiGe/Si quantum structures grown by molecular beam epitaxy. Appl Phys Lett 67:1642–1644
22. Chen WM, Buyanova IA, Henry A, Ni WX, Hansson GV, Monemar B (1996) Nonradiative defects in Si and SiGe/Si heterostructures grown by molecular beam epitaxy. Appl Phys Lett 68:1256–1258
23. Chen WM, Buyanova IA, Ni WX, Hansson GV, B. Monemar (B (1996) Identification of grown-in efficient nonradiative recombination centers in molecular beam epitaxial silicon. Phys Rev Lett 77:4214–4217
24. Buyanova IA, Chen WM, Pozina G, Monemar B, Ni WX, Hansson GV (1997) Mechanism for thermal quenching of luminescence in SiGe/Si structures grown by molecular beam epitaxy: Role of nonradiative defects. Appl Phys Lett 71:3676–3678
25. Chen WM, Buyanova IA, Ni WX, Hansson GV, B. Monemar B (1997) Postgrowth hydrogen treatments of nonradiative defects in low-temperature molecular beam epitaxial Si. Appl Phys Lett 70:369–371
26. Chen WM, Monemar B, Janzén E, Lindström JL (1991) Direct observation of intercenter charge transfer in dominant nonradiative recombination channels in silicon. Phys Rev Lett 67:1914–1917
27. Köhler J, Disselhorst JAJM, Donckers MCJM, Groenen EJJ, Schmidt J, Moerner WE (1993) Magnetic resonance of a single molecular spin. Nature 363:242–244
28. Wrachtrup J, von Borczyskowski C, Bernard, Orrit JM, Brown R (1993) Optical detection of magnetic resonance in a single molecule. Nature 363:244–245
29. Gammon D, Brown SW, Snow ES, Kennedy TA, Katzer DS, D. Park D (1997) Nuclear spectroscopy in single quantum dots: nanoscopic Raman scattering and nuclear magnetic resonance. Science 277:85–88
30. Gruber A, Dräbenstedt AA, Tietz C, Fleury L, Wrachtrup J, von Borczyskowski C (1997) Scanning confocal optical microscopy and magnetic resonance on single defect centers. Science 276:2012–2014
31. Rugar D, Yannoni CS, Sidles JA (1992) Mechanical detection of magnetic resonance. Nature 360:563–566
32. Rugar D, Budakia R, Mamin H, Chui B (2004) Single spin detection by magnetic resonance force microscopy. Nature 430:329–332

General Appendices

Tables G1–G5 and G7 below were adapted from the Appendix in [Anders Lund, Masaru Shiotani and Shigetaka Shimada: Principles and Applications of ESR Spectroscopy (Springer, 2011)] with permission from Springer

Table G1 Fundamental Constants[a]

Quantity	Symbol	Value	SI unit
Speed of light	c	$2.997\,924\,58 \times 10^{8}$	$\mathrm{m\ s^{-1}}$
Elementary charge	e	$1.602\,176 \times 10^{-19}$	C
Faraday constant	$F = N_\mathrm{A} e$	$9.648\,456 \times 10^{4}$	$\mathrm{C\ mol^{-1}}$
Boltzmann constant	k	$1.380\,65 \times 10^{-23}$	$\mathrm{J\ K^{-1}}$
Gas constant	$R = N_\mathrm{A} k$	8.314 47	$\mathrm{J\ K^{-1}\ mol^{-1}}$
Planck constant	h	$6.626\,068 \times 10^{-34}$	J s
	$\hbar = h/2\pi$	$1.054\,571 \times 10^{-34}$	J s
Avogadro constant	N_A	$6.022\,14 \times 10^{-23}$	$\mathrm{mol^{-1}}$
Atomic mass unit	u	$1.660\,54 \times 10^{-27}$	kg
Mass			
Electron	m_e	$9.109\,38 \times 10^{-31}$	kg
Proton	m_p	$1.672\,62 \times 10^{-27}$	kg
Neutron	m_n	$1.674\,93 \times 10^{-27}$	kg
Vacuum permittivity	$\varepsilon_0 = 1/c^2\mu_0$	$8.854\,188 \times 10^{-12}$	$\mathrm{F\ m^{-1}}$

[a]CODATA recommended values of the fundamental physical constants 2006, National Institute of Standards and Technology, Gaithersburg, Maryland 20899–8420, USA; http://physics.nist.gov/cuu/Constants/

A. Lund and M. Shiotani (eds.), *EPR of Free Radicals in Solids II*, Progress in Theoretical Chemistry and Physics 25, DOI 10.1007/978-94-007-4887-3,

Table G2 Magnetic Constants in SI Units[a]

Quantity	Symbol	Numerical value	Unit
Magnetic constant	$\mu_0 = 4\pi \times 10^{-7}$	$12.566\,370 \times 10^{-7}$	$N\,A^{-2}$
Bohr magneton	μ_B (β_e)	$927.400\,915\,(23) \times 10^{-26}$	$J\,T^{-1}$
Nuclear magneton	μ_N (β_N)	$5.050\,783\,24(13) \times 10^{-27}$	$J\,T^{-1}$
Electron *g*-factor	g_e	2.002 319 304 361 7(15)	
Electron gyromagnetic ratio	γ_e	$1.760\,859\,770\,(44) \times 10^{11}$	$s^{-1}\,T^{-1}$
μ_B/h	μ_B/h	$13.996\,246\,4(35) \times 10^{9}$	$Hz\,T^{-1}$
μ_B/hc	μ_B/hc	46.686 451 5(12)	$m^{-1}\,T^{-1}$
μ_N/h	μ_N/h	7.622 593 84(19)	$MHz\,T^{-1}$

[a]CODATA recommended values of the fundamental physical constants 2006, National Institute of Standards and Technology, Gaithersburg, Maryland 20899–8420, USA; http://physics.nist.gov/cuu/Constants/

Table G3 Conversion Factors for EPR (ESR) Coupling Constants[a, b]

Unit	MHz	mT	cm^{-1}
MHz	1	0.071 447 66/g	$0.333\,564\,095 \times 10^{-4}$
mT	13.996 25·g	1	$4.668\,645 \times 10^{-4}$ ·g
cm^{-1}	$2.997\,924\,58 \times 10^{4}$	$0.214\,194\,9 \times 10^{4}$/g	1

A coupling given in a unit of the 1st column is calculated in other units by multiplication with the factor in the corresponding row.
Calculations of g from measured values of microwave frequency ν_e (GHz) and resonance field B (T), of resonance field, and of nuclear frequency ν_N (MHz):

$$g = \frac{h}{\mu_B} \cdot \frac{\nu_e}{B} = 0.071447656 \frac{\nu_e(GH_Z)}{B(T)}, B(T) = \frac{h}{\mu_B} \cdot \frac{\nu_e}{g} = 0.071447656 \frac{\nu_e(GH_Z)}{g}$$

$$\nu_N(MH_Z) = \frac{\mu_N}{h} \cdot g_N B = 7.62259384 \cdot g_N B(T)$$

[a]The factors were obtained from CODATA recommended values of the constants in Table G1; http://physics.nist.gov/cuu/Constants/
[b]Mohr PJ, Taylor BN, Newell DB, Rev Mod Phys 80:633 (2008); J Phys Chem Ref. Data 37:1187 (2008)

Table G4 Other Useful Conversion Factors

1 eV	$1.602\,18 \times 10^{-23}$ J
	96.485 kJ mol^{-1}
	8065.5 cm^{-1}
1 cal	4.184 J
1 atm	101.325 kPa
1 cm^{-1}	$1.986\,4 \times 10^{-23}$ J
1 D (Debye)	$3.335\,64 \times 10^{-30}$ C m
1 Å	10^{-10} m
1 T	10^{-4} G (or gauss)
1 L atm	= 101.325 J
θ/°C	= T/K − 273.15

Table G5 Symbols, Variables and Units in EPR (ESR)

Symbol	Name or description	Unit and/or value
A, a	Hyperfine coupling (splitting) constant	MHz, mT (milli-Tesla)
D	Zero-field splitting, Fine structure	cm^{-1}, MHz, mT
B (H)	External magnetic field	T (Tesla)
e	Electron charge	$1.602\ 177 \times 10^{-19}$ A·s
g	g-factor	Dimensionless
G	Radiation yield	$\mu molJ^{-1}$
h	Planck constant	$6.626\ 068 \times 10^{-34}$ J·s
I	Nuclear spin angular momentum	J·s
I	Nuclear spin quantum number	Dimensionless
J	Heisenberg exchange coupling	cm^{-1}, MHz, mT
k	Boltzmann constant	1.380658×10^{-23} $J{\cdot}K^{-1}$
L	Orbital angular momentum	J·s
l	Orbital quantum number	Dimensionless
m_e	Electron mass	0.910939×10^{-30} kg
m_I	Nuclear magnetic quantum number	Dimensionless
m_S	Electron magnetic quantum number	Dimensionless
P	Microwave power	Js^{-1}
Q	Nuclear quadrupole coupling	cm^{-1}, MHz, mT
S	Electron spin angular momentum	J·s
S, s	Electron spin quantum number	Dimensionless
v	Speed	$m{\cdot}s^{-1}$
λ	Spin-orbit coupling constant	cm^{-1}
μ	Magnetic moment	A·s
μ_B, (β_e)	Bohr magneton	9.274015×10^{-24} $J{\cdot}T^{-1}$
μ_N, (β_N)	Nuclear magneton	5.050787×10^{-27} $J{\cdot}T^{-1}$
ν	Frequency	Hz

Table G6 Abbreviations

Abbreviation	Name or description
Magnetic resonance:	
ADMR	Absorption detected magnetic resonance
ALC-MuSR	Avoided level crossing MuSR
BP	Breit-Pauli
CPMG	Carr-Purcell-Meiboom-Gill
CW, cw	Continuous wave
DEER	Double electron electron resonance
DQC-ESR (EPR)	Double quantum coherence ESR (EPR)
ED-EPR (EchoEPR)	Echo-detected EPR
ELDOR	Electron electron double resonance
EMR	Electron magnetic resonance
ENDOR	Electron nuclear double resonance
ENTOR	Electron nuclear triple resonance
EPR	Electron paramagnetic resonance
EPR-COSY	EPR correlation spectroscopy

(continued)

Table G6 (continued)

Abbreviation	Name or description
EPR-SECSY	EPR spin echo correlated spectroscopy
ESE	Electron spin echo
ESEEM	Electron spin echo envelope modulation
ESR	Electron spin resonance
ESTN	Electron spin transient nutation
FID	Free induction decay
FT	Fourier transform
HF, hf	Hyperfine
HF-EPR (ESR)	High frequency EPR (ESR)
HFC, hfc (Hfi or Hfs)	Hyperfine coupling (interaction or structure)
HYSCORE	Hyperfine sublevel correlation
IHC	Isotropic hyperfine coupling
LF-MuSRx	Longitudinal (magnetic) field muon spin-relaxation
MIDP	Microwave induced delayed phosphorescence
MRFM	Magnetic resonance force microscopy
MW, mw	Micro wave
MuSR (μSR)	Muon spin rotation
NMR	Nuclear magnetic resonance
NMRD	Nuclear magnetic relaxation dispersion
NQC, Nqc	Nuclear quadrupole coupling
OD(N)MR	Optically detected (nuclear) magnetic resonance
PELDOR	Pulsed electron electron double resonance
QC-ENDOR (NMR)	Quantum computing ENDOR (NMR)
QTM	Quantum tunneling of magnetization
RF, rf	Radio-frequency
SHF, shf	Super-hyperfine
SMM	Single-molecule magnet
SO(MF)	Spin-orbit (meanfield)
SOO	Spin-other-orbit
SS/EPR dosimeters	Solid state EPR dosimeters
TF	Transverse-field
TPPI	Time proportional phase increment
Quantum chemistry:	
AMFI	Atomic mean field
B3LYP	Becke, three-parameter, Lee-Yang-Parr
CAS	Complete active space
CC	Coupled-cluster
CI	Configuration interaction
CNDO	Complete neglect of differential overlap
CP	Car–Parrinello
CP(CM)	Conducter-like polarized (continuum method)
CP(KS)	Coupled-perturbed (Kohn-Sham)
DFT	Density functional theory
DIM	Diatomics-in-molecules
DKH	Douglas-Kroll-Hess

(continued)

Table G6 (continued)

Abbreviation	Name or description
DZ(P)	Double-zeta (plus polarization)
GGA	Generalized gradient approximations
GIAO	Gauge including atomic orbitals
HDV	Heisenberg-Dirac-Van Vleck
HF	Hartree-Fock
HOMO	Highest occupied molecular orbital
IEF	Integral equation formalism
IGLO	Individual gauges for localized orbitals
INDO	Intermediate neglect of differential overlap
J-T	Jahn-Teller
L(S)DA	Local (spin) density approximation
LUMO	Lowest unoccupied molecular orbital
MCSCF	Multi-configuration SCF
MD	Molecular dynamics
MM	Molecular mechanics
MO	Molecular orbital
MP	Møller-Plesset
MRCI	Multi-reference configuration-interaction
MRMP2	Second-order multi-reference Møller–Plesset
NBMO	Non-bonding molecular orbital
NDDO	Neglect of diatomic differential overlap
PCM	Polarizable continuum models
QM/MM	Quantum-mechanics/molecular-mechanics
(Q)RO	(Quasi) restricted orbital
ROHF	Restricted open-shell Hartree-Fock
SAC-CI	Symmetry-adapted cluster configuration interaction
SCF	Self-consistent field
SCIPCM	Self-consistent isodensity PCM
SCRF	Self-consistent reaction field
SD(T)	Single, double (and perturbative triple)
SECI (CIS)	Single excitation configuration interaction
SO-CI	Spin–orbit configuration interaction
SOMO	Singly occupied molecular orbital
SOS	Sum-over-states
TZ	Triple-zeta
UDFT	Uncoupled density functional theory
UHF	Unrestricted Hartree-Fock
ZFS	Zero-field splitting
ZORA	Zero order regular approximation
ZPVE	Zero point vibrational energy
Chemistry and biochmistry:	
2-MTHF	2-Methyltetrahydrofuran
$AlPO_4$	Aluminum orthophosphate
ArO	Phenoxide
a-Si:H	Hydrogenated amorphous silicon

(continued)

Table G6 (continued)

Abbreviation	Name or description
BQ	1,4-Benzoquinone
BSS	Benzylsuccinate synthase
CU	Coupling unit
CuHis	Copper(II)-histidine
Cyt	Cytochrome
DCMU	3-(3,4-Dichlorophenyl)-1,1-dimethylurea
DMBQ	2,3-Dimethyl-1,4-benzoquinone
DMC	2,3-Dimethylenecyclohexane-1,4-diyl
DME	Dimethylether
DMEQ	2,3-Dimethyl-5-ethyl-1,4-benzoquinone
DMNQ	2,3-Dimethyl-1,4-naphthoquinone
DPNO	Diphenylnitroxide
DQ	Duroquinone: 2,3,5,6-tetramethyl-1,4-benzoquinone
DTBN	di-tert-Butyl nitroxide
Et_3N	Triethylamine
FA	Ferredoxin A
FB	Ferredoxin B
Freon-11	Fluorotrichloromethane (CCl_3F)
Freon-113	1,1,2-Trifluoro-1,2,2-trichloroethane (CCl_2FCClF_2)
Freon-114B2	1,2-Dibromotetrafluoroethane (CF_2BrCF_2Br)
GO	Galactose oxidase
GT	Gauche-trans
HAS	Human serum albumin
HCA II	Human carbonic anhydrase II
IN	Iminonitroxide
MES	2-(n-Morphorino)ethansulfonic acid
MTBE	Methyl tert-butyl ether
NADP	Nicotinamide adenine nucleotide phosphate
NAG	n-Acetyl-glycine radical
NN	Nitronyl nitroxide
NO	tert.-Butyl-nitroxide
NQ	1,4-Naphthoquinone
OEC	Oxygen-evolving complex
P680	Pigment 680 nm
P700	Pigment 700 nm
PE	Polyethylene
PFL	Pyruvate formate lyase
PQ	Plastoquinone
Pr_3N	Tripropylamine
PS	Photosynthetic reaction center
Q	Quinone
Q_K	Phylloquinone
QOX	Quinol oxidase
Rg	Rare gases
RNR	Ribonucleotide reductase
RO•	Alkoxy radicals

(continued)

Table G6 (continued)

Abbreviation	Name or description
RO_2•	Organic peroxyl radical
Rps	Rhodpseudomonas
S_H2	Bimoleclar homolytic substitution
Tempone	4-Oxo-2,2,6,6-tetramethylpiperidine-N-oxyl
TME	Tetramethyleneethane
TMM	Trimethylenemethane
TMQ	2,3,5-Trimethyl-1,4-benzoquinone
TMS	Tetramethylsilane
TPA	Triphenylamine
TPM	Triphenylmethyl
Tris	Tris(hydroxylmethyl)aminomeethane
Trp	Tryptophan
USQ	Ubisemiquinone
VCP	Vinyl cyclopropane
V-O	Vacancy-oxygen (complex)
VOCs	Volatile organic compounds
VP	Versatile peroxidase
VZ	Verdazyl
WOC	Water oxidizing complex
ZSM	Zeolite socony mobil
Others:	
CNOT	Controlled-not
CORBA	Common object request broker architecture
ETE	Extended time excitation
EXAFS	Extended X-ray absorption fine structure
FCC (fcc)	Face centered cubic
FFT	Fast Fourier transform
FTIR	Fourier transform infrared
HCP, hcp	Hexagonal closed-packed
IAEA	International Atomic Energy Agency
IDAS	International Dose Assurance Service
IP	Ionization potential
LET	Linear energy transfer
MBE	Molecular beam epitaxy
NIST	National Institute for Standards and Technology
NPL	National Physical Laboratory
NSERC	Natural Sciences and Engineering Research Council of Canada
PL	Photo-luminescence
PPTV (pptv)	Parts-per-trillion-by-volume
QC	Quantum computing
QIP	Quantum information processing
SDC	Super dense coding
SQUID	Superconducting quantum interference device
SS/ES	Solid state electron spectroscopy
UV/VIS	Ultraviolet ultraviolet/visible (absorption spectroscopy)
XANES:	X-ray absorption near edge structure

Table G7 Magnetic Properties of Stable Isotopes[a, b, c]

Isotope	Atomic number (Z)	Natural abundance (%)	Nuclear spin (I)	Nuclear g-factor (g_N)
^{1}H	1	99.985	0.5	5.58569
^{2}H	1	0.0148	1	0.85744
^{3}He	2	0.00014	0.5	−4.25525
^{6}Li	3	7.5	1	0.82205
^{7}Li	3	92.5	1.5	2.17096
^{9}Be	4	100	1.5	−0.785
^{10}B	5	19.8	3	0.60022
^{11}B	5	80.2	1.5	1.79242
^{13}C	6	1.11	0.5	1.40482
^{14}N	7	99.63	1	0.40376
^{15}N	7	0.366	0.5	−0.56638
^{17}O	8	0.038	2.5	−0.75752
^{19}F	9	100	0.5	5.25773
^{21}Ne	10	0.27	1.5	−0.4412
^{23}Na	11	100	1.5	1.47839
^{25}Mg	12	10	2.5	−0.34218
^{27}Al	13	100	2.5	1.4566
^{29}Si	14	4.67	0.5	−1.1106
^{31}P	15	100	0.5	2.2632
^{33}S	16	0.75	1.5	0.42911
^{35}Cl	17	75.77	1.5	0.54792
^{37}Cl	17	24.23	1.5	0.45608
^{39}K	19	93.26	1.5	0.26099
^{40}K	19	0.0117	4	−0.32453
^{41}K	19	6.73	1.5	0.14325
^{43}Ca	20	0.135	3.5	−0.37641
^{45}Sc	21	100	3.5	1.35906
^{47}Ti	22	7.4	2.5	−0.31539
^{49}Ti	22	5.4	3.5	−0.31548
^{50}V	23	0.25	6	0.55659
^{51}V	23	99.75	3.5	1.46836
^{53}Cr	24	9.5	1.5	−0.3147
^{55}Mn	25	100	2.5	1.3819
^{57}Fe	26	2.15	0.5	0.1806
^{59}Co	27	100	3.5	1.318
^{61}Ni	28	1.13	1.5	−0.50001
^{63}Cu	29	69.2	1.5	1.484
^{65}Cu	29	30.8	1.5	1.588
^{67}Zn	30	4.1	2.5	0.35031
^{69}Ga	31	60.1	1.5	1.34439
^{71}Ga	31	39.9	1.5	1.70818
^{73}Ge	32	7.8	4.5	−0.19544
^{75}As	33	100	1.5	0.95965
^{77}Se	34	7.6	0.5	1.0693
^{79}Br	35	50.69	1.5	1.40427

(continued)

Table G7 (continued)

Isotope	Atomic number (Z)	Natural abundance (%)	Nuclear spin (I)	Nuclear g-factor (g_N)
^{81}Br	35	49.31	1.5	1.51371
^{83}Kr	36	11.5	4.5	−0.2157
^{85}Rb	37	72.17	2.5	0.54125
^{87}Rb	37	27.83	1.5	1.83427
^{87}Sr	38	7	4.5	−0.24291
^{89}Y	39	100	0.5	−0.27484
^{91}Zr	40	11.2	2.5	−0.52145
^{93}Nb	41	100	4.5	1.3712
^{95}Mo	42	15.9	2.5	−0.3656
^{97}Mo	42	9.6	2.5	−0.3734
^{99}Ru	44	12.7	2.5	−0.249
^{101}Ru	44	17	2.5	−0.279
^{103}Rh	46	100	0.5	−0.1768
^{105}Pd	46	22.2	2.5	−0.256
^{107}Ag	47	51.83	0.5	−0.22725
^{109}Ag	47	48.17	0.5	−0.26174
^{111}Cd	48	12.8	0.5	−1.19043
^{113}Cd	48	12.2	0.5	−1.2454
^{113}In	49	4.3	4.5	1.22864
^{115}In	49	95.7	4.5	1.23129
^{115}Sn	50	0.38	0.5	−1.8377
^{117}Sn	50	7.75	0.5	−2.00208
^{119}Sn	50	8.6	0.5	−2.09456
^{121}Sb	51	57.3	2.5	1.3455
^{123}Sb	51	42.7	3.5	0.72876
^{123}Te	52	0.89	0.5	−1.4736
^{125}Te	52	7	0.5	−1.7766
^{127}I	53	100	2.5	1.1253
^{129}Xe	54	26.4	0.5	−1.55595
^{131}Xe	54	21.2	1.5	0.46124
^{133}Cs	55	100	3.5	0.73785
^{135}Ba	56	6.59	1.5	0.55884
^{137}Ba	56	11.2	1.5	0.62515
^{138}La	57	0.089	5	0.74278
^{139}La	57	99.911	3.5	0.7952
^{141}Pr	59	100	2.5	1.6
^{143}Nd	60	12.2	3.5	−0.3076
^{145}Nd	60	8.3	3.5	−0.19
^{147}Sm	62	15.1	3.5	−0.2322
^{149}Sm	62	13.9	3.5	0.1915
^{151}Eu	63	47.9	2.5	1.389
^{153}Eu	63	52.1	2.5	0.6134
^{155}Gd	64	14.8	1.5	−0.1723
^{157}Gd	64	15.7	1.5	−0.2253
^{159}Tb	65	100	1.5	1.342

(continued)

Table G7 (continued)

Isotope	Atomic number (Z)	Natural abundance (%)	Nuclear spin (I)	Nuclear g-factor (g_N)
^{161}Dy	66	19	2.5	−0.189
^{163}Dy	66	24.9	2.5	0.266
^{165}Ho	67	100	3.5	1.192
^{167}Er	68	22.9	3.5	−0.1618
^{169}Tm	69	100	0.5	−0.466
^{171}Yb	70	14.4	0.5	0.9885
^{173}Yb	70	16.2	2.5	−0.27195
^{175}Lu	71	97.39	3.5	0.63943
^{176}Lu	71	2.61	7	0.452
^{177}Hf	72	18.6	3.5	0.2267
^{179}Hf	72	13.7	4.5	−0.1424
^{181}Ta	73	99.9877	3.5	0.67729
^{183}W	74	14.3	0.5	0.23557
^{185}Re	75	37.4	2.5	1.2748
^{187}Re	75	62.6	2.5	1.2878
^{187}Os	76	1.6	0.5	0.1311
^{189}Os	76	16.1	1.5	0.488
^{191}Ir	77	37.3	1.5	0.097
^{193}Ir	78	62.7	1.5	0.107
^{195}Pt	78	33.8	0.5	1.219
^{197}Au	79	100	1.5	0.09797
^{199}Hg	80	16.8	0.5	1.01177
^{201}Hg	80	13.2	1.5	−0.37348
^{203}Tl	81	29.5	0.5	3.24451
^{205}Tl	81	70.5	0.5	3.2754
^{207}Pb	82	22.1	0.5	1.1748
^{209}Bi	83	100	4.5	0.938
^{235}U	92	0.72	3.5	−0.11

[a]Raghavan P, At Data Nucl Data Tables 42:189 (1989)

[b]http://ie.lbl.gov/toipdf/mometbl.pdf

[c]Values for the isotropic and anisotropic hyperfine couplings of the isotopes are reported in Weil JA, Bolton JR, Electron paramagnetic resonance: elementary theory and practical applications, 2nd edn. Wiley (2007)

Index

A. Lund and M. Shiotani (eds.), *EPR of Free Radicals in Solids I*, Progress in Theoretical Chemistry and Physics 25, DOI 10.1007/978-94-007-4887-3,